Investigation of fundamental mechanisms of CO2 plasmas

Ana-Sofia Morillo-Candas

▶ **To cite this version:**

Ana-Sofia Morillo-Candas. Investigation of fundamental mechanisms of CO2 plasmas. Plasma Physics [physics.plasm-ph]. Université Paris Saclay (COmUE), 2019. English. NNT : 2019SACLX091 . tel-03014566

HAL Id: tel-03014566

https://polytechnique.hal.science/tel-03014566

Submitted on 2 Jan 2022

HAL is a multi-disciplinary open access archive for the deposit and dissemination of scientific research documents, whether they are published or not. The documents may come from teaching and research institutions in France or abroad, or from public or private research centers.

L'archive ouverte pluridisciplinaire **HAL**, est destinée au dépôt et à la diffusion de documents scientifiques de niveau recherche, publiés ou non, émanant des établissements d'enseignement et de recherche français ou étrangers, des laboratoires publics ou privés.

Thèse de doctorat

NNT: 2019SACLX091

Investigation of fundamental mechanisms of CO_2 plasmas

Thèse de doctorat de l'Université Paris-Saclay préparée à l'École Polytechnique

École doctorale n° 572: Ondes et matières (EDOM)
Spécialité de doctorat: Physique des Plasmas

LPP (LPP UMR 7648 Laboratoire de Physique des Plasmas)

Thèse présentée et soutenue à Palaiseau, le 4 Décembre 2019, par

Ana Sofía Morillo Candás

Composition du Jury

Dr. Erik Johnson Dir. de Recherche CNRS, École Polytechnique, LPICM, France	Président
Dr. Gilles Cartry Professeur, Aix-Marseille Université, France	Rapporteur & Examinateur
Dr. Timo Gans Professeur, York University, United Kingdom	Rapporteur & Examinateur
Dr. Giorgio DiLecce Senior Researcher CNR, Trento University, Italy	Examinateur
Dr. Richard Engeln Professeur associé, Eindhoven University, The Netherlands	Examinateur
Dr. Andrew Gibson Professeur adjoint, Bochum University, Germany	Examinateur
Dr. Olivier Guaitella Ing. de Recherche, École Polytechnique, LPP, France	Directeur de thèse
Dr. Vasco Guerra Professeur, Instituto Superior Tecnico, Portugal	Co-Directeur de thèse

Investigation of fundamental mechanisms of CO_2 plasmas

Étude des mécanismes fondamentaux des plasmas de CO_2

Ana Sofía Morillo Candás

Supervisor / Directeur de thése: Olivier Guaitella

Co-supervisor / Co-directeur de thése: Vasco Guerra

Thesis presented for the degree of
Doctor of Philosophy (Physics)

Thèse présentée pour le diplôme de Docteur en
Philosophie (Physique)

Laboratoire de Physique des Plasmas (LPP)

Ecole Polytechnique-Université Paris-Saclay

This work was funded by LabEx Plas@par receiving financial aid from the French National Research Agency (ANR) under project number ANR-11-IDEX-0004-0 and project ANR-JCJC SYCAMORE ANR-16-CE06-0005-01.

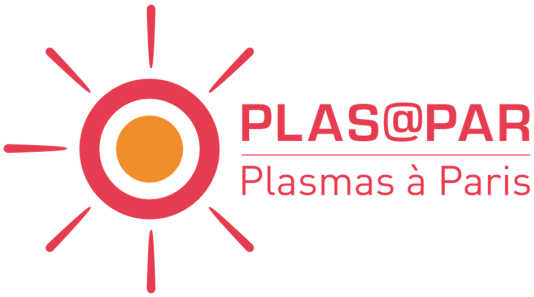

Resumé

Les plasmas froids constituent l'une des voies les plus prometteuses pour recycler efficacement le CO_2 en carburants de synthèse ou en molécules de base pour la chimie organique "verte". Pour obtenir des rendements énergétiques satisfaisants, il est nécessaire de bien contrôler les transferts d'énergie vibrationnelle dans la molécule de CO_2 considérés bénéfiques pour la dissociation, mais aussi l'énergie transférée aux états électroniquement excités ainsi que les processus de recombinaison de O avec CO. Toutefois, en dépit d'une littérature conséquente sur les lasers CO_2 et les plasmas de rentrée atmosphérique, de nombreux processus essentiels à la description des plasmas de CO_2 sont encore très mal compris. Cette thèse a donc pour objectif de réaliser des mesures dans des conditions suffisamment bien contrôlées pour identifier et étudier certains de ces mécanismes.

Deux types de sources de plasma, une décharge luminescente DC et une décharge radiofréquence (RF) ont été étudiées à basse pression (27-1000 Pa) ce qui ralentit les temps caractéristiques des différents processus. Ces sources plasmas ont été étudiées à l'aide de techniques optiques de pointe complémentaires *in situ* et résolues en temps afin d'obtenir dans un même système, tous les paramètres pertinents pour une description complète du plasma. Ainsi les densités et températures vibrationelles de CO_2 et CO ont été mesurées par spectroscopie d'absorption infrarouge (FTIR), la densité et les fréquences de perte des atomes d'oxygène par TALIF haute résolution, actinométrie et CRDS, alors que des mesures d'échanges isotopiques ont donné des informations notamment sur le rôle de $O(^1D)$. La plupart de ces techniques permettent également de déterminer la température du gaz illustrant simultanément la précision et la cohérence des mesures obtenues par différentes techniques.

Les données expérimentales ont permis d'obtenir de nombreux résultats parmi lesquels l'identification de la meilleure section efficace de dissociation du CO_2 par impact électronique, ou la quantification de la désexcitation vibrationelle du CO_2 par les atomes d'oxygène. Les principaux mécanismes d'oxydation de CO ont été identifiés et discutés, révélant un rôle clé de l'état métastable $CO(a^3\Pi_r)$. Les données obtenues ont également permis la validation de modèles cinétiques développés à l'IST Lisbonne. En particulier les taux de réaction de processus de transfert d'énergie vibration-vibration ou vibration-translation ont pu être validés pour les niveaux vibrationels de CO_2 de faible énergie.

Un aspect important du travail a également porté sur l'influence des surfaces sur le plasma. Les processus de perte d'atomes de O dominés par la recombinaison en surface, se sont avérés dépendre de la température des atomes près de la surface. Il a aussi été montré qu'un plasma de CO_2 peut passiver la surface de SiO_2 diminuant la probabilité de recombinaison des atomes d'oxygène aux

parois, et la rendant identique sous exposition au plasma et en post-décharge contrairement a ce qui est observé en plasma de O_2. Une comparaison préliminaire avec un modèle de surface donne un bon éclairage sur les mécanismes de surface impliqués. En utilisant des fibres de SiO_2 de grandes surfaces spécifiques, la formation de CO_2 en surface a été mise en évidence ce qui limite l'efficacité de dissociation. Au contraire des surfaces à base de carbone ont permis une augmentation importante de la conversion du CO_2 en piégeant les atomes d'oxygène. Ceci démontre le rôle essentiel que des surfaces catalytiques pourraient jouer dans l'efficacité de conversion du CO_2 et l'importance de contrôler la réactivité des atomes d'oxygène.

L'ensemble de ces résultats offre une vision beaucoup plus détaillée de la cinétique des plasmas de CO_2. Il s'agit donc d'un travail utile non seulement pour développer de nouveaux procédés efficaces de conversion du CO_2 avec ou sans catalyseurs, mais également dans des domaines tels que les traitements de surfaces utilisant des plasmas contenant du CO_2 ou les problèmes d'entrée atmosphériques pour Mars ou Vénus. Plus généralement, la compréhension des plasmas de CO_2 détaillée dans cette thèse, représente un cas modèle pour appréhender la cinétique des plasmas en gaz moléculaire tri-atomique dans lesquels les échanges entre état excités et les produits de réactions sont encore plus riches et complexes que pour des gaz rares, ou moléculaires di-atomiques.

Abstract

The use of non thermal plasmas is one of the most promising paths to efficiently recycle CO_2 into more complex organic molecules, such as energy-dense hydrocarbon fuels, and it is compatible with the use of intermittent renewable energy sources. To obtain satisfactory energy yields, it is necessary to properly control the energy transfer processes, including the vibrational energy of the CO_2, believed to be beneficial for the CO_2 conversion, or the energy stored in electronically excited species. Recombination processes producing CO_2 from the dissociation products (the so-called back reaction) must also be prevented. However, despite the extensive literature in the fields of CO_2 lasers, atmospheric entry plasmas or CO_2 conversion, many of the basic mechanisms essential for the description of CO_2 plasmas are still very poorly understood. The objective of this thesis is therefore to perform experiments under sufficiently well controlled conditions to identify and study some of these fundamental mechanisms.

Two types of plasma sources, a DC glow discharge and a radio frequency (RF) discharge were studied at low pressures (27-1000 Pa) to slow down characteristic times of various processes. Advanced optical diagnostic techniques were used *in situ* and time-resolved to obtain all the relevant parameters for a complete description of the plasma. The densities and vibrational temperatures of CO_2 and CO were measured by infra-red absorption spectroscopy (FTIR), giving also insight in back reaction mechanisms. The density and loss frequencies of oxygen atoms were obtained with High Resolution Two photon Absorption Laser Induced Fluorescence (HR-TALIF), actinometry and Cavity Ring Down Spectroscopy (CRDS), while isotopic exchange measurements provided information on the role of $O(^1D)$. Most of these techniques were also used to determine the gas temperature, showing simultaneously the consistency and accuracy of the different techniques.

The experimental results made possible, for instance, the identification of the most accurate cross section for CO_2 dissociation by electron impact, or the quantification of the vibratory de-excitation of CO_2 by oxygen atoms. The main back reactions mechanisms were identified and discussed revealing a key role of the metastable state $CO(a^3\Pi_r)$. The obtained data were also used to validate a 0D kinetic model developed at IST Lisbon, which allowed the validation of the rates for vibration-vibration or vibration-translation energy transfer processes for the low vibrational levels of CO_2.

Another important part of the work focused on the role of the surfaces on the CO_2 plasma kinetics. The O atoms loss processes were found to be dominated by surface recombination, dependent on the temperature of the O atoms near the surface, similarly to a pure O_2 plasma. However, it

was found that CO_2 plasma can passivate SiO_2 surfaces, reducing the recombination probability of oxygen atoms at the walls, and making it identical under plasma exposure and in post-discharge, unlike what is observed in O_2 plasma. A preliminary comparison with a surface model provided a valuable insight into the surface mechanisms involved. Large specific SiO_2 surfaces were found to induce CO_2 formation in the surfaces under high O atom flux regimes, limiting the dissociation efficiency, whereas the use of carbon-based surfaces showed an enormous potential to re-use the oxygen atoms to enhance the final CO_2 conversion, demonstrating the key role of the surfaces in the efficiency of the CO_2 conversion and the importance of a proper handling of the oxygen atoms. These results are therefore very valuable to understand which materials would be relevant to be used as catalysts to improve the CO_2 conversion efficiency by plasma.

The thesis provides a detailed view on the fundamental mechanisms controlling the kinetics of CO_2 plasmas. The results presented are therefore useful not only for developing more efficient CO_2 conversion processes, with or without catalysts, but they are also relevant in fields such as surface treatment and surface functionalization using O_2/CO_2-containing plasmas or atmospheric entry studies for Mars or Venus. More generally, the study of CO_2 plasmas detailed in this thesis, represents a model case to approach the study of the kinetics of tri-atomic molecular gas plasmas, in which the exchanges between ground and excited states of the initial gas and the dissociation products are richer and more complex than for plasmas of rare gases or di-atomic molecular gases.

List of publications and oral presentations

In the scope of this PhD thesis, several articles have been published in international peer-reviewed journals. The obtained results have also been presented in international conferences, in the format of oral or poster presentations. All research papers and the most relevant oral and poster presentations are listed below. More articles are submitted or in preparations to disseminate the contents of this thesis work in the near future.

Papers

Papers in peer-reviewed journals

- Morillo-Candas, A.S., Guerra, V. and Guaitella, O. (2020) "Time evolution of the dissociation fraction in RF CO_2 plasmas: impact and nature of back reaction mechanisms" Submitted to The Journal of Physical Chemistry.

- Morillo-Candas, A.S., Silva, T., Klarenaar, B.L.M., Grofulović, M., Guerra, V. and Guaitella, O. (2020) "Electron impact dissociation cross section of CO_2" Plasma Sources Science and Technology 29 01LT01.

- Terraz, L., Silva, T., Morillo-Candas, A.S., Guaitella, O., Tejero-del-Caz, A., Alves, L., and Guerra, V. "Influence of N_2 on the CO_2 vibrational distribution function and dissociation yield in non-equilibrium plasmas" (2019) Journal of Physics D: Applied Physics 53(09) 094002

- Morillo-Candas, A.S., Drag, C., Booth, J.-P., Dias, T.C., Guerra, V. and Guaitella, O. (2019) "Oxygen atom kinetics in CO_2 plasmas ignited in a DC glow discharge" Plasma Sources Science and Technology. 28(7), 075010.

- Klarenaar, B.L.M., Morillo-Candas, A.S., Grofulović, M., Van de Sanden, R., Engeln, R., and Guaitella, O. (2019) "Excitation and relaxation of the asymmetric stretch mode of CO_2 in a pulsed glow discharge". Plasma Sources Science and Technology. 28(3), 035011.

- Grofulović, M., Silva, T., Klarenaar, B.L.M., Morillo-Candas, A.S., Guaitella, O., Engeln, R., Pintassilgo, C.D. and Guerra, V. (2018) "Kinetic study of CO_2 plasmas under non-equilibrium conditions. II. Input of vibrational energy." Plasma Sources Science and Technology 27 (11), 115009.

- Klarenaar, B.L.M., Grofulović, M., Morillo-Candas, A.S., van den Bekerom, D.C.M., Damen, M.A., Van De Sanden, M.C.M., and Engeln, R. (2018). "A rotational Raman study under non-thermal conditions in a pulsed CO_2 glow discharge". Plasma Sources Science and Technology, 27(4), 045009

- Silva, T., Grofulović, M., Klarenaar, B.L.M., Morillo-Candas, A.S., Guaitella, O., Engeln, R., and Guerra, V. (2018). Kinetic study of low-temperature CO_2 plasmas under non-equilibrium conditions. I. Relaxation of vibrational energy. Plasma Sources Science and Technology, 27(1), 015019

- Klarenaar, B.L.M., Engeln, R., Van Den Bekerom, D.C.M., Van de Sanden, M.C.M., Morillo-Candas, A.S., and Guaitella, O. (2017). Time evolution of vibrational temperatures in a CO_2 glow discharge measured with infrared absorption spectroscopy. Plasma Sources Science and Technology 26(11), 115008.

Conference papers

- Ogloblina, P., Guerra, V., Morillo-Candas, A.S., Guaitella, O. (2019) "Plasma reforming for oxygen production on Mars" 8th European Conference for aeronautics and aerospace sciences (EUCASS)

- Engeln, R., Klarenaar, B. L. M., Morillo-Candas, A. S., Grofulović, M., van de Sanden, M. C. M., and Guaitella, O. (2018). "Diagnostics to study the vibrational excitation kinetics of CO_2 for renewable energy storage". In Optics and Photonics for Energy and the Environment (pp. EM2A-6). Optical Society of America.

Oral contributions

Oral contributions in conferences and workshops

- Morillo-Candas, A.S., Klarenaar, B.L.M., Silva, T., Engeln, R., Guerra, V., Guaitella, O. "Time-evolution of the CO_2 conversion studied by in situ FTIR absorption and isotopic exchange" 3-min poster pitch presentation awarded with the Prize to the Best 3-min poster pitch in the 24th International Symposium on Plasma Chemistry (ISPC) Naples Italy June 9-14th 2018. [Poster pitch presentation]

- Morillo-Candas, A.S., Gonçalves, C. Klarenaar, B.L.M., Booth, J.P., Drag, C., Guerra, V., Guaitella, O. "Effect of the O atoms in the vibrational kinetics of CO_2 plasmas" Workshop PREMiERE - CO_2 Plasmas: a fRIendly MEdium for Renewable Energy, Ericeira, Portugal, 23-24 November 2018. [Contributed talk]

- Morillo-Candas, A.S., Gonçalves, C. Klarenaar, B.L.M., Booth, J.P., Drag, C., Guerra, V., Guaitella, O. "Effect of high surface-area on CO_2 plasma kinetics" 24th Europhysics Conference on Atomic and Molecular Physics of Ionized Gases (ESCAMPIG), Glasgow, Scotland, 17-21 July, 2018. [Contributed talk]

- Morillo-Candas, A.S., Klarenaar, B.L.M., Engeln, R., Chatterjee, A., Booth, J-P., Drag, C., Silva T., Guerra, V., Guaitella, O. "O atom kinetics in CO_2 glow discharges", XXXIII

International Conference on Phenomena in Ionized Gases (ICPIG), Estoril, Portugal, 9-14 July 2017. [Contributed talk]

Other oral presentations

- Morillo-Candas, A.S., Guerra, V., Guaitella, O. "Effect of the O atoms in CO_2 plasmas", PhD days of LPP (Laboratoire de Physique des Plasmas). Palaiseau, France, March 2019.
- Morillo-Candas, A.S., Klarenaar, B.L.M., Engeln, R., Chatterjee, A., Booth, J-P., Drag, C., Silva, T., Guerra, V. and Guaitella O. "O atom kinetics in CO_2 plasmas", EDOM (Ecole Doctorale Ondes et Matiere) Scientific days, Paris, France, May 2018.
- Morillo-Candas, A.S., Guerra, V., Guaitella, O. "Diagnostics for Characterization of O2 and CO_2 plasma", PhD days of LPP (Laboratoire de Physique des Plasmas). Palaiseau, France, February 2018.
- Morillo-Candas, A.S., Klarenaar, B.L.M., Engeln, R., Chatterjee, A., Booth, J-P, Silva, T., Guerra, V., Drag, C., and Guaitella, O. "O atom kinetics in CO_2 glow discharges". Plas@Par Young Researcher's day, Paris, France, May 2017.
- Morillo-Candas, A.S., Guerra, V., Guaitella, O. "CO_2 plasma kinetics", PhD days of LPP (Laboratoire de Physique des Plasmas). Palaiseau, France, February 2017.

Posters

- Morillo-Candas, A.S., Klarenaar, B.L.M., Silva, T., Engeln, R., Guerra, V., Guaitella, O. "Time-evolution of the CO_2 conversion studied by in situ FTIR absorption and isotopic exchange" 24th International Symposium on Plasma Chemistry (ISPC) Naples Italy June 9-14th 2018.
- Morillo-Candas, A.S., Klarenaar, B.L.M., Grofulović, M. Drag, C., Booth, J-P., Guerra, V. and Guaitella O. "Comparison of gas temperature measurements with Raman, FTIR and HR-TALIF" 24th Europhysics Conference on Atomic and Molecular Physics of Ionized Gases (ESCAMPIG), Glasgow, Scotland, 17-21 July, 2018.

Acknowledgements

At the beginning of October 2016, I started my PhD in the Laboratoire de Physique des Plasmas (LPP, École Polytechnique) and an awesome period of time from professional and personal point of view, and for this in the first place I want to thank my PhD supervisor, Olivier Guaitella. Thank you very much on the one hand for all the great ideas, the cool experiments, the wish to do a good job, the constant help and support, the commitment with your students, the respect and the way you encourage us to investigate our own ideas. On the other hand, thank you very much for the good mood, the good atmosphere you create in the lab, all the fun, the drinks, the basketball,... thanks for everything! And of course thanks for having hired me.

This last comment is also applicable to Vasco Guerra, co-supervisor of this PhD. Thanks for the always interesting ideas and reflections, dedication and enormous patience to answer all the questions I asked. I truly appreciate all the discussions we had, not only about science and I still hope that I can put in practice many of the things I learned and I admire from you. Olivier and Vasco created a very rich environment where I could move and learn to look at things from different points of view. I could discover the world of simulations and understand what are their needs, and in that way I could improve myself as experimentalist. It is not easy to end up in the centre of such a great collaboration with their combined expertise.

Apart from my official supervisors, I want to thank particularly Cyril Drag and Bart Klarenaar. Both have been very important for me during these years. I spent a lot of time with Cyril in the lab, where we shared a lot of fun and where I discovered many things. He also inspired me to try to learn more about atomic and molecular physics. Cyril somehow represents the dreamed life of a experimentalist (before becoming boss of the team): spending time in the lab, playing with fancy diagnostics, trying cool experiments and exploring new ideas. I wish I could be like that in the future. I also learned a lot with Bart about how to face problems, deal with research and how to do a good job. He has also been very supportive and helpful during all my thesis. Both have been real mentors in my research life.

I also want to thank Jean-Paul Booth for his help and advise. His door is always open and he never refuses to answer kindly, quickly and precisely any question you could have. Thanks for letting me join many of the very interesting measurement campaigns you planned in the lab and in Synchrotron and for all the equipment I borrowed during my stay in the lab! Thanks to Dmitry Lopaev and Sergey Zyrianov from MSU for their kindness and patience. I learned a lot from them, how to discuss, argue, challenge things and how to work hard. My first experiment campaign in

LPP was with them, and had a great and good influence on the rest of my PhD. I also want to mention Enric García-Caurel, Garret Curley and Nelson de Oliveira, we did not have too many opportunities to work together but every time we meet you were extremely kind and nice with me, thanks.

During these years I had the opportunity to visit the lab of Richard Engeln during 1 month and to visit Técnico (IST) in Lisbon for about 2 months and in multiple trips. It was a great time and therefore I want to thank Richard, Bart and Mark Damen, for the help, the honesty and directness, and also the good mood. It was really enlightening. In Lisbon I want to thank all the people there that kindly helped me including Vasco, Marija Grofulović, Tiago Silva, Antonio Tejero(-del-Caz), Luis Alves, Loann Terraz and Joao Vargas. Not only for everything I learned but for all the fun and the warm welcome I always had. It was a real pleasure to go there.

If there is something important in research is the work of the technicians. So I want to warmly thank all the technicians who helped me during my PhD and I want to mention specially Jean Michel Wierniezky, the glass blower of École Polytechnique. Absolutely all the experiments I did these years worked thanks to the reactors of Jean-Michel. The practical life in the lab improved a lot after Pascal Pariset arrived. He has been always helpful and it was nice to find him in the corridors and make jokes with him. Another special mention is deserved by Philippe Auvray, who had to deal with me in a few panic situations including CO alarms (uhm) and an explosion in the lab (uhm again, my fault this time). He always stayed calm, which is good if you are the safety responsible of the lab! I also want to thank Nicolas Marsac for saving me when I burned my hard disk (twice) or when the computer crashed or did not started (many times), also to Stephane and Catherine and other members of the lab that have been kind and helpful when needed.

During my PhD I had the opportunity to work with many nice master and PhD students: Henrique, Carolina A., Ana Filipa, Tiago D., Edmond, Carolina G., Joost, Polina and Loann. Thanks for the good times and for everything I learned from you. Sometimes trying to teach or guide others makes you improve more and develop clearer ideas than spending all the time alone working in your own project. I also want to apologize for those times where I was not clear or not patient or when I did not help enough. I want to thank all the friends who made my PhD a great time, one of the best periods of my life, including Marija, Abhyuday, Elmar, Bart, Pedro, Victor and my mentor in life, Ralph. Thanks to the people that makes the lab a better place like Marlous, Thomas, Tat Loon, with his great sense of humour, Audrey, Gautier, Kishor, Victor, Malik, Pierre and Ozgur, Inna, Sergey and Nikita. Thanks to all my office (the PhDarium) mates, who varied during these years but most of the time included Antoine, Thomas, Abhyuday, Marlous and Florian. I was very lucky to be in that office. I want also to thank all the people that participated and made the musical soirées and international cooking night such great evenings like Olivier, Ralph, Cyril, Audrey, Jean-Paul, Antoine, etc. to the secretary of LMS lab, who lend us the piano, all the people that helped to move the piano and Cyril again for the motivation to move the piano. Thanks to the football team of LPP, it was awesome, and specially thanks to Abhyuday who inspired the team, and to Thomas Charoy who has been great continuing with it. I want to mention also those people that I am always happy to meet from time to time in conferences or in the lab and with whom is great to have a beer like Andrew, Zdenek Bonaventura, Petr and the czeck students.

I would like to thank all the members of my jury Erik Johnson, Giorgio diLecce, Richard Engeln and Andrew Gibson, with a special mention to the rapporteurs Gilles Cartry and Timo Gans, and

including again my supervisors, to agree to read my thesis and to come to Paris for the defense. Thank you for being kind with the questions and for the good mood and great atmosphere you created during the defense. Thanks my family for coming, thanks again Bart for the support, and thanks to all the people that helped with the "pot". Thanks also for the nice presents I got and in general thanks to everyone that participated in a day that was one of the happiest days of my life.

I want to thank my friends Barbara and Edu, who warn me about what really means doing a PhD, Alberto, Jose, Sergio, Ismael and also Roberto for his support, especially when I decided to come to France to do the PhD and during the beginning of my time here. Thanks Sarah and Marija for chatting and gossiping and for making me feel better when I was needing it. I want to mention also that I found some nice people in my residence in Cité Universitaire, especially Amadou.

Although I loved the lab, holidays are also important! And I of course want to thank my friends in Asturias, particularly Amor and Jose Manuel, and all the mountain group. The mountains of Asturias are one of the things I missed the most being in Paris, along with all the nice people there, even those family members and friends that were all time asking: but when are you finally going to start working...(*sic*)?

Finally, I want to thank my family, my mother Rita, my aunt Tona and my uncle Eloy, for all the support in the difficult times, for the advises, critics and, sometimes even more important, for all the jokes. I thank them because of their different points of view and opinions about everything, because they make look trivial most of the problems and because we laugh a lot with all the stories and anecdotes of life. Gracias mamá porque siempre crees en mí y me apoyas en todo lo que hago, aunque preferirías que estuviera mas cerca, porque siempre escuchas mis problemas y batallitas y porque nos reímos mucho de ellas. Gracias también a todos los que se precupan por mí y crean esa sutil red the apoyo que no siempre se ve pero siempre está ahí, que conforman las familias Tona, Eloy, Alejando, mi tío Victor, mi tía Mari Carmen, Mari Reyes y Luis, Mari Balbi. Y también a los que ya no están pero que lo hicieron en el pasado, mi padre Manuel, mis abuelos Rita y Eliseo, y mis tíos abuelos Jesús y Balbina. Thanks Iván for the good mood and attitude and for coming to the defense.

I have been really very lucky for this opportunity, for the research I could do and for the people I shared my time with. Very lucky.

Thanks to all of you.

Ana Sofía

Contents

Resumé i
Abstract iii
List of publications and oral presentations v
Acknowledgements ix

1 Introduction and state of the art **1**
1.1 Context and importance of CO_2 plasmas 1
1.2 Basic properties of CO_2 plasmas 3
1.2.1 Main CO_2 dissociation mechanisms 3
1.2.2 The complexity of CO_2 plasmas 5
1.3 Current approaches to study CO_2 plasmas 8
1.3.1 Experimental point of view 8
1.3.2 Modelling point of view 10
1.4 What is unknown? 11
1.5 Approach and objectives of the thesis 16
1.6 Outline of the thesis 18

I Description of the diagnostics and general characterization of the glow discharge **21**

2 Diagnostics for the characterization of CO_2 plasmas **23**
2.1 Introduction 23
2.2 Description of the discharges used 24
2.2.1 Glow discharge reactor 24
2.2.2 RF reactor 25
2.2.3 Gas line 26
2.3 Diagnostics for the determination of the CO and CO_2 densities and their vibrational temperatures 27
2.3.1 Fourier Transform Infra-Red (FTIR) spectroscopy 28
2.3.2 Raman spectroscopy 33
2.4 Diagnostics for the determination of the O atom density 36
2.4.1 Actinometry 36

2.4.2 High Resolution - Two photon Absorption Laser Induced Fluorescence (HR-TALIF) . . . 40
2.4.3 Cavity Ring Down Spectroscopy (CRDS) . . . 47
2.5 Summary . . . 51

3 General characterization of the CO_2 glow discharge and the dissociation products 53
3.1 Introduction . . . 54
3.2 Gas temperature in CO_2 plasmas . . . 54
3.2.1 Accuracy of the gas temperature diagnostics techniques . . . 55
3.2.2 Gas temperature dependence . . . 56
3.2.3 Residence time and diffusion time toward the walls . . . 58
3.2.4 Radial temperature profile and effect of the wall temperature . . . 60
3.3 Electric field (E_{field}), specific energy input (SEI) and electron energy distribution function (EEDF) . . . 62
3.4 CO_2 dissociation fraction . . . 64
3.4.1 Dissociation fraction in continuous CO_2 plasma measured downstream . . . 64
3.4.2 Dissociation fraction in continuous CO_2 plasma measured *in situ* . . . 65
3.4.3 Longitudinal profile measured with Raman scattering . . . 67
3.4.4 Effect of the gas flow and residence time . . . 68
3.4.5 Comparison of FTIR and Raman in continuous plasma . . . 72
3.4.6 CO_2 and CO densities for comparison with oxygen data . . . 73
3.5 O atom densities . . . 74
3.5.1 Validity of the diagnostics . . . 74
3.5.2 Oxygen atom density variation . . . 77
3.5.3 O atom densities as a function of gas flow . . . 78
3.5.4 O atom loss frequency . . . 78
3.6 Discussion . . . 81
3.6.1 CO and O atom densities . . . 81
3.6.2 O atom loss processes . . . 83
3.7 CO and oxygen atom densities in pulsed plasma . . . 87
3.7.1 CO densities . . . 88
3.7.2 O atom densities . . . 90
3.8 Summary and conclusions . . . 91

II Vibrational kinetics in CO_2 plasmas 93

4 CO_2 vibrational kinetics in continuous and pulsed DC glow discharge 95
4.1 Introduction . . . 95
4.2 Experimental details and data treatment . . . 96
4.3 Vibrational temperatures in continuous CO_2 glow discharge . . . 97
4.4 Experimental results in pulsed glow discharge . . . 101
4.4.1 Time evolution of the vibrational temperatures in a repetitive pulsed discharge 101
4.4.2 Effect of the gas composition . . . 102

4.4.3 Effect of fast consecutive pulses . . . 104
4.4.4 Influence of the discharge current and pressure . . . 107
4.5 Discussion . . . 108
4.6 Comparison with a kinetic model . . . 114
4.7 Summary and conclusions . . . 117

5 Effect of the oxygen atoms on the CO_2 vibrational kinetics 119
5.1 Introduction . . . 120
5.2 Experimental details . . . 120
5.2.1 Discharge reactor and diagnostics . . . 120
5.2.2 Surface configurations . . . 121
5.3 O atom density, gas temperature, electric field and dissociation fraction . . . 122
5.3.1 Gas temperature . . . 122
5.3.2 Electric field and dissociation fraction . . . 123
5.3.3 O atom densities . . . 124
5.4 Effect of the oxygen atoms in the vibrational temperatures of CO_2 and CO . . . 126
5.4.1 Temperature of the bending and symmetric vibrational modes, $T_{1,2}$ . . . 126
5.4.2 Temperatures of the asymmetric stretch mode of CO_2, T_3, and of CO, T_{CO} . . . 127
5.4.3 Correlation with the O atom densities . . . 130
5.5 Discussion . . . 132
5.5.1 Quenching of the vibrations of CO_2 by O atoms . . . 132
5.5.2 Quenching of the CO_2 vibrations of at the walls . . . 136
5.5.3 Dissociation fraction . . . 139
5.6 Time resolved evolution of the vibrational temperatures along a plasma pulse . . . 139
5.6.1 Effect on the vibrational temperatures . . . 140
5.6.2 Dissociation fraction along a plasma pulse . . . 144
5.7 Summary and conclusions . . . 147

III Time evolution of the dissociation fraction 149

6 Time evolution of the dissociation fraction in CO_2 RF and glow discharges 151
6.1 Introduction . . . 151
6.2 Description of the experiment and experimental set-up . . . 152
6.2.1 Experimental set-up . . . 152
6.2.2 Protocol for building-up experiments . . . 153
6.2.3 Data treatment . . . 156
6.3 RF discharge results . . . 158
6.3.1 Pure CO_2 plasma . . . 158
6.3.2 Gas mixtures . . . 174
6.4 Building-up in glow discharge . . . 181
6.4.1 Experimental results and comparison of rate coefficients . . . 182
6.4.2 Comparison with a kinetic model . . . 185
6.5 Summary and conclusions . . . 186

7 Investigating the chemistry of CO_2 plasmas by isotopic exchange 189
7.1 Introduction . . . 189
7.2 Experimental set-up . . . 190
7.3 Data treatment . . . 191
7.3.1 Description of the fitting script . . . 191
7.3.2 Example of isotopic measurement . . . 194
7.4 Experimental results: CO_2-CO-O_2 mixtures . . . 196
7.4.1 CO_2-O_2 mixtures with isotopically labelled species . . . 196
7.4.2 CO-O_2 mixtures . . . 201
7.4.3 Comparison of gas mixtures . . . 206
7.5 Discussion . . . 208
7.5.1 Initial time steps: fast growth of isotopically-labelled CO_2 and CO . . . 208
7.5.2 "Turning region": back reaction and effect of the vibrational kinetics . . . 211
7.6 Conclusions and perspectives . . . 214

IV Surface processes in CO_2 plasmas 215

8 Surface processes in CO_2-O_2 plasmas 217
8.1 Introduction . . . 217
8.2 Preliminary comparison between CO_2 and O_2 plasmas . . . 219
8.2.1 O atom densities and loss frequencies in CO_2 and O_2 plasmas . . . 219
8.2.2 O atom loss probabilities in CO_2 and O_2 plasmas . . . 220
8.3 Experimental details and basic parameters in CO_2-O_2 plasmas . . . 224
8.3.1 Experimental details . . . 224
8.3.2 Gas temperature . . . 225
8.3.3 Electric field . . . 226
8.4 O atom densities and loss probabilities in CO_2-O_2 plasmas . . . 226
8.4.1 O atom densities and surface losses under plasma exposure . . . 226
8.4.2 O atom losses in post-discharge . . . 231
8.5 Effect of the wall temperature on the O atom loss processes . . . 234
8.6 Wall reactivity with large SiO_2 effective surfaces . . . 239
8.7 Investigation of surface processes by isotope implantation . . . 243
8.7.1 Oxygen atoms *versus* carbon compounds . . . 244
8.7.2 Effect of the large effective surfaces on isotopic exchange . . . 245
8.8 Preliminary comparison with a surface model . . . 246
8.8.1 Brief description of the model . . . 246
8.8.2 Model results and comparison with experiments . . . 249
8.9 Epilogue: Carbon-based surfaces for enhanced CO_2 dissociation . . . 257
8.10 Conclusions . . . 264

9 Conclusions 267

Bibliography i

Chapter 1

Introduction and state of the art

Contents

1.1 Context and importance of CO_2 plasmas 1
1.2 Basic properties of CO_2 plasmas 3
1.2.1 Main CO_2 dissociation mechanisms 3
1.2.2 The complexity of CO_2 plasmas 5
1.3 Current approaches to study CO_2 plasmas 8
1.3.1 Experimental point of view 8
1.3.2 Modelling point of view 10
1.4 What is unknown? 11
1.5 Approach and objectives of the thesis 16
1.6 Outline of the thesis 18

1.1 Context and importance of CO_2 plasmas

A growing number of applications such as indoor air pollution abatement, assisted combustion and more recently molecule synthesis (NO, NH_3, for instance) require to understand and control the development of Non Thermal Plasmas (NTP) in molecular gases at relatively high pressure. The recycling of CO_2 by plasma for environmental purposes is one of the most important within these applications, which alone justifies a considerable interest in studying CO_2 plasmas. However, the interest in a fundamental study of CO_2 and/or CO_2-containing plasmas is not limited solely to CO_2 recycling. On the one hand, other applications, briefly discussed below, are based on the use of CO_2-containing plasmas; on the other hand, CO_2 molecule is an ideal case study for any molecular gas plasma. The CO_2 molecule has been already studied enough to benefit from a significant amount of spectroscopic data, but, at the same time, it is a tri-atomic molecule that implies a great complexity of mechanisms under plasma conditions. Nevertheless, the main current motivation for studying CO_2 plasmas remains to successfully recycle CO_2 with a minimum energy cost.

The increasing concentration of CO_2 in the atmosphere due to anthropogenic emissions is widely established to be a major cause of global warming *Stocker et al.* [2013]. The associated climate change and its consequences are motivating the development of different strategies to either reduce the emissions of CO_2 or to capture and store it from industrial sources. The use of renewable energy

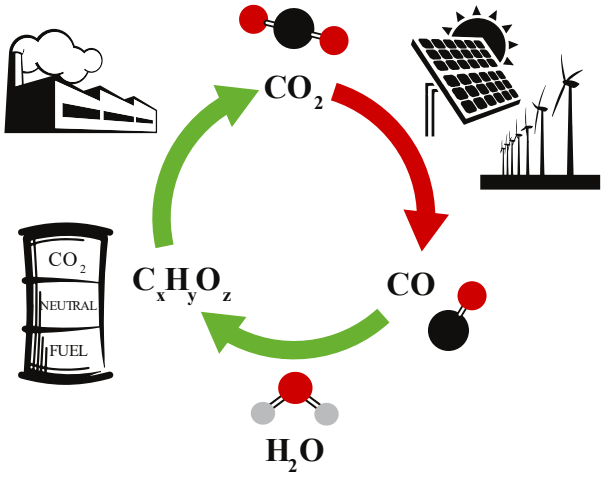

Figure 1.1: Ideal closed carbon cycle. *Picture credits: B. Klarenaar.*

sources can help to reduce CO_2 emissions. However, several problems prevent a more extensive use of these energies such as their intermittency, the optimal production locations, usually far from the consumption points, and the lack of efficient energy storage technologies.

CO_2 recycling is an attractive possibility for energy storage which is also in line with the necessity of finding new sources of fuels and chemicals *Perathoner and Centi* [2014]. Instead of considering CO_2 as a waste, CO_2 emissions could be used as a raw material for the synthesis of more complex organic compounds, such as energy-dense hydrocarbon fuels *Centi and Perathoner* [2009]. An efficient storage of energy in chemical compounds produced from industrial CO_2 would allow creating a closed carbon cycle, schematically represented in figure 1.1 and contributing to mitigate the climate change. It would also help the development of renewable energies, such as solar and wind energies, at a larger scale.

Consequently, CO_2 recycling technologies have been attracting growing interest for the last few years and different technologies have emerged including thermolysis and thermochemical cycles, electrolysis and photo-electrolysis or bio-fixation *Graves et al.* [2011]; *Jones et al.* [2014]; *Halmann* [2018]. Compared to these techniques, the use of Non Thermal Plasmas could have several advantages. NTP are potentially more efficient than thermal dissociation *Adamovich et al.* [2017] and efficiencies close to 90% have been reported *Fridman* [2008]. Another advantage of NTP for CO_2 recycling is the possibility to be integrated into the electrical network. The immediate on/off operation of plasma allows to take advantage of the available energy from intermittent renewable sources *van Rooij et al.* [2017]; *Bogaerts and Neyts* [2018]. The scalability of plasma reactors gives also flexibility to adapt to various CO_2 sources. A detailed comparison between CO_2 plasma conversion and other CO_2 recycling technologies can be found in *Snoeckx and Bogaerts* [2017].

As already mentioned, the study of CO_2 plasmas is also important for other fields. CO and CO_2 molecules are often studied in the context of astrophysical plasmas, for instance in the detection of emission/absorption bands of excited states of these molecules in comet tails *Wyckoff and Theobald* [1989]. An important research field is focused on simulating the entry of space-crafts in the atmospheres of Mars and Venus, where CO_2 is the dominant compound in order to design proper protecting shields *Bykova et al.* [1997]; *Kolesnikov et al.* [2000]; *Herdrich et al.* [2002]; *Marieu et al.* [2007]; *Vacher et al.* [2008]; *Lin et al.* [2018]. A related topic focuses on the *in situ* resource

utilization with the aim of producing oxygen directly from Mars atmosphere, composed of 96% CO_2 at a few hundreds of Pa *Wu et al.* [1996]; *Guerra et al.* [2017]; *Premathilake et al.* [2019].

The use of plasmas for surface treatment processes on carbon-containing substrates such as polymers *Bousquet et al.* [2007], glassy carbon *Pérez-Mendoza et al.* [1999], carbon nano-structures *Babu et al.* [2014]; *Ramos et al.* [2010] or graphene *Gokus et al.* [2009]; *Nourbakhsh et al.* [2010] or polymer deposition at low pressures *Médard et al.* [2002]; *Gancarz et al.* [1999]; *Fahmy and Schönhals* [2016] is also a growing subject. Surface treatment processes can either use CO_2 plasma, or O_2 plasma, forming CO_2 molecules at the surface *Koizumi et al.* [2013].

For all these applications a deep understanding of the fundamental mechanisms involved in CO_2 plasmas is essential to control the induced chemistry.

1.2 Basic properties of CO_2 plasmas

The intense research effort initiated about 10 years ago on CO_2 recycling by plasma is built on the knowledge of CO_2 plasmas acquired in the 1960s and 1970s. Apart from the "warm" planetary entry plasmas, CO_2 low temperature plasmas were first studied for the development of CO_2 lasers *Moore et al.* [1967]; *Witteman* [2013]. These works focussed on the vibrational kinetics of the very first levels of CO_2, while trying to keep its dissociation as low as possible. The study of CO_2 dissociation itself started in the seventies *Capezzuto et al.* [1976]; *Andreev et al.* [1971] motivated by the impossibility to describe the experimental dissociation rates of CO_2 solely by direct electron impact dissociation process. At that time, some experiments showed energy efficiencies for the dissociation process up to 90% in supersonic microwave plasmas *Asisov et al.* [1983]. Nowadays, in spite of the intense research being done by many research groups, these efficiencies have not been reproduced yet, and the maximum values are close to ∼45% *Bongers et al.* [2017], equivalent to the theoretical maximum energy efficiency for the thermal dissociation of the CO_2 molecule.

The basic properties of CO_2 plasma known from the literature are briefly reviewed in this section. Different approaches currently being pursued to investigate CO_2 plasmas will be described in the following section.

1.2.1 Main CO_2 dissociation mechanisms

CO_2 plasma conversion can be obtained by exciting the molecule electronically or vibrationally to make it reactive towards other molecules, or by dissociating it into CO:

$$CO_2 \rightarrow CO + O,\ \Delta H{=}5.5\ \text{eV/mol}$$

This is a strongly endothermic process and thermal decomposition of pure CO_2 starts only at temperatures higher than 2000 K *Gordon et al.* [1984]. In low temperature plasmas the two main dissociation mechanisms are direct electron impact dissociation *Polak and Slovetsky* [1976]; *Hake and Phelps* [1967]; *Itikawa and Mason* [2005] and vibrational up-pumping, also called ladder climbing *Fridman* [2008]. The direct electron impact dissociation has an energy threshold above 7 eV, producing CO or O in an electronically excited state (the production of ground state $CO(X^1\Sigma^+)$ + $O(^3P)$ is spin-forbidden). The lowest energy process leads to the formation of $CO(X^1\Sigma^+)$ and $O(^1D)$, but higher energy processes can produce other excited states such as $O(^1S)$ *LeClair and McConkey* [1994] or $CO(a^3\Pi_r)$ *Cosby and Helm* [1992]; *Itikawa and Mason* [2005], requiring energies above 10

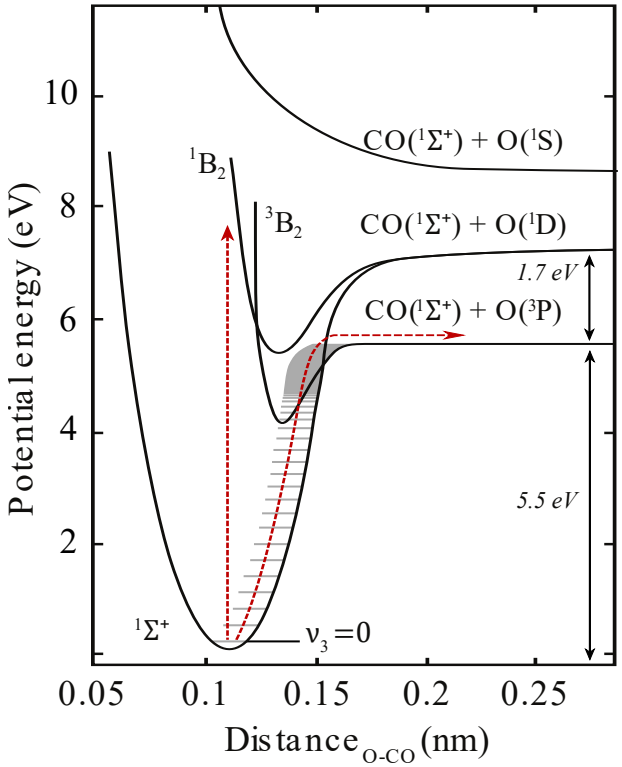

Figure 1.2: Qualitative representation of the potential energy diagram of CO_2 as a function of the CO-O distance. Figure adapted from *Fridman* [2008]; *Klarenaar* [2018].

eV. Note that the electron impact dissociation is also possible from vibrationally excited molecules, which would reduced the energy threshold for this processes but would also lead to the creation of electronically excited states.

The so-called vibrational up-pumping mechanism is an indirect dissociation route where the energy given by low energy electrons $\sim$ 1eV is transferred to the asymmetric stretch vibrational mode of CO_2 *Armenise and Kustova* [2018]. The exchange of vibrational quanta between molecules may lead to highly excited vibrational levels until it reaches a potential crossing of the CO_2 ground state ($CO_2(^1\Sigma^+)$) with the electronically excited $CO_2(^3B_2)$ state at $\sim$5.5 eV. CO molecules and O atoms would then be both produced in ground state *Fridman* [2008], as shown schematically in figure 1.2. It must be noted that this representation is an idealization, since CO_2 is a tri-atomic molecule, therefore described not with potential curves but with potential surfaces *Huang et al.* [2012]. In this representation the electronic excited states are plotted for their equilibrium angles, different than the ground state equilibrium angle *Vargas et al.* [2019].

The vibrational up-pumping of the asymmetric-stretch vibrational mode of CO_2 has been proposed to be the most efficient CO_2 dissociation path *Fridman* [2008]. Most of the discharge energy is carried by low energy electrons, which effectively transfer it to vibrational excitation of CO_2 and other molecules *Rusanov et al.* [1981]. This can be clearly observed in figure 1.3, which presents the fraction of electron energy transferred to different channels as a function of the reduced electric field, including of vibrational excitation, electronic excitation, dissociation and ionization *Grofulović et al.* [2016]. Nevertheless, in many plasma regimes electron impact dissociation is the main path for the CO_2 dissociation, especially in discharges with high reduced electric field, such as DBDs or

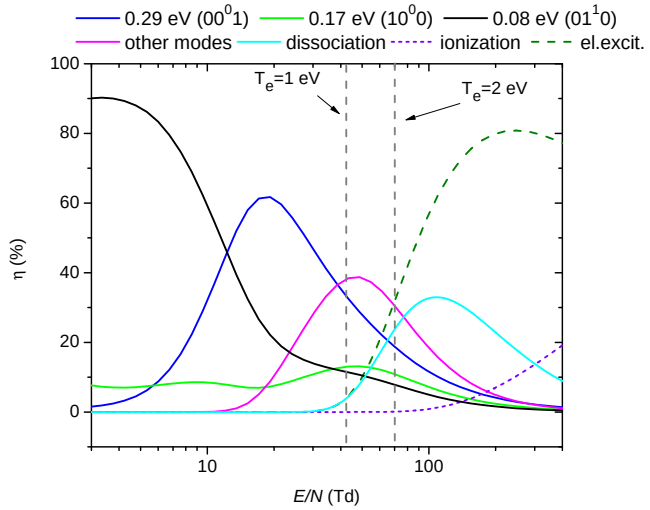

Figure 1.3: Fraction of electron energy transferred to vibrational excitation, electronic excitation, dissociation and ionization as a function of the reduced electric field. Figure extracted from *Grofulović et al.* [2016].

nano-second discharges. However, even in a dissociation regime dominated by electron impact, the vibrational kinetics may have a strong influence on the dissociation rates through their influence on the electron distribution function (EEDF), as well as in post-discharge chemistry *Capitelli et al.* [2017].

Many other species can play a direct or indirect role in the dissociation of CO_2. For instance, in order to achieve the highest energy efficiencies for the CO_2 conversion, the O atoms produced from the primary CO_2 dissociation should react with vibrationally excited CO_2 molecule to produce CO and O_2 *Fridman* [2008]. Electronically excited states can also undergo chemical reactions leading to dissociation *e.g.* $CO(a^3\Pi_r) + CO_2 \rightarrow 2CO + O$, or play a key role on the vibrational and electron kinetics. These species are described in the next section.

1.2.2 The complexity of CO_2 plasmas

CO_2 plasma is a complex mixture of numerous species including neutrals in ground state or excited states (electronically, vibrationally etc.), positive and negative ions, electrons, radicals, short-lifetime intermediates, etc. Some of the main gas phase species are summarized in table 1.1. A basic energy diagram including some of main neutral species is also shown in figure 1.4. The corresponding dissociation and ionization levels are indicated. This simplified diagram, which does not show levels of ions or vibrational levels of electronic states, illustrates the large number of species involved in the kinetics of CO_2 plasmas.

The first column in figure 1.4 shows the CO_2 electronic excited states on the left. The three other sub-columns correspond to vibrational states of the pure vibrational modes. CO_2 is a linear molecule with three vibrational modes represented by the quantum numbers ν_1, ν_2 and ν_3, which correspond respectively to the symmetric stretch, bending, and asymmetric stretch modes. The bending mode is doubly degenerate because of the linear symmetry of the CO_2 molecule. Therefore the contribution of ν_2 to the angular momentum is described using an extra quantum number l_2, which takes values ν_2, $\nu_2 - 2$, $\nu_2 - 4$,...1 or 0. The energies of the CO_2 vibrational levels can be

Neutrals (ground state)	CO_2, CO, O_2, O, C, O_3, C_2, C_2O,...
Electronically excited states	$O(^1D)$, $O(^1S)$, $CO(a^3\Pi_r)$, $O_2(a^1\Delta_g)$, $O_2(b^1\Sigma_g^+)$...
Vibrationally excited states	$CO_2(\nu_1,\nu_2^l,\nu_3)$, $CO(\nu)$, $O_2(\nu)$,
	$X^e(\nu)$*, $X^{+/-}(\nu)$,*
Positive ions	CO_2^+, CO_4^+, CO^+, $C_2O_2^+$, $C_2O_3^+$, $C_2O_4^+$,
	C^+, C_2^+, O^+, O_2^+, O_4^+,...
Negative ions	CO_3^-,CO_4^-,O^-, O_2^-, O_3^-, O_4^-,...

* Vibrationally excited states of electronically excited states and ions.

Table 1.1: Non-exhaustive list of the main gas phase species in CO_2 plasmas.

calculated using the anharmonic oscillator approximation *Treanor et al.* [1968]. The energy of one ν_1 quantum and two ν_2 quanta is very close. Therefore there is a strong Fermi resonance between states of the form $(\nu_1, \nu_2^{l_2}, \nu_3)$ and $((\nu_1 - 1), (\nu_2 + 2)^{l_2}, \nu_3)$.

For an average electron energy around 2 eV, typical of a glow discharge, the vast majority of electrons will have enough energy only to populate vibrational levels (see figure 1.3). Nevertheless, even at this low energy range and because of the three vibrational modes of CO_2, there are already hundreds of combined vibrational levels of CO_2 that can be populated. Vibrationally excited molecules can be populated by direct electron impact but their population also depends on many other mechanisms, such as:

- Electron impact de-excitation through super-elastic collisions with low energy electrons
- Vibrational energy exchange reactions or V-V' transfers, including exchange of vibrational quanta between different modes of vibration of CO_2 or with other molecules. For instance CO has *quasi* resonant energy levels with the CO_2 asymmetric mode.
- Vibrational-translational/rotational relaxation, V-T, through collisions with other particles or with the reactor walls.
- Molecules can become vibrationally excited through collisions with electronically excited states *Harding et al.* [1988]; *Chen et al.* [2009]; *Huestis et al.* [2002].
- Vibrationally excited molecules can promote chemical reactions if the vibrational energy can help to overcome the activation energy barrier of the reaction, as suggested for example for the production of CO from $CO_2(\nu^*)$ reacting with O atoms *Fridman* [2008].

When the rates for V-T transfers are slower than the rates of V-V energy exchanges, a fast redistribution of the energy within a vibrational mode can happen. This fast V-V relaxation, together with the anharmonic energy levels lead to the establishment of the so-called Treanor vibrational distribution *Treanor et al.* [1968]. In CO_2, a Treanor distribution is more easily obtained in the asymmetric mode, because the low energy gap between the energy levels corresponding to the bending and symmetric stretch modes favours an efficient V-T relaxation.

Even in the low energy range (∼2 eV) corresponding to most of the electrons in a NTP, important electronic states can be populated in CO_2 plasmas. As can be seen in the two right columns in figure 1.4, several excited states of O_2 and O can be efficiently populated. In particular states such as $O_2(a^1\Delta_g)$, $O_2(b^1\Sigma_g^+)$ or $O(^1D)$ can play an important role in chemical reactions or energy transfer to

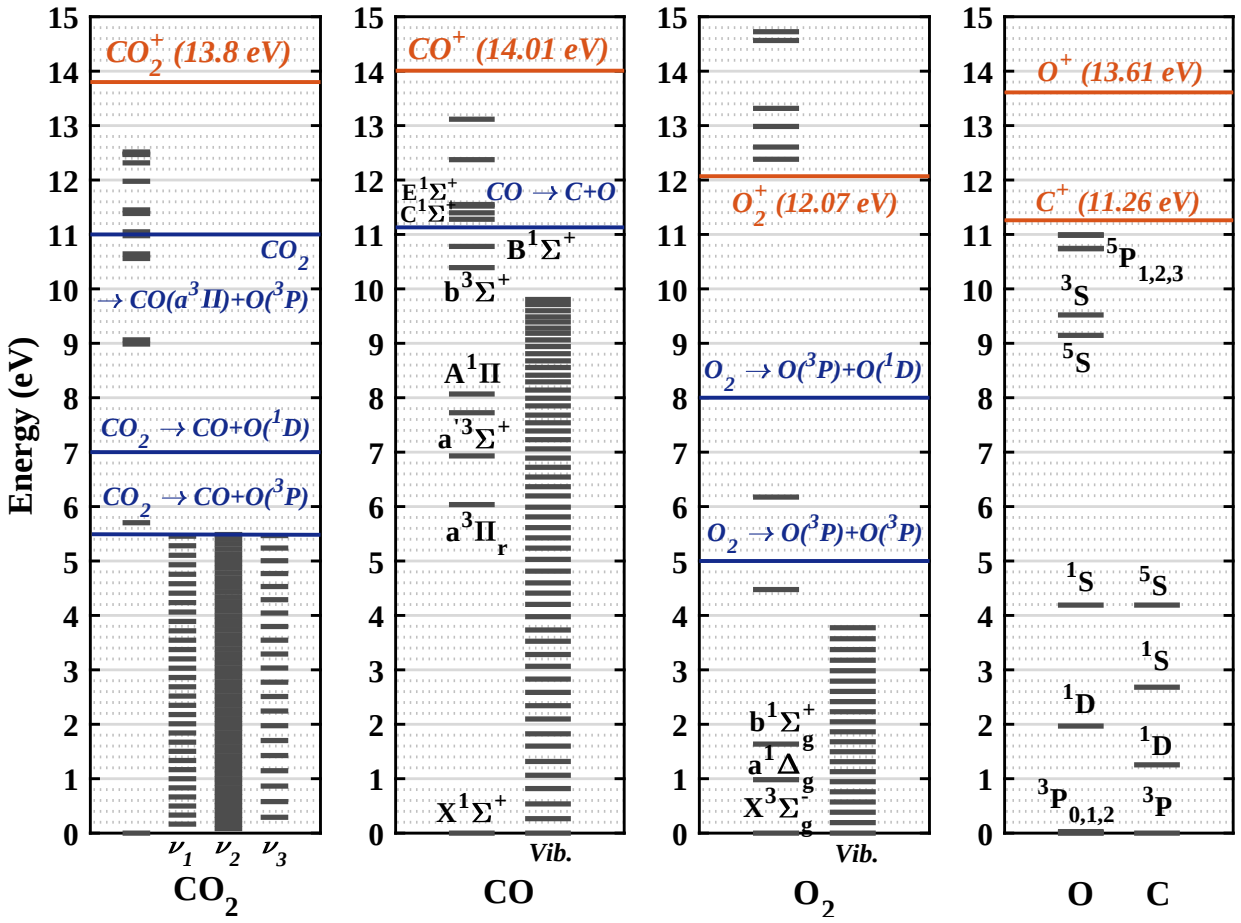

Figure 1.4: Energy level diagram of main vibrational and electronic states of neutral components in CO_2 plasmas. CO and CO_2 electronic states taken from *Herzberg* [1950, 1991] and vibrational levels from HITEMP database *Rothman et al.* [2010]; *Patel* [1965], O_2 levels taken from *Krupenie* [1972] and O and C atoms levels from NIST database.

vibrations *Zhu et al.* [1990]. Typically, not more than a few percent of electrons in a glow discharge will have enough energy for dissociating CO_2 by direct electron impact (from 7 eV and above). Close to this energy threshold, another electronic state may again be important: $CO(a^3\Pi_r)$, which has a relatively long life-time, ~2.5-7.5 ms *Mori et al.* [2002]; *Gilijamse et al.* [2007] and can be populated by electron impact or radiative cascade transitions. In an even higher energy range (≥10 eV), the relatively close ionization potentials of CO_2, CO and O makes the *a priori* assessment of the main ions difficult, because it will strongly depend on the gas mixture composition and therefore on the dissociation rate. O_2 can be more easily ionized but starting from pure CO_2, its density can not be more than half of CO. In this high energy range, electronically excited states, even though less populated than lower levels, are sometimes claimed to play an important role on the electron kinetics via super-elastic collisions, as reported for the 10.5 eV electronic state of CO_2 by *Capitelli et al.* [2017].

To address specific aspects of CO_2 plasma kinetics, relevant information can be found in a wide range of past and present research areas. The extensive literature on the development of CO_2 lasers is obviously an important source of information. These lasers are based on a population inversion of the first level of the asymmetric mode (ν_3=1). Therefore these works provide very valuable

information about the very first vibrational levels of CO_2 *Shields et al.* [1973]; *Huddleston and Weitz* [1981]; *Dang et al.* [1982]; *Dang et al.* [1983]; *Zasavitskii et al.* [1990]; *Toebaert et al.* [1995]; *Witteman* [2013]. However, they often study low pressure continuous plasmas in gas mixtures of CO_2-He-N_2, with the aim of minimizing the dissociation of CO_2. Experimental works on combustion and shock tube experiments for atmosphere entry provide also important information, for instance on reaction rates *Bykova et al.* [1997]; *Kovalev et al.* [2005]. The study of the chemistry induced by photolysis/photo-ionization in the upper atmosphere of Mars, Venus and the primordial Earth brings also information, especially on reactivity of electronically excited states *Fox and Dalgarno* [1979]; *Krauss et al.* [1971]; *Donahue* [1971]; *Perri et al.* [2004]. These planetary science works have often motivated electron beam and/or molecular beam experiments to investigate individual excitation or chemical reactions *Mumma et al.* [1975]; *Zhu et al.* [1990]; *Perri et al.* [2004]. Beam experiments are certainly very useful and provide reaction rates or lifetime of species but they do not directly reveal the role of excited states inside a gas discharge. The vibrational kinetics of CO_2 above the very first levels relevant for CO_2 lasers remains also very poorly documented. Therefore, in spite of all the useful literature available, the complexity of CO_2 plasmas and the difficulties to describe accurately the processes influencing the CO_2 dissociation under plasma conditions implies that significantly more experimental and modelling work is still required.

1.3 Current approaches to study CO_2 plasmas

1.3.1 Experimental point of view

Over the past 10 years, most of the work conducted on CO_2 plasmas has focused on optimizing dissociation efficiency for environmental purposes. To this aim, many different plasma sources have been investigated over a large range of pressure and frequencies: from 10 to 1000 Pa with DC glow or radio frequency discharges *Spencer and Gallimore* [2011]; *Premathilake et al.* [2019]; *Huang et al.* [2017]; *Yang et al.* [2018], from few kPa to tens of kPa with RF and microwave discharges *Heijkers et al.* [2015]; *Silva et al.* [2014]; *den Harder et al.* [2017]; *Bongers et al.* [2017], at atmospheric pressure with gliding arc *Nunnally et al.* [2011]; *Wang et al.* [2017]; *Liu et al.* [2016], dielectric barrier discharges *Aerts et al.* [2014]; *Brehmer et al.* [2014]; *Duan et al.* [2015] or micro-hollow cathode discharges *Taylan and Berberoglu* [2014] or even above atmospheric pressure with nanosecond discharges *Bak et al.* [2015]; *Scapinello et al.* [2016]. These plasma sources and others have been listed and compared in terms of conversion efficiency in several review articles *Snoeckx and Bogaerts* [2017]; *Britun et al.* [2018]; *Qin et al.* [2018].

These works are carried out either in pure CO_2 ?*Brehmer et al.* [2014]; *Britun et al.* [2018]; *Sun et al.* [2017], or in mixtures with noble gases (Ar, He) *Yap et al.* [2015]; *Ramakers et al.* [2015]; *Ray et al.* [2017] to improve the dissociation efficiency by modifying the EEDF, or diluted in N_2 *Xu et al.* [2017b]; *Heijkers et al.* [2015] to benefit from the resonance between vibrational levels. Many works are also carried out by mixing CO_2 with H_2 (methanation) *de la Fuente et al.* [2017]; *Azzolina-Jury et al.* [2017], H_2O *Martini et al.* [2017]; *Chen et al.* [2017b] or CH_4 (gas reforming) *Scarduelli et al.* [2011]; *Bouchoul et al.* [2019] with the aim of directly converting CO_2 into hydrocarbons.

In order to enhance the energy efficiency and to have a better control on the by-products formed when CO_2 is mixed with other molecules, many works are coupling the plasma with catalytic surfaces *Mei et al.* [2016]; *Chen et al.* [2017a]; *Zhang et al.* [2017]; *Puliyalil et al.* [2018]; *Chen et al.*

[2019]. This is an additional degree of complexity not only because of surface chemical reactions but also because the presence of a surface in contact with the plasma can modify the electric field, the charge loss mechanisms, the radical recombination or numerous other processes strongly affecting the plasma behaviour. A few works look specifically at the influence of the size of catalytic material particles *Butterworth et al.* [2016]; *Uytdenhouwen et al.* [2018]. However, until now the most commonly used configuration for plasma/catalyst coupling is packed bed DBD *Xu et al.* [2018], which is not a convenient configuration for *in situ* diagnostics.

All these investigations aim to maximize the amount of CO_2 converted while minimizing the energy cost but they are conducted in very complex configurations that do not facilitate the understanding of the mechanisms involved in the CO_2 dissociation. Even studies of pure CO_2 plasmas without catalysts often use configurations that are challenging to investigate *in situ* and cannot be understood without taking into account complex fluid dynamics *Ponduri et al.* [2016]; *Liu et al.* [2016]; *den Harder et al.* [2017].

For instance **Microwave discharges (MW)** are among the most investigated plasma sources in pure CO_2 because they have been used to achieve the highest reported energy efficiencies, most likely through their ability to strongly populate high vibrational levels. However, MW discharges tend to reach high gas temperatures, and the CO_2 dissociation becomes dominated by thermal splitting at elevated pressure. This gas heating induces strong convective structures and often imposes the use of vortex gas flow configurations to prevent the reactor walls from melting *Bongers et al.* [2017]. The strong non-uniformity of these discharges requires time and space resolved diagnostics, for example laser scattering experiments *van den Bekerom et al.* [2019].

Radio-frequency discharges (RF), one of the first plasma sources reported for plasma dissociation through vibrational excitation *Capezzuto et al.* [1976], are also interesting plasma sources especially with the recent development of frequency mixing in order to taylor the EEDF, even at elevated pressure *Korolov et al.* [2019], which could help favouring the most efficient dissociation processes. However, RF discharges can be difficult to ignite at elevated pressure without diluting CO_2 with noble gases *Urbanietz et al.* [2018], and short electrode gap distances, in the order of ∼few millimetres, are often necessary. The gas heating can also be strong, requiring electrode cooling.

Gliding arc discharges (GAD) and **Nanosecond repetitively pulsed discharges (NRP)** are two other promising configurations that can be used at atmospheric pressure, while keeping higher energy efficiency than **dielectric barrier discharges (DBD)**, whose main interest for CO_2 conversion is related to the ease of coupling with catalysts. In GAD a thermal arc is translated quickly in the direction of gas flow between two electrodes separated by increasing distance. When the discharge filament becomes long enough, a non-thermal plasma is obtained in which vibrational excitation could help the dissociation *Indarto et al.* [2007]; *Wang et al.* [2017]. This "classical" GAD configuration, highly transient and unstable, is sometimes replaced by a "reverse vortex" configuration that allows achieving higher dissociation rates but makes *in situ* measurement extremely challenging *Ramakers et al.* [2017]; *Li et al.* [2019]. NRP are commonly generated between two pin electrodes by applying short high voltage pulses of few nanoseconds which ignites transient filamentary discharges (usually streamers or sparks). During the ionization wave propagation, the very strong electric field, with even higher E/N than in classical corona or DBD discharges, favours the dissociation through electron impact *Moss et al.* [2017] and/or through CO_2 electronically excited states *Bak et al.* [2015]. After this initial discharge development, also responsible for shock

waves generation *Dumitrache et al.* [2019], vibrational excitation may also play a role in the dissociation process *Heijkers et al.* [2019]. For NRP like for other discharges presented here, in situ measurements require high spatial and time resolution, which could be achieved in NRP with LIF diagnostics *Martini et al.* [2017].

All these configurations have their merits but none of them, even in pure CO_2, is simple to compare with numerical models, nor allow for using simple diagnostics techniques and identifying main mechanisms controlling the kinetics of the plasma.

1.3.2 Modelling point of view

Because of the importance of the vibrational kinetics in CO_2 plasmas in particular (but not only) for efficient dissociation, many modelling works focused on the description of the vibrational kinetics of CO_2 plasmas from different approaches, already back to CO_2 lasers literature *Siemsen et al.* [1980]; *Spiridonov et al.* [1994]; *Witteman* [2013]. One of the most common approaches to model vibrational kinetics is the state-to-state (STS) modelling based on the numerical solution of a system of non-linear balance rate equations. Different complementary STS models have been developed, that can be differentiated depending on the level of detail used for describing the population densities of the three vibrational modes of CO_2. The most complete description consists in taking into account all the vibrational levels and corresponding V-V' and V-T transfers. This approach has been developed for the study of non-equilibrium flows (mostly for atmospheric entry) *Armenise and Kustova* [2013, 2018] and takes into account about 10000 levels. It can be very useful to help improving simplified schemes, but it does not account for electron impact reactions and it is difficult to include in models describing complex plasma sources because of the computational requirements.

In order to compare modelling results with experimental configurations such as MW or DBD, reduced schemes that allow for the coupling with large chemical reaction sets must used. For instance, *Aerts et al.* [2012]; *Kozák and Bogaerts* [2014a, b] described a few low-lying symmetric stretch and bending mode levels along with all the levels (21) in the asymmetric mode, up to the dissociation energy (estimated in 5.5 eV). This description assumes that the three vibrational modes are independent, significantly limiting the number of transitions considered. However, one of the peculiarities of the CO_2 kinetics is to have multiple channels of vibrational energy relaxation, such as energy transfer between different vibrational modes (inter-mode V-V').

The model developed at IST Lisbon *Silva et al.* [2018]; *Grofulović et al.* [2018] is also a STS model with a reduced scheme that takes into account about 75 energy levels, with coupled vibrational modes. It includes electron-impact mechanisms of excitation and de-excitation of the different vibrational levels (e-V). Moreover, the system of rate balance equations describing the vibrational kinetics is coupled to the electron Boltzmann equation. One of the goals of this thesis is to provide a step by step validation of this model by comparing experimental data in well controlled conditions with modelling results. The comparison of the experimental results concerning the vibrational kinetics of CO_2 with the model description is discussed in chapter 4. Once the vibrational kinetics is validated, the model can be coupled with gas phase chemical reactions or surface reactions, as discussed in chapter 6, or even include a self consistent gas temperature calculation *Grofulović* [2019].

Similarly to the IST Lisbon approach, a self-consistent model coupling the electron equation with the STS vibrational kinetics of CO_2 is developed by the group from Bari (Italy) *Pietanza et al.*

[2016a]; *Capitelli et al.* [2017]. This time-dependent model was used to investigate the relative contribution of vibrational excitation or direct electron impact on the dissociation of CO_2 for typical conditions of MW and NRP discharges *Pietanza et al.* [2016c]. This model emphasizes also the influence of super-elastic collisions transferring energy from vibrationally excited molecules to electrons and the corresponding modifications on the Electron Energy Distribution Function (EEDF), especially during post-discharge.

State-to-state models are very detailed but can become computationally demanding. Therefore, several methods have been developed to reduce the computational cost of kinetic models, while keeping the main features of vibrational kinetics in CO_2, with the aim of coupling the vibrational models with complex physical phenomena, such as fluid dynamics, to describe plasma reactors or atmospheric entry conditions. These approaches include lumping vibrational levels *de la Fuente et al.* [2016]; *Berthelot and Bogaerts* [2016], adaptative bining of levels *Sahai et al.* [2017] or multi-temperature models *Armenise et al.* [2016]; *Kustova et al.* [2019]. The description of the CO_2 vibrational kinetics by the Fokker-Planck (FP) equation, based on replacing the individual vibrational levels by a continuum in the vibrational energy space and using transport parameters to describe the vibrational kinetics, is another approach *Rusanov et al.* [1979]; *Capitelli* [2012]; *Diomede et al.* [2018]; *Viegas et al.* [2019]. The description of chemical reactions can also include thousands of reactions for which the rates coefficients are not always well known. Reduced chemistry sets with pathway analysis to identify the main mechanisms in CO_2 plasma chemistry are then necessary *Colonna et al.* [2006]; *Koelman et al.* [2019]. In some particular configurations in which the vibrational kinetics can be neglected as a first approximation, for instance for packed bed DBD reactors, modelling approaches including only electron kinetics and chemistry of heavy species have been explored *Saidia et al.* [2019]; *Liu et al.* [2017], due to the easier coupling with a fluid dynamics description *Ponduri et al.* [2016]. Streamers in CO_2 starts also to be described with fluid models or even particle-in-cell (PIC) simulations *Levko et al.* [2017]. PIC/MCC (Monte Carlo collision) simulations have been recently used to show that specific catalytic materials could promote vibrational excitation in the asymmetric stretch mode in field emission driven micro-discharges *Tan and Go* [2019].

1.4 What is unknown?

Many different types of discharges have been studied in the last years mainly focusing on increasing both the energy efficiency and the conversion. In spite of the extensive literature, several basic processes essential for describing the CO_2 plasma kinetics, are not yet well understood. The lack of knowledge on some fundamental mechanisms brings difficulties to the very formulation of the models, resulting in discrepancies between experimental data and model predictions and making difficult to conceive more efficient conversion processes.

Among the mechanisms that are still surrounded by large uncertainties, we can mention five, which are more extensively described bellow: (i) scaling of V-V and V-T rate coefficients, (ii) rates for chemical reactions involving vibrationally excited CO_2 or CO, (iii) role of electronically excited states ($CO(a^3\Pi_r)$, $O(^1D)$, etc.) in chemical reactions and/or in super-elastic collisions, (iv) direct electron impact dissociation cross section, and (v) surface reactivity of CO_2 plasmas.

(i) Scaling of V-V and V-T rate coefficients

CO_2 decomposition in non-equilibrium plasmas is strongly influenced by the population of the CO_2 vibrational levels. Therefore, an accurate estimation of the corresponding reaction rates up to the dissociation limit is of critical importance for a proper investigation of the CO_2 vibrational kinetics. However, whereas experimental data for vibrational exchanges at high quantum numbers are available for diatomic molecules such as CO, NO, and O_2 *Adamovich et al.* [1998]; *Annušová et al.* [2018], only rates for the energy transfer between vibrational-vibrational and vibrational-translational degrees of freedom (V-V and V-T) for the first levels of CO_2 are available in the literature (the first 14 levels in *Blauer and Nickerson* [1973]), most of the time from old experiments motivated by the study of CO_2 lasers. Schwartz-Slawsky-Herzfeld (SSH), a first-order perturbation theory *Schwartz et al.* [1952]; *Seeber* [1971], is often used to extrapolate the state-specific rate coefficients up to the dissociation limit, for which no experimental data are available. However, SSH theory provides unrealistically high values for reaction rates with high vibrational quantum numbers and/or for high translation temperatures. Other possible theories for the scaling of rate coefficients are: Sharma and Brau theory *Sharma and Brau* [1969], a first order perturbation theory which takes into account long range interactions, quantum classical trajectory (QCT) or forced harmonic oscillator (FHO) approaches, as discussed in detail by *Silva et al.* [2018]. Only comparison with experimental data can determine the accuracy and applicability of the different theories.

There is even less information about the state-specific calculation of V-V' and V–T rate coefficients between excited CO_2 and molecules such as O_2 or CO, or with C and O atoms. Only data for the lowest vibrational levels are available *Buchwald and Wolga* [1975]; *Lopez-Puertas et al.* [2001]. A related source of inaccuracy of kinetics models is the unknown proper scaling of electron impact dissociation processes on vibrationally excited CO_2. For electron impact dissociation, usually a simple shift of the cross section threshold with the energy of the vibrational state considered is applied.

(ii) Chemical reactions involving vibrationally excited molecules

The reactivity of ground state species is usually well known from classical chemistry and the rate coefficients for most of the reactions are available in NIST database. Under plasma conditions, vibrational state-dependent rate coefficients of chemical reactions are rarely known. For some reactions, it is often assumed that the vibrational excitation of CO or CO_2 can lower the corresponding activation energy. Commonly, this effect is taken into account by subtracting a contribution to the activation energy in an Arrhenius-type reaction rate equation, as in *Kozák and Bogaerts* [2014a]:

$$k(E_v, T) = A_0 \cdot exp\left(-\frac{E_{act} - \alpha E_v}{T}\right) \tag{1.1}$$

where E_{act} is the activation energy of the reaction, E_v is the vibrational energy and α is in this case a parameter determining the efficiency of lowering the reaction energy barrier by vibrational excitation. The values of α are calculated with the Fridman–Macheret α-model *Fridman* [2008]. Note that for high vibrational levels $E_{act} - \alpha E_v$ may reach values <0, generating negative activation energies, and a condition of $E_{act} - \alpha E_v$=0 must be imposed *Capitelli et al.* [2017]. Example of reactions for which this activation energy lowering is assumed are $CO_2^{*v} + M \rightarrow CO + O + M$ or $CO_2^{*v} + O \rightarrow CO + O_2$. On the contrary, reactions such as $CO + O + M \rightarrow CO_2 + M$ or

$CO_2 + C \rightarrow CO + CO$ are usually considered with the same rate coefficient for all vibrational states and different descriptions can be found in literature for the reaction $CO^{*v} + O_2 \rightarrow CO_2 + O$ *Beuthe and Chang* [1997]; *Kozák and Bogaerts* [2014a]; *Fridman* [2008]. An experimental validation of these rate coefficients would be necessary, in particular for processes that can lead to the oxidation of CO into CO_2 (so called "back reaction mechanisms") such as CO(ν^*) and O or O_2, $CO(\nu) + CO(\omega) \rightarrow CO_2 + C$ *Gorse and Capitelli* [1984]; *Essenhigh et al.* [2006]; *Capitelli et al.* [2017] or in the associative ionization $CO(\nu) + CO(\omega) \rightarrow CO_2^+ + C + e$ *Adamovich et al.* [1993].

It is worth mentioning the critical role of oxygen atoms, which can either be beneficial or detrimental for the dissociation. O atoms can contribute to the dissociation of CO_2 through the reaction $CO_2 + O \rightarrow CO + O_2$, which has a rather low activation energy $E_a \approx 0.5 - 1$ eV/mol. This reaction has been claimed to be faster than the three-body recombination of atomic oxygen ($O + O + M \rightarrow O_2 + M$) and to produce an extra CO molecule when the vibrational temperature is $T_v \geq$0.1 eV (∼1160 K) *Fridman* [2008]. A value of $\alpha = 0.5$ in equation (1.1) is given for the reaction $CO_2 + O \rightarrow CO + O_2$ *Kozák and Bogaerts* [2014a]; *Fridman* [2008]. On the other hand, O atoms can act as efficient quenchers of the CO_2 vibrational excitation. The quenching of the vibrational excitation of the bending (ν_2) and the asymmetric stretch (ν_3) by O atoms modes have been discussed in the fields of atmospheric studies *Sharma and Wintersteiner* [1990]; *Lopez-Puertas et al.* [2001] or wave-guide CO_2 lasers *Zasavitskii et al.* [1990]. In the latter case, at only 1% concentration of O atoms in the gas mixture, the contribution of the oxygen atoms to the relaxation of the asymmetric stretch mode was found to be approximately equal to the contribution of all the remaining components *Spiridonov et al.* [1994]. However, the possible relaxation of CO_2 vibrations with O atoms is not taken into account in several models describing the CO_2 vibrational kinetics such as *Kozák and Bogaerts* [2014a]; *Armenise and Kustova* [2018], where only V-T relaxation by collisions with CO_2, CO or O_2 is considered. Including the relaxation of the vibrations by O atoms may lead to very different results, as shown by *Terraz et al.* [2019].

(iii) Role of electronically excited states

The role of electronically excited states, some of them metastable, is also unclear although their importance has been pointed out in several papers. An interesting example is CO($a^3\Pi_r$), that can be created by electron impact dissociation of CO_2 *Cosby and Helm* [1992], by electron impact excitation at an energy close to 6 eV (see figure 1.4), by radiative cascade from higher states, or by dissociative recombination ($CO_2^+ + e$). CO($a^3\Pi_r$) can play a role in shaping the EEDF, especially in the post-discharge, through super-elastic collisions ($e(E = 0\ eV) + CO(a^3\Pi_r) \leftrightarrow e(E = 6\ eV) + CO$ and $e(E = 6\ eV) + CO(a^3\Pi_r) \leftrightarrow e(E = 12\ eV) + CO$) *Capitelli et al.* [2013, 2017]. It can also be involved in chemical reactions either enhancing the dissociation ($CO(a^3\Pi_r) + CO_2 \rightarrow 2CO + O$) or in "back reaction mechanisms" ($CO(a^3\Pi_r) + O_2 \rightarrow CO_2 + O$ and $CO(a^3\Pi_r) + CO \rightarrow CO_2 + C$) *Cenian et al.* [1994]. The electronically excited state of CO_2 at 10.5 eV has been also claimed to affect the EEDF in the early post-discharge *Capitelli et al.* [2017]. In addition, electronic states of O and O_2 with energies mostly below 2 eV could also play an important role in the vibrational and chemical kinetics. O(^1D) state is directly created by electron impact dissociation of CO_2 and can therefore be largely produced, $O_2(a^1\Delta_g)$ at ∼1 eV can store energy with a very long life-time *Schweitzer and Schmidt* [2003] (the radiative life-time reaches values close to 72 minutes), however these states are rarely taken into account and their influence on the CO_2 plasma kinetics is usually

not described.

(iv) Direct electron impact cross section

A striking example of a poorly known, yet crucial parameter is the direct electron impact dissociation cross section of CO_2, addressed hereinafter in more detail because of its relevance and importance in this thesis. Direct electron impact dissociation is obviously one of the most important processes in CO_2 plasmas, and in general in any CO_2-containing gas discharge. In many types of discharges it constitutes the main dissociation mechanism (glow or DBD, for instance). The electron impact dissociation cross section is reported by several authors. However, the proposed values differ significantly both in threshold and in magnitude as a function of the electron energy *Grofulović et al.* [2016] (see figure 1.5). Consequently, the derived rate coefficients are orders of magnitude different (see figure 1.6). The CO_2 electron impact dissociation cross section is perhaps the most surprising source of uncertainties for the description of CO_2 plasma, and has a direct impact in the modelling predictions *Bogaerts et al.* [2016]. A detailed review of the available electron impact cross sections is given by Grofulović *et al.* *Grofulović et al.* [2016], only a short summary is given here.

Itikawa *Itikawa and Mason* [2005] reports a single mechanism with a threshold energy around 11.9 eV, leading to the production of $O(^1S)$, based on measurements by LeClair and McConkey *LeClair and McConkey* [1994]. This cross section was adopted for example by *Ponduri et al.* [2016]; *Koelman et al.* [2017]. A similar variation as a function of the reduced electric field, although up to a factor 5 larger, and with slightly higher energy threshold is given by Cosby & Helm *Cosby and Helm* [1992], obtained by crossed beam experiments and claimed to correspond to two dissociation channels giving $CO(X^1\Sigma^+)$ + $O(^1S)$ and $CO(a^3\Pi)$ + $O(^3P)$. This cross section is used for example by *Capitelli et al.* [2017]. The cross sections reported by Phelps *Lowke et al.* [1973]; *Hake and Phelps* [1967] are widely used in the literature *Pietanza et al.* [2016d, a, b]; *Kozák and Bogaerts* [2014a]; *Berthelot and Bogaerts* [2017]. Phelps' cross section was derived from the comparison between predicted and measured swarm parameters (transport coefficients) for pure CO_2 and CO_2 laser gas mixtures (CO_2-He-N_2 *Nighan* [1969]; *Wiegand et al.* [1970]). The set contains two electronic excitation cross sections, with thresholds at 7 eV and 10.5 eV. The 7 eV cross section is often used to calculate the dissociation rate coefficient *Pietanza et al.* [2016d, a, b]; *Kozák and Bogaerts* [2014a]; *Berthelot and Bogaerts* [2017]. The cross section calculated theoretically by Polak and Slovetsky *Polak and Slovetsky* [1976], used in *Fridman* [2008]; *Grofulović et al.* [2016], also includes two excitation/dissociation channels, but smaller in magnitude and with thresholds shifted towards higher energy values (∼7.5 and 11.9 eV). Corvin and Corrigan *Corvin and Corrigan* [1969] built a cross section from their measured rate coefficient assuming a Maxwellian distribution of electron energies, defining a single process with threshold at 6 eV. The corresponding rate coefficient falls in between those calculated using Phelps' and Polak's cross section for the high reduced electric field (E/N, where E is the electric field and N the gas density) range, but they are up to two orders of magnitude higher for low E/N *Grofulović et al.* [2016].

This short compilation illustrates the discrepancies found in the literature for the CO_2 electron-impact dissociation cross section. The lack of experimental data and validation for this cross section is a bottleneck for the understanding of CO_2-containing plasmas. An inaccurate electron impact cross section may lead to under- or over-estimation of the CO_2 dissociation through a pure vibrational mechanism or by electron impact. In addition, the choice of cross section affects

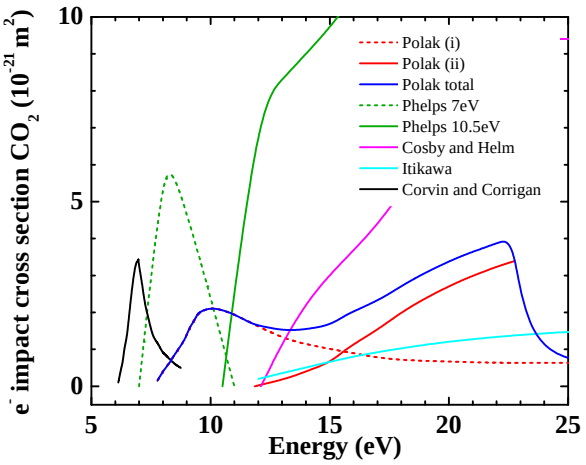

Figure 1.5: Electron impact dissociation cross sections of CO_2 as a function of the electron energy available in the literature. Figure extracted from *Grofulović et al.* [2016].
.

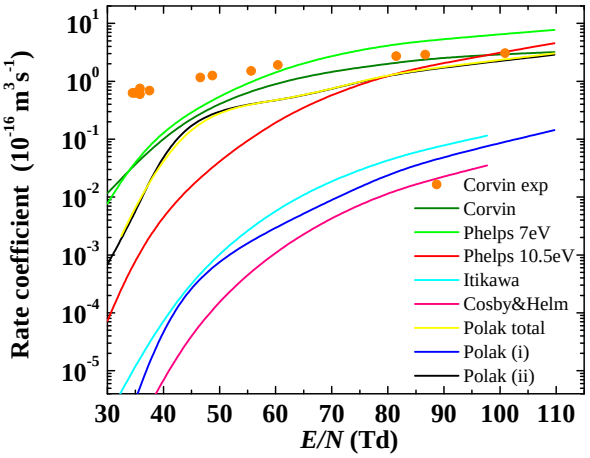

Figure 1.6: Dissociation rate coefficients of CO_2 as a function of E/N, calculated from dissociation cross sections in figure 1.5. The symbols represent measurements by Corvin and Corrigan. Figure extracted from *Grofulović et al.* [2016].
.

the calculation of other electron impact processes (electronic excitation, ionization) through its influence in the EEDF. For instance, differences up to an order of magnitude were found in the two ionization rates due to the differences in the EEDF obtained using two different CO_2 electron impact dissociation cross sections (*Hake and Phelps* [1967]; *Cosby and Helm* [1992]) in the Boltzmann solver *Capitelli et al.* [2017]. The validity of scaling laws of dissociation and ionization cross sections as a function of the vibrational state based on a threshold shift of the cross section *Capitelli et al.* [2017]; *Grofulović et al.* [2018] should also be verified *Laricchiuta et al.* [2018].

(v) Surface chemistry

As mentioned in section 1.3.1, many studies are coupling plasmas with catalytic materials to enhance the CO_2 conversion. However, beyond the knowledge of adsorption capabilities and surface reactivity coming from regular catalysis activated by heat, very little is known concerning surface processes under direct CO_2 plasma exposure. The electric field induced on a catalyst surface by a plasma could, for instance, modify the CO_2 adsorption energy *Bal et al.* [2018]. Plasma reactors always have walls, made either of metal (for the electrodes) or of dielectric materials (often glass or quartz). Certain metals are known to have a catalytic activity towards CO and CO_2 (for example copper for methanol formation *Studt et al.* [2015]), but the catalycity of metals under plasma exposure is very little documented (except Ni for methanation *Dębek et al.* [2019]). Studies dedicated to spacecraft shields development for Mars atmosphere entry give only scarce data about CO_2 plasma interaction with metal or dielectric surfaces *Sepka et al.* [2000], and usually only for high gas temperatures *Kolesnikov et al.* [2000]; *Bykova et al.* [1997].

Catalysts are often used in complex gas mixtures but even for pure CO_2 plasma, basic data on the recombination probability of oxygen atoms (γ_O), or accommodation coefficients for vibrational de-excitation at the wall are missing, which is detrimental for the accuracy of surface kinetic models.

Several studies have been dedicated to measure γ_O in pure O_2 plasmas *Kim and Boudart* [1991]; *Macko et al.* [2004]; *Cartry et al.* [2006]; *Booth et al.* [2019]. The de-excitation of vibrationally excited N_2 has also been documented *Pintassilgo et al.* [2014]; *Popov* [2001]; *Marinov et al.* [2012b]. Unfortunately data for CO_2 plasma are much more scarce, even for simple SiO_2 surfaces *Doyennette et al.* [1974]; *Bousquet et al.* [2007].

Comparison model/experiments

The five main "unknowns" discussed above are clear obstacles for the development of predictive models and optimized CO_2 conversion processes. An additional issue would be to include a proper calculation of gas heating in models *Grofulović* [2019], since the gas temperature is a key parameter affecting not only the chemical reactions rate coefficients but also the EEDF by modifying the gas density (and therefore E/N).

The comparison between theoretical and modelling results with experimental values, often missing in the studies available in the literature, is also of critical importance to validate the accuracy of models and in particular to establish a consistent set of parameters. Models can provide useful information about parameters that cannot be measured, allowing to extract meaningful information and real understanding of the most relevant mechanisms in CO_2 plasmas.

1.5 Approach and objectives of the thesis

If all these uncertainties remain, it is largely due to the lack of experimental data under discharge conditions capable of distinguishing the contribution from different mechanisms. The approach adopted for this thesis aims to cover some of these needs in two complementary ways: (i) by selecting experimental conditions appropriate to emphasize the contribution of one particular mechanism, (ii) by measuring as many different parameters as possible in the same plasma source to constrain a plasma model in which all the different processes are coupled.

Our objective is therefore to design and carry out dedicated "benchmarking" experiments to study fundamental processes under plasma conditions, but still simple enough to measure sufficient parameters to constraint and validate step-by-step kinetic models. In addition, these measurements provide a large set of new data and a thorough experimental characterisation of CO_2 plasmas in controlled conditions, allowing the investigation of the kinetic mechanisms from a purely experimental point of view. Therefore, our main purpose is not to improve the efficiency of our discharge or increase the conversion but to gain basic understanding and physical insight into the elementary processes ruling the complex kinetics of CO_2 plasmas.

This thesis is part of a joint effort to investigate fundamental aspects of the kinetics of CO_2 plasmas between the Laboratoire de Physique des Plasmas (LPP, École Polytechnique) where the experiments presented here were performed, and Instituto Superior Técnico (IST, Lisbon) where kinetic models to be validated against the experimental data are developed. The collaboration is actually tripartite and measurements complementary to those done at LPP, are carried out at the PMP group from the Technical University of Eindhoven (TU/e), using exactly the same plasma sources.

The choice of plasma sources studied in this thesis was therefore driven by four main ideas:

- Allow an easy comparison between experiments and 0D models and give the possibility to take into account complex kinetics.
- Allow the use of many diagnostics giving access to the most complete possible set of parameters in a single system.
- Allow the use of simple control parameters (pressure, gas flow, current, etc...) to study different operating conditions in terms of dissociation rate, vibrational excitation or interaction with surfaces.
- Allow having multiple reactors with slightly different characteristics to test the sensitivity to the geometrical characteristics of the reactor, and allow to have identical set-ups in different laboratories.

To this aim, we have chosen to use a **DC glow discharge** as primary plasma source, because it is simple, reproducible and homogeneous (in the positive column *Raizer* [1991]). It provides several advantages from a diagnostics point of view: (i) the determination of the electric field is straightforward, allowing an easy and accurate estimation of the reduced electric field and the electron density, (ii) the plasma volume is well defined and constrained between the electrodes, and (iii) it allows line-of-sight integrated diagnostics, such as *in situ* FTIR (Fourier Transform Infra-Red) absorption spectroscopy or Cavity Ring Down Spectroscopy (CRDS). Comparison with spatially resolved diagnostics can still be performed to insure the homogeneity of the system.

Some experiments were done using a **capacitively coupled RF discharge** with no direct contact of metal electrodes with the plasma, and ignited in a similar glass tube as the glow discharge. This configuration provides also an homogeneous and stable plasma. It does not allow a quantification of the electric field as easy as the glow discharge, but it can have a more stable ignition in some conditions (see chapters 6 and 7). Both discharges allow the use of multiple and complementary diagnostic methods. Considering that one of our goals is to give accurate constraints for the 0D model, the accuracy of the measurements techniques is also critical. The flexibility offered by these two simple discharges makes them also good test cases to cross-check and validate diagnostics. An important point throughout the whole thesis will be to show for each parameter measured the comparison of several diagnostic methods and evaluate their consistency (see chapters 2 and 3).

The low pressure range chosen (0.2-7.5 Torr), in addition to its relevance for some applications, has the advantage of slowing down characteristic times, which eases the monitoring of the time evolution of various parameters. Lower pressures also allows the study of surface processes under well controlled conditions.

A special care was taken in the study of oxygen atoms. An important objective of this thesis is to determine accurately the absolute O atom densities under conditions where the CO_2 and CO densities are also well characterized, and to study its role on the CO_2 plasma kinetics. Surprisingly, to the best of our knowledge, absolute densities of CO_2, CO and O have never been measured *in situ* in the same plasma conditions. The main O atom loss mechanisms are also studied in detail. Notice that in our experimental conditions the O atom loss processes are *a priori* strongly influenced by surface recombination at the reactor walls, giving us the opportunity to study both surface and gas phase processes involving oxygen atoms.

In summary, we have used a simple discharge along with multiple advanced diagnostics (described in chapter 2) to investigate fundamental mechanisms in CO_2 plasmas. The experimental

data are used as a basis for validating kinetic models, from which only a few results will be mentioned in this thesis. By choosing carefully the conditions in which the glow and the RF discharges are used, the different chapters of the thesis will give insights into the five main sources of uncertainties (the "unknowns") mentioned above.

1.6 Outline of the thesis

The thesis is structured in four parts: Part I describes the different diagnostics used and presents a basic characterization of the studied discharges in their "default" configuration. Knowing these initial characteristics, the next three parts can focus on individual mechanisms separately, using the most favourable experimental conditions to study them. Thus Part II will focus on vibrational kinetics, Part III on dissociation and "back reaction" mechanisms and on the role of excited states on the CO_2conversion. Finally Part IV will focus on surface processes, in particular on the recombination of oxygen atoms. In more detail:

- **Part I: Description of the diagnostics and general characterization of the glow discharge**. Chapter 2 describes the experimental methods and measurement techniques used during all the thesis. A basic characterization of the main plasma source, the glow discharge, with a careful study of the fundamental parameters describing and driving the chemistry in our plasma conditions, such as the reduced electric field, the gas temperature and the densities of the main gas phase compounds is given in chapter 3. Most of the parameters studied were measured by at least two different diagnostics, a good opportunity to benchmark many of these experimental techniques, that will be compared and discussed.

- **Part II: Vibrational kinetics in CO_2 plasmas**. Chapter 4 provides a general study of the vibrational kinetics in continuous and pulsed glow discharges, mainly from an experimental point of view. At the end of the chapter a brief summary of the comparison with the kinetic model developed in IST Lisbon is also shown, as an example of the valuable information extracted from the comparison between the experiments performed and the model. The effect of the dissociation products on the CO_2 vibrational kinetics is briefly discussed at the end of the chapter, and acts as an introduction of chapter 5, which focusses on the effect of oxygen atoms, one of the main dissociation products, on the vibrational kinetics of CO_2 and CO.

- **Part III: Time evolution of the dissociation fraction**. Chapters 6 and 7 focus on the time evolution of the dissociation fraction, both in the glow discharge and in an RF discharge. In chapter 6 we introduce a different experimental method so-called "building-up", which allow us to study the dissociation processes for various gas mixtures and under different experimental conditions (pressures, pulse duration, etc.). In chapter 7 we make use of isotope labelling experiments to trace the exchange of oxygen atoms between different species, and to identify the mechanisms involved during the different phases of the time evolution of the dissociation fraction.

- **Part IV: Surface processes in CO_2 plasmas**. The effect of the surface of the reactor, made of Pyrex and in principle chemically inert, will be discussed in chapter 8. In particular, the recombination mechanisms of oxygen atoms and their possible influence on the dissociation

fraction of CO_2 will be investigated. A comparison with pure O_2 plasma and CO_2-O_2 gas mixtures will help to emphasize the modifications on surface processes under CO_2 plasma exposure. A preliminary comparison with a surface model will be introduced. Finally, going one step further towards a more efficient conversion and at the same time illustrating many of the effects shown in previous sections, at the end of the chapter preliminary results using of a more complex surface to consume the oxygen atoms produced and increase the dissociation fraction is studied.

Except in a few cases, duly identified, all the experimental results shown in this manuscript have been obtained during my thesis at LPP. A research stay of few months at IST Lisbon provided a better view on the possibilities offered by the kinetic models, and allow to participate in the development of surface kinetic models. As mentioned above, the work carried out during this thesis is part of a broader research effort conducted in collaboration with IST Lisbon and TU/e, and the work presented here has benefit from the infra-red spectra analysis method developed during Bart Klarenaar's PhD thesis *Klarenaar et al.* [2017], in joint investigation involving LPP and TU/e. We could also benefit from a collaboration within LPP with C. Drag, J.-P. Booth and A. Chatterjee, and with D. Lopaev and S. Zyrianov from Moscow State University. The obtained experimental data led to several joint publications, often including comparison with models and/or other measurement techniques. For instance the vibrational temperatures of CO_2 and CO measured in a pulsed DC discharge both with FTIR and Raman scattering *Klarenaar et al.* [2017, 2019] has been shown to give good agreement with a kinetic model describing CO_2 vibrational kinetics under conditions of very low dissociation fraction *Silva et al.* [2018]; *Grofulović et al.* [2018]. The influence of N_2 add-mixtures in the vibrational kinetics of CO_2 has also been recently shown both experimentally and by modelling *Terraz et al.* [2019]. Other publications focussed on the role of O atoms in CO_2 plasmas *Morillo-Candas et al.* [2019] or on the validation of the CO_2 electron impact dissociation cross section *Morillo-Candas et al.* [2020].

Part I

Description of the diagnostics and general characterization of the glow discharge

Chapter 2

Diagnostics for the characterization of CO_2 plasmas

Contents

2.1 Introduction **23**

2.2 Description of the discharges used **24**

2.2.1 Glow discharge reactor 24

2.2.2 RF reactor 25

2.2.3 Gas line 26

2.3 Diagnostics for the determination of the CO and CO_2 densities and their vibrational temperatures **27**

2.3.1 Fourier Transform Infra-Red (FTIR) spectroscopy 28

2.3.2 Raman spectroscopy 33

2.4 Diagnostics for the determination of the O atom density **36**

2.4.1 Actinometry 36

2.4.2 High Resolution - Two photon Absorption Laser Induced Fluorescence (HR-TALIF) 40

2.4.3 Cavity Ring Down Spectroscopy (CRDS) 47

2.5 Summary **51**

2.1 Introduction

This chapter details the diagnostics used for the experiments described throughout this thesis in addition to the data treatment process carried out to analyse the experimental data. The description of the diagnostics techniques is organized in this chapter according to the main gas phase species detected, however many of them also provide information about other plasma parameters. Moreover, several parameters were measured by more than one diagnostic technique, which allow us to confirm and cross check both the experimental results and the validity of the experimental approach in our discharge conditions. In following chapters, the experimental values obtained from different methods will be compared whenever possible. For every diagnostic a brief introduction of the basic principles

is given, followed by the experimental set-up details and the data analysis procedure. In the case of HR-TALIF, preliminary observations required for the data treatment of TALIF and Actinometry data are also included.

2.2 Description of the discharges used

Two different types of discharges were studied in a similar reactor configuration: a DC glow discharge and a capacitively coupled radio frequency (RF) discharge. In both cases the plasma reactors were 2 cm inner-diameter cylindrical Pyrex tubes closed by CaF_2 or BaF_2 windows at the sides. In the pressure range studied (0.2-7.5 Torr) both discharges develop an spatially homogeneous discharge (in the positive column in the case of the glow discharge), allowing line-of-sight integrated diagnostics techniques such as FTIR absorption or CRDS. A schematic representation of some of the reactors used for both discharges is shown in figure 2.1 (a). Three discharge regimes were explored with the glow discharge: continuous, partial-modulation and full-modulation (pulsed) regimes, schematically represented in figure 2.1 (b).

2.2.1 Glow discharge reactor

Several types of glow discharge reactors were used in the experiments described in this thesis. The basic reactor is represented in figure 2.1 (a.1). Two different reactor lengths were used, 67 cm for TALIF and CRDS and 23 cm for *in situ* FTIR and Raman experiments. Actinometry experiments were performed in both reactors. For continuous and modulated plasma experiments in general, and in particular for experiments studying surface processes in any discharge regime, a doubled-walled (DW) reactor was used to allow control of the wall temperature, T_{wall}, by circulating a mixture of distilled water and ethanol at a fixed temperature. T_{wall} was varied between -25^{o}C to 50^{0}C. Pulsed plasma experiments with FTIR absorption and Raman scattering were done in a single-walled (SW) reactor. Two other reactors were used: (1) a SW reactor surrounded by an insulator box. This reactor was used exclusively to reach wall temperatures down to -50^{o}C, by filling the box with a mixture or carbo-ice and ethanol (more details are given in section 8.5); (2) L-shaped reactor, represented in figure 2.1 (a.2), which allows to switch between *in situ* FTIR configuration, *i.e.* with the plasma volume in the path of the IR beam, and downstream FTIR configuration, where the IR beam diagnoses the effluent of the glow discharge. More details of these experiments are given in section 3.4.4.

The glow discharge was established between two cylindrical metallic electrodes located in perpendicular side tubes, 17 or 53 cm apart, depending on the tube length, in front of the gas in- and outlet. This configuration ensures that absorption measurements (line-of sight-integrated) are taken only through the positive column of the glow discharge. The anode was connected to a DC high voltage power supply (Fug) through a 4kΩ or 68 kΩ non-inductive ballast resistor. The axial electric field was determined from the voltage drop between two tungsten probes, embedded in the Pyrex tube, located 12 or 20 cm apart in the discharge reactor. The electric field measurements along with the values of the discharge current imposed in the power supply allow the calculation of the power dissipated in the positive column of the glow discharge. This power differs from the total power feeding the discharge due to the power dissipated in regions such as the cathode fall *Raizer* [1991].

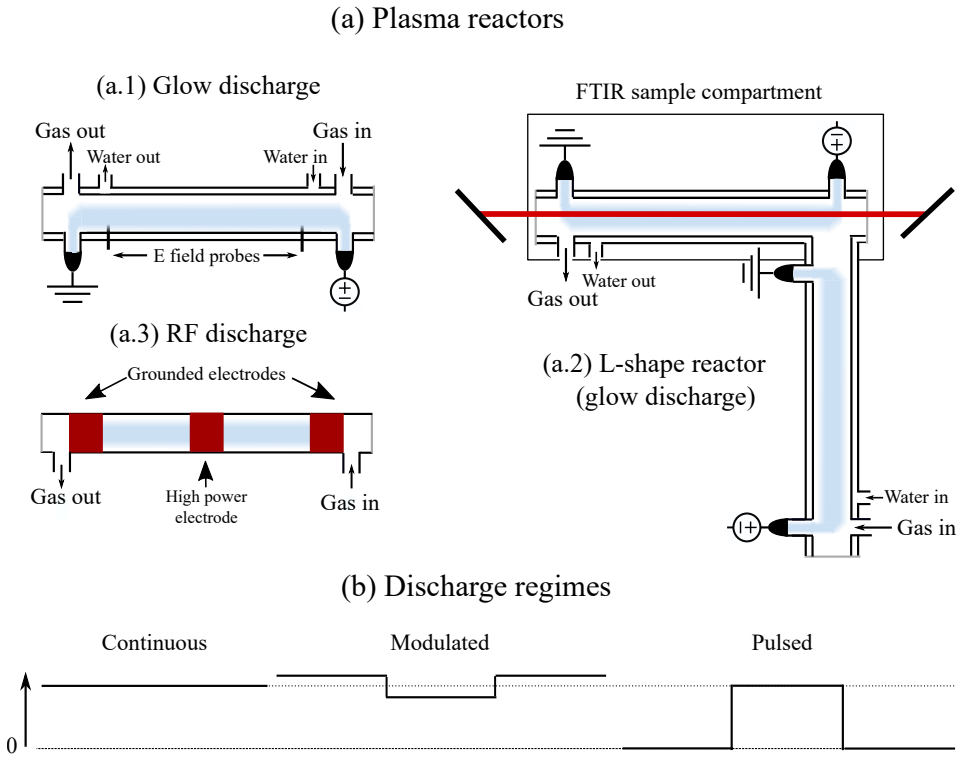

Figure 2.1: (a) Schematic representation of the basic plasma reactors used during the experiments: (a.1) usual short glow discharge reactor (doubled-walled (DW) in the figure), (a.2) DW L-shape glow discharge reactor used for the comparison of *in situ* and downstream FTIR data, with the representation of the IR beam of the FTIR and the sample compartment (see figure 2.5), (a.3) RF discharge reactor. (b) Schematic representation of the discharge regimes studied in the experiments.

The discharge current in continuous and pulsed discharges was varied between 10 and 50 mA. In partial-modulation experiments (for time-resolved actinometry), the discharge current was partially modulated using a circuit between the cathode and the ground comprising a 15 kΩ resistor in parallel with a transistor switch, triggered by a data acquisition card controlled with a Labview program. More details of the modulated regime and the actinometry set-up are given in section 2.4.1. For time-resolved pulsed glow discharge, the FTIR and the pulsed DC power supply were triggered by pulse generators (TTi, TGP110), producing square pulses with rise/fall times in the order of a few μs. The voltage along the plasma pulse was measured with a high-voltage probe (LeCroy, PPE 20kV) and the current was obtained from the voltage drop across a small resistor (18.4 Ω) connected in series with the glow discharge tube. The trigger signals for the FTIR and the power supply, and the voltage and current in the discharge were monitored with an oscilloscope (LeCroy, LT584M or Waverunner LT584M). The plasma was pulsed typically in a cycle of 5-10 ms On-Off. An example of the current and voltage measured in a pulsed CO_2 glow discharge at 5 Torr, 50 mA is given in figure 2.2. More details about the pulsed glow discharge are given in chapter 4.

2.2.2 RF reactor

The RF discharge was used for static measurements in the "building-up" experiment, thoroughly described and explored in chapters 6 and 7. The RF was more stable and easier to run than the glow

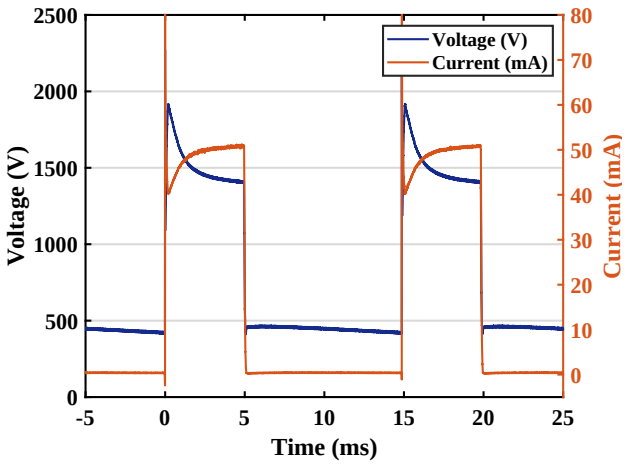

Figure 2.2: Voltage and current traces measured in the glow discharge in a pulsed plasma of 5-10 ms On-Off at 5 Torr, 50 mA.

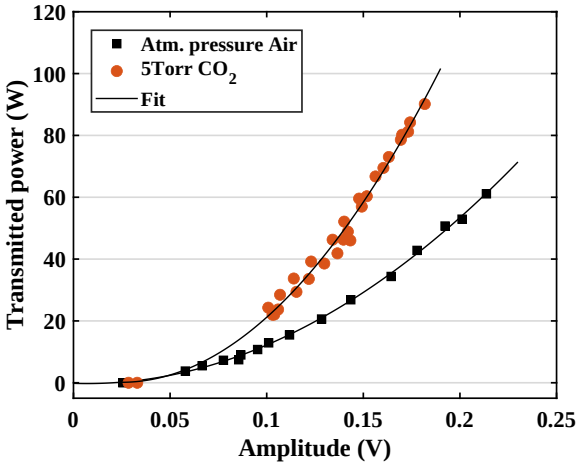

Figure 2.3: Power calibration curve of the RF discharge.

discharge in this experiment. A radio frequency generator (Advanced Energy, RFX 600) powers the reactor through a match box (custom-made by Solayl) at 13.6 kHz. The transmitted and reflected power were measured with a RF probe (Vigilant Power Monitor, Solayl SAS) placed between the RF generator and the match box. The RF power is transmitted to the plasma by a three-electrode system consisting in three copper sheets rolled around the Pyrex tube. Two grounded electrodes are located in the extremes of the reactor (15 cm apart) and one high power electrode is placed the middle. An schematic representation of the RF reactor is shown in figure 2.1 (a.3). This configuration helps to control the plasma volume (in between the two grounded electrodes) and the homogeneity of the discharge, and allows for a adequate calibration of the power dissipated in the plasma via subtraction method *Godyak and Piejak* [1990]. The calibration curve is given in figure 2.3. The amplitude in this curve corresponds to the current measured by a current probe (Pearson, 2868) placed around the high power electrode, which had a typical value of ∼3 A at 40 W imposed power. In our experiments, the power was varied typically between 40 and 80 W, reading powers, which correspond to real powers dissipated in the discharge ∼27.7, 36.3 and 44.2 W. An error ∼20%, is estimated for this power, based on the reproducibility of the amplitude measured with the current probe for similar plasma conditions, and on the slightly variable overall shape of the amplitude profile, particularly at the beginning of the pulse, for different plasma conditions and from pulse to pulse. FTIR was used as diagnostic technique for RF experiments. A "Faraday cage" was build around the plasma reactor to avoid any possible electromagnetic noise that could influence the performance of the FTIR.

2.2.3 Gas line

Most of the measurements were done in flowing conditions. The gas flow was set by Brooks SLA5850S1 or Bronkhorst F-201CV flow controllers) using gas from bottles of pure CO_2, CO, O_2, Ar and Xe (Air Liquide Alphagaz 1 for CO_2 and Ar, and Alphagaz 2 for O_2 and Xe). Unless otherwise specified the constant total gas flow was 7.4 sccm. The pressure in the tubes was varied between 0.2 and 7.5 Torr, and it was measured with a capacitance manometer (Pfeiffer CMR263/

MKS 122AA). The gas was evacuated by a scroll pump (Edwards, XDS35) through a pressure-regulating valve (Pfeiffer EVR116 + controller RVC300). For measurements in static conditions, *i.e.* without gas flow, a buffer volume was installed in parallel to the reactor to prepare gas mixture in isotopic measurements and to by-pass the reactor when needed. More details are given in chapters 6 and 7.

2.3 Diagnostics for the determination of the CO and CO_2 densities and their vibrational temperatures

The main diagnostic technique to study the dissociation fraction in CO_2 plasmas will be Fourier Transform Infra-Red (FTIR) spectroscopy. This diagnostic provides not only information about the densities of both CO_2 and the main dissociation product CO, but also the vibrational temperatures of CO_2 and CO and the rotational temperature of both molecules. FTIR is a line-of-sight integrated technique, that requires homogeneous plasma conditions and it is therefore ideal to study the positive column of the glow discharge. Another experimental technique that provides similar information is rotational Raman scattering, able to measure the rotational temperature and number densities of CO_2, CO and O_2 molecules. Raman scattering presents two main advantages in comparison with FTIR: the spatial resolution, which gives the possibility to study the homogeneity of the positive column and the longitudinal profile and the possibility of measuring *in situ* O_2 densities. O_2 is not infra-red active and therefore cannot be detected with FTIR. However, rotational Raman scattering experiments at the working pressures are challenging. In addition, only the symmetric stretch vibrational mode of CO_2 is Raman active. The technique can provide an estimation of the overall degree of vibrational excitation, but it cannot give population densities of vibrational levels for the asymmetric stretch and bending modes. Both diagnostics are therefore complementary and were carefully compared in *Klarenaar et al.* [2018, 2019].

Similar parameters can be measured with other diagnostic not explored in this thesis, such as quantum cascade lasers (QCL) *Röpcke et al.* [2012] or tunable diode lasers (TDL), which have been frequently used to determine vibrational level densities in CO_2 lasers *Dang et al.* [1982]. These systems scan very narrow frequency ranges (in the order of single wavenumbers) and are a good tool to diagnose high vibrational levels *Dang et al.* [1983] due to the high spectral resolution, contrary to broadband absorption sources. At low pressure, QCL measurements can also be affected by the rapid passage effect, which modifies the shape of each absorption line depending on the scan speed of the laser *Welzel et al.* [2010]. QCL lasers could provide measurement with high time resolution (typically down to 100 ns). However, to determine both rotational and vibrational temperatures of CO and CO_2, the narrow bandwidth and the complex line shape seemed more difficult than FTIR, as a first approach. In future work higher vibrational levels requiring better signal to noise ratio could be reached with new generation of IR lasers (such as External Cavity QCL) or even frequency combs. These measurements would be very complementary with the work presented here. We could also have performed IR spectroscopy in emission with the same FTIR spectrometer. It would have the advantage of the spatial resolution and it would allow the determination of the vibrational state absolute densities providing similar information as IR absorption *Plönjes et al.* [2000]; *Depraz et al.* [2012b, a]. However, the absolute values would depend on a proper accounting of the "self absorption" and the spatial resolution would depend on the precision of the light collection optics.

Broadband IR absorption spectroscopy seems therefore a good compromise to measure at once a large frequency range with a spectral resolution that is lower than with laser-based diagnostics, but high enough for an accurate determination of vibrational state densities in a low excitation regime as is the case for the plasma sources used in this thesis.

2.3.1 Fourier Transform Infra-Red (FTIR) spectroscopy

Principles

A FTIR spectrometer is a Michelson interferometer allowing to measure interferograms on a large bandwidth of infra-red light. By doing a Fourier transform, a broadband spectrum can be determined with a relatively good spectral resolution. The IR spectral range is used to take advantage of the large line strength of molecular ro-vibrational transitions. When the beam of the FTIR passes through an active medium, as for any absorption technique the decrease of light intensity, in absence of non-linear effects, is given by the Lambert-Beer law:

$$I(\nu) = I_0(\nu) \cdot exp(\sum_j n_j \sigma_j \times L) \qquad (2.1)$$

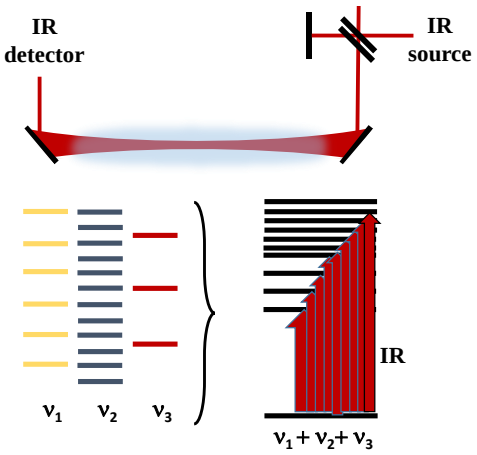

Figure 2.4: FTIR scheme

where $I(\nu)$ is the intensity after passing through the medium, $I_0(\nu)$ the intensity before, n_j is the density of absorbing species j, $\sigma(\nu)$ is the absorption cross section of a transition of species j and L is the absorption path length. The absorption cross section can be expressed as:

$$\sigma_j(\nu - \nu_0) = S(T) \cdot (\phi(\nu - \nu_0)) \qquad (2.2)$$

where $S(T)$ is the line strength of the transition and $\phi(\nu - \nu_0)$ is the normalised line profile, determined by the natural line width and the broadening of the line given by instrumental broadening along with temperature broadening (Gaussian profile) or pressure (Lorentzian). When the cross section of the absorbing medium is known, the density of absorbing species can be directly determined from the ratio of $I(\nu)$ and $I_0(\nu)$ without any calibration procedure.

The CO_2 molecule has three vibrational modes. The vibrations corresponding to the bending and the asymmetric stretch modes are infra-red active, since they induce an dipole moment in the CO_2 molecule. The CO molecule, created in the dissociation process, also presents infra-red active vibrations corresponding to a single vibrational mode. Therefore the densities of ground state and ro-vibrationally excited CO_2 and CO molecules can be detected by FTIR absorption.

Experimental set-up and measurement procedure

FTIR measurements were performed with an FTIR spectrometer (Bruker, Vertex 70), with a spectral resolution of 0.2 cm^{-1}. The diaphragm aperture was set to 2.5 mm. The experimental set-up for *in situ* measurements with a short plasma reactor (23 cm length maximum) positioned in the sample compartment of the FTIR is shown schematically in figure 2.5. For basic continuous plasma experiments, the FTIR was operated in conventional mode, averaging 20 scans. For time-resolved

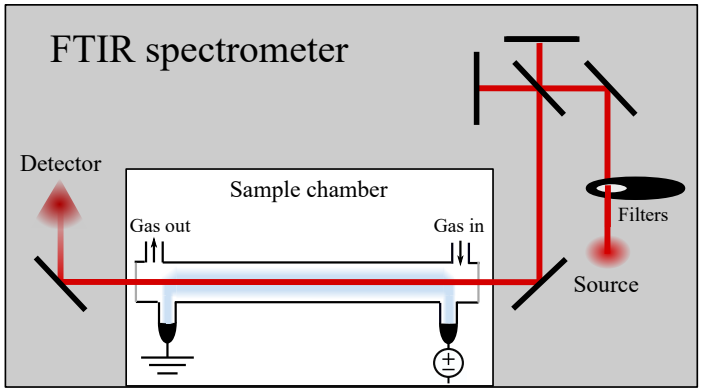

Figure 2.5: Schematic representation of the experimental set-up used for the FTIR experiments.

pulsed plasma measurements, the FTIR is operated in Step-scan mode. In this mode, the interferometer assumes a mirror position, relaxes for a certain time set to 60 ms and waits for a trigger signal. After receiving a trigger, the DC signal of the IR detector is repetitively read out with a certain period defined by the time resolution. The time-resolution and the number of time slices were set to 10 μs and 1100 respectively in most of our time-resolved experiments, which results in a measured time period of 11 ms. Each of these series per interferometer position was average four times. Subsequently, the mirror of the interferometer moves to the next position (53.323 in total), and the procedure is repeated. The Fourier transform of the 2D interferogram gives a time-resolved absorption spectrum of 10 μs time resolution. The Step-scan mode will be used to study the time evolution of the vibrational excitation of CO_2 and CO in chapters 4 and 5. The FTIR can also be operated in a Rapid-scan mode. In this case, the FTIR scanning process is similar as in conventional mode but we can define a "method", which consists on a small set of lines of code describing an experiment and allowing for instance to use FTIR as a trigger for the plasma. In this mode, the FTIR completes the whole experiment detailed in the method, before the Fourier transform is done, allowing to follow a relatively fast chain of events. This FTIR working mode will be used only in the so-called "building-up" experiments. More details are given in chapters 6 and 7. In the case of *in situ* plasma ON measurements, the infra-red light arriving to the detector is a combination of three contributions:

- Light emitted by the IR source of the FTIR spectrometer, going through the interferometer and then through the plasma reactor, where is partially absorbed, towards the detector.
- Spontaneous emission from the plasma, directly emitted towards the detector.
- Spontaneous emission from the plasma that first enters the interferometer and is reflected back through the reactor towards the detector.

The light emitted from the plasma directly towards the detector is not spectrally resolved and only induces an offset in the interferogram that disappears after the Fourier transformation. However, the plasma emission that is reflected towards the interferometer and subsequently reabsorbed by the plasma is spectrally resolved since it depends on the position of mirror of the interferometer. The absorption spectrum should be corrected for this contribution. Therefore, in order to

obtain the final absorption spectrum, two complementary measurements must be performed: an absorption measurement, taken with the infra-red source of the interferometer ON, and an emission measurement performed with the infra-red source OFF and placing a black filter in front of the IR source, in order to record the plasma emission spectrum. Background measurements are taken after purging the reactor with N_2, providing the spectral profile of the IR source. The emission spectrum is subtracted from the absorption spectrum and the final transmittance is obtained by dividing the remainder by the background profile of the IR source. Downstream measurements were also performed during this thesis either by passing the effluent from the discharge through a measurement cell placed in the sample compartment of the FTIR or by using the L-shape reactor (see figure 2.1 (a.2)). These experiments were done for the comparison of downstream and *in situ* data and in order to check that the dissociation fractions obtained with both long and short plasma reactors are similar for a given gas residence time (more details are given in section 3.4).

Data treatment

The IR spectra studied all along this thesis corresponds to absorption bands of the asymmetric stretch of CO_2 (between ~2200 cm^{-1} and ~2400 cm^{-1}) corresponding to all the transitions absorbing a photon changing the ν_3 level and the CO ro-vibrational band (between ~2000 cm^{-1} and ~2250 cm^{-1}). These bands can be fitted to obtain information on densities of each ro-vibrational level of these two molecules. However, vibrational excitation of CO_2 and CO is commonly described by the corresponding vibrational temperatures T_ν, which will be widely used along this thesis. The concept of vibrational temperature relies on the assumption that the vibrational level populations of each vibrational mode can be characterized by a certain distribution, which in thermal equilibrium is a Boltzmann distribution but that may differ under non-equilibrium conditions and follow a so-called Treanor distribution for the low energy levels *Treanor et al.* [1968]; *Dang et al.* [1982] (at energies close to the dissociation energy, the vibrational levels can be more depopulated and their population deviates from a Treanor distribution).

In practice, the obtained FTIR spectra are fitted with a MATLAB script developed by B. Klarenaar which can either fit individual population densities of vibrational levels, or take advantage of the assumption of a vibrational distribution. Here we only summarize the main characteristics and approximations done with regard to the data treatment process. More details about the fitting algorithm are given in *Klarenaar et al.* [2017] and in his PhD thesis. Several versions of the script were used to treat different types of data:

- **Equilibrium script**: It fits molecules included in HITRAN database *Gordon et al.* [2017] assuming thermal equilibrium. Therefore, this script is used only to fit data acquired in plasma OFF, either in spatial (downstream) or temporal post-discharge. The script is ready to fit molecules such as NO, NO_2 N_2O, H_2O, O_3, CH_4, C_2H_2 and other hydrocarbons, which are out of the scope of this thesis. The script will be mostly used to fit molecular densities of different isotopes of CO_2 (12 isotopes of CO_2 and 6 isotopes of CO), recently added in HITRAN database and to the script. More details are given in chapter 7. Hereinafter this version will be called "**thermal script**".
- **Out of equilibrium script with free fitting of the vibrational population densities**. The algorithm uses the information contained in HITEMP-2010 database *Rothman et al.*

Symbol	Description	Guess value
T_{rot}	Rotational temperature	600 [273,2000] K
$T_{1,2}$	Vibrational temperature of ν_1 and ν_2 modes of CO_2	600 [273,4000] K
T_3	Vibrational temperature of the ν_3 mode of CO_2	600 [273,8000] K
T_{CO}	Vibrational temperature of CO	600 [273,8000] K
c_{Tth}	Thermal variable	0.1 [0,1]
α	Dissociation fraction	0.3 [0,1]
P	Pressure	PressureSet [0.1,50] Torr

Table 2.1: List of fitting parameters in the FTIR data treatment script, including symbol, description, and guess value with the fitting interval.

[2010], concerning transition energies, Einstein coefficients, broadening constants, etc. to calculate the line strength (see equation (2.2)) and the population densities of vibrational levels corresponding to the three vibrational modes ν_1, ν_2 and ν_3, using the information corresponding to the ro-vibrational transitions up to ν_3=6→7 for CO_2 and up to ν=14→15 for CO, in addition to the rotational temperature T_{rot} and the conversion factor α. Note that only transitions corresponding to ν_3 fall in the IR region examined, but these transitions are enough to diagnose all the modes because of the coupling of the different levels ($(\nu_1, \nu_2^{l_2}, \nu_3) \rightarrow (\nu_1, \nu_2^{l_2}, (\nu_3 + 1))$). The script will be called hereinafter "**OoE Free script**".

- **Out of equilibrium script with imposed vibrational population distribution** (hereinafter called **Treanor OoE (TOoE)** script). The script is similar to the previous version (OoE Free) but it imposes a Treanor distribution to obtain the population of the vibrational levels for the three vibrational modes of CO_2, bending, symmetric and asymmetric stretch. It also assumes that the bending and the symmetric modes are Fermi coupled, *i.e.* T_1=T_2=$T_{1,2}$. This script is extensively discussed in *Klarenaar et al.* [2017].

It is worth mentioning that the values of T_{rot}, α and the vibrational temperatures deduced from the population densities obtained by the OoE Free script are in very good agreement with those from the Treanor OoE fitting *i.e.* the Fermi resonance is directly observed in the data and not artificially imposed. As default, the *in situ* plasma ON FTIR spectra will be treated with the Treanor OoE script, and only in few cases that will be pointed out in the text, the OoE Free script will be used.

Several assumptions are made in the code: The energies of vibrational states and rotational states are assumed to be independent, common approximation in literature for lower vibrational levels. The distributions over rotational levels are assumed to be Maxwellian (described by T_{rot}). The script makes the assumption that the rotational temperature is the same for CO_2 and CO molecules and that it is equal to the translational temperature *Dang et al.* [1982]. This assumption is verified in section 3.2.1.

The list of fitting parameters, the guess values and the fitting intervals are given in Table 2.1. The dissociation fraction, α, is defined as:

$$\alpha = \frac{[CO]}{[CO] + [CO_2]} \tag{2.3}$$

and assumes that the number densities of CO and CO_2 are described by the reaction:

$$CO_2 \rightarrow CO + \frac{1}{2}O_2 \tag{2.4}$$

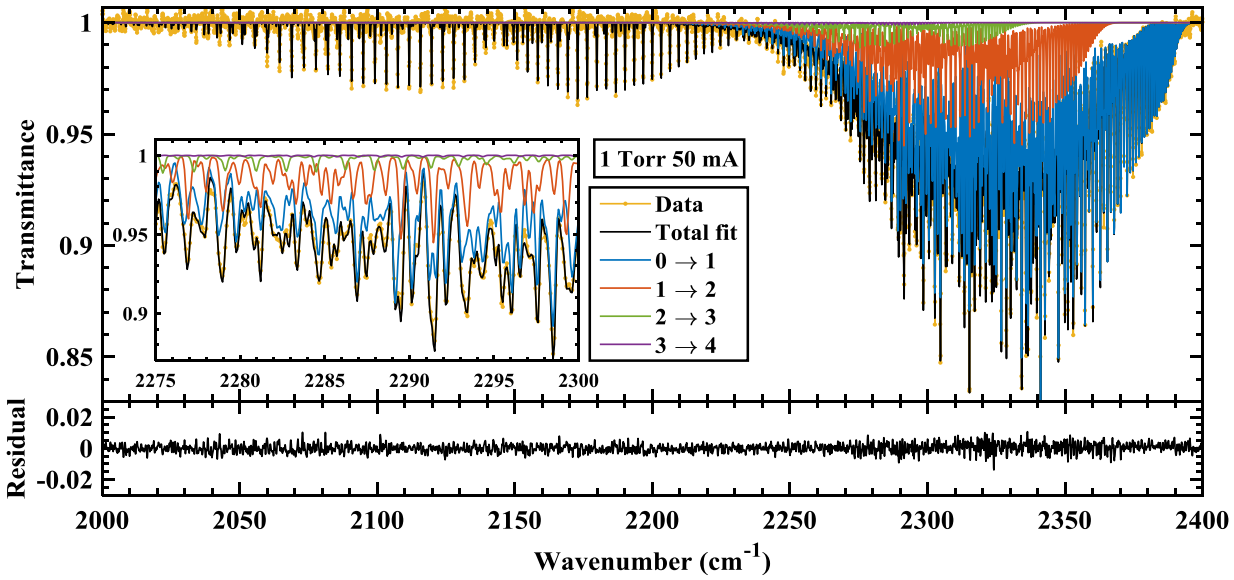

Figure 2.6: Example of an FTIR spectra, background and emission corrected, taken at 1 Torr 50 mA in the glow discharge in a pulsed plasma (5-10 ms On-Off) at t=4.9 ms after the beginning of the pulse, and the corresponding fit detailing the contributions of the different transitions to the CO_2 spectra. The inner figure shows a zoom for a narrower wavenumbers range. The residual of the fit is included in the bottom panel.

The fraction of O_2 is assumed to be equal to half the fraction of CO, *i.e.* all the O atoms are assumed to be recombined into O_2. The fractions of CO and CO_2 can then be calculated with the expressions:

$$f_{CO_2} = \frac{1-\alpha}{1+\alpha/2} \qquad f_{CO} = \frac{\alpha}{1+\alpha/2} \tag{2.5}$$

The fact that the electrodes are not in the extremes of the discharge tube but in perpendicular side tubes (see figure 2.5), implies that there is a certain volume in the plasma reactor, between the electrodes and the windows, not filled by the plasma. The properties of the gas in this volume, which is in the absorption path of the FTIR beam, are significantly different than in the discharge. To account for this difference, a parameter so-called thermal volume was introduced. In this volume all the temperatures are assumed to be in thermal equilibrium at a temperature T_{th}. The temperature in the thermal volume, T_{th}, is fitted using a thermal variable c_{Tth} defined as a function of the rotational temperature T_{rot} such that T_{th} is always between 273 K and the rotational temperature in the discharge volume, according to the expression:

$$T_{th} = c_{Tth} \cdot (T_{rot} - 273K) + 273K \tag{2.6}$$

It is possible to keep the thermal volume as fitting parameter, but it increases the fitting time and the noise in the fitting. Hence, it was fixed according to the fraction determined from the positions of the electrodes. The effect of including or not this thermal volume is discussed in detail in *Klarenaar et al.* [2017]. The pressure and the fractions of CO and CO_2 are considered equal in both the thermal gas and the non-thermal plasma. It is worth mentioning that imposing a value of the thermal volume=1 in the Treanor OoE script (imposing that all the gas is in thermal

equilibrium) is possible to fit gas in thermal equilibrium (plasma OFF) and the results obtained are similar to those obtained with thermal script.

Figure 2.6 shows an example of a *in situ* FTIR spectra measured at 1 Torr, 50 mA in a pulsed plasma (5-10 ms On-Off) at t=4.9 ms after the beginning of the pulse and the corresponding fit (TOoE). The residual of the fit is included in the bottom panel. The data is shown in orange (the dots represent the individual data points) and the total fit is shown in black. Lines between 2250 and 2400 cm^{-1} correspond to the CO_2 absorption band, whereas lines between 2100 and 2250 cm^{-1} belong to CO. The inner figure shows a zoom of the CO_2 band where the coloured lines represent the individual contributions of transitions $CO_2(\nu_1, \nu_2^{l_2}, \nu_3) \rightarrow CO_2(\nu_1, \nu_2^{l_2}, (\nu_3+1))$. Although the fitting script accounts for transitions up to ν_3=7, already the transition ν_3=3→ν_3=4 shows a negligible contribution to the spectra.

The sensitivity of the fitted transmittance to the different temperatures gives an indication of their error, which was estimated as 30 K and 27 K for T_{rot} and $T_{1,2}$ respectively, 67 for T_3 and 357K for T_{CO} *Klarenaar et al.* [2017]. The accuracy with which T_{CO} is determined is significantly less than for the other temperatures and below 500 K the peaks in spectra corresponding to vibrationally excited CO are at the noise level.

2.3.2 Raman spectroscopy

The Raman scattering set-up is installed in the laboratory of Richard Engeln in Eindhoven University of Technology (Technische Universiteit Eindhoven, TU/e). Most of the experimental data was taken by Bart Klarenaar and Marija Grofulović. In this context, the contribution can be summarized as helping in the installation of the experimental set-up and in the direct acquisition of data during a measurement campaign of 1 month in TU/e. The data measured in a pulsed glow discharge has been included here for the comparison between FTIR and Raman techniques and will not be discussed in detail, more information can be found in *Klarenaar et al.* [2018, 2019]. Additionally, new data taken in continuous plasma is presented in this thesis with the same purpose: to compare with other diagnostic techniques providing information about the same plasma parameters, for instance HR-TALIF or CRDS, and as extra validation of the measured values. Only a brief introduction of the experimental set-up and the data treatment process is given. More details on the experiments and the data treatment can be found in *Brehmer et al.* [2015]; *Klarenaar et al.* [2015, 2018]; *Grofulović et al.* [2019] and in the PhD thesis of Bart Klarenaar and Marija Grofulović. Theoretical information about Raman spectroscopy in which the data treatment process is based, can be found in *Long* [2002]; *Hoskins* [1975]; *Chedin* [1979].

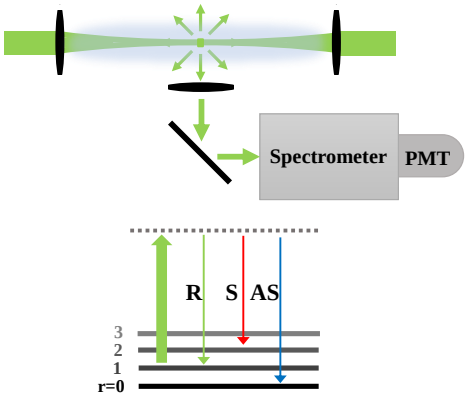

Figure 2.7: Raman scheme

Raman scattering experimental set-up

Figure 2.8 (a) shows an schematic representation of the Raman scattering set-up extracted from *Klarenaar et al.* [2018]. The beam of a Nd:YAG laser (SpectraPhysics, Quanta-Ray, Lab-190-100),

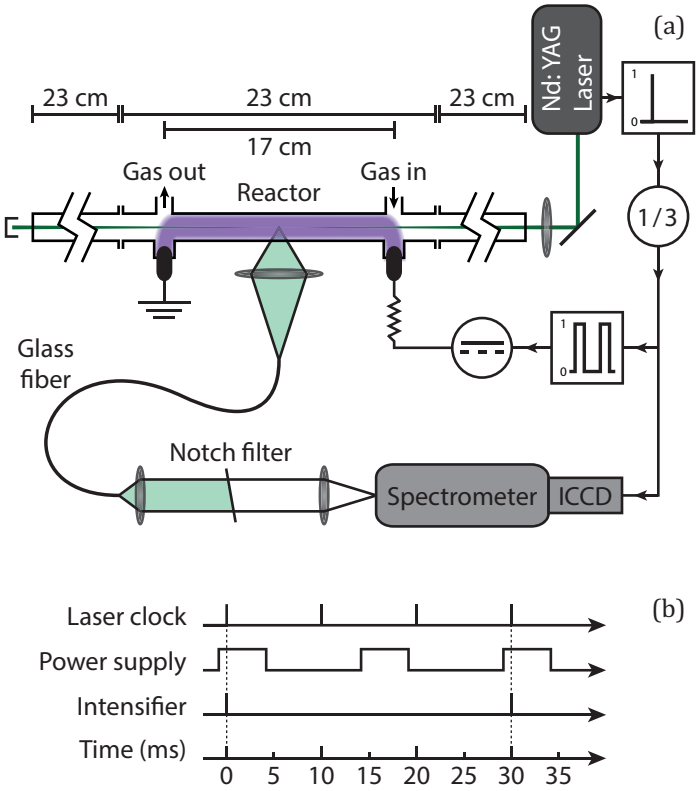

Figure 2.8: (a) Schematic representation of the Raman scattering set-up and (b) trigger scheme, including the laser clock, which provides the trigger for the power supply and for the intensifier of the ICCD camera. Figure extracted from extracted from *Klarenaar et al.* [2018].

operating at 100 Hz with 140 mJ per laser pulse is frequency doubled (532 nm) and focused in the centre of the short glow discharge reactor (the beam waist in the focus was 70 μm). Two Pyrex cylinders (23 cm length) were connected in both sides of the reactor to avoid damaging the anti-reflective coated windows by the laser. The distance between the electrodes remains unchanged, not varying the residence time of the molecules under plasma exposure. The scattered light is collected perpendicularly to the laser beam direction, focused into an optical fiber and collimated to pass through an ultra-narrow-band notch filter (OptiGrate, BragGrage, BNF-532-OD4-12.5M), in order to remove Rayleigh scattered and stray light (FWHM 0.2nm=7 cm^{-1}) *Klarenaar et al.* [2015, 2018]. The remaining light is focused into the entrance slit of spectrometer (Jobin-Yvon, HR 640) to an intensified ICCD camera (EPM102G-04-22F, KATOD + Bigeye G-132B Cool, Allied Vision) with a spectral resolution of 0.143 cm^{-1} and a frequency range of 193 cm^{-1}. The instrumental broadening presents a Voigt profile with a FWHM of 1.55 cm^{-1}.

Raman scattering experiments were performed in both continuous and pulsed plasma. In the latter case the discharge was pulsed with 5-10 ms plasma On-Off cycle, *i.e.* a plasma duty cycle ratio of 33.3 Hz. The laser clock provides the trigger for both the plasma power supply and the intensifier of the camera for the data acquisition. To match the laser at 100 Hz with the plasma pulses, the intensifier of the camera is gated only once every three laser pulses and once out of two plasma pulses. The trigger scheme is shown in figure 2.8 (b). In order to vary the measurement time-point in time-resolved pulsed plasma experiments a delay is imposed between the laser clock and the plasma pulse. The detection point along the longitudinal axis of the plasma reactor (to study the spacial homogeneity) is varied by translating the reactor with respect to the focal point of

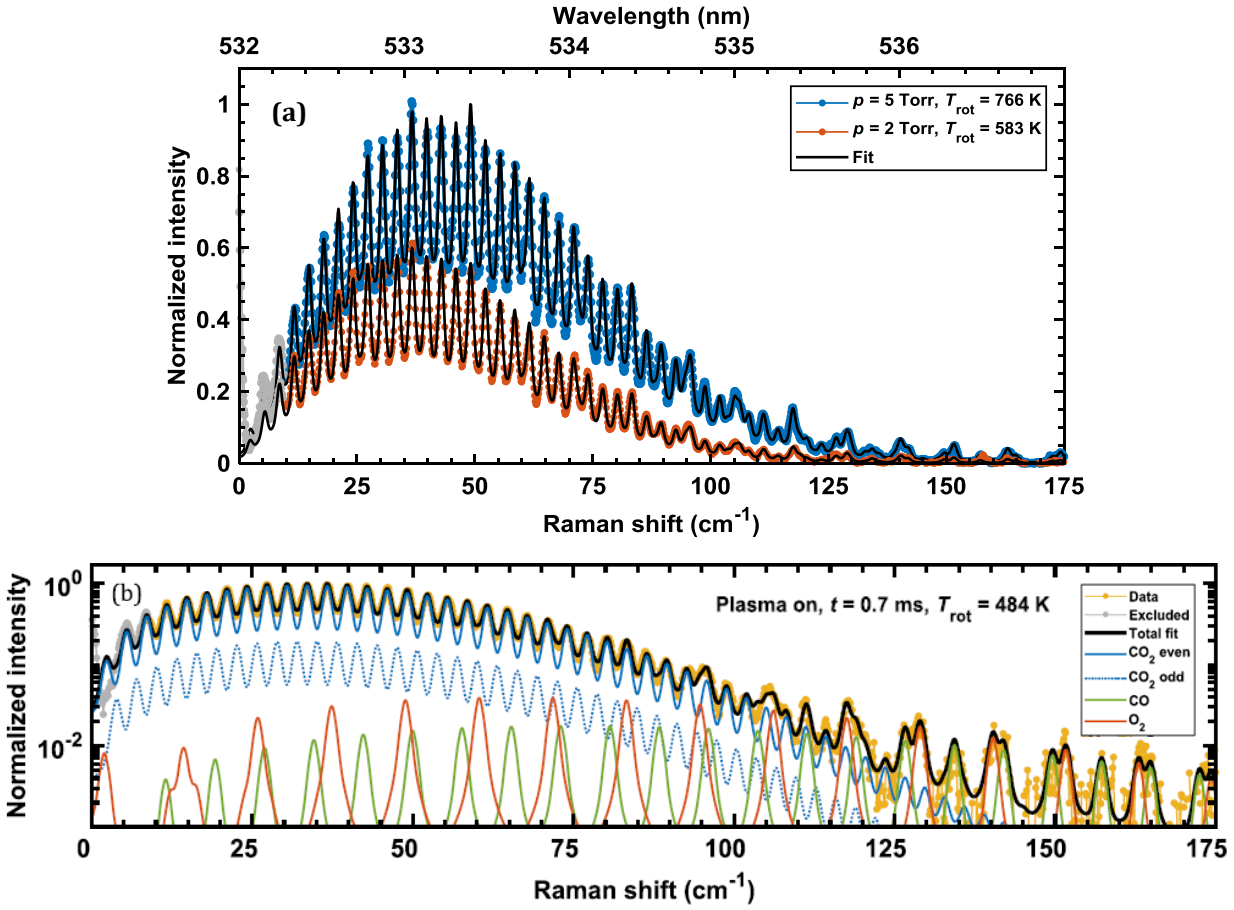

Figure 2.9: (a) Raman stokes spectra taken in continuous plasma at 2 and 5 Torr, 40 mA and the corresponding fits. (b) Raman stokes spectra taken in a pulsed plasma of 5-10 ms On-Off at 0.7 ms after the beginning of the plasma pulse and the corresponding fit, detailing the contribution of the CO_2 odd and even peaks, CO and O_2. Figure (b) is extracted from *Klarenaar et al.* [2018].

the laser. Note that the longitudinal profile along the axis of the discharge reactor can be diagnose in this way, but it is not possible to measure radial profiles due to the focalized beam used for the Raman scattering experiments. More details on the experimental set-up can be found in *Klarenaar et al.* [2018].

Data treatment and measured quantities

The Stokes branch of the Raman spectra is recorded and analysed using an algorithm described in detail in *Klarenaar et al.* [2018], which has five fitting parameters: T_{rot}, describing the densities of rotational levels assuming a Maxwellian distribution, the number densities of CO_2, CO, and O_2, obtained from their scattering contributions and the odd average nuclear degeneracy of CO_2. Excitations of vibrational modes affect the symmetry of the molecule and therefore its nuclear degeneracy *Klarenaar et al.* [2018]. The rotational Raman spectrum of CO_2 is affected by the vibrational temperatures $T_{1,2}$ and T_3 through the nuclear degeneracies of even and odd rotational states *van den Bekerom et al.* [2018], impacting the intensity ratio between even and odd rotational peaks. The ratio can therefore be used to study the vibrational excitation. Comparing the fitted odd vibrationally averaged nuclear degeneracy to the expected thermal averaged degeneracy (T_{vib}=T_{rot}),

it is possible to give estimation of the level of vibrational excitation. The use of rotational Raman scattering for the study of vibrational excitation of CO_2 molecules will not be discusses in this thesis, but the estimated vibrational excitation is in good agreement with the vibrational temperatures measured with FTIR (see *Klarenaar et al.* [2019]).

Figure 2.9 (a) shows an example of a Raman stokes spectra taken in continuous plasma at two different pressures (2 and 5 Torr) and therefore at very different rotational temperatures, as illustrative example of the effect of T_{rot} on the Raman spectra (the evolution of the rotation temperature as a function of pressure is discussed in section 3.2). Figure 2.9 (b) shows the example of a spectra taken during a pulsed plasma of 5-10 ms On-Off at t=0.7 ms after the beginning of the plasma pulse (maximum of vibrational excitation, as discussed in chapter 4) and the corresponding fit detailing the contribution of the CO_2 odd and even peaks, and of CO and O_2 to illustrate the scattering contributions of CO_2, CO, and O_2, and the even/odd peaks ratio.

2.4 Diagnostics for the determination of the O atom density

Three different diagnostic techniques were used to determine the atomic oxygen density in continuous, modulated and pulsed DC glow discharges: Actinometry, High-Resolution Two photon Absorption Laser Induced Fluorescence (HR-TALIF) and Cavity Ring Down Spectroscopy (CRDS). These techniques will be discussed in detail to assess the level of accuracy of the absolute O atom densities obtained, both in this section and in section 3.5. In addition to the O atom density, HR-TALIF and CRDS provide values of the translational temperature of the oxygen atoms, which will be compared to the rotational temperature of CO_2, CO (and O_2) provided by FTIR and Raman spectroscopy in section 3.2.

2.4.1 Actinometry

Principles

Actinometry is a widely used emission spectroscopy technique described extensively in literature and originally developed for atomic fluorine *Coburn and Chen* [1980]. With actinometry, the density of a reactive species of interest is determined from the ratio of the intensity of emission from an excited state of the probed species to that from a rare gas (actinometer), which is added in small amount to the gas mixture. It assumes that the observed emitting electronically excited states are predominantly populated by electron impact from the ground state. In this case, the observed emission intensity is given by *Pagnon et al.* [1995]:

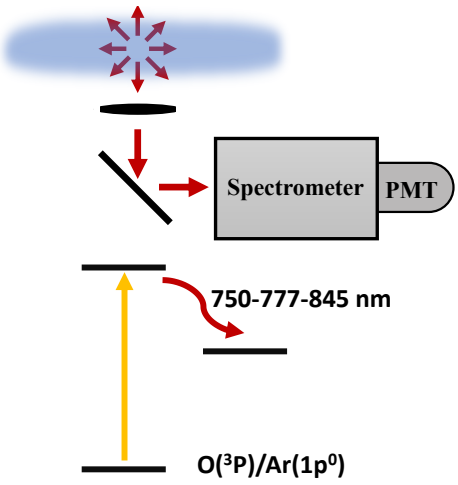

Figure 2.10: Actinometry scheme

$$I_X = C_X \cdot h\nu_{ij}^X \cdot k_e^X \cdot n_e \cdot \frac{A_{ij}^X}{\sum A_i^X + \sum_Q k_Q^X [n_Q]} [n_X] \quad (2.7)$$

where C_X is a constant dependent on the detection system, in our case calculated with the calibration

Excitation processes	De-excitation processes
Electron impact	Radiative de-excitation
$O(2p^4\,{}^3P) + e \xrightarrow{k_e^{3P}} O(3p\,{}^3P) + e$	$O(3p\,{}^3P) \xrightarrow{A_{ij}^{3P}} O(3s\,{}^3S) + h\nu(844.6\,nm)$
$O(2p^4\,{}^3P) + e \xrightarrow{k_e^{5P}} O(3p\,{}^5P) + e$	$O(3p\,{}^5P) \xrightarrow{A_{ij}^{5P}} O(3s\,{}^5S) + h\nu(777.4\,nm)$
$Ar(1p^0) + e \xrightarrow{k_e^{2P_1}} Ar(2p_1) + e$	$Ar(2p_1) \xrightarrow{A_{ij}^{2P_1}} Ar(1p_0) + h\nu(750.4\,nm)$
Dissociative excitation	Quenching processes
$O_2 + e \xrightarrow{k_{de}^{3P}} O + O(3p\,{}^3P) + e$	$O(3p\,{}^3P) + Q \xrightarrow{K_Q^{3P}} O(3s\,{}^3S) + Q$
$O_2 + e \xrightarrow{k_{de}^{5P}} O + O(3p\,{}^5P) + e$	$O(3p\,{}^5P) + Q \xrightarrow{K_Q^{5P}} O(3s\,{}^5S) + Q$
	$Ar(2p_1) + Q \xrightarrow{K_Q^{2P_1}} Ar(1p_0) + Q$

Table 2.2: Excitation and de-excitation processes taken into account for actinometry calculations.

factors described in section 2.4.1, $h\nu_{ij}$ is the energy of the emitted photons, n_e is the electron density and $[n_X]$ is the density of the atoms in the ground state. k_e^X is the excitation rate coefficient, calculated with the expression *Hagelaar and Pitchford* [2005]:

$$k_e^X = \left(\frac{2e}{m}\right)^{1/2} \int_{\epsilon_{th}}^{\infty} \sigma_i(\epsilon) f(\epsilon) \epsilon d\epsilon \tag{2.8}$$

where $\sigma_i(\epsilon)$ is the collision cross section with threshold energy ϵ_{th} for the excitation of the level i and $f(\epsilon)$ is the electron energy distribution function (EEDF), normalized by $\int_0^\infty f(\epsilon)\epsilon^{1/2} d\epsilon = 1$. The effective branching ratio is:

$$a_{ij}^X = \frac{A_{ij}^X}{\sum_i A_i^X + \sum_Q k_Q^X [n_Q]} \tag{2.9}$$

This term represents the ratio of the detected emission to the sum of all de-excitation processes, where A_{ij}^X is the Einstein coefficient for the measured transition and $\sum A_i^X$ is the sum over all the possible radiative de-excitation processes. The ratio $A_{ij}^X / \sum A_i^X$ is the pure optical branching ratio. $k_Q^X [n_Q]$ represents the non-radiative de-excitation processes, where k_Q^X is the rate coefficient for collisional quenching by species Q of density $[n_Q]$. In the case of oxygen-containing plasmas, dissociative excitation can also be a significant source of emitting atoms. This can be taken into account by substituting the term $k_e^X [n_X]$ in equation (2.7) by $k_e^X [n_X] + k_{de}^O [O_2]$, where k_{de}^O is calculated with equation (2.8) with the corresponding cross section. Rearranging the different terms and using argon as actinometer, the O atom density can be obtained from the expression *Tsutsumi et al.* [2017]:

$$[O] = \frac{I_O}{I_{Ar}} \frac{C_{Ar} \cdot h\nu_{ij}^{Ar}}{C_O \cdot h\nu_{ij}^O} \frac{k_e^{Ar}}{k_e^O} \frac{a_{ij}^{Ar}}{a_{ij}^O} \cdot [Ar] - \frac{k_{de}^O}{k_e^O} [O_2] \tag{2.10}$$

where the last term in equation (2.10) represents the contribution of dissociative excitation. Therefore, the calculation includes excitation through electron impact and dissociative excitation of O_2 by electron collisions, along with radiative and non-radiative (quenching) de-excitation processes (see table 2.2).

Actinometry set-up

The atomic oxygen (777.4 and 844.6 nm, hereinafter O777 and O845) and argon (750.4 nm, Ar750) emission intensities were collected perpendicular to the reactor axis (see schematic representation of actinometry and TALIF set-ups in figure 2.12), by a collimating lens with the focal point at the centre of the discharge tube. The collimated beam was steered by mirrors and focused into the entrance slit of a spectrometer (Princeton Isoplane STC-320). The light at the output slit was detected with an IR-sensitive photomultiplier (Hamamatsu H7422-50) and recorded by a data acquisition card (National Instruments NI-USB-6210). The fraction of argon in the total gas mixture was kept constant at 5% in order to minimize its effect on the CO_2 plasma dynamics.

The wavelength dependence of the relative sensitivity of the full optical detection system was calibrated for the three emission lines used for actinometry. The infra-red output of a single-mode continuous Ti:Sa laser described in section 2.4.2 was directed through the discharge tube following the same optical path as the light emitted by the plasma. The power of the laser was attenuated by using several beam splitters, and a diffuser (Thorlabs) was used to reproduce a diffuse light source. The diffused light was focussed into the entrance slit of the spectrometer. The response of the beam splitters and the diffuser was checked, and showed the same response for the three wavelengths studied. With no plasma in the discharge tube, and using constant laser power, the relative intensities of the signals obtained at each wavelength were recorded, providing two correction factors ($I_{O777}/I_{Ar} = 1.44$ and $I_{O845}/I_{O777} = 3.20$) that were applied to the actinometry formula (equation (2.10)).

Data analysis

The cross sections used to calculate the excitation rate coefficients for direct electron impact and dissociative excitation for oxygen were taken respectively from Laher *Laher and Gilmore* [1990] and Schulman *Schulman et al.* [1985], and for the electron impact excitation of argon were taken from Puech *Puech and Torchin* [1986]. These cross sections were chosen since they were found by Pagnon *et al.* *Pagnon et al.* [1995] to give the best agreement between actinometry and VUV measurements for pure O_2 plasma. The cross sections for the calculation of the EEDF (see details bellow) were obtained from IST-Lisbon database for CO_2, O_2, O and Ar, available in LxCat *IST-LXCat* [2018], and for CO *Guerra* [2019].

The Einstein coefficient values used in equation (2.9) were taken from the NIST database *Kramida et al.* [2018]: $A_{ij}^{O^3P} = 3.22 \times 10^7\, s^{-1}$, $A_{ij}^{O^5P} = 3.69 \times 10^7\, s^{-1}$, $A_{ij}^{Ar} = 4.45 \times 10^7\, s^{-1}$. The optical branching ratio $A_{ij}^X / \sum A_i^X$ is equal to 1 for oxygen and to 0.994 for argon *Nick and Helbig* [1984]. The rate coefficients for quenching of the emitting oxygen states by O_2 molecules used here were *Tsutsumi et al.* [2017] $K_Q^{O^3P} = 9.4 \times 10^{-16}\, m^3 s^{-1}$ *Niemi et al.* [2005], $K_Q^{O^5P} = 10.8 \times 10^{-16}\, m^3 s^{-1}$ *Dagdigian et al.* [1988]. These coefficients were measured in pure O_2 with an average error around 10%. However, other sources report significantly different values (*e.g.* $K_{O_2}^{O^3P} = 7.8 \times 10^{-16}\, m^3 s^{-1}$ *Dagdigian et al.* [1988]). To the best of our knowledge, there is no data available for the quenching of atomic oxygen lines by CO_2, CO or O. Therefore, we assumed these species have the same quenching rate coefficients as for O_2. We checked the validity of this assumption by measuring the decay time of the TALIF fluorescence signal while varying the gas mixture between pure CO_2 and pure O_2 (discussed in section 2.4.2). $[n_Q]$ was considered in this case equal to the total gas density (jus-

tified also in section 2.4.2). In the case of the Ar line, values are available for other quenchers: CO_2: $K_{CO_2}^{Ar\,2P_1} = 6.2\times10^{-16} m^3 s^{-1}$, CO: $K_{CO}^{Ar\,2P_1} = 1.1\times10^{-16} m^3 s^{-1}$ and O_2: $K_{O_2}^{Ar\,2P_1} = 7.6\times10^{-16} m^3 s^{-1}$ *Sadeghi et al.* [2001]. Two methods were followed for the data treatment process:

- **Method 1: Manual method with Bolsig+** In a first state, the EEDF was calculated using the two term approximation Boltzmann solver BOLSIG+ *Hagelaar and Pitchford* [2005]. The experimental values of CO_2 dissociation were used to define the CO_2 and CO fractions for the calculation of the EEDF. The values of O and O_2 used for the calculation of the EEDF were "guess" values based on preliminary calculations. The EEDF was calculated with the corresponding reduced electric field (E/N) value for each plasma condition. The excitation rate coefficients were calculated through integration over the EEDF, according to equation (2.8), and are used in equation (2.10) to calculate the O atom densities from the experimental emission line ratios. In this method, the density of O_2 used in equation (2.10) was assumed to be equal to half of the CO density determined with FTIR, *i.e.* the O_2 density that would be obtained if all the O atoms were recombined into molecular oxygen, which could lead to an overestimation of the dissociative excitation term. However, since the excitation rate coefficients for this process are at least two orders of magnitude smaller than the rate coefficients for direct excitation, the contribution of this term was found to be negligible. The percentage of Ar in the input gas flow was 5%, but under plasma conditions the dissociation reduces the fraction of Ar over the total gas density, an effect that was taken into account in the calculations, also assuming that the O_2 fraction was equal to half of the CO fraction.

- **Method 2: Self consistent calculation with LoKI**. The equation to calculate the O atom density depends on the densities of all the species and therefore requires to make assumptions, particularly for the densities of Ar and O_2. We can overcome this issue by calculating the O atom density in a self-consistent cycle, schematically represented in figure 2.11. The EEDF in this case is calculated by the Boltzman solver LoKI *Tejero-del Caz et al.* [2019], programmed in MATLAB. The calculation requires as input values the gas temperature, the electric field, the initial fractions of CO_2, Ar, other add mixtures (typically O_2 for the data treatment in chapter 8) and the dissociation fraction, α, for the calculation of the CO fraction. A first guess for the fractions of O and O_2, $^{O}/_{O_2}$, is still required.

  A MATLAB script was built to automatically modify the input files of Loki according to the

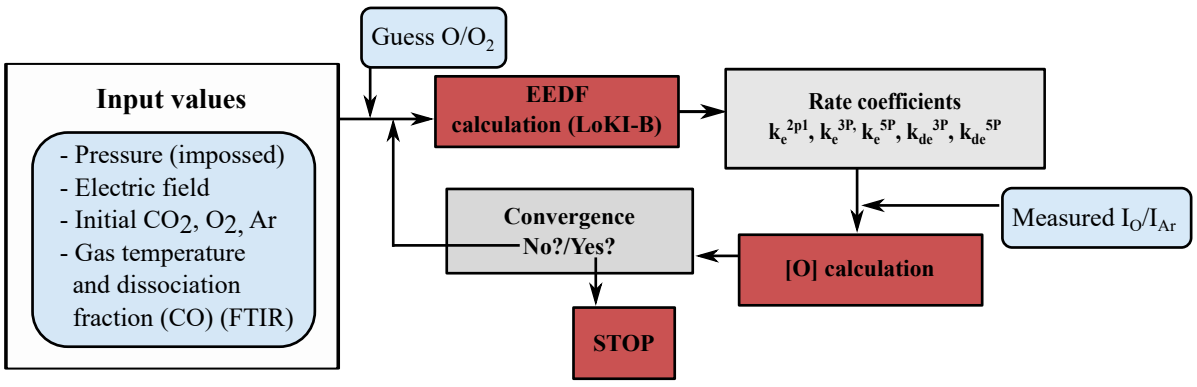

Figure 2.11: Flow chart followed in the actinometry calculation method 2.

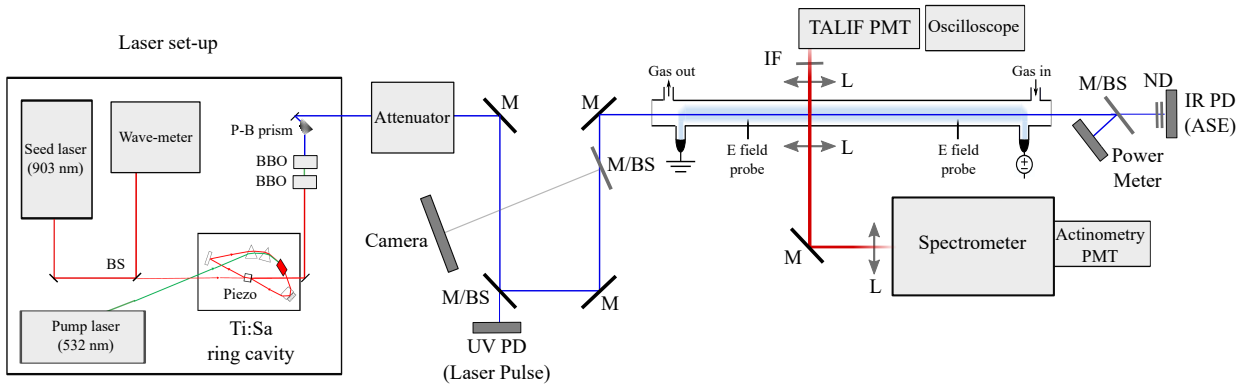

Figure 2.12: Experimental set-up used (non-simultaneously) for TALIF and actinometry experiments. M: Mirror, BS: Beam splitter, L: Lens, PD: Photo-diode, PMT: Photomultiplier, IF: Interference filter, ND: Neutral density filter. The laser set-up is shown with a simplified version of the optics.

plasma conditions under study and call the Boltzmann solver using the input data. With the EEDF and the corresponding cross sections, the excitation rate coefficients for the emission lines studied are calculated. Introducing the experimental emission line ratios, we calculate a first value of the O atom density for each emission line with equation (2.10). This values is taken as guess value for the next iteration. The fractions of all the gases involved (O_2, O an Ar) are recalculated keeping the carbon and oxygen balance. The new fractions are used again to calculate the EEDF, repeating the procedure until the convergence condition is matched: when the value of the oxygen density differs less than 1% from the O atom density obtained in the previous two iterations. We have checked that the initial guess for $^{O}/_{O_2}$ does not influence the final O atom density results and, as example, initial values of 0 or 1 lead to the same final atomic oxygen density. The calculations according to the detailed method converge fast, typically after 5 iterations. This method automatically calculates the O atoms density from the input values avoiding the manual calculation in Bolsig+ and is not dependent on the initial guess values. The method is easily adaptable to other gas mixtures apart from those investigated in this thesis.

As final remark, in order to record the actinometry signal, the wavelength of the spectrometer is fixed at the peak of intensity of every emission line. Therefore, in principle, we should include a term to account for the Doppler broadening (and pressure broadening if needed), which reduces the intensity peak value, as it is done for HR-TALIF (see section 2.4.2) *Kunze* [2009]. However in actinometry measurements the instrumental broadening is dominant, and the Doppler effect is negligible in comparison.

2.4.2 High Resolution - Two photon Absorption Laser Induced Fluorescence (HR-TALIF)

Principles

Contrary to actinometry, Two-photon Absorption Laser Induced Fluorescence (TALIF) directly probes the atoms in their ground state *Niemi et al.* [2005]; *Amorim et al.* [2000]; *Amorim and*

Baravian [2001]; these are pumped by the absorption of laser light to an electronically-excited state, which decays radiatively, emitting the detected fluorescence photons. We used the conventional TALIF scheme in which O atoms in the ground state are excited by two photons at 225.65 nm, emitting a fluorescence signal through the $3p\,^3P_J \rightarrow 3s\,^3S^o$ transitions at 844.6 nm. The relation between the ground state density and the detected signal is given, for a collimated beam (confocal parameter $\gg$ fluorescence viewing region) by the expression *Bamford et al.* [1986]:

$$N_{h\nu} = \frac{a_{ij}^X \cdot C_X \; \hat{\sigma}_X^{(2)} L \; E^2 \cdot n_X}{\pi \cdot w^2 \cdot (h\nu)^2} \cdot \int_{-\infty}^{\infty} F^2(t)dt \tag{2.11}$$

where $N_{h\nu_i}$ is the fluorescence signal ($\sim$ total number of fluorescence photons), a_{ij}^X is the effective branching ratio described in equation (2.9), C_X is a constant dependent on the detection system, $\hat{\sigma_X}^{(2)}$ is the two-photon absorption cross section, L is the effective length of the light-collection system, E is the laser energy, w is the beam waist, n_X is the ground state density and $\int_{-\infty}^{\infty} F^2(t)dt$ is the integral of the temporal profile of the laser pulse.

In order to deduce absolute densities, we followed the calibration process first proposed by Goehlich *et al.* *Goehlich et al.* [1998] and further developed by Niemi *et al.* *Niemi et al.* [2005]. This method is based on a reference measurement with a noble gas of known concentration, performed ideally with the same spatial, spectral, and temporal intensity distribution of the laser radiation, removing the necessity to know these distributions explicitly. This condition is best fulfilled if the two-photon resonances are spectrally close. Accordingly, xenon is commonly used as calibration gas to measure O atom densities *Goehlich et al.* [1998]. Two possible Xe fluorescence transitions have been used in the literature for the calibration of O atom density, $6p'[3/2]_2 \rightarrow 6s'[1/2]_1$ and $7p[3/2]_2 \rightarrow 6s[3/2]_2$. We used the first one, which is excited by 224.31 nm photons and emits fluorescence at 834.91 nm. The term $\int_{-\infty}^{\infty} F^2(t)dt$ is similar for the measurements of O atom and Xe (the maximum difference was determined to be less than 8%). After normalizing the signal by the square of the laser pulse energy $S_X \sim {}^{N_{h\nu}^X}/_{E^2}$, the O atom density is deduced from the following expression *Niemi et al.* [2005]:

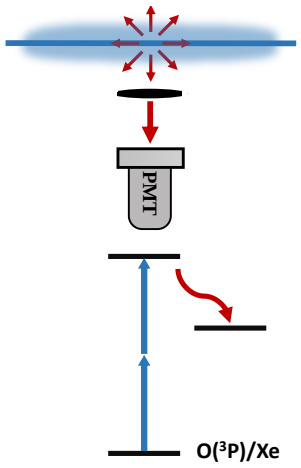

Figure 2.13: TALIF scheme

$$n_{O_{atom}} = \frac{T_{Xe}}{T_O} \cdot \frac{\xi_{Xe}}{\xi_O} \cdot \frac{\sigma_{Xe}^{(2)}}{\sigma_O^{(2)}} \cdot \frac{a_{Xe}}{a_O} \cdot \frac{S_O}{S_{Xe}} \cdot \frac{w_O^2}{w_{Xe}^2} \cdot \frac{(h\nu_O)^2}{(h\nu_{Xe})^2} \cdot \frac{1}{n_{J=2}/\sum_J n_J} \cdot n_{Xe} \tag{2.12}$$

where T_X is the transmittance of the windows and ξ_X is the sensitivity of the detection system ($C_X = T_X \cdot \xi_X$), including the spectral responses of the photomultiplier (measured similarly as described in section 2.4.1) and of the interference filter (obtained from the data-sheet), for both wavelengths. ${}^{\sigma_{Xe}^{(2)}}/_{\sigma_O^{(2)}}$ is the ratio of the two-photon absorption cross sections. To our knowledge, the Xe two-photon absorption cross section has not been published. Therefore we used the value of the ratio of both cross sections ${}^{\sigma_{Xe}^{(2)}}/_{\sigma_O^{(2)}} = 1.9$ determined by Niemi *et al.* *Niemi et al.* [2005], based on a titration method, with an estimated uncertainty $\sim$20%. However, recent preliminary,

direct, measurements of the Xe two-photon absorption cross section *Drag* [2020], seem to indicate that this value could be over-estimated, and point towards a $\sigma^{(2)}_{Xe}$ value smaller by a factor ~ 2 than the value determined by titration. The impact of this cross section on the final O atom density results will be discussed in section 3.5.1. The fluorescence quantum yield, ${}^{a_{Xe}}/_{a_O}$, was defined above in equation (2.9). The pure optical branching ratio ${}^{A^X_{ij}}/_{\sum A^X_i}$ is 1 for oxygen, while for Xe it is 0.733 *Aymar and Coulombe* [1978]; *Horiguchi et al.* [1981]. In the case of Xe, the radiative decay rate and quenching coefficient were taken from Niemi *et al.* *Niemi et al.* [2005] and are, respectively, $A_{Xe} = 2.45 \times 10^7\ s^{-1}$ and $k_q^{Xe} = 3.6 \times 10^{-10}\ cm^3 s^{-1}$. The density of Xe, n_{Xe}, in the discharge tube was calculated from the pressure and temperature with the ideal gas law. In the case of oxygen, a single effective quenching coefficient was used, therefore the total gas density was used as the quencher density (see section 2.4.2).

${}^{S_O}/_{S_{Xe}}$ is the experimentally observed ratio of the fluorescence, integrated either over time, for the TALIF fluorescence ratio, or over time and wavelength, for the TALIF excitation profile ratio (see section 2.4.2), and normalized to the squared laser energy, for the two species. Although ideally the beam spatial profile should be identical in the O and Xe measurements, in practice when the laser wavelength is varied, the position of the beam in the frequency doubling crystals changes slightly, affecting the beam shape. According to equation (2.11), the size of the beam must be taken into account and the term ${}^{w_O^2}/_{w_{Xe}^2}$ in equation (2.12) represents the ratio of the laser beam waist diameters estimated using the laser beam profiler in the respective cases. ν_i is the frequency of the absorbed photons. Finally, the ground state of oxygen comprises three fine structure components, but we only determine the absolute density by TALIF in the level J=2; therefore we must include a term accounting for the fraction of O atoms in this level. We assume the fine-structure components are described by a Boltzmann distribution and are in equilibrium with the gas temperature. Consequently, the fraction of O atoms in the level J=2 is given by:

$$\frac{n_J}{\sum_J n_J} = \frac{(2J+1) \cdot \exp\left(-E_J/k_B \cdot T_g\right)}{\sum_J (2J+1) \cdot \exp\left(-E_J/k_B \cdot T_g\right)} \tag{2.13}$$

which is equal to 0.67 for oxygen at 1 Torr 40 mA ($T_{gas} \approx 500\ K$), the condition for which the absolute calibration was made.

HR-TALIF set-up

The laser set-up used for HR-TALIF measurements (shown schematically in figure 2.12), uses a commercial single-mode continuous Titanium:Sapphire (Ti:Sa) laser (Coherent MBR 110 pumped by a 10W Verdi Nd:YVO_4 laser) to seed a home-built nanosecond pulsed ring cavity Ti:Sa laser, pumped by a 20Hz 532nm Nd:YAG laser (Quantel CFR200) *Booth et al.* [2015]; *Marinov et al.* [2016]; *Cabaret and Drag* [2010]; *Lottigier et al.* [2019]. The seed laser is injected co-linearly with the pump laser into a Ti:Sa crystal. The cavity also contains two prisms to coarsely select the output wavelength range with a spectral resolution of about 15 cm^{-1}. The cavity is locked to the frequency of the seed laser by adjusting the cavity length using a piezoelectric actuator on one of the mirrors, in order to operate the ring cavity in a single longitudinal mode. The wavelength of the seed laser is monitored by a wave-meter (Angstrom WSU from High Finesse, measurement resolution 5 MHz FWHM).

The output pulses from the ring laser (at around 903 nm) are then frequency-doubled twice

by non-linear BBO crystals, generating ultraviolet pulses around 225.6 nm with an energy of approximately 1 mJ. The spectral width of the ultraviolet pulses is around 0.006 cm^{-1} FHWM, close to the Fourier transform limit of the pulse duration. The ultraviolet beam is spatially separated from the longer-wavelength components using a fused silica Pellin-Broca prism and passed through a home-made attenuator (allowing the laser energy to be varied without changing the spatio-temporal profile), towards the long discharge tube, which is closed with two CaF_2 windows. The beam was not focused (the reason for this is explained below). The laser pulse duration is approximately 7.5 ns and a reflection from a mirror/beam splitter was monitored with a fast UV photo-diode to trigger the data acquisition. After exiting the tube, the beam is reflected by a dielectric mirror at 45^0 (97% of the laser energy) towards a laser energy meter (Sensor PE10-C + controller Pulsar, Ophir). Behind this last mirror we installed an IR photo-diode with two neutral density filters in order to detect the onset of the amplified spontaneous emission (ASE) signal from the transmitted (IR) light. All TALIF data was recorded using a laser energy below the threshold for ASE.

The fluorescence from the laser-excited atoms at 844.6 nm was collected perpendicularly to the laser beam by a f=35.5 mm lens, imaged onto a horizontal slit, passed through an interference filter (840 nm centre wavelength, 13 nm FWHM), and detected with a photomultiplier (Hamamatsu R13456, with a time response of 2.7 ns) fitted with a gated voltage-divider circuit (Hamamatsu C1392-56) to avoid saturation by the plasma emission. The fluorescence signal, the laser pulse signal (UV photo-diode) and the ASE signal (IR photo-diode) were monitored with a digital oscilloscope (LeCroy HDO4104). A Labview program was used to record the fluorescence intensity, the laser energy and the seed laser wavelength. The laser beam profile was measured with a camera beam profiler (Thorlabs BC106N) and the beam waist was derived assuming a Gaussian spatial profile.

Measurement procedure

For the absolute calibration, the excitation wavelength was scanned at a fixed laser pulse energy, for both gases. An example of the excitation spectra obtained from the integral of the TALIF fluorescence over time is shown in figure 2.14. As can be seen, the high spectral resolution of the laser allows us to partially resolve the fine structure of the excited level O ($3p\ ^3P$); the contributions of the levels J=1 (88630.59 cm^{-1}, fluorescence transition $3p\ ^3P_{J=1} \rightarrow 3s\ ^3S_{J=1}$) and J=2 (88631.15 cm^{-1}, transition $3p\ ^3P_{J=2} \rightarrow 3s\ ^3S_{J=1}$) are easily distinguished. The J=0 (88631.30 cm^{-1}) contribution is weaker and convoluted with that from J=2 one *Marinov et al.* [2017a]. In the conditions studied in this work, these profiles are dominated by Doppler broadening (*i.e.* pressure broadening, natural line-width and laser line-width are negligible), and can be fitted with a sum of three Gaussian functions to determine the temperature of the O atoms. The ratio of the TALIF signals, S_O/S_{Xe} in equation (2.12) is in this case simply the ratio of the TALIF signals integrated over time and wavelength and normalized to the laser intensity squared for both species *i.e.* an integral of the TALIF profiles shown in figure 2.14.

The absolute calibration can also be achieved by recording only the TALIF fluorescence signal as a function of time, with the laser wavelength set to the maximum of the signal (at the peak of the resonance). An example is shown in figure 2.15, recorded by the oscilloscope and averaged over 300 laser shots. This signal must be corrected for the Doppler broadening, which reduces the signal at the peak. In the case of Xe, we take into account the contribution of the different isotopes by including a correction factor equal to 0.54 *Kono et al.* [2016]; *Saloman* [2004]. Therefore, in this case, S_O/S_{Xe}

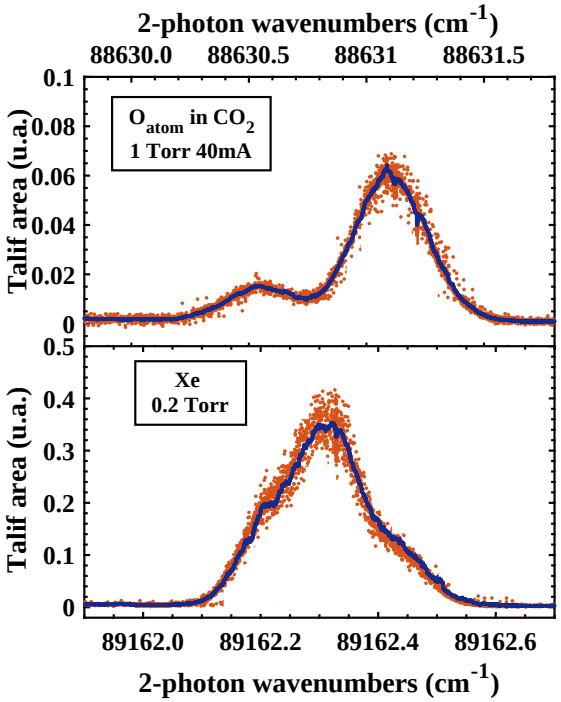

Figure 2.14: TALIF excitation profile for O atoms in a CO_2 plasma and for Xe. In red the raw data points, in blue the smoothed data (averaging 50 points) used for the integral calculation.

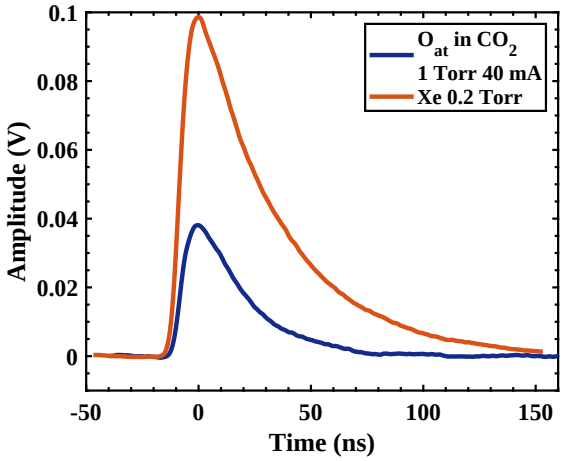

Figure 2.15: TALIF fluorescence signal over time for O atoms in CO_2 at 1 Torr 40 mA (transition $3p\ ^3P_{J=2} \rightarrow 3s\ ^3S_{J=1}$), and Xe at 0.2 Torr. The profile is an average over 300 laser shots.

in equation (2.12) is the ratio of the TALIF fluorescence signal, not integrated over wavelength but only over time, corrected for the Doppler broadening and the isotope contribution and normalized to the laser energy squared. The values of the absolute O atom densities obtained by this method were within 11% of the densities found by integrating over the complete TALIF excitation profile, and the data acquisition is much faster, being less affected by possible instabilities of the laser, and reducing the uncertainties caused by fluctuations in the laser beam spatial profile when scanning over wavelength. Therefore the measurements of the relative variation of the O atom density as a function of discharge parameters (pressure and current) were subsequently determined just from the signal at the peak wavelength corresponding to the transition $3p\ ^3P_{J=2} \rightarrow 3s\ ^3S_{J=1}$, corrected also for the quenching, as follows from equation (2.12). The transition $3p\ ^3P_{J=1} \rightarrow 3s\ ^3S_{J=1}$ was found to be give consistent O atom relative variation with pressure and current, finding a difference lower than 4%, which means that both transitions can be indifferently used to assess the variation of O atom density for different plasma parameters.

The temporal shape of the fluorescence signal is a convolution of the laser pulse duration (around 7.5 ns), the time response of the PMT (2.7 ns) and the lifetime of the fluorescing state. In order to evaluate the lifetime of the exited states (and therefore compensate for quenching in the calculation), we reject the first 7.5 ns after the peak (15 ns in total) to avoid any influence of the laser profile or the response of PMT in the fitting of the fluorescence decay. Concerning the integral of the TALIF fluorescence signal to obtain the absolute density, the effect of the response time of the PMT (assuming a Gaussian profile and convolving it with the exponential decay of the TALIF signal) gives an error in the integral below 0.5% for both O and Xe. The maximum effect of the laser pulse duration, also assuming a Gaussian profile, is around 3.5%; therefore both contributions

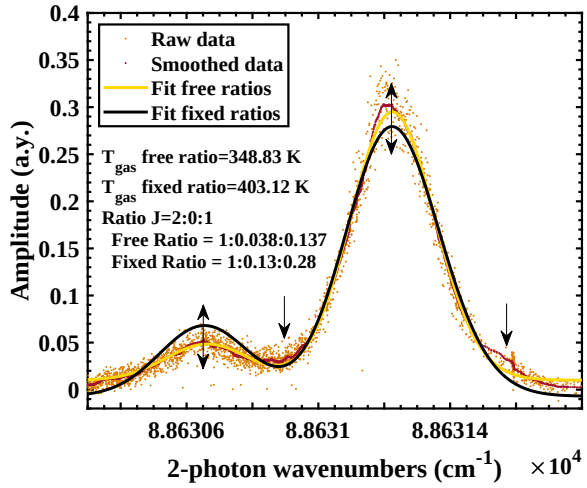

Figure 2.16: Example of the TALIF excitation profile for O atoms in an O_2 plasma at 1 Torr, 20 mA measured with a focalised beam along with two fits, keeping free or fixing the J-ratio for the fine structure of $O(3p\,^3P_J)$ to the theoretical values. The obtained temperature values are indicated.

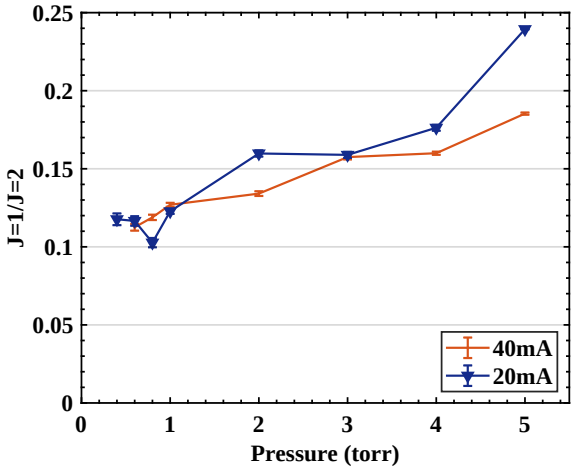

Figure 2.17: Pressure dependence of the ratio between $O(3p\,^3P_{J=1})$ and $O(3p\,^3P_{J=2})$ derived from a gaussian fit of the excitation profile keeping free the J-ratio for the fine structure of $O(3p\,^3P_J)$, measured in an O_2 plasma at 20 and 40 mA.

were considered negligible. The laser beam shape, which is close to a gaussian profile, was recorded after each TALIF profile scan for absolute calibration in order to obtain the beam waist. For Xe $w^Y_{Xe} \approx 916.6\ \mu m$ and $w^X_{Xe} \approx 1083.8\ \mu m$ while for oxygen $w^Y_O \approx 892.1\ \mu m$ and $w^X_O \approx 733.5\ \mu m$.

It is worth mentioning that all TALIF data were obtained without focusing the laser beam. In initial measurements we did focus the beam, but we found that the two-photon absorption excitation line profile was distorted; the intensity ratio of the three fine-structure components of the upper $O(3p\,^3P^J)$ state did not match the theoretical values *Saxon and Eichler* [1986], and wide "wings" appeared. An example is shown in figure 2.16, which plots the excitation spectra obtained from the integral of the TALIF fluorescence and the 3-gaussian fit carried out to deduce the gas temperature. Two fits are included: (1) imposing the theoretical J-ratio for the fine-structure of $O3p\,^3P_J$ (fixed ratio); (2) keeping the ratio free in the fitting. In the figure, the free fitting evidently follows better the experimental data but it is far from the theoretical predictions. The obtained gas temperatures are ~50K different. Figure 2.17 plots the variation of the ratios between $O3p\,^3P_{(J=1)}$ and $O3p\,^3P_{(J=2)}$ obtained from similar free fittings in different plasma conditions, as a function of pressure for two currents. The values show a certain pressure dependence. Possible origins of these effects include J-dependent photo-ionization of the emitting state, and production of hot O atoms by photo-dissociation of vibrationally-excited O_2 *Niemi et al.* [2005]; *Amorim et al.* [1996]. Without laser focusing these effects disappeared. As a default approach the gas temperature was fitted always with fixed and free J-ratio. Only data with a difference in the fitted temperatures with both methods <5% was kept as final TALIF T_{gas} data. An example of the good agreement between the temperatures obtained with both fits is given in figure 3.8.

The quadratic dependence of the TALIF signal on the laser pulse energy was also verified, since any deviation from this dependence would indicate a significant perturbation by photo-ionization and/or amplified stimulated emission (ASE), leading to errors in the determined O atom density.

The laser energy threshold for ASE was detected with the IR photo-diode as the laser energy was varied and, during subsequent measurements, the power of the laser was always kept below this threshold. For all TALIF data, laser shots where the laser energy fell below 75% of the average were rejected since they correspond to a failure of the cavity seeding.

Preliminary observations: Quenching

The temporal decay of the TALIF fluorescence signal allows the quenching rate of excited O atoms to be measured as a function of the gas mixture, which is necessary for the analysis of actinometry data. Measurements of the temporal decay of the TALIF fluorescence signal after the laser pulse (such as those shown in figure 2.15), give the effective decay rate of the O atoms in the exited state, which is related to the quenching rate coefficients by the expression:

$$A^* = \frac{1}{\tau^*} = \frac{1}{\tau_0} + \sum_Q k_Q[n_Q] \Rightarrow A^* = \sum_i A_i^X + \sum_Q k_Q[n_Q] \tag{2.14}$$

where A^* is the measured effective decay rate, τ^* is the effective lifetime, τ_0 is the natural lifetime accounting for all the possible radiative de-excitation processes, k_Q is the quenching coefficient and $[n_Q]$ is the density of quenchers. The experimental values of the effective decay rate, A^*, for the level $3p\,^3P_{J=2}$ as a function of pressure and current can be seen in figure 2.18. The level $3p\,^3P_{J=1}$ gave the same decay rate values and variation with pressure and current within an average difference of $\pm$ 0.0022 ns^{-1} (~4.5%).

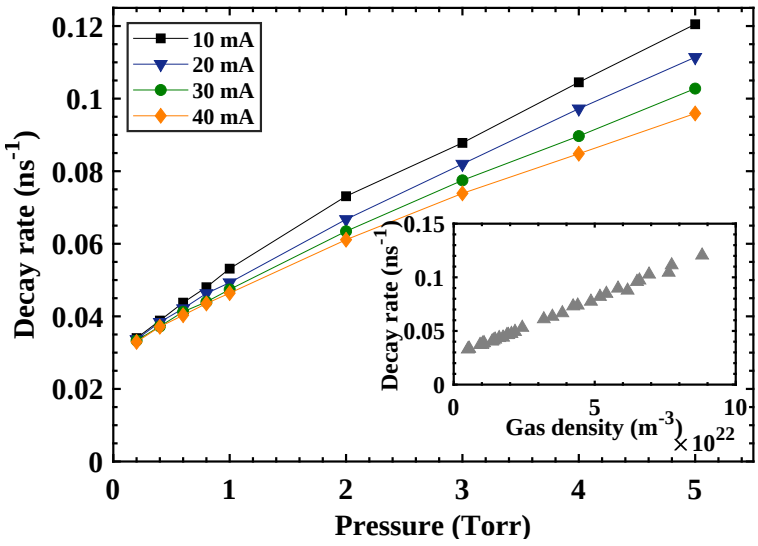

Figure 2.18: Variation of the effective decay rate of the $3p\,^3P_{J=2}$ state with pressure and current. In the inner figure, the same decay rates are plotted *versus* total gas density.

As expected, we see an increase of the decay rate with pressure. We also see a small decrease with increased current, which can be explained by the decrease in gas density due to a temperature increase. The inner figure shows the same data but plotted as function of the total gas density. The clear linear dependence shows that it is reasonable to assume that the decay rate depends only on the total gas density and is insensitive to the gas composition (in our experimental conditions). Therefore, $\sum_Q k_Q[n_Q] \rightarrow k_Q[N]$, with N being the total gas density. The natural lifetime is obtained from the inverse of the intercept at zero pressure of a linear fit to this data. The value found is around

$\tau_0 = 37.3$ ns, which is close to experimental values found in literature, 34.7 ± 1.7 ns in *Niemi et al.* [2005] and 35.1 ± 3.0 ns in *Niemi et al.* [2001], but slightly higher than the theoretically calculated value given by the NIST (31.1 ns).

The O atom densities were calculated from the TALIF signal using our experimental values for the natural lifetime and the measured decay rates for each plasma condition (*i.e.* a_O in equation (2.12) is equal to $A(=1/\tau_0)/A^*$). For the actinometry calculation the quenching rates for the two oxygen lines, O777 and O845, are required. Due to the lack of data in CO_2, we used the quenching rate coefficients available for pure O_2 plasma. The fact that the gas density is the main parameter in the quenching process gives us confidence in that the error induced is insignificant for the final result. Nevertheless, we determined experimentally how the quenching coefficient for the O845 line (from $O(3p^3P)$), changes with gas composition, from pure O_2 plasma to pure CO_2 plasma in our experimental conditions.

The average value for k_Q obtained in pure O_2 is $k_Q^O = 9.35 \times 10^{-16}\ m^3 s^{-1}$, very close to the value taken from literature. The addition of CO_2 has only a small effect, between 2 and 10%, and the average value is $k_Q^O = 9.59 \times 10^{-16} m^3 s^{-1}$. Therefore, we make the same assumption for both oxygen emission lines used for actinometry, and assume that the quenching coefficients for O_2 plasma are also valid for CO_2 plasma, with a maximum error around 10%. *A posteriori* analysis showed that varying all these quenching coefficients by 10% causes a change of less than 1.5% in the absolute O atom values obtained by actinometry.

2.4.3 Cavity Ring Down Spectroscopy (CRDS)

CRDS experiments were performed during a short measurement campaign in collaboration with Jean-Paul Booth, Abhyuday Chatterjee, Dmitry Lopaev Sergey Zyrianov and the master student under my co-supervision, Tiago C. Dias. The CRDS results are only preliminary and should be confirmed with future measurements. More details about the diagnostic and the experimental set-up can be found in the PhD thesis of Abhyuday Chatterjee.

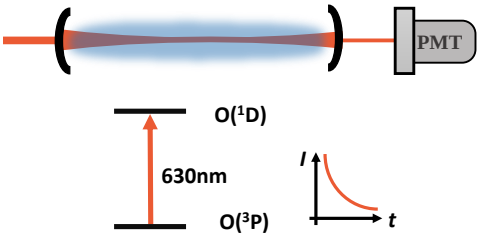

Figure 2.19: CRDS scheme

Principles

Cavity Ring Down Spectroscopy (CRDS) is an absorption technique which measures the rate of absorption rather than directly the magnitude of the absorption of a light pulse confined in an optical cavity consisting of two highly reflective mirrors *Berden et al.* [2000]. The light intensity trapped in the optical cavity decays exponentially in time. The decay rate is related to the total losses inside the cavity and can be used to determine the absolute densities of gas phase species with very high sensitivity *Busch and Busch* [1999]; *Berden et al.* [2000]. Under conditions of weak absorption, the transmitted intensity of a light source $I(\nu)$ through a homogeneous gas is given by the Beer-Lambert law *Stancu et al.* [2010]:

$$I(\nu) = I_0(\nu) \cdot e^{[-\alpha(\nu) \cdot l]} \tag{2.15}$$

where $I_0(\nu)$ is the incident intensity, $\alpha(\nu)$ is the frequency-dependent absorption coefficient of the

cavity medium at the light of frequency ν and l is the absorption path length.

In this technique a monochromatic tunable laser pulse is confined in an optical cavity by two high reflectivity mirrors. The laser light is injected through one of the two mirrors, which can also serve to close the gas cell or plasma reactor. The light is reflected back and forth inside the cavity and every time that the light is reflected a small fraction of this light leaks out of the cavity. When the laser is tuned to an absorption transition of the species present inside the cavity, the decay of pulses is faster. The difference of the decay time τ for ON- and OFF-resonance measurements is proportional to the absorption coefficient *Macko et al.* [2001]:

$$I(t) = I_0 \cdot e^{\left[-\left(\frac{1}{\tau_e}+c\alpha\right)\cdot t\right]} = I_0 \cdot e^{\left(-\frac{t}{\tau}\right)} \tag{2.16}$$

where τ is the total decay time (ring-down time). The decay time is affected by 3 contributions: (1) the "cavity losses" for a given mode injected inside the cavity, (2) the broadband absorption of the gas filling the cavity, (3) the narrow wavelength dependant absorption of the transition studied:

1. The cavity losses depend on the transmittivity T of the mirrors and the losses L they induce because of diffusion and diffraction. These two parameters are related to the reflectivity of the mirrors by the relation $R + T + L = 1$. The characteristic ring-down time for a given cavity mode with the cavity being empty is given by $\tau_e = \frac{l}{c(T+L)}$, which is almost frequency independent over a few tens of cm^{-1}. l is the optical path between the mirrors. In our case, τ_e was typically in the order of 25μs. Note that certain "pollution" of the mirrors, which can simply be water adsorption, can affect L and therefore τ_e.

2. Several processes can lead to light absorption on a broader spectral range than the one scanned for the CRDS measurement. In our conditions photo-detachment from negative ions as well as broad band absorption from ozone can produce an almost wavelength independent absorption in the $\sim$1 cm^{-1} range scanned. This contribution can be taken into account with the absorption coefficient (α_p). As a result, for all our measurements, either the full line profile must be acquired, or at least the level of the baseline on both sides of the O atom absorption line must be acquired in the same plasma conditions (see example on figure 2.21).

3. Finally the absorption due to the transition of interest can be described with the wavelength dependant absorption coefficient ($\alpha_l(\lambda)$).

With all these contributions, the time evolution of the intensity detected at the output of the cavity can then be described by the expression:

$$I(t) = I_0 \cdot e^{\left[-\left(\frac{1}{\tau_e}+c\alpha_p+c\alpha_l\right)\cdot t\right]} = I_0 \cdot e^{\left(-\frac{1}{\tau_0}+c\alpha_l\right)\cdot t} \tag{2.17}$$

where τ_0 is defined as:

$$\frac{1}{\tau_0} = \frac{1}{\tau_e} + c\alpha_p \tag{2.18}$$

includes all the wavelength independent terms. Measuring the total ring down time τ and subtracting the wavelength independent contribution we can obtain the absorption coefficient:

$$\alpha_l = \frac{1}{c} \cdot \left(\frac{1}{\tau} + \frac{1}{\tau_0}\right) \tag{2.19}$$

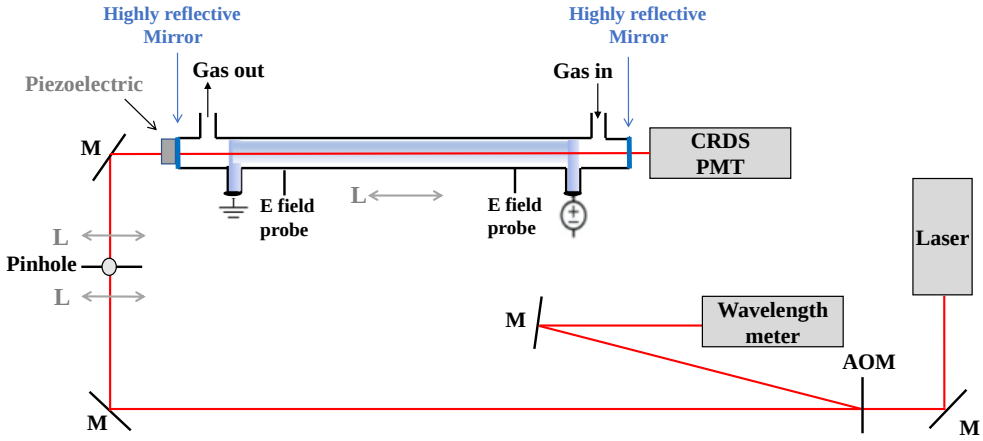

Figure 2.20: Experimental set-up used for CRDS experiments.

Equation (2.19) is valid if the density of the absorbing species is constant during the decay time *Stancu et al.* [2010] (although CRDS can also be used for density measurements changing faster than ring-down time as shown in *Yalin et al.* [2002]; *Brown et al.* [2000]). In our case, O atom density will not significantly vary during the ∼25 μs of ring-down. The density of adsorbing species can then be calculated knowing the absorption cross section σ_a with *Grangeon et al.* [1999]:

$$n_a = \frac{\alpha_l}{\sigma_a} = \frac{1}{\sigma_a c} \cdot \left(\frac{1}{\tau} + \frac{1}{\tau_0} \right) \tag{2.20}$$

The absorption cross section is deduced from the Einstein coefficient A_{ul}=5.65x10^{-3} s^{-1} given in the NIST database for the transition $^3P_2 \rightarrow ^1D_2$ at 630.03 nm (15867.862 cm^{-1}), and coming from *Baluja and Zeippen* [1988]; *Slanger et al.* [2011]. This transition is electric-dipole forbidden which explains why CRDS is needed to detect an absorption signal.

CRDS set-up

The CRDS scheme followed is based on continuous-wave cavity ring-down spectroscopy (CW-CRD) similar to that presented in *Romanini et al.* [1997]. The schematic representation of the experimental set-up used for CRDS experiments is presented in figure 2.20. The output of a continuous wave (CW) single frequency laser (Toptica DL100 at 630.03nm) is directed towards an acousto-optic modulator (AOM) with a time response of ∼2 μs, which redirects part of the beam towards a wave-meter (Angstrom WSU from High Finesse, measurement resolution 5 MHz FWHM), for the laser wavelength calibration. The rest of the beam goes towards the plasma reactor/cavity through two plano-convex lenses and a pinhole to obtain a well defined Gaussian beam. Each mode of the cavity can have different ring-down time. It is therefore important to minimize as much as possible mode jumps in the injection of the cavity with transverse mode. The laser enters plasma reactor through a highly reflecting mirror (curvature 1000 mm (±1%) and transmittance ∼0.005%) mounted in a piezoelectric transducer, which allows the tuning of the cavity length.

A PMT (Hamamatsu R928) placed behind a second mirror closing the plasma chamber detects the time variation of the laser intensity. A bandpass interference filter (centered at 630 nm, 10 nm FWHM) was placed in front of the PMT to reject visible and IR emission from the plasma.

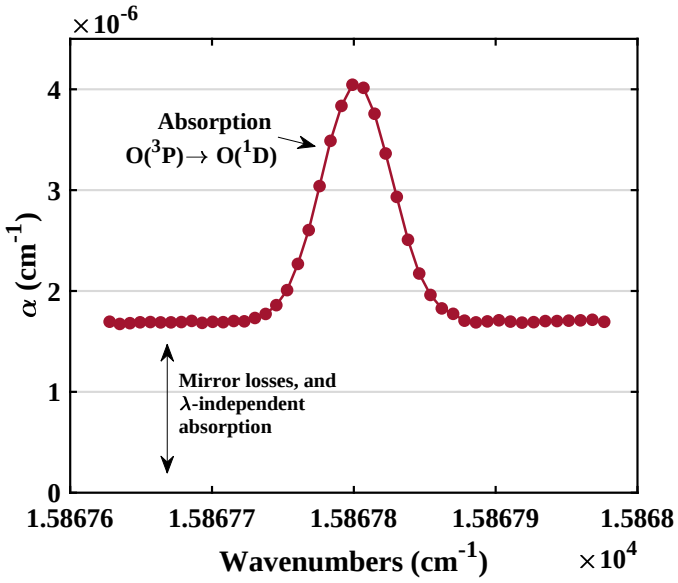

Figure 2.21: Example of absorption as a function of wavenumbers used to determine the translational temperature of oxygen atoms (measured in an O_2 plasma at 1 Torr, 40 mA).

A data acquisition card (NI-DAQ) and a Labview program were used to control the equipment, acquire data, and pre-treat the data. The PMT signal was recorded with an oscilloscope (LeCroy, HDO4104). A threshold circuit controlled the AOM to cut the laser beam when sufficient build-up of number of photons in the cavity was detected (threshold). For time-resolved experiments in pulsed discharges, when the laser is cut and the acquisition starts, the program records the time point along the plasma pulse (delay with regard to the trigger of the plasma pulse). The time evolution of the absorption spectra is re-constructed afterwards relating the recorded ring down times (only the events higher than threshold of injection of the cavity) with the corresponding time point along the pulse.

CRDS data analysis

In the context of this thesis CRDS was used to determine the O atom density in continuous, and pulsed DC discharges. Similarly to HR-TALIF, CRDS probed the ground state O atom density. The transition used is $(2s^4 2p^4)O(^3P_2) \rightarrow O(^1D_2)$, spin-forbidden which absorbs light at a wavelength of 630 nm (15867.862 cm^{-1}). As to treat TALIF data, we must take into account that we detect only a fraction of all the O atoms in ground state since the transition is from level J=2, assuming a Boltzmann distribution for the fine-structure components. An example of an absorption spectrum is shown in figure 2.21. The laser is scanned in wavelength to record each data point. The gaussian fit of this spectrum (pressure broadening is negligible < 0.005 cm^{-1}) allows to obtain the translational temperature of the O atoms, similarly to HR-TALIF, and the area is providing the O atom density.

In pulsed plasma, the full line profile was not always recorded. Measurements were done in the same conditions on both sides of the absorption line, far enough to have only contributions of broadband absorption processes (photo-detachment and ozone absorption), together with the cavity losses. This first measurement gave us the baseline as a function of time during plasma pulses. The same measurement was then taken at the maximum of absorption of the line. The gas temperature

was taken from from FTIR data to recalculate the full line profile from the maximum of absorption.

In addition, to calculate O atom densities in pulsed plasma, the variation of total gas density between ON and OFF phases must be taken into account. For short plasma pulses (5-10 ms On-Off) the time evolution of the rotational temperature measured with FTIR was used (see sections 3.2.2 for temperature variation and 3.7.2 for the calculated O atom densities). For long plasma pulses (196-196 ms On-Off) used to study surface loss processes we considered that the gas temperature with plasma ON and the room temperature were immediately reached because the characteristic time for the temperature evolution is significantly shorter (<5ms) than the time evolution of the O atom density. This assumption and more details are discussed in section 8.4.2).

It is important to be sure that the laser width is not comparable to the absorption line-width. In our case the absorption spectra is dominated by the Doppler broadening (the pressure broadening can be considered negligible), which allows to obtain the translational temperature of the O atoms, similarly to TALIF. For these measurements the laser wavelength was scanned around the peak of the absorption line while CRDS measures were consecutively acquired. An example of the obtained gaussian profile is shown in figure 2.21. Careful attention was paid to avoid optical saturation because of too high intensity of the laser inside the CRDS cavity, which could cause depletion of the absorbing species, *i.e.* underestimation of the density of the absorbing species, and inducing non-single exponential decay of the ring-down signal *Gao et al.* [2005] .

2.5 Summary

In this chapter we have described the experimental details of the main diagnostics techniques used in this thesis. As a summary of these techniques, figure 2.22 shows an energy diagram of the different gas phase species probed, including the noble gases used for calibration, and the transitions used for the different diagnostics.

All the techniques used have advantages and limitations but they are complementary. For instance, CRDS and FTIR are line-of sight integrated and while actinometry, HR-TALIF and Raman scattering are spatially resolved. However, they are absorption techniques that do not require a calibration, in contrast with actinometry or TALIF. The different diagnostics will be discussed in more detail along the different chapters where the experimental results are compared (mainly in chapter 3) in order to assess the level of accuracy of the absolute values obtained. Indeed, most of the parameters discussed in this thesis were measured at least by two different diagnostics, giving confidence in the experimental results obtained. To illustrate this important point of our approach, the table 2.3 is summarizing the main characteristics of all techniques, detailing the measured parameters.

The colours in the measured parameters emphasize the different techniques used for a given parameter. This is an important point in particular to use these data as benchmark for the validation of models. The detection limits, temporal and spatial resolution indicated are only those obtained in our experimental set-ups but higher performance can sometimes be achieved with similar techniques. In our conditions and with the techniques used, the minimum absolute densities of species measured corresponds typically to 0.02% of the total gas density.

Because of the multiplicity of reactors and diagnostics discussed throughout this thesis, a summary of the experimental conditions will always be reminded with the so-called **"Experimental**

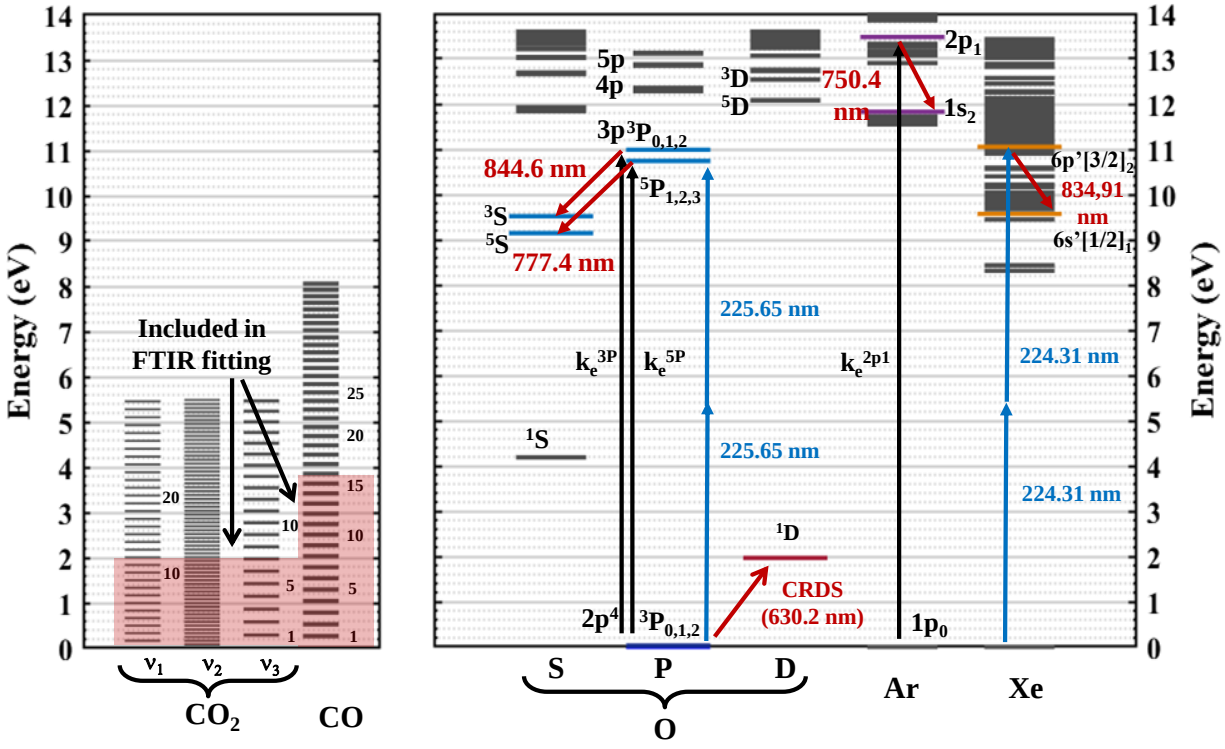

Figure 2.22: Schematic representation of the transitions studied by the different diagnostics in this thesis.

boxes". In the following chapters these "Experimental boxes", with blue borders, will gather the main diagnostic details, discharge and reactor used, in addition to the main parameters varied for a given section in order to help the reader through all the different experimental configurations studied.

Technique	Measured Parameter	Detection limit	Time resolution (s)	Spatial resolution
FTIR	$[CO_2]$, $[CO] \rightarrow \alpha$ T_{rot} ($\sim T_{gas}$) T_{12}, T_3 T_{CO}	2.10^{19}m^{-3} precision $\leq$30 K precision $\sim$60 K precision $>$150 K	10^{-5} (step scan) $\sim$0.5 (rapid scan) $>$1 (normal scan)	line of sight integrated
RAMAN (@TU/e)	$[CO_2]$, $[CO]$, $[O_2]$ T_{rot} ($\sim T_{gas}$) $\sim$ratio T_{12}/T_3	5.10^{20}m^{-3} $\leq$30 K	10^{-8} (used only for ms)	axial only (focussing beam) $\sim$100 μm
TALIF	$[O]$ T_{gas}	10^{19}m^{-3} $\leq$30 K	10^{-8} (not done)	axial and radial $\sim$100 μm
ACTINOMETRY	$[O]$ ν_O (plasma ON)	10^{19}m^{-3}	10^{-6} (acq. card)	possible but not done
CRDS	$[O]$ ν_O (also plasma OFF) T_{gas}	10^{19}m^{-3} $\leq$30 K	$\sim 10^{-6}$	line of sight integrated

Table 2.3: List of all measurement techniques used for this thesis. The colours in the measured parameters show the redundancy between measurements for checking the accuracy of obtained values. Other parameters given in the table correspond to the experiments discussed in this work, *i.e.* they do not necessarily represent the best possible performance of each technique.

Chapter 3

General characterization of the CO_2 glow discharge and the dissociation products

Contents

3.1 Introduction . . . 54

3.2 Gas temperature in CO_2 plasmas . . . 54

3.2.1 Accuracy of the gas temperature diagnostics techniques . . . 55

3.2.2 Gas temperature dependence . . . 56

3.2.3 Residence time and diffusion time toward the walls . . . 58

3.2.4 Radial temperature profile and effect of the wall temperature . . . 60

3.3 Electric field (E_{field}), specific energy input (SEI) and electron energy distribution function (EEDF) . . . 62

3.4 CO_2 dissociation fraction . . . 64

3.4.1 Dissociation fraction in continuous CO_2 plasma measured downstream . . . 64

3.4.2 Dissociation fraction in continuous CO_2 plasma measured *in situ* . . . 65

3.4.3 Longitudinal profile measured with Raman scattering . . . 67

3.4.4 Effect of the gas flow and residence time . . . 68

3.4.5 Comparison of FTIR and Raman in continuous plasma . . . 72

3.4.6 CO_2 and CO densities for comparison with oxygen data . . . 73

3.5 O atom densities . . . 74

3.5.1 Validity of the diagnostics . . . 74

3.5.2 Oxygen atom density variation . . . 77

3.5.3 O atom densities as a function of gas flow . . . 78

3.5.4 O atom loss frequency . . . 78

3.6 Discussion . . . 81

3.6.1 CO and O atom densities . . . 81

3.6.2 O atom loss processes . . . 83

3.7 CO and oxygen atom densities in pulsed plasma . . . 87

3.7.1 CO densities . . . 88

3.7.2 O atom densities . . . 90

3.8 Summary and conclusions 91

3.1 Introduction

The discharges used in this thesis are deliberately simple, but they are homogeneous and reproducible, and can be easily adjusted to multiple experimental configurations and diagnostics, as detailed in the previous chapter. This gives us the opportunity to isolate and study individual processes. Nevertheless, to achieve this goal, it is first necessary to have sufficient knowledge of the system under study in its "normal" operating mode, and be confident in the experimental results. This chapter has therefore two main objectives:

- Provide a general characterization of the system under study in our basic working conditions.
- Validate the diagnostics that will be used all along this thesis.

We will start with the study of two basic plasma parameters: gas temperature and reduced electric field. These are key parameters in any gas discharge strongly determining the chemistry through their influence on the rate coefficients of many processes. Subsequently a study of the densities of the main dissociation products in different discharge conditions is presented. Experiments were performed at pressures in the range of 0.2-5 Torr (26.7-666.6 Pa) and discharge currents from 10 to 50 mA, in continuous, modulated and pulsed regimes.

FTIR absorption spectroscopy and Raman spectroscopy were used to determine the densities of CO and CO_2 in the discharge, and thus the dissociation rate. Special care has been taken to determine accurately the absolute O atom densities under the same conditions where the CO_2 and CO densities are also well characterized. Therefore, three different experimental techniques were used: actinometry, High Resolution-Two photon Absorption Laser Induced Fluorescence (HR-TALIF) and Cavity Ring-Down Spectroscopy (CRDS), described in chapter 2, which will be discussed in detail to assess the level of accuracy of the absolute values obtained. In this chapter we also determine the O atoms loss frequency under direct plasma exposure using a time-resolved actinometry technique in partial modulated discharges, allowing the discussion of the main O atom loss mechanisms in our discharge conditions.

3.2 Gas temperature in CO_2 plasmas

The gas temperature, T_{gas}, is an essential parameter required for a good description of the CO_2 plasma kinetics. The gas temperature was determined independently in different conditions by three diagnostic techniques: HR-TALIF, Raman scattering and infra-red absorption (FTIR). Preliminary measurements with CRDS will be also briefly introduced. The accuracy of the techniques and consistency between them is discussed first. The variation of T_{gas} as a function of pressure and current and its evolution along a plasma pulse are subsequently discussed. Finally, the radial temperature profile in the discharge is analysed at the end of the section. The different experimental details are summarized in the experimental box 3.1.

Diagnostics: FTIR (TOoE), HR-TALIF, Raman, CRDS **Discharge**: Glow - Continuous FTIR Raman HR-TALIF & CRDS - Pulsed (5-10ms On-Off) FTIR & Raman	**Reactor**: DW/SW Short FTIR, DW Long TALIF & CRDS, SW Short+ extensions Raman T_{wall}: Continuous: HR-TALIF 5 & 50^{o}C , FTIR 50^{o}C CRDS 25^{o}C; Pulsed: not controlled (FTIR & Raman)	**Pressure**: - **0.4-5** Torr Continuous - **1-5** Torr Pulsed **Current**:**10-50** mA **Flow**: 7.4 sccm (τ_{res} ≈0.15-1.65 s) (short tube)

Experimental box 3.1: Gas temperature determination.

3.2.1 Accuracy of the gas temperature diagnostics techniques

A complete parametric study in terms of current and pressure was done with two diagnostics in continuous discharge: FTIR and TALIF. These measurements were taken in a doubled-walled reactor with controlled wall temperature fixed at 50^{o}C. The rotational temperature of CO_2 and CO (T_{rot}) was obtained by fitting the FTIR absorption spectra *Klarenaar et al.* [2017]. The translational temperature of the oxygen atoms was obtained by fitting the Doppler broadening of the TALIF profile *Booth et al.* [2015]. Figure 3.1 shows the variation of both as a function of current and pressure. Rotational Raman scattering *Klarenaar et al.* [2018] and CRDS measurements in continuous plasma (preliminary tests) were also taken for two currents, 20 and 40 mA. Raman data was taken without controlling the wall temperature, and CRDS with a T_{wall}=25^{o}C. Figure 3.2 shows the comparison between T_{rot} obtained with Raman and the translational temperature of O atoms measured with CRDS with the other two techniques. The temperatures obtained by the four diagnostics are very comparable, showing a monotonous increase of temperature with pressure and current. This consistency allows us to assume that T_{rot} is in equilibrium with the gas temperature and confirms that O atoms and CO_2, CO and O_2 molecules are in thermal equilibrium in our discharge conditions.

Beyond the general good agreement between the four diagnostic techniques and looking in more detail, we observe that the temperatures obtained with TALIF and Raman are very similar and both tend to be slightly higher than those obtained with FTIR. The difference increases with pressure and current and can be explained by the radial temperature gradient in the discharge tube, further discussed in section 3.2.4. The gas temperature at the centre of the tube and the radial gradients increase with both pressure and current. The laser beams used for TALIF and Raman scattering are relatively small, measuring therefore the temperature at the tube axis (the hottest point). Note that in the case of Raman the beam is focused in the centre of the discharge tube, and the wall temperature is not controlled. The good agreement with TALIF, obtained with the wall temperature at 50^{o}C using a collimated beam confirms that both techniques diagnose the maximum temperature in the discharge tube. In contrast, the infra-red beam used for FTIR measurements is larger, filling a large part of the tube radius; the temperature obtained is therefore an average over the radial profile of the discharge tube.

For the following calculations, the temperature obtained with TALIF is used to obtain O atom densities from the TALIF signal, whereas the rotational temperature obtained by FTIR is used to treat FTIR data, actinometry and to obtain the reduced electric field. CRDS agrees well with Raman and TALIF at 40 mA, whereas at 20 mA is slightly higher. More tests should be carried

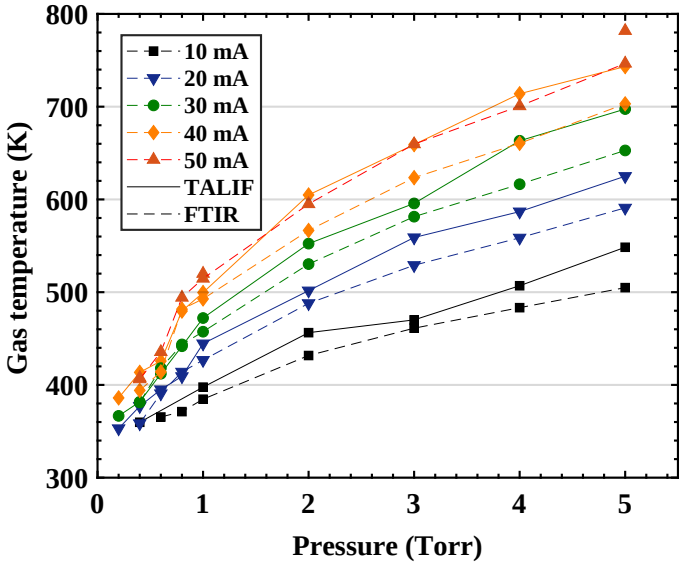

Figure 3.1: Gas temperature variation *versus* pressure for currents between 10 and 50 mA obtained from the FTIR spectra (rotational temperature of CO_2 and CO) and from the Doppler broadening of TALIF signal (translational temperature of O atoms).

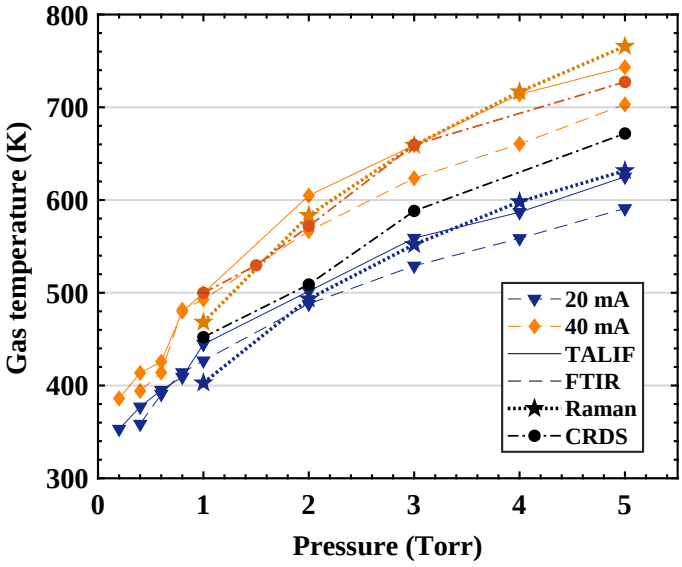

Figure 3.2: Gas temperature variation as a function of pressure for 20 and 40 mA obtained from the Doppler broadening of TALIF and CRDS signals, and rotational temperatures of CO_2, CO (and O_2) obtained with Raman scattering and FTIR.

out to validate the gas temperatures measured with CRDS and in the following these temperatures will be used only to calculate the O atom density in continuous plasma with CRDS.

3.2.2 Gas temperature dependence

In figures 3.1 and 3.2 we see that T_{gas} increases with both current and pressure. Such a trend can be explained by the higher power dissipated in the plasma as the current is increased, and the higher voltage (and therefore power) required to maintain the current as the pressure is increased.

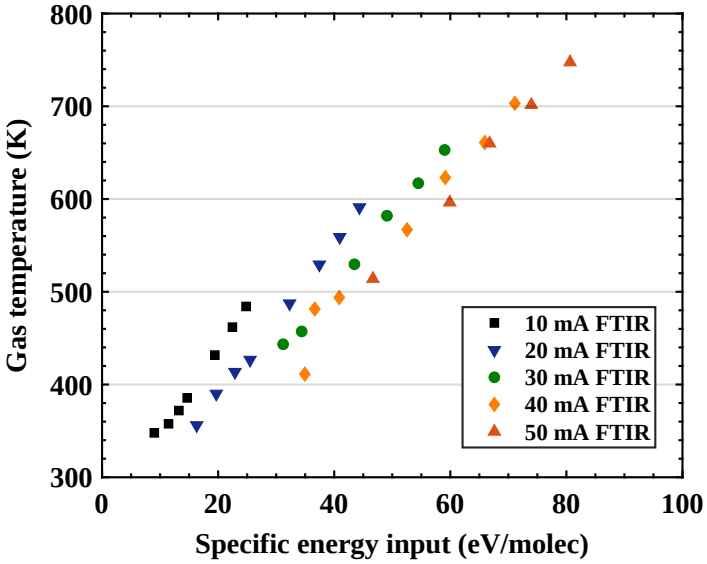

Figure 3.3: Gas temperature variation for currents between 10 and 50 mA obtained from the FTIR spectra (rotational temperature of CO_2 and CO) as a function of the specific energy input (SEI).

This dependence is clear when plotting T_{gas} *versus* the energy input, shown in figure 3.3. An almost linear increase of the gas temperature with the specific energy input (SEI) can be observed. The SEI is calculated from the discharge power dissipated in the positive column divided by the molecular flow, and takes into account the residence time of the gas in the plasma (see the details about the calculation of the SEI in section 3.3). The exact mechanisms responsible for the conversion of electrical energy into gas heating are complex, but could include enhanced V-T transfers at higher pressure, and possible exothermic reactions *Grofulović* [2019]. Additionally, the increased diffusion time towards the reactor walls when increasing pressure results in a reduced number of collisions with the wall compared to the number of molecules. The heat release through the walls is then reduced contributing to the increase of the gas temperature as a function of pressure.

Temperature measurements in pulsed plasma were done both with Raman and FTIR (without

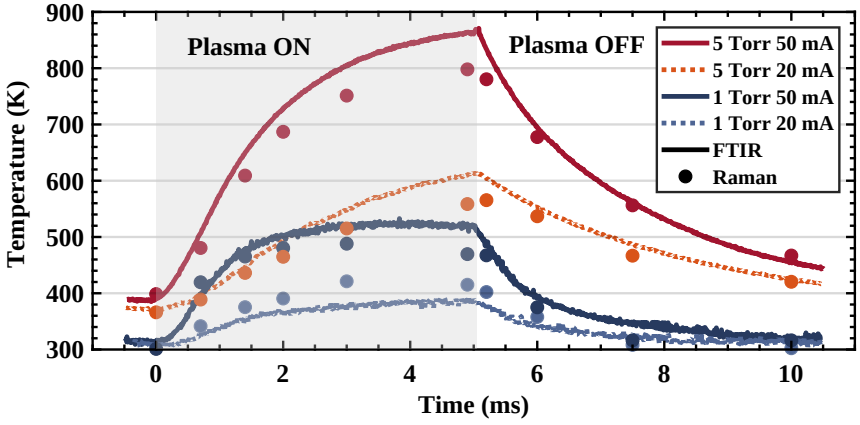

Figure 3.4: Time evolution of the rotational temperature along a plasma pulse of 5-10 ms On-Off for 1 and 5 Torr, 20 and 50 mA measured with FTIR and rotational Raman scattering.

controlling the wall temperature in any case). The obtained time-resolved evolution of T_{rot} in both cases is presented in figure 3.4 for a plasma pulse of 5-10 ms On-Off at 1 and 5 Torr, and 20 and 50 mA. The agreement between both techniques is very good, although in this case the values obtained with Raman are slightly lower than those measured with FTIR, except at 1 Torr, 20 mA. Similarly to the continuous data, the gas temperature increases with pressure and current. Nevertheless, the main interest of time resolved pulsed measurements is the information about the characteristic time of the temperature variation. In general, the values at the end of the pulse match relative well the temperatures in continuous plasma, except at 5 Torr 50 mA, where in the case of FTIR are slightly higher. The time variation of the gas temperature is faster at 1 Torr and it reaches a steady-state value at around ∼3 ms, whereas at 5 Torr at the end of the pulse T_{gas} is barely reaching the steady-state.

3.2.3 Residence time and diffusion time toward the walls

The residence time τ_{res} of the molecules under plasma exposure affects the specific energy input per molecule and therefore the dissociation fraction, as will be discussed in section 3.4.4. Assuming a laminar flow, τ_{res} depends directly on the gas temperature and the flow according to the expression:

$$\tau_{res} = \frac{N}{f} = \frac{{}^{PV}/_{KT_{gas}}}{\phi_{(sccm)} \cdot ({}^{P^oV^o}/_{KT^o})} \tag{3.1}$$

where N is the gas density in the positive column of the glow discharge (using the distance between the electrodes to calculate the plasma volume) and ϕ is the gas flow, measured in units of sccm (standard cubic centimetres per minute). P^o, T^o and V^o represent the different variables in standard conditions of pressure and temperature. 1 sccm therefore is equivalent to 4.4779×10^{17} ${}^{molec}/_{s}$. Figure 3.5 plots τ_{res} in our typical conditions, to give an order of magnitude for this parameter. τ_{res} increases with pressure and decreases with current due to the effect of the gas temperature. Values of τ_{res} for different gas flows will be presented in section 3.4.4.

Another relevant parameter dependent on the gas temperature is the diffusion time towards the

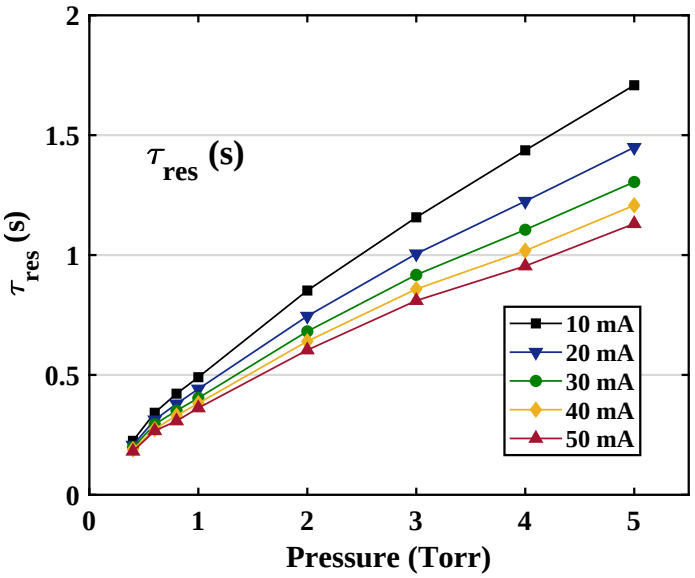

Figure 3.5: Variation of the residence time, τ_{res}, as a function of pressure and current.

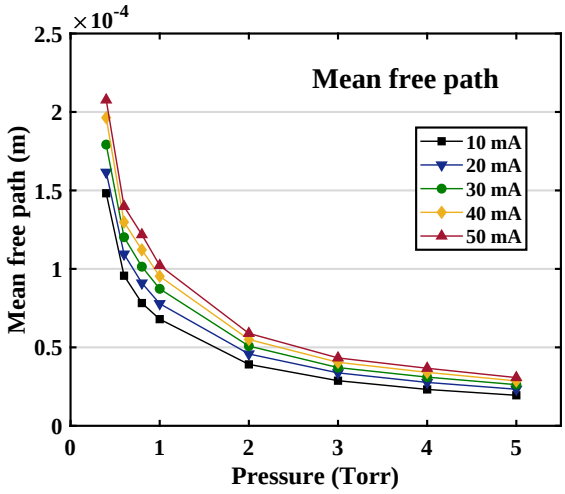

Figure 3.6: Mean free path of oxygen atoms as a function of pressure and current.

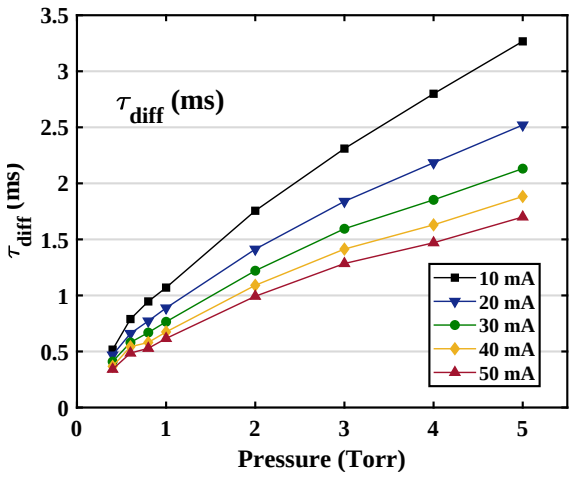

Figure 3.7: Diffusion time τ_{diff} towards the walls of oxygen atoms.

reactor walls τ_{diff}, given by the expression:

$$\tau_{diff} = \frac{\Lambda_O^2}{D} \tag{3.2}$$

where D is the diffusion coefficient and Λ_O is the diffusion length given, for a cylindrical reactor, by:

$$\frac{1}{\Lambda_O^2} = \left(\frac{\pi}{L}\right)^2 + \left(\frac{2.405}{R}\right)^2 \tag{3.3}$$

where L is the length and R is the radius of the cylindrical reactor, in our case $\Lambda_O \sim 0.42$ cm. D can be calculated with the equation:

$$D = \frac{1}{3} l v_{th} = \frac{1}{3}\left(\frac{k_B T}{\sqrt{2}\cdot P\pi d^2}\right)\cdot\sqrt{\frac{8k_B T}{\pi\cdot m_o}} \tag{3.4}$$

where l is the mean free path, d is the kinetic diameter and v_{th} is the thermal velocity. The diffusion coefficient differs for different molecules or atoms due to the effect of the mass and the kinetic diameter. Values of d for different molecules are given in *Mehio et al.* [2014]: 376 pm for CO, 330 pm for CO_2 and 346 for O_2. No values could be found for oxygen atoms and the same radius as for O_2 was assumed in the calculations. However, estimations from diffusion measurements suggest that the value of the kinetic diameter for O could be lower, close to 300 pm *Booth* [2019]. The diffusion coefficients for different molecules and oxygen atoms with both values of the kinetic diameter are shown in the following section. Figures 3.6 and 3.7 plot the variation with pressure and current of the mean free path and τ_{diff} (for an oxygen atom with d=346 pm). The mean free path decreases significantly with pressure, as expected, whereas τ_{diff} increases with pressure and decreases with current similarly to τ_{res}. The maximum of τ_{diff} ≈3.27 ms at 5 Torr 10 mA.

A more accurate calculation of the diffusion coefficient for different molecules towards the walls could be done considering Wilke's formula *Terraz et al.* [2019] and the binary diffusion coefficient given by *Bird et al.* [1954] which takes into account the different diffusion coefficients for excited species. This correction was considered negligible in our case as it becomes relatively small as the

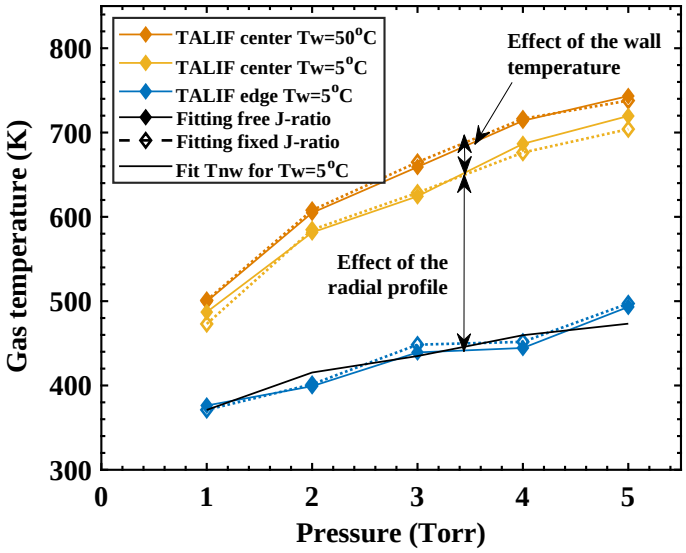

Figure 3.8: Gas temperature variation as a function of pressure for a current of 40 mA obtained from the Doppler broadening of TALIF signal measured at the centre of the plasma reactor for wall temperatures of 5^{o}C and 50^{o}C and at the edge of the plasma reactor, T_{nw} at 5^{o}C. The fitted T_{nw} according to equation (3.6) is also included.

temperature increases *Kovacs et al.* [1968]; *Doyennette et al.* [1974].

3.2.4 Radial temperature profile and effect of the wall temperature

The radial temperature profile will be especially important when discussing surface processes in chapter 8 because of two reasons:

- The diffusion time towards the wall, τ_{diff} is long enough so that the particles thermalize to the temperate close to the wall before reaching the surface.
- The radial temperature profile induces a density profile and therefore affects the density of particles close to the surface.

To study the radial temperature profile, the collimated TALIF laser beam was translated along the radial axis of the reactor in order to measure the temperature as close as possible to the reactor walls, the so-called temperature near-the-wall, T_{nw}. In practice, the beam was moved until a decrease of the fluorescence signal was noticeable, indicating that we were touching the reactor walls. Then, the position was slightly corrected to avoid being in contact with the tube. The wall temperature can affect both the temperature in the center of the tube and the temperature near the wall. Figure 3.8 shows measurements done with TALIF with T_{wall}=50^{o}C and 5^{o}C in the centre of the discharge tube, to illustrate the effect of T_{wall} and measurements of T_{nw} for T_{wall}=5^{o}C to illustrate the effect of the radial profile, for pressures between 1 and 5 Torr at 40 mA. The figure includes the temperature values obtained keeping free the ratio between the J-components of the fine structure of TALIF signal or fixing them to the theoretical values (as discussed in section 2.4.2), to give an idea of the accuracy in the determination of the temperature by HR-TALIF. We observe that the wall temperature induces an "offset" in the temperatures measured at the centre of the tube, slightly lower than the change in the wall temperature (∼30-40K).

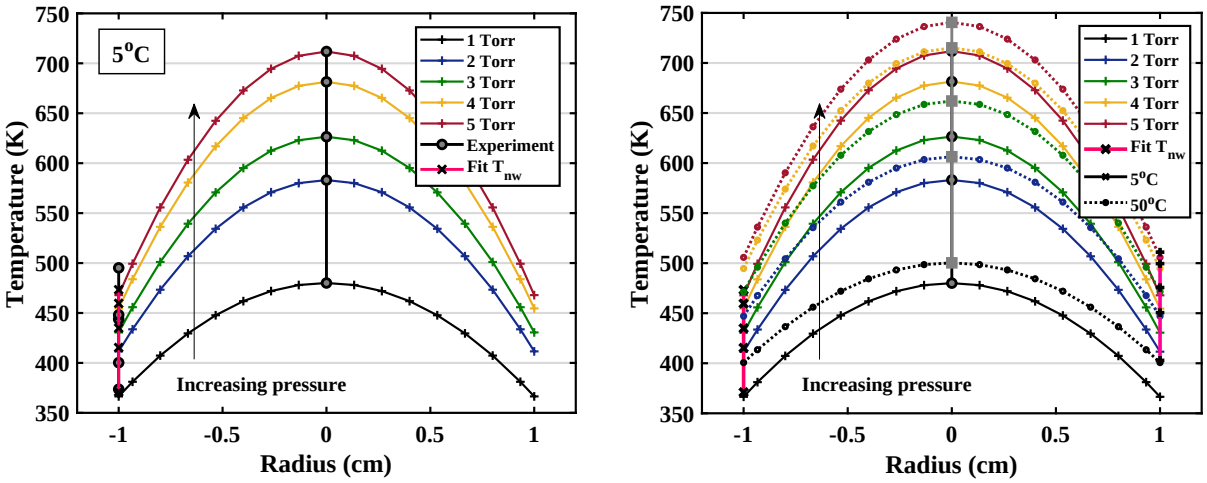

(a) Gas temperature profile for T_{wall}=5°C.

(b) Gas temperature profiles for T_{wall}=5°C and 50°C.

Figure 3.9: Gas temperature radial profiles calculated from the experimental $T_{gas}(max = TALIF)$ and the fitted T_{nw} for pressures between 1 and 5 Torr, 40 mA. The experimental values of $T_{gas}(max = TALIF)$ and T_{nw} at T_{wall}=5°C are included.

T_{nw} is considerably lower than the gas temperature in the center of the tube but still higher than the fixed wall temperature. Provided that the temperature drop across the Pyrex tube wall can be considered negligible (less than 2 K), there is a temperature jump between the wall temperature and the gas temperature in contact with it, δT=T_{nw}-T_w, which depends on the pressure, the heat flux to the walls and the thermal accommodation coefficient of the gas particles hitting the tube surface *Booth et al.* [2019]. In an O_2 discharge in similar experimental conditions, a comparison between modelling results and experimental data allowed to deduce a simple relation between T_{nw}, T_{gas} and T_{wall}:

$$T_{nw} = T_w + 0.28 \cdot (T_{gas} - T_w) \tag{3.5}$$

For CO_2, the experimental T_{nw} values could be fitted with a similar expression:

$$T_{nw} = T_w + 0.45 \cdot (T_{gas} - T_w) \tag{3.6}$$

An example of the fit is included in figure 3.8 (solid black line). The different "slopes" in equations (3.5) and (3.6) could be related to the different accommodation coefficients for the molecules involved *Wachman* [1962]. We assume that these expressions are valid for every wall temperature and they will be used in chapter 8 to calculate T_{nw}, required, for instance, for the calculation of the O atom loss probabilities.

We assume a parabolic temperature profile according to the expression:

$$T_{gas}(r) = T_{gas}(max) - (T_{gas}(max) - T_{nw}) \cdot \left[\frac{r}{R}\right]^2 \tag{3.7}$$

where $T_{gas}(max)$ is T_{gas}(TALIF, Raman). Based on this assumption, figure 3.9 plots the temperature profile for T_{wall}=5°C (panel (a)) using T_{gas}(TALIF) data as $T_{gas}(max)$ and the fitted T_{nw} values. Figure 3.9 plots the same magnitude for both T_{wall}=5°C and T_{wall}=50°C for comparison. From the temperature profile we obtain the corresponding gas density profile, plotted in figure

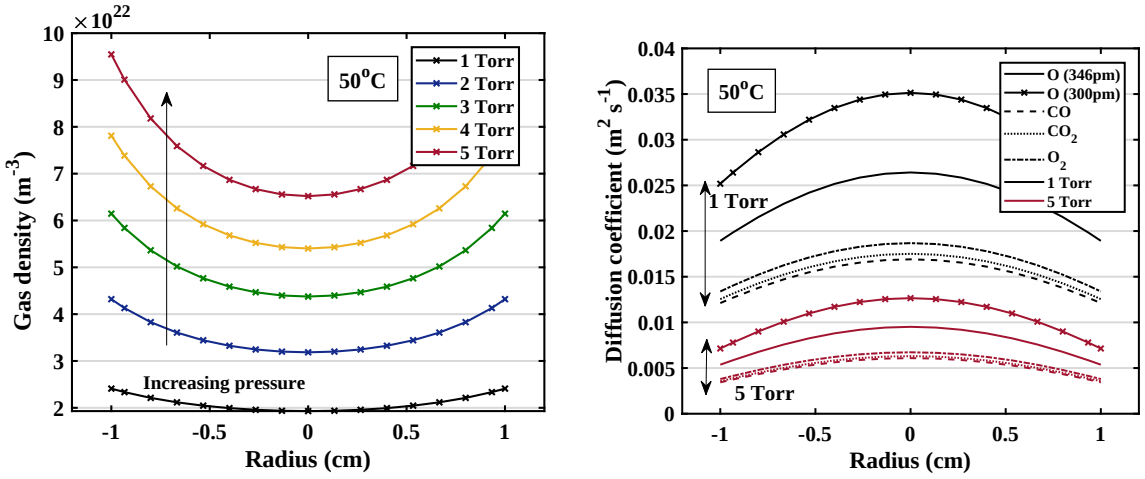

(a) Gas density radial profile at T_{wall}=50°C.

(b) Diffusion coefficient for 1 and 5 Torr at T_{wall}=50°C for CO, CO_2, O_2 and O atoms

Figure 3.10: Radial profiles of gas density (panel (a)) for pressures between 1 and 5 Torr, 40 mA and diffusion coefficient (panel (b)) for only 1 and 5 Torr, 40 mA, for CO, CO_2, O_2 and O atoms, for two values of the kinetic radius, 300 pm and 346 pm, in the latter case.

3.10(a). The profile in the diffusion coefficient calculated for the main neutral gas components is plotted in figure 3.10 for 1 and 5 Torr. Oxygen atoms diffuse significantly faster, with both possible kinetic diameters compared to CO, CO_2 or O_2, which are very similar.

3.3 Electric field (E_{field}), specific energy input (SEI) and electron energy distribution function (EEDF)

The axial electric field was obtained from the voltage drop across the positive column of the glow discharge between the two tungsten probes, as described in section 2.2.1. The measured values and the corresponding reduced electric fields are shown *versus* pressure and gas density in figures 3.11 (a) and (b) respectively. For a given current, the reduced electric field decreases with pressure (opposite trend to the electric field), whereas at a given pressure the reduced field increases with current due to the effect of gas heating on the gas density. A single monotonous dependence with gas density is observed for all currents and pressures measured. As expected, a higher field is required to sustain the plasma when the gas density is higher, but the reduced electric field is smaller. The E/N values along with the gas temperature allow the calculation of the electron distribution function (EEDF). As an illustrative example, the EEDF calculated for 2 and 5 Torr, 40 mA with the Boltzmann solver LoKI *Tejero-del Caz et al.* [2019] using the densities of CO_2, CO, O_2 and O atoms measured in the long discharge tube (see sections 3.4.6 and 3.5) is plotted in figure 3.12. The energy levels of several excited states and the threshold for different dissociation processes of CO_2, CO and O_2, according to the energy levels presented in figure 1.4 are detailed.

The power dissipated in the positive column can be calculated from the electric field and the discharge current, giving values up to 35.5 W for the short tube (17 cm between electrodes) and up to 106.5 W in the long discharge tube (54 cm between electrodes) for the highest pressure. This power differs from the total power feeding the discharge due to the power dissipated in regions such

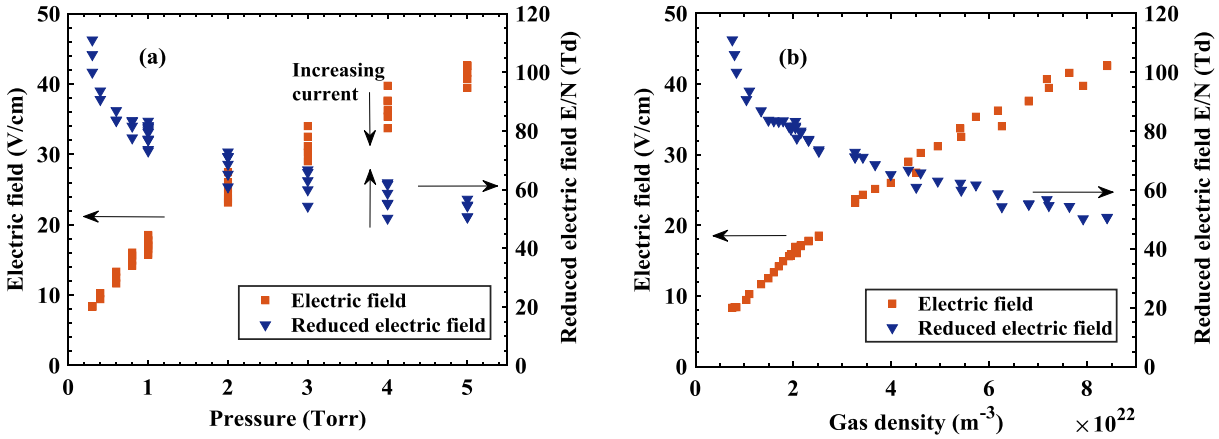

Figure 3.11: Variation of the electric field (left axis) and reduced electric field (right axis) as a function of pressure (panel(a)) and gas density (panel (b)).

as the cathode fall *Raizer* [1991], which do not contribute significantly to the total dissociation. This has been verified by comparing downstream FTIR measurements with two discharge tubes lengths, which gave the same dissociation rate as a function of residence time.

In order to calculate the specific energy input (SEI) we use the following expression:

$$SEI = \frac{P \cdot \tau_{res}}{N(T_{gas} = 300K)} = \frac{I \cdot V \cdot N(T_{gas})}{\phi \cdot N(T_{gas} = 300K)} \tag{3.8}$$

Note that in general the SEI is defined as a ratio between the dissipated power and the molecular flow. However such an expression would not take into account the effect on the flow of the gas

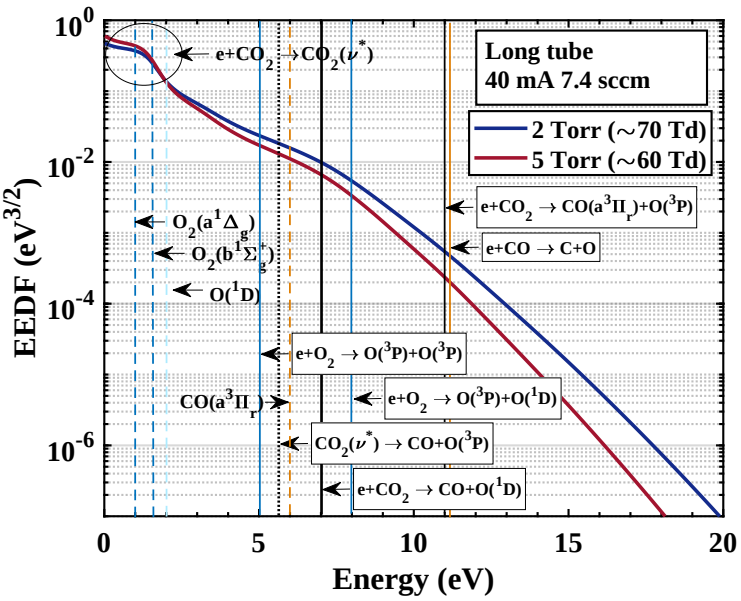

Figure 3.12: EEDF calculated for 2 and 5 Torr 40 mA. The energy levels of several excited states and the threshold for several dissociation processes of CO_2, CO and O_2 are included, according to the energy levels presented in figure 1.4.

expansion due to heating in the discharge. Equation (3.8) takes into account the real residence time of the molecules under discharge conditions. $N(T_{gas} = 300K)$ represents the number of molecules "to be exposed" to the plasma.

3.4 CO_2 dissociation fraction

The dissociation fraction measured in different experimental conditions is presented in this section. We discuss two basic set-up configurations: (1) *In situ*, in which the infra-red absorption measurements were performed directly through the short discharge tube (23 cm) placed in the sample compartment of the FTIR (see figure 2.5); and (2) Downstream, in which the same plasma reactor is placed upstream a measurement cell (of similar geometry as the plasma reactor) installed in the FTIR sample compartment. In a second step, an especially designed reactor ("L-shape") with two branches: one to measure *in situ* and one to measure downstream was used (see figure 2.1 (a.2)). The "L-shape" configuration allowed to switch fast between both experiments and makes sure that no other surface material but Pyrex is in contact with the effluent of the discharge (more details are given in section 3.4.4). The main diagnostic technique will be FTIR. Only a a few measurements done with Raman scattering (performed at TU/e) are included to provide insight in the longitudinal profile along the discharge tube, taking advantage of its spatial resolution. The experimental details are summarized in the experimental box 3.2.

Diagnostics: FTIR	**Reactor**: DW Short,	**Pressure**: **0.4-5** Torr
Raman	DW L-shape, SW	**Current**: **10-50** mA
Discharge: Glow	Short+extension (Raman)	**Flow**: **0.1-7.4** sccm
Continuous plasma	$\boldsymbol{T_{wall}}$: 50^{o}C FTIR, not	($\boldsymbol{\tau_{res}}$: **0.2-110** s)
In situ & downstream	controlled Raman	

Experimental box 3.2: Measurements of the dissociation fraction in flowing conditions.

3.4.1 Dissociation fraction in continuous CO_2 plasma measured downstream

Measuring densities or fractions of different gas compounds downstream the gas discharge is the most common way to study the chemical reactivity in plasmas. Many diagnostic techniques such as mass spectrometry, gas chromatography, etc., work downstream and FTIR is also very often used in this configuration. Figure 3.13 shows the measured dissociation fraction α (panel (a)), the (molar) fractions of CO and CO_2 (panel (b)) and the absolute densities of CO, CO_2 along with the total gas density as a function of pressure for currents between 10 and 50 mA measured downstream for a gas flow of 7.4 sccm. The equations relating these parameters are discussed in section 2.3.1.

Figure 3.13 (a) shows that the dissociation fraction depends only on the discharge current in these experimental conditions. No variation with pressure is observed in α or in the CO or CO_2 fractions. CO and CO_2 absolute densities increase with pressure due to the increase of the total gas density, which does not vary with current since the gas temperature is close to room temperature in the measurement cell. We now wonder if these data is representative of the dissociation fraction in the discharge. In the following section we compare the downstream data with the values measured *in situ*.

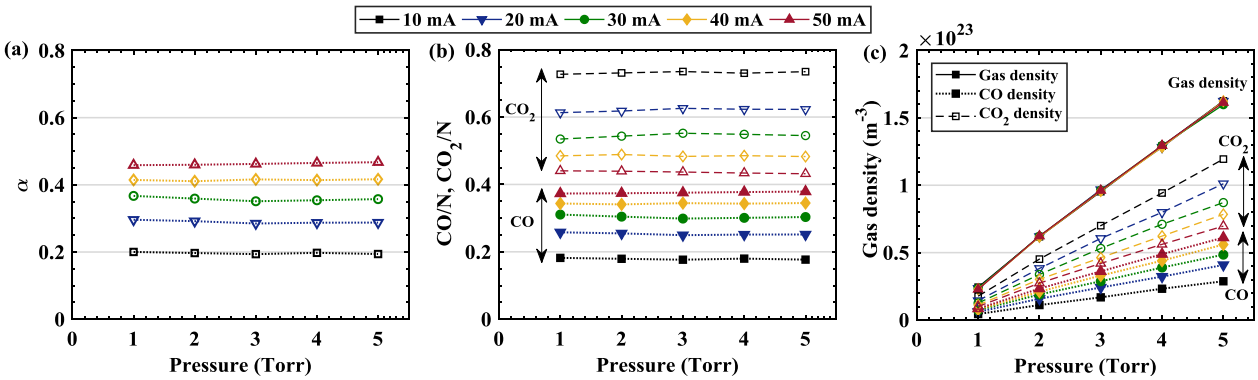

Figure 3.13: Variation of α (a), CO and CO_2 fractions (b) and CO and CO_2 densities along with the total gas density (c) measured downstream for pressures between 1 and 5 Torr and currents between 10 and 50 mA.

3.4.2 Dissociation fraction in continuous CO_2 plasma measured *in situ*

In situ measurements were taken placing the same plasma reactor in the measurement compartment of the FTIR. Figure 3.14 (a) shows the variation of α as a function of pressure for both *in situ* and downstream configurations at a constant gas flow of 7.4 sccm. Solid lines with filled symbols represent the data taken with the plasma reactor *in situ*. Dashed lines with empty symbols present the data obtained with the measurement cell placed downstream the discharge. Panel (b) in figure 3.14, plots the same data but as a function of current, for only three pressures (for readability) 0.6, 2 and 5 Torr in the case of *in situ* measurements and only for 2 and 5 Torr for downstream data. Lower pressures than 1 Torr were not possible in the downstream configuration due to the longer gas line.

In the case of *in situ* measurements we observe that the dissociation fraction increases only very slightly with pressure, especially for the highest currents whereas downstream data shows a

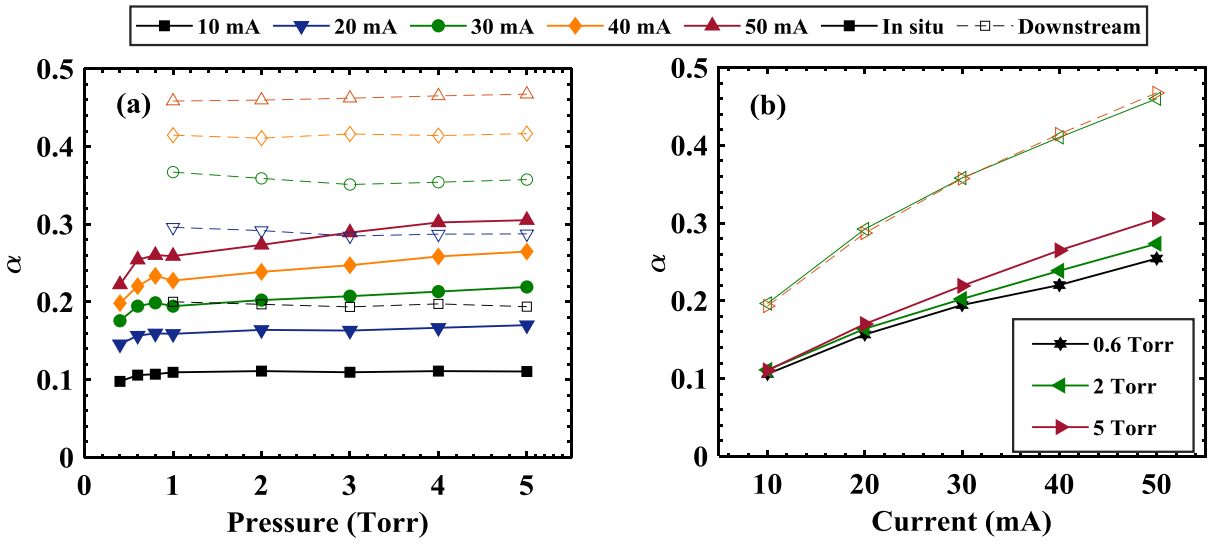

Figure 3.14: Variation of α as a function of pressure (a) and current (b) measured *in situ* and downstream.

constant α. In both cases the dissociation increases with current, as expected from the higher electron density, although both graphs show a certain saturation at higher currents. Nevertheless, the most striking feature in these graphs is the significant difference in the dissociation fraction between *in situ* and downstream configurations. Several hypothesis can be put forward:

1. Effect of the density profile
2. Effect of electronically excited states
3. Artefact of the fitting script
4. Longitudinal profile along the discharge tube
5. Post-discharge chemistry

The first three options suppose a certain under-estimation of the dissociation fraction *in situ*. We have seen that the diffusion coefficient of CO and CO_2 is very similar (see figure 3.10(b)) therefore even though there is a radial density profile, the parameter α should be radially ∼constant. Electronically excited states of CO, such as CO($a^3\Pi_r$), may exist in the discharge and could deplete the ground state CO density affecting *in situ* measurements, although their density is not expected to be very high due to the fast reaction rate *Cenian et al.* [1994] and their short lifetime ∼2.5-7.5 ms *Mori et al.* [2002]; *Gilijamse et al.* [2007]. The excitation of vibrational levels of CO($a^3\Pi_r$) falls in a region (between 1635 and 1780cm^{-1} *Davies and Martin* [1990]) that could be detected by the FTIR, but no clear absorption band was visible in the measured spectra, indicating that the density of CO($a^3\Pi$) is under the detection limit of the FTIR. Higher excited states would have even lower densities.

Finally the fitting results (hypothesis 3) could be affected by some of the assumptions done in the fitting script, such as the recombination of the O atoms into O_2, or the definition of thermal and non-thermal volumes. We have done an experiment dedicated to test these three hypothesis together: repetitive measurements switching the plasma ON and OFF in static conditions (no flow), that will be presented in section 6.3.1. The experiment shows very good agreement between the α values obtained when the plasma in ON and fitted with the TOoE script, and when it is OFF and fitted with the thermal script, discarding an effect of electronically excited states, different radial profiles for CO and CO_2, or an artefact of the fitting script. The ON/OFF comparison, directly in the same reactor and with the same gas mixture (just during the plasma pulse *versus* the post-discharge) is a good condition to benchmark the out-of-equilibrium script (OoE) against the simpler thermal equilibrium script. The good agreement between the dissociation fractions measured with Raman and FTIR (shown in the following sections) also supports the accuracy of the fitting script.

The two last hypothesis (longitudinal profile or post-discharge chemistry) are discussed in the following sections. FTIR *in situ* measurements are line-of-sight integrated and give an averaged value along the longitudinal axes of the discharge tube. If there is a steep longitudinal profile, lower α values could be expected *in situ* (see schematic representation in figure 3.15 (a)). Downstream measurements would represent then the "last" value of dissociation, at the end of the tube, explaining the higher values. In this case, if we increase the residence time we would tend to the results obtained downstream (having a very steep profile at the very beginning, close to the gas entrance and flat afterwards (see 3.15 (b)). This possibilities are explored in sections 3.4.3 and 3.4.4.

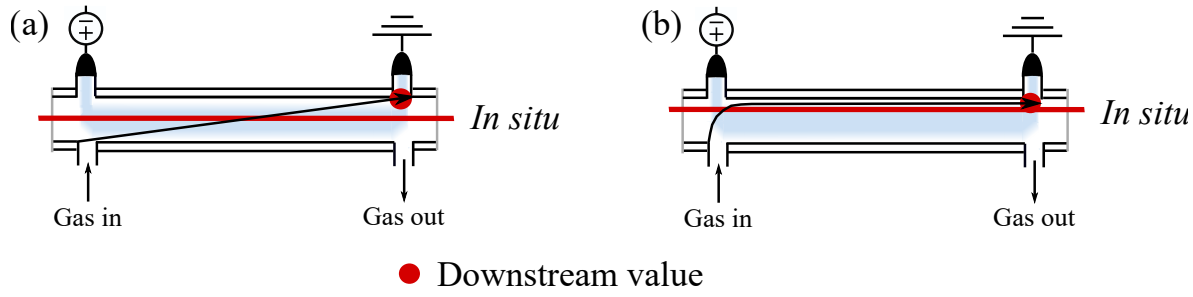

Figure 3.15: Schematic representation of the hypothetical dissociation profile and the values measured *in situ* and downstream for short residence time (linear profile) (a) and long residence time (steep profile at the gas entrance and flat in the rest of the tube) (b).

✓ Dissociation fractions measured downstream are significantly higher than *in situ*. Artefacts from the measurement technique itself are excluded.
✓ α increases with current but does not show any dependence with pressure at a constant gas flow of 7.4 sccm.

3.4.3 Longitudinal profile measured with Raman scattering

Raman scattering, contrary to FTIR, is a spatially resolved technique. As detailed in section 2.3.2, in order to study the longitudinal profile the reactor was translated along the focal point of the laser beam. Figure 3.16 shows the longitudinal profile measured for two pressures, 2 and 5 Torr, 30 mA. The entrance of gas is located at L=0 cm. Both CO_2 and CO traces show a certain longitudinal profile. CO_2 decreases monotonically towards the exit of the discharge, whereas CO slightly increases. The variation of O_2 is apparently flat, but O_2 is the molecule fitted with less precision due to the low density and the convolution of the peaks with those of CO (see figure 2.9 (b)). However, the ratio between α at the output (L=12 cm), as it would be measured downstream,

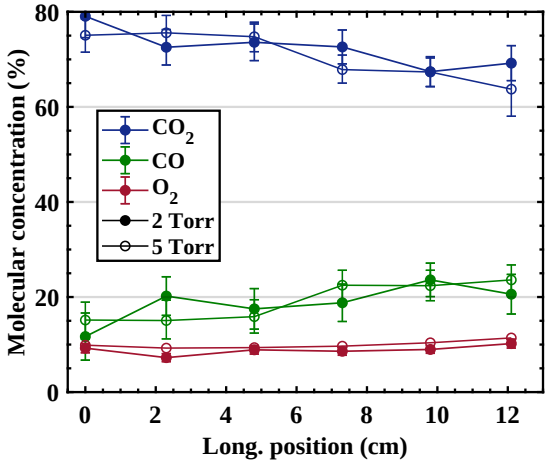

Figure 3.16: Variation of fractions of CO_2, CO and O_2 measured along the longitudinal axis of the discharge tube for 2 and 5 Torr at 30 mA. The gas inlet is located at the position 0 cm and the outlet at 12 cm.

and the average value of α, as it would be measured by FTIR, is only slightly above 1. Therefore, there is indeed a small longitudinal profile but not enough to explain the ratio between downstream and *in situ* between 1.5 and 2 seen in figures 3.14 or 3.18. To explain such an effect, the profile should be much steeper.

The reason of the small profile is because the diffusion tends to homogenize the concentrations in the tube. To assess the contribution of diffusion to the gas mixing we calculate the Péclet number, which represents the ratio of mass transfer by motion in the longitudinal direction due to the gas flow to the mass transfer by diffusion and it is defined as *Klarenaar et al.* [2018]:

$$P_e = \frac{L \cdot u}{D} \tag{3.9}$$

where L is the length of the discharge volume, u is the average flow velocity (L divided by the residence time) and D is the pressure and temperature dependent diffusion coefficient. The closest the Péclet number is to one, the more important is the diffusion. In our conditions this number varies from 1.8 to 5, implying that diffusion dominates over the motion due to the gas flow, homogenizing the concentrations.

✓ The longitudinal profile measured with Raman does not justify the different α values measured downstream and *in situ*.

3.4.4 Effect of the gas flow and residence time

In order to vary the average residence time of the molecules under plasma exposure in our experimental conditions, we simply need to vary the gas flow, as derived from equation (3.1). The measured flows were 0.1, 0.3, 0.5, 1, 2, 3.7, 5.55 and 7.4 sccm (the default flow). Note that the lowest flow values are in the limit of precision of the flow-meters used (3 and 10 sccm full range), therefore the precision with which the lowest gas flows were set (and kept) during the acquisition time is lower, causing the data in these conditions to be slightly more scattered. The gas flow variation

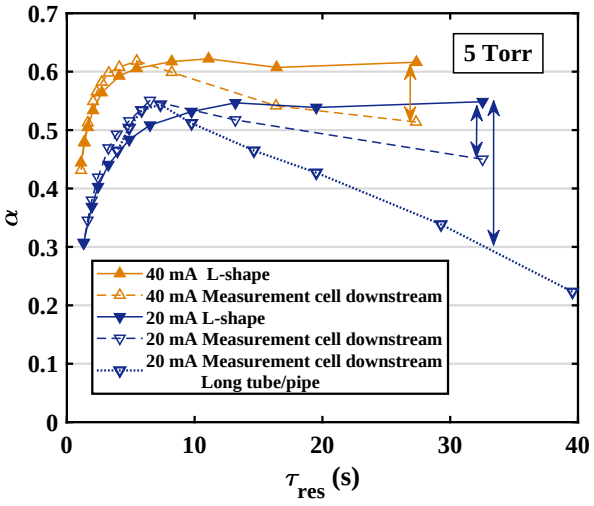

Figure 3.17: Variation of the dissociation fraction measured downstream as a function of the residence time for 5 Torr 20 and 40 mA for different set-up configurations: "L-shape" and *in situ*/downstream for the short and the long tube (the latter with a longest gas pipe).

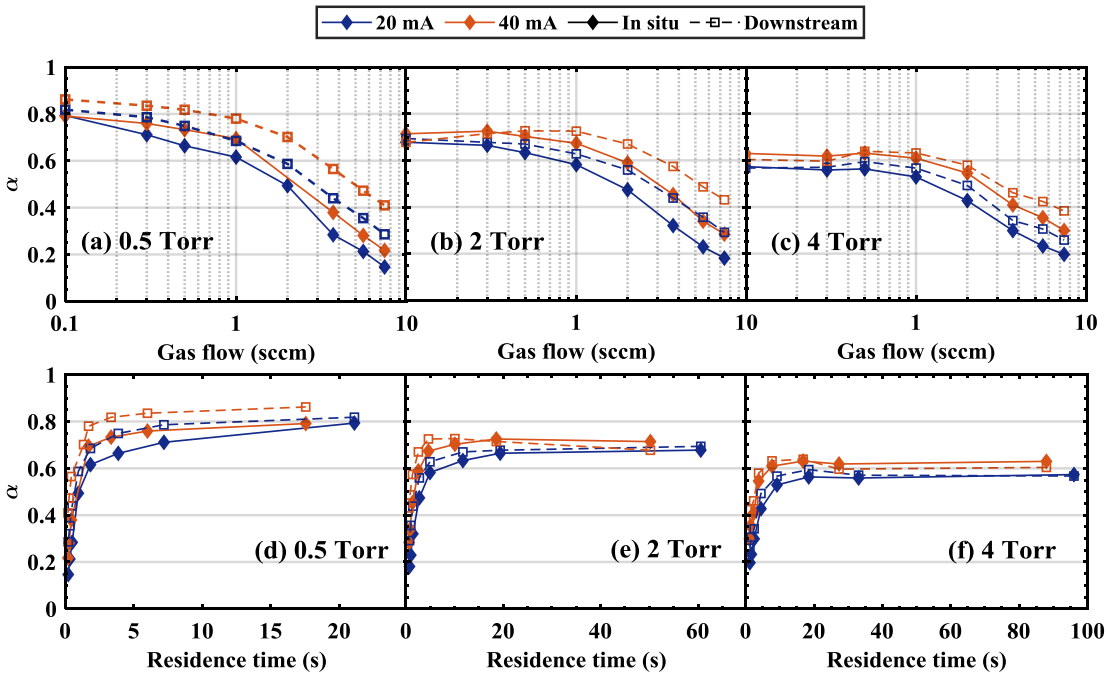

Figure 3.18: Variation of the dissociation fraction, α measured *in situ* and downstream for three different pressures, 1, 2 and 4 Torr and two currents, 20 and 40 mA, plotted as a function of gas flow (panels (a), (b) and (c) respectively) and as a function of the residence time (panels (d), (e) and (f) respectively).

experiments were done with the "L-shape" reactor, schematically represented in figure 2.1 (a.2). Initial measurements were done similarly to the downstream measurements presented in previous sections, *i.e.* the plasma reactor was placed upstream the measurement cell located in the sample compartment of the FTIR, and connected to it through stainless steel corrugated gas pipes. However, evidences of chemistry in the pipes advised to avoid those gas connections and keep a similar, inert, surface material. As example of this effect, figure 3.17 compares the variation of α measured downstream as a function of τ_{res} with the initial measurement cell configuration, downstream the discharge and connected through metal pipes, and with the "L-shape" for 5 Torr, 20 and 40 mA. An extra measurement taken in the downstream of the long tube after a longest metal pipe is also included. Evidently, set-up configurations including metal gas pipes show a significant decrease of the dissociation fraction for long residence times. On the contrary with the L-shape reactor, when the steady-state α is reached, it remains stable for longer residence time. This graphs suggest the existence of post-discharge chemistry ("back reaction" mechanisms) at the metal surface. As a consequence, gas flow variation experiments were done with the L-shape reactor where the surface material between the discharge and the measurement volume is the same (Pyrex).

Figure 3.18 shows the gas flow variation measurements for three different pressures, 0.5, 2 and 4 Torr (panels (a), (b) and (c)), and two currents, 20 and 40 mA, measured *in situ* and downstream. Panels (d), (e) and (f) plot the same data but as a function of the residence time. We can observe in the upper panels of figure 3.18 that the conversion factor increases significantly with decreasing gas flow. The increase is very fast for high gas flow values, and tends to saturate roughly from 1 sccm, reaching the steady-state α value. The lower panels of figure 3.18 shows the increase of α with the residence time. For short τ_{res}, α increases very fast as τ_{res} increases. Note that the X axis in these

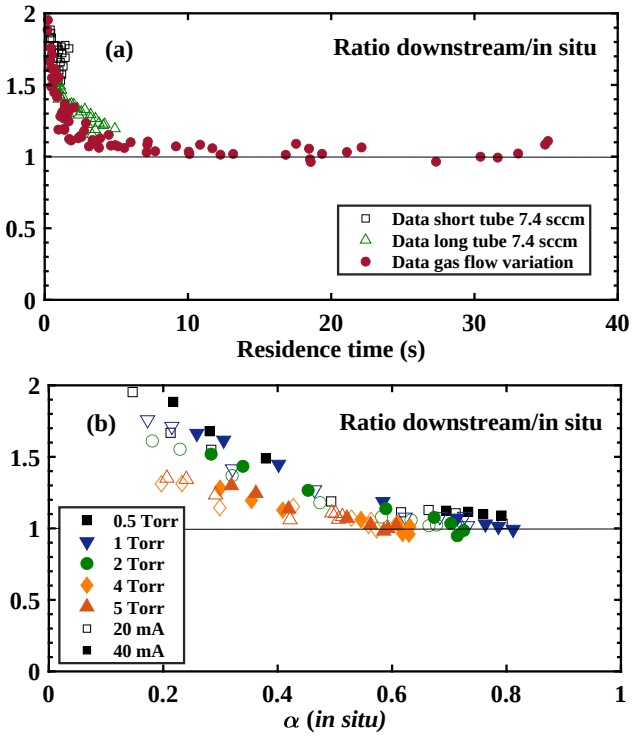

Figure 3.19: Variation of the ratio $R_{d/i} = {}^{\alpha(downstream)}/_{\alpha(in\ situ)}$ as a function of the residence time (panel (a)) and of α measured *in situ* (panel (b)). In panel (a) the data for pressure/current variation plotted in figure 3.14 and the data for the long tube (discussed in section 3.4.6) are included, along with the gas flow variation data (figure 3.18). Panel (b) shows only the data from gas flow variation experiments differentiated by pressure and current.

graphs is different for the three pressures plotted; the steady state is reached for longer residence times at higher pressures. As a reminder, the largest gas flow plotted in figure 3.18 is the same as for the data presented in figure 3.14, 7.4 sccm, which corresponds to the shortest residence time.

It is clear that downstream and *in situ* dissociation values tend to converge for low gas flow *i.e.* for long residence times. The ratio between α downstream and *in situ* ($R_{d/i}$) is plotted versus residence time (only up to τ_{res}=40 s) in figure 3.19 (a). $R_{d/i}$ decays with an exponential-like trend with increasing residence time. For short τ_{res} the ratio reached values as high as 2, and stabilizes around 1 for long residence times. The data presented in figure 3.14 are also included, confirming that for the flow used (7.4 sccm) we are still far from steady-state conditions. Small differences are due to the different distance and configuration of the electrodes, but the trend is the same. α values calculated for the long tube (see section 3.4.6) used for the comparison with oxygen data are also included, showing good agreement with the variation of the ratio $R_{d/i}$ obtained from the gas flow variation experiments.

The exact mechanisms to explain the behaviour seen in figure 3.19 are at this point still unclear but they could be related to a mechanism involving CO (possibly in an excited state). This is suggested by the trends showed in 3.19 (b), where two clearly differentiated regions can be observed. For low α values $R_{d/i}$ decreases ~linearly as a function of α with a slope that depends on the pressure. An abrupt change of slope happens around α=0.5 for all pressures, where the ratio reaches a value ~1.

Another interesting feature is the fact that the dependence of α with pressure is strongly modified

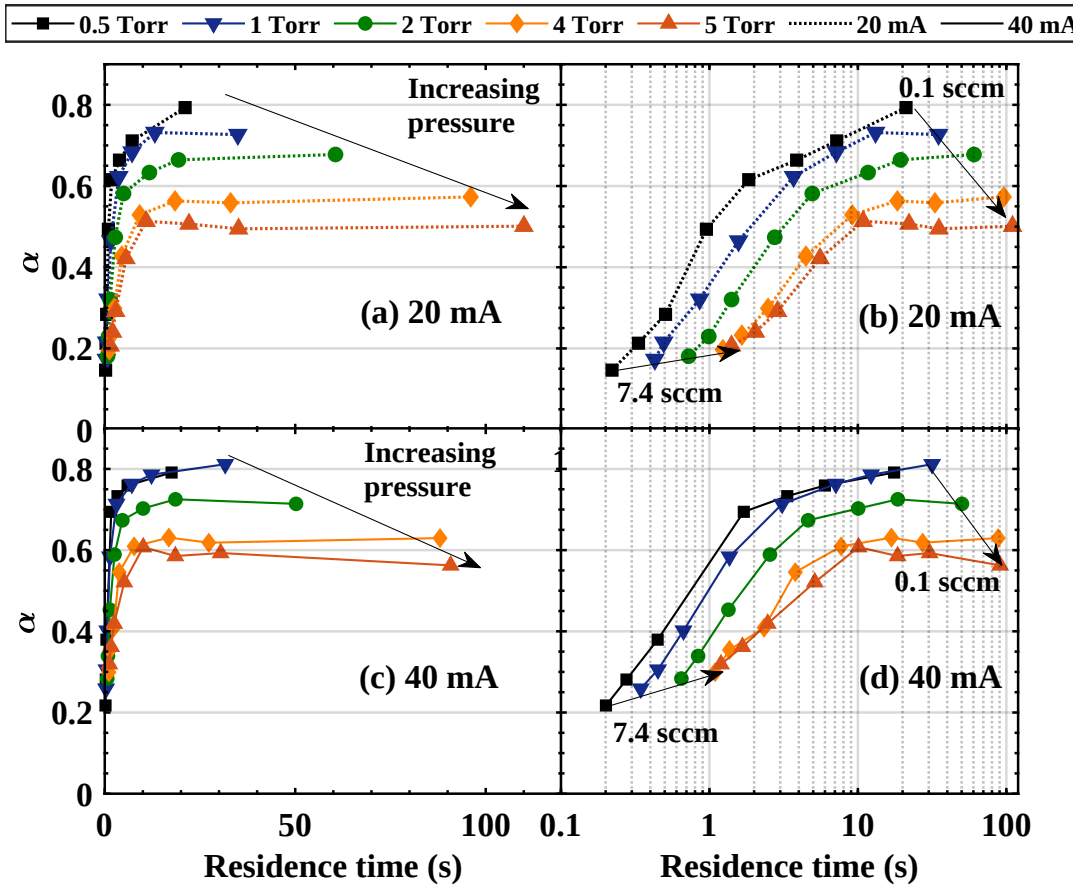

Figure 3.20: Variation of α measured *in situ* with τ_{res} in linear (panels (a) and (c)) and logarithmic (panels (b) and (d)) time scale for 20 ((a) and (b)) and 40 ((c) and (d)) mA and pressures between 0.5 and 5 Torr.

by the residence time. Figure 3.20 plots the variation of α measured *in situ* as a function of the residence time for all the pressures measured and for the two currents, 20 (plots (a) and (b)) and 40 mA (plots (c) and (d)), in linear ((a) and (c)) and logarithmic ((b) and (d)) time scale. The first data point in each curve, indicated in panels (b) and (d) (in logarithmic scale), corresponds to 7.4 sccm and reproduces the little increase of α as a function of pressure seen in figure 3.14. When increasing the residence time the variation of α with pressure tends to level off, and for longer residence times, α clearly decreases with pressure.

Although the residence time variation data could be consistent with the hypothesis of a longitudinal profile, the information obtained from Raman supports the hypothesis of a contribution of post-discharge chemistry, which could be influenced by the residence time due to the different chemical composition of the gas at different τ_{res}. The static measurements (On-Off) do not show any post discharge chemistry *in situ* (in the discharge tube), suggesting that it could be happening only at the output of the plasma reactor (spatial and temporal post-discharge). The distance between the plasma branch and the measurement branch in the L-shape reactor is only 3 cm, but it is enough to reach the dissociation fraction measured downstream.

✓ Evidences of post-discharge chemistry on the metal surfaces.
✓ The ratio downstream vs. in situ $R_{d/i}$ depends on τ_{res} and/or on α.
✓ The dependence of α with pressure is related to the τ_{res}. For similar τ_{res}, α decreasses as a function of pressure.
✓ τ_{res} variation tests and longitudinal Raman experiments suggest the possibility of post-discharge chemistry in the gas phase.

3.4.5 Comparison of FTIR and Raman in continuous plasma

We compare now the dissociation fractions measured with both FTIR and Raman scattering. Figure 3.21 presents the data taken *in situ* at a gas flow of 7.4 sccm obtained by FTIR with the basic short reactor and the L-shape reactor (same data as in figures 3.14 and 3.18) and the data obtained by Raman in the same conditions. In general, *in situ* FTIR in the L-shape reactor matches well with Raman and both give slightly higher α values than FTIR in the short reactor. In addition, Raman values at 40 mA reproduce the small increase of α with pressure seen with FTIR *in situ*. Raman data at 20 mA is somewhat scattered because of the low signal of CO at low current (see figure 2.9 (b)).

The small differences between both *in situ* FTIR sets of data could be related to a slightly different distance between electrodes, an influence of electrode ageing or a certain effect of larger dead volume in the L-shape reactor (downstream volume) and in Raman reactor (the extensions). Nevertheless, the differences between reactors and/or set-up configurations are much smaller than the large difference between the dissociation fractions measured downstream and *in situ*. The agreement between FTIR and Raman confirms that the TOoE fitting script is not giving artificially lower α values and that FTIR is not somehow under-estimating the CO densities.

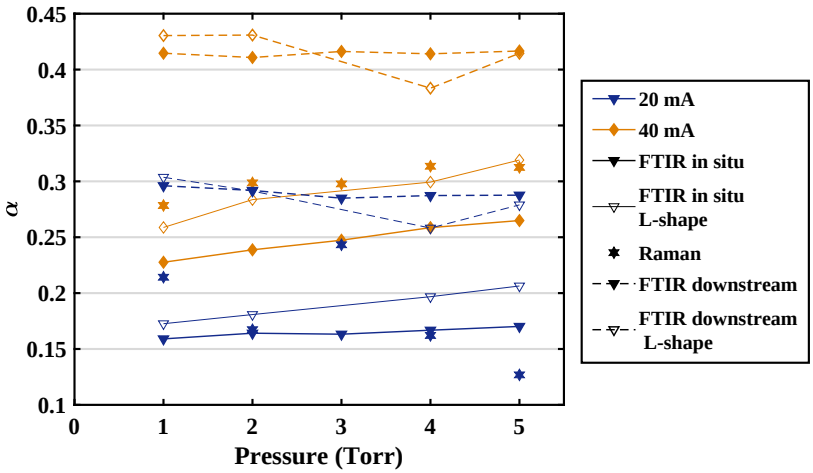

Figure 3.21: Variation of α as a function of pressure for 20 and 40 mA measured *in situ* by FTIR (with the usual DW short reactor and with the DW L-shape reactor) and by Raman scattering (SW short reactor+extensions) and measured downstream by FTIR (with both reactors).

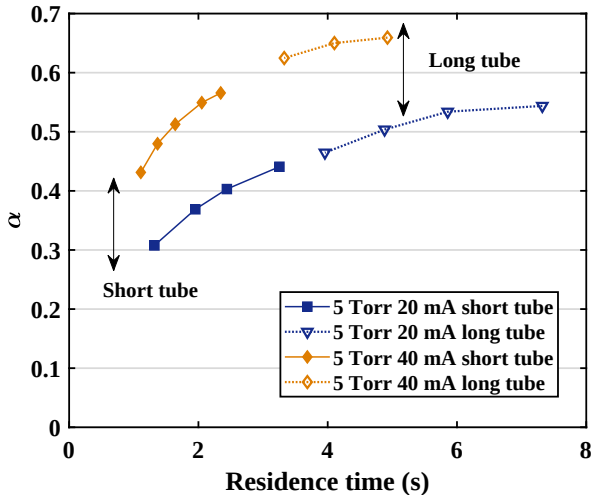

Figure 3.22: Variation of the dissociation fraction α as a function of the residence time at 5 Torr, 20 and 40 mA for the short and long discharge tubes.

3.4.6 CO_2 and CO densities for comparison with oxygen data

The atomic oxygen measurements were made in the long discharge reactor (67 cm), because of the advantages for absorption techniques, such as CRDS. In order to compare the measured O atom densities with CO densities we need to estimate the dissociation fraction in the long discharge tube. The *radii* of this tube is the same as in short tube (23 cm length), and the axial gradient along the tube can be neglected, as discussed in section 3.4.4. Therefore, the main difference between the two discharge tubes is the length between the electrodes, which for a given flow, implies a different residence time (τ_{res}) in the plasma. To estimate the CO produced in the long tube, we used the dependence of α as a function of τ_{res} measured *in situ* in the short tube as shown in previous section 3.4.4. In addition, downstream measurements using both long and short tubes confirmed

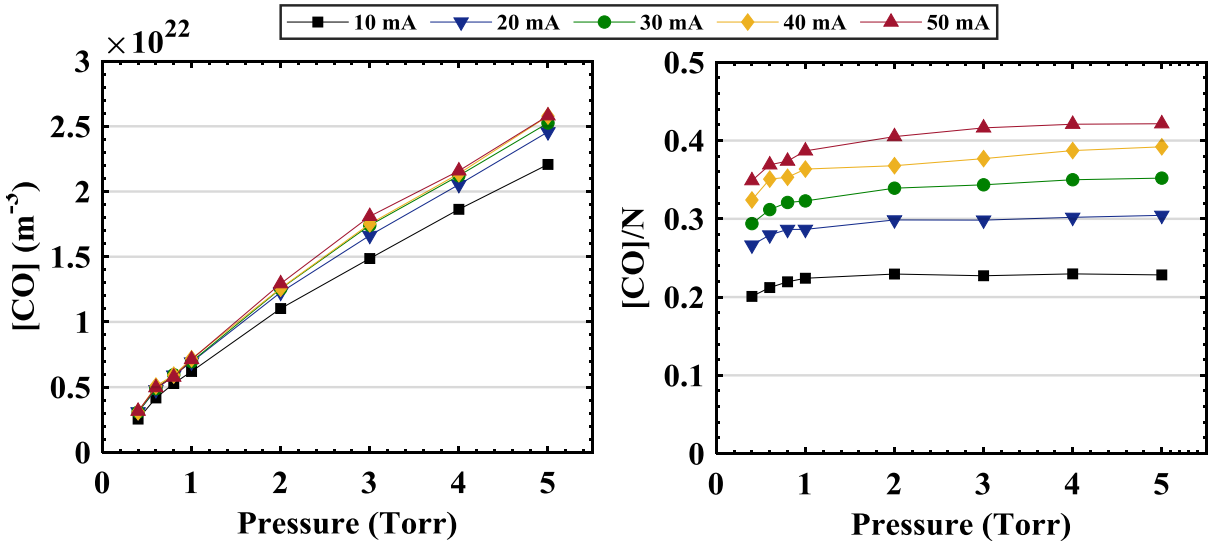

Figure 3.23: Variation of the CO fraction (a) and CO absolute density (b) as a function of pressure for different currents (10-50 mA) calculated for the long discharge tube.

that the CO_2 dissociation fraction follows a similar trend for both reactors as a function of τ_{res}. An example of these measurements is shown in figure 3.22 for 5 Torr, 20 and 40 mA illustrating the single dependence of α with τ_{res} in both short and long tube reactors.

Figure 3.23 shows the measured variation of the absolute CO density and the CO fraction, normalized over total gas density N, for different currents and pressures in the long discharge tube. The absolute CO density increases monotonically with pressure, whereas the CO fraction over total gas density first increases slightly with pressure up to 1 Torr, and then becomes almost constant at higher pressures. Both graphs show a saturation at higher currents. It is worth noting that during these measurements the CO_2 densities were also measured and that the carbon balance was always fulfilled for all pressures and currents. Therefore the CO densities presented in figure 3.23 give an upper limit to the O atom densities that can be expected in the gas mixture.

3.5 O atom densities

The atomic oxygen densities are determined with three diagnostic techniques: actinometry, HR-TALIF and CRDS in the same experimental set-up. The experimental details are summarized in the experimental box 3.3. We first discuss the accuracy of the diagnostic techniques and subsequently the variation of the O atom density as a function of pressure, current and gas flow.

Diagnostics: HR-TALIF, Actinometry, CRDS	**Reactor**: DW Long	**Pressure**: **0.4-5** Torr
Discharge: Glow Continuous plasma	$\boldsymbol{T_{wall}}$: 50^{o}C HR-TALIF & actinometry, 25^{o}C actinometry & CRDS	**Current**: **10-50** mA
		Flow: 7.4 sccm (τ_{res} ≈0.46-5 s)

Experimental box 3.3: Measurements of the oxygen atom density.

3.5.1 Validity of the diagnostics

A complete parametric study of the O atom density variation in terms of current and pressure was done with two diagnostics: actinometry and TALIF (TALIF data was taken between 10 and 40 mA). CRDS (preliminary) measurements were taken only for 20 and 40 mA between 1 and 5 Torr and will be discussed below. The absolute O atom densities and O atom fraction measured by actinometry and TALIF are shown in figure 3.24 as a function of pressure and current. The graph to the left (a) shows the absolute O atom density and panel (b) (on the right) presents the O atom fraction (absolute O atom density divided by the total gas density). The TALIF data in these graphs were obtained with the absolute calibration based on the TALIF fluorescence method (see section 2.4.2) and using $\sigma^{(2)}_{Xe}/\sigma^{(2)}_{O} = 1.9$ from *Niemi et al.* [2005]. Three main observations can be made:

- Both O atom emission lines used for actinometry give very similar values.
- The trends of O atom absolute density variation as a function of pressure obtained with both HR-TALIF and actinometry is the same. It shows an increase in density below 1-2 Torr and then a saturation, which results in a clear decrease in the O atom fraction, $^O/_N$, above 1 Torr.

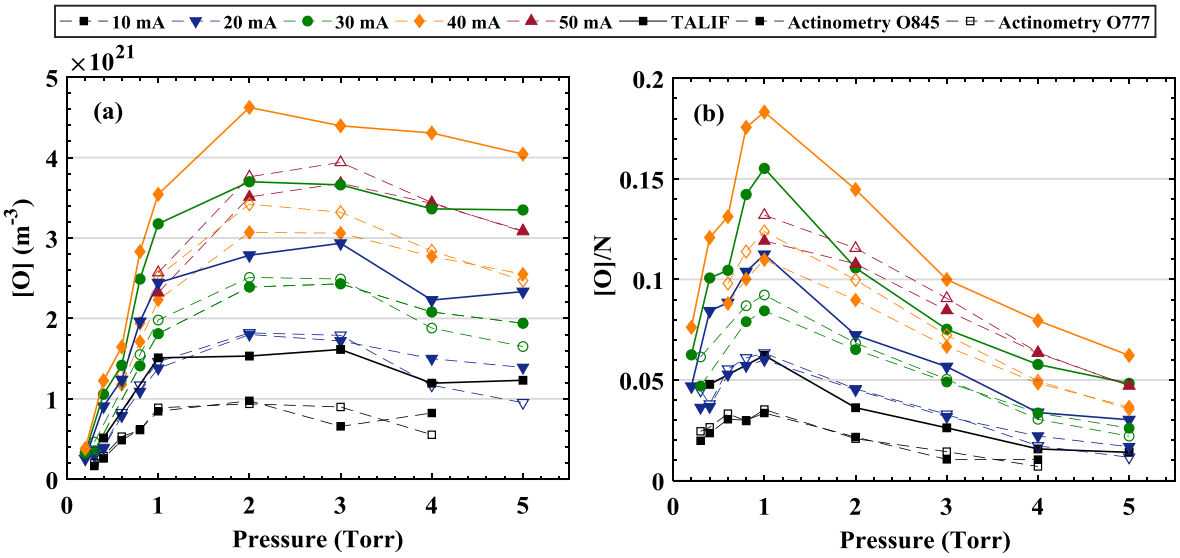

Figure 3.24: Variation of the absolute O atom density (left, (a)) and the O atom fraction normalized to the total gas density (right, (b)) with pressure for different currents measured with both TALIF and actinometry. N is the total gas density, calculated using T_{gas} measured with TALIF for TALIF O_{atom} densities and with T_{gas} measured by FTIR for actinometry O_{atom} densities. The TALIF data in these graphs correspond to the absolute calibration based on the TALIF fluorescence and using $\sigma^{(2)}_{Xe}/\sigma^{(2)}_{O} = 1.9$ *Niemi et al.* [2005].

- The densities obtained with actinometry are systematically lower than with TALIF.

Let us first discuss the accuracy of the absolute values obtained with actinometry. The CO fractions shown in the previous section were used as input for the Boltzmann solver in order to obtain the EEDF and the excitation rate coefficients, required to obtained the O atom densities, as detailed in section 2.4.1 for the so-called method 1 (M1). These CO densities, although determined with a line-of-sight integrated technique, correspond to the correct values necessary to process the O emission data because of the spatial homogeneity in the CO densities (discussed in section 3.4.3).

The fact that both O777 and O844 give similar densities suggests that processes populating the detected excited states other than direct electron impact excitation of atoms are not significant in our plasma conditions *Katsch et al.* [2000] (*i.e.* two-step excitation via metastable states or cascading from higher excited levels can be neglected). When looking more closely, the line O777 gives slightly higher O atom densities in the low pressure range. In the case of a pure O_2 plasma, it is commonly considered that the line O777 is less reliable because it can have a stronger contribution from dissociative excitation of ground state or metastable O_2 molecules *Katsch et al.* [2000]. The dissociative excitation of ground state O_2 was accounted for in our calculations; however its contribution is very small due to the low O_2 fraction in a CO_2 plasma *Bousquet et al.* [2007] and the higher energy threshold for this process. Similarly, the dissociative excitation from metastable states of O_2 is expected to be very low. Dissociative excitation from CO_2 could 'occur, but it was not included in our calculations due to lack of cross-section data for this process.

In spite of the consistency between the results obtained with the two oxygen emission lines, the absolute densities measured can still be sensitive, for instance, to the electron impact excitation

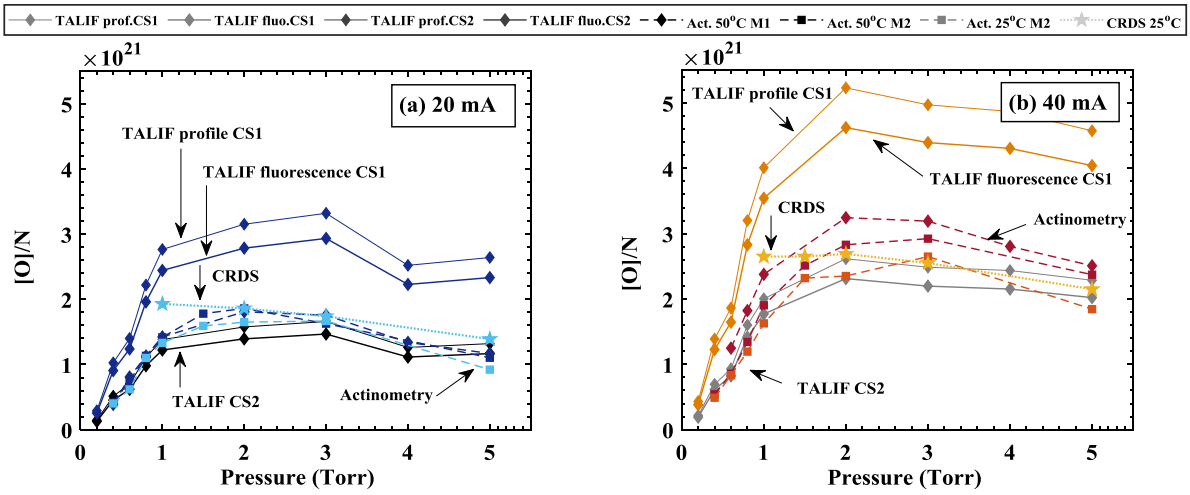

(a) O atom absolute density

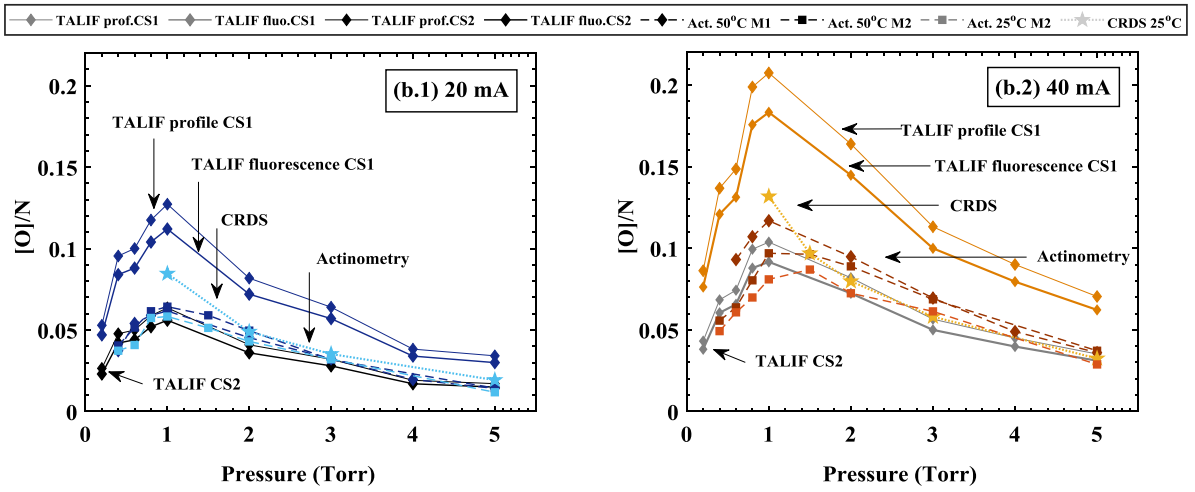

(b) O atom fraction

Figure 3.25: Variation of the O atom absolute density (figure (a)) and O atom fraction (figure (b)) for 20mA (left, (x.1)) and 40 mA (right, (x.2)) with pressure measured with TALIF, Actinometry and CRDS. TALIF profile and TALIF fluorescence are calculated with the cross sections from *Niemi et al.* [2005](CS1) and *Drag* [2020](CS2). Actinometry is calculated for two methods: M1 (Bolsig+) applied to the first data set (see figure 3.24) and M2 (Self-consistent calculation with Loki) applied to the second data set (see chapter 8). Actinometry data in this figure is always an average of the results obtained with the two emission lines O777 and O845. TALIF data was taken at T_{wall}=50^{o}C, actinometry at T_{wall}=25 and 50^{o}C and CRDS at T_{wall}=25^{o}C. N is the total gas density is calculated with $T_{gas}(TALIF)$, $T_{rot}(FTIR)$ and $T_{gas}(CRDS)$ for TALIF, actinometry and CRDS data.

cross sections used in the calculations, as discussed in *Pagnon et al.* [1995]. In addition, the cross section set used to calculate the electron distribution function (EEDF) may also affect the estimated densities. As an example, when calculating the O atom densities with a different set of cross sections (Morgan + Phelps) for a similar gas composition, the O atom densities obtained are about 20% higher than with the IST set. Therefore, the disagreement between TALIF and actinometry could be partially explained by inaccuracies in the cross sections used. On the other hand, the densities

obtained from TALIF measurements could also be overestimated.

In figure 3.24 (a) and (b) the solid lines represent the TALIF data obtained with the absolute calibration based on the TALIF fluorescence and using $\sigma^{(2)}_{Xe}/\sigma^{(2)}_{O} = 1.9$ *Niemi et al.* [2005]. Figure 3.25, shows the data only for 20 and 40 mA, separately for readability, for the absolute O atom density (a) and fraction (b) obtained with the two methods (TALIF fluorescence and TALIF profile), in good agreement. It also includes the average of both actinometry lines shown in figure 3.24 and the average value of actinometry measurements in the same conditions (T_{wall}=50^o) taken during another measurement campaign and analysed with the method 2 (M2) calculating densities self-consistently with the Boltzmann solver LoKI (see details in section 2.4.1). Both TALIF curves give densities markedly higher than actinometry. These absolute O atom densities determined with TALIF are directly proportional to the ratio of the two-photon absorption cross section of xenon *versus* oxygen, determined by titration *Niemi et al.* [2005]. Recent preliminary measurements obtained by direct laser absorption *Drag* [2020] indicate that the value of the Xe cross section may be significantly lower than the previously reported value, roughly half of the previous value (for oxygen the two-photon absorption cross section is known *Bamford et al.* [1986]). This would tend to decrease the results obtained with TALIF. Figure 3.25 includes a preliminary calculation of the O atoms densities and fractions determined by TALIF but using this new cross section value. With this cross section the densities estimated by TALIF are in very good agreement with actinometry. Preliminary measurements by cavity ring down spectroscopy (CRDS) in the similar experimental conditions (T_{wall}=25^o) were also performed, and are included in figure 3.25 along with actinometry measurements at the same wall temperature to show that the impact of the small change on T_{wall} is not significant in the measured densities.

It is clear that actinometry measurements, CRDS data and TALIF densities calculated with the cross section from *Drag* [2020] show a remarkably good agreement, whereas the TALIF densities estimated with the cross section from *Niemi et al.* [2005] are significantly higher. The new value of the Xe two-photon absorption cross section is to be confirmed. In any case, this cross section is the biggest source of uncertainty in TALIF measurements. Additionally, small deviations of the laser beam spatial distribution from the assumed Gaussian profile can affect significantly the final O atom density results because of the square dependence of the TALIF signal with the beam waist.

3.5.2 Oxygen atom density variation

The absolute O atom density values still have significant uncertainties due to their sensitivity to the parameters detailed above, and an error not lower than 30% is estimated. However, beyond these uncertainties O atoms represent in any case a large proportion of the total gas mixture in our conditions. The maximum of $[O]/_N \sim$ at 1 Torr, shown in figure 3.24 (b) is 0.12 for actinometry. The ratio $[O]/_{CO}$ reaches a maximum value close to 35% for 1 Torr 50 mA, meaning that for some conditions a significant amount of the atomic oxygen resulting from CO_2 dissociation remains in the form of free O atoms and do not recombine into oxygen molecules. In addition, the consistency in the trends shown in figure 3.24 for both actinometry and TALIF when the current and pressure are varied is remarkable.

The atomic oxygen density monotonically increases with current over the range measured, not showing the same saturation seen for CO (see figure 3.23). The O atom density increases with pressure up to around 2 Torr and then further reaches a "plateau", showing only a slight decrease

with increasing pressure. This trend indicates that there is a change of regime around 1-2 Torr which is even more evident in O atom fraction (the graph to the right in figure 3.24). $[O]/N$ increases up to 1 Torr, passes through a maximum and then decreases rapidly. Therefore, two distinct regimes are observed with a transition between 1 and 2 Torr, which could be caused either by a change in the production of O atoms or due to a change in their loss processes.

The variation of the CO and O atom fraction with pressure shown in figures 3.23 and 3.24, is noticeably different. Both CO and O densities show an increase below 1 Torr, but for higher pressures $[CO]/N$ becomes almost constant, while $[O]/N$ decreases markedly. Since the creation rate of both O and CO from CO_2 dissociation should be similar (assuming a negligible contribution to $[O_{atom}]$ from the dissociation of CO), the loss rate of O atoms must increase faster than for CO with increasing pressure. The losses of O will be examined in section 3.5.4.

3.5.3 O atom densities as a function of gas flow

Only a few tests of oxygen density variation as a function of gas flow were done at 1 Torr, 20 and 40 mA, presented in figure 3.26, obtained from the average of both oxygen emission lines O777 and O845 measured with actinometry. Although these data cannot be directly compared to the variation of the dissociation fraction as a function of gas flow presented in section 3.4.4, because of the different length of the discharge tubes, it is worthwhile showing that both dissociation products behave similarly and tend to accumulate when decreasing the gas flow, *i.e.* when increasing τ_{res}.

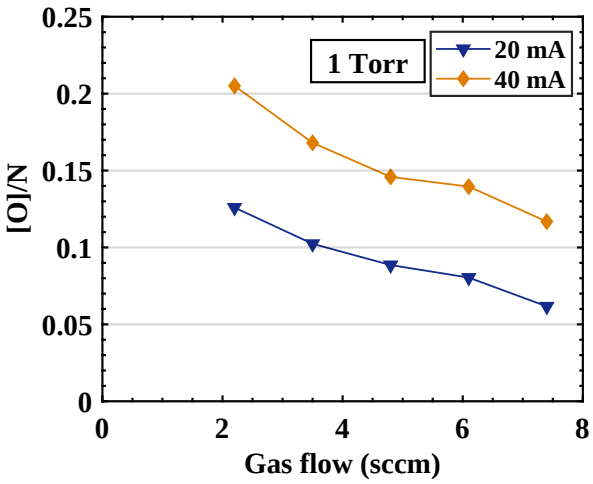

Figure 3.26: Variation of the O atom fraction as a function of the gas flow for 20 and 40 mA at 1 Torr.

3.5.4 O atom loss frequency

O atom loss processes must be investigated in order to understand the variation of the O atom densities as a function of pressure. In a glow discharge at a few Torr, it is expected that the recombination of oxygen atoms at the walls will be the major loss process although gas phase losses must also be considered (see section 3.6.2). To get insight into the loss mechanisms and obtain reliable data on the role of oxygen atoms on the kinetics of a CO_2 plasma, it is important to determine the loss frequencies of oxygen atoms in the same conditions as the atomic oxygen density

was measured, keeping the reactor surface directly exposed to CO_2 plasma.

To determine the lifetime of the O atoms under plasma exposure we have followed a similar method to that used by Lopaev and Smirnov *Lopaev and Smirnov* [2004]; *Booth et al.* [2019] which is based on a partial modulation of the discharge current (square modulation, with a current variation around 15%, depending on the plasma conditions). In this way, the gas composition and the flux of various species (atoms, ions) towards the surface is only slightly modulated during the cycle. As the surface temperature is known to change the recombination probability at the wall, the surface temperature is kept constant at 323 K (50^0C). Given that TALIF and actinometry provide consistent trends, these measurements can be made simply by recording the variation of the actinometry signal over time. The modulation period was fixed at 146 ms, long enough to fit the decay time for all conditions.

The measurements of the current and the optical emission intensities for argon and both oxygen lines are shown in figure 3.27, as an illustrative example, for 2 Torr, 50 mA. Clearly, the Ar line follows the same trend as the current, while both atomic O lines show an exponential increase or decay as the current is modulated. The figure in the bottom shows the ratio between the O lines and the Ar line, with a single exponential fit *Bousquet et al.* [2007]; *Macko et al.* [2004]. A single exponential curve fits very well the experimental data, which was the case for all pressures studied. The error in the exponential fit of this decay (residual of the fit), is very small and on average around 0.5%. The single exponential behaviour suggests that the loss mechanism is controlled by

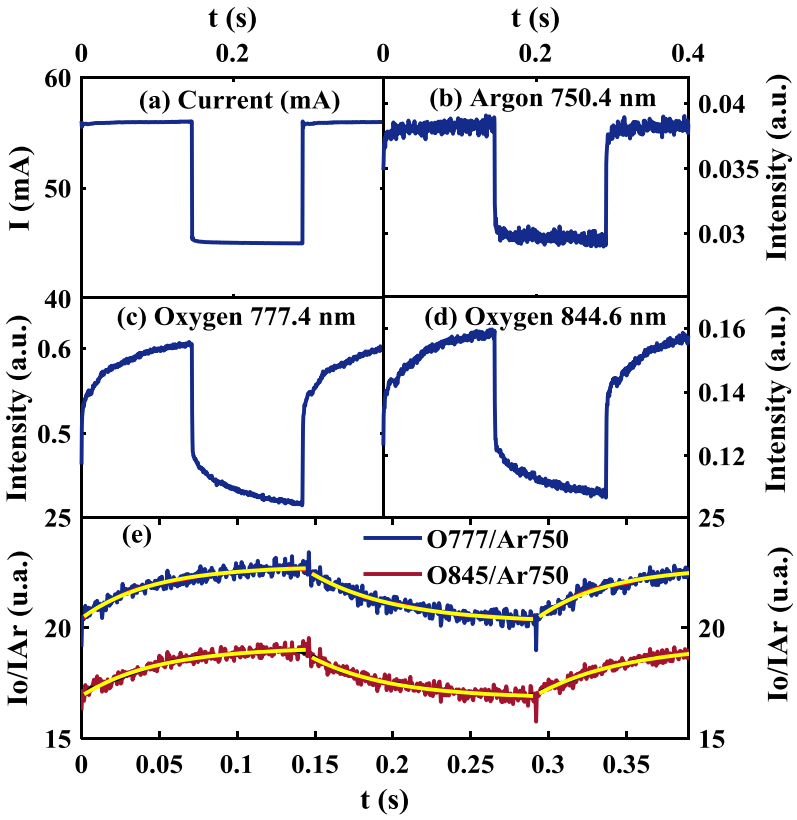

Figure 3.27: Temporal variation of: (a) Current flowing in the discharge; (b) Intensity of the Ar750 nm line; (c) Intensity of the O777 nm line; (d) Intensity of the O845 nm line and (e) Ratios I_O/I_{Ar} for both O lines and the corresponding exponential fit.

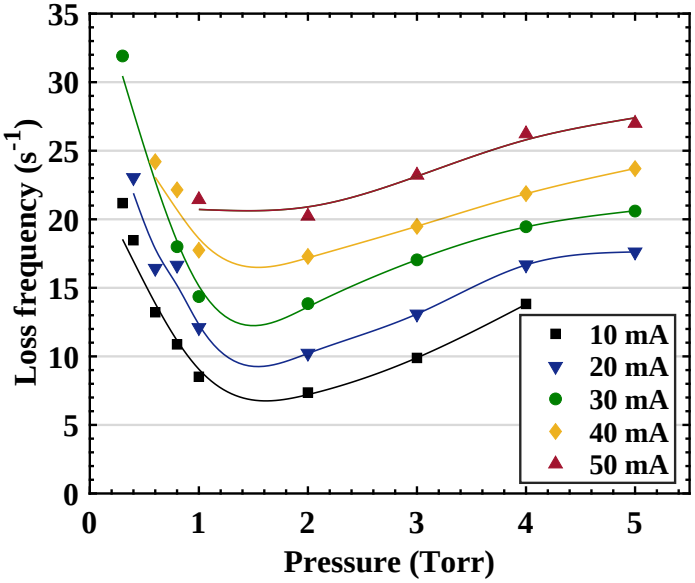

Figure 3.28: Variation of the loss frequency, ν_O^{loss}, with pressure and current.

a first order process, which will be discussed in section 3.6.2. A second order mechanism would lead to an hyperbolic decay $\sim 1/t$, but this type of fitting was not following the data as well as the exponential fit, giving a residual value 36% higher.

From equation (2.10), we can assume that the temporal variation of the O atom fraction $[O]/N$, is well represented by the temporal variation of the emission line intensity ratios I_O/I_{Ar}. This supposes that both the reduced electric field and the gas temperature do not change significantly during modulation, or that they change so fast as to not influence the O atom kinetic measurement. In the case of the electric field, the highest variation during modulation happens for 5 Torr, 50 mA, reaching around 4% for a change of 21% of the current. Additionally the time variation of the electric field is relatively fast, around 10 μs. Concerning the gas temperature (which affects E/N though its influence in the gas density), in the worst case the induced variation on the total gas density is around 7% with a characteristic time lower than 5 ms (see figure 3.4), considerably faster than the O atom lifetime. Consequently, the O atom loss frequency ν_O^{loss} can be obtained directly from the time variation of the ratio of the intensities.

The loss frequencies, obtained from the average of the values for the two atomic oxygen lines, are plotted for different currents and pressures in figure 3.28. The error in the loss frequency is more related to the reproducibility and the small differences between the exponential increase and decay than to the error in the exponential fitting; the estimated error is of the order of 15%. The obtained ν_O^{loss} values fall mostly between 10 and 25 s^{-1} and we can again clearly differentiate two regions. The loss frequency first decreases with pressure, passes through a minimum around 1-2 Torr and then increases slowly with pressure above 2 Torr. This correlates very well with the pressure trend in the O atom density. The loss frequency increases markedly with current at all pressures. This change of regime, the strong increase of the O atom loss frequency at low pressure and the corresponding variation of the O atom density is similar to that observed in pure oxygen plasma with a similar discharge in *Booth et al.* [2019]. However, loss frequencies up to ~2 times higher were measured in the case of O_2 plasma compared to CO_2 plasma. Therefore CO and CO_2 molecules

appear to influence the loss mechanisms of O atoms as it will be discussed chapter 8.

3.6 Discussion

The O atom densities, measured *in situ* in a glow discharge tube of 1 cm radius, show two regimes when varying the pressure: the O atom fraction increases with pressure below 1 Torr, passes through a maximum and then decreases for higher pressures. The corresponding O atom loss frequencies measured under plasma exposure show the opposite behaviour, decreasing with pressure up to 1 Torr and subsequently increasing for higher pressures. Both are strongly correlated. The CO trend at low pressure is similar but differs form the O atom at higher pressures. One might expect the dissociation fraction of CO_2 to depend mostly on the energy density dissipated in the plasma. Therefore figure 3.29 summarizes all the O atom and CO data, plotted as a function of the energy density (*i.e.* specific energy input, SEI).

3.6.1 CO and O atom densities

For all currents the O atom density and the O atom fraction pass through a maximum as a function of the SEI, a maximum which is broader for higher currents and which increases linearly with the energy density. A similar trend was observed by Vesel *et al.* *Vesel et al.* [2011] in the spatial post-discharge of a microwave plasma ignited in a 0.25 cm radius quartz tube. As a function of pressure, while a maximum was observed at 1 Torr for all discharge currents in our experiments, Vesel *et al.* shows a maximum in the relative O atom density around 20 Pa (0.15 Torr) for all microwave powers.

The fact that the maximum of O atom density occurs at higher SEI for higher current can be simply explained by the increase in the electron density, leading to an increase of the dissociation rate. The subsequent decrease when increasing pressure is claimed by Vesel *et al.* *Vesel et al.* [2011] to be due to a decrease in the production rate (related to a decrease of the electron temperature caused by the lower mean free path), along with an increase of the gas phase recombination processes. The bottom graph of figure 3.29 shows that the minimum of the O atom loss frequency also increases linearly with the SEI, similarly to the maximum of the O atom density. This suggests that the maximum in O atom density is more related with a change in the loss processes rather than a change in the kinetics of the creation processes when the pressure is increased.

The similar trends in the O atom density for the two different types of discharges are noteworthy and could be related to similarities in the surface of the reactors (quartz and Pyrex). The different pressure at which the maximum of $[O]/N$ occurs (1 Torr here and 0.15 Torr in the case of Vesel *et al.*) could be due to the different geometry (different radius, 1 cm *versus* 0.25 cm) of the reactor, which may affect both the electric field and the loss processes, impacting the O atom densities obtained *Pagnon et al.* [1995]. Other possible differences are the higher ion flux in microwave plasmas compared to DC *Cartry et al.* [2006], slightly different surface composition (quartz versus Pyrex), different surface and/or gas temperature or the usual differences in the O atom loss frequencies in a spatial post-discharge *versus* in steady state plasma (as discussed in chapter 8 and *Sabadil and Pfau* [1985]; *Cartry et al.* [2006]; *Bousquet et al.* [2007]).

The CO density is equal to the maximum density of O atoms that either remain as free atoms or that recombine into molecular oxygen. This may be different to the total amount of O atoms

produced, since the recombination of CO with O is possible and cannot be excluded, but this would not be detected from the measurements of CO. It is clear that the O atoms are more affected by loss processes than CO over the whole range of pressures and currents studied, otherwise their densities (and trends with pressure and current) should be similar. The atomic oxygen density represents between 10 to 35% of the CO, and is therefore always a significant part of the gas mixture in our conditions. At low SEI, the quantity of O atoms produced is low, and almost all are recombined, most likely into O_2 (O_3 can be considered to be a minor specie in our pressure range *Lopaev et al.* [2010b]). However at around 50 eV/molecule the O atom density reaches values above 35% of the density of CO (according to actinometry). For all currents, the O atom fraction first increases linearly with SEI, in spite of the high loss frequency observed for these conditions. In contrast, at higher SEI, the O atom fraction decreases linearly. The loss mechanisms of O atoms are therefore

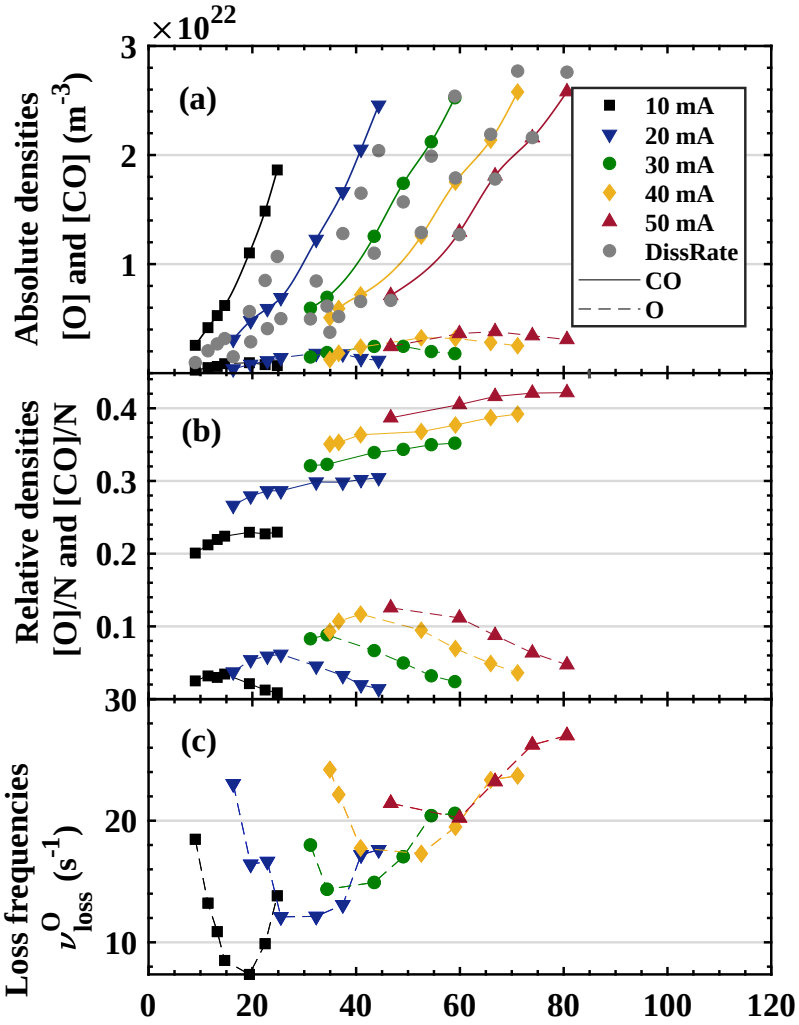

Figure 3.29: (a) Variation of the absolute densities and (b) fractions of CO and O atom (average of actinometry lines in figure 3.24) along with the calculated dissociation fraction (using Polak's cross section *Polak and Slovetsky* [1976]) and (c) the corresponding O atom loss frequencies as a function of the specific energy input.

more efficient at high SEI, which will be discussed more in detail in section 3.6.2.

Contrary to the case of O atoms, the CO density increases with the energy input, although tends to saturate at high current and SEI. This is expected since the more we dissociate, the more probable are collisions between electrons and other molecules instead of CO_2. The increase of CO with energy input can be mostly explained by direct electron impact dissociation. The rate for this process is also included on the top graph of figure 3.29 for comparison. This dissociation rate was calculated with the expression:

$$R = n_{e-} \cdot K_{diss} \cdot [CO_2] \cdot \tau_{res} \tag{3.10}$$

where n_{e-} is the electron density calculated from the measured current and the drift velocity (calculated from fitting the data from *ETH Zurich* [2018]), K_{diss} is the dissociation rate coefficient from Polak and Slovetsky *Polak and Slovetsky* [1976], $[CO_2]$ are the measured CO_2 densities and τ_{res} is the residence time. The use of Polak's cross section here follows the recommendation in *Grofulović et al.* [2016] and is only to illustrate that the CO trends follow what would be expected from electron impact dissociation. An investigation dedicated to establish the value of the electron impact dissociation rate coefficient will presented in chapter 6. Nevertheless, the results in figure 3.29 suggest the validity of the rate coefficients calculated from the cross section from Polak and Slovetsky *Polak and Slovetsky* [1976].

3.6.2 O atom loss processes

The measured loss frequencies can be the result of both surface loss processes and/or due to gas phase reactions:

$$\nu_{loss}^{O} = L_{gp} + \frac{\gamma_O \cdot \upsilon_{th}}{2R} \tag{3.11}$$

where L_{gp} represents the contribution of the gas phase losses, γ_O is the O atom surface loss probability, υ_{th} is the thermal velocity of the O atoms and R is the radius of the discharge tube. In

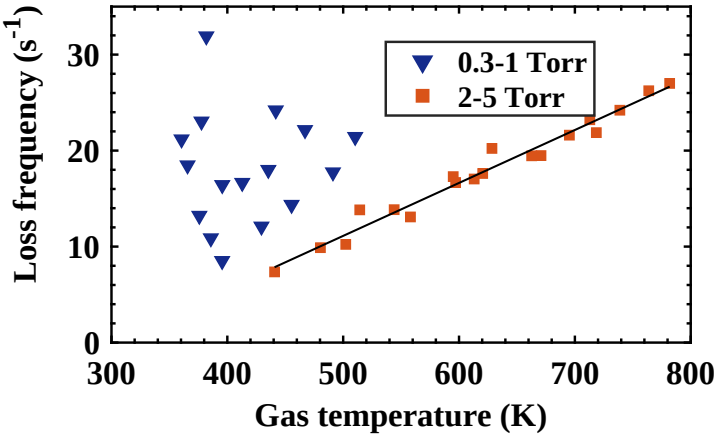

Figure 3.30: Loss frequencies plotted as a function of the gas temperature. In blue triangles, the data for pressures from 0.3 to 1 Torr, included, and in red squares the data from 2 Torr up to 5 Torr. A linear fit for the data at higher pressures is also included.

principle, ν_{loss}^{O} can have a very complex dependence with different plasma parameters including gas temperature *Booth et al.* [2019], wall temperature *Macko et al.* [2004], flux of O atoms, etc. as discussed in detail by Guerra *Guerra* [2007]. Figure 3.29 shows that for higher pressures (above 1 Torr) the O atom loss frequency increases linearly with the energy input. This dependence is in fact related to the linear increase of the gas temperature with the SEI (shown in figure 3.3), which is clearly observed in figure 3.30, showing the measured loss frequencies plotted as a function of T_{gas}. For higher pressures, from 2 to 5 Torr, we see a direct correlation of the loss frequency with the gas temperature, which increases with pressure and current as shown in figure 3.1. We checked the dependence of the measured loss frequencies with many other variables, such as the O atom density, the electron density, etc. However, no obvious correlation with any other variable except the gas temperature was found. Therefore we conclude that in our conditions the gas temperature plays a dominant role in the recombination process and the effect of other possible variables is less relevant. The gas temperature can affect the recombination processes in two possible ways: either by an increase of the gas phase recombination processes, whose rates are temperature dependent, or due to an increase of the kinetic energy of the O atoms reaching the reactor walls, and therefore with higher energy to overcome an activation energy for recombination with adsorbed species at the wall (*e.g.* O_{ad} or CO_{ad}), as proposed in the case of pure O_2 discharges by *Booth et al.* [2019].

Gas phase recombination

There are several gas phase reactions reported in the literature *Cenian et al.* [1994, 1995]; *Kozák and Bogaerts* [2014a]; *Beuthe and Chang* [1997]; *Byron and Apter* [1992]; *Slovetsky* [1980] that can remove atomic oxygen from the gas mixture. Only a selection of them is listed in table 3.1, and the corresponding reaction rates obtained for the most relevant reactions (underlined in the table, and discussed bellow) are plotted in figure 3.31, along with the measured loss frequencies. Note that reactions 10 and 11 correspond to a gas-phase effective way of describing reactions at the surface (wall). They are further discussed at the end of this section.

- **O+O and O+CO (+M)**. Comparing both reactions and their variation with gas temperature, the recombination of O atoms into oxygen molecules is more efficient than the reaction with CO giving back CO_2. This is consistent with *Sepka et al.* [2000], where a mixture of CO and O atoms in the post-discharge of an O_2 plasma showed that the presence of CO in gas phase did not affect the O recombination processes and that the CO concentration in gas phase was not significantly altered by the presence of oxygen atoms. However, the rates for these reactions are strongly temperature dependent. Indeed, the rate of the recombination reaction between oxygen atoms increases by one order of magnitude over the range of gas temperatures studied, while the rate of recombination with CO increases by about two orders of magnitude. Consequently, at the highest temperatures, which correspond to the highest pressures, the rates for both processes tend to converge reaching the same order of magnitude.

- **Vibrationally excited molecules**. The reaction between O and CO could be enhanced by the vibrational excitation of CO, which has been measured under similar plasma conditions (see chapter 4). No rates are available in the literature, to our knowledge, for the reaction of O with vibrationally excited CO. A reaction between atomic oxygen and vibrationally excited CO_2, producing CO and O_2, is also possible. The rate for this reaction, as presented in

Type	Reaction R	N^{er}	Rate coefficients	Reference
Gas phase	$O + O + M \rightarrow O_2 + M$	1	$5.2 \cdot 10^{-34} \cdot exp(^{900}/_{T_{gas}})$	*Cenian et al.* [1994]
Gas phase	$O + CO + M \rightarrow CO_2 + M$	2	$8.2 \cdot 10^{-34} \cdot exp(^{-1510}/_{T_{gas}}) \quad M = CO/O_2$	*Cenian et al.* [1994]
		3	$1.6 \cdot 10^{-33} \cdot exp(^{-1510}/_{T_{gas}}) \quad M = CO_2$	*Cenian et al.* [1994]
Gas phase	$O + CO \rightarrow CO_2 + h\nu$	4	$4.15 \cdot 10^{-18} \cdot exp(^{-1600}/_{T_{gas}})$	*Beuthe and Chang* [1997]
Gas phase	$O + CO_2 \rightarrow CO + O_2$	5	$2.8 \cdot 10^{-11} \cdot exp(^{-26500}/_{T_{gas}})$	*Beuthe and Chang* [1997]; *Kozák and Bogaerts* [2014a]
Gas phase	$O + O_2 + M \rightarrow O_3 + M$	6	$5.5 \cdot 10^{-31} \cdot T_{gas}^{-1.2} \quad M = O_2$	*Cenian et al.* [1994]
		7	$5.5 \cdot 10^{-31} \cdot T_{gas}^{-1.2} \quad M = CO$	*Cenian et al.* [1994]
		8	$1.7 \cdot 10^{-30} \cdot T_{gas}^{-1.2} \quad M = CO_2$	*Cenian et al.* [1994]
Gas phase	$O + O_3 \rightarrow 2O_2$	9	$3.1 \cdot 10^{-14} \cdot T_{gas}^{0.75} \cdot exp(^{-1575}/_{T_{gas}})$	*Cenian et al.* [1994]
Gas / surface	$O + CO + wall \rightarrow CO_2 + wall$	10	$^{7.4 \cdot 10^{-17}}/_{R} \quad cm^3\ s^{-1}$ *	*Slovetsky* [1980]; *Cenian et al.* [1994]
Gas / surface	$O + O + wall \rightarrow O_2 + wall$	11	$^{5 \cdot 10^{16}}/_{[CO]} \quad cm\ s^{-1}$ **	*Slovetsky* [1980]; *Cenian et al.* [1994, 1995]

* R is the radius of the reactor in cm. **[CO] in $cm\ s^{-3}$. The effective rate constant for this reaction is calculated with equation 3.12.

Table 3.1: Main reactions involving oxygen atoms in CO_2 plasmas found in literature. For the gas phase reactions the units are $cm^3\ s^{-1}$ or $cm^6\ s^{-1}$ for two or three body reactions respectively. For gas/surface reactions the units are specified. The number of the reactions corresponding to the rates plotted in figure 3.31 are underlined.

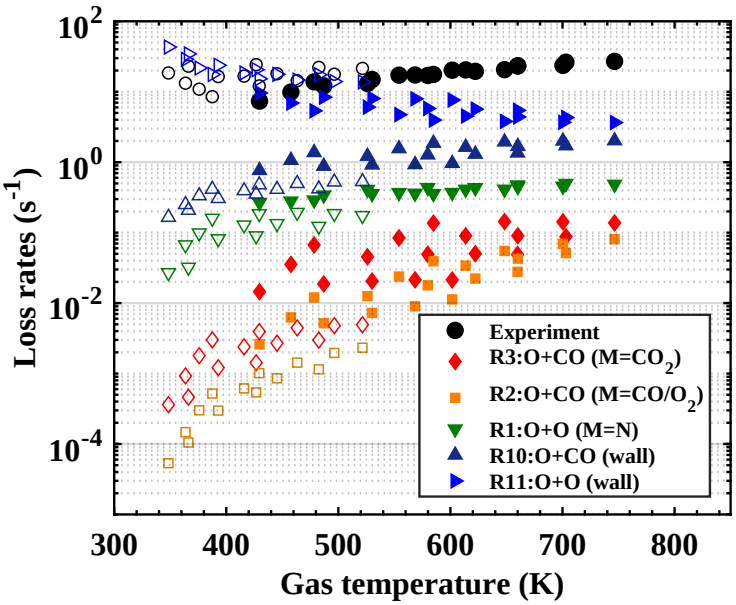

Figure 3.31: The experimentally observed loss frequencies ν_{loss}^{O} plotted versus T_{gas} along with the calculated rates for different reactions summarized in table 3.1. The empty symbols are for data between 0.3 and 1 Torr and the full symbols are for data between 2 and 5 Torr.

table 3.1, is rather low, however it is expected to increase with the vibrational excitation of CO_2 *Kozák and Bogaerts* [2014a] and could contribute to the different behaviour of O atom and CO as a function of the energy density. Nevertheless, in a glow discharge the CO_2 dissociation is believed to be mostly due to electron impact and, at the same time, the vibrational excitation of CO_2 decreases with increasing pressure (see chapter 4). Additionally, the higher the vibrational excitation, the lower the density of vibrationally excited particles, as can be deduced from the vibrational distribution function *Kozák and Bogaerts* [2014a].

- **Ozone formation and oxidation**. The reaction between atomic oxygen and molecular oxygen to create ozone (reactions 6-8 in in table 3.1), has a rate constant between those of reactions 1 (O+O) and 3 (O+CO), plotted in figure 3.31. This reaction could be followed by further reaction of the created ozone with O atoms (creating two O_2 molecules), consuming an extra O atom (reaction 9). However the density of the reactants (O_3 and O) is relatively low *Marinov et al.* [2013a] and therefore this reaction may contribute but will not play an important role in the overall O atom loss rate.

- **C atom oxidation reactions**. The carbon balance was checked by means of FTIR, and was found to be basically fulfilled with the measured amounts of CO and CO_2. Therefore reactions with C atoms are not expected to have a significant impact on the overall O atom balance. If some carbon is created by dissociation of CO, it will be subsequently oxidized rapidly back to CO.

In spite of the increase of the rates of the above-mentioned gas phase recombination reactions with the gas temperature, the rates are still at least one order of magnitude lower than the observed loss rates. The potential contribution of reactions of O with vibrationally excited CO, or CO_2,

cannot be excluded, and potentially can have reaction rates that are higher than for vibrational ground state molecules, but it is not probable that this type of reactions can increase the gas phase reaction rates enough to reach the experimental loss frequencies.

Reactions at the wall. Reactions 10 and 11 in table 3.1, plotted in figure 3.31, account for the recombination of gaseous oxygen atoms with either oxygen atoms or with CO at the walls *Cenian et al.* [1994]. They represent therefore surface processes, without specifying their nature, since they come from fitting of experimental data *Slovetsky* [1980], and are valid for the conditions of those experiments (1-2 Torr, T_{wall}=300-390K and between 1 and 10 mA cm^2). The loss rates corresponding to reaction 10 can be calculated by multiplying directly by the measured [CO]. In the case of reaction 11, the corresponding effective rate constant in s^{-1} is calculated by the expression *Cenian et al.* [1995]:

$$k_{eff} = \frac{k \cdot {}^{S}/_{V} \cdot K_{diff}}{k \cdot {}^{S}/_{V} + K_{diff}} \tag{3.12}$$

where k_{eff} is the effective rate constant, plotted in figure 3.31, k is the rate coefficient in table 3.1, S is the surface area in contact with the plasma, V is the volume of the plasma and K_{diff} is the diffusion rate towards the wall $= 1/\tau_{diff}$. The loss rate values obtained with these expressions are higher than the rates previously discussed, and are much closer to the experimental values, especially for the reaction $O + O + wall \rightarrow O_2$, and particularly in the range between 1 and 2 torr (400-600K). This suggest that surface recombination dominates over gas phase reactions of O atoms under our experimental conditions. The O atom surface loss processes in CO_2-O_2 plasma will be thoroughly studied in chapter 8.

3.7 CO and oxygen atom densities in pulsed plasma

After analysing the variation of the densities and fractions of CO and O atoms in continuous plasma, in this section we investigate their evolution in pulsed plasma (full modulation) for pulses of 5-10 ms On-Off. The choice of this pulse duration will be justified in the following chapters but already seeing the time evolution of the gas temperature (see figure 3.4) we observe that 5 ms is ∼enough to reach the steady-state values of gas temperature in continuous plasma. In this section, we will discuss only CO and O atom fractions (and exceptionally α to comparison with continuous plasma) because the absolute densities tend to follow the variation of the total gas density that decreases during the pulse due to the effect of the gas temperature. The information extracted from this analysis will be of interest to analyse the data in the next two chapters, where the vibrational kinetics of CO_2 plasma will be investigated. The experimental conditions are summarized in the experimental box 3.4.

Diagnostics: FTIR (TOoE), CRDS, Raman **Discharge**: Glow - Pulsed (5-10ms On-Off) Downstream & *in situ*	**Reactor**: SW Short (FTIR), SW Short+ extensions (Raman), DW Long (CRDS) ***T_{wall}***: CRDS: 25ºC; FTIR & Raman: not controlled	**Pressure**: **1-5** Torr **Current**:**10-50** mA **Flow**: **0.74-7.4** sccm (FTIR) **7.4-25** sccm (CRDS)

Experimental box 3.4: Measurements of CO and O fractions in pulsed plasma

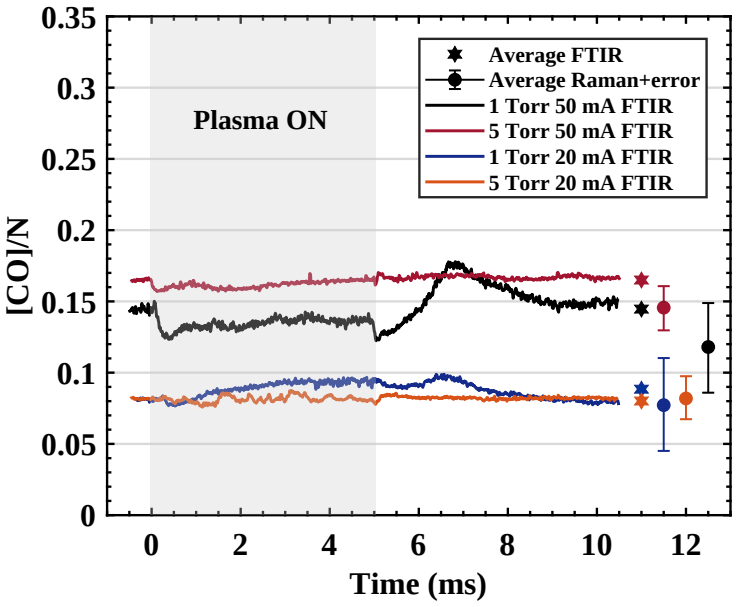

Figure 3.32: Time evolution of the CO fraction long a 5-10 ms On-Off pulse for 1 and 5 Torr, 20 and 50 mA measured with FTIR (full traces), average value plotted (stars) at the end of the measurement. Raman averaged values for the 11 measured time-points (see *Klarenaar et al.* [2018]) are also plotted (circles) with the corresponding error bars at the end of the measurement. The plasma ON-time is indicated with a shaded area.

3.7.1 CO densities

Time-resolved measurements of the dissociation fraction were done with FTIR and Raman *Klarenaar et al.* [2019]. The gas temperature values corresponding to this measurements were already shown in figure 3.4. Figure 3.32 shows the time evolution of the CO fraction measured with FTIR and compares it with the average of Raman results for 1 and 5 Torr, 20 and 50 mA. Raman data fluctuates significantly from one time point to another due to the low signal of CO and O_2 compared to the signal of CO_2 at low pressure which makes the determination of CO (and O_2) densities very challenging in pulsed plasma (see figure 2.9 (b)). Therefore, only the mean value of the eleven Raman data points is shown with the corresponding error bar (given by a 95% confidence interval). The average values of the FTIR measurements are also shown. At 20 mA the average fractions agree well between FTIR and Raman. At 50 mA the agreement is less good and FTIR tends to give slightly higher values than Raman, especially at 1 Torr, but still reasonable since the Raman error bars are large.

In general, the traces are flat, indicating that no significant amounts of CO are created during the pulse or recombined in the 10 ms afterglow. However a small conversion peak is visible within the first 2 ms of post-discharge. The peak value and delay with regard to the end of the pulse decreases with increasing pressure. This peak is visible for different conditions of pressure and current (see figures 3.33(a) and 5.22 (a)). The reason for the increase in the dissociation and the subsequent creation the dissociation peak is not clear. It could be related to dissociation by vibrational up-pumping of ν_3 such as in N_2 discharges, where the densities of high vibrational levels increase right after the end of the plasma *Guerra et al.* [2003]. It could be also related to de-excitation of electronically excited states of CO such as $CO(a^3\Pi_r)$. The lifetime of this state is very close to the

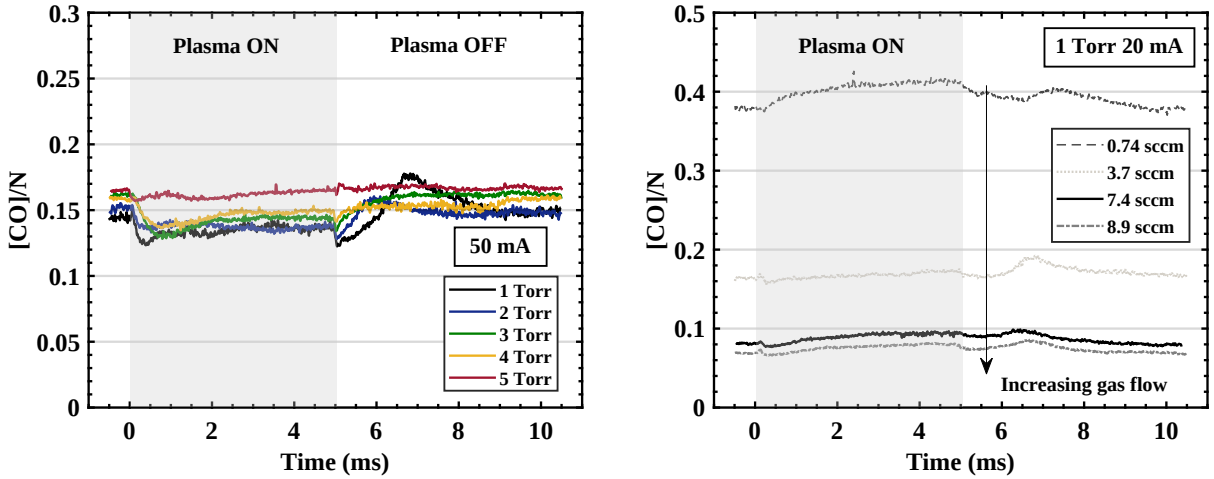

(a) Pressure variation at 50 mA.

(b) Gas flow variation at 1 Torr 20 mA.

Figure 3.33: Time evolution of the CO fraction along a 5-10 ms On-Off pulse (a) for pressures between 1 and 5 Torr at 50 mA and (b) for gas flows between 0.74 and 7.4 sccm at 1 Torr 20 mA. The ON-time is indicated with a shaded area.

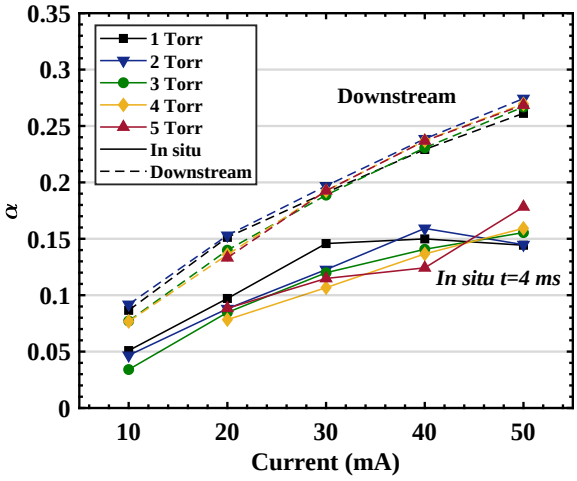

Figure 3.34: Variation of the dissociation fraction α as a function of current measured downstream a pulsed plasma of 5-10 ms On-Off and *in situ* at a time point t=4 ms for pressures between 1 and 5 Torr.

time delay of the dissociation peak ∼2.5-7.5 ms *Mori et al.* [2002]; *Gilijamse et al.* [2007], and is consistent with lower peak values and short delay times at higher pressures. The average values of $^{CO}/_{N}$ increase with current, but not with pressure, similarly to the continuous data. This is clearly visible in figure 3.33(a), which plots the time evolution of $^{CO}/_{N}$ for pressures between 1 and 5 Torr at 50 mA.

Figure 3.33(b) presents the FTIR traces for different gas flows at 1 Torr 20 mA, showing an increase of the dissociation fraction with decreasing gas flow, as observed in continuous data (see section 3.4.4). Finally, figure 3.34 plots the CO fraction measured downstream the pulsed discharge and compares it with the $^{CO}/_{N}$ values measured *in situ* taken at t=4 ms. This figure is qualitatively very similar to figure 3.14 (b), confirming the strong increase of dissociation when the current is

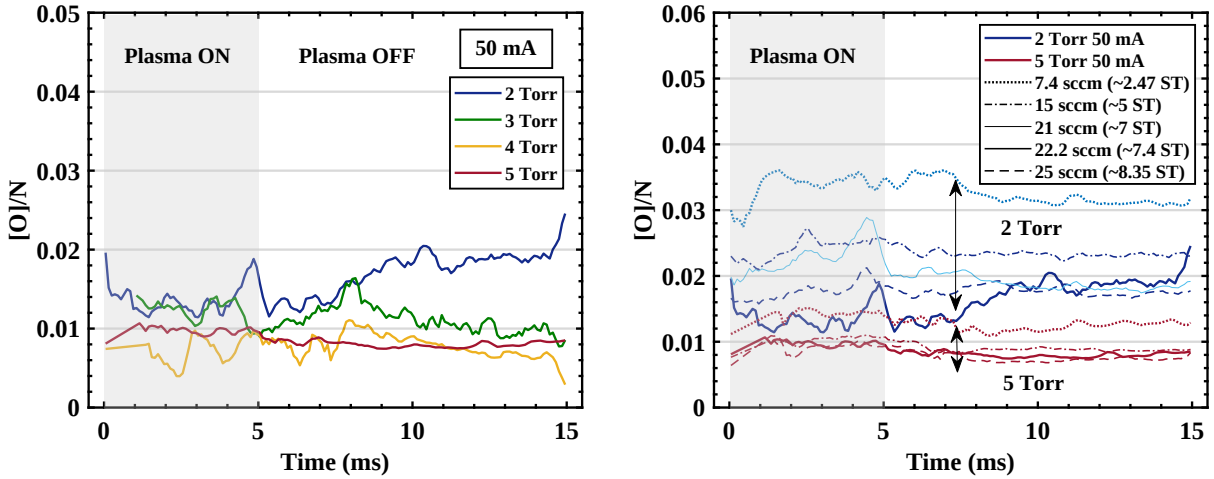

(a) Time evolution of the O atom fraction for pressures between 2 and 5 Torr.

(b) Time evolution of the O atom fraction for 2 and 5 Torr for gas flows between 7.4 and 25 sccm.

Figure 3.35: Time evolution of the O atom fraction along a plasma pulse of 5-10 ms On-Off (a) for different pressures between 2 and 5 Torr and (b) for only 2 and 5 Torr for different flows between 7.4 and 25 sccm. The ON-time is indicated with shaded area. Measurements taken at 22.2 sccm in the long tube reactor are equivalent in terms of τ_{res} to 7.4 sccm in the short tube (ST).

increased. Additionally, a similar ratio downstream *versus in situ* is apparent in pulsed plasma. Raman measurements done along the longitudinal axis of the tube in pulsed plasma show a negligible longitudinal profile *Klarenaar et al.* [2018], even less evident than in continuous plasma (see section 3.4.3).

3.7.2 O atom densities

Preliminary measurements of the O atom density in pulsed plasma were done with CRDS in the long discharge tube. In order to have a similar residence time as for the CO fractions in the short tube, these measurements were taken at a gas flow around 22 sccm. The CRDS signal (absorbance) is corrected by the change of gas density using the time-resolved temperatures measured with FTIR, presented for some conditions in figure 3.4 and for all conditions in the following chapter. Figure 3.35(a) shows the time evolution of the atomic oxygen fraction along the same plasma pulse discussed in the previous section: 5-10 ms On-Off, for pressures between 2 and 5 Torr at 50 mA. The O atom fraction is very similar for all the pressures, although it is slightly higher for the lowest pressures. Gas flow variation measurements, plotted in figure 3.35(b) further confirm the small pressure effect. Gas flow variation in pulsed plasma follows a similar trend as in continuous plasma: the O atom density increases when the gas flow decreases. The effect of the gas flow is higher at 2 Torr than at 5 Torr. Two main points can be underlined for the following chapters:

- In all cases the measurements show a flat profile *versus* time during pulses of 5-10 ms On-Off.
- The fraction of oxygen atoms compared to the CO fraction is significantly lower than in continuous plasma. Figures 3.33(a) and 3.35(a) show data for the same conditions (at 2 Torr 50 mA), and the $^{O}/_{CO}$ is on average $\lesssim 0.1$, whereas in continuous plasma it was close to 0.3.

A lower O atom fraction compared to the CO fraction could be expected because the losses are

more important for oxygen atoms than for CO, as discussed in section 3.6. However the lifetime of oxygen atoms is considerably longer than the OFF time in these experiments. In principle, the O atom loss processes could be different in post-discharge than under plasma exposure (this topic will be investigated in chapter 8), but if there is any difference, the lifetime of O atoms should be longer in post-discharge. This is actually consistent with observations since no significant decrease of oxygen density is detected in the post discharge in figure 3.35. More experiments, for instance with different On-Off cycles are required to confirm these results and to fully understand the lower average O atoms densities with short pulses.

✓ CO and O atom fractions are ∼constant along a short plasma pulse of 5-10 ms On-Off.
✓ In pulsed plasma the ratio $^{O}/_{CO}$ is $\lesssim$10% (at 50 mA), lower than in continuous plasma.
✓ Gas flow variation and downstream *vs. in situ* trends are consistent with continuous plasma data.

3.8 Summary and conclusions

This chapter aimed at providing a general characterization of the CO_2 glow discharge. The presented results are also relevant for the RF discharge under low excitation regime studied in chapters 6 and 7. The main results relevant for the discussion in the following chapters are summarized here. Concerning the gas temperature and electric field:

- The electric field and the reduced electric field are a monotonous function of total gas density ranging from E_{field} ∼10-40 V/cm, $^{E}/_{N}$ ∼110-50 Td in our pressure and current range (0.2-5 Torr, 10-50 mA).
- The gas temperature is at the first order a linear function of specific energy input, reaching maximum values ∼750-800 K at 5 Torr and 50 mA.
- The rotational temperature of CO_2, CO and O_2 measured with FTIR and Raman scattering is in equilibrium with the translational temperature of O atoms measured with HR-TALIF and CRDS.
- The characteristic time for reaching temperature stabilization ranges from ∼3-6 ms.
- The radial temperature profile implies that the temperature close to the reactor walls is significantly lower than in the centre of the discharge tube.

With regard to the densities of the main dissociation products:

- The CO_2 dissociation fraction increases with the SEI and in the first order seems to be well described by the direct electronic impact dissociation rate.
- The dissociation fraction α and its dependence as a function of pressure are strongly dependent on the residence time of the gas under plasma exposure. At the "reference" gas flow (7.4 sccm) the dissociation fraction does not reach the steady-state.
- The hypothesis of post-discharge chemistry seems to explain measured downstream α values higher than *in situ*.

- O atom densities reach relatively high values in continuous plasma, in the order of 1-5$\times 10^{21}$ m^{-3}. The maximum O atom fraction reaches values up to 35% of the CO density at 1 Torr, meaning that atomic oxygen represents a large proportion of the total gas in continuous discharge.
- Two clearly differentiated regimes as a function of pressure were found with regard to the O atom density in the range of pressures studied: (1) below 1 Torr the O atom density increases with pressure due to the increase of production rate along with the decrease of the O atom loss frequency. (2) Above 1 Torr the O atom density decreases with pressure, while the loss frequency increases with both pressure and current.
- The variation of the CO and O densities as a function of the specific energy input, is remarkably different, suggesting different loss processes. In our experimental conditions the O atom densities are shown to depend on surface loss processes.
- Both CO and O atoms densities are almost constant over short plasma pulses cycles of 5-10 ms On-Off, *i.e.* the characteristic time of loss/production mechanisms is significantly longer.

It is also worth mentioning that several diagnostic techniques were studied in detail and have been carefully cross checked and compared in this chapter. The main conclusions in this regard are the following:

- The gas temperature determined with FTIR, Raman, HR-TALIF and CRDS are generally in very good agreement within a difference $\lesssim$5%. The small differences are believed to be only due to the different regions sampled by laser (TALIF, CRDS and Raman) and IR (FTIR) beams.
- CO and CO_2 densities measured with FTIR and Raman are consistent. This validates in particular the Out of Equilibrium (OoE) script for IR spectra analysis.
- O atoms densities measured with Actinometry, HR-TALIF and CRDS show in general good agreement. The comparison of the absolute values points toward a possible over-estimation of HR-TALIF due to the two-photon absorption cross section of Xe commonly used for calibration

The experimental results shown in this chapter demonstrate the complexity of CO_2 plasmas even in simple discharge conditions. In the following chapters specific experimental configurations, such as static conditions (no flow), or absence of O atoms, will be studied in order to focus on individual mechanisms.

Part II

Vibrational kinetics in CO_2 plasmas

Chapter 4

CO_2 vibrational kinetics in continuous and pulsed DC glow discharge

Contents

4.1 Introduction 95
4.2 Experimental details and data treatment 96
4.3 Vibrational temperatures in continuous CO_2 glow discharge 97
4.4 Experimental results in pulsed glow discharge 101
4.4.1 Time evolution of the vibrational temperatures in a repetitive pulsed discharge 101
4.4.2 Effect of the gas composition 102
4.4.3 Effect of fast consecutive pulses 104
4.4.4 Influence of the discharge current and pressure 107
4.5 Discussion 108
4.6 Comparison with a kinetic model 114
4.7 Summary and conclusions 117

4.1 Introduction

The vibrational kinetics in any molecular gas discharge are mainly controlled by the balance between three basic mechanisms:

- **e-V** Electron impact excitation and de-excitation processes.
- **V-V** Vibrational energy transfer within the same vibrational mode, between different vibrational modes (V-V') of the same molecule or between different molecules (V-V').
- **V-T** Energy transfer from vibrational to translational/rotational degrees of freedom.

Energy exchanges as a result of collisions with electronically excited molecules, creation and/or destruction of vibrationally excited molecules in chemical reactions and de-excitation at the reactor walls can also be important. Most of the available literature concerning studies on vibrational excitation of CO_2 comes from the field of CO_2 lasers *Siemsen et al.* [1980]; *Dang et al.* [1982];

Andreev et al. [2004]; *Spiridonov et al.* [1994]; *Witteman* [2013]. These measurements are usually performed in continuous glow discharges in order to study the vibrational excitation as a function of different parameters, such as gas composition, pressure, plasma current, etc. However, time evolution analysis in transient discharges could provide a valuable insight into the mechanisms involved in the vibrational excitation and de-excitation processes and their characteristic times, and can be used for comparison and validation of kinetic models of CO_2 discharges.

Time-resolved measurements on pulsed CO_2 discharges have been rarely performed but *Rivallan et al.* [2010] already showed the possibility of using Fourier transform infra-red absorption (FTIR) to follow on time, with a micro-second resolution, the evolution of CO_2 absorption lines in a glow discharge in an air/CO_2 mixture. We will use this diagnostic to study the time evolution and the different processes involved in the vibrational excitation and de-excitation in a continuous and pulsed CO_2 glow discharge. The spacial homogeneity of the positive column of the glow discharge *Raizer* [1991] makes it suitable for this line-of-sight integrated technique.

This chapter is organized as follows: we first remind a few details of the experimental conditions. Subsequently we analyse the vibrational kinetics in continuous discharges and afterwards in pulsed discharges. Finally, we provide a comparison with a kinetic model developed in IST Lisbon. A great part of the data presented in this chapter has been obtained in collaboration with Bart Klarenaar. More details and analysis can be found in *Klarenaar et al.* [2017, 2019] and in his PhD thesis.

4.2 Experimental details and data treatment

The experimental details are summarized in the experimental box 4.1. All the data presented in this chapter have been acquired with a short glow discharge reactor (23 cm length and 2 cm inner-diameter) placed in the sample compartment of the FTIR spectrometer. Continuous plasma data were taken with a double-walled reactor, fixing the temperature of the water+ethanol circulating mixture at T_{wall}=50^{o}C for all the experiments. Pulsed plasma experiments were performed without controlling the wall temperature.

In the case of pulsed plasma, a master signal generator triggers the FTIR and a second pulse generator, which triggers the pulsed DC power supply with a delay of 0.5 ms. The trigger scheme is shown in figure 4.1. The plasma was pulsed typically in a cycle of 5-10 ms On-Off, but other duty cycle ratios were explored and will be detailed in the corresponding sections. Two experimental conditions are particularly important: (1) the "reference repetitive pulse" conditions to which other pulsed measurements will be compared, and (2) the so-called "single pulse" which allows to renew enough the gas between pulses to remain at very low dissociation fraction. These two particular conditions are detailed in the experimental box 4.2 and will be discussed in detail in section 4.4.2.

For continuous plasma experiments, the FTIR was operated in conventional mode, averaging 20 scans. For time resolved pulsed plasma measurements, the FTIR is operated in step scan-mode, as described in section 2.3.1. The experimental data was treated with the MATLAB scripts described in section 2.3.1. As default approach we will show the results obtained with the TOoE script (assuming a Treanor distribution for the population density of the vibrational levels), and we will use the vibrational temperatures defined in section 2.3.1 to describe the vibrational excitation. The results obtained with the OoE Free script, fitting the population density of vibrational levels without imposing any distribution, will be used for the comparison with the kinetic model in section 4.6.

Diagnostics: FTIR (TOoE, OoE Free) **Discharge**: Glow: Continuous & **pulsed** (5-10ms On-Off*, 0.3-0.3, 0.75-0.75-5-10 ms On-Off + single pulse*)	**Reactor**: SW short (cont.) DW short (pulsed) T_{wall}=50^{o}C in continuous, not controlled for pulsed **Flow**: 7.4 sccm (τ_{res} ≈0.23-2.5s + single pulse*)	**Pressure**: - **0.4-5** Torr Continuous - **1-5** Torr Pulsed **Current**: - **10-50** mA

Experimental box 4.1: General experimental conditions.

* **Reference repetitive pulse**:
-**Pulse**: 5-10 ms On-Off
-**Flow**: 7.4 sccm (τ_{res} ≈ 2.25 s ∼150 discharges during τ_{res})
-Reference conditions **Pressure**: 5 Torr, **Current**: 50 mA

* **Single pulse**: 1 single plasma pulse during τ_{res}
- **Pulse**: 5-150 ms On-Off, **Flow**: 166 sccm (τ_{res} ≈ 123 ms)
- **Pressure**: 5 Torr, **Current**: 50 mA

Experimental box 4.2: Description of the reference experiments.

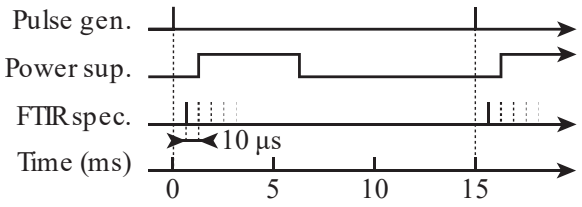

Figure 4.1: Scheme of the trigger for time-resolved FTIR experiments.

4.3 Vibrational temperatures in continuous CO_2 glow discharge

The vibrational temperatures of CO_2, corresponding to the bending and symmetric vibrational modes (Fermi-coupled), $T_{1,2}$, and to the asymmetric stretch vibrational model, T_3, the vibrational temperature of CO, T_{CO}, and the rotational temperature, T_{rot}, for different currents (between 10 and 50 mA) and pressures (between 0.4 and 5 Torr) in a continuous CO_2 glow discharge are shown in figure 4.2. The data at 50 mA is plotted with solid lines and for currents between 10 and 40 mA the data is plotted with dotted lines for readability. The plotted temperatures are deduced from the same spectra as the *in situ* dissociation data presented in figure 3.14. The rotational temperature has been already discussed and compared with the translational temperature of the O atoms measured with HR-TALIF and with the rotational temperature of CO_2, CO and O_2 measured by Raman scattering in section 3.2.2. The three techniques give very comparable values confirming that the rotational temperature T_{rot} is representative of the gas temperature in our discharge conditions. Several observations can be extracted from these data, summarized as follows:

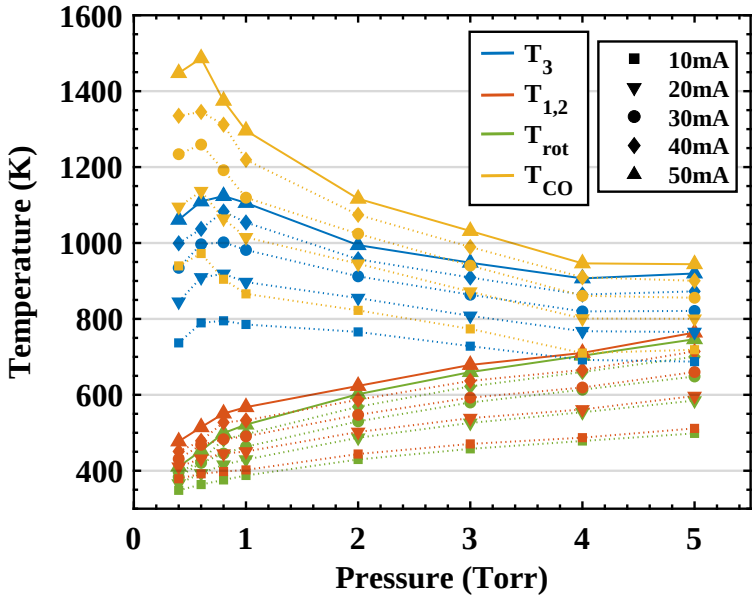

Figure 4.2: Variation of the rotational temperature, T_{rot}, and the vibrational temperatures of CO_2, $T_{1,2}$, T_3, and CO, T_{CO}, as a function of pressure for currents between 10 and 50 mA. Data at 50 mA is plotted with solid lines and for currents between 10 and 40 mA the data is plotted with dotted lines for readability.

- $T_{1,2}$ is strongly thermalized with T_{rot} for most of the range of pressures scanned. Only for the lowest pressures slightly higher values of $T_{1,2}$ compared to T_{rot} can be noticed. The maximum difference (at 0.4 Torr 50 mA) is approximately 70 K.
- $T_{1,2}$ and T_{rot} increase monotonically with pressure and current.
- T_3 reaches values between 700 and 1150 K for the lowest pressures, remarkably higher than T_{rot} (between 350 and 500 K in the same range of pressures), and shows a decreasing trend as a function of pressure from ~0.8 Torr hereinafter, opposite to the variation of T_{rot} and $T_{1,2}$.
- T_{CO} follows similar trend to T_3. Both show a maximum between 0.6-1 Torr, although T_{CO} values are surrounded by a bigger fitting error (see section 2.3.1).
- The difference between T_3 and T_{CO} is maximum in the low pressure range (the maximum difference ~380 K, is reached at 0.6 Torr) and decreases with increasing pressure, similarly to the difference between $T_{1,2}$ and T_{rot}.
- Towards higher pressures all temperatures tend to converge.
- All the temperatures show a similar, increasing, variation as a function of current.

The increase of T_{rot} has already been discussed in section 3.2.2. $T_{1,2}$ is strongly thermalized, probably due to efficient V-T relaxation *Blauer and Nickerson* [1973], expected from the small energy separation between consecutive bending modes (~0.08 eV) and the close energy levels between bending and symmetric vibrational modes *Herzberg* [1966]. T_3 and T_{CO} follow a remarkably different trend, not being thermalized with T_{rot} for most of the pressure range studied. They show a maximum at pressures between 0.6 and 1, which could be related to a balance point between

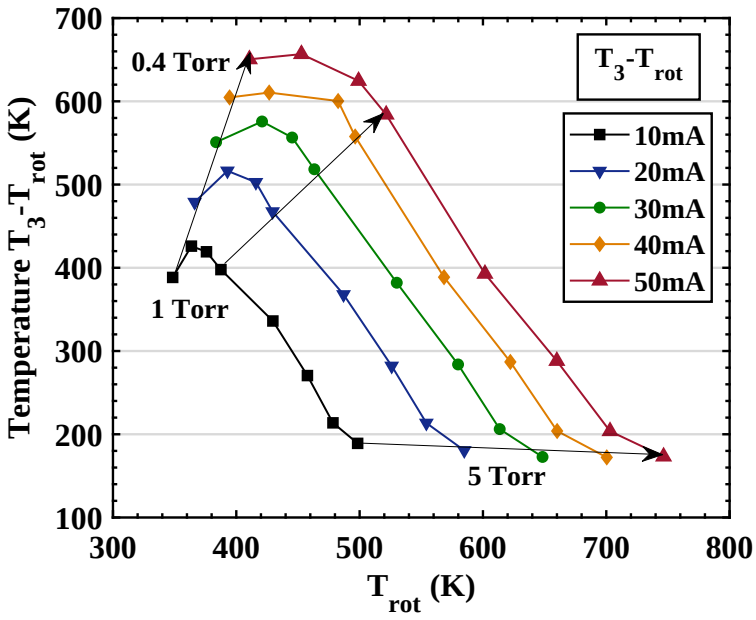

Figure 4.3: [T_3-T_{rot}] plotted as a function of T_{rot}, for currents between 10 and 50 mA. The variation as a function of current for pressures 0.4, 1 and 5 Torr is indicated with arrows pointing towards the highest current.

wall de-excitation and gas phase de-excitation processes. At a constant gas temperature, the relaxation rate of vibrationally excited molecules in the reactor walls decreases typically as a function of pressure up to a minimum which is around 1 Torr *Margottin-Maclou et al.* [1971], followed by an increase of the relaxation rate with pressure, agreeing well with the measured variation. The wall relaxation processes are discussed more in detail in the next chapter.

The excitation of the asymmetric stretch vibration of CO_2 is claimed to be beneficial for an efficient dissociation *Capezzuto et al.* [1976]; *Fridman* [2008]. The difference between T_3 and T_{rot}, [T_3-T_{rot}], is therefore interesting as a tracer of preferential energy transfer to the asymmetric mode and describes the "non-equilibrium" character of $CO_2(\nu_3)$. Figure 4.3 shows the variation of [T_3-T_{rot}] plotted as a function of T_{rot}. We observe that [T_3-T_{rot}] increases with current for the lowest pressures, whilst it remains almost constant (or even decreases slightly) for the highest pressures. In other words, for pressures between 0.4 and 1 Torr, an increase of current, *i.e.* electron density, induces an increase of the vibrational excitation, while for pressures above 1 Torr no increase of [T_3-T_{rot}] is observed, but only an increase of T_{rot}. Similar variation is followed by [T_{CO}-T_{rot}] (not shown). Note that the variation of the dissociation fraction α with pressure for a given current at the working flow (7.4 sccm) is almost negligible, whereas there is a strong increase of dissociation with current for all pressures (see figure 3.14). To understand this graph it is worth analysing the extreme cases:

- A perfectly vertical variation of [T_3-T_{rot}] with increasing current would mean that all the extra energy put in the vibrational excitation when increasing the discharge current would go to the excitation of the asymmetric stretch mode. It represents therefore an "ideal" excitation of the vibrations, without V-T, *i.e.* without heating.
- An horizontal line would imply that even though the electron density increases, the energy

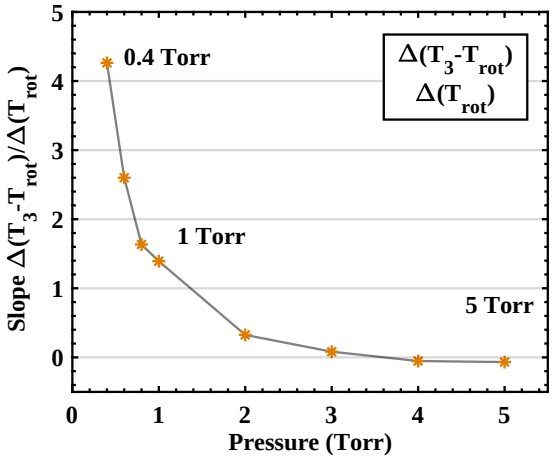

Figure 4.4: Slope of the variation [T_3-T_{rot}] as a function of T_{rot} when increasing current for all the pressures plotted in figure 4.3.

stored in the vibrations would remain the same and the extra vibrational energy would be preferentially transferred to translational energy.

The slope of the variation of [T_3-T_{rot}] as a function of T_{rot} for increasing current (*e.g.* qualitatively indicated by arrows in figure 4.3) is potted as a function of pressure in figure 4.4. The higher slope means a more dominant role of e-V processes compared to V-V and V-T. At low pressures the reduced electric field is higher. However, the electrons exciting the vibrations of CO_2 or CO are low energy electrons (∼1 eV) and the discharge power is more effectively transferred from the electrons to the vibrations when the electron temperature T_e is around 1-2 eV (equivalent to E/N ∼40-80 Td) *Grofulović et al.* [2018]. Therefore the high reduced electric field at lower pressures is not expected to be the cause of the increase of non-equilibrium with the plasma current, and the observed trends are probably not related to changes in e-V processes.

We can tentatively conclude that the trend at high pressures is more related to losses of vibrational excitation (quenching, V-V' and V-T) related to the larger collision rate, as well as an increase in efficiency of the de-excitation process, for instance because of the higher gas temperature at higher pressures (see figure 4.2).

✓ T_{rot} and $T_{1,2}$ are almost thermalized and increase monotonically with pressure. T_3 and T_{CO} (T_{CO}>T_3) decrease as a function of pressure.
✓ Increasing current leads to stronger out-of-equilibrium character, ↑ [T_3-T_{rot}], only for low pressures.
✓ [T_3-T_{rot}] decreases when the collision frequency increases (pressure and/or temperature effect).

Pulsing the plasma could give the possibility to differentiate the effect of gas temperature from the effect of pressure. Keeping T_{gas} low enough could extend the pressure range where V-T transfer do not dominate the vibrational kinetics. It will bring in addition, information about the e-V processes by looking at the characteristic time of vibrational excitation.

4.4 Experimental results in pulsed glow discharge

The analysis of the time evolution of the vibrational temperatures of CO_2 and CO, $T_{1,2}$, T_3 and T_{CO}, and the rotational temperature, T_{rot}, for currents between 10 and 50 mA and pressures between 1 and 5 Torr is presented in this section. In the first place we discuss the time evolution of the vibrational and rotational temperatures along a plasma pulse for the reference condition: 5 Torr 50 mA for a pulse of 5-10 ms On-Off. The influence of the gas mixture and the pre-pulse conditions is subsequently discussed. Finally, the influence of pressure and current is analysed in the last part of this section. More information and analysis about these experimental results can be found in *Klarenaar et al.* [2017, 2019] and in the PhD thesis of Bart Klarenaar.

4.4.1 Time evolution of the vibrational temperatures in a repetitive pulsed discharge

Figure 4.5 plots the time evolution of the fitted T_{rot}, $T_{1,2}$, T_3, T_{CO} and T_{therm}, the temperature of the thermal volume (see section 2.3.1), along a plasma pulse of 5-10 ms On-Off at 5 Torr 50 mA as illustrative example of a time-resolved pulsed plasma measurement. The shaded area indicates the plasma pulse. The current trace is also included and shows a certain over-shoot when the plasma is ignited followed by a fast stabilization that does not have any impact in the measured temperatures. The FTIR measurement starts 0.5 ms before the plasma is switched ON and it lasts until t=10.5 ms. The total measurement time is therefore 11 ms (corresponding to a 1100 time slices and a time resolution of 10 μs), less than the total plasma cycle, but we can assume a smooth evolution until the pre-pulse conditions of the next pulse.

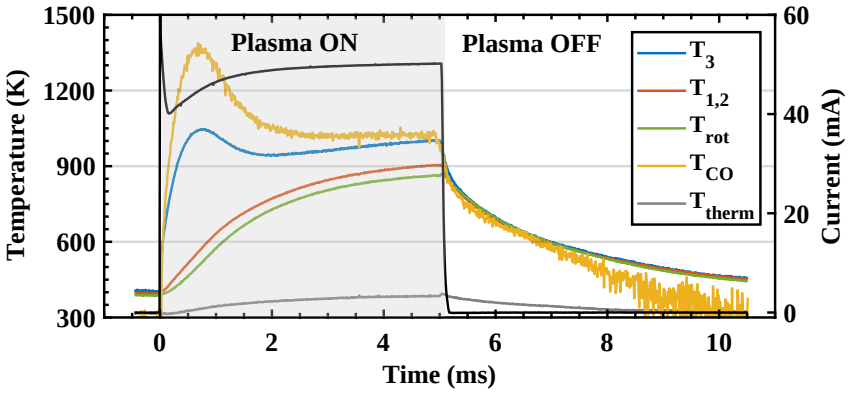

Figure 4.5: Time evolution of the rotational temperature T_{rot}, the vibrational temperatures of CO_2 and CO, $T_{1,2}$, T_3 and T_{CO}, and the temperature of the thermal volume, T_{therm}, measured along a plasma pulse of 5-10 ms On-Off at 5 Torr, 50 mA. The current trace is plotted as a solid black line.

Before the pulse, T_{rot}, $T_{1,2}$ and T_3 are in thermal equilibrium at a temperature close to 400 K. T_{CO} is not well fitted around this temperature; below 600 K the peaks in spectra corresponding to vibrationally excited CO are at the noise level and the fitted T_{CO} values become meaningless. When the plasma starts all the temperatures increase, but with different characteristic times: T_{rot} and $T_{1,2}$, show a similar time-evolution increasing monotonically with time, reaching a *quasi* steady-state at t$\sim$4.5 ms. T_3 and T_{CO} follow also a similar trend, with a fast initial increase until they reach a maximum at t$\approx$0.7 ms, compatible with e-V excitation. Thereafter, both T_3 and T_{CO} decrease but,

around t=2 ms, T_3 seems to be slightly pushed up by the increase of T_{rot} and $T_{1,2}$. The difference between T_3 and T_{CO} is maximum at the maximum of vibrational excitation but they converge to the same value at the end of the pulse. All temperatures tend to evolve towards a non-thermal equilibrium between 850 (T_{rot}, $T_{1,2}$) and 1050 K (T_3, T_{CO}) at the end of the pulse. T_3 and T_{CO} remain roughly 200 K higher than T_{rot} and $T_{1,2}$. These temperatures are slightly higher than the temperatures acquired in continuous plasma (see figure 4.2). The most probable reason is the use of a non-doubled walled reactor for the pulsed plasma (no wall temperature controlled). At t=5 ms the plasma is turned off and all temperatures equilibrate within a few μs. The thermal temperature T_{therm} only increases and decreases slightly between 300 and 400 K during and after the pulse.

✓ The characteristic time for reaching steady-state values of T_{rot} and $T_{1,2}$ is ∼4-5 ms at 5 Torr 50 mA.
✓ T_3 and T_{CO} show a faster excitation, reaching a maximum value at 0.7 ms.
✓ [T_3-T_{rot}] can reach much higher values (up to 522 K) than in continuous plasma for the same pressure, when the gas temperature is still low enough.

4.4.2 Effect of the gas composition

The data presented in the previous section was taken in a repetitive pulse configuration of 5-10 ms On-Off, meaning that every molecule receives many discharge pulses before leaving the reactor. At 5 Torr 50 mA for example, the residence time is around 2.25 s (considering 2/3 of the time at 300K and 1/3 at the continuous T_{rot} temperature) and therefore a molecule experiences on average ∼150 discharges during its way through the discharge tube. Although during one plasma pulse of 5-10 ms On-Off the dissociation and therefore the change in the dissociation fraction, α, is negligible (below detection), the cumulative effect of the pulses causes that we reach a stable dissociation fraction all along the experiment time (around 2.5 h). At 5 Torr 50 mA, the condition plotted in figure 4.5, α is around 0.17 (see figure 3.32). Over one period of 5-10 ms On-Off plasma α is basically constant for any pressure or current, as discussed in section 3.7. Therefore, the time evolution of the vibrational temperatures is not affected by a temporal change in the gas composition of ground state species. However, the time variation of vibrationally or electronically excited states of background molecules and atoms could still affect the vibrational temperature of CO_2 during the pulse, for instance by vibrational energy exchanges with CO (or even O_2) or collisions with other short life species such as oxygen atoms.

To investigate the effect of the gas composition, we have done an experiment in which the molecules only see one discharge pulse during its way through the plasma rector: the "single pulse" experiment. The gas flow is increased from the usual 7.4 sccm to 166 sccm of CO_2 and the plasma OFF time is increased from 10 ms to 150 ms (pulses of 5-150 ms On-Off). In this case, the residence time of the gas is ∼123 ms, significantly lower than the OFF time, purging the reactor of most of the CO, O and O_2 produced before the next plasma pulse, but keeping the renewal of the gas during the discharge reasonably low (∼5%). As a consequence, the dissociation fraction α is virtually zero and T_{CO} cannot be fitted for the single pulse measurement.

Figure 4.6 compares the "single pulse" with the repetitive pulse reference data (the same plotted in figure 4.5) for 5 Torr 50 mA. Comparing figures 4.6 (a.1) and (a.2), we observe that the general

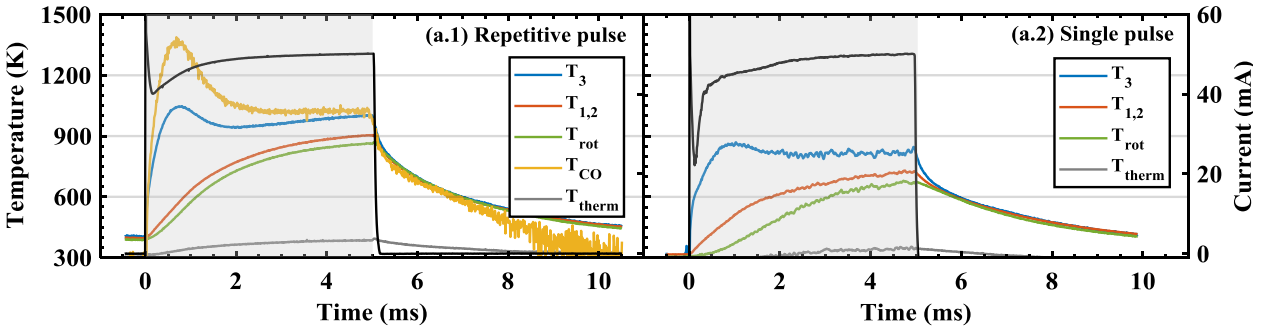

(a) Repetitive pulse and single pulse measurements at 5 Torr 50 mA

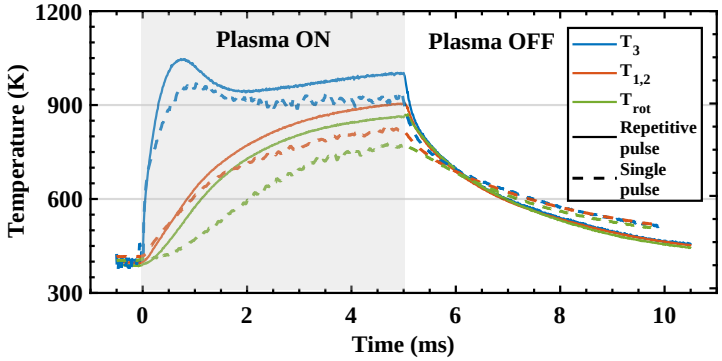

(b) Comparison between repetitive pulse and single pulse +100 K

Figure 4.6: Time evolution of T_{rot}, $T_{1,2}$ and T_3 for the repetitive pulse (panel a.1, including also T_{CO}) and for the single pulse (panel a.2) measurements, at 5 Torr 50 mA. Panel (b) shows the same data but shifting the single pulse values by the background temperature difference, 100K. The current traces are plotted in solid black lines.

evolution of the fitted temperatures as a function of time is qualitatively similar. T_3 shows an initial fast increase, passes through a maximum and then decreases, while T_{rot} and $T_{1,2}$ monotonically increase; all temperatures level off towards the end of the pulse. The temperatures quickly thermalize after the end of the plasma pulse, taking slightly longer in the single-pulse measurement. The irregularities in the single pulse data (between t=2 and 5 ms) are caused by variations between single discharges. When the plasma OFF time is small the discharge is more stable, evident also in the current trace.

There are, nevertheless, a few differences between both measurements. The most evident one is the difference in absolute values of the temperatures, already visible before the plasma pulse starts. This difference of ∼100K could be partly explained by the full renewal with cold gas in the single pulse experiment before the next plasma pulse, but also due to the effect of reactor walls, not cooled, which keep a relatively high temperature during the repetitive pulse experiment. Figure 4.6(b) presents the traces corresponding to T_{rot}, $T_{1,2}$ and T_3 for both experiments together but "shifting" the single pulse data by the initial 100K difference. We can now appreciate some more subtle differences between both experiments. This analysis is only qualitative since starting the pulse from a different temperature could already be influencing the time evolution of vibrational temperatures (see next section). Nevertheless, the following observations can be mentioned:

- Both measurements show a similar initial rise of $T_{1,2}$ and T_3 at the beginning of the pulse.

- The trends of $T_{1,2}$ and T_{rot} are qualitatively similar in both experiments, but the values in the single pulse remain clearly lower than in the repetitive pulse. The difference between both temperatures is larger.
- The rise of T_{rot} in the single pulse is delayed compared to the repetitive pulse case.
- The maximum of T_3 is slightly shifted in time from t=0.7 ms to t=1 ms for the "single pulse" compared to the repetitive pulse, and it is slightly lower in absolute value.
- After passing the maximum of T_3 (>1.5 ms), with repetitive pulses T_{rot} seems to push up T_3 at the end of the pulse, while for single pulse experiment T_3 remains constant (∼900K).

These observations suggest a similar excitation of the vibrations by e-V processes in both experiments, for both ν_3 and $\nu_{1,2}$, in spite of the differences in the EEDF induced by the presence of CO, O_2, O and other minor species. V-V' and V-T transfer processes appear to be more affected by the presence of dissociation products and/or by the lower initial T_{rot}. The lower peak of T_3 in the single pulse could suggest an effect of the lower initial temperature. It is therefore relevant to investigate how a short pre-pulse could affect the development of the 5 ms plasma pulse, which will be done in the next section. Another possibility is the enhancement of the ν_3 excitation due to V-V' transfer from CO which would happen only for the repetitive pulse case. T_{CO} shows similar evolution as T_3, but at higher temperature, and CO and $CO_2(\nu_3)$ have near-resonant transitions *Witteman* [2013]. The delayed T_{rot} rise (and lower values) in the "single pulse" measurement suggests a reduction of V-T processes in the absence of dissociation products, which could also explain the longer thermalization in the early post-discharge.

✓ The decrease of T_3 after the excitation peak is related to the increase of T_{rot} and/or $T_{1,2}$. When T_{rot} is delayed as in the singe pulse, the maximum is also delayed.
✓ The presence of dissociation products, such as CO, O or O_2, increases significantly V-T processes.
✓ Vibrational energy transfer from CO probably enhances the increase of T_3 at the beginning of repetitive plasma pulses.

4.4.3 Effect of fast consecutive pulses

The time evolution of the vibrational temperatures seen in previous sections suggests that short pulses could be beneficial to take advantage of the non-equilibrium at the beginning of the pulse, when the gas temperature is still low. We could wonder however how the pre-pulse conditions affect the development of the following pulse. Or even if the accumulation of short pulses with fast repetition rate could further increase the maximum of ν_3 excitation. To examine these questions two different pulse configurations are studied:

1. **Double pulse: 0.75-0.75-5-10 ms On-Off-On-Off** → the usual 5-10 ms On-Off pulse but preceded by a short 0.75-0.75 ms On-Off pulse, to study the effect of a short pre-pulse in the development of the usual pulse.
2. **Fast pulse: 0.3-0.3 ms On-Off** → to study the possible cumulative effect on the excitation of ν_3.

Figures 4.7 (a) and (c) show the usual pulse (to the left) compared to the two study cases described (to the right, in panels (b) and (d)). Vertical lines in the reference case (panels (a) and (c)) indicate the time duration of the short pulses in the study cases (panels (b) and (d)). In panel (b), the temperature variation during the pre-pulse is similar to the first 0.75 ms in the reference pulse (panel (a)) for all temperatures (T_{CO} is slightly lower but within the error associated to this temperature). After the pre-pulse, the relaxation of T_3 is remarkably slower than at the end of the reference pulse or in the single pulse (see figure 4.6): After the 5 ms pulse, the thermalization with T_{rot} takes a few tens μs, whereas after the 0.75 ms pulse the OFF time of 0.75 ms is too short to relax T_3 and T_{CO} to T_{rot}. When the second pulse starts T_3 and T_{CO} are not completely relaxed yet. The second pulse develops similarly to the reference case. T_3 and T_{CO} reach a maximum at ~0.7 ms again, but the temperature value at the peak is lower than in the 5 ms pulse without pre-pulse. The difference [T_3-T_{rot}] is significantly lower because of the higher T_{rot}. The end of the second pulse is similar to the reference case and the final temperatures are essentially the same.

Figure 4.7 (d) plots the short pulses with fast repetition rate. The maximum in T_3 is approximately the same as in the reference pulse for the same ON time, not higher. No cumulative effect, *i.e.* a further increase, on the excitation of T_3 is observed. After the pulse, T_3 does not relax completely, staying between 750 and 900 K. T_{rot} and $T_{1,2}$ stay relatively high during the ON and OFF phases, between 650 and 725 K because the OFF time (0.3 ms) is not long enough to cool down the gas. A cumulative effect is therefore seen in the case of T_{rot} and $T_{1,2}$, also observed in panel (b).

The gas temperature appears to be essential for the analysis of the characteristic times of vibra-

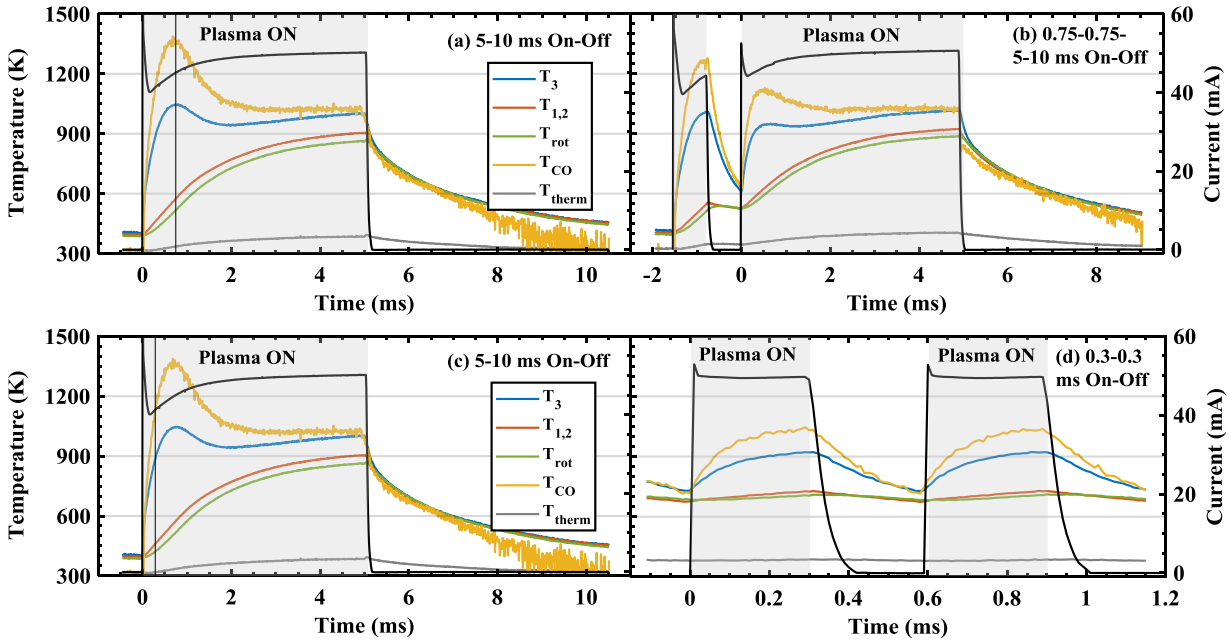

Figure 4.7: Time evolution of the rotational and vibrational temperatures of CO_2 and CO, T_{CO} for different pulse durations at 5 Torr 50 mA: (a) and (c) 5-10 ms On-Off (reference), (b) 0.75-0.75-5-10 ms On-Off-On-Off, similar to (a) but with a short pre-pulse and (d) 0.3-0.3 ms On-Off. Vertical lines in panels (a) and (c) indicate the time duration of the first pulse in panels (b) and (d) for comparison. Black solid lines represent the discharge current.

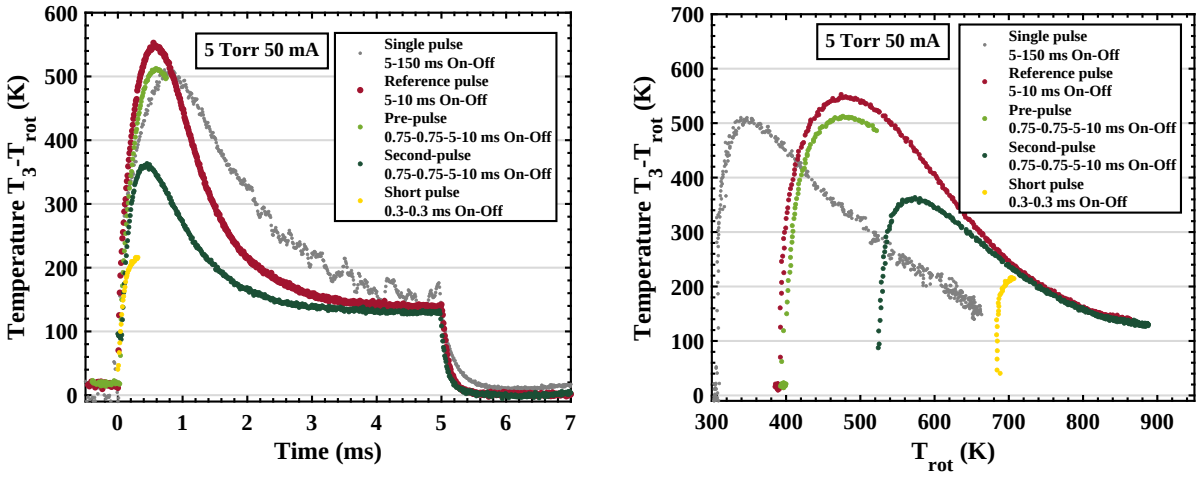

(a) T_3-T_{rot} plotted as a function of time.

(b) T_3-T_{rot} plotted as a function of T_{rot}

Figure 4.8: $[T_3\text{-}T_{rot}]$ plotted as a function of time (panel (a)) and as a function of T_{rot} (panel (b)) for different pulse configurations at the same pressure and current (5 Torr 50 mA).

tional temperatures. Figure 4.8 plots $[T_3\text{-}T_{rot}]$, representative of the out-of-equilibrium character, as a function of time (panel (a)) and as a function of T_{rot} (panel (b)) for the different pulse durations shown in figure 4.7, including also the "single pulse" data. The pre-pulse of 0.75-0.75 ms On-Off is treated separately from the second pulse, which has the same duration as the reference condition (5-10 ms On-Off). Note that all the measurements plotted are taken at the same pressure and current, 5 Torr 50 mA, but the dissociation values are different. The single pulse has practically α=0, for the reference pulse α=0.17, for the double pulse α=0.19 and for the fast pulse α=0.25. Panel 4.8(a) shows that the initiation of the pulse (the first μs) is similar for all the conditions, regardless the initial temperature or dissociation fraction, implying that these parameters do not affect the e-V excitation of ν_3. Several differences are evident for longer ON times, though. The peak value in $[T_3\text{-}T_{rot}]$ is relatively similar for the cases of single pulse, the reference (repetitive) pulse and the pre-pulse, but significantly lower for the second pulse in the double pulse experiment and for the fast pulse. The cause is clear looking at the graph 4.8(b), which plots the same data as in 4.8(a) but as a function of T_{rot} only for the active part of the discharge. Except for the single pulse, all the measurements are aligned in a general trend, following a fast increase at low T_{rot}, pass through the peak and then a sluggish decrease for higher T_{rot}. This single decaying trend with T_{rot} confirms the increased efficiency of V-T with gas temperature.

✓ Higher T_{rot} and/or $T_{1,2}$ values at the beginning of the pulse reduce the maximum in $[T_3\text{-}T_{rot}]$.
✓ Lower T_{rot} and/or $T_{1,2}$ at the end of the pulse increase the relaxation time of T_3.
✓ Re-starting from an already excited gas does not lead to a further elevation of T_3, but to an increase of the average gas temperature.

These results will be relevant for the discussion in chapter 6, where the effect of pulsing on the CO_2 dissociation is studied.

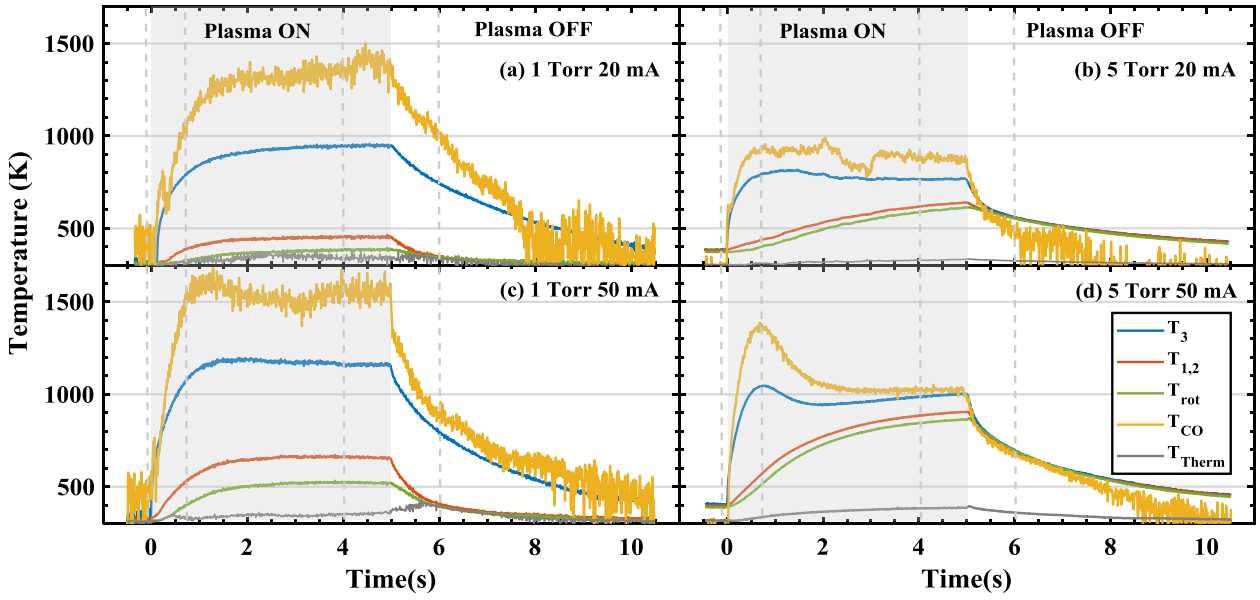

Figure 4.9: Variation of the rotational temperature of CO_2, T_{rot}, the temperature of the thermal volume T_{Them} and the vibrational temperatures of CO_2, $T_{1,2}$ and T_3, and CO, T_{CO}, *versus* time along a plasma pulse of 5-10 ms On-Off, for four different conditions of pressure and current: 1 Torr 20 (a) and 50 mA (c) and 5 Torr 20 (b) and 50 mA (d).

4.4.4 Influence of the discharge current and pressure

Time-resolved pulsed measurements were performed for pressures between 1 and 5 Torr and currents between 10 and 50 mA. Figure 4.9 presents similar data as in 4.5, for 1 and 5 Torr, 20 and 50 mA to illustrate the effect of current and pressure on the time evolution of the rotational and vibrational temperatures of CO_2 and CO. The plasma pulse is indicated by a shaded area.

- When the plasma pulse starts, T_3 and T_{CO} show a fast increase in all conditions. T_{CO} is always higher than T_3 and both temperatures are significantly higher than the rotational temperature T_{rot}.
- The difference between T_3 and T_{rot}, *i.e.* the non-equilibrium [T_3-T_{rot}], decreases significantly with pressure. A similar relation is shown between T_{CO} and T_{rot}.
- T_{rot} increases clearly both with pressure and current, similarly to the continuous plasma experiments (see section 3.2).
- $T_{1,2}$ is slightly above T_{rot} for all conditions, and it is always significantly lower than T_3. The difference between $T_{1,2}$ and T_{rot} decreases with pressure and slightly increases with current, especially at 1 Torr.

T_3 shows different behaviour for the different pressure/current conditions. At 1 Torr, the temperatures rapidly increase and then, from t=1.5-2 ms remain stable around 950 K and 1175 K for 20 mA and 50 smA, respectively. At 5 Torr, T_3 first increases to a maximum after which it slightly decreases and then stabilizes at a lower temperature, around 760 K and 980 K for 20 mA and 50 mA, respectively, showing a certain re-increase in the case of 5 Torr 50 mA, already discussed. The maximum value of T_3, is shifted towards shorter ON times for the higher currents (t=0.7 *vs.* t=1.5

ms at 5 Torr (50 and 20 mA respectively), probably related to the slower increase of T_{rot} and $T_{1,2}$ at lower current, as in the single pulse. In the afterglow, at the highest pressure, T_3 and $T_{1,2}$ relax very quickly to T_{rot}, in a few μs whereas at low pressure the non-thermal conditions remain significantly longer, more than 5 ms in the case of T_3 and ~1 ms for $T_{1,2}$. T_{CO} shows similar behaviour as T_3, stabilizing around 1350 K (20 mA) and 1550 K (50 mA) at 1 Torr, and 790 K (20 mA) and 1000 K (50 mA) at 5 Torr.

The time evolution along a plasma pulse obtained for pressures from 1 to 5 Torr and currents between 10 and 50 mA allows to create time-resolved temperature maps *versus* current and pressure by inter/extrapolating the values of T_3, $T_{1,2}$ and T_{rot}. The maps corresponding to four time points indicated with dashes lines in figure 4.9 are presented in figure 4.10:

1. **t=-0.1 ms** at thermal equilibrium, before the beginning of the plasma pulse.
2. **t=0.7 ms** at the peak of vibrational excitation of ν_3 at 5 Torr (close to the maximum for other pressures) while $T_{1,2}$ and T_{rot} are still relatively low.
3. **t=4.0 ms** close to the end of the plasma pulse, when all the temperatures stabilize.
4. **t=6.0 ms** 1 ms after the pulse, when the temperatures are thermalized and decreasing.

The three sheets represent the data for T_3 (top layer), $T_{1,2}$ (middle layer) and T_{rot} (bottom layer). The left and right graphs show the same data, but from a different angle, to allow clear view on the maps. Panels (a) and (b) in figure 4.10 show that for every condition the gas is in thermal equilibrium before the beginning of the plasma pulse (t=-0.1 ms), with a small temperature gradient towards higher pressures. In panels (c) and (d) corresponding to the maximum, or close to the maximum, of vibrational excitation of the asymmetric stretch mode ν_3 (t=0.7 ms) we see that T_3 increases drastically for all conditions. The increase seems to be related to the discharge current, but not to the pressure. Note that an increase of current implies an increase of the dissociation fraction α (see section 3.7.1). $T_{1,2}$ remains low, close to T_{rot}.

When we approach the end of the plasma pulse (t=4 ms, panels (e) and (f)) we observe that the excitation of T_3 decreases with increasing pressure for pressures between 1 and 3 Torr, but then it re-increases again for 4 and 5 Torr creating a saddle point. The reason, as pointed out in figure 4.9, is the increase of T_{rot} and $T_{1,2}$, proportional to both the plasma current and the pressure, clearly visible in panel (f). It is also evident that when we are at ~steady-state the non-equilibrium [T_3-T_{rot}] decreases with pressure for every current, similarly to the continuous plasma case (see figure 4.2). After the end of the plasma pulse (t=6 ms, panels (g) and (h)), the thermalization rate is directly related to pressure. The time required to reach the steady-state during the plasma pulse for all the temperatures was between 2 and 4.5 ms for the conditions studied. This is therefore the characteristic time for the vibrational equilibrium in our discharge conditions.

4.5 Discussion

Effect of the gas temperature on the vibrational kinetics of CO_2

Looking at the data in continuous plasma (see figure 4.3) we saw that for higher pressures an increase of current had no effect on the non-equilibrium parameter [T_3-T_{rot}]. Apart from the increase on the dissociation fraction, increasing the current was only leading to an increase of the rotational

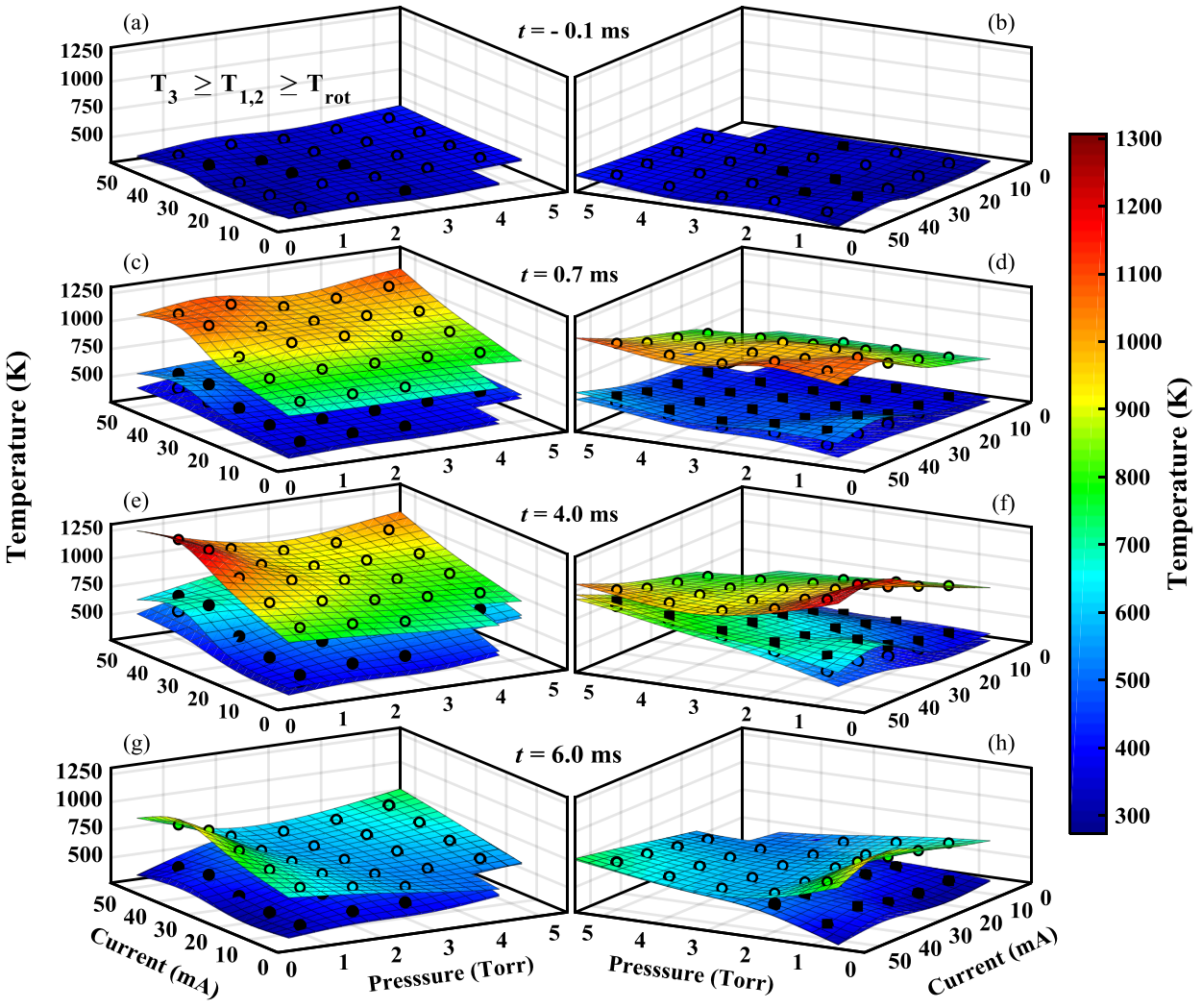

Figure 4.10: Temperature maps of T_{rot} (bottom layer), $T_{1,2}$ (middle layer) and T_3 (top layer) as a function of pressure and current, for four characteristic time-points during the plasma cycle: (a) and (b) -0.1 ms (before the beginning of the pulse); (c) and (d) 0.7 ms (maximum of vibrational excitation for ν_3 and CO); (e) and (f) 4.0 ms (close to the end of the pulse, with already stabilized temperatures); (g) and (h) at 6.0 ms (1.0 ms after the end of the discharge). The maps were created interpolating (and extrapolating when needed) from the data points, indicated by square and circular symbols. The left ((a), (c), (e) and (g)) and right ((b), (d), (f) and (h)) graphs show the same data from different perspective.

temperature. However, in pulsed plasma we do observe a positive impact of the current on the vibrational excitation, but it is a transient effect. Figure 4.11(a) plots the time evolution of [T_3-T_{rot}] along the plasma pulse for different pressures at 40 mA and figure 4.11(b) for different currents for the highest pressure studied, 5 Torr. For all currents and pressures we see the same rapid increase at the beginning of the pulse, when T_{rot} is still low. Subsequently, [T_3-T_{rot}] passes through a maximum, whose peak value does increase with current even at 5 Torr, and decreases with pressure. It is noticeable however, that after the peak the decrease is faster for higher currents and especially for high pressures. This behaviour again points out towards an effect of higher T_{rot} and $T_{1,2}$ which could enhance V-T processes and V-V' inter-mode exchanges. For the single pulse, however the decrease after the maximum resembles more the behaviour at lower current, i.e. at lower temperature or

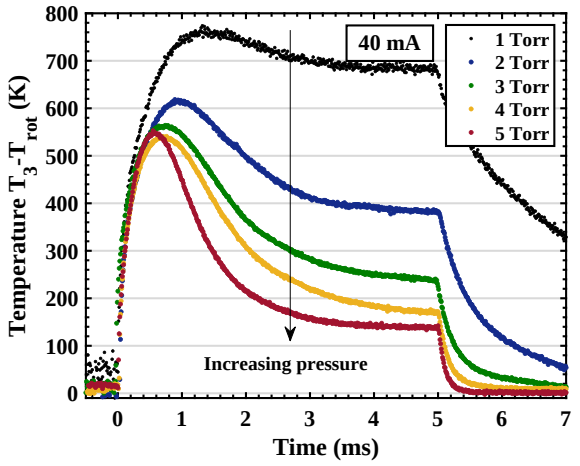

(a) Pressure effect at constant current (40 mA) plotted as a fucntion of time

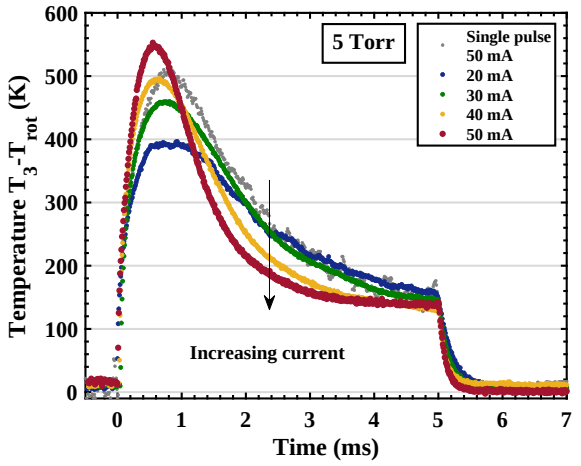

(b) Current effect at constant pressure (5 Torr) plotted as a fucntion of time

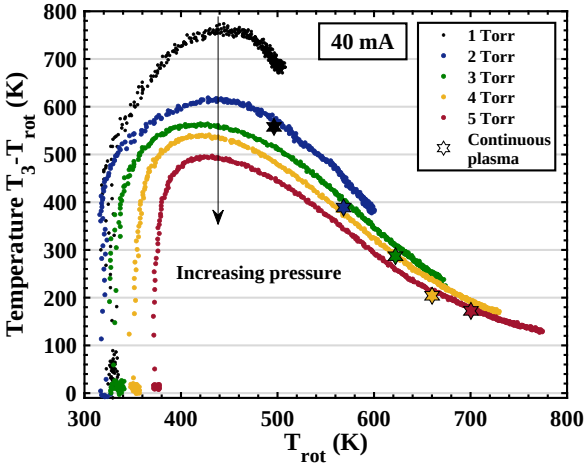

(c) Pressure effect at constant current (40 mA) plotted as a fucntion of T_{rot}

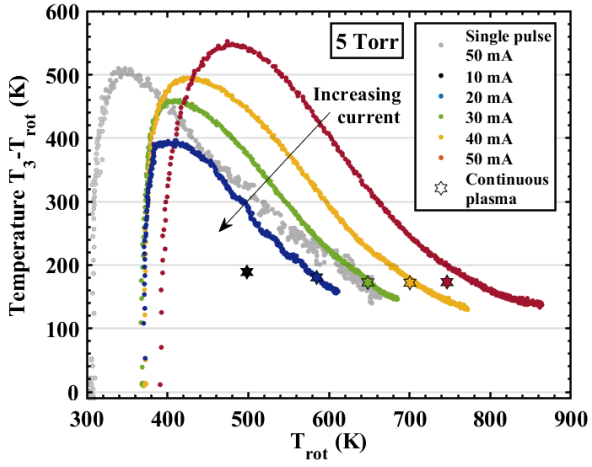

(d) Current effect at constant pressure (5 Torr) plotted as a fucntion of T_{rot}

Figure 4.11: [T_3-T_{rot}] plotted as a function of time (panels (a) and (b)) and as a function of T_{rot} (panels (c) and (d)) along a plasma pulse of 5-10 ms On-Off. (a) and (c) show the effect of pressure for a constant current of 40 mA. (b) and (d) show the effect of current for a constant pressure of 5 Torr. The single pulse (5-150 ms On-Off) data is included in panels (b) and (d).

lower densities of dissociation products.

Figures 4.11(c) and 4.11(d) plot the same data but as a function of T_{rot} only for the active part of the discharge. The continuous data are plotted for the same plasma conditions with stars. The values are very consistent, only slightly shifted towards lower temperatures and higher [T_3-T_{rot}], due to the effect of cooling the reactor walls (only present for the continuous plasma data). The discrepancy at 1 Torr is however quite noticeable in figure 4.11(c). Either at 1 Torr we are far from reaching the steady-state at the end of a 5 ms pulse, which does not seem to be the case in figure 4.9, or there is a clear effect of de-excitation of T_3 in the walls, more pronounced in continuous plasma. As pointed out by *Margottin-Maclou et al.* [1971], 1 Torr is somewhat the frontier in which the wall de-excitation can be competitive with gas phase de-excitation processes (for a similar tube radius). In this regard, a cooler wall temperature would enhance this process since the accommodation coefficient increases with decreasing surface temperature *Doyennette et al.* [1974]. The vibrational de-excitation in the reactor walls at 1 Torr will be confirmed in the next chapter.

Since the dissociation fraction is basically constant along the plasma pulse, the variation of [T_3-T_{rot}] points towards a negative effect of the increasing gas temperature in the vibrational excitation. Another phenomena that suggests the detrimental effect of the gas temperature on the vibrational excitation is the behaviour after the end of the pulse. Figure 4.12 plots the time evolution of [T_3-T_{rot}] for the first milliseconds after the end of the pulse for 1, 2, 3 and 5 Torr and currents between 20 and 50 mA. The decay rate of [T_3-T_{rot}] increases with pressure and current. This time evolution is fitted with a single exponential decay and the obtained decay rate is plotted as a function of the mean rotational temperature in figure 4.13 (the temperature value of T_{rot} for twice the characteristic time of relaxation, see *Klarenaar et al.* [2019] for more details). Note that this figure provides information only about V-V' and V-T processes, not e-V. The decay rates fitted for the different pulse configurations discussed in section 4.4.3 are also included (as stars) being in good agreement with the variation as a function of T_{rot} shown by the rest of the data. The graph shows a ∼exponential increase of the decay rate with increasing rotational temperature, although the slightly different trend for the different currents suggest that there is more than a single parameter involved. It is noticeable in figure 4.12 that the decay rate of the single pulse is different than the repetitive pulse for the same pressure and current, it is slower, confirming the impact of the gas temperature and the dissociation products in the V-T processes taking place after the end of the pulse.

It is also worth remembering the information obtained from the different pulse configurations (section 4.4.3). The increase of the gas temperature is not only the consequence of the quenching of the vibrational states, but also the cause. Starting from a gas at already high gas temperature prevents the efficient excitation of the vibrations, even though the e-V excitation by electron collisions should be similar. Available rate constants for the relaxation of ν_3 through V-T (to translational degrees of freedom) and V-V' (to other vibrational modes) increase with temperature *Blauer and Nickerson* [1973]:

$$k(cm^3 s^{-1}) \propto exp\left(A + BT^{(-1/3)} + CT^{(-2/3)}\right) \tag{4.1}$$

where A is a positive constant, whereas either B or C is negative in a way that k increases with the gas temperature T.

The observed trends are consistent with the rate coefficients available and we can conclude that

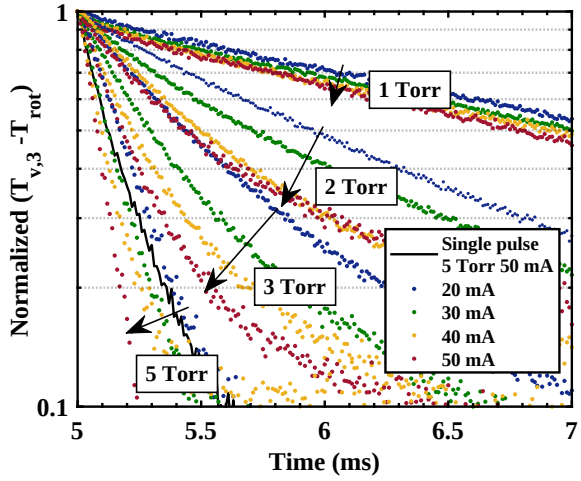

Figure 4.12: Time evolution of [T_3-T_{rot}] normalized to the end of the pulse (t=5ms) for pressures 1, 2, 3 and 5 Torr and currents between 20 and 50 mA for the repetitive pulse (5-10 ms On-Off). The single pulse data 5-150 ms On-Off at 5 Torr 50 mA is also included for comparison. The graph is colour coded according to current.

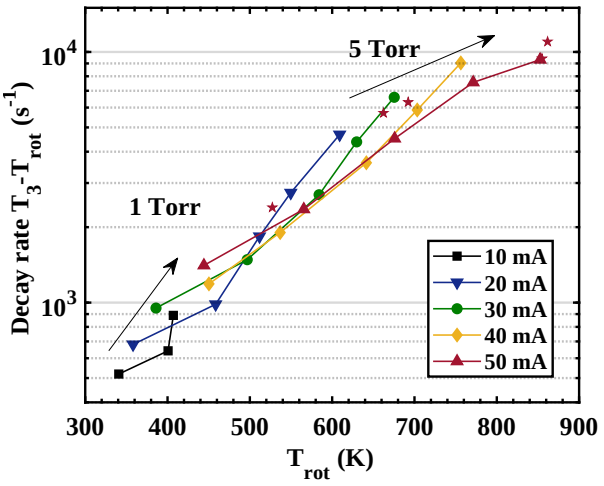

Figure 4.13: Variation of the decay rate of [T_3-T_{rot}] *versus* time after the end of the pulse (such as in 4.12) for all pressures and currents for the repetitive pulse (5-10 ms On-Off). The graph is colour coded according to current. Data for other pulse durations (section 4.4.3) at 5 Torr 50 mA is included, represented by stars.

they are caused by an excitation/de-excitation equilibrium in which the de-excitation processes are dominated by the increase of both the collision rate and the efficiency of the de-excitation processes *per* collision with the gas temperature. Nevertheless, from an experimental point of view it is difficult to isolate the effects of V-V' and V-T in the relaxation of T_3 because $T_{1,2}$ and T_{rot} tend to follow a very similar evolution, and a comparison with kinetic models is convenient.

Effect of the dissociation products

Concerning the effect of the dissociation products on the CO_2 vibrational kinetics, the variability of conditions scanned, with several parameters varying at the same time, makes it difficult to correlate the information about the vibrational kinetics with the densities of different species. There is only one case where we can perceive the effect of dissociation products: the comparison between the "single pulse", where the amount of CO, O_2, O and other minor products is negligible, and the repetitive pulse in the reference condition. Nevertheless, isolating the effect of the different by-products is still challenging. It is known from literature that the vibrational energy transfer between CO and $CO_2(\nu_3)$ is nearly resonant *Witteman* [2013]. Several experimental details point towards such phenomena in our discharge:

- Similar qualitative time variation along a plasma pulse and as a function of pressure and current of T_3 and T_{CO}, also observed in continuous plasma.
- Convergence of the vibrational temperatures of CO and CO_2 at higher pressures both in continuous and in pulsed plasma towards the end of the plasma pulse.
- Slightly higher [T_3-T_{rot}] peak value (50K) (figure 4.11(d)) even for a higher initial T_{rot} for the repetitive pulse compared to the single pulse.

Provided that the energy transfer between ν_3 and ν_{CO} is *quasi* resonant, it is expected that at higher pressures, and therefore higher collision rates, the relaxation of CO to ν_3 is more effective, resulting in the de-excitation of CO and a smaller difference between the temperatures T_{CO} and T_3, as confirmed by the experiments. This is consistent with modelling results *Gorse and Capitelli* [1984] showing a decrease of T_{CO} when the fraction of CO_2 in the gas mixture grows.

The high T_{CO} values in our discharge can be explained because of the lower de-excitation rate compared to $CO_2(\nu_{1,2})$, less effective V-V' from CO to $CO_2(\nu_{1,2})$, compared to V-V' from $CO_2(\nu_3)$ to $CO_2(\nu_{1,2})$, effective vibrational CO up-pumping ("ladder climbing") *Powell* [1973]; *Liu et al.* [1975]; *Pietanza et al.* [2017], or even effective energy transfer from collisions with excited species such as $O(^1D)$, created for example from the electron impact dissociation of CO_2 or O_2. In this regard, it was concluded that up to 25% of the electronic energy in $O(^1D)$ is converted to CO vibrational energy *Harding et al.* [1988] (other references suggest up to 40% *Slanger and Black* [1974]). Energy transfer from $O(^1D)$ to CO_2 is also possible, and some references suggest that up to 44% of the available energy of the $[O(^1D)+CO_2]$ system could be converted into vibrational energy of CO_2 *Huestis et al.* [2002]; *Chen et al.* [2009]. The energy transfer from electronically excited states, not only from O atoms, but also of CO, O_2 or even CO_2 *Capitelli et al.* [2017], has not yet been considered in our discussion. The amount of energy stored may be significant and if there is no low-lying excited level it must be transmitted all at once *Zhu et al.* [1990], eventually leading to highly excited vibrational levels, which would not be detected in our experiment. However, if these processes involving CO, O or O_2 in electronically excited states, were very relevant in our discharge conditions we should observe more evident differences between the single and the repetitive pulse.

Although a careful study of the CO_2-CO vibrational exchanges should be carried out, for instance by doing single pulse measurements in CO_2-CO mixtures, some experiments were already done in CO_2-N_2, to study the possible enhancement of the vibrational excitation by V-V' resonant transitions between $CO_2(\nu_3)$ and N_2, well known in the field of CO_2 lasers *Witteman* [2013]; *Taylor and Bitterman* [1969]; *Wiegand et al.* [1970]. Figure 4.14 shows, as an illustrative example, the reference measurement in a repetitive pulse at 5 Torr, 50 mA starting from a initial pure CO_2 gas mixture, and a measurement in similar conditions but starting from a 50%CO_2-50%N_2. N_2 behaves as a reservoir of vibrational energy, that can be transferred to $CO_2(\nu_3)$ or CO *Benedictis et al.* [1987]; *Flament et al.* [1992]. The increase in the experimental vibrational temperature is highly

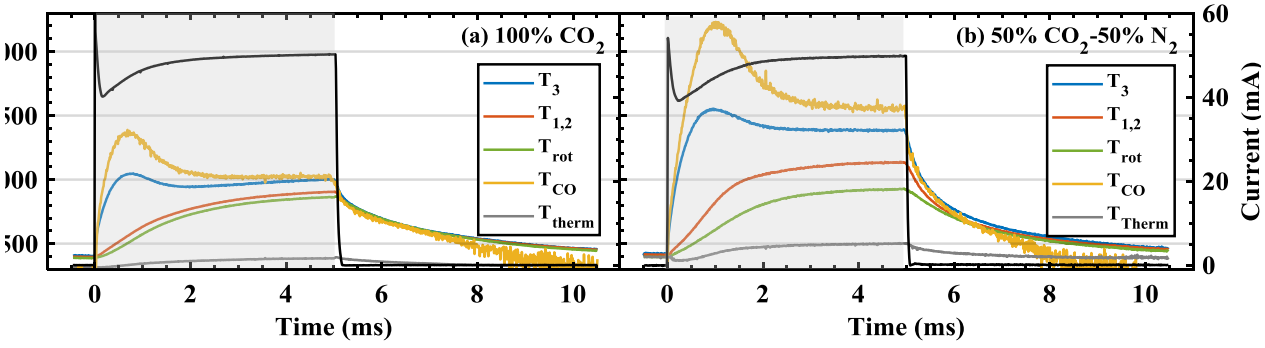

Figure 4.14: Time evolution of T_{rot}, T_{Therm}, $T_{1,2}$, T_3 and T_{CO} at 5 Torr, 50 mA for initial gas mixtures of: (a) pure CO_2 and (b) 50%CO_2-50%N_2.

remarkable (from peak values in T_3 around 1050 K for pure CO_2 to 1550 K in the CO_2-N_2 mixture, or from 1380 K to 2200 K in the case of T_{CO}). This measurement cannot be extrapolated to a pure CO_2-CO case, due to the different energy transfer probabilities and the different gas mixture due to the higher dissociation fraction, or the low fractions of O_2 and O atoms, for instance. However, it gives a qualitative example of the effect of resonant or quasi-resonant V-V' transitions (between CO_2 and N_2, and between CO and N_2). The vibrational kinetics in CO_2-N_2 mixture are out of the the scope of this thesis, more details are given in *Terraz et al.* [2019]; *Grofulović et al.* [2019] and in the PhD thesis of Loann Terraz.

O_2 is not expected to have a very relevant impact in the vibrational kinetics of CO_2 for the low levels in the conditions under study *Zasavitskii et al.* [1990]. There is no resonant energy exchange for the low vibrational levels and the rate coefficients for the relaxation of vibrational excited CO_2 by collisions with O_2 are rather low *Lopez-Puertas et al.* [2001]. For higher vibrational levels of O_2, where energy resonance conditions are much more easily met, there are indeed resonant transitions, for instance $O_2(X^3\Sigma_g^-, \nu = 18 \rightarrow 16)$ is nearly resonant with $CO_2(000 \rightarrow 001)$ and for the symmetric mode $O_2(X^3\Sigma_g^-, \nu = 10) + CO_2(000) \rightarrow O_2(X^3\Sigma_g^-, \nu = 9) + CO_2(100)$ *Mack et al.* [1996]. However, the high vibrational states of O_2 are very effectively quenched by O atoms *Esposito et al.* [2008], and the density of these levels in our discharge is expected to be very low. V-V' transfer from $CO_2(\nu_3 = 1)$ to lower levels of $CO_2(\nu_{1,2})$ is only slightly more efficient in collisions with O_2 than with CO or N_2, which are similar *Blauer and Nickerson* [1973].

Finally, another feature in figure 4.13 is that the de-excitation rate of T_3 to T_{rot} in the after glow shows a different variation with current for 1 and 2 Torr, when compared to that at 4, 5 Torr. A "twisting" point appears in between 2-3 Torr. The conversion factor α increases with current, but it does it only slightly more at higher pressures at the working flow (7.4 sccm), therefore it does not seem to be cause of this behaviour. The decay rates at low pressure are probably more affected by de-excitation in the walls, but there is another parameter that increases more with current at pressures around 1-2 Torr than at 4-5 Torr: the oxygen atom fraction in the total gas mixture (see section 3.5). O atoms are known to affect and interact with vibrationally excited CO_2 *Buchwald and Wolga* [1975]; *Lopez-Puertas et al.* [2001]; *Fridman* [2008]; *Kozák and Bogaerts* [2014a]. The impact of the oxygen atoms in the vibrational kinetics of CO and CO_2 is studied in chapter 5, where the wall de-excitation is also discussed.

4.6 Comparison with a kinetic model

The experimental time-resolved evolution of the population densities along a plasma pulse was used to validate a 0D kinetic model solving the time evolution of the electron kinetics and vibrational kinetics of CO_2 in the active discharge and in the after-glow, developed in IST-Lisbon by the group led by V. Guerra. More information about the model can be found in *Silva et al.* [2018]; *Grofulović et al.* [2018] and in the PhD thesis of Marija Grofulović. Here, we only present the comparison between the output from the model and the experimental data, previously discussed, and summarize the main outcome of this comparison. The kinetic model has been recently extended to study CO_2-N_2 glow discharges and compared with similar measurements as those presented in this chapter but in CO_2-N_2 mixtures (*e.g.* figure 4.14) *Terraz et al.* [2019].

The state-to-state model calculates the population density in a certain CO_2 vibrational level

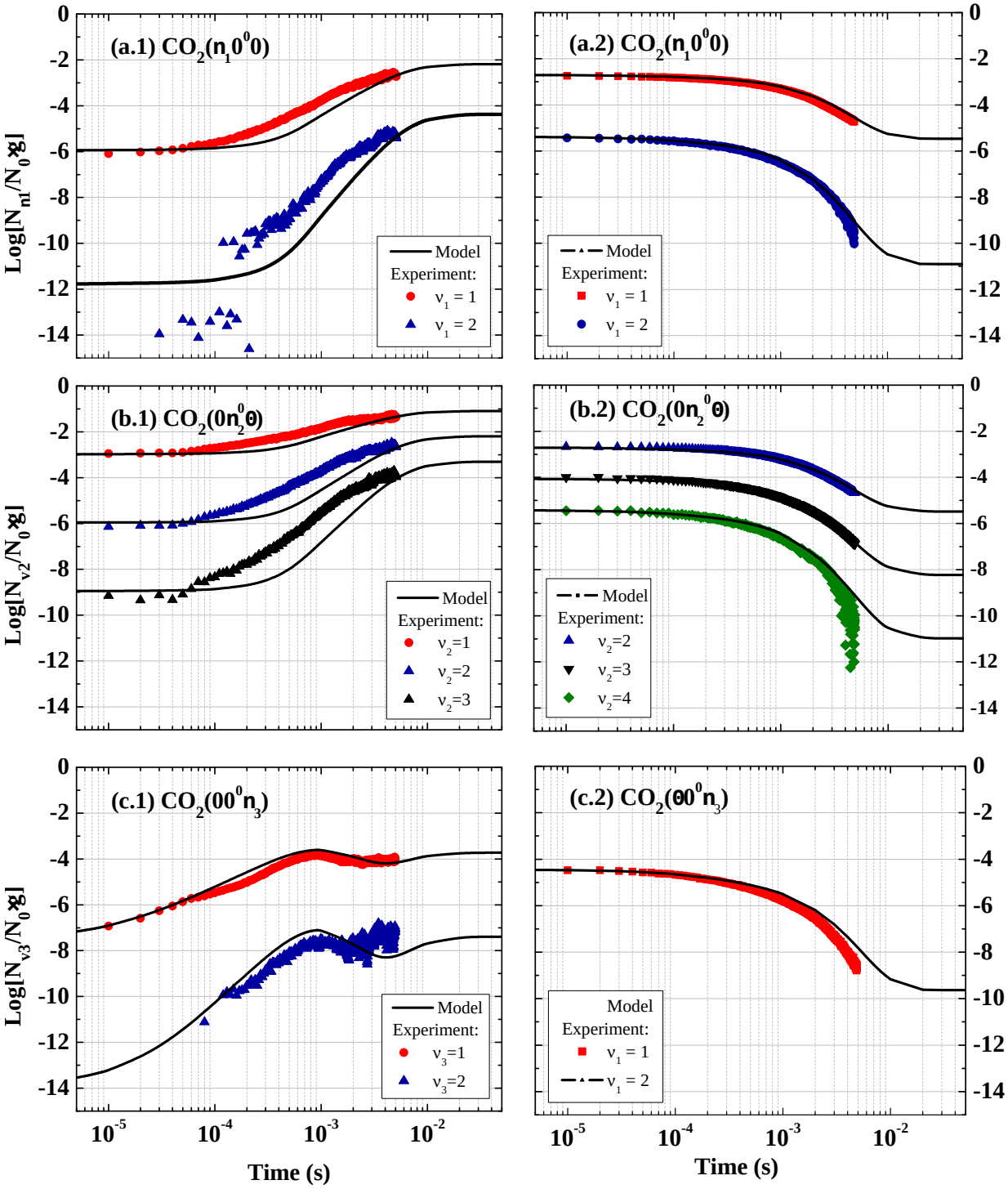

Figure 4.15: Normalized densities calculated from the model for the CO_2 vibrational levels associated with the asymmetric mode (top panel), symmetric mode (middle panel) and bending mode (bottom panel) in the active discharge (left), extracted from *Grofulović et al.* [2018] and in the post-discharge (right), extracted from *Silva et al.* [2018], compared with the "single pulse" experimental data (5 Torr, 50 mA, 5-150 ms On-Off).

from a system of time-dependent rate balance equations. It accounts for the vibrational kinetics of the lower levels of ground-state $CO_2(X\ ^1\Sigma^+)$ in each vibrational mode, corresponding to quantum numbers up to ν_1^{max}=2 and ν_2^{max}=ν_3^{max}=5 and of the lower mixed levels (∼70 individual vibrational

levels). The experimental data for the "single pulse" measurement is used for the comparison, since the density of dissociation products, CO, O, O_2, etc., is negligible and does not affect the CO_2 vibrational kinetics. The relevant rate coefficients were validated in two sequential steps:

1. **Validation of V-V' and V-T rate coefficients**: In the first place, the simulation of the time relaxation of vibrationally excited CO_2 molecules during the afterglow (no e-V) of a pulsed glow discharge was used to validate the rate coefficients of vibration–translation (V–T) and vibration–vibration (V–V') energy exchanges among low vibrational levels *Silva et al.* [2018]. The rate constants for the low-lying levels were obtained from the survey of Blauer and Nickerson *Blauer and Nickerson* [1973], while for the higher levels and missing transitions, scaling laws based on the Schwartz–Slawsky–Herzfeld (SSH) *Schwartz et al.* [1952] and Sharma–Brau (SB) *Sharma and Brau* [1969] theories were used.

2. **Validation of e-V rate coefficients**: In a second step, the model is extended to the active discharge with the inclusion of electron impact processes of vibrational excitation and de-excitation (e-V) and ionization *Grofulović et al.* [2018]. The objective was to validate the electron impact cross sections and rate coefficients for the individual e-V processes and get an insight into the input of vibrational energy in the plasma by electron impact. The cross sections for individual processes were calculated from the deconvolution of available cross sections *Grofulović et al.* [2016], or through approximations such as Fridman's approximation *Fridman* [2008] or shifting the threshold for step-wise excitations.

The comparison between the single pulse experimental data, fitted with the OoE Free script, and the output of the model is shown in figure 4.15. The model reproduces very well the relaxation of of the vibrational excitation in the post discharge in the case of the single pulse measurements, whilst the repetitive pulse (not shown in the figure, see *Silva et al.* [2018]), especially at lower pressures slightly underestimates the relaxation time, pointing out again towards the role of the dissociation products not only in the enhancement of excitation during the discharge but also in the relaxation processes after the plasma pulse.

In the active discharge *Grofulović et al.* [2018], the calculations are able to reproduce remarkably well the evolution of population of the two first levels of ν_3, including the maximum at around 0.7-0.9 ms after the beginning of the pulse. When the discharge is initiated, levels ν_3=1 and 2 are mainly populated by electron impact from the ground-state. When the population of the second asymmetric level becomes large enough, V–V reactions within the asymmetric mode depopulating ν_3=2 and populating ν_3=1, become the dominant creation mechanism of ν_3=1. Subsequently, the gas temperature starts to increase and V–T processes starts to play an important role, explaining the decrease in the population for plasma ON times around 0.7-1 ms. The population densities of ν_3 calculated with the model are slightly over-estimated, while for ν_1 and ν_2 are lower than the experiment, suggesting a little underestimation of the V-V' transfer rates from ν_3 to $\nu_{1,2}$. The model results reveal a higher population for excited ν_3 level at lower gas temperatures, confirming the close relation between ν_3 and T_{rot} observed in the experiments. Calculations made at constant gas temperature do not show the peak in the population of ν_3, suggesting that this effect is caused by the modification of the V–V' and V–T rate coefficients with the gas temperature.

4.7 Summary and conclusions

In this chapter we have studied the vibrational kinetics of CO_2 plasmas ignited in a DC glow discharge in continuous and pulsed regimes. The non-equilibrium character of low temperature CO_2 plasmas was demonstrated. The temperature of the asymmetric stretch mode, T_3, is significantly higher than the rotational temperature, in equilibrium with the gas temperature in our discharge conditions. The temperature of the bending and symmetric vibrational modes, $T_{1,2}$ is strongly thermalized. In continuous plasma we have seen that the vibrational excitation of CO_2 and CO decreases when the pressure is increased and only for low pressures a positive effect of the current is observed. However, time-resolved experiments in pulsed plasma revealed that T_3 and T_{CO} show a faster excitation/slower de-excitation compared to $T_{1,2}$ and T_{rot} with a maximum at 0.7 ms after the beginning of the plasma pulse. Additionally, it was shown that it is possible to have peaks of non-equilibrium, [T_3-T_{rot}], above 500 K dependent on current, even for the highest pressures studied, when the gas temperature is still low. Two parameters were found to have a strong influence in the vibrational kinetics of CO_2 and CO:

- **Gas temperature**. The initiation of plasma pulses is similar for all pressures, current or pulse configurations, suggesting similar e-V excitation processes in all cases. However, a list of phenomena points to a significant impact of the gas temperature: (1) The maximum of [T_3-T_{rot}] and the steady-state value at the end of the pulse decrease with pressure; (2) when T_{gas} at the end of the pulse is higher the de-excitation of T_3 to T_{rot} in the post-discharge is faster; (3) starting the pulse at higher temperatures lead to lower excitation peaks; (4) the maximum in [T_3-T_{rot}] is not caused by the excitation mechanisms, but it is as consequence of the increase of T_{rot}. The gas temperature appears to be the key parameter controlling the vibrational de-excitation in CO_2 plasmas through its influence in the V-V' and V-T relaxation processes.

- **Dissociation products**. In order to study the influence of the dissociation products, a single pulse measurement, where the density of dissociation products is negligible, is compared to a repetitive pulse measurement where the accumulation of dissociation products lead to non-negligible densities of CO, O atoms and O_2 and other minor species. Both show similar development of temperatures over time. The maximum of [T_3-T_{rot}] increases with current but for similar current, the gas mixture containing a significant amount of dissociation products reaches higher excitation peaks. CO, whose concentration also increases with current, is the most probable responsible of this effect due to the near-resonant V-V' transfer between CO(ν) and CO_2(ν_3). On the other hand, the de-excitation after the pulse is faster in the repetitive pulse. The dissociation products are therefore significantly affecting the vibrational kinetics of CO_2 and are involved both in excitation and de-excitation mechanisms.

The results presented in this chapter suggest that keeping the gas temperature low could be beneficial in order to take advantage of the non-equilibrium of CO_2(ν_3) in the first milliseconds of the discharge when the gas temperature is still relatively low. The contribution of the vibrational excitation to the dissociation in our discharge conditions is still unclear at this point and will be studied in more detail in chapters 6 and 7. The dissociation products are believed to have a significant impact on the vibrational kinetics of CO_2, and the role and energy exchanges with CO

should be addressed in a future work. The effect of oxygen atoms will studied in the following chapter (5).

Chapter 5

Effect of the oxygen atoms on the CO_2 vibrational kinetics

Contents

5.1 Introduction . . . 120

5.2 Experimental details . . . 120

5.2.1 Discharge reactor and diagnostics . . . 120

5.2.2 Surface configurations . . . 121

5.3 O atom density, gas temperature, electric field and dissociation fraction 122

5.3.1 Gas temperature . . . 122

5.3.2 Electric field and dissociation fraction . . . 123

5.3.3 O atom densities . . . 124

5.4 Effect of the oxygen atoms in the vibrational temperatures of CO_2 and CO . . . 126

5.4.1 Temperature of the bending and symmetric vibrational modes, $T_{1,2}$ . . . 126

5.4.2 Temperatures of the asymmetric stretch mode of CO_2, T_3, and of CO, T_{CO} 127

5.4.3 Correlation with the O atom densities . . . 130

5.5 Discussion . . . 132

5.5.1 Quenching of the vibrations of CO_2 by O atoms . . . 132

5.5.2 Quenching of the CO_2 vibrations of at the walls . . . 136

5.5.3 Dissociation fraction . . . 139

5.6 Time resolved evolution of the vibrational temperatures along a plasma pulse . . . 139

5.6.1 Effect on the vibrational temperatures . . . 140

5.6.2 Dissociation fraction along a plasma pulse . . . 144

5.7 Summary and conclusions . . . 147

5.1 Introduction

After the dissociation of CO_2 the main products are CO and O atoms, which partially recombine into O_2. Other species, including neutrals in ground state (C, O_3), or in excited states ($CO(a^3\Pi_r)$, $O_2(a^1\Delta_g)$, $O_2(b^1\Delta_g^+)$, $O(^1D)$, etc.) and ions, are also present in the discharge, but their densities are expected to be lower. All these species can have an impact on the vibrational kinetics of CO_2. Already in the previous chapter we observed differences in the time evolution of the vibrational temperatures between a repetitively pulsed CO_2 discharge, where the amount of dissociation products accumulated is significant, and a "single pulse" CO_2 discharge, which can be considered as a pure CO_2 discharge. Having discussed briefly the effect of CO, the objective of this chapter is to study the effect of the oxygen atoms in the vibrational kinetics of CO_2. As outlined in section 1.4, oxygen atoms are claimed to enhance the CO_2 dissociation through the reaction $CO_2^* + O \rightarrow CO + O_2$ *Fridman* [2008]; *Kozák and Bogaerts* [2014a]. On the other hand, they can quench the vibrational excitation of CO_2 *Buchwald and Wolga* [1975]; *Spiridonov et al.* [1994]; *Lopez-Puertas et al.* [2001].

In order to investigate the effect of oxygen atoms on the CO_2 vibrational kinetics, we could study CO_2-O_2 mixtures. However, in this case the dissociation fraction also changes, *i.e.* the density of CO, in addition to other relevant parameters such as the electric field or the gas temperature (more details about CO_2-O_2 mixtures will be given in chapter 8). Ideally, the vibrational kinetics of CO_2 and CO should be compared in the same conditions with and without oxygen atoms in the gas mixture, *i.e.* we must "remove" the oxygen atoms without changing significantly any other relevant plasma parameter. In chapter 3, it was shown that the recombination of O atoms into O_2 in our experimental conditions was dominated by surface processes. We take advantage of this fact and, in order to reduce the density of O atoms in the gas mixture, we enhance the O atom recombination by increasing the effective surface area in contact with the plasma. To avoid any extra catalytic effect we change minimally the chemical nature of the surface by using a layer of micro-structured silica (SiO_2) fibers, similar to the Pyrex reactor. The use of a large effective surface can also affect directly the vibrational kinetics for example by increasing the de-excitation of vibrationally excited molecules in the walls. This possibility is discussed along this chapter.

Most of the analysis will be based on continuous plasma because the effect of removing the oxygen atoms is expected to be higher. In continuous plasma in our discharge conditions, the fraction of free O atoms over the total gas density reaches values above 10% (see section 3.5). Atomic oxygen is therefore a relevant compound in the gas mixture. In pulsed plasma the O atom fraction is lower ∼1-2% (see section 3.7.2). Nevertheless, at the end of the chapter time-resolved pulse plasma data are also included to show that even such a low amount of oxygen atoms has a significant effect on the time evolution of the vibrational kinetics of CO_2.

5.2 Experimental details

5.2.1 Discharge reactor and diagnostics

The CO_2 glow discharge was ignited in a short Pyrex reactor (23 cm length) in continuous, modulated or pulsed regimes for currents between 10 and 50 mA and pressures between 0.4 and 5 Torr. Continuous and modulated plasma measurements were performed with a double-walled reactor to control the wall temperature by distilled water + ethanol circulation. This wall temperature was

kept at 50^{o}C for all the experiments. Pulsed plasma experiments were done without controlling the wall temperature for consistency with the previous data (see chapter 4). The experimental details are summarized in the experimental box 5.1.

Two diagnostics will be used along this chapter: *in situ* FTIR measurements were done with the plasma reactor positioned in the sample compartment of the FTIR spectrometer. In continuous plasma, the spectra was obtained operating the FTIR in normal mode, averaging 20 scans; for pulsed plasma measurements, the plasma in pulsed in a 5-10 ms On-Off cycle and the FTIR is operated in step scan-mode with a temporal resolution of 10 μs and recording 1100 time slices, similarly to the previous chapter. Oxygen atom densities were measured by actinometry in continuous and partial modulation regimes, similarly to the measurements presented in section 3.5.

Diagnostics: FTIR (TOoE, OoE Free), Actinometry **Discharge**: Glow Continuous, modulated & pulsed (5-10ms On-Off) (+ single pulse 4.2)	**Reactor**: DW Short (cont.) SW short (pulsed) $\boldsymbol{T_{wall}}$=50^{o}C in cont. & mod., not controlled for pulsed **Flow**: 7.4 sccm ($\boldsymbol{\tau_{res}}$ ≈0.23-2.5s) (+ single pulse 4.2)	**Pressure**: - **0.4-5** Torr Continuous - **1-5** Torr Mod. & pulsed **Current**: - **10-50** mA Cont. & mod. - 50 mA Pulsed

Experimental box 5.1: General experimental conditions.

5.2.2 Surface configurations

We have played with the surface structure to change the density of O atoms in gas phase. In this chapter we will compare two surface configurations: The "**bare tube**", which refers to the usual Pyrex reactor and which has a surface area in contact with the plasma around 0.0110 m^2 (assuming a perfectly polished surface); and the "**fibers**", which refers to a layer of silica fibers (SiO_2) similar to a textile (see figure 5.1) that is rolled around the inner wall of the plasma reactor. The thickness of the layer is less than 200 micron, changing minimally the diameter of the tube, but increasing significantly the effective surface in contact with the plasma, up to around 10 m^2 (estimated from specific surface data provided by the manufacturer). This increase is due to the microscopic structure of the fibers (a SEM microscope image is shown in figure 5.2). Before any experiment, and for both surface configurations, the surface is exposed to pure O_2 plasma at 1 Torr, 40 mA in continuous discharge, during at least 30 minutes to remove any pollutant adsorbed in the surface, especially water, which can strongly influence the CO_2 plasma dynamics. The evolution of the absorption lines corresponding to water are checked with the FTIR during this time verifying that they decrease down to the usual background level.

All along this chapter we will use the same notation to identify the two surface conditions: **bare tube** and (silica) **fibers** summarized in the experimental box 5.2. In order to make easier for the reader to perceive the differences or similarities between both configurations a simplified colour code was adopted: dark blue lines + triangles for the bare tube and red lines + squares for the fibers. We have previously seen that generally most of the parameters studied, such as the dissociation fraction α, T_{rot}, $T_{1,2}$, T_3 or T_{CO}, show an increasing trend with current. Therefore, no distinction in terms of colour or line/symbols style is done for different plasma currents, except for the highest

Figure 5.1: Photo of the silica fibers layer rolled around the inner wall of the reactor.

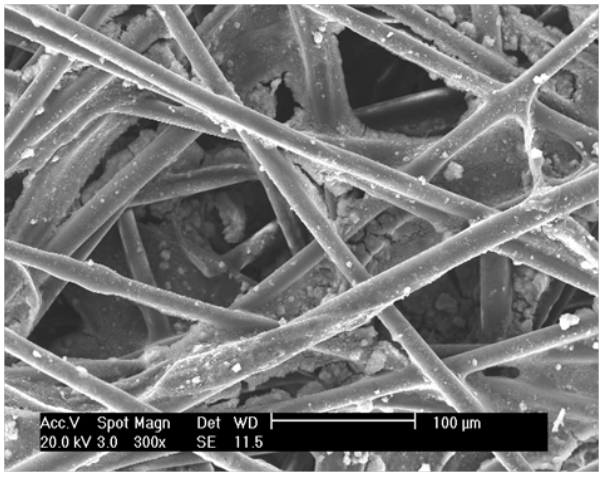

Figure 5.2: Microscopic structure of the silica fibers measured with a SEM microscope.

current (50 mA) presented with solid lines, whereas currents from 10 to 40 mA are presented with dotted lines.

Bare tube:	**Fibers**:
- **Material**: Pyrex	- **Material**: SiO_2
- **Surface area**: 0.0110 m^2	- **Surface area**: ~10 m^2
▲ **Bare tube**	■ **Fibers**

Experimental box 5.2: Summary of the surface configurations.

5.3 O atom density, gas temperature, electric field and dissociation fraction

In order to study the impact of the oxygen atoms on the vibrational kinetics of CO_2 we must verify on the one hand that we manage to change significantly the density of oxygen atoms and, on the other hand, that we do not change significantly any other plasma parameter that can disturb the analysis of the results. Thus, this section provides information about atomic oxygen density and about three key parameters in the description of a DC CO_2 plasma: gas temperature, electric field and dissociation fraction.

5.3.1 Gas temperature

We concluded in chapter 3, section 3.2.2, that the rotational temperatures of CO_2 and CO, measured from FTIR spectra are in equilibrium with the translational temperature, based on the consistency between FTIR, rotational Raman scattering and HR-TALIF temperature measurements in continuous plasma. Hence, we can analyse the effect of the SiO_2 fibers on the gas temperature by checking the values of T_{rot} deduced from the FTIR spectra. Note that a large change in the gas temperature would have a direct impact in the gas density and therefore in the reduced electric

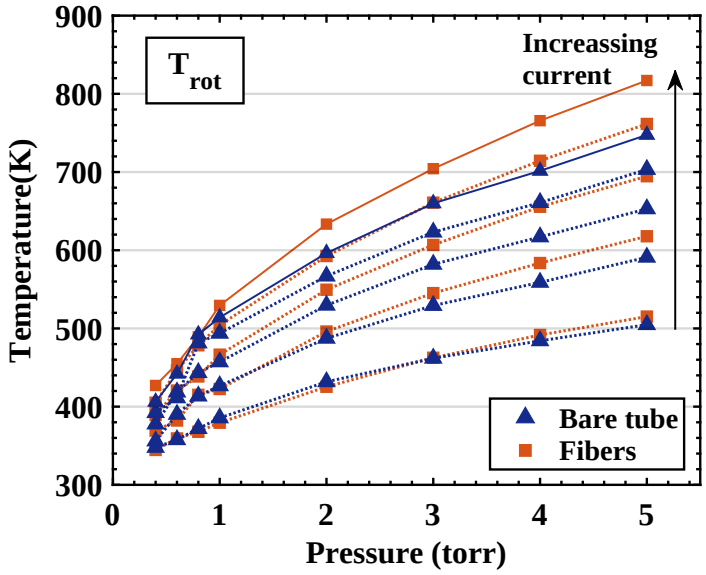

Figure 5.3: Variation of the rotational temperature, T_{rot} obtained with the bare tube and with fibers as a function of pressure for currents between 10 and 50 mA.

field. It would also affect many chemical processes, both in gas phase and in the surface, in addition to the vibrational-vibrational-translational (VV'-VT) relaxation processes through its influence on the rate coefficients (see chapter 4).

Figure 5.3 shows the evolution of T_{rot} as a function of pressure for currents between 10 and 50 mA, with the bare tube and with the silica fibers. We see very little difference (maximum ~70 K), although the temperatures obtained with the fibers tend to be slightly higher than with the bare tube for the highest pressures and currents. The most probable reason is that the fibers act somewhat as an insulation layer for the heat flux towards the reactor wall. The wall temperature in these measurements was controlled, but the SiO_2 layer would reduce the efficiency of the heat exchange between the plasma and the mixture of water and ethanol circulating at 50^{o}C (323 K). This hypothesis is supported for instance by the fact that the temperatures obtained with the fibers are closer to the temperatures obtained at the end of the pulse in pulsed plasma measurements (see figure 4.9 as example), taken without cooling the reactor walls. The small difference in the gas temperature is not expected to have a significant impact in the plasma dynamics.

5.3.2 Electric field and dissociation fraction

Figure 5.4 presents the electric field, measured between 1 and 5 Torr and from 10 to 40 mA, and the corresponding reduced electric field with the bare tube and the fibers. Previous data (discussed in section 3.3) in a close range of pressures and currents is included for comparison. Figure 5.5 shows the dissociation fraction α measured *in situ* with the bare tube and with fibers. None of these two parameters show any significant difference between both surface configurations within the reproducibility error. Concerning the electric field, the average difference is around 3.4% and the maximum is approximately 9%, not following any specific trend with any plasma parameter, representing rather the error in the electric field determination than a systematic change in the electric field. The electric field values and the reduced electric fields are well aligned with previous

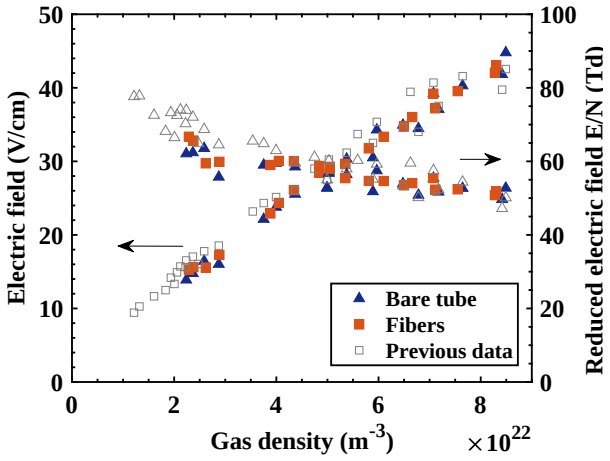

Figure 5.4: Variation of the electric field as a function of gas density measured for pressures between 1 and 5 Torr and for currents between 10 and 40 mA with the bare tube and with fibers.

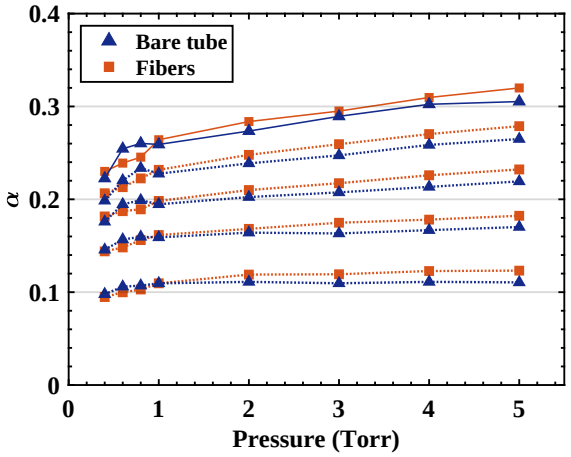

Figure 5.5: Variation of the conversion factor α measured *in situ* as a function of pressure for currents between 10 and 50 mA with the bare tube and with fibers. The data with the bare tube is the same shown in figure 3.14.

data as a function of the gas density. The slightly higher gas temperatures are compensated by a slightly different fitted pressure, giving very similar reduced electric fields. The similar electric field for both surface configurations is somehow surprising since one could expect an increase of the charge losses due to the larger surface area, and therefore an increase of the electric field to compensate these additional losses. The reason is probably that the sheath is relatively "thick" compared to the characteristic dimension of the fibers. The minimum Debye length, λ_D, in our discharge is ~100 μm. The "sheath width", estimated as $\sim 5\lambda_D$ *Chen and Chang* [2012], is then significantly higher than the width of the individual fibers that form the fibers tissue, which is around 20 μm, as can be seen in figure 5.2. Therefore the sheath does not follow the shape of the individual fibers and the "sheath surface area" that the charges and the charged species "see" is similar to the bare tube, *i.e.* the fibers do not change significantly the loss of charged species on the surface.

Concerning the CO_2 conversion, again no significant difference is observed. Therefore, any possible change in the vibrational excitation should not be associated with enhanced V-V' transfers between CO and ν_3 due to *quasi*-resonant transition, as previously discussed. The absence of effect on α suggests no "back reaction" neither in gas phase nor in the surface. Nevertheless it is possible that the characteristic time for surface reactions is longer than the residence time, τ_{res}, at the working gas flow (7.4 sccm). The possibility of back reaction in the surface is thoroughly explored in chapter 8, and the dissociation fraction with and without fibers is discussed more in detail in section 5.5.3.

5.3.3 O atom densities

It is essential to check if by using the SiO_2 fibers we have changed relevantly the density of oxygen atoms. In chapter 3 we have seen that the amount of O atom that remained free and did not recombine into O_2 or CO_2, for the long discharge tube, was between 10 and ~35%, depending on the discharge current and pressure. We also showed that the O atom densities measured by means

of actinometry were consistent with the results obtained with CRDS and HR-TALIF (with the cross section from *Drag* [2020]). Therefore actinometry is considered a valid diagnostic technique to measure absolute O atom densities in our experimental conditions, and also suitable to follow the time evolution of the O atom density under plasma exposure in modulated discharges. In this section, we used this diagnostic to quantify the effect of the fibers in the O atom densities and their life-time.

Figure 5.6 shows, for one plasma condition, 1 torr 40 mA, as illustrative example, the effect of the fibers in the O atom density in a modulated discharge of 146 ms-146 ms Up-Down. The O atom density is normalized to the maximum in the bare tube. It is clear that when we introduce the fibers, the absolute density decreases drastically, down to ∼5% of the O atom density with the bare tube. Similar measurements were taken for pressures between 1 and 5 Torr and currents between 10 and 40 mA. For all the conditions, the ratio $O_{fibers}/O_{bare\ tube}$ varies between 5 and 8%. Only for 5 Torr the values are slightly higher, between 10 and 12%, confirming that the O atom density with fibers is controlled by the diffusion time towards the wall, which is maximum at 5 Torr, 20 mA. In the inner figure, where both signals are normalized, we can appreciate better the differences in the O atoms life-time both with the bare tube and with fibers. With the bare tube the calculated lifetime is, on average, around 60 ms and varies between ∼30 ms for the lowest pressures (0.3 Torr) and ∼130 ms (at 2 Torr, 10 mA), whereas with the fibers it is significantly lower. The fitted τ_{loss} values for all the conditions studied is below 7 ms, close to the diffusion time towards the reactor walls. We can conclude therefore that the O atoms are effectively recombined as soon as they reach the reactor walls covered by the silica fibers.

In summary, adding the SiO_2 fibers keeps the reduced electric field, dissociation fraction (α) and gas temperature unchanged but reduces significantly the atomic oxygen density. The fibers are therefore a good tool to investigate the effect of ground state oxygen atoms in the vibrational kinetics of CO_2 and CO. It is worth mentioning that the density of electronically excited states

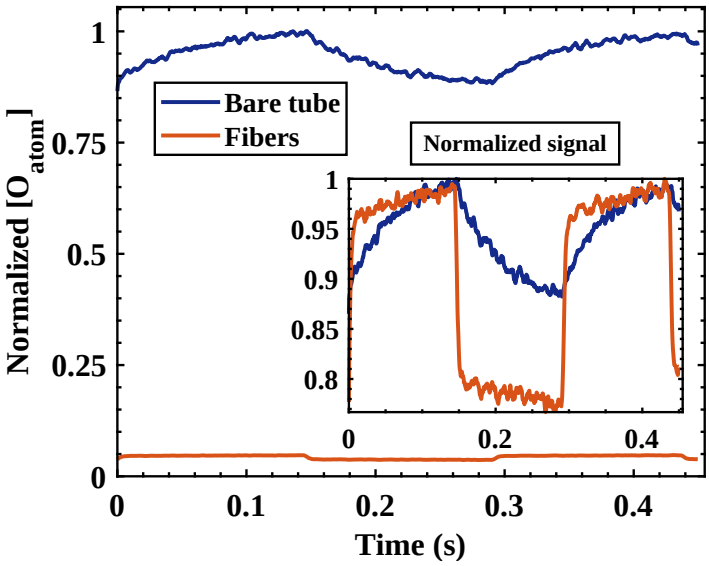

Figure 5.6: Temporal variation of the relative O atom density of 1 torr 40 mA with the bare tube and with fibers, normalized to the maximum in the bare tube. The inner figure shows both traces normalized to their respective maximum values.

with long life-time, such as $O_2(a^1\Delta_g)$, can be affected by the fibers, since they can be de-excited in the surface. For excited species which react fast, such as $O(^1D)$ reacting almost at gas kinetic rate *Perri et al.* [2004], their densities and effect on vibrational kinetics are not expected to be affected by the presence of fibers.

✓ The fibers keep E/N, α and T_{rot} unchanged.
✓ $[O]$ is drastically reduced by the fibers to 10% of $[O]_{bare\ tube}$, limited only by τ_{diff}.

5.4 Effect of the oxygen atoms in the vibrational temperatures of CO_2 and CO

5.4.1 Temperature of the bending and symmetric vibrational modes, $T_{1,2}$

The vibrational temperature corresponding to the bending and symmetric vibrational modes of CO_2, $T_{1,2}$ obtained from the fitting of the FTIR spectra with the bare tube and with fibers is presented in figure 5.7. The difference between the values obtained with both surface configurations is evident and highly remarkable. With the fibers, the obtained vibrational temperatures are in all cases noticeably higher than with the bare tube. The difference between bare tube and fibers tends to increase with pressure up to 1 Torr and then slightly decrease towards higher pressures.

In chapter 4 we saw that $T_{1,2}$ tends to be thermalized with T_{rot} in the bare tube. This is clear when plotting directly $T_{1,2}$ *versus* T_{rot}, shown in figure 5.8 (a). The values obtained with the bare tube follow a linear dependence with the gas temperature and the slope is very close to a complete thermalization (represented by a dotted black line). Higher pressures give closer values to the thermal line. However, with the fibers, $T_{1,2}$ is not thermalized with T_{rot}. For pressures between 0.4 and 1 Torr all the data points follow a single linear evolution as a function of the gas temperature

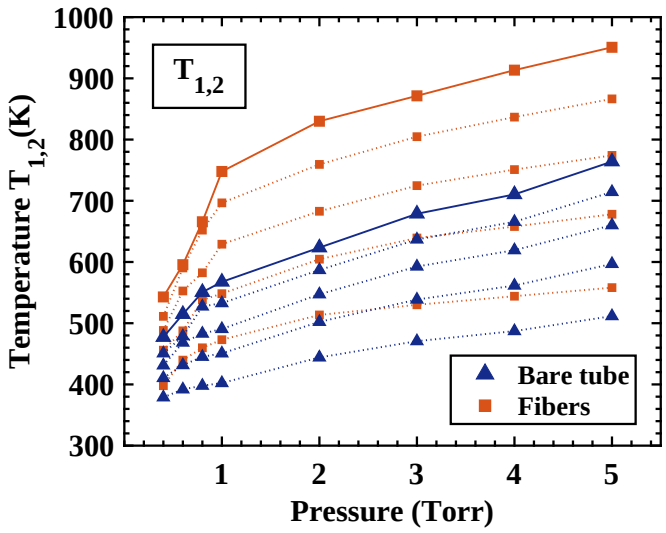

Figure 5.7: Variation of the vibrational temperature corresponding to the bending and symmetric vibrational modes of CO_2, $T_{1,2}$, as a function of pressure for currents between 10 and 50 mA obtained with the bare tube and with fibers.

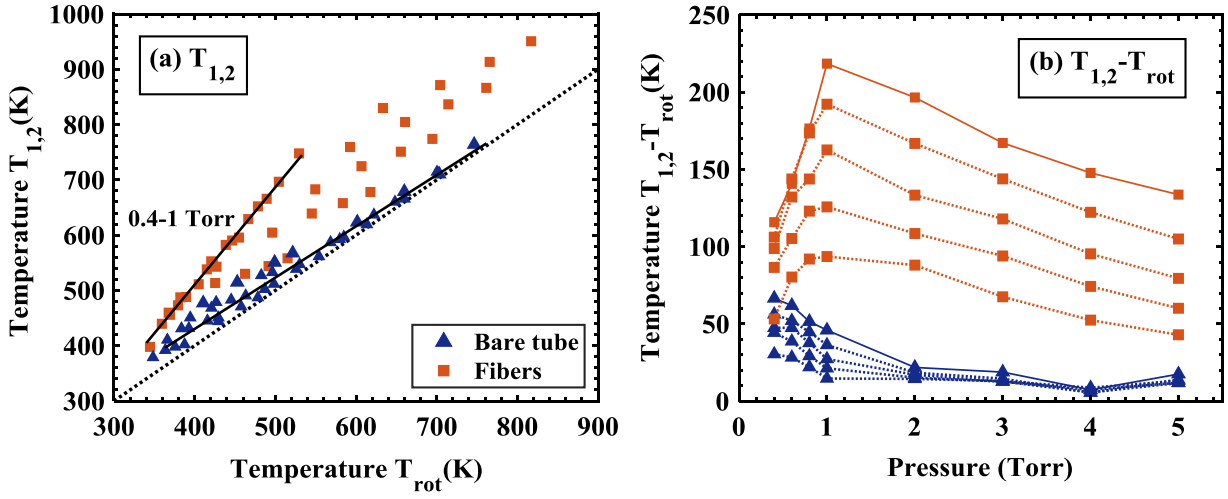

Figure 5.8: Comparison between $T_{1,2}$ and T_{rot} for the bare tube and with fibers: (a) Variation of $T_{1,2}$ as a function of T_{rot}. A linear fit for all the data points in the bare tube is included as well as a linear fit for the data points corresponding to pressures between 0.4 and 1 torr. The dotted line represents T_{rot} *versus* T_{rot} *i.e.* thermal equilibrium. (b) Difference between $T_{1,2}$ and T_{rot} plotted as a function of pressure.

with a slope that diverges from the thermal one. The data between 2 and 5 Torr fall in the middle of both lines representing a tendency towards thermalization. These two different trends below and above 1 Torr are well visible in figure 5.8 (b), where the difference between $T_{1,2}$ and T_{rot} is plotted as a function of pressure. [$T_{1,2}$-T_{rot}] increases with current and pressure up to a maximum at 1 Torr, 50 mA, where the thermal non-equilibrium reaches values above 220 K, decreasing when the pressure is further increased. With the bare tube [$T_{1,2}$-T_{rot}] is negligible, except for the lowest pressures, which show an opposite variation as a function of pressure compared to the fibers.

5.4.2 Temperatures of the asymmetric stretch mode of CO_2, T_3, and of CO, T_{CO}

The temperatures corresponding to the asymmetric stretch vibrational mode of CO_2, T_3, and the vibrational temperature of CO, T_{CO}, were shown to follow a similar variation as a function of pressure in chapter 4. The effect of using the fibers on both temperatures is shown in figure 5.9: panel (a) shows the variation of T_3 as a function of pressure and panel (b) the variation of T_{CO}. For the very low pressures (0.4-0.6 Torr) T_3 is similar with the bare tube and with the fibers. When the pressure is increased, with the bare tube it passes through a maximum around to 0.8 torr and starts decreasing significantly. With the fibers, however, it keeps increasing up to 1 Torr, when it starts decreasing slowly, at a lower pace than without the fibers. T_{CO} follows qualitatively a very similar variation as a function of pressure. It shows a few values at the lowest pressures which seem to be higher with the bare tube than with the fibers. A possible reason could be an efficient de-excitation of vibrationally excited CO on the surface (γ_ν^{CO}) in this pressure range, leading to lower T_{CO} with the fibers. CO is believed to de-excite more efficiently in Pyrex surfaces than CO_2 *Black et al.* [1974] and could explain why we do not see a similar effect in T_3 or $T_{1,2}$ (more details are given in section 5.5). Nevertheless, it is worth reminding that T_{CO} is by far the vibrational temperature determined with a bigger error from the fitting of the FTIR spectra in any condition. Moreover, the intensity of the FTIR signal at very low pressures is quite low and, consequently, the signal-to-noise ratio is

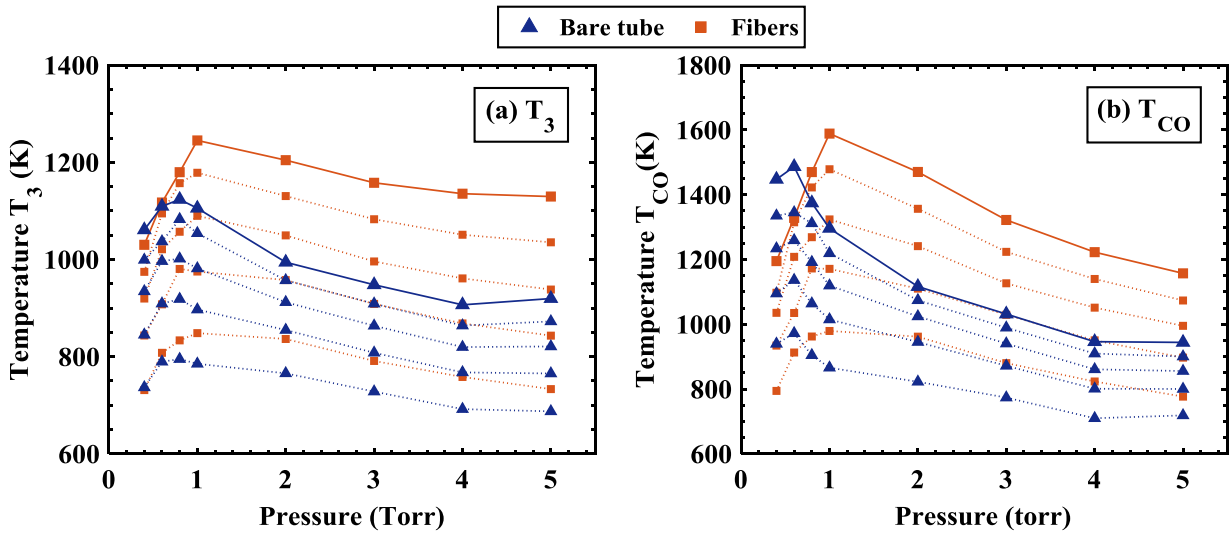

Figure 5.9: Variation of the vibrational temperatures corresponding to: (a) asymmetric stretch mode of CO_2, T_3, and (b) CO, T_{CO}, as a function of pressure measured with the bare tube and with fibers.

high. It is important to underline that it is *a priori* surprising to observe, in almost all conditions, an increase of the vibrational temperatures ($T_{1,2}$, T_3 and T_{CO}) in the presence of fibres because we could expect an increase of the vibrational de-excitation at the walls (γ_v) as a consequence of the increase of surface area in contact with the plasma.

Let us analyse now the relation between T_3 and T_{rot}. It was shown in the previous chapter that the increase of T_{rot} affects negatively the values of T_3, decreasing the level of non-equilibrium, believed to be potentially beneficial for the CO_2 dissociation. The difference between T_3 and T_{rot} is plotted *versus* pressure in figure 5.10 (a), for both the bare tube and the fibers separately (panels (a.1) and (a.2) respectively) for readability of the graph. [T_3-T_{rot}] decreases with pressure with the bare tube and there is no effect of the current on the vibrational excitation of ν_3 except for the lowest pressures (from 0.4 to 1 Torr), already discussed in section 4.3 (see figure 4.3). It is also consistent with figure 4.11 (b), where towards the end of the pulse all the currents tend to give the same level of excitation of T_3 over T_{rot} (around 180 K). However, with the fibers (panel (a.2)) we do see an increase of the non-equilibrium when increasing the discharge current, for all the pressures studied. In this case, an increase of current leads to a higher excitation of T_3, and not only to an increase of T_{rot}, even at high pressure. It is also visible in figure 5.10 (a) that whereas in the bare tube the asymmetric non-equilibrium always decreases as a function of pressure, with the fibers there is a clear increasing trend up to 1 Torr, where higher values than in the bare tube (above 700 K) are reached. For pressures between 1 and 5 Torr, [T_3-T_{rot}] decreases with pressure, similarly to the variation of $T_{1,2}$ shown in figure 5.8 (b).

Figure 5.10 (b) plots the same data as a function of T_{rot}. It is therefore the same representation shown in figure 4.3, but adding the data obtained with fibers. Similarly to the bare tube, two distinct behaviours are observed at low (0.4-1 Torr) and high (2-5 Torr) pressures:

- Low pressure: In the bare tube clearly different slopes were observed for the different pressures. With the fibers all the data between 0.4 and 1 Torr falls on the same curve.

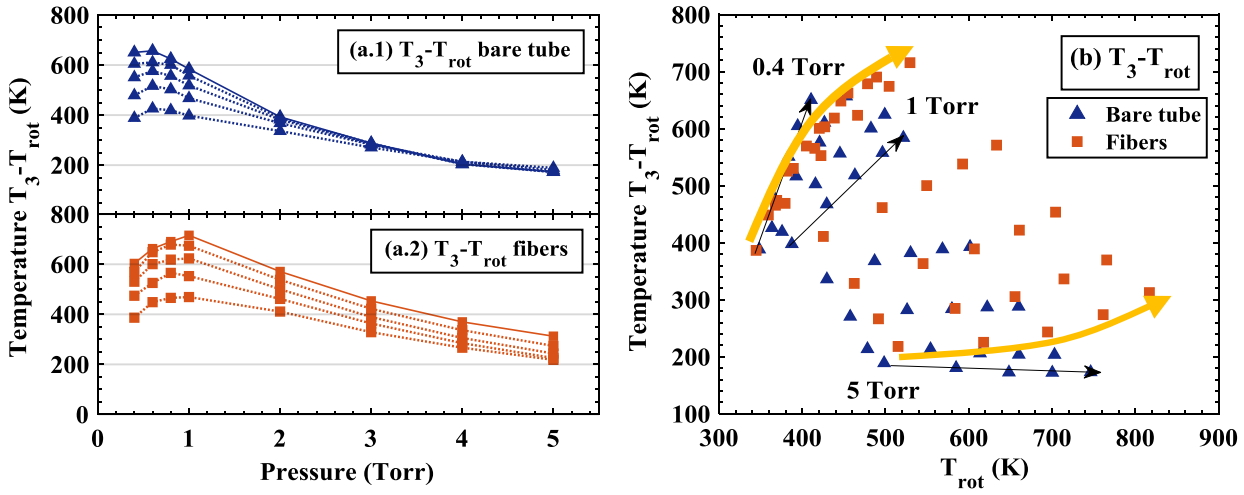

Figure 5.10: Difference between T_3 and T_{rot} plotted *versus* pressure (panel (a)) and *versus* T_{rot} (panel (b)). The top graph of panel (a), (a.1), shows the data for the bare tube and the bottom panel, (a.2), for the fibers. Different curves correspond to different currents between 10 and 50 mA. Data for 10-40 mA are plotted with dotted lines and for 50 mA with solid lines.

- High pressure: The data with the fibers show an increase of [T_3-T_{rot}] when increasing current, contrary to the bare tube.

In the previous chapter we concluded that the trend at high pressures was related to an efficient vibrational quenching (V-T and V-V' where V-V' designates inter-modes exchange or energy transfer towards other molecules than CO_2) due to the higher collision rate, and the increase in the efficiency of the de-excitation process with T_{rot}. The trend with fibers suggests that the V-T and V-V' processes are less efficient than with the bare tube. At low pressure, the observed variation is caused by a balance between the reduction of V-T and V-V' processes and the increase of surface de-excitation (γ_ν). τ_{diff} decreases with T_{rot}, which explains the tendency to level off when increasing current (indicated by the yellow arrow in figure 5.10 (b)).

The relation between T_{CO} and T_{rot}, shown in figure 5.11, is qualitatively similar to that of T_3

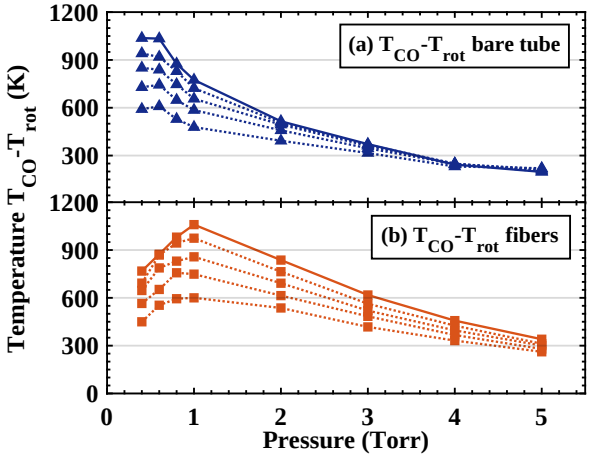

Figure 5.11: Variation of [T_{CO}-T_{rot}] as a function of pressure. The top graph (panel (a)) shows the data for the bare tube and the bottom panel (b) for the fibers.

and T_{rot}, but reaching higher values of [T_{CO}-T_{rot}], up to 1000 K. We do not observe any influence of the current in the vibrational excitation of CO for the bare tube, but there is an increasing degree of vibrational excitation with current in the presence of the fibers.

✓ $T_{1,2}$, T_3 and T_{CO} increase significantly with fibers compared to the bare tube.
✓ [T_{vib}-T_{rot}] increases with current for pressures between 2 and 5 Torr with the fibers, contrary to the bare tube.
✓ [T_{vib}-T_{rot}] increases with pressure up to 1 Torr but decreases when the pressure is further increased.

In summary, we have increased the effective surface area in contact with the plasma and, in principle, we could have expected an enhanced quenching of the vibrations in surface ($\uparrow \gamma_\nu$). However, the vibrational excitation increases in all the pressure range studied, suggesting a more dominant effect of the decrease of V-T and V-V' de-excitation processes. Considering the conclusions from section 5.3.3, the increase in T_{vib} is likely to be related with the removal of O atoms. This possibility will be checked by comparing the change in vibrational excitation with the variation of the O atom density in the next section.

5.4.3 Correlation with the O atom densities

In order to confirm that the effect induced by the fibers in the vibrational kinetics is due to the removal of the oxygen atoms, we compare in this section the difference in the vibrational temperature with and without fibers with the oxygen atom data. $[T_{vib}(fibers) - T_{vib}(bare\ tube)]$ is plotted as a function of pressure in figure 5.12. Panel (a) plots the difference being T_{vib}=$T_{1,2}$ and panel (b) for T_{vib}=T_3. We measured O atom densities in continuous CO_2 plasma, with actinometry, TALIF and CRDS (see section 3.5) in the bare (long) tube finding consistent trends as a function of current and pressure. In figure 5.13 we show similar data measured with actinometry but for the short discharge bare tube. An average of the absolute densities and O atom fractions measured with both emission lines is plotted. The trend is similar to that of the long tube (see figure 3.24). The absolute and relative atomic oxygen densities are slightly lower than in the long tube, as expected, similarly to the case of CO (see section 3.4). The maximum of absolute O atom density appears at 2 Torr, whereas for the relative oxygen density it is at 1 Torr. For lower pressures both [O] and $^{O}/_{N}$ show an increasing trend with pressure, which is related to higher CO_2 dissociation. Above 2 Torr, the absolute density slightly decreases, while the relative O atom density starts decreasing significantly from 1 Torr towards increasing pressure. Comparing the O atom absolute density graph with the variation of $[T_{vib}(fibers) - T_{vib}(bare\ tube)]$ for both T_3 and $T_{1,2}$, the similarities are evident.

Figure 5.14 plots directly $[T_{vib}(fibers) - T_{vib}(bare\ tube)]$ as a function of the O atom density measured in the bare tube (same data as in figure 5.13) for both T_{vib}=$T_{1,2}$ and T_{vib}=T_3. A single linear dependence is observed, confirming the correlation with the oxygen atoms density and suggesting that the effect of other possible species or radicals is less relevant. We could wonder why the variation of $[T_{vib}(fibers) - T_{vib}(bare\ tube)]$ does not follow the trend given by the O atom fraction $^{O}/_{N}$ instead of the absolute O atom values (a plot of $[T_{vib}(fibers) - T_{vib}(bare\ tube)]$ as a function of the $^{O}/_{N}$ does not show any clear correlation). However, if collisions with other molecules have

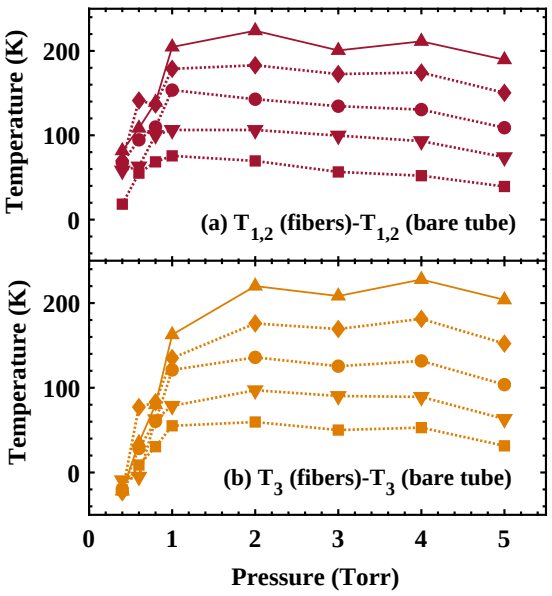

Figure 5.12: Variation of the difference $T_{vib}(fibers) - T_{vib}(bare\ tube)$ as a function of pressure, being T_{vib}=$T_{1,2}$ (panel (a)) or T_{vib}=T_3 (panel (b)).

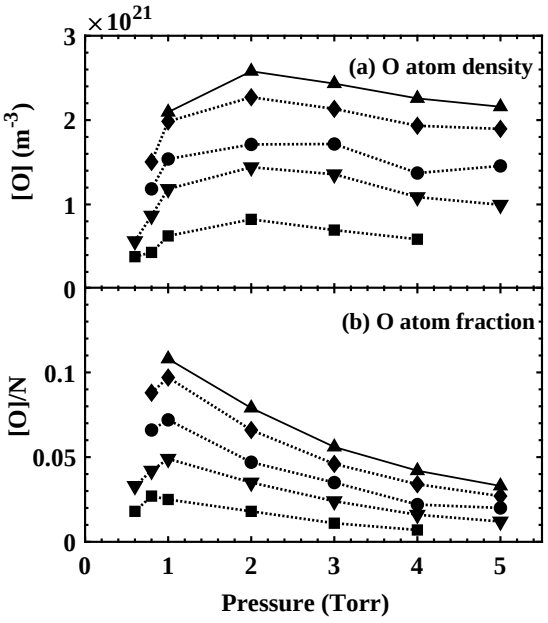

Figure 5.13: Variation of the the O atom density (panel (a)) and O atom fraction (panel (b)) as a function of pressure. Average of actinometry lines O777 and O845 measured for the short discharge tube.

a negligible effect compared to collision with oxygen atoms, only the absolute number of oxygen atoms matters.

✓ $[T_{vib}(fibers) - T_{vib}(bare\ tube)]$ shows a direct linear variation as a function of the absolute O atom density

✓ The removal of oxygen atoms leads to an increase of the vibrational excitation.

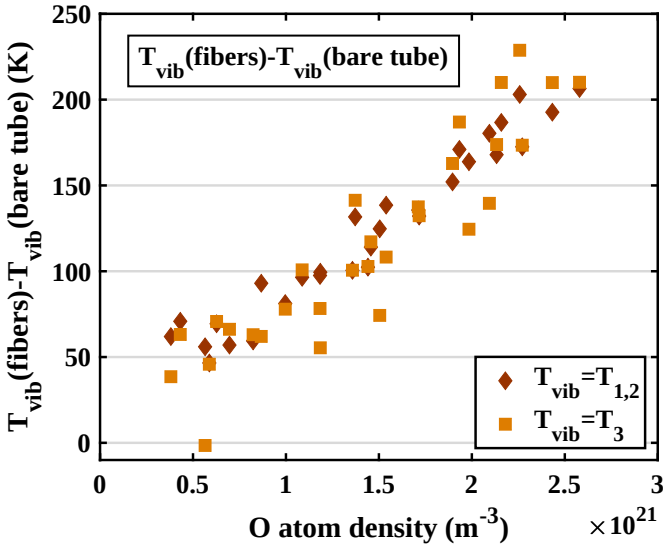

Figure 5.14: $[T_{vib}(fibers) - T_{vib}(bare\ tube)]$ plotted as a function of the absolute O atom density measured in the bare tube (figure 5.13) with T_{vib}=$T_{1,2}$ and T_{vib}=T_3.

5.5 Discussion

In the previous section we have observed a strong influence of the fibers on the vibrational kinetics in continuous plasma. The conclusions extracted can be summarized in three main points:

1. Direct linear correlation of $[T_{vib}(fibers) - T_{vib}(bare\ tube)]$ with the O atom density, which suggests an efficient deactivation of the CO_2 and CO vibrations through collisions with oxygen atoms.
2. Two-regimes dependent on the pressure range in the variation of $[T_{vib} - T_{rot}]$ as a function of pressure and/or T_{rot}:
   - Between 0.4 and 1 Torr $[T_{vib} - T_{rot}](fibers)$ increases with pressure and follows a single dependence as a function of $[T_{rot}]$, which seem to level off when increasing current for the three vibrational temperatures: $T_{1,2}$, T_3 and T_{CO}.
   - Above 1 Torr $[T_{vib} - T_{rot}](fibers)$ decreases with pressure but still increases with current, contrary to the bare tube.

   The two regimes suggest a low pressure range influenced by the surface de-excitation of the vibrations and a high pressure range dominated by gas phase de-excitation.
3. No influence of the higher vibrational excitation in the dissociation fraction α (see figure 5.5).

These three points are discussed in detail in this section.

5.5.1 Quenching of the vibrations of CO_2 by O atoms

Quenching of the first vibrational levels

The quenching of CO_2 vibrational excited states has been studied in the literature for the very first levels of ν_2 *Center* [1973]; *Sharma and Wintersteiner* [1990]; *Shved et al.* [1991]; *Pollock et al.* [1993]; *Lopez-Puertas et al.* [2001]; *Castle et al.* [2006] and ν_3 *Buchwald and Wolga* [1975]; *Cramp and Lambert* [1973]; *Lopez-Puertas et al.* [2001] due to their importance in the energy balance of the upper atmospheres of Earth, Mars and Venus. A small representative collection of rate coefficients available in literature for the quenching of both ν_2 and ν_3 is included in table 5.1.

The available data for ν_2 is more abundant, but also less consistent than in the case of ν_3. For example, the rate coefficients for the $CO_2(\nu_2)$ quenching by oxygen atoms obtained from laboratory measurements *Castle et al.* [2006]; *Pollock et al.* [1993]; *Shved et al.* [1991] do not match with field measurements in the upper atmosphere, with values in the order of in the order of (5-6)$\times 10^{-12}$ cm^3s^{-1}, approximately 2-3 times larger than the values obtained in the laboratory *Sharma and Wintersteiner* [1990]; *López-Puertas et al.* [1992]; *Gusev et al.* [2006]; *Feofilov et al.* [2012]. The laboratory values at room temperature (300 K) from *Castle et al.* [2012] matches very well theoretical calculations for ν_2 with a quenching rate 1.8×10^{-12} cm^3s^{-1} *de Lara-Castells et al.* [2006], but the variation with temperature is different (discussed in the next section).

Vibrational relaxation by collisions with "closed-shell" species is usually described by the so-called Landau-Teller mechanism, an impulsive-type theory which distinguishes between atomic colliders based only on the mass and the interaction parameters. The measured $CO_2(\nu_2)$ de-excitation

Process	Rate coefficient	Range and reference
	Bending and symmetric modes	
	$3.0\times10^{-12}(T/300)^{(1/2)}$ (cm^3s^{-1})	*Lopez-Puertas et al.* [2001]
	$(1.8\pm0.3)\times10^{-12}$ (cm^3s^{-1})	(300K) *Castle et al.* [2006]
$CO_2(\nu_2)$+ $O(^3P)$	$(2.7\pm0.4)-(1.3\pm0.2)\times10^{-12}$ (cm^3s^{-1})	(142-490K) *Castle et al.* [2012]
⇕	$(1.2\pm0.2)\times10^{-12}$ ($cm^3molec^{-1}s^{-1}$)	(300K) *Pollock et al.* [1993]
$CO_2(\nu_2$-1)+ $O(^3P)$	$(1.5\pm0.5)\times10^{-12}$ ($cm^3molec^{-1}s^{-1}$)	(300K) *Shved et al.* [1991]
	$(6\pm3)\times10^{-12}$($cm^3molec^{-1}s^{-1}$)	*Sharma and Wintersteiner* [1990]*
	$(1.9-9.2)\times10^{-12}$ ($cm^3molec^{-1}s^{-1}$)	(1972-3875K) *Center* [1973]
	Asymmetric stretch mode	
$CO_2(\nu_3=1)$+ $O(^3P)$	$2.0\times10^{-13}(T/300)^{(1/2)}$ (cm^3s^{-1})	*Lopez-Puertas et al.* [2001]
⇕	$(6.69\pm1.2)\times10^3$ $s^{-1}Torr^{-1}$**	*Buchwald and Wolga* [1975]
$CO_2(\nu_2=2,3,4)$+ $O(^3P)$	6.25×10^3 $s^{-1}Torr^{-1}$***	*Cramp and Lambert* [1973]

* Determined from rocket-borne radiometric data in the upper atmosphere
** According to *Lopez-Puertas et al.* [2001] equivalent to 2×10^{-13} cm^3s^{-1}.
*** According to *Buchwald and Wolga* [1975].

Table 5.1: Brief compilation of rate coefficients for the vibrational de-excitation processes through collisions with oxygen atoms available in the literature.

rates by collisions with oxygen atoms are up to three orders of magnitude higher than those predicted by Landau-Teller based calculations *Pollock et al.* [1993]. Abnormally efficient relaxation rates have also been found experimentally for O_2^* + O collisions and N_2^* + O collisions. Moreover, it has been observed that hydrogen, deuterium or nitrogen (atomic S states) relax CO_2 much more slowly than atomic P states such as oxygen, chlorine, and fluorine *Buchwald and Wolga* [1975]. Relaxation efficiencies of quenching by rare gases, fall into the ranges measured for hydrogen, deuterium and nitrogen, lower than for oxygen atoms. For instance, the V-T relaxation time CO_2*-O collisions is two orders of magnitude shorter than for CO_2*-Ne collisions, in spite of the similar reduced mass and collision rate *Cramp and Lambert* [1973]. The rates for atomic P state atoms are faster than any rare gas atom and would require unrealistic interaction parameters to explain their high efficiency by the Landau-Teller mechanism *Buchwald and Wolga* [1975].

The investigation of the detailed mechanisms causing the efficient quenching by O atoms is out of the scope of this thesis. Nevertheless, several suggestions are available in the literature for mechanisms of vibrational relaxation when one of the colliders has an unpaired electron, including chemical reactions with the aid of vibrational excitation or the formation of a stable intermediates *Lambert* [1972], which has been suggested to be responsible for the abnormally low relaxation times shown by NH_3, H_2O, CH_3CN and SO_2 in self-collisions, caused by strong intermolecular attractive forces. A similar effect could occur in CO_2 + O collisions and evidence for the existence of a collision complex, CO_3^*, is given by *Zipf* [1969]. Atmospheric studies show the formation of CO_3^* intermediate after collisions between CO_2 and $O(^1D)$ *Mebel et al.* [2004]; *Perri et al.* [2004], leading to isotope enrichment, also observed in our plasma conditions (see chapter 7), but no isotope exchange was found with $O(^3P)$ *Katakis and Taube* [1962]; *Baulch and Breckenridge* [1966]; *Perri et al.* [2004].

It is also possible that the very effective relaxation of CO_2 by atoms in electronic P states, "open-shell" species such as $O(^3P)$ with degenerate electronic angular momentum, is due to interaction

between electronic and vibrational degrees of freedom *Pollock et al.* [1993], such as vibrational-to-electronic energy transfer where some of the vibrational energy is converted to excited spin-orbit states of the colliding atom *Nikitin* [1964]. This type of process has already been observed in the bromine atom-hydrogen halide system *Buchwald and Wolga* [1975], and it was suggested to explain the abnormally short relaxation times shown in collisions involving NO, O and Fe *Nikitin* [1964].

Temperature dependence and quenching of higher vibrational states

There is no clear agreement in the literature about the temperature dependence of the quenching rate coefficients of $CO_2(\nu^*)$ by O atoms. Slightly negative temperature dependence was measured in a temperature range between 142 and 490 K by *Khvorostovskaya et al.* [2002]; *Castle et al.* [2012], but an increasing variation was also determined by *Center* [1973]; *Lopez-Puertas et al.* [2001]. Quantum scattering calculations based on *ab initio* potential energy surfaces *de Lara-Castells et al.* [2006] predict a weak positive temperature dependence of the quenching rate for $CO_2(\nu_2)$ dependent upon the O atom fine structure. For $O(^3P_{J=0,1})$ spin-orbit states, the rate coefficient is proportional to $\exp(T^{-1/3})$ (Landau-Teller behaviour) while for $O(^3P_{J=2})$ the rate coefficient shows a $T^{1/2}$ dependence, as proposed by *Lopez-Puertas et al.* [2001] (see table 5.1). The $(^3P_{J=2})$ spin sub-level is dominant in our discharge conditions (see figure 2.14 for instance) and, in general, below ∼2000 K. The weak positive temperature dependence predicted would then be caused by the varying Boltzmann distribution of the fine structure as a function of temperature *Castle et al.* [2012]. Above 2000 K, higher than our temperature range, a stronger increasing temperature dependence is described experimentally by *Center* [1973] and confirmed by calculations carried out by *Pollock et al.* [1993], predicting also a small temperature dependence of the quenching rate up to about 2000 K, and therefore suggesting different quenching mechanisms below and above 2000 K.

Note that the dependence of the V-V' and V-T rate coefficients discussed in section 4.5, predicted by *Blauer and Nickerson* [1973] and validated for pure CO_2 in our discharge (see section 4.6 and in more detail in *Silva et al.* [2018]; *Grofulović et al.* [2018]) is $\propto exp\left(A + BT^{(-1/3)} + CT^{(-2/3)}\right)$. Similar dependence is suggested for the quenching by CO and O_2.

To illustrate the temperature effect and give an idea of the predominance of the quenching by O atoms compared to the quenching by other species, figure 5.15 plots the rate coefficients for the de-excitation of the first vibrational levels of CO_2, for ν_2 and ν_3, by CO_2, O_2, CO and O atoms according to *Blauer and Nickerson* [1973] and *Lopez-Puertas et al.* [2001]. Only a few reactions, indicated in the figure, are plotted as illustrative examples. More information and rate coefficients for other reactions can be found in *Blauer and Nickerson* [1973]; *Lopez-Puertas et al.* [2001]; *Silva et al.* [2018] and the references therein. Several comments can be pointed out:

- The rate coefficient for the quenching of $CO_2(\nu_{2,3})$ by O atoms, k_O, is always higher than the quenching by CO_2, CO and O_2.
- The quenching of $CO_2(\nu_2)$ by O atoms is more than one order of magnitude higher than for $CO_2(\nu_3)$.
- In the case of $CO_2(\nu_2)$, k_O is at least two orders of magnitude higher than the rate coefficient for the quenching of CO_2 by CO_2, CO or O_2, $k_{CO_2,CO\&O_2}$, for the range of temperatures corresponding to our experimental conditions.
- For $CO_2(\nu_3)$, k_O is between 1.5 to ∼ 0.5 orders of magnitude higher than $k_{CO_2,CO\&O_2}$.

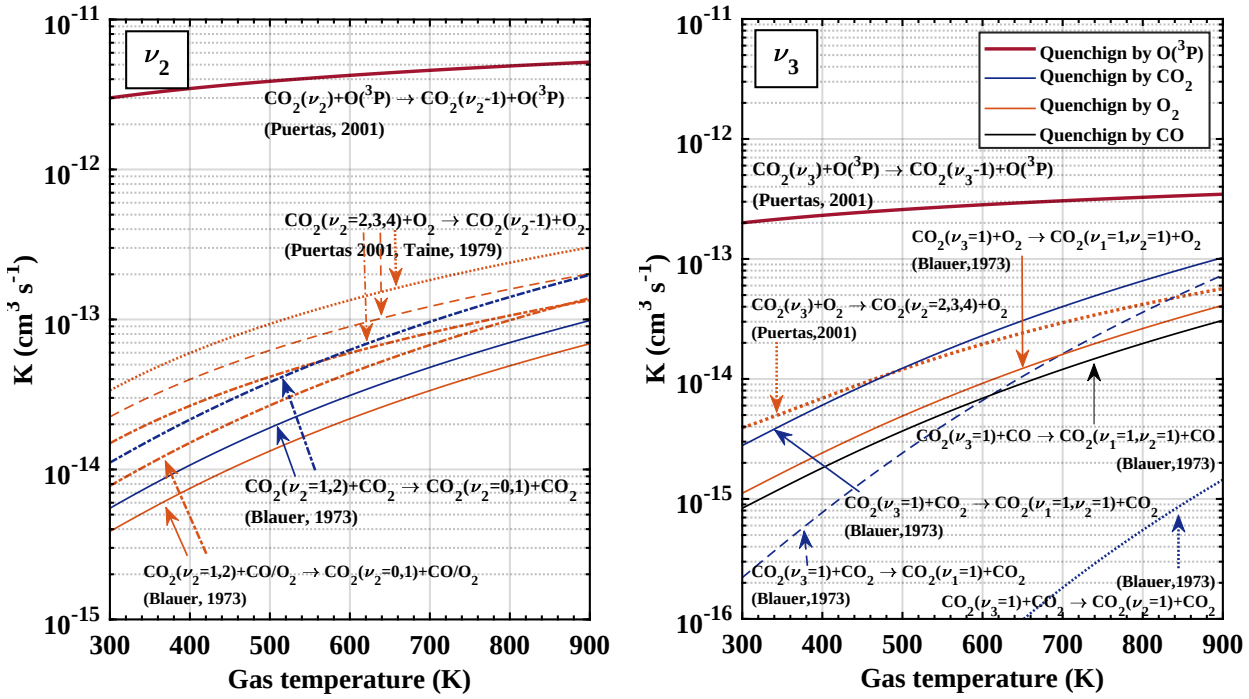

(a) Bending mode (ν_2)

(b) Asymmetric mode (ν_3)

Figure 5.15: Evolution of rate coefficients for the vibrational de-excitation of the bending mode (left graph) and the asymmetric stretch mode (right) as a function of gas temperature.

- When comparable, the rate coefficients listed by *Lopez-Puertas et al.* [2001] are in reasonable agreement with the values reported by *Blauer and Nickerson* [1973] (for example for k_{O_2}).

The plotted rate coefficients can be debatable. For some reactions the agreement between *Blauer and Nickerson* [1973] and *Lopez-Puertas et al.* [2001] such as de-excitation rate of CO_2 by CO_2 (not plotted) is not complete and only the rate coefficients from *Blauer and Nickerson* [1973] have been validated in our experimental conditions (see section 4.6). There are also certain discrepancies in the literature about the rate coefficients for the quenching of $CO_2(\nu_2)$ (see table 5.1), although the quenching by of $CO_2(\nu_3)$ by O atoms is in good agreement with other experimental data reported in literature *Buchwald and Wolga* [1975]; *Cramp and Lambert* [1973]. A comparison of the quenching rate with our experimental results would require a comparison with a kinetic model (in progress). However, qualitatively, the available rate coefficients are consistent with our experimental results in terms of the importance of the quenching by atomic oxygen.

The rate coefficients available in literature for the quenching of ν_2 and ν_3 by atomic oxygen are given only for the first vibrational levels. For higher levels a scaling based on the harmonic oscillator approximation is suggested by *Lopez-Puertas et al.* [2001] for both vibrational modes. To investigate the variation of the quenching rate with the quantum number figure 5.16 plots the comparison of the population densities for ν_2 and ν_3 with the fibers and with the bare tube for levels up to ν_2=4 and ν_3=3 (higher levels are in the noise level in our experimental conditions) for all pressures at 50 mA. The same spectra used in previous sections was fitted in this case with the Free OoE fitting script (see details in section 2.3.1). The difference in population density of vibrational levels between fibers and bare tube increases significantly with the quantum number for both ν_2

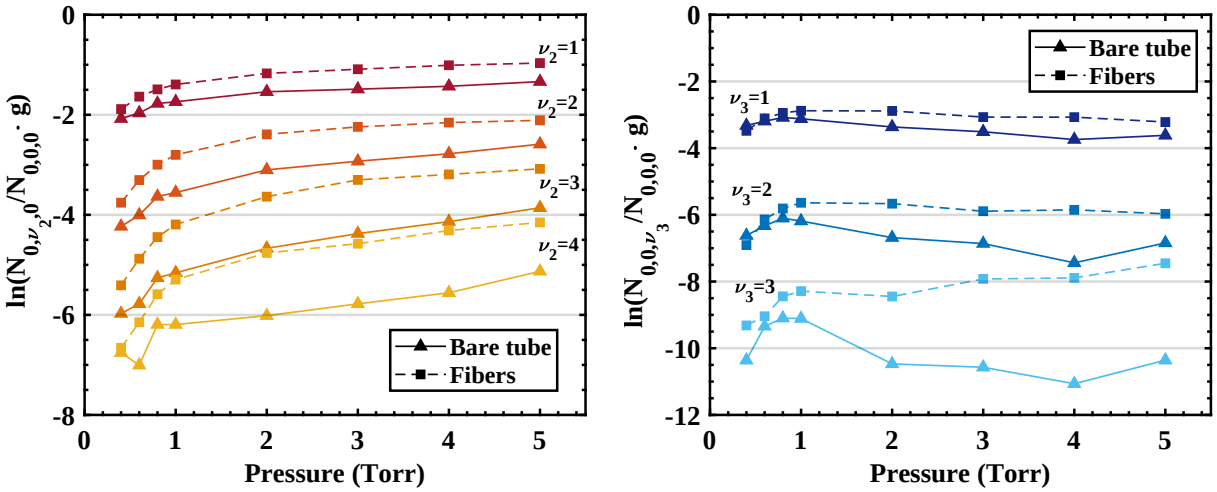

(a) Bending mode (ν_2)

(b) Asymmetric mode (ν_3)

Figure 5.16: Ratio of the population density of excited vibrational levels to the population of ground state corresponding to the bending vibrational mode (ν_2) up to $\nu_2 = 4$ (panel (a)) and the asymmetric stretch vibrational mode (ν_3) up to $\nu_3 = 3$ (panel (b)) with the bare tube and with the fibers. g is the degeneracy of the vibrational mode.

and ν_3. The pressure and/or temperature dependence is however different. In the case of ν_2 both fibers and bare tube evolve similarly with pressure, in agreement with the rate coefficients plotted in figure 5.15. However, in the case of ν_3 there is a clear pressure dependence. The difference between bare tube and fibers is negligible at the lowest pressures and increases significantly with pressure (and/or temperature) suggesting a different scaling law.

5.5.2 Quenching of the CO_2 vibrations of at the walls

Several observations point towards an effect of the quenching of vibrational excitation in the walls for the lowest pressures. Generally speaking, the de-excitation of vibrationally excited molecules can happen through three basic mechanisms: Gas phase collisions (V-e, V-V' and V-T), surface collisions and spontaneous emission.

An illustrative graph of the qualitative variation of the three mechanisms as a function of pressure (for constant gas temperature) is shown in figure 5.17, extracted from *Doyennette et al.* [1974]. This figure represents qualitatively the vibrational de-excitation rate of N_2O and $CO_2(\nu_3 = 1)$ in a pure gas. The rate of gas phase de-excitation, here represented by the parameter K, is proportional to the collision rate and it becomes significantly higher than the other two contributions when the pressure increases. In the previous chapter we have seen that under discharge conditions, this parameter also increases significantly with the gas temperature. The de-excitation in the walls, represented by δ depends on the diffusion coefficient and on the probability of de-excitation by collision with the walls. When the vibrational energy of a molecule is much higher than the energy that a molecule in thermal equilibrium with the surface would have, the de-excitation probability at the wall, γ_ν, is equivalent to the accommodation coefficient, α_ν, *Houston and Merrill* [1988]. This mechanism is dominant at low pressures. δ depends on the radius (the geometry) of the discharge tube through τ_{diff} and increases as the radius decreases. The rate of de-excitation at the wall can

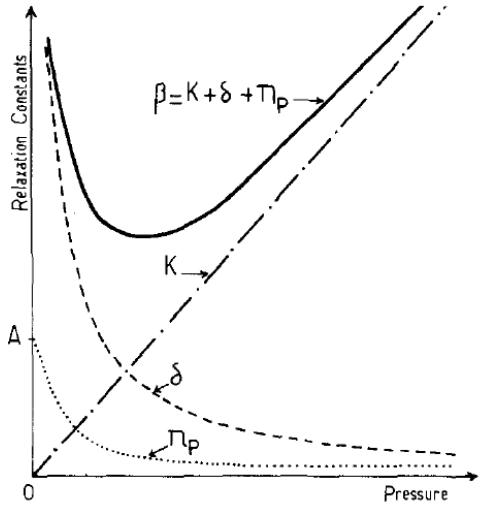

Figure 5.17: Pressure dependence of the rates (per second) of de-excitation by gas phase collisions, by collisions on the reactor walls, and by radiative process, represented by the parameters K, δ and Π_P, respectively. The general variation of the relaxation constant β (in s^{-1}) is given by the relation $\beta = K + \delta + \Pi_P$. Figure extracted from *Doyennette et al.* [1974].

thus be estimated by the expression *Margottin-Maclou et al.* [1971]; *Doyennette et al.* [1974]:

$$r_{wall}(=\delta) = \frac{\mu^2 D}{R^2} \tag{5.1}$$

where R is the radius of the tube, D is the diffusion coefficient and μ is a parameter dependent on α_ν. The accommodation coefficient α_ν is therefore a critical parameter determining the efficiency of the de-excitation process and the neutral gas temperature *Gibson et al.* [2017]. α_ν is temperature dependent and for $CO_2(\nu_3 = 1)$ hitting on quartz it was found to be ∼0.34 at 300 K, rapidly decreasing with temperature down to a value of 0.12 at T=600 K and then more slowly down to 0.07 at 900 K *Doyennette et al.* [1974]. α_ν can also be affected by the molecules adsorbed at the surface *Marinov et al.* [2013b]; *Liang et al.* [2013]. In fact, the rapid decrease of the accommodation coefficient from 300 K to 600 K was suggested to be caused by the desorption of the molecules from the surface, whereas at higher temperatures, the slow decrease should depend on the nature and temperature of the surface *Doyennette et al.* [1974]. Therefore, the real value of the accommodation coefficient might vary both with the gas mixture and the gas temperature under plasma exposure.

A more accurate estimation of the wall de-excitation, described in terms of wall de-excitation probability could be done by using the common expression (used also to calculate the O atom loss probability, see section 8.2.2) *Chantry* [1987]; *Kutasi et al.* [2010]; *Guerra et al.* [2019]:

$$\tau = \frac{1}{K_{wall}} = \tau_{diff} + \tau_{loss} = \frac{\Lambda_O^2}{D} + \frac{V}{S}\frac{2(2-\gamma_\nu)}{\upsilon_{th}\gamma_\nu} \tag{5.2}$$

where γ_ν is here the wall de-excitation/loss probability , V and S are the volume and surface of the discharge tube, υ_{th} is the thermal velocity and D is the diffusion coefficient of atomic oxygen. Λ_O is the diffusion length given, defined in equation 3.3.

Values of γ_ν for $CO_2(00^01)$ in the literature range from 0.18-0.22 to 0.4 on Pyrex *Kovacs et al.* [1968]; *Margottin-Maclou et al.* [1971]; *Black et al.* [1974]. The deactivation probability of $CO_2(10^01)$ seems to be higher than that of $CO_2(00^01)$ for a similar material. For instance for polycrystalline

silver $CO_2(10^01)$ showed a γ_ν value of 0.72 at 300 K, whereas for $CO_2(00^01)$ it was reported to be 0.16 by *Misewich et al.* [1985]. For $CO(\nu = 1)$ there are values significantly lower than for CO_2, between 1.86-4$\times10^{-2}$ *Black et al.* [1974] in Pyrex. A certain dependence on the vibrational level is expected, similar to the case of N_2, where a linear dependence of γ_ν with the vibrational level is reported by *Yaney and Parish* [1999]. As a matter of interest, the relaxation time for the vibrational deactivation in the surface can be rather long, *e.g.* τ_{vib} $\sim10^{-3}-10^{-4}$ s for N_2 *Black et al.* [1974], compared to the vibrational time of the surface atoms $\sim10^{-12} - 10^{-14}$ s. The mechanisms involved on the surface relaxation are out of the scope of this thesis, but could include vibrational-to-rotational energy transfer (V-T), excitation of surface phonons, etc. More information can be found in *Misewich et al.* [1983]; *Zangwill* [1988]; *Houston and Merrill* [1988]; *Muiño and Busnengo* [2013].

Finally the de-excitation rate through spontaneous emission, represented by Π_P, also scales inversely with pressure but it is generally much lower than the other two, and lower than the Einstein coefficient of spontaneous emission because of the self-absorption of the radiation. It can be therefore considered negligible *Doyennette et al.* [1974]; *Klarenaar et al.* [2019].

The sum of the three contributions gives a two-regime variation as a function of pressure which first decreases, passes through a minimum and then increases with pressure. The pressure at which the minimum of the vibrational de-excitation happens depends on the balance between gas and surface de-excitation, and therefore depends on the tube radius, the surface characteristics, and the gas temperature. For $CO_2(\nu_3)$ it was found to be between 0.5 and 1 Torr for a quartz tube of radius between 2.77 cm and 1.33 cm in a range of temperatures between 300 K and 900 K. An increase of temperature or tube radius tends to shift the minimum point towards lower pressures. Although this is a somewhat simplified view, not directly applicable to our discharge conditions, where the measured vibrational temperatures are also influenced by a constant e-V excitation (and de-excitation), V-V' and V-T interactions with other molecules, etc., this estimation matches relatively well with the values observed for T_3 in the bare tube (with a maximum of T_3 around $\sim$0.6-0.8 Torr). Considering now the use of fibers in the surface, we expect a reduction of the gas phase de-excitation (*i.e.* the slope of K in figure 5.17) and probably a certain increase of δ, which should shift the minimum point towards higher pressures. This is consistent with what we observed in figures 5.9, 5.10 (a) and 5.11, where the maximum of T_3 and T_{CO} is shifted up to 1 Torr. The case of $T_{1,2}$ is particular because in the bare tube $T_{1,2}$ is thermalized with T_{rot} due to the very strong de-excitation by O atoms, but with the fibers it shows a similar behaviour as T_3 and T_{CO} with a maximum at 1 Torr.

✓ At low pressure surface de-excitation is the main vibrational de-excitation mechanism.
✓ At higher pressure (>1 Torr) V-T de-excitation through collisions with O atoms becomes the dominant de-excitation mechanism.
✓ The increase of surface and decrease of O atom density with the SiO_2 fibers shifts to higher pressure ($\sim$1 Torr) the transition from a regime dominated by wall de-excitation to a regime dominated by V-T with O atoms as main vibrational energy loss mechanism.
✓ The effect of quenching by O atoms increases with quantum number for both $\nu_{1,2}$ and ν_3, but increases with pressure only for ν_3.

5.5.3 Dissociation fraction

The removal of O atoms by the fibers attached to the surface of the reactor wall decreases the quenching of vibrationally excited CO_2 and CO molecules. Additionally, the removed O atoms do not participate any more in any mechanism inducing "back reaction" in the gas phase. Nevertheless, we do not perceive any effect on the dissociation fraction. A plausible explanation would be that in the glow discharge we do not excite enough the highest vibrational states and the CO_2 is dissociated basically through electron impact, as discussed in section 3.6.1. The main parameter controlling the dissociation would then be the reduced electric field which remains essentially unchanged. Indeed, the highest vibrational temperatures are only at the limit suggested by *Fridman* [2008] for the reaction $CO_2 + O \rightarrow CO + O_2$, ∼1160 K, and the rates for the gas phase recombination between CO and O are low, as discussed in section 3.6.2. In that case, gas phase O atoms and surface processes would not influence at all the CO_2 dissociation, and the dissociation fraction would follow a single dependence with the electron impact dissociation process, with no influence of any "back reaction mechanism". Nevertheless there are two other possibilities: (1) The "back reaction" does not involve directly free O atoms and therefore is not affected by the fibers; and (2) other reactions compensate the possible positive effect of the removal of oxygen atoms. Two of these possible reactions are:

- **Reaction between CO and O_2, to produce CO_2 and O**. The rate coefficient for this reaction is believed to increase with the vibrational excitation of CO *Kozák and Bogaerts* [2014a], which is clearly increased when removing the O atoms. Additionally with the fibers the O atoms are more efficiently recombined into O_2, increasing the O_2 density and thus the rate for this reaction.
- **Enhanced back reaction in the surface**. The O atoms that disappear from the gas phase could follow three possible paths leading to "back reaction" in the surface: $O_{ads} + CO \rightarrow CO_2$, $O + CO_{ads} \rightarrow CO_2$ or $O_{ads} + CO_{ads} \rightarrow CO_2$. These reactions would be enhanced by the higher amount of adsorbed species due to the larger surface available.

The rate for the reaction $CO(\nu*) + O_2 \rightarrow CO_2 + O$ is still rather low compared with other processes. In addition, under our low excitation conditions the vibrational excitation of CO is not expected to be high enough to increase significantly the rate of the reaction. However, the participation of electronically excited states could present higher rate coefficients. These reactions and the possibility of "back reaction" mechanisms not involving O atoms are explored and discussed in detail in chapters 6 and 7. The possibility of "back reactions" in the surface will be further studied in chapter 8.

5.6 Time resolved evolution of the vibrational temperatures along a plasma pulse

Time-resolved FTIR measurements were taken with the fibers in a pulsed plasma (for the reference pulse, 5-10 ms On-Off) for pressures between 1 and 5 Torr at a current of 50 mA. These measurements are compared to the data taken with the bare tube, presented in chapter 4 in order to study the influence of the O atoms on the time evolution of the vibrational temperatures in a CO_2 glow discharge.

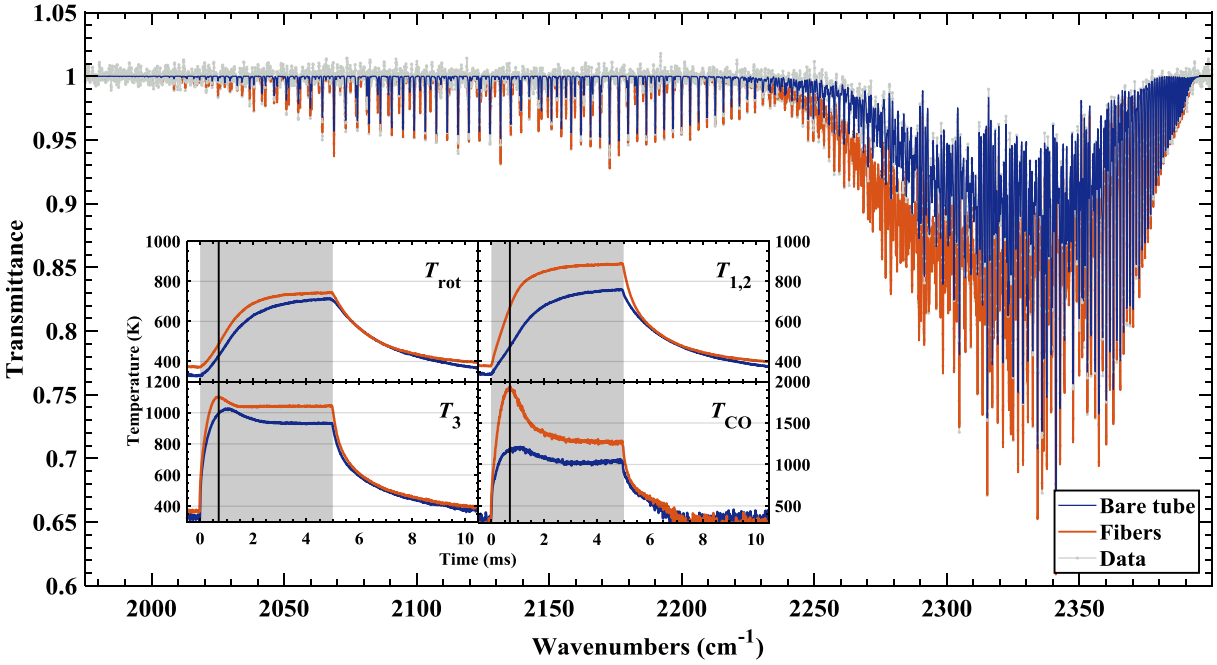

Figure 5.18: Example of the FTIR spectra obtained with the bare tube and with fibers for a pulsed plasma of 5-10 ms On-Off at 3 Torr 50 mA. The inner panels show the time evolution of the fitted rotational temperature (T_{rot}) and the vibrational temperatures of CO_2 and CO ($T_{1,2}$, T_3 and T_{CO}). The shown spectra corresponds to the time point 0.7 ms after the beginning of the plasma pulse as shown by the time bar in the inner panels, *i.e.* at the peak of excitation of T_3 and T_{CO}.

5.6.1 Effect on the vibrational temperatures

Figure 5.18 shows the FTIR spectra and the total fit for both surface configurations at a given time point (t=0.7 ms after the beginning of the plasma pulse, ∼maximum of vibrational excitation of CO and $CO_2(\nu_3)$) for 3 torr 50 mA, as representative example. The spectrum itself is clearly different, demonstrating that the fitting results reflect a real change in the absorption spectra and are not caused by a misfit of the data.

The time evolution of T_{rot}, $T_{1,2}$, T_3 and T_{CO} is shown in the inner panels. The fitting results are qualitatively consistent with those observed in continuous plasma, showing a clear increase of the vibrational excitation represented by $T_{1,2}$, T_3 and T_{CO} with the fibers. The increase is more significant in the case of $T_{1,2}$ than for T_3, in agreement with the de-excitation rate coefficients for collisions with O atoms shown in figures 5.15 (a) and (b). In the very first μs of the pulse, the kinetics of T_3 and T_{CO} both with the bare tube and the fibers are similar, but the peaks in the excitation of T_3 and T_{CO} are higher and slightly shifted towards shorter ON time values when compared with the time evolution in the bare tube. The rise of $T_{1,2}$ at the beginning of the pulse with the fibers is clearly much faster and the time required to reach the steady-state is shorter than with the bare tube.

In continuous plasma we observed that T_{rot} was slightly higher with the fibers than with the bare tube. The increased temperatures with the fibers were suggested to be due to their role as thermal insulator, reducing the efficiency of the cooling circulation used for continuous plasma measurements. This hypothesis is confirmed by the pulsed plasma results. The difference between the bare tube and the fibers is slightly lower here because the wall temperature is not controlled

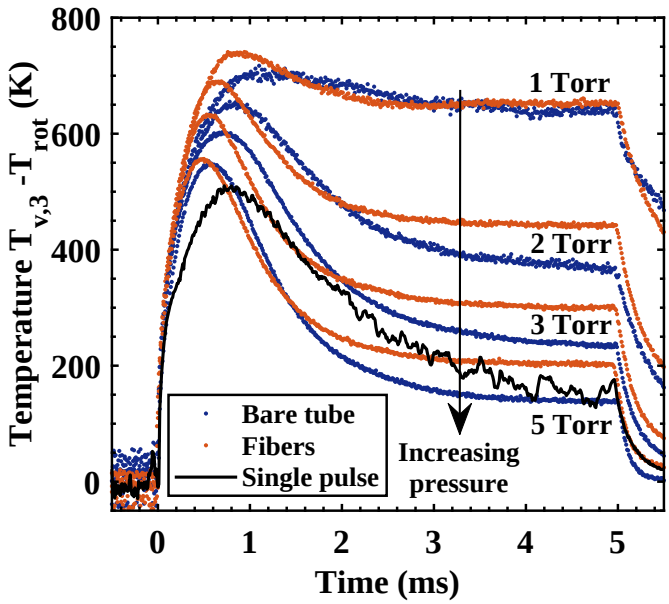

Figure 5.19: Time evolution of [T_3-T_{rot}] during the plasma pulse for pressures between 1 and 5 Torr, excluding the data at 4 Torr for readability, at 50 mA. The "single pulse" measurement (see section 4.4.2) is also included for comparison.

in this case and the role of the fibers as an insulation layer is less significant. Additionally the same temperature difference appears both during the ON and OFF phases, showing that it is not a phenomenon related with the plasma, but with the less efficient heat release through the walls.

As previously, we can look at [T_3-T_{rot}] as characterization of the non-equilibrium of the asymmetric stretch mode. We first discuss the active part of the discharge in figure 5.19, and subsequently the post-discharge (figure 5.21). Figure 5.19 presents the time evolution [T_3-T_{rot}] for pressures between 1 and 5 torr 50 mA (4 Torr is not plotted for readability of the graph) during the plasma pulse. The data corresponding to the "single pulse" measurement, at 5 Torr 50 mA, described in section 4.4.2 is also included. In general, for all conditions, [T_3-T_{rot}] first sharply increases, passes through a maximum and then decreases until it reaches a *quasi* steady-state value close to the end of the pulse, at t∼4 ms. Looking in more detail:

- The initialization of the pulse is the same for the different pressures and for both surface configurations.
- The value of the maximum is slightly higher with the fibers than with the bare tube and it is shifted towards shorter plasma ON times.
- The maximum slightly drifts towards shorter ON times when the pressure increases for both the bare tube and the fibers.
- The shape of the maximum is sharper with the fibers than with the bare tube. After the peak, [T_3-T_{rot}] decreases faster with the fibers but also stabilizes earlier.
- With the bare tube, the maximum of T_3 occurs later than with fibers and stabilizes at lower values towards the end of the pulse, causing two crossing points between the fibers and the bare tube data that occurs earlier for higher pressures.
- The steady-state value of [T_3-T_{rot}] after the maximum significantly decreases with increasing

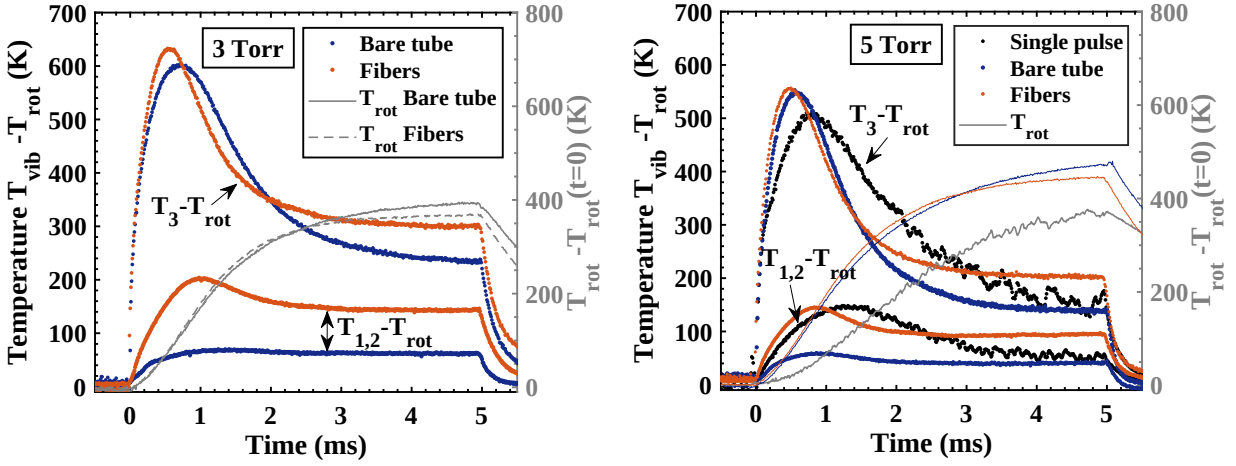

(a) 3 Torr, 50 mA

(b) 5 Torr, 50 mA

Figure 5.20: Time evolution of [T_3-T_{rot}] and [$T_{1,2}$-T_{rot}] (left axis) for 3 Torr 50 mA (a) and 5 Torr (b) with the bare tube and with fibers. Panel (b) includes the data corresponding to the "single pulse". Right axis plots the time evolution of $T_{rot} - T_{rot}(t = 0)$ for the same conditions.

pressure for both the bare tube and the fibers, leading to a sharper maximum for higher pressures.

- The steady-state value of [T_3-T_{rot}] at the end of the pulse is higher with the fibers, except at 1 Torr, which is very similar. The difference between the fibers and bare tube increases with pressure.
- The "single pulse" measurement has a noticeably different shape compared to the other two measurements in the same condition. The maximum is clearly delayed on time and the evolution after is slower, causing a less sharp excitation peak.

The similar initialization of the pulse indicates equivalent e-V excitation processes for all conditions. The maximum is reached earlier for the higher pressures not due to a faster kinetics but to a stronger influence of V-T and V-V' de-excitation processes, explaining the lower peak values when the pressure is increased. The higher peak value in [T_3-T_{rot}] with the fibers could be partly explained by the higher T_{CO} values (see figure 5.18) and V-V' transfer processes between CO and $CO_2(\nu_3)$, along with a reduced de-excitation through collisions with O atoms. The faster decay after the peak with the fibers could be related to the rapid rise of $T_{1,2}$ and the consequent increase of the V-V' de-excitation of ν_3 towards $\nu_{1,2}$. To illustrate this effect, figure 5.20 plots the time evolution of [T_3-T_{rot}] and [$T_{1,2}$-T_{rot}] (left axis) for 3 Torr 50 mA (panel (a)), again taken as illustrative example, with the bare tube and with fibers. The right axis plots the time evolution of $T_{rot} - T_{rot}(t = 0)$, *i.e.* the increase of T_{rot} along the pulse, for the same conditions, to keep in mind the characteristic time of the gas temperature evolution. Panel (b) plots similar data for 5 Torr 50 mA, adding the "single pulse" data for comparison.

From an experimental point of view it is usually difficult to isolate the contributions of V-V' and V-T de-excitation, but in this case, thanks to the similar time evolution of T_{rot} with the bare tube and the fibers it is clear that the faster de-excitation after the peak with the fibers corresponds very well with a maximum in $T_{1,2}$, not observed in the bare tube. For longer ON times, when T_{rot} increases both [T_3-T_{rot}] and [$T_{1,2}$-T_{rot}] decrease. It is evident that from the beginning of the pulse

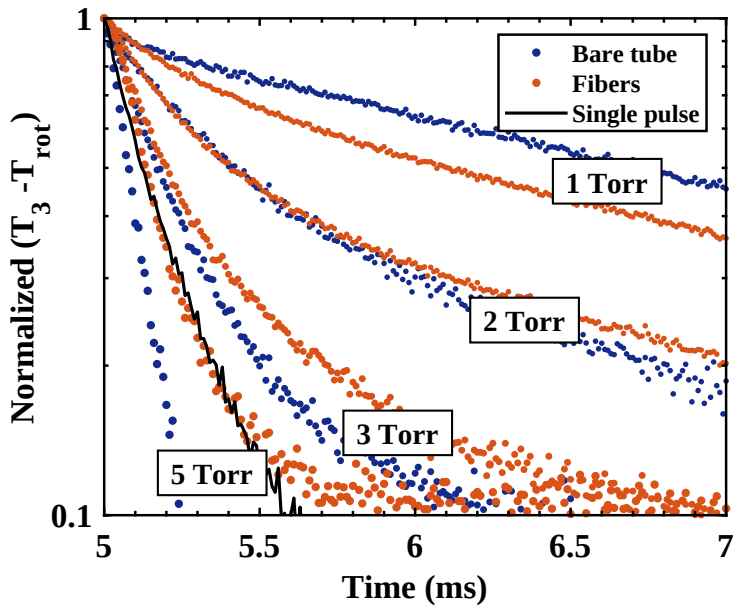

Figure 5.21: Normalized time evolution of [T_3-T_{rot}] for pressures between 1 and 5 Torr, excluding the data at 4 Torr for readability, at 50 mA after the end of the puls. The "single pulse" measurement (see section 4.4.2) is also included for comparison.

all the mechanisms involved in the vibrational kinetics (e-V, V-V' and V-T) are active but their role and influence varies with time. Figure 5.20 nicely highlights three time-regions of influence in the mechanisms driving the development of the vibrational excitation of T_3 over T_{rot} along a plasma pulse:

1. e-V excitation in the first $\sim 100\mu$s of the pulse
2. V-V' T_3 excitation due to near resonant energy transfer from CO + V-V' relaxation to $T_{1,2}$ up to $\sim$2 ms
3. V-T relaxation due to the increase of T_{rot} until the end of the pulse.

In the bare tube, the relaxation of T_3 after the peak is slower due to the lower value of $T_{1,2}$, but towards the end of the pulse the V-T relaxation is stronger due to the higher V-T de-excitation rate with oxygen atoms compared to other gas phase compounds. For $T_{1,2}$ the mechanisms are similar but the V-T processes are always more efficient, minimizing the effect of e-V excitation. A combined effect of the enhanced vibrational excitation by CO and de-excitation through V-V' and the lower relaxation to T_{rot} due to the reduced number of collisions with O atoms explains the different time evolution with the bare tube and with fibers. Similar arguments explain why in the active discharge the "single pulse" data do not resemble more the time-evolution seen with the fibers. Figure 5.20 (b) shows that in the "single pulse" both the decrease in [T_3-T_{rot}] and the maximum in [$T_{1,2}$-T_{rot}] are delayed with regard the repetitive pulse, similarly to T_{rot}. The maximum in [$T_{1,2}$-T_{rot}] is similar as with the fibers, but the maximum in [T_3-T_{rot}] is lower confirming the effect of CO(ν) in the rise of $CO_2(\nu_3)$ at the beginning of the pulse.

In order to investigate the relaxation processes in the post discharge, controlled by V-V, V-V' and V-T processes, figure 5.21 plots the time evolution of [T_3-T_{rot}] normalized to the end of the

plasma pulse for the bare tube and the fibers for the first 2 ms of post-discharge. Several observations can be pointed out:

- At lower pressures (1 Torr) the decay with fibers is faster than with the bare tube, suggesting a dominant effect of de-excitation in the surface.
- At higher pressures (3-5 Torr) the decay with the fibers is slower than with the bare tube, demonstrating the "positive effect" of removing the O atoms and thus reducing the quenching of the vibrations in gas phase.
- At 2 Torr the decay rate is the same with and without the fibers, and seems to be the "frontier" between regimes dominated by either de-excitation in the walls or by gas phase collisions.
- At 5 Torr, the "single pulse" data, taken in pure CO_2 without significant amounts of CO, O or O_2 (or other minor species), matches remarkably well the data with fibers.

Figure 5.21 confirms that the fibers do increase the de-excitation of $CO_2(\nu^*)$ in the surface at low pressures, clearly evident at 1 Torr. At higher pressures the gas phase de-excitation is dominant and the comparison with the single pulse suggest that the relaxation of T_3 to T_{rot} in the early post-discharge of repetitive pulses is strongly controlled by the quenching by O atoms.

To conclude, in general the increase of vibrational temperatures with the fibers in pulsed plasma is less pronounced than in continuous plasma. For instance, at 3 Torr (50 mA) $[T_3 - T_{rot}](fibers)$-$[T_3 - T_{rot}](bare\ tube)$ is around 80 K, while in continuous discharge is around 170 K. The reason is the lower atomic oxygen density in these conditions, ∼1-2% of the total gas mixture (see section 3.7.2), compared to continuous plasma ∼5-12% of the total gas mixture (see section 3.5). Still, despite the low O atom density in pulsed plasma, the effect on the vibrational kinetics is significant, in agreement with *Spiridonov et al.* [1994] who reported that at only 1% concentration of O atoms in the gas mixture, the contribution of the oxygen atoms to the relaxation of the asymmetric stretch mode was approximately equal to the contribution of all the remaining components.

✓ Similar vibrational excitation by e-V processes at the begining of the pulse with and without fibers.
✓ Time-resolved pulsed plasma measurements confirm the strong effect of V-T with O atoms observed in continuous plasma.
✓ $CO_2(\nu_3)$ relaxation in post-discharge is controlled by V-T with O atoms at high pressures and affected by surface de-excitation at low pressures.
✓ Strong indication of energy transfer from $CO(\nu)$ towards $CO_2(\nu_3)$ pulling up T_3.

5.6.2 Dissociation fraction along a plasma pulse

We have seen in section 5.3.2 that the use of fibers does not change the measured dissociation fraction in continuous plasma. We also saw in section 3.7.1 that α does not vary significantly along a plasma pulse with the bare tube. Only a slight decrease is perceived during the pulse, followed by a small bump in the first milliseconds of post-discharge, whose magnitude and delay with regard to the end of the pulse increases with decreasing pressure (see figure 5.22 (a), for a plasma current

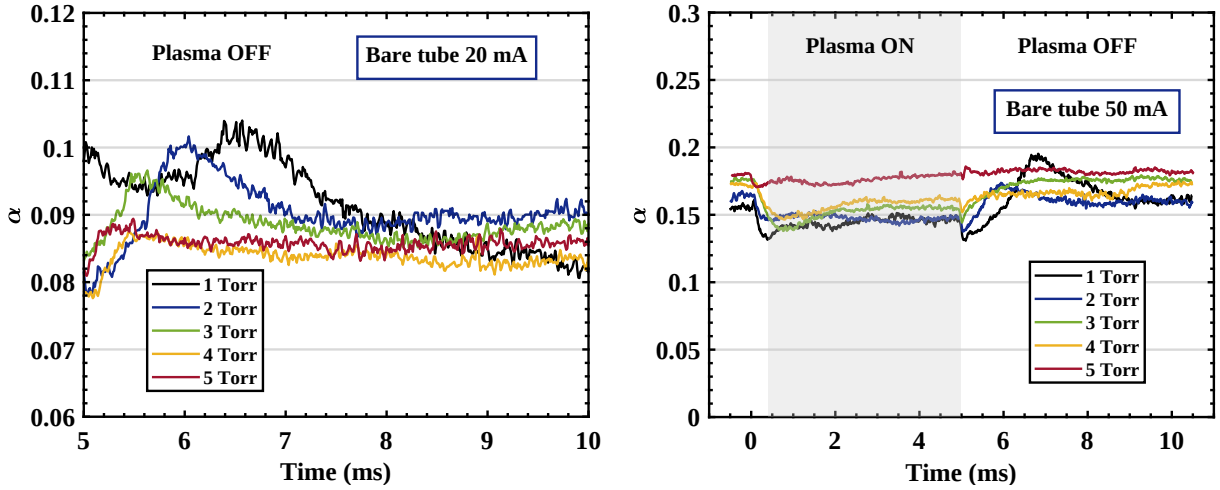

(a) Post-discharge bare tube 20 mA

(b) Bare tube 50 mA

Figure 5.22: Time evolution of the dissociation fraction, α, measured with the bare tube for pressures between 1 and 5 Torr along a plasma pulse of 5-10 ms On-Off (a) in the post-discharge of the plasma pulse at 20 mA and (b) along the whole pulse at 50 mA.

of 20 mA). We investigate now the effect of the fibers on the dissociation along a plasma pulse and compare it with the bare tube.

Figure 5.22 (b) shows the time evolution of the conversion factor α along the usual plasma pulse of 5-10 ms On-Off for pressures between 1 and 5 Torr at a plasma current of 50 mA for the bare tube. Figure 5.23 plots the same data for the fibers, colour-coded according to pressure. Both plots show similarities but also evident differences. In both cases, the conversion fraction is similar during the OFF phase, ranging from α=0.15 to 0.2 and showing a little increase with pressure. The similar dissociation fraction between fibers and bare tube and the variation with pressure are consistent with the continuous plasma data. The behaviour during the plasma pulse is however noticeably different. Contrary to the bare tube, with the fibers the dissociation factor increases

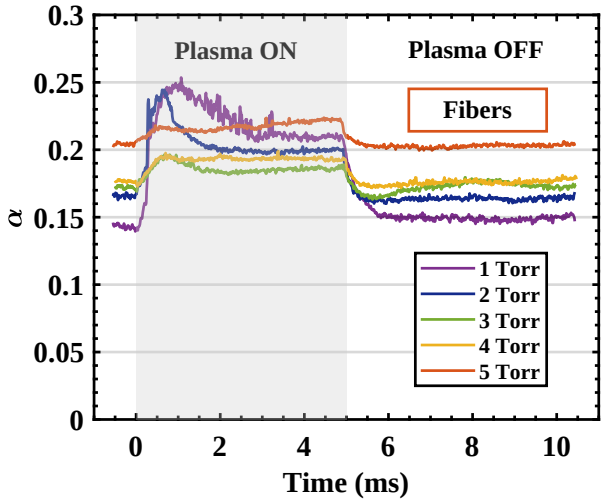

Figure 5.23: Time evolution of the conversion factor α along a plasma pulse of 5-10 ms On-Off for pressures between 1 and 5 Torr at a plasma current of 50 mA with the fibers.

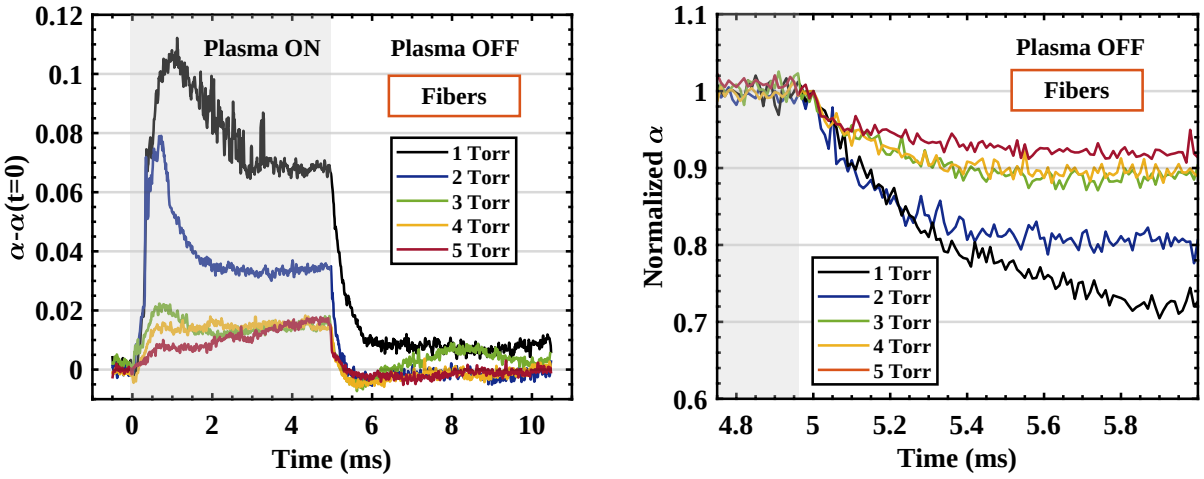

(a) Increase of α during the plasma pulse over the steady-state value before the pulse

(b) α in the post-discharge normalized to the end of the pulse

Figure 5.24: Time evolution of the conversion factor α along a plasma pulse of 5-10 ms On-Off for pressures between 1 and 5 Torr at a plasma current of 50 mA, normalized either to the beginning or to the end of the plasma pulse.

during the pulse. For the lowest pressures it shows a certain bump at the beginning (around t=1 ms) and then decreases slightly. When increasing the pressure, the initial bump decreases whereas a small re-increase is noticeable towards the end of the pulse. In the after-glow, the bump seen in the post-discharge with the bare tube (see figure 5.22 (a)) disappears, and α simply decays down to the pre-pulse level. To allow better visualization of this behaviour, figure 5.24 plots the increase of α along the plasma pulse (panel (a)) and the decay of α in the early post-discharge normalized to one at the end of the pulse (panel (b)). Two hypothesis could explain these graphs:

1. An increase of CO_2 dissociation during the pulse, followed by destruction/adsorption processes.
2. "Extraction" of adsorbed CO from the surface during the plasma pulse followed by re-adsorption after the end of the pulse.

An increase of dissociation could be related, for instance, to the reaction $CO_2^* + O \rightarrow CO + O_2$, possibly in the surface with adsorbed O atoms. At 1 Torr T_3 reaches values as high as 1170 K with a peak of excitation happening at a similar time as the maximum in α. However, the change in α is rather large to be caused by a single pulse of 5 ms. In chapter 6 we will see that accumulation of several pulses at 50 mA is necessary to cause a detectable increase of α. The fast "destruction" at the end of the pulse would also be difficult to justify. An adsorption of molecules at the end of each pulse without a mechanism removing the adsorbed CO from the surface would eventually saturate the surface since the total experiment time is close to 2.5 hr.

Therefore, the most probable cause of the increase of α along the pulse is the desorption of weakly bonded species (physisorbed). After the end of the pulse the desorbed CO would get adsorbed again, in a adsorption-desorption cycle. The desorption rate depends on temperature (see chapter 8) and therefore it should be favoured by an increase of pressure, contrary to our results. However, a

certain increase of α towards the end of pulse is visible at higher pressures (3-5 Torr), when the gas temperature increases. Moreover, for a given amount of CO molecules desorbing from the surface, their contribution to α is more diluted at higher pressure. At low pressure, it is also possible that "bombardment" of the surface by ions, atoms, molecules, etc. is more efficient and could explain an increase of the desorption processes. After the end of the pulse, the variation of τ_{diff} with pressure (see figure 3.7) is consistent with the faster decrease in α at lower pressures at the end of the pulse in figure 5.24 (b).

5.7 Summary and conclusions

The evolution of the vibrational excitation of CO_2 and CO along with the dissociation rate in pure CO_2 plasma has been analysed with two surface configurations, a bare Pyrex tube with smooth surface for which the total surface area in contact with the plasma is around 110 cm^2 (supposing perfectly smooth surface) and a configuration with a larger surface area, but similar chemical nature, by using a layer of SiO_2 fibers attached to the reactor wall, which increases the effective surface area up to 10 m^2. In principle, we could have expected an enhanced quenching of the vibrations in surface ($\uparrow \gamma_\nu$). However, the vibrational excitation increases in all the pressure range studied.

The positive effect of the fibers is believed to be caused by their capacity to recombine the O atoms, which act as an effective quencher of the vibrational excitation of CO_2 and CO. Continuous and pulsed plasma show consistent results and revealed two regimes in the variation of the vibrational excitation $[T_{vib} - T_{rot}]$ as a function of pressure: a low pressure range (between 0.4 and 1-2 Torr) influenced by the surface de-excitation of the vibrations and a high pressure range (above 2 Torr) dominated by gas phase de-excitation of the CO_2 and CO vibrations through collisions with oxygen atoms. In addition, time-resolved experiments with the fibers support the hypothesis of an important effect of the vibrational energy exchange between $CO(\nu)$ and $CO_2(\nu_3)$. They have also revealed a significant effect of V-V' relaxation from $CO_2(\nu_3)$ to $CO_2(\nu_{1,2})$.

No influence of the higher vibrational excitation in the dissociation fraction α was observed. Different hypothesis are:

1. Negligible effect of the "back reaction" and no influence of the vibrational excitation in the dissociation in our discharge conditions.
2. Insignificant role of the O atoms in the "back reaction" mechanisms, which could be dependent on O_2 with excited CO.
3. Surface back reaction, supported by the evident of CO absorption in the fibers revealed by the time-resolved pulsed experiments.

These hypothesis will be thoroughly discussed in the following chapters. On the other hand, the reaction $CO_2 + O \rightarrow CO + O_2$ in the gas phase, which should be enhanced by the vibrational excitation of CO_2 *Kozák and Bogaerts* [2014a], seems to be hindered by the quenching reaction in our discharge conditions. More investigation is required to study the role of this reaction in order to assess its rate coefficients and the conditions were it may become important.

Part III

Time evolution of the dissociation fraction

Chapter 6

Time evolution of the dissociation fraction in CO_2 RF and glow discharges

Contents

6.1 Introduction . . . 151
6.2 Description of the experiment and experimental set-up . . . 152
6.2.1 Experimental set-up . . . 152
6.2.2 Protocol for building-up experiments . . . 153
6.2.3 Data treatment . . . 156
6.3 RF discharge results . . . 158
6.3.1 Pure CO_2 plasma . . . 158
6.3.2 Gas mixtures . . . 174
6.4 Building-up in glow discharge . . . 181
6.4.1 Experimental results and comparison of rate coefficients . . . 182
6.4.2 Comparison with a kinetic model . . . 185
6.5 Summary and conclusions . . . 186

6.1 Introduction

In previous chapters we have studied continuous and pulsed discharge regimes. In both cases we are in steady-state or *quasi* steady-state conditions in terms of the chemistry of the main neutral species. The amount of CO created during a plasma pulse of a few milliseconds is negligible and the fraction of CO can be considered basically constant. Longer pulses cannot be followed by the FTIR working in step scan mode and the measurements would be affected by the renewal of the gas in the discharge tube due to the continuous gas flow. Therefore, with the previous experimental configuration we cannot follow the time evolution of the dissociation fraction.

In this chapter we present a different approach to face this problem. We have designed an experiment so-called "building-up", which is performed in static conditions (closed reactor, without gas flow) and allows to follow the evolution of a fixed number of CO_2 molecules and their dissociation into CO. In this experiment, consecutive plasma pulses are ignited while the densities of CO and CO_2

are monitored in time by infra-red absorption, until the dissociation fraction reaches the steady-state value. This experiment has several advantages: (1) working in static conditions, without renewing the gas, allows to remove the possible influence of residence time on the CO_2 conversion, (2) playing with the plasma pulse duration and frequency allows to investigate the influence of processes with different characteristic times while being able to measure the cumulative effect of multiple pulses on the dissociation fraction. Therefore, in addition to pressure and current, in this chapter we have varied the pulse duration, pulse frequency and the initial gas mixture. Note that in static conditions the ratio between molecules in gas phase and molecules adsorbed in the surface is fixed, contrary to the case of flowing conditions, where the renewal of the gas affects the balance between gas phase and surface species. In the range of pressures and working in static conditions, the surface may affect the evolution of the dissociation fraction and a careful measurement procedure was developed to obtain reproducible results.

We performed "building-up" experiments in two types of discharges: a pulsed DC glow discharge and a pulsed capacitively coupled radio frequency (RF) discharge. The glow discharge has several advantages previously described, including the straightforward determination of the electric field and an easy estimation of the electron density. These parameters were required for the experimental validation of the direct electron impact dissociation cross section of CO_2, an important result of this chapter (see section 6.4), and for the comparison with a 0D kinetic model. However, the ignition of the pulsed DC glow discharge in the "building-up" experiment may become unstable, particularly for higher pressures and low currents. Therefore, a broader parametric study was done using the RF discharge, more stable in a wider range of conditions. The RF discharge does not allow an easy quantification of the electric field but it provides significant qualitative results.

This chapter is organized as follows: An introductory part describing the experimental set-up, the measurement procedure and the data treatment process, common for both types of discharges. The second part will focus on the experimental results obtained in the RF discharge. Finally, the experimental data obtained with the glow discharge will be used to estimate the electron impact dissociation cross section of CO_2 and for the comparison with a 0D kinetic model.

6.2 Description of the experiment and experimental set-up

6.2.1 Experimental set-up

Both the glow and the RF discharges were generated in a reactor of similar configuration, a cylindrical Pyrex tube of 2 cm inner diameter and 23 cm length, positioned in the sample compartment of the FTIR spectrometer. The experimental set-up in the RF version is shown schematically in figure 6.1. For the glow discharge experiment the set-up is similar substituting the RF generator, RF probe and match box by a pulsed DC power supply, and the RF reactor by the usual glow discharge tube. The gas line around both plasma reactors remained the same. A buffer volume including a by-pass valve is connected to the reactor by two glass pipes through two Teflon valves, minimizing as a much as possible the dead volume. After setting the pressure in the buffer + reactor volume and before starting the building-up experiment, these valves are closed, isolating the gas contained in the plasma reactor from the rest of the gas line. The buffer volume allows a fine adjustment of the pressure in the reactor but its main purpose is the preparation of appropriate gas mixtures for isotopic measurements that will be described in chapter 7. The pressure, varied between 0.5 and 5

Torr, was measured with a pressure gauge placed in the upstream part of the by-pass valve in the buffer volume. The RF power was varied between 40 and 80 W (reading of the RF generator). The real power dissipated in the RF can be determined after using the subtractive calibration method (see section 2.2.2). More information about the discharge set-ups can be found in section 2.2. A summary of the experimental details is given in the experimental box 6.1.

Diagnostics: FTIR (Thermal)	**Reactor**: Short (23 cm)	**Pressure**: **0.4-5** Torr
Discharge: RF & glow	$\boldsymbol{T_{wall}}$=not controlled	**Current (glow)**: **10-50** mA
Pulse: variable t_p^{ON}, t_p^{OFF}, N_p, etc. (Table 6.1)	**Flow**: 0 (Static)	**Power (RF)**: **40-80** W (reading)

Experimental box 6.1: General experimental conditions for the building-up experiment.

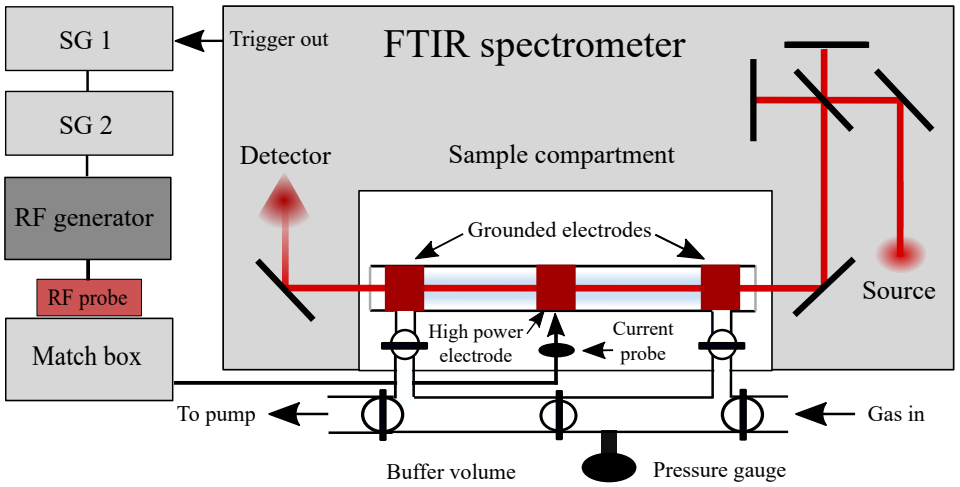

Figure 6.1: Schematic representation of the experimental set-up used for the RF experiments. SG: Signal generator

6.2.2 Protocol for building-up experiments

The reactor is filled with pure CO_2 at the targeted pressure and closed. Before any plasma an IR absorption spectrum is taken. Subsequently a trigger signal provided by the FTIR working in Rapid Scan mode, triggers a train of plasma pulses whose characteristics are defined by two signal generators (SG): SG1, triggered by the FTIR, defines the number of pulses within a train by adjusting the gate duration; SG2, gated by SG1, controls the pulse duration and the delay between pulses within a train, and triggers the RF generator or the DC pulsed power supply. After each train of plasma pulses, an IR absorption measurement with the plasma OFF (gas in thermal equilibrium) is acquired with a mirror scan speed of 80 KHz, before the next TTL trigger is sent to SG1.

The default train configuration is 10 pulses of t_p^{ON}=5 ms plasma ON and t_p^{OFF}=10 ms plasma OFF, similar to the reference pulse duration studied in chapter 4, which corresponds to a total plasma ON time per train $t_{tr}^{ON} = \sum t_p^{ON}$= 50 ms. This procedure is repeated until the total accumulated plasma ON time $T^{ON} = \sum t_{tr}^{ON}$ is around 25 s (500 trains), long enough to reach the

steady-state equilibrium for all the conditions studied. Other pulse configurations will be studied and are detailed in following sections. Table 6.1 summarizes the notation used to define the pulse characteristics for all the experiments. The measurement procedure is schematically presented in figure 6.2 (a) ("Measurement" box) and (b). In order to run the experiment without gas flow, two preliminary steps must be carefully followed: (1) adjustment of the RF power or DC voltage/current conditions and (2) pre-treatment of the reactor walls.

- **RF power or DC current/voltage adjustment**: In both RF or glow discharge experiments, the operating conditions have to the adjusted in advance (before the pre-treatment process, see next step). In the case of the RF, the optimal functioning point of the match box varies with the pressure and the gas mixture. The reactor is filled and closed at the measurement conditions. Under continuous plasma at the targeted power, the matching is adjusted by tuning the load and tune capacitors until the reflected power measured by the RF probe is zero. For the glow discharge, we need to ensure the stability of the discharge. Therefore, the reactor is filled and pulse series similar to the "real building-up" experiment are ignited. The pulse DC power supply was set to work in current limitation, whereas the voltage was carefully set slightly higher than the voltage limitation value. A too high over-voltage lead to a significant over shoot in the discharge current when starting the measurement. On the contrary if the over-voltage was too low, the plasma showed problems to re-ignite after the absorption measurements, especially when the amount of CO in the discharge tube is large and for high pressures and low currents. After the adjustment step, the reactor was pumped and the power supply settings remained untouched.
- **Pre-treatment of the reactor wall**: It consists of two steps: a first step of 15 minutes of pure O_2 continuous plasma (RF or DC) at 1.5 Torr (maximum of O atom density in similar experimental conditions *Booth et al.* [2019]), 40 W/40 mA, in flowing conditions (7.4 sccm gas flow), followed by 10 minutes of CO_2 gas flow (no plasma) at similar pressure and flow. These steps are summarized in figure 6.2 (a) ("Pre-treatment" box). In order to keep the power supply settings set in the "adjustment step", for the pre-treatment of the glow discharge reactor another power supply was used to ignite the continuous O_2 plasma. In the range of pressures studied (between 0.4 and 5 Torr) and working in static conditions, the initial surface state of the reactor walls was found to influence the final steady-state ("plateau") value, probably due to slow chemical reactions at the surface, leading to non-reproducibility issues. The choices made for the two steps of the pre-treatment can be debatable (and have certain consequences that will be briefly discussed in section 6.3.2), but the objective of the pre-treatment step is to start always from the same surface conditions. This procedure made possible to achieve very good reproducibility (shown below).

After the pre-treatment step, the reactor is filled again with the investigated gas mixture and closed. The measurement starts following the method defined to control the FTIR working in Rapid Scan mode and the pulse configuration defined by the signal generator, as shown schematically in figure 6.2 (a) ("Measurement" box). The default train configuration is summarized in the experimental box 6.2. Note that the total "measurement" time per train of plasma pulses is around 2.08 seconds, which includes the time the FTIR waits for the ignition of the train of plasma pulses (500 ms), the "settings" time of the FTIR and the real scanning time (*i.e.* the time required by the

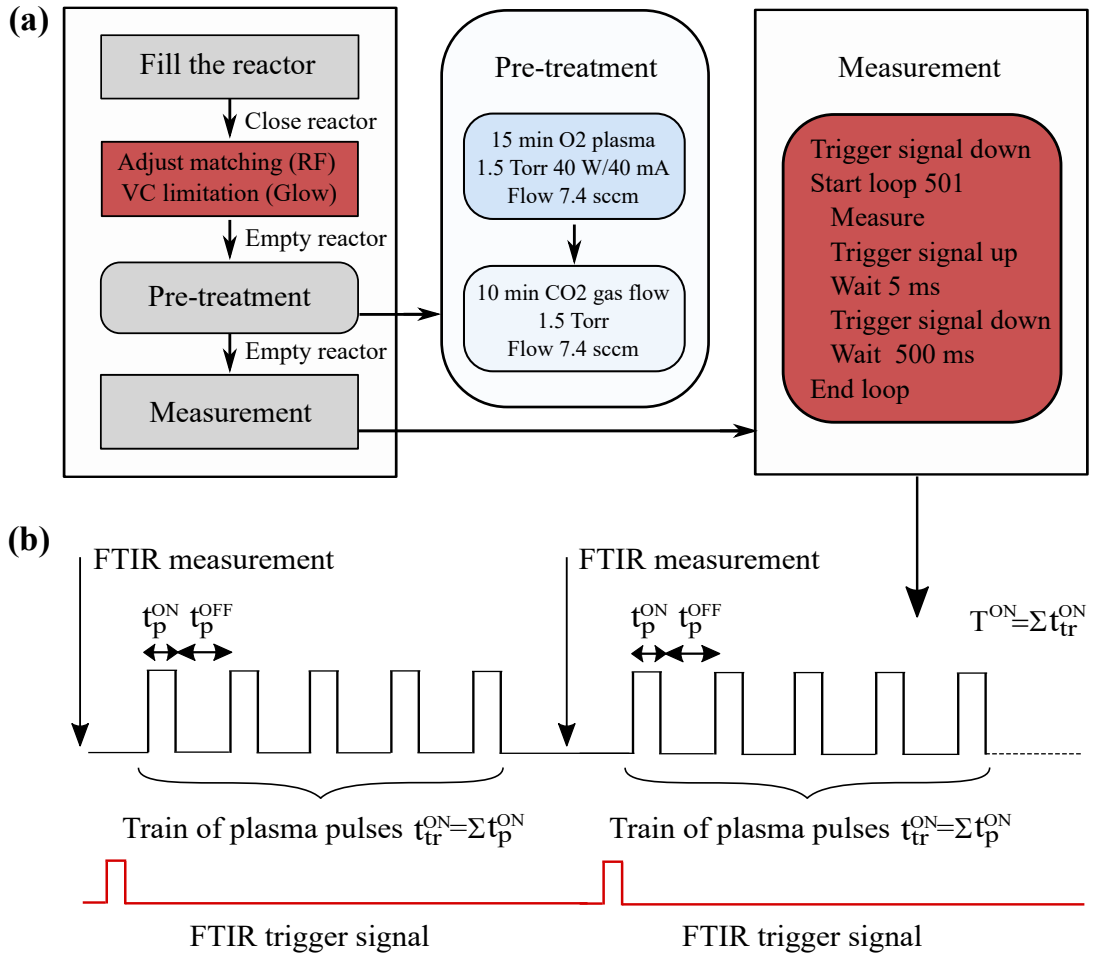

Figure 6.2: (a) Complete experimental procedure and (b) detail of the FTIR measurement.

mirror of the FTIR to scan the whole wavelength range, ∼1 s at 80 kHz). Therefore the OFF time in between consecutive trains is roughly 1.5 s. The total experiment time is around 17 minutes for each plasma condition. The influence of the measurement time and the choice of the experiment parameters will be briefly discussed in section 6.3.1.

Symbol	Definition
N_p	Number of pulses per train of plasma pulses
N_{tr}	Total number of trains of plasma pulses
t_p^{ON}	Pulse duration (plasma ON)
t_{tr}^{ON}	Total plasma ON time per train of plasma pulses $t_{tr}^{ON} = \sum t_p^{ON} = N_p \cdot t_p^{ON}$
t_p^{OFF}	Delay between consecutive plasma pulses (plasma OFF)
t_{tr}^{OFF}	Total plasma OFF time per train of plasma pulses $t_{tr}^{OFF} = \sum t_p^{OFF} = N_p \cdot t_p^{OFF}$
T^{ON}	Total plasma ON time in the experiment $T^{ON} = \sum t_{tr}^{ON} = N_{tr} \cdot t_{tr}^{ON}$

Table 6.1: Parameters defining the pulse characteristics for a “building-up” experiment.

Reference pulse configuration:
- **Pulse**: 5-10 ms On-Off ($t_p^{ON} - t_p^{OFF}$)
- N_p: 10 pulses per train
- N_{tr}: 500 trains
- t_{tr}^{ON}: 50 ms total plasma ON per train
- t_{tr}^{OFF}: 100 ms total plasma OFF per train
- T^{ON}: 25 s total plasma ON per experiment

* **Notation → (500)×10×5-10 ms On-Off**

Experimental box 6.2: Description of the reference pulse configuration.

6.2.3 Data treatment

The IR absorption spectra is fitted with a Matlab script that considers only gas mixtures in thermal equilibrium, described in section 2.3.1, *i.e.* the script does not take into account any vibrational excitation. The determination of the molecular densities of the different species is in this case more accurate (less fitting parameters). In addition, the IR spectra are measured during the post-discharge and the characteristic time of the relaxation of the vibrational excitation is significantly shorter than the time scales attainable with the Rapid Scan mode. Figure 6.3 shows an example of the output of the fitting corresponding to a measurement taken at 5 Torr 40 W. The fit provides directly number densities off all the molecules included in the script (figure 6.3, (a)) along with

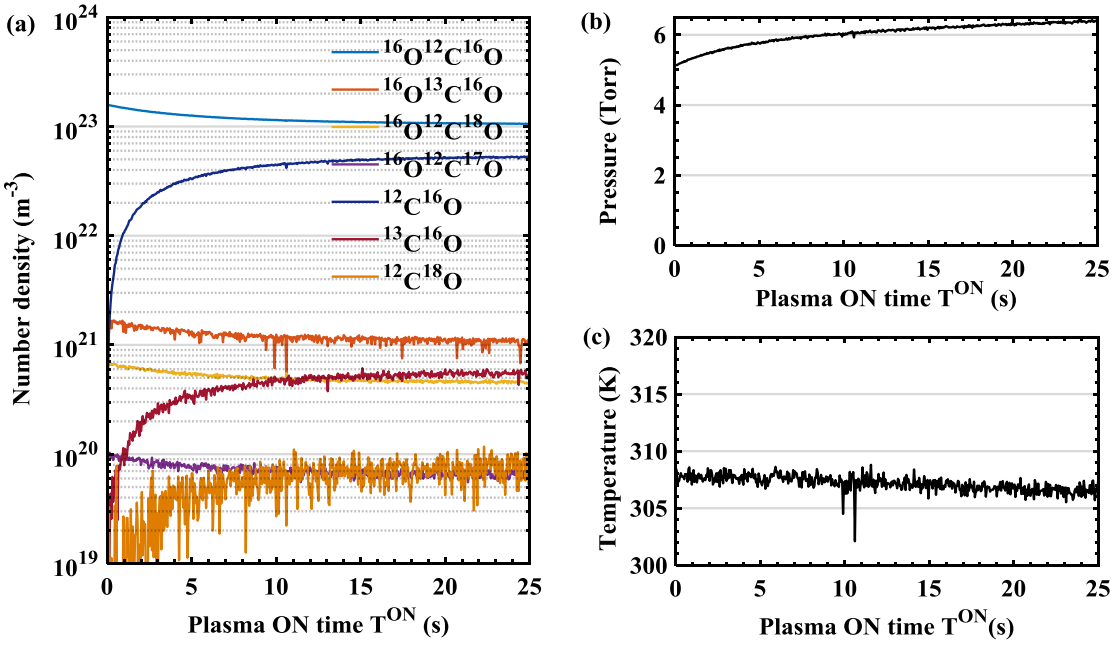

Figure 6.3: Example of the output of the fitting script obtained for a measurement in the RF discharge at 5 Torr 40 W. (a) Time evolution of the number densities of all the molecules (isotopologues of CO_2 and CO) included in the fitting as a function of the total plasma ON time T^{ON}, (b) and (c) fitted pressure and gas temperature in the same condition

the pressure (figure 6.3, (b)) and the gas temperature (figure 6.3, (c)). As expected the pressure is increasing with the dissociation of CO_2 into CO and O_2 while the gas temperature measured during the post-discharge remains close to room temperature.

The script was adapted to include several isotopologues of CO_2 and CO (more details will be given in chapter 7). The version used to treat the experimental data in this chapter includes four isotopologues of CO_2: $^{16}O^{12}C^{16}O$, $^{16}O^{13}C^{16}O$, $^{16}O^{12}C^{18}O$ and $^{16}O^{12}C^{17}O$, and three isotopologues of CO: $^{12}C^{16}O$, $^{13}C^{16}O$ and $^{12}C^{18}O$. These isotopologues were included because their natural abundance in the CO_2 gas bottle used (Air Liquide, Alphagaz 1), is such that their contribution to the IR spectra is clearly distinguishable and therefore can be fitted. Not taking them into account seriously disturbs the fitting. In figure 6.3 (c), it is noticeable that all the isotopologues of CO_2 and of CO follow the same variation as a function of the total plasma ON time. Other isotopologues, included for the measurements with isotopically marked species (see chapter 7) are only at the noise level for the measurements presented in this chapter. Therefore, they are not taken into account here to avoid increasing the fitting error. The script also accounts for the possibility of gas mixtures with other gases not infra-red active by introducing a dilution factor.

The pressure in the script is calculated from the initial pressure and taking into account the dissociation measured. It also includes the effect of the leak rate, which tends to increase the pressure in the reactor. As in any system under vacuum a small leak is unavoidable. This leak was verified to come from the purge chamber around the IR beam and the reactor windows, set to avoid absorption of the IR beam by CO_2 from the room. The leak consist therefore in pure N_2 (no CO_2 was found in the spectra after the leak test, discarding a leak of air from the room) and was estimated to be approximately 0.5 Torr/hour (~0.15 Torr during the experiment). The pressure at the end of experiment was also measured thanks to a calibration of the volume of the reactor and buffer volume. After experiment, the buffer volume was pumped and closed again. The Teflon keys closing the reactor were open and the gas from the reactor filled the reactor+buffer volume, allowing a measurement of the pressure. The measured pressures were found to match the pressures given by the fitting script with an error <8%.

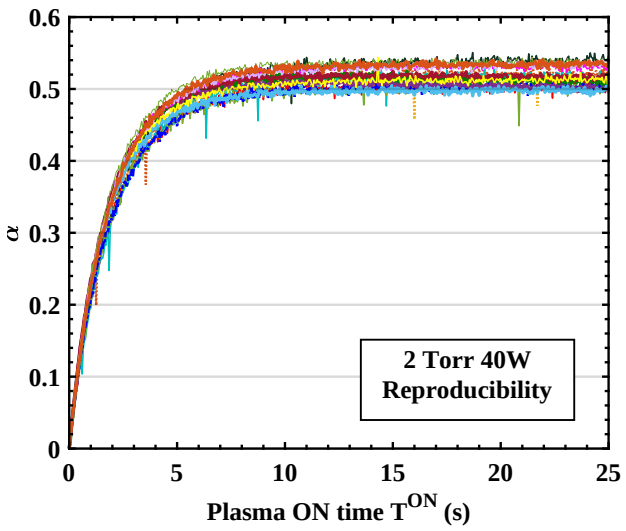

Figure 6.4: Reproducibility tests for the time evolution of the dissociation fraction α taken for the same condition (2 Torr, 40 W RF power) on different days.

For the analysis of the experimental results, we will look mostly at the dissociation fraction represented by the parameter $\alpha = {}^{CO}/_{CO+CO_2}$. Figure 6.4 shows the evolution of this parameter as a function of the total (accumulated) plasma ON time T^{ON}. The graph superimposes multiple measurements in the same condition, 2 torr, 40 W, measured on different days, to give an idea of the reproducibility of the experiment. Systematically, every time a parameter is scanned, a test measurement for the reference pulse condition (see experimental box 6.2) is taken at 2 or 5 Torr to check the reproducibility. The general trend for every plasma condition presents an initial fast increase followed by a saturation towards longer total plasma ON times. Small "artefact peaks" can be noticed along the time evolution of α, which do not affect the overall trend. These peaks are caused by mis-fitting induced by the inclusion of isotopes with low densities (see figure 6.3 (a)).

Teflon keys are used in both RF and DC discharge tubes to isolate the reactor and to be able to work in static conditions. The valves are placed relatively close to the plasma, in order to minimize the dead volume. Moreover, CaF_2 IR windows mounted with Teflon rings in the RF case, or glued with VacSeal in the glow discharge reactor, are also in the vicinity of the discharge. In static conditions, these two set-up details could be a source of pollution, for instance due to oxidation of these materials by the O atoms produced in the discharge. To evaluate this pollution and compare it with the measured CO_2 and CO densities in the experiments, several tests were carried out with both RF and DC discharges consisting in running a full building-up measurement but in pure O_2 at 1.5 Torr, to maximize the possible oxidation of the Teflon keys and rings. These tests showed that the sum of CO and CO_2 molecules created after the O_2 plasma represented only 0.47% and 0.51% of the total gas density for the RF and the glow discharge respectively. Hence, the contribution of possible pollution was considered negligible.

6.3 RF discharge results

This section presents the experimental results obtained with the RF discharge. Several parameters such as pressure, power or pulse configuration were varied to study their impact on the time evolution of the dissociation fraction, α. Additionally, several gas mixtures were investigated: CO_2-O_2, CO-O_2, CO_2-Ar and CO_2-N_2, with the purpose of changing respectively the initial oxygen content, the electron energy or the influence of vibrational excitation of CO_2 molecules.

6.3.1 Pure CO_2 plasma

Pressure and power variation

Figure 6.5 presents the temporal evolution of the dissociation fraction α as a function of the total plasma ON time, T^{ON}, for the reference pulse configuration, *i.e.* N_{tr}=500 trains × N_p=10 pulses per train × t_p^{ON}=5 ms plasma ON - t_p^{OFF}=10 ms plasma OFF per pulse for different pressures and powers. The graph to the left (figure 6.5 (a)) shows the effect of the initial pressure for the same imposed RF power, 40 W. The graph to the right (figure 6.5 (b)) shows the effect of the RF power for two pressures, 2 and 5 Torr. Note that according to the RF power calibration shown in section 2.2.2, the power values imposed by the generator (40, 60 and 80 W) correspond to real values of power transmitted to the plasma of ∼27.7, 36.3 and 44.2 W respectively, with an estimated error ∼20%. For simplicity, all along this chapter and the following one we keep the notation of the imposed power.

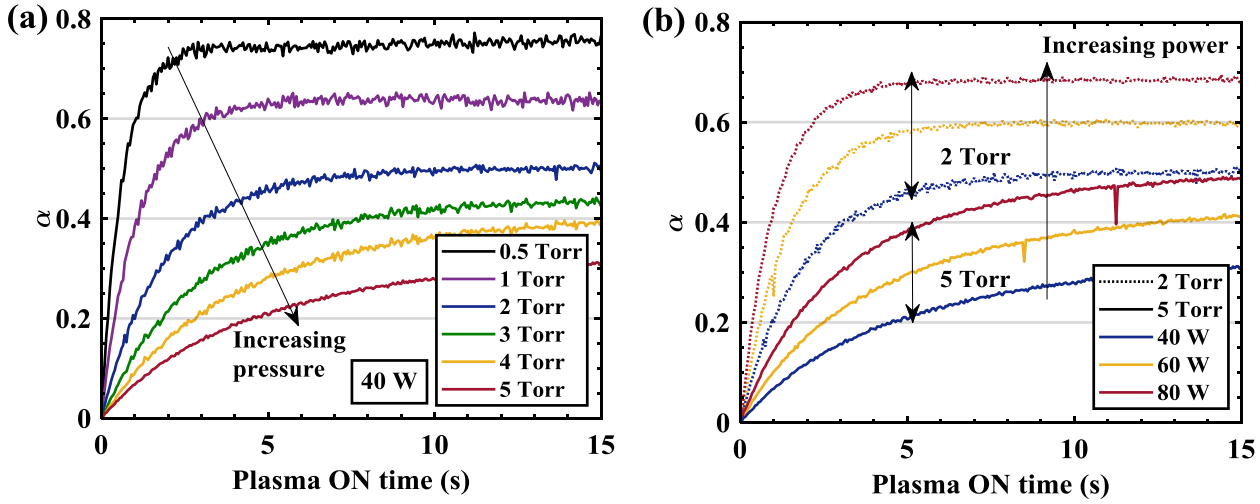

Figure 6.5: Time evolution of the dissociation fraction α as a function of the total plasma ON time T^{ON} for: (a) different initial pressures from 0.5 to 5 Torr for the same RF power, 40 W, and (b) for different RF powers between 40 and 80 W for two pressures, 2 and 5 Torr

Pressure and power have a clear impact in the time evolution of the dissociation fraction, both in the kinetic evolution at the beginning of the experiment and in the final dissociation value. In figure 6.5, as well as in figure 6.4, we can distinguish three time "regions" schematically represented in figure 6.6:

1. "Initial slope": for short plasma ON times (until $T^{ON} \sim 0.3{,}1$ s) α follows a ~linear evolution with T^{ON} (straight line in linear scale).
2. "Turning region" shows an exponential-like variation (~linear variation in logarithmic scale),

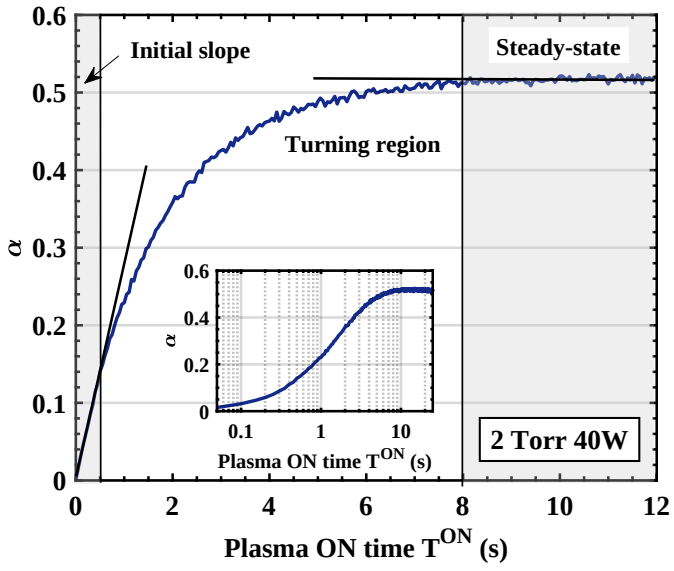

Figure 6.6: Time evolution of the dissociation fraction α as a function of the total plasma ON time T^{ON} (only up to T^{ON}=12 s) for 2 Torr 40 W, pointing out three different regions discussed in the current and following sections. The inner figure shows the same data in log scale up to T^{ON}=25 s.

followed by a transition to the next region.

3. Final steady-state equilibrium ("plateau") where the dissociation fraction remains constant as a function of time.

The time-points for which every region is reached depend strongly on both pressure and power. In general, lower pressures and higher powers lead to a faster evolution of the gas mixture: The initial slope is steeper and the gas composition reaches the final steady-state for shorter T^{ON}. At higher pressures a significantly slower evolution of the gas mixture is observed. As an example, at 0.5 Torr, the lowest pressure studied, the gas reaches the chemical equilibrium after $T^{ON} \sim 2.5$ s while at 5 Torr it requires up to T^{ON} ~25 s (not shown) to reach the steady-state. When the steady-state ("plateau") value is reached, even though the gas continues receiving plasma pulses, the chemical composition does not evolve any more because dissociation and recombination processes are balanced.

Figure 6.7 panel (a) shows the slope values calculated with the data for the first 0.3 s of plasma ON time and panel (b) plots the steady-state dissociation value, calculated as the average of the α values between T^{ON}=20 s and T^{ON}=25 s for the different plasma conditions in figure 6.5. The variation of initial slope as a function of pressure resembles the variation of the reduced electric field observed in the glow discharge (see figure 3.11). In the glow, the electric field increases as a function of pressure but the reduced electric field still decreases due to the increase of gas density. Even though the electric field has not been measured in the RF, a similar behaviour is expected. Increasing the power makes the time evolution faster, *i.e.* increases the slope. However, the impact on the initial slope is smaller at 5 Torr than at 2 Torr due to smaller increase in the energy density.

The final steady-state value of α decreases significantly as a function of pressure, more than a factor of 2 between 0.5 and 5 Torr, and increases with power. This dependence can be partly explained by the decrease of the reduced electric field, but also by the decrease in the specific

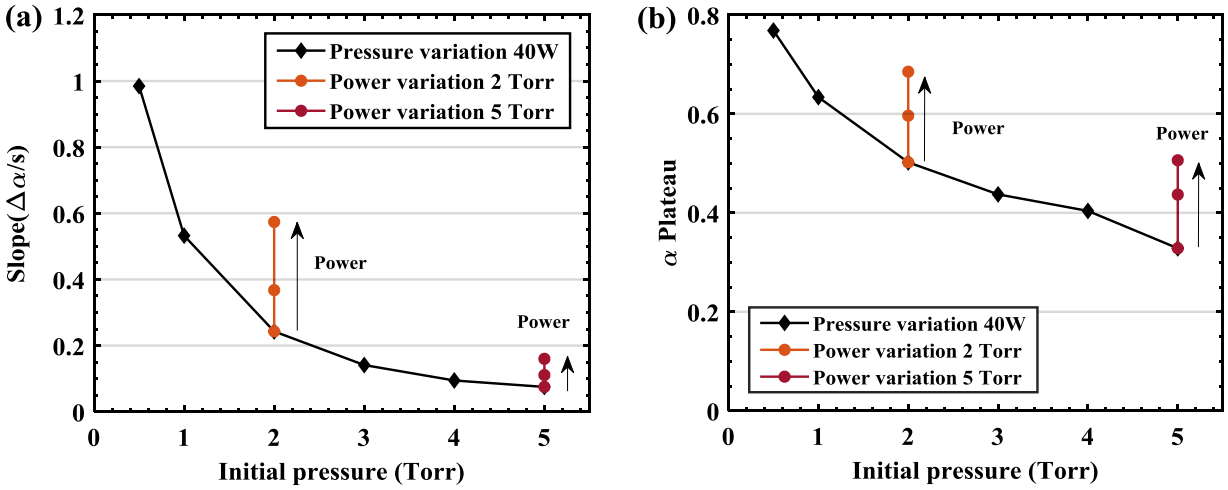

Figure 6.7: (a) Variation of the initial slope, calculated up to T^{ON}=0.3 s, and dissociation fraction at the steady-state (α(plateau)), calculated as the average of the α values between T^{ON}=20 s and T^{ON}=25 s (not shown in figure 6.5) as a function of the initial pressure for 40 W imposed power (~27.7 W real transmitted power) for all the pressures and, additionally, for 60 and 80 W imposed power (~36.3 and 44.2 W real transmitted power, respectively) for 2 and 5 Torr.

energy input per molecule (SEI). The total gas density increases with pressure and, consequently, for similar power and plasma ON time, the SEI decreases. The relation between the dissociation fraction at the "plateau" and the power is basically linear with a similar effect for both pressures studied. Electric field and electron density measurements in the RF discharge would be helpful to differentiate the effect of possible electric field variation from the change in energy density, and would allow a more detailed comparison with the glow discharge. Nevertheless, the measurements in the RF are qualitatively in good agreement with the trends observed in the glow.

The variation of the dissociation fraction with pressure and power suggests that the dissociation process is strongly controlled by the electron kinetics through electron impact dissociation, which, in any case, should be one of the main dissociation mechanisms in our experimental conditions. However, the effect of vibrational excitation of CO_2 molecules could contribute to the measured dissociation fraction either through vibrational up-pumping mechanism or due to electron impact on vibrationally excited molecules. In the following section the effect of the vibrational excitation on the time evolution of the dissociation fraction is investigated by varying the pulse series configuration.

✓ Three time regions are observed in the time evolution of the dissociation fraction: initial slope, "turning region" and steady-state equilibrium.
✓ Both the initial slope and α(plateau) decrease with pressure but increase with the discharge power.

Pulse duration (t_p^{ON}) and delay between pulses (t_p^{OFF}) variation

Playing with the pulse configuration within a train of pulses can provide an insight in the role of the vibrational excitation or the gas temperature on the time evolution of α, since the characteristic times of excitation and relaxation of the temperatures T_{rot}, $T_{1,2}$, T_3 and T_{CO} are different. Only preliminary time-resolved measurements in flowing conditions (similar to those discussed in chapter 4) were done in the RF discharge, to confirm that the time evolution of the vibrational excitation of CO_2 and CO follows similar trends as those observed in the glow discharge. Figure 6.8 shows the evolution of T_{rot}, $T_{1,2}$, T_3 and T_{CO} along a plasma pulse of 5-10 ms On-Off, similar to the reference pulse configuration, detailed in the experimental box 6.2, for the glow discharge (panel (a)) and the RF(panel (b)) at 5 torr, 50 mA and 40 W respectively. RF measurements are noisier, increasing the error for all temperatures shown in figure 6.8 (b) compared to the glow discharge, especially for T_{CO}. Nevertheless, except for the larger difference between T_{CO} and T_3, the evolution of temperatures is remarkably similar in the RF and the glow. In particular, the overshoot of T_{CO} and T_3 before 1 ms of plasma pulse and the slower increase of T_{rot} and $T_{1,2}$ over the 5 ms of the pulse are observed for both discharges. The similarities between glow and RF discharges allow us to interpret the effect of t_p^{ON} and t_p^{OFF} variation in the RF based on the time evolution already studied in the glow discharge.

Figure 6.9 shows, as a reminder, the traces measured in the glow for the two pressures that will be studied in this section, 2 and 5 Torr, at 50 mA. In this figure, the vertical bars show some of the values of pulse duration t_p^{ON} (in red) or delay between pulses t_p^{OFF} (in blue) that will be analysed along this section, as detailed in table 6.2. It is clear that varying the pulse duration or the delay between pulses in the range of a few milliseconds, will allow us to play with the average level of

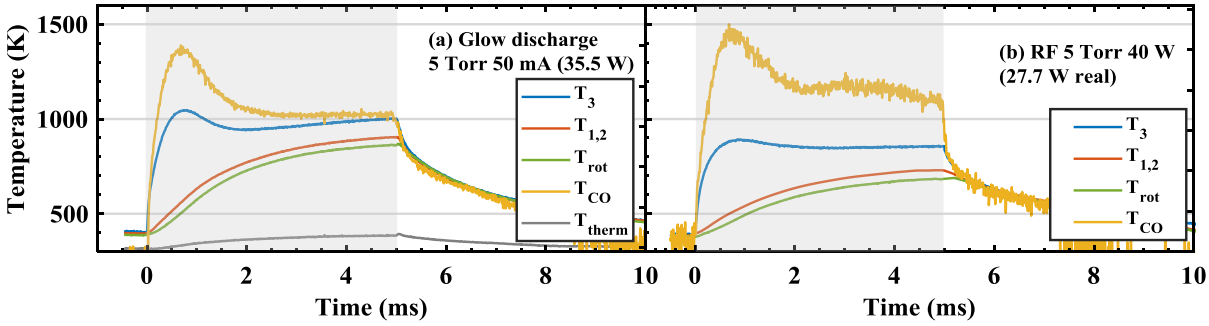

Figure 6.8: Time evolution of the rotational temperature T_{rot} and the vibrational temperatures of CO_2 and CO, $T_{1,2}$, T_3 and T_{CO}, along a plasma pulse of 5-10 ms On-Off ignited in a glow discharge at 50 mA (panel (a)) and in the RF at 40 W (panel (b)), in flowing conditions (7.4 sccm gas flow) at a pressure of 5 Torr.

vibrational excitation or to study the effect of the gas temperature. A brief summary of the key points to be kept in mind concerning the variation of these parameters is the following:

- The vibrational excitation of T_3 and T_{CO} shows a maximum around 0.7-1 ms after the beginning of the pulse. Therefore, short pulses provides higher non-equilibrium conditions, $\uparrow T_{3,CO}$ and $[T_{3,CO}\text{-}T_{rot}]$, compared to longer pulses. Moreover $T_{3,CO}$ and $[T_{3,CO}\text{-}T_{rot}]$ are higher at 2 Torr than at 5 Torr.
- T_{rot} and $T_{1,2}$ increase along pulse duration t_p^{ON} and are higher at 5 Torr. Longer pulses have higher average T_{rot} values.

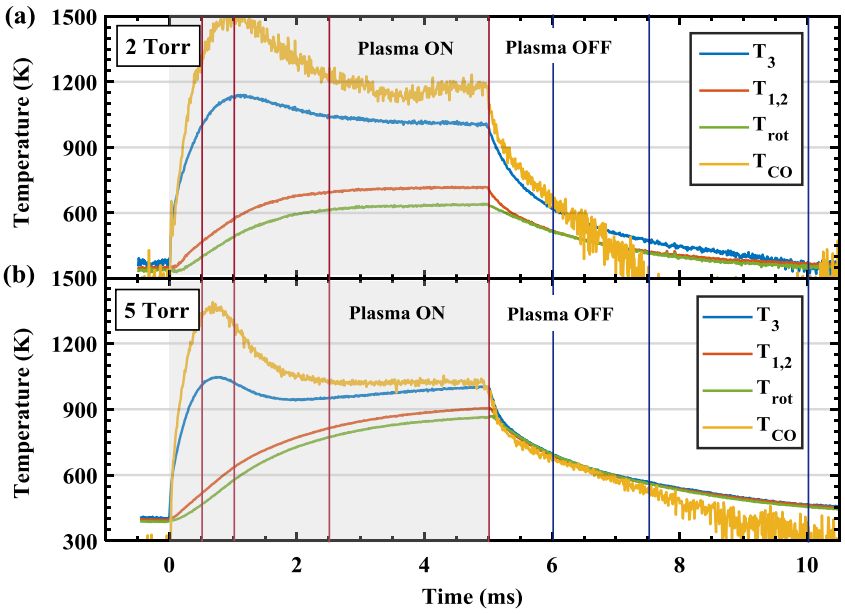

Figure 6.9: Time evolution of the rotational temperature T_{rot} and the vibrational temperatures of CO_2 and CO, $T_{1,2}$, T_3 and T_{CO}, along a plasma pulse of 5-10 ms On-Off ignited in a glow discharge at 50 mA for two pressures: 2 Torr (top graph, (a)), and 5 Torr (bottom graph, (b)). Vertical lines indicate times points of interest for the pulse duration (red lines) and delay between pulses (blue lines) variation experiments with the RF.

- After the end of the pulse, for short delay times (1, 2.5 ms), T_{rot} and T_{vib} do not relax completely before the next pulse starts. When the plasma is switched on again it re-starts in a gas that is at higher temperature than room temperature for both pressures and out of equilibrium at 2 Torr (see effect in section 4.4.3). As example, at 2 Torr, for t^{OFF}=1 s, T_3=T_{CO}=600K but T_{rot}=$T_{1,2}$ 500K. At 5 Torr T_{vib}=T_{rot}=700K.
- For delay times of 5 ms or longer, all the temperatures have relaxed completely down to room temperature before the next pulse starts.

Note that these measurements were obtained for a certain dissociation degree, however in the building-up experiment the dissociation fraction changes for every pulse, particularly for short T^{ON}. For the first pulses, the time evolution of the rotational and vibrational temperatures should be closer to the "single pulse" measurement. It is also worth remembering that the life-time of the O atoms is in the order 50-100 ms under plasma exposure depending on the plasma conditions (see figure 3.5.4). These values are only slightly lower in post-discharge for CO_2 plasmas (see chapter 8) implying that at least part of the O atoms created in each pulse will accumulate and the O atom density can increase during a train of pulses. However these O atoms recombine mostly into O_2, and/or possibly into CO_2, during the plasma OFF time in between trains ($\sim$ 1.5 s).

Other exited species, such as electronically excited atoms or molecules like $CO(a^3\Pi_r)$, $O_2(a^1\Delta_g)$, $O_2(b^1\Sigma_g^+)$, $O(^1D)$, $O(^1S)$, etc. can be created by electron impact excitation or dissociation during the pulse. Some of them, meta-stable states, may have a relatively long life-time such as $O_2(a^1\Delta_g)$ *Schweitzer and Schmidt* [2003] or $CO(a^3\Pi_r)$ *Mori et al.* [2002]; *Gilijamse et al.* [2007]. However, the rates for the quenching of these states are high, in the order of 10^{-11} cm^3s^{-1} *Young and Black* [1967]; *Davidson et al.* [1978]; *Cenian et al.* [1994]. A build up of their densities during a train of plasma pulses for short t_p^{OFF} times can not be discarded but they certainly de-excite/recombine in between trains.

In summary, we can consider that within a train the density of O atoms and maybe some meta-stable states can increase, but between trains they will recombine and/or de-excite. When the next train begins, we re-start from a gas mixture of CO_2 + CO + O_2, all in ground state and at room temperature, as shown by the fitting of the gas temperature shown in figure 6.3 (c).

Pulse variation experiments

Figures 6.10 and 6.11 present in linear time scale (plots (a), (c) and (e)) and logarithmic time scale (plots (b), (d) and (f)) the time evolution of the dissociation fraction, α, as a function of total plasma ON time, T^{ON}, for 2 and 5 Torr respectively, in three experimental cases:

1. Top panels ((a) and (b)) show the variation of the pulse duration t_p^{ON} keeping constant the plasma OFF time in between pulses, t_p^{OFF}=10 ms.
2. Middle panels ((c) and (d)) show pulse duration t_p^{ON} variation but keeping constant the duty cycle ratio (DCR, t_p^{ON}/t_p^{OFF}).
3. Bottom panels ((e) and (f)) present the data obtained varying the plasma OFF time (delay) in between pulses, t_p^{OFF}, for a fixed pulse duration t_p^{ON}=5 ms.

All the data in figures 6.10 and 6.11 were taken keeping constant the total plasma ON per train t_{tr}^{ON}=50 ms, the number of trains N_{tr}=500, and the total plasma ON time T^{ON}=25 s. A detailed

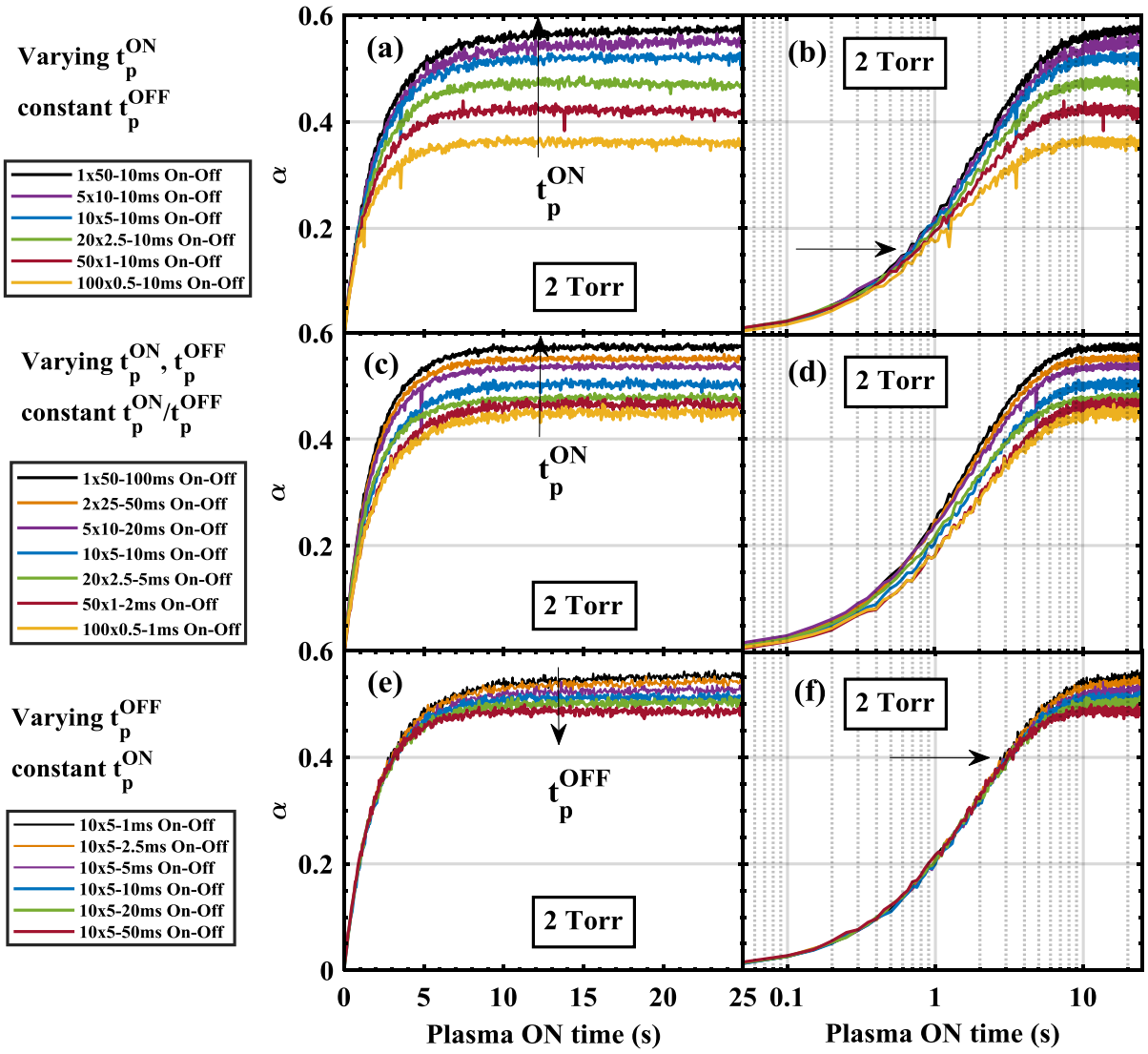

Figure 6.10: Time evolution of the dissociation fraction α as a function of the total plasma ON time T^{ON} in linear time scale (panels (a), (c) and (e)) and logarithmic time scale (panels (b), (d) and (f)) measured at 2 Torr, 40 W. Graphs (a) and (b) present data for different pulse duration (t_p^{ON}) but same delay between pulses (t_p^{OFF}), panels (c) and (d) present data for different pulse duration (t_p^{ON}) but same duty cycle ratio (t_p^{ON}/t_p^{OFF}) and graphs (e) and (f) present data for different delay times between pulses (t_p^{OFF}) but the same pulse duration (t_p^{ON}). The number of pulses N_p is varied to keep always the same plasma ON per train (t_{tr}^{ON}).

description of the different times involved in each experiment is given in table 6.2. Several general observations can be made about these results:

- The initial slope (T^{ON} <∼0.5 s) is the same for any pulse configuration.
- Both t_p^{ON} and t_p^{OFF} have a strong effect on the "turning region" and consequently on the final dissociation fraction at the "plateau".
- An increase of the pulse duration t_p^{ON} leads to a significant increase of the dissociation fraction α at the "plateau", both when the t_p^{OFF} is kept constant (panels (a) and (b)) and when it is varied to keep the duty cycle ratio t_p^{ON}/t_p^{OFF} and t_{tr}^{OFF} constant (panels (c) and (d)).
- The increase of α with t_p^{ON} is more important for constant t_p^{OFF} than for constant t_p^{ON}/t_p^{OFF}.
- An increase of t_p^{OFF}, *i.e.* longer delay between pulses, leads to a decrease of α(plateau) (panels (e) and (f)).
- At 2 Torr, the time T^{ON} at which the curves diverge in t_p^{ON} variation experiments is clearly shorter, T^{ON}∼0.5 s, compared to the time at which they diverge in the t_p^{OFF} variation experiment, T^{ON} ∼3 s.
- The time at which the effect of varying t_p^{ON} becomes noticeable is similar at 2 and 5 Torr, but the effect of varying t_p^{OFF} happens earlier at 5 Torr T^{ON} ∼0.5-1 s.

Concerning the initial slope, it is noticeable that for short total plasma ON times (typically T^{ON} <∼ $0.5s$), the evolution of the dissociation fraction with time is *quasi* linear and it remains unchanged for any pulse configuration, *i.e.* only the initial pressure and power affect the initial slope. This behaviour can be explained by a first-order dissociation process, the electron impact dissociation of CO_2: $e^- + CO_2 \rightarrow CO + O$, which can be described by the first-order rate equation:

$$\frac{d[CO]}{dt} = K_{diss} \cdot n_e \cdot [CO_2] \rightarrow [CO] = n_e \cdot K_{diss} \cdot [CO_2] \cdot T^{ON}, \tag{6.1}$$

Varying t_p^{ON} constant t_p^{OFF}

Notation	N_p	t_p^{ON}	t_p^{OFF}	t_{tr}^{OFF}
1x50-10	1	50	10	10
5x10-10	5	10	10	50
10x5-10	10	5	10	100
20x2.5-10	20	2.5	10	200
50x1-10	50	1	10	500
100x0.5-10	100	0.5	10	1000

Varying t_p^{OFF} constant t_p^{ON}

Notation	N_p	t_p^{ON}	t_p^{OFF}	t_{tr}^{OFF}
10x5-1	10	5	1	10
10x5-2.5	10	5	2.5	25
10x5-5	10	5	5	50
10x5-10	10	5	10	100
10x5-20	10	5	20	200
10x5-50	10	5	50	1000

Varying t_p^{ON} & t_p^{OFF}, constant t_p^{ON}/t_p^{OFF}

Notation	N_p	t_p^{ON}	t_p^{OFF}	t_{tr}^{OFF}
1x50-100	1	50	100	100
2x25-50	2	25	50	100
5x10-20	5	10	20	100
10x5-10	10	5	10	100
20x2.5-5	25	2.5	5	100
50x1-2	50	1	2	100
100x0.5-1	100	0.5	1	100

Table 6.2: Pulse parameters used in the experiments presented in figures 6.10 and 6.11. t_{tr}^{ON}=50 ms, N_{tr}=500 and T^{ON}=25 s are constant for all the experiments.

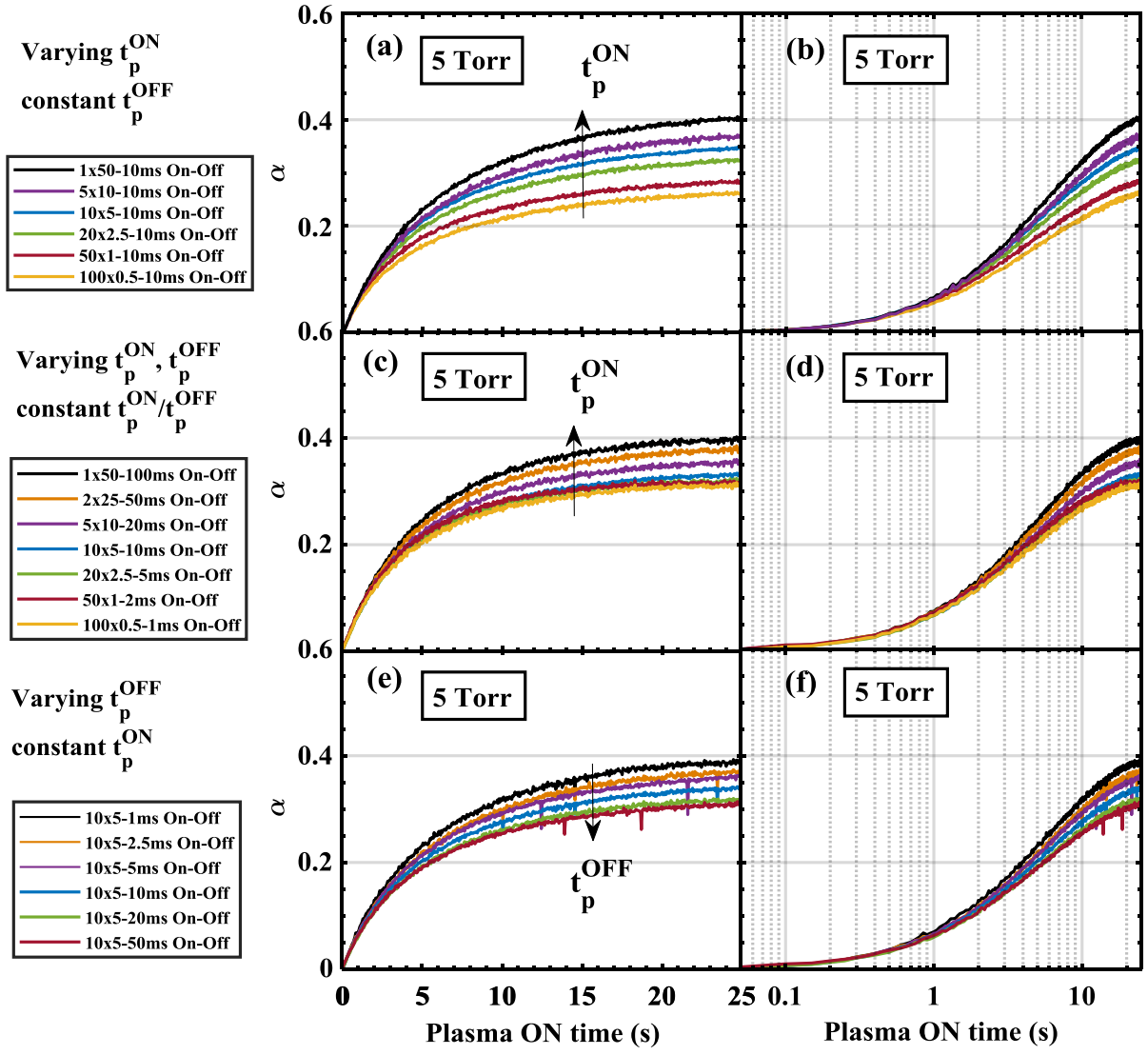

Figure 6.11: Time evolution of the dissociation fraction α as a function of the total plasma ON time T^{ON} in linear time scale (panels (a), (c) and (e)) and logarithmic time scale (panels (b), (d) and (f)) measured at 5 Torr, 40 W. Graphs (a) and (b) present data for different pulse duration (t_p^{ON}) but same delay between pulses (t_p^{OFF}), panels (c) and (d) present data for different pulse duration (t_p^{ON}) but same duty cycle ratio (t_p^{ON}/t_p^{OFF}) and graphs (e) and (f) present data for different delay times between pulses (t_p^{OFF}) but the same pulse duration (t_p^{ON}). The number of pulses N_p is varied to keep always the same plasma ON per train (t_{tr}^{ON}).

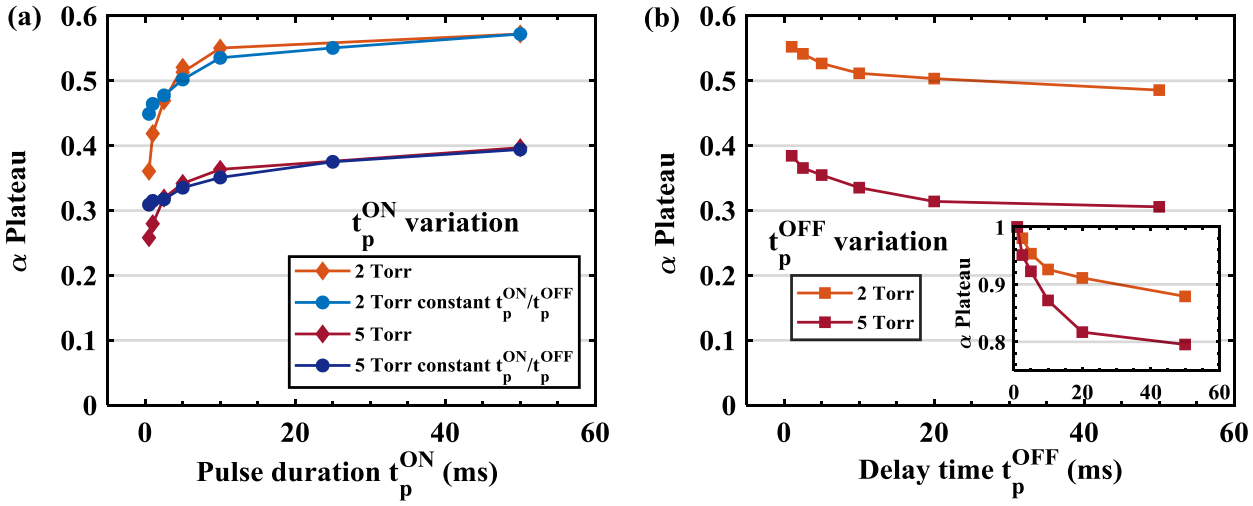

Figure 6.12: Variation of α at the plateau (average of T^{ON}=20-25 s) as a function of (a) pulse duration, t_p^{ON}, and (b) delay time between pulses, t_p^{OFF}, for 2 and 5 Torr extracted from figures 6.10 and 6.11.

where n_e is the electron density, K_{diss} the dissociation rate coefficient, $[CO_2]$ and $[CO]$ the CO_2 and CO densities and T^{ON} is the plasma ON time. The dependence with pressure is then explained through the density of CO_2 in equation (6.1), whereas the dependence with power is related to the electron density.

More verifications are required to confirm this single dependence, which will be done in the following sections, but we can already tentatively conclude that the initial time evolution is driven only by electron impact dissociation of CO_2 and that the vibrational excitation of CO_2 molecules is not contributing to the dissociation in our experimental conditions for short T^{ON}, since it would not be a first order process. This is in agreement with the results obtained in the glow discharge, preliminary discussed in section 3.6.1 and discussed in more detail in section 6.4.

Deviations from the initial linear evolution start when the amounts of CO and O_2 in the total gas mixture become significant. A less efficient CO_2 dissociation, as the CO_2 density decreases and CO and O_2 densities increase is expected simply due to energy spent in the excitation and dissociation of O_2 and to a lesser of extent of CO (due to the higher dissociation threshold compared to O_2). No effect of t_p^{ON} or t_p^{OFF} would be expected in a time evolution purely driven by electron impact dissociation of CO_2. Nevertheless, a clear effect of the pulsing starts from $T^{ON} \gtrsim 0.5$ s. The pulse configuration defines what happens in the "turning region", and consequently strongly impacts the final dissociation value in the steady-state, where no evolution of the chemistry is noticeable any more. The differences in the time evolution of α for different pulse configurations provide an evidence of the influence of chemical reactions between heavy species in ground state or electrically/vibrational excited states, induced by temperature and/or by the excitation degree.

In order to discuss the variation of α(plateau), figure 6.12 summarizes the results from figures 6.10 and 6.11 by plotting the values of α at the "plateau" (average over the last 5 s of T^{ON}) either as a function of the pulse duration for the t_p^{ON} variation experiments (panel (a)) or as a function of the delay between pulses, t_p^{OFF} (panel (b)).

→ t_p^{ON} ***variation experiments***

Figure 6.12 (a) shows a significant increase of α(plateau) in t_p^{ON} variation experiments for variable or constant duty cycle ratio (DCR). Longer plasma pulses lead to higher steady-state dissociation values compared for the same total accumulated plasma ON time, T^{ON}. For the longest pulses t_p^{ON} ≥2.5 ms (→ t_p^{OFF}=5 or 10 ms), both types of experiments give the same dissociation fraction. The difference between keeping constant or not the DCR is noticeable only for very short t_p^{ON} (t_p^{ON}=0.5 & 1 ms).

The pulse duration effect is more important at low pressure (2 Torr) than at high pressure (5 Torr). As example, for variable duty cycle ratio, for the shortest pulse, α(plateau) at 2 Torr is ∼0.36 and for the longest pulse is ∼0.57, whereas at 5 Torr for the shortest pulse α(plateau)∼0.26 and for the longest pulse is 0.39. Similar effect, but less pronounced, is noticeable when keeping constant t_p^{ON}/t_p^{OFF}, the difference at 2 Torr is ∼0.12 and at 5 Torr is ∼0.085.

The stronger influence of t_p^{ON} at low pressure could be related either to higher vibrational excitation (see figure 6.9) or higher reduced electric field at low pressures (see section 3.3). Higher E/N may cause, for instance, higher density of electronically excited states, that are in addition less efficiently quenched at low pressure. The effect of the pulse duration, t_p^{ON}, is somehow contradictory with literature *Britun et al.* [2017]; *Vermeiren and Bogaerts* [2019], where pulsing is claimed to be helpful for an efficient dissociation, due to the lower gas temperature compared to continuous plasma. However, this is only true if there is a significant contribution of the vibrational excitation to the dissociation. In that case, as the vibrational excitation decreases with temperature (see chapter 4), it is interesting to keep the gas temperature as low as possible, which would also reduce "back reactions" dependent on T_{gas}. In such situation short pulses are expected to have a positive effect on the dissociation, opposite to our experimental results. To understand why, it is important to have in mind several things:

- When varying the pulse duration t_p^{ON}, with or without constant DCR, the number of times that the plasma is switched OFF in a train is varying (see N_p in table 6.2)
- In experiments varying the DCR, t_p^{ON}/t_p^{OFF}, the vibrational excitation is higher for shorter pulses. The t_p^{OFF} is constant, and therefore every pulse restarts from the same gas condition for all t_p^{ON}. However, the total OFF time per train t_{tr}^{OFF} varies.
- For constant duty cycle ratio t_p^{ON}/t_p^{OFF}, the pulses re-start from different gas conditions, especially for short t_p^{OFF} but t_{tr}^{OFF} is constant.

We first discuss the common trend for both experiments ($t_p^{ON} \geq 2.5$ ms, $t_p^{OFF} \geq 5$ ms). Keeping constant or not t_p^{ON}/t_p^{OFF}, both show an increase of α when t_p^{ON} is increased. The total OFF time per train t_{tr}^{OFF}, different in both cases, does not seem to affect the results when t_p^{OFF} is long enough (> 5 ms). Both experiments have in common N_p and t_p^{ON}, and α decreases with increasing N_p or decreasing t_p^{ON}. Therefore either the higher average vibrational excitation of T_3 and/or T_{CO} for short pulses or an increase of N_p have a detrimental effect on the dissociation. A possibility would be that a "back reaction" mechanism happening only in the early post-discharge becomes more prominent when the plasma is switch OFF more times. In this hypothesis, there would be a short duration (<5 ms) in the post-discharge when CO would be lost.

Differences between both experiments appear for short t_p^{ON} (=0.5 or 1 ms). We observe that the longer the OFF time, t_p^{OFF}, after a short pulse of t_p^{ON}=0.5 or 1 ms, the lower the final dissociation

fraction (10 ms *versus* 1 or 2 ms). These results support the hypothesis of a "back reaction" in the early post-discharge for short t_p^{OFF}, from the end of the pulse to 5-10 ms after switching OFF. This characteristic time is in agreement with the relaxation times of T_{rot} and T_{vib} seen in figure 6.9, but also of some electronically excited levels such as CO($a^3\Pi_r$), whose lifetime is ~2.5-7 ms *Mori et al.* [2002]; *Gilijamse et al.* [2007]. The difference between variable or constant t_p^{ON}/t_p^{OFF} decreases from 2 to 5 Torr, suggesting more an effect of vibrational or electronic excitation than a gas temperature effect. An influence of vibrational excitation (which should be stronger during short pulses t_p^{ON}), beneficial or not, could be hidden by the effect of the post-discharge in these experiments. t_p^{OFF} variation experiments may provide more insight in this regard.

→ t_p^{OFF} ***variation experiments***

Figure 6.12 (b) shows a decrease in the dissociation fraction α(plateau) as a function of t_p^{OFF}. The decrease is fast for short t_p^{OFF} values, following an exponential-like variation with t_p^{OFF}. For longer t_p^{OFF} the effect tends to becomes negligible. The inner graph in figure 6.12 (b) plots the same data normalized to the shortest t_p^{OFF} (1 ms) and shows that for higher pressures (5 Torr) α decreases more and faster that for lower pressures (2 Torr). This effect seems to support the hypothesis of a "back reaction mechanism" during the first milliseconds of the OFF phase, in between pulses, which would be inhibited when the next plasma pulse is ignited. The back reaction mechanism either in gas phase and/or on the surface, could be influenced by the gas temperature, exited species or oxygen O atoms created during the pulse.

The larger effect of the t_p^{OFF} variation at 5 Torr (which seems contradictory with the analysis of the t_p^{ON} variation) could suggest a more efficient "back reaction" in the post-discharge related to higher gas temperature. The variation of α with t_p^{OFF} follows qualitatively a similar variation as in the case of a nano-second discharge *Martini et al.* [2018], where a correlation with the time variation of the gas temperature in the post-discharge was found. The known rates *Cenian et al.* [1994] for the "back reaction" between ground state CO and O are temperature dependent, and therefore this reaction could be more efficient during the cooling-down time of the gas, *i.e.* during the first 5-10 ms. However, estimations done for the glow discharge indicate that the rate for this reaction is at least two orders of magnitude lower than the reaction between two oxygen atoms to produce O_2 (see section 3.6.2), pointing towards a participation of excited states and an influence of pressure and/or temperature via higher collision rate. Both experiments agree on the hypothesis of "back reaction" is the post discharge. The stronger effect at 2 Torr for the t_p^{ON} variation experiments suggest the possibility of "back reaction" also during the ON phase, possibly caused by a higher density of vibrationally and electronically excited states. Apart from the direct reaction between CO and O atoms, that could be also influenced by the vibrational excitation of CO, other possible "back reaction" mechanisms have been proposed in the literature:

- Reactions involving vibrationally excited CO, for example *Gorse and Capitelli* [1984]; *Adamovich et al.* [1993]; *Essenhigh et al.* [2006]; *Capitelli et al.* [2017]: $CO(\nu) + CO(\omega) \rightarrow CO_2 + C$, or in the associative ionization reaction: $CO(\nu) + CO(\omega) \rightarrow CO_2^+ + C + e$.
- Reactions involving CO($a^3\Pi_r$), which has been claimed to enhance the dissociation when the total CO density is low *Cenian et al.* [1994]: $CO(a^3\Pi) + CO_2 \rightarrow 2CO + O$, but to contribute to the "back reaction" when the concentrations of CO and O_2 increase: $CO(a^3\Pi) + O_2 \rightarrow CO_2 + O$, $CO(a^3\Pi) + CO \rightarrow CO_2 + C$.

These mechanisms will be discussed in more detail in following sections. In any case, these results suggest that the steady-state dissociation values are strongly controlled by the back reaction, which seems to happen efficiently at the beginning of the post-discharge. Any possible positive effect of the vibrational excitation seems hindered by the back reaction mechanisms in our discharge conditions. To conclude, pulsed plasmas are often believed to be more efficient for the CO_2 dissociation by limiting the gas heating and favouring the vibrational excitation. However, pulsing the plasma increases the proportion of "early post-discharge" time during which significant "back reaction" processes seem to take place.

✓ The initial slope remains the same for any pulse configuration.
✓ Varying the pulse configuration significantly affects the steady-state dissociation fraction.
✓ Evidences of post-discharge back reaction mechanisms, possibly involving excited states in the early post-discharge.
✓ The possible back reaction mechanisms during the ON and OFF phases hinders the beneficial role of vibrational excitation during the ON-phase (if any).

Influence of the plasma ON per train and the measurement time

1. Number of trains N_{tr} and total plasma ON per train t_{tr}^{ON}.
2. The delay between trains, *i.e.* the time required by the FTIR to measure after every train.

In the previous section we have varied the pulse duration t_p^{ON}, the delay between pulses t_p^{OFF} and the ratio between them t_p^{ON}/t_p^{OFF}, but always keeping constant the total plasma ON per train t_{tr}^{ON}=50 ms, the number of trains N_{tr}=500, and the total plasma ON time T^{ON}=25 s. For all these experiments the "measurement" time per train is ∼2.08 s, which includes the time during which the FTIR waits for the train of plasma pulses (500 ms), and the FTIR measurement time ∼1.5 s. The total experiment time is approximately 17 minutes. In this section we briefly address the effect of varying two other parameters in the experiment:

Varying N_{tr} and t_{tr}^{ON}

Notation	N_{tr}	N_p	t_p^{ON}(ms)	t_p^{OFF}(ms)	t_{tr}^{ON}(ms)	t_{tr}^{OFF}(ms)	T^{ON}(s)	Meas†(s)	Exp‡(min)
100x50x5-10	100	50	5	10	250	500	25	2.08	3.47
250x20x5-10	250	20	5	10	100	200	25	2.08	8.67
500x10x5-10*	500	10	5	10	50	100	25	2.08	17.34
1000x5x5-10	1000	5	5	10	25	50	25	2.08	34.67
Varying delay between trains									
500x10x5-10+2s	500	10	5	10	50	100	25	4.161	34.67
500x10x5-10+4s	500	10	5	10	50	100	25	6.241	52.01

* Default train configuration, see experimental box 6.2.
† Measurement time per train.
‡ Total experiment time.

Table 6.3: Pulse parameters used in the experiments presented in figure 6.13.

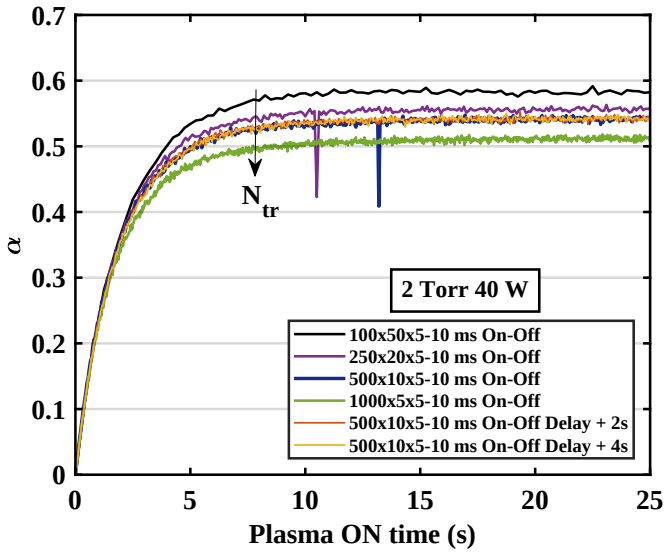

Figure 6.13: Time evolution of α for the experiments described in table 6.3, at 2 Torr 40 W.

The experimental parameters are summarized in table 6.3. The pulse configuration, t_p^{ON} and t_p^{OFF}, and the total plasma ON in the experiment, T^{ON}=25 s, were kept the same for all the experiments.

The initial slope remains the same for any experiment configuration, in agreement with the hypothesis of a time region dominated by electron impact dissociation. Introducing a delay in between trains, which is equivalent to enlarge the measurement time of the FTIR, does not affect the time evolution of α. The default measurement, which requires 2.08 s per train and a total experiment time of 17.34 minutes, perfectly overlaps with two measurements where the FTIR has been forced to wait either 2 or 4 extra seconds, which increases significantly the total experiment time to 34.67 and 52.01 minutes respectively.

Varying the train configuration (N_{tr} and t_{tr}^{ON}), however, does affect the values of α at the plateau. The lower the number of trains (and higher number of pulses per train), the higher the dissociation fraction value. Although the total experiment time significantly increases with the number of trains because of the number of FTIR measurements (number of FTIR measurements=N_{tr}), this should not be the cause of the difference since no difference is observed when varying the delay between trains. The variation with N_{tr} could suggest a CO destruction at the end of each train. Therefore in addition to the "back reaction" after every pulse, there could be a certain "back reaction" after every train for instance caused by long-lived species such as oxygen atoms or meta-stable states like $O_2(a^1\Delta_g)$, or slow chemical reactions on the surface.

Building-up Plasma On and Building-up On-Off

In this section we investigate how very long pulses or a continuous discharge affect the time evolution of the dissociation fraction, as extreme case of the previous experiment configurations. Instead of trains of pulses defined by signal generators, the FTIR trigger signal directly controls the RF generator. Two variants were investigated:

1. "Building-up On-Off": the plasma is consecutively switched ON and OFF. At every phase,

ON and OFF, an absorption measurement in taken. The duration of the pulse (ON phase) and the delay between pulses (OFF phase) is only limited by the time required by the FTIR to adcquire the interferogram. We therefore obtain consecutively measurements with plasma ON and measurements with plasma OFF.

2. "Building-up ON": the plasma is switched ON after the initial trigger signal and it is kept ON while consecutive absorption measurements are taken until the end of the experiment, without switching off the discharge.

A schematic of the measurement procedure for both variants is shown in figure 6.14. Similar pre-treatment procedure as for the usual building-up experiment were carried out. Note that, as for any *in situ* FTIR measurement, an extra measurement is required to subtract the IR emission from the plasma (see section 2.3.1). The ON phase data is treated with the Treanor Out of Equilibrium script detailed in section 2.3.1. The OFF phase data is treated with the same thermal equilibrium script used throughout this chapter. Note that for the ON phase measurements in both variants of the experiment, the gas mixture is evolving while the interferogram is being recorded by the FTIR spectrometer. This may introduce a certain error in α values especially at the beginning of the experiment for the lowest pressures corresponding the fastest growth of α. To minimize this error, the scan speed of the IR mirror was set at the fastest speed possible 160 kHz. In these conditions the total scan time is ∼0.5 s. The total measurement time is around 1 s, including settings time and scan time, defining the pulse duration in the building-up On-Off experiment. The measurement stops after T^{ON}=20 s. The total experiment time is significantly shorter than in the reference building-up experiment 20-50 s.

Figure 6.15 shows the comparison between the usual building-up measurements with the refer-

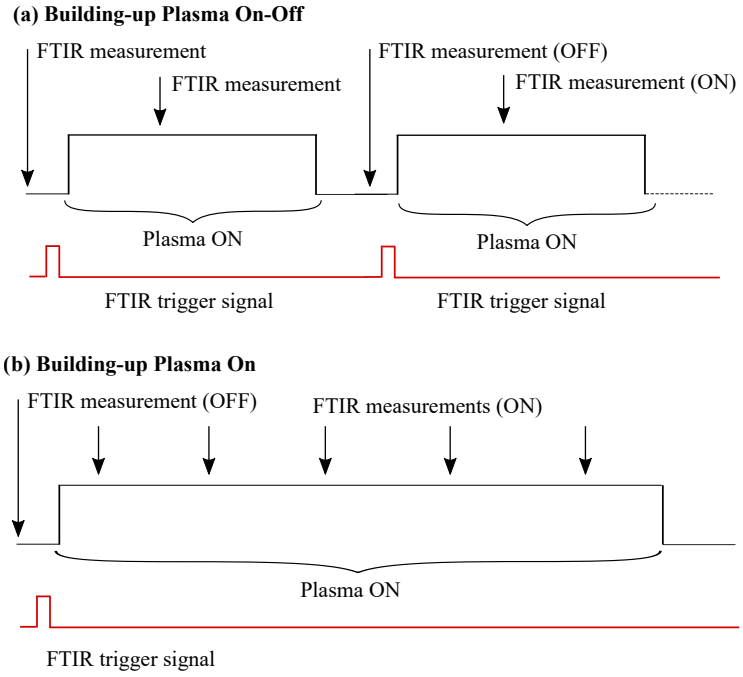

Figure 6.14: Measurement schemes for the building-up plasma On and for the building-up plasma On-Off experiments.

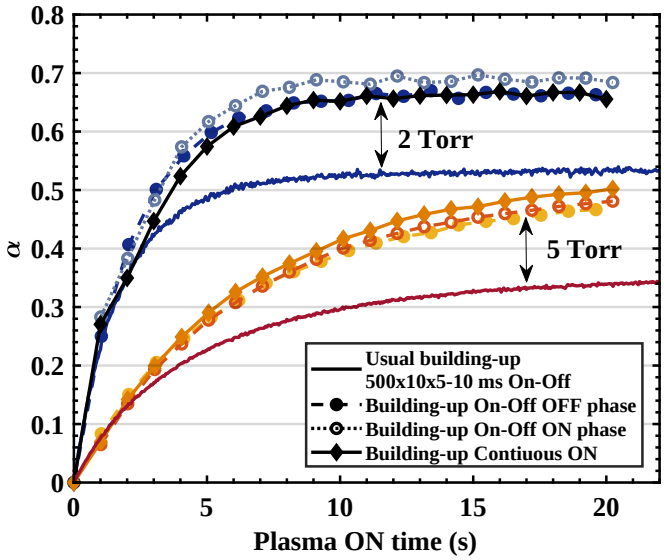

Figure 6.15: Time evolution of the dissociation fraction α at 2 and 5 Torr, 40W for the usual building-up in the reference pulse configuration (500 trains × 10 pulses × 5-10 ms On-Off), for the building-up plasma On experiment and for the building-up plasma On-Off experiment plotting separately the results for the ON and OFF phases.

ence pulse configuration and the two variants described above, for 2 and 5 Torr at 40W. The results for the ON and OFF phases in the case of the building-up plasma On-Off experiment are plotted separately. Several observations can be made:

- The two variants of the building-up experiment investigated in this section give similar α(plateau), significantly higher than for the usual building-up.
- All the measurements show a similar evolution for short T^{ON}.
- For the building-up plasma On-Off experiment the results for the ON and OFF phases are consistent within the reproducibility error of the experiment.

These results are in good agreement with the previous observations: initial slope only controlled by electron impact dissociation of CO_2 for all the experiments, and higher dissociation fraction in the steady-state for longer pulses. The α(plateau) values observed in figure 6.15 are higher than those for the longest pulses in the previous experiments, but the number of pulses is significantly lower (20 *vs.* more than 500) supporting the hypothesis of "back reaction" in the early post-discharge. It is also worth noting the consistency between the ON and OFF phase measurements during the "building-up plasma On-Off" experiment. It gives a validation of the α values obtained with the Out of Equilibrium script, significantly more complex and with more fitting parameters than the thermal equilibrium script. In section 3.4 we showed significant discrepancies between the dissociation measured *in situ versus* the measurements downstream. The agreement between the ON and OFF phase results confirms that the reason for the different α measured downstream vs *in situ* is not an artefact of the Out of Equilibrium script (used only for the *in situ* data). The consistency between α measured in the ON and OFF phases also implies that the post-discharge chemistry becomes significant when the number of post-discharge events is large and it always tends to decrease the final dissociation fraction. Therefore, temporal *in situ* post-discharge chemistry

cannot be the explanation for the discrepancy *in situ versus* downstream, pointing out towards either spatial post-discharge and/or an effect of the gas flow/τ_{res}.

✓ The initial slope remains the same for any train of plasma pulses configuration.
✓ Measurements taken with plasma On and OFF in similar conditions are consistent, validating the OoE script.
✓ Post-discharge "back reaction" mechanisms require cumulative effect over several post-discharge events to be significant.

6.3.2 Gas mixtures

Different gas mixtures were investigated, CO_2-O_2, CO-O_2, CO_2-N_2 and CO_2-Ar with "building-up" experiments. CO_2-O_2 and CO-O_2 mixtures are interesting in order to study the effect of the O atoms on the dissociation fraction and on the time evolution of any possible "back reaction" mechanism. The vibrational levels of N_2 are known to be resonant with the vibrational levels of the asymmetric stretch mode of CO_2 (ν_3), as briefly discussed in section 4.5. N_2 can act therefore as a reservoir of vibrational energy. The presence of N_2 has been proven to be beneficial to increase the dissociation in CO_2-N_2 mixtures *Grofulović et al.* [2019]; *Terraz et al.* [2019]. Several reasons can cause this effect: the increased vibrational excitation due to resonant energy exchanges, the change in the EEDF and the higher electric field in CO_2-N_2 mixtures, an effect simply of the dilution of CO_2 reducing the "back reaction" due to lower oxygen density, or different surface processes. To get more insight on the results obtained in CO_2-N_2, a comparison is made with CO_2-Ar with similar dilution factor. The EEDF is also changed differently by the addition of Ar, and the electric field decreases when compared to the addition of N_2.

CO_2-O_2 mixtures

The time evolution of the CO_2 conversion in different CO_2-O_2 gas mixtures was investigated with the reference pulse condition (500 trains × 10 pulses × 5-10 ms On-Off). Figure 6.16 presents the variation of the dissociation parameter α as a function of the total plasma ON time, T^{ON} for initial gas mixtures ranging from 100%CO_2 to 25%CO_2-75%O_2. Graphs (a) and (b) show the time evolution for 2 Torr up to T^{ON}=25 s in linear time scale (a) and logarithmic scale (b) to focus on the initial rising of the dissociation fraction. Panels (c) and (d) show the same data but for 5 Torr (40 W). Two main observations can be noticed from these graphs:

- The initial rise-up until T^{ON} ~0.5 s is not affected, within the experimental error, by the O_2 fraction in the initial gas mixture for any of the pressures studied.
- The steady-state value of the dissociation fraction α is strongly affected by the initial O_2 content. Increasing the amount of O_2 in the initial gas mixture leads to a clear decrease in the final dissociation value.

The similar initial slope agrees with the previous observations when varying the pulse duration or the delay between pulses, suggesting that indeed these first steps in the dissociation are only

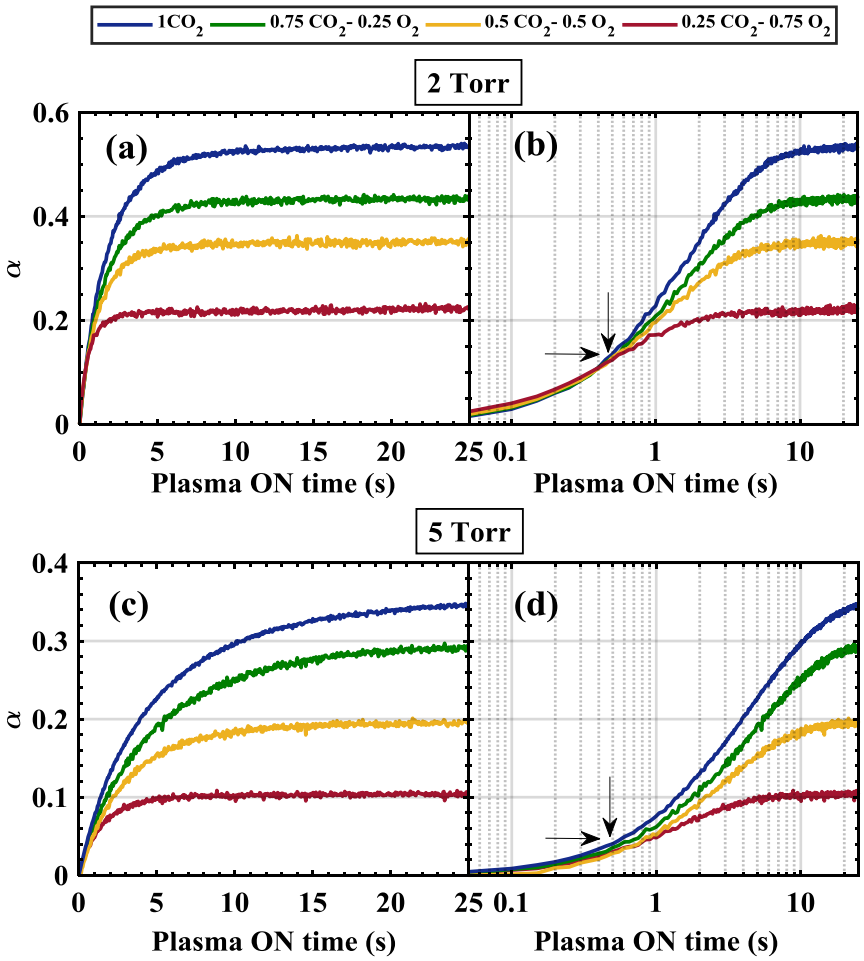

Figure 6.16: Time evolution of the dissociation parameter α for different initial CO_2-O_2 mixtures, for 2 Torr (panels (a) in linear time scale and (b) in logarithmic scale) and 5 Torr (panels (c) and (d)), 40 W.

controlled by the electron impact dissociation of CO_2. This also implies that the population of electrons having enough energy for the dissociation of CO_2 is not affected in presence of O_2.

After $\sim$ T^{ON}=0.5 s, the curves corresponding to different gas mixtures start diverging from each other. When increasing the O_2 content the steady-state region is reached earlier. As example at 2 Torr α reaches the steady-state at T^{ON} $\sim$3 s for 0.25CO_2-0.75O_2, whereas for 100% CO_2 it reaches it at T^{ON} $\sim$8 s. The case of 5 Torr is even more pronounced and for 0.25CO_2-0.75O_2 the steady-state is reached at T^{ON} $\sim$5 s, whereas at 100% CO_2 is barely reached at the end of the experiment, T^{ON}=25s.

The most noticeable feature in figure 6.16 is the clear threshold at which this "back reaction" becomes prominent (around $T^{ON}\approx$0.5 s, qualitatively indicated by arrows in the figure). It is remarkable that the threshold is independent of the % of O_2 in the initial gas mixture. Although at first we could think that the threshold is related with time, the experiment configuration based on trains of pulses does not seem to support such idea. There is no accumulative effect for example on the gas temperature, or on the O atom density (O atoms recombine in between trains), when progressing along the T^{ON} axis. The only thing that changes between trains is the initial gas mixture, evolving from pure CO_2/CO_2-O_2 towards a mixture CO_2-CO-O_2 with increasing CO density. It is

therefore more probably a threshold in concentration. The lower α value for which the threshold occurs at 5 Torr (α ~0.04) compared to 2 Torr (α ~0.1) could then be related to the different total gas density.

Increasing the O_2 content could in principle increase the O atom density. Nevertheless, in chapter 3 we have seen that the O atoms are preferentially lost in the reactor walls in our experimental conditions, and more probably through a recombination with oxygen to produce O_2 than with CO. We expect similar O atom loss processes in the RF because of the similar reactor configuration, and the similar range of gas temperatures. In gas phase, the rate for the reaction between CO and O in ground state is rather low (see figure 3.31), as expected from a spin-forbidden recombination reaction ($CO(^1\Sigma^+) + O^3P) \rightarrow CO_2(^1\Sigma_g^+)$) *Xu et al.* [2017a]. Direct recombination reaction involving one of the species in an electronically excited state $O(^1D)$, $O(^1S)$ or $CO(a^3\Pi_r)$, could have higher rate coefficients but it is worth remembering that the O atom density in pulsed plasma is significantly lower than in continuous plasma (see section 3.7.2) and O atoms recombine in between trains. Therefore, it is not very probable that the mechanism responsible for the effect of O_2 ad-mixtures in pulsed plasma involves oxygen atoms.

As briefly discussed at the end of section 6.3.1, there is a back reaction mechanism involving the $CO(a^3\Pi_r)$ state, that can explain our results. For gas mixtures with high amounts of CO_2 the following reactions could take place and compete:

$$CO(a^3\Pi_r) + CO_2 \rightarrow 2CO + O$$
$$CO(a^3\Pi_r) + CO \rightarrow CO_2 + C$$

The first reaction would be dominant when the amount of CO is not very high but the density of CO_2 is still large, and it enhances the dissociation. The second one tends to decrease the final dissociation rate and would become dominant as the CO density increases. Assuming the created C atom is oxidized to CO (through different mechanisms, involving O_2, O, C_2O, etc.) *Cenian et al.* [1994]; *Kozák and Bogaerts* [2014a], only one CO molecule would be destroyed. In the dissociation of CO_2 we create O atoms that may recombine into O_2 and start participating in another mechanism that involves directly O_2 molecules *Cenian et al.* [1994]:

$$CO(a^3\Pi_r) + O_2 \rightarrow CO_2 + O$$

This last reaction could explain the experimental data observed in figure 6.16. A minimum amount of CO is necessary for this mechanism to start playing a role, explaining the threshold. For CO_2-O_2 mixtures with high amount of O_2 the total CO density is lower, but it is compensated by the increase of O_2 density. The energy of the $CO(a^3\Pi_r)$ state is ~ 6eV. Considering the EEDF in our system, and an electron impact-driven dissociation mechanism dominating the dissociation in our discharge (at ~7 eV) this state is expected to be significantly populated. The density of $CO(a^3\Pi_r)$ in the discharge may also be affected by de-excitation through super elastic collisions *Capitelli et al.* [2017] and by quenching reactions:

$$CO(a^3\Pi_r) + O_2 \rightarrow CO + O_2$$
$$CO(a^3\Pi_r) + CO \rightarrow CO + CO$$
$$CO(a^3\Pi_r) + CO_2 \rightarrow CO + CO_2$$

The quenching and the "forward" reactions producing either CO_2 or CO have close reaction rate coefficients, significantly higher than the reactions involving ground state species *Slovetsky* [1980]; *Cenian et al.* [1994]; *Skrzypkowski et al.* [1998]. For example, the rate coefficient for the reaction $CO(a^3\Pi_r) + O_2 \rightarrow CO_2 + O$ is between 3-5$\times 10^{-11}$ cm^{-3} s^{-1} and for the quenching reaction is 5×10^{-11} cm^{-3} s^{-1} *Cenian et al.* [1994]. These rates are orders of magnitude higher than the recombination between CO and O atoms. Reactions involving electronically excited states are more probable that reaction involving vibrationally excited CO, such as $CO(\nu) + CO(\omega) \rightarrow CO_2 + C$ *Gorse and Capitelli* [1984]; *Adamovich et al.* [1993]; *Essenhigh et al.* [2006]; *Capitelli et al.* [2017] since the pulse duration experiments are not showing any clear effect of the different vibrational excitation on α. The possible role of electronic states in back reactions is in any case discussed in more detail in the following chapter (section 7.5).

✓ The addition of O_2 to the initial gas mixture decreases strongly the steady-state α but it does not change the initial slope.
✓ A clear threshold is observed in the occurence of the "back reaction", probably related to a threshold in CO density.
✓ Plausible role of $CO(a^3\Pi_r)$ in back reaction mechanisms.

CO-O_2 mixtures

Mixtures of CO+O_2 are interesting because they represent the final "ideal"gas mixture in case we could dissociate all the CO_2 available and no recombination/oxidation of the CO produced would happen. Two gas mixtures were investigated:

- 0.4 CO + 0.6 O_2: 1 carbon atom for 4 oxygen atoms → similar proportion $^C/_O$ as in a mixture of 0.5 CO_2 + 0.5 O_2.
- 0.666 CO + 0.333 O_2: 1 carbon atom for 2 oxygen atoms → similar to a 100% CO_2 plasma.

Figure 6.17, presents for 2 and 5 Torr the time evolution of the dissociation fraction α for these two gas mixtures compared to the equivalent CO_2-O_2 measurements shown in figure 6.16. We observe, similarly to the experiments in CO_2 or CO_2-O_2 mixtures three-regions: an initial fast evolution, in this case decreasing the value of α, a "turning region" and the final steady-state. These experimental results confirm that the time evolution of α in CO_2 initial mixtures (pure or mixed with O_2) is not only given by a constant decrease in the dissociation efficiency due to the presence of dissociation products but also given by "back reaction" mechanisms, which are active and significant in our plasma. Three additional observations can be pointed out:

1. The evolution of α for both CO-O_2 mixtures diverged from the beginning of the building-up experiment contrary to the common threshold observed in CO_2-O_2 mixtures.
2. The evolution of the gas mixture is faster when starting from CO-O_2 than when the initial gas mixture is CO_2-O_2 (qualitatively indicated with arrows in figure 6.17). Consequently the steady-state is reached for shorter T^{ON}. For example, at 2 Torr the measurement of 0.5CO_2-0.5O_2 reaches the steady-state approximately at T^{ON} ∼8-9 s, whereas 0.4CO-0.6O_2 is stable already at T^{ON} ∼5-6 s.

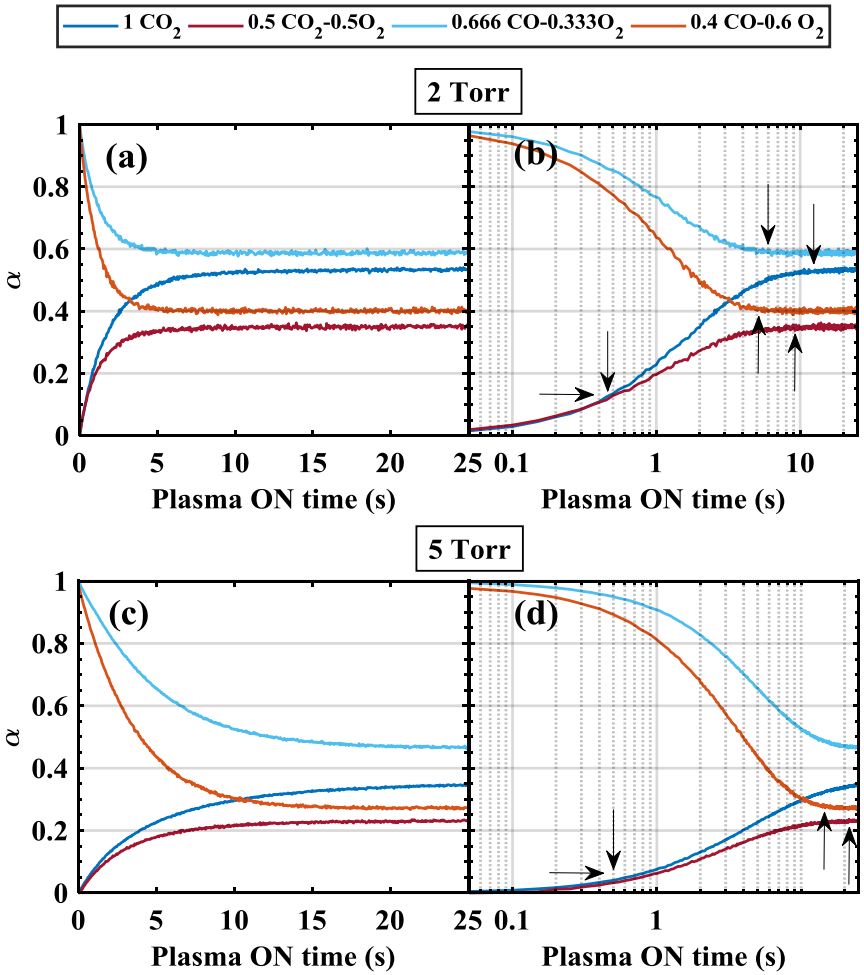

Figure 6.17: Time evolution of the dissociation parameter α for CO_2/CO_2-O_2 and CO-O_2 mixtures for two carbon *vs.* oxygen ratio 1/4 and 1/2 for 2 Torr (panels (a) and (b)) and 5 Torr (panels (c) and (d)) in linear (panels (a) and (c)) and logarithmic (panels (b) and (d)) time scales.

3. The steady-state dissociation value is higher for CO-O_2 mixtures than for CO_2-O_2.

The absence of threshold in these experiments supports the previous conclusion of a threshold related to concentration of reactants (and not time-related). Assuming that the molecules involved in the back reaction mechanism are CO and O_2 (or even O), the higher amount of reactants in the initial gas mixture induces a faster overall evolution and explains the shorter T^{ON} required to reach the steady-state. If the mechanism involving $CO(a^3\Pi_r)$ is driving the "turning region", the faster decrease for higher amounts of initial O_2 suggest a more dominant role of the reaction $CO(a^3\Pi_r)+O_2 \rightarrow CO_2+O$ compared to $CO(a^3\Pi_r)+CO \rightarrow CO_2+C$ in agreement with the higher reaction rate coefficient given in literature ($k = 3-5\times10^{-11}$ cm^{-6}s^{-1} for the first one compared to $k = 1.4\times10^{-12}$ cm^{-6}s^{-1} for the latter one) *Cenian et al.* [1994].

Measurements done starting from a CO-O_2 mixture give systematically higher steady-state dissociation fractions. The difference between α(CO_2-O_2) and α(CO-O_2) seems to decrease with the initial amount of O_2 for both pressures, *i.e.* [α(0.666CO-0.333O_2)-α(1 CO_2)] > [α(0.4CO-0.6O_2)-α(0.5 CO_2-0.5 O_2)], and with pressure. The reason is still unclear, although a plausible hypothesis would be that α(plateau) is affected by surface processes, that can be relevant when working in static conditions. This would imply different surface reactivity (and/or adsorption) of CO_2 and CO

on the glass surface. This hypothesis agrees with the fact that the difference between both initial gas mixtures decreases when the O_2 content is increased. More experiments are required to confirm this hypothesis, but already an indication of the importance of surface processes was observed when modifying the pre-treatment procedure (see section 6.2.2). In the first step of the pre-treatment, O_2 plasma and CO_2 plasma were giving similar final α(plateau), but slightly higher than with Ar plasma (∼6% higher). In the second step, O_2 gas flows seems to give higher steady-state α than CO_2 flows (∼8% higher). These pre-treatment tests show the same initial slope, but suggest that surface reactions play a role for long T^{ON}. The effect of the gas mixture in surface processes is investigated in more detail in chapter 8.

✓ CO-O_2 experiments confirm the results from CO_2-O_2 gas mixtures and suggest an important role of the reaction $CO(a^3\Pi_r) + O_2 \rightarrow CO_2 + O$.
✓ Surface reactions involving CO and CO_2 seem to influence the dissociation fraction on long time scale.

Other gas mixtures

Preliminary experiments in gas mixtures with Ar and N_2 were done to investigate the effect of modifying the electron kinetics and/or the possible contribution of vibrational excitation on the evolution of the dissociation fraction.

Figure 6.18 shows the time evolution of α up to T^{ON}=5 s for a better observation of the initial slope, for the reference pulse configuration in gas mixtures of CO_2-N_2 and CO_2-Ar at 2 Torr (panel (a)) and 5 Torr (panel (b)). The addition of N_2 or Ar leads to a remarkable increase in the dissociation fraction. This increase is already visible for very short T^{ON}, *i.e.* both gas add-mixtures affect the initial slope. The addition of argon leads to a steeper slope and a faster evolution of the gas mixture compared to N_2, particularly for the gas mixtures with lowest CO_2 content. The change of slope is not necessarily in contradiction with an initial dissociation dominated by electron impact dissociation. Both Ar and N_2 change significantly the electron kinetics in the discharge. Measurements of the reduced electric field in a CO_2-Ar glow discharge show that the reduced electric field is lower (*e.g.* ∼53 for 0.5CO_2-0.5Ar vs. 60 Td in pure CO_2 for the same conditions), but the electron density calculated with the drift velocity obtained from the Boltzmann solver LoKI *Tejero-del Caz et al.* [2019], is higher than in pure CO_2 plasma. Consequently the product $n_e \cdot K_{diss}$ (see equation (6.1)) is higher (see also K_{diss} variation as a function of E/N in figure 6.21).

In the case of N_2 ad-mixtures, the reduced electric field is higher (*e.g.* ∼72 *vs.* 60 Td for 0.5CO_2-0.5N_2 *vs.* pure CO_2). In addition, the contribution of vibrational excitation to the total dissociation enhanced by the addition of N_2 has been claimed in the literature *Silva et al.* [2014], even in similar experimental conditions (glow discharge) *Terraz et al.* [2019]. A relevant change in the dissociation mechanism, for instance due to a significant dissociation through vibrational-up pumping or electron impact on vibrationally excited molecules, would affect the initial slope. Note that the vibrational temperatures in CO_2-N_2 mixtures are significantly higher than in pure CO_2 (see figure 4.14). Future experiments varying the pulse duration in CO_2-N_2 mixtures may provide insight into the role of this mechanism on the evolution of the dissociation fraction in CO_2-N_2 plasmas.

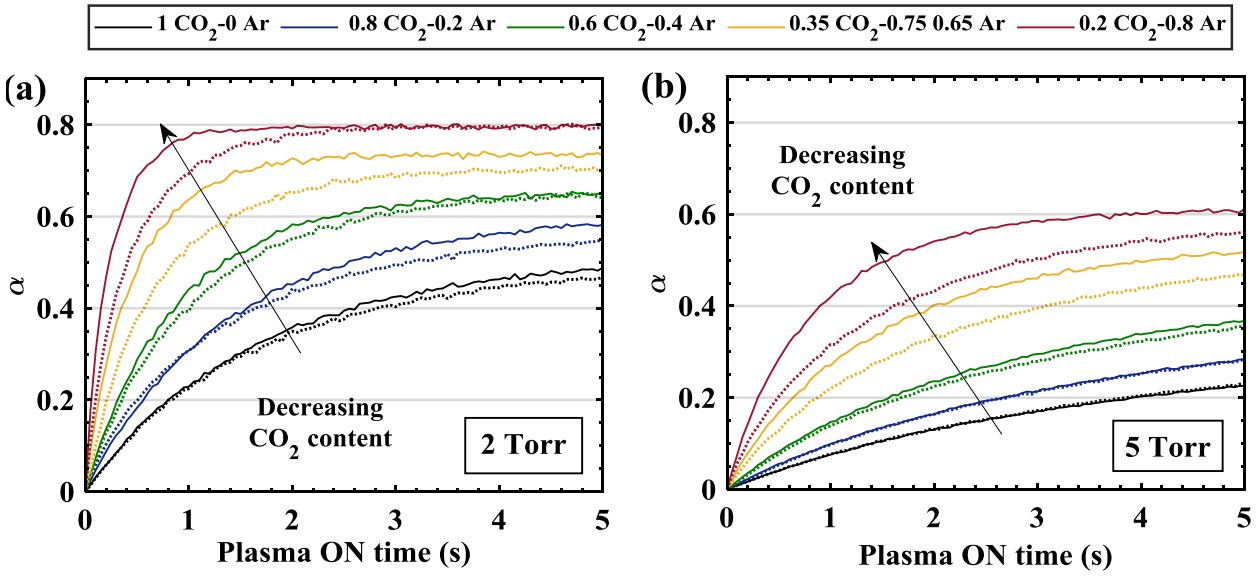

Figure 6.18: Time evolution of the dissociation parameter α for CO_2-Ar mixtures (solid lines) and CO_2-N_2 mixtures (dotted lines) for 2 (panel (a)) and 5 (panel (b)) Torr. The mixtures indicated in the legend are approximated. The real gas mixtures are shown in figure 6.19.

In order to investigate the effect of ad-mixtures on the final dissociation rate, figure 6.19 (a) plots the average of the α values between T^{ON}=20 s and T^{ON}=25 s as a function of the initial CO_2 for CO_2-N_2 and CO_2-Ar mixtures, including also CO_2-O_2 mixtures. Both N_2 and Ar ad-mixtures show a single linear dependence, decreasing with the CO_2 content. At the same time, CO_2-O_2 linearly increases with the amount of CO_2. If we now plot the same data as a function of a so-called "extractable" O in the initial fraction, calculated as $[1\times f_{CO_2} + 2\times f_{O_2}]$ (*i.e.* considering that CO is not dissociated), shown in figure 6.19 (b), we observe that all the data taken at the same pressure, fall in a single line. The data for CO-O_2 mixtures is also included and are in good agreement with the other gas mixtures. Assuming that CO is not dissociated is a rough estimation of course, and the data for CO-O_2 mixtures at 2 Torr are slightly lower than the others. At low pressure, $^{E}/_{N}$ is higher and CO dissociation may become relevant in that case, increasing the "extractable" O and shifting these values towards the right of the graph. The single linear dependence of the steady-state dissociation value with the overall oxygen content provides another indication of a steady-state α strongly controlled by "back reaction" mechanisms. Considering the differences between Ar, N_2 and O_2, the dominant "back reaction" mechanism does not seem to be dependent on the nature of a 3^{rd} body, as it would be in reactions such as $CO + O + M \rightarrow CO_2 + M$, supporting again the idea of a 2-body mechanism. As a final comment, 6.19 (c) plots the steady state CO fraction ($^{CO}/_{N}$), and shows that even though the addition of N_2 and Ar increases significantly the value of α, ($^{CO}/_{N}$) is always higher for pure CO_2 initial gas mixtures.

✓ Ar and N_2 significantly modify the chemical kinetics for short T^{ON}, as expected for an initial slope dominated by direct electron impact dissociation.
✓ The steady-state dissociation fraction for all gas mixtures studied follow a single linear dependence with the total oxygen content, supporting the idea of an important back reaction mechanism via 2-body reaction.

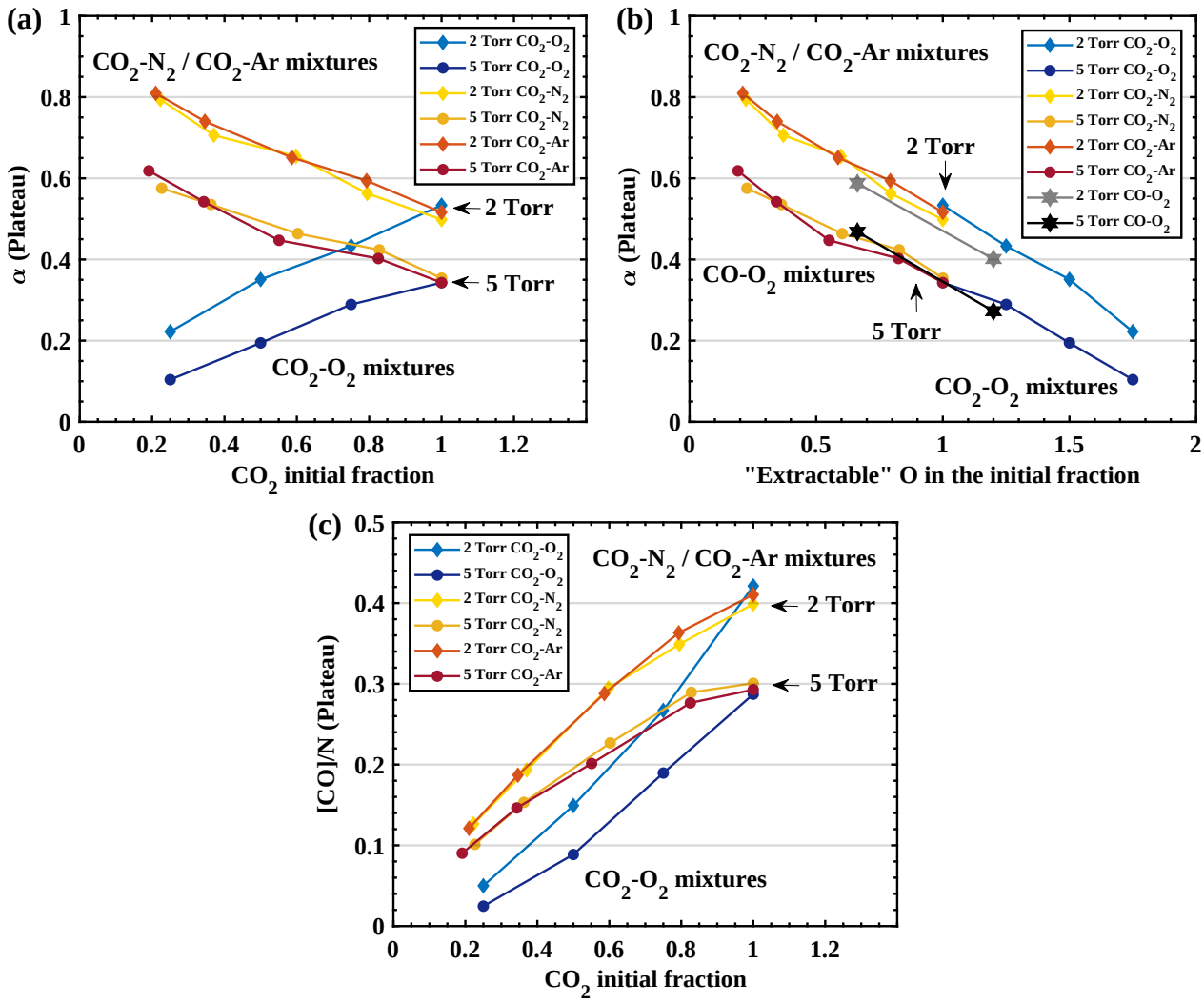

Figure 6.19: (a) & (b) Variation of α(plateau), calculated as the average of the α values between T^{ON}=20 s and T^{ON}=25 s, for different gas mixtures of CO_2-O_2, CO_2-N_2 and CO_2-Ar as a function of: (a) initial CO_2 fraction and (b) the initial "extractable" O in the initial fraction, calculated as $[1\times f_{CO_2} + 2 \times f_{O_2}]$ (*i.e.* as if CO could not be dissociated). Data for CO-O_2 mixtures is also included in panel (b). (c) Variation of the CO fraction over the total gas density as a function of the initial CO_2 fraction.

6.4 Building-up in glow discharge

Throughout this chapter we have observed that the initial linear evolution ("initial slope") after starting the building-up experiment is not affected by any of the parameters studied, such as pulse duration, delay between pulses, number of trains, number of pulses, or even the initial O_2 content, except by two parameters: pressure and discharge power. In section 6.3.1, we already suggested that this linear time evolution could be related to the first-order process: electron impact dissociation of CO_2: $e^- + CO_2 \rightarrow CO + O$, which would depend only on the electron density, *i.e.* the reduced electric field, and the fractions of CO and CO_2, as derived from equation (6.1). As expected, the initial slope is only affected when modifying significantly the electron kinetics, like in mixtures with argon or N_2.

As discussed in the introduction (chapter 1), the electron impact dissociation cross section of CO_2

has been reported by several authors but the proposed values differ significantly both in threshold and in magnitude as a function of the electron energy, as shown in figure 1.5. The derived rate coefficients are orders of magnitude different *Grofulović et al.* [2016], hindering the understanding of CO_2 plasmas *Bogaerts et al.* [2016]; *Capitelli et al.* [2017]. The objective of doing building-up experiments in the glow discharge is, first, to verify that the initial steps in the time evolution of the dissociation fraction are indeed purely related to electron impact dissociation and then to use the information from the initial slope to provide an experimental validation of the electron impact dissociation cross section of CO_2. Two complementary methods will be followed:

1. A comparison of the rate coefficients calculated from our experimental results with those derived from cross sections available in literature.
2. A comparison of the experimental time evolution of the dissociation fraction with the simulations of a 0D model.

For this purpose, a reduced set of experiments were done with the glow discharge, for which the determination of the electric field and therefore the estimation of the electron density are straightforward. The aim of these measurements is not to scan a wide set of parameters, already done with the RF discharge, but in the first place to check that the conclusions extracted from the RF discharge are still valid for the glow discharge and, as second goal, to extract enough data to compare with available rate coefficients and with the kinetic model over a range of E/N as large as possible.

6.4.1 Experimental results and comparison of rate coefficients

The time evolution of the dissociation fraction for some representative conditions in the glow discharge is shown in figure 6.20. Qualitatively the results are similar to the RF plasma: lower pressures and higher currents show faster time evolution and higher dissociation fraction. For every plasma condition, α shows an initial fast increase followed by a saturation towards longer T^{ON} times. Figure 6.20 (a) plots the variation of α as a function of T^{ON} for two pressures, 1 and 2 Torr, and three discharge currents: 20, 30 and 40 mA. In the case of the glow discharge, the controlled parameter is the discharge current and not the power as in the RF, but both are proportional. Evidently, higher currents make the time evolution *i.e.* the kinetics of the discharge faster. This graph includes two measurements for the same condition, 2 Torr and 40 mA, to show the reproducibility of the experiment in the glow discharge. Figure 6.20 (b) presents the time evolution of α for several pressures at a given current (40 mA). Lower pressures show a faster increase of the dissociation fraction and the final equilibrium concentration is reached for shorter T^{ON} than at higher pressures. The effect of the current can be explained mostly by the increase of the electron density when the current increases, along with a small contribution of the slightly higher reduced electric field (in these conditions the electric field decreases slightly with current but the E/N increases due to the higher gas temperature). The time variation of α for different pressures is mostly dominated by the effect of the reduced electric field. Although the electric field increases as a function of pressure, the reduced electric field decreases significantly (see section 3.3). These results are in good agreement with those observed in the RF in section 6.3.1. For short total plasma ON times the evolution of the dissociation fraction with time is still ∼linear (small deviations for low pressures are discussed below).

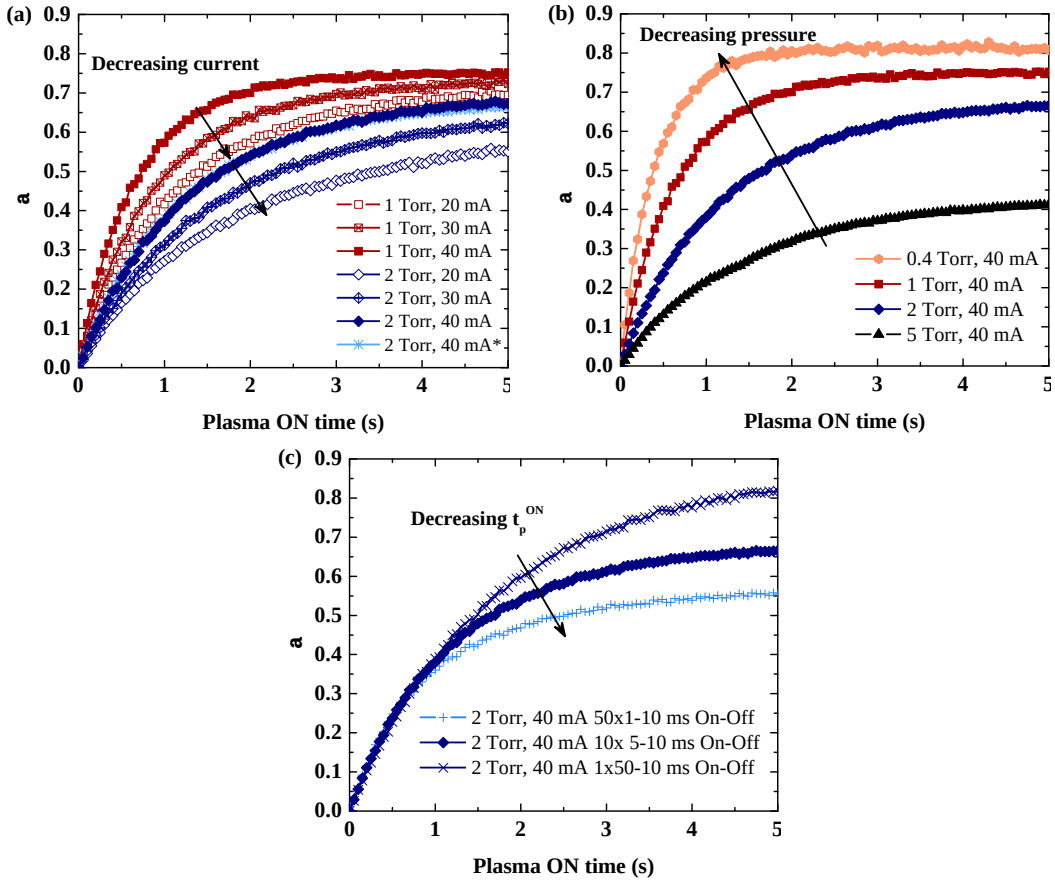

Figure 6.20: Time evolution of the dissociation fraction (a) for two pressures (1 and 2 Torr) and three different currents 20, 30 and 40 mA, and (b) for different pressures at 40 mA (c) for different pulse durations at 2 Torr, 40 mA.

In order to be sure that the initial slope is defined only by direct electron impact dissociation of CO_2 and that it can be used to determine the corresponding rate coefficient, we must verify that neither the dissociation through vibrational up-pumping nor the possible occurrence of "back" reactions", affect the measured CO and CO_2 densities in the relevant time range. Firstly, the dissociation through vibrational up-pumping is not expected to show a linear time evolution since it is not a first order process. In addition, the density of the individual vibrationally excited levels has been measured in similar experimental conditions (see chapter 4), and was shown to be relatively low, as expected in a glow discharge regime. The maximum of vibrational excitation in the asymmetric stretch mode of CO_2 was reached $\sim$ 0.7-1ms after the beginning of the plasma pulse, followed by a relaxation due to V-V and V-T energy exchanges *Grofulović et al.* [2018]. As example, at 5 Torr 50 mA, at the maximum of vibrational excitation the density of CO_2 molecules in $\nu_3 = 1$ was found to be 0.018 times the density in ground state ($\nu_3 = 0$). For $CO_2(\nu_3 = 2)$ is $3.4{\times}10^{-4}$ times the ground state density (see figure 4.15).

Additionally, varying the pulse duration in RF experiments was not showing any influence in the initial slope, despite the different average vibrational excitation. We have varied the pulse duration in the glow discharge only for one discharge condition, 2 Torr and 40 mA, to confirm that the behaviour is similar. Figure 6.20 shows the measured time evolution of α for three different pulse

durations: 50 × t_p^{ON}= 1 ms ON - t_p^{OFF}=10 ms OFF and 1 × t_p^{ON}= 50 ms ON - t_p^{OFF}=10 ms OFF and the reference pulse configuration. This figure confirms that in the glow discharge the effect of pulsing is similar to the observations with the RF: longer pulses lead to higher dissociation in the steady-state, and the vibrational excitation does not contribute to measured dissociation fraction for short T^{ON}.

Concerning a possible influence of recombination reactions producing back CO_2, the measurements with O_2 add-mixtures in the RF showed that adding O_2 to the gas mixture had no effect on the initial slope, whereas a clear effect starts to be noticeable after a certain time point (∼0.5 s of T^{ON}) (see section 6.3.2). Hence, only data corresponding to T^{ON} <0.3 s were kept for the calculation of the rate coefficient. The relatively high amount of CO for low pressures could suggest the possibility of CO dissociation by electron impact. However, it is not expected to be very relevant due to the high energy threshold, estimated to be above 10 eV *Polak and Slovetsky* [1976], and the typical EEDF (electron energy distribution function) in our conditions. Still, only data with a CO/N ratio below 30% and showing a clearly linear time variation in α *versus* T^{ON} were kept to insure a minimal influence of other processes on the determination of the rate coefficients.

The electric field was measured for each data point matching these conditions. Note that CO affects the electric field in the discharge in particular for low pressures. As example, at 1 torr, 20 mA the electric field changes from 19.3 V/cm at T^{ON}=0.05 s to 16.4 V/cm at T^{ON}=0.3 s. From the reduced electric field (E/N), we calculate the electron drift velocity through a fitting of data available in LXCat database *ETH Zurich* [2018]. The electron density is calculated with the equation:

$$n_e = \frac{J}{e \cdot v_d} \tag{6.2}$$

where J is the current density ($J = \frac{I}{S}$, I being the discharge current and S the transversal area of the plasma reactor), e is the electron charge and v_d the electron drift velocity. For low pressures, the first 2 or 3 trains of pulses present a certain over-shoot in the discharge current (∼20% higher than targeted). The real current was recorded by the oscilloscope and taken into account in the calculations. The measured CO and CO_2 densities as well as the calculated n_e values are used in the equation for the electron impact dissociation rate to obtain the rate coefficients for the electron impact dissociation of CO_2:

$$\frac{d[CO]}{dt} = K_{diss} \cdot n_e \cdot [CO_2] \rightarrow [CO] = n_e \cdot K_{diss} \cdot [CO_2] \cdot T^{ON}, \tag{6.3}$$

These values are plotted in figure 6.21 along with the rate coefficients calculated from the available cross sections by direct integration over the EEDF *Grofulović et al.* [2016], according to the expression:

$$K_{diss} = \left(\frac{2}{m_{e-}}\right)^{\frac{1}{2}} \int_0^\infty \epsilon \sigma(\epsilon) f(\epsilon) d\epsilon$$

where m_{e-} is the electron mass, $f(\epsilon)$ is the electron distribution function (EEDF) normalized so that $\int_0^\infty \epsilon^{\frac{1}{2}} f(\epsilon) d\epsilon = 1$ and $\sigma(\epsilon)$ is the cross section for dissociation by electron impact.

The agreement between our experimental rate coefficients and the values obtained from the cross section proposed by Polak and Slovetsky *Polak and Slovetsky* [1976] is remarkable. These values

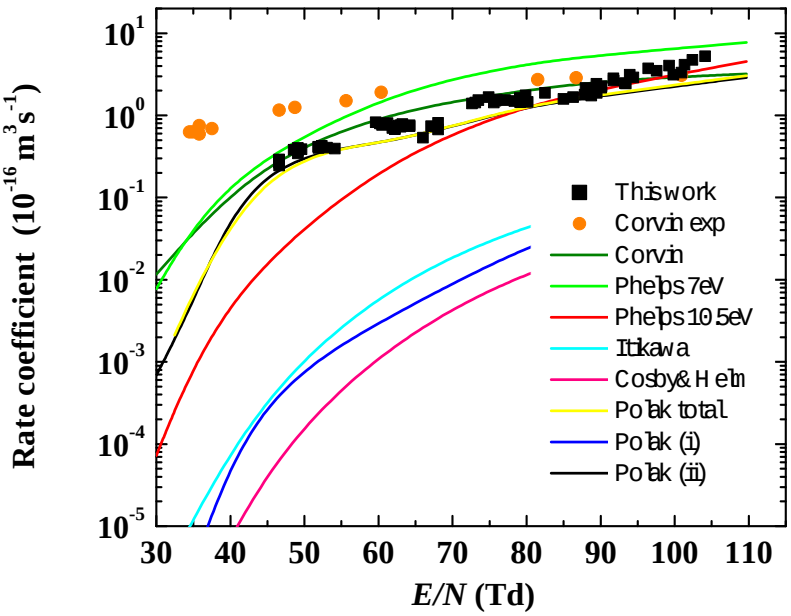

Figure 6.21: Rate coefficients for the electron impact dissociation of CO_2 calculated from the experimental data compared with the values obtained from the cross sections available in the literature *Grofulović et al.* [2016].

are significantly lower than those calculated from the 7 eV cross section from Phelps, widely used in the literature.

6.4.2 Comparison with a kinetic model

The experimental time evolution is compared with the results of a 0D kinetic model in this section. The model, developed in IST Lisbon *Silva and Guerra* [2020], solves on time the electron and vibrational kinetics of CO_2 *Silva et al.* [2018]; *Grofulović et al.* [2018] and takes into account the time evolution of the gas temperature and the electric field along a plasma pulse. The results concerning the vibrational kinetics have been already discussed and compared with our experimental data in section 4.6. A simple set of reactions describing CO_2 dissociation and recombination (detailed in table 6.4) was added for completeness.

Figure 6.22 shows the comparison between the experimental data at 4 Torr, 40 mA as illustrative example, and the output from the model calculated for two different cross sections: Polak and

Reaction	Reference
$e^- + CO_2(v^*) \rightarrow e^- + CO + O$	*Polak and Slovetsky* [1976] or *Hake and Phelps* [1967]
$CO + O + M \rightarrow CO_2(000) + M$	*Capitelli et al.* [2017]; *Cenian et al.* [1994]
$e^- + O_2 \rightarrow e^- + O + O$	*Phelps* [1985]
$O + wall \rightarrow 1/2\ O_2$	Exp.values(chapter 8)
$O + O + M \rightarrow O_2 + M$	*Annušová et al.* [2018]

Table 6.4: Set of chemical reactions included in the model. Reactions accounting for the electron and vibrational kinetics of CO_2 are detailed in *Silva et al.* [2018]; *Grofulović et al.* [2018].

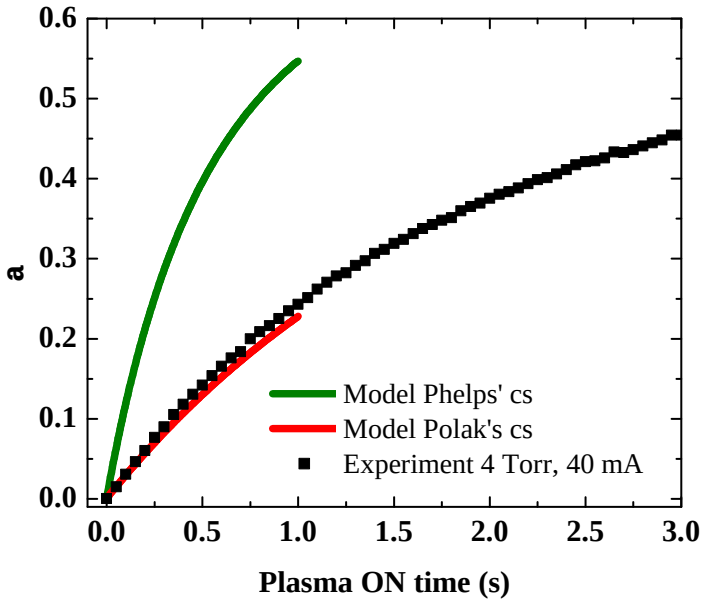

Figure 6.22: Comparison of experimental data at 4 Torr, 40 mA with a 0D model using Polak's or Phelps' electron impact dissociation cross sections.

Slovetsky's *Polak and Slovetsky* [1976] and Phelps' *Hake and Phelps* [1967]; *Phelps* [1985]. The model reproduces very well the experimental data for short T^{ON} when using Polak's cross section, whereas Phelps' clearly over-estimates the dissociation. Note that the electron impact dissociation from $CO_2(010)$ level was taken into account either with the same rate coefficient as from the ground (000) state or using a threshold shift in the cross section *Kozák and Bogaerts* [2014a]. The results are not affected by the assumption considered. Moreover, the contribution to dissociation coming from higher vibrationally excited levels was found to be negligible in our experimental conditions. Additionally we have verified that the inclusion of the reactions detailed in table 6.4 leads to differences in the modelled evolution of less than 1% up to T^{ON}=0.4 s. This comparison confirms the conclusions derived from the good agreement between the experimental rate coefficient with the rate coefficients calculated from Polak and Slovetsky's cross section discussed in the previous section.

✓ Glow discharge experiments agree qualitatively with the conclusions extracted from the RF experiments, and prove that the initial slope is given by the electron impact dissociation in our experimental conditions.
✓ The comparison of the rate coefficients derived from the glow discharge data with those calculated from available electron impact dissociation cross sections validate the theoretical cross section calculated by *Polak and Slovetsky* [1976].
✓ A comparison with the output from a 0D model confirms the previous conclusions.

6.5 Summary and conclusions

Performing measurements in a "static reactor" (*i.e.* without gas flow) brings practical difficulties to achieve good reproducibility, but it allowed a more detailed analysis of the time evolution of the

dissociation fraction. The large parametric study done with the RF discharge allowed by the stability of the power, has shown an initial region dominated by direct electron impact dissociation. When the CO density becomes large enough an important contribution of back reaction mechanisms controlled by excited states, have been evidenced. The linear dependence of this "back reaction" with the total oxygen content of the initial gas mixture for very different diluting gases in mixtures with CO_2 seem to exclude three body reactions to explain the back reaction. The characteristic time relevant to influence this mechanisms in the early post-discharge (a few milliseconds) as well as the rates found in literature strongly suggest an important role of the reaction $CO(a^3\Pi_r)+O_2 \rightarrow CO_2+O$. Working in static conditions is also a good way to emphasize a possible contribution of surface reactivity. The difference between the steady-state values of α obtained in CO-O_2 and CO_2-O_2 mixtures suggest the possibility of chemical reactions involving CO and/or CO_2 at the walls.

Finally a careful experimental approach allowed to use the initial slope data measured in the glow discharge to validate the electron impact dissociation cross section of CO_2 calculated by Polak and Slovetsky. A remarkable good agreement was found comparing our experimental rate coefficients with those derived from their theoretical calculations, confirmed by the comparison with a 0D model. This validation suggest and agrees with the hypothesis that the cross sections proposed by Phelps probably include other energy loss processes in addition to the pure electron impact dissociation *Grofulović et al.* [2016]. The determination of what appears to be the most correct effective cross-section for CO_2 electron impact dissociation is particularly important for the development of kinetic models of pure CO_2 or CO_2-containing plasmas.

Chapter 7

Investigating the chemistry of CO_2 plasmas by isotopic exchange

Contents

7.1 Introduction . . . 189
7.2 Experimental set-up . . . 190
7.3 Data treatment . . . 191
7.3.1 Description of the fitting script . . . 191
7.3.2 Example of isotopic measurement . . . 194
7.4 Experimental results: CO_2-CO-O_2 mixtures . . . 196
7.4.1 CO_2-O_2 mixtures with isotopically labelled species . . . 196
7.4.2 CO-O_2 mixtures . . . 201
7.4.3 Comparison of gas mixtures . . . 206
7.5 Discussion . . . 208
7.5.1 Initial time steps: fast growth of isotopically-labelled CO_2 and CO . . . 208
7.5.2 "Turning region": back reaction and effect of the vibrational kinetics . . . 211
7.6 Conclusions and perspectives . . . 214

7.1 Introduction

The "building-up" experiments presented in the previous chapter showed that the time evolution of the dissociation fraction follows three time-regions: (1) Initial fast increase dominated by electron impact dissociation (2) "turning region", from T^{ON} ≈0.5s, when a significant "back reaction" mechanisms, both under plasma exposure and in post-discharge, is noticeable (3) steady-state, with no evolution of the gas mixture due to a balance between creation and recombination processes. The role of the vibrational excitation of CO_2 and CO molecules, if existing, remains unclear.

In this chapter we present a different approach to study the time evolution of the chemistry of neutral species in CO_2 plasmas. Similar building-up experiments in CO_2-CO-O_2 gas mixtures will be presented, but using isotopically labelled species. The primary objective is to trace the exchange of oxygen atoms between different species and study the mechanisms that activate the

"back-reaction". The use of isotopes in this context is interesting because the electron kinetics, the electron impact dissociation processes and the chemical reactions between neutral species are *a priori* similar for different isotopes *Mori et al.* [2002]. However the vibrational kinetics of different isotopologues may be significantly different. The reason is the change in the energy spacing between vibrational levels due to the change of weight in one (or two) of the atoms in the molecule *Herzberg* [1966].

The use of isotopes to study the chemical reactivity in low temperature plasmas is not very extended. They have been mostly used to investigate surface processes *Janssen and Tuzson* [2010]; *Marinov et al.* [2014] and for isotope separation by differentiated vibrational pumping *Gordiets and Mamedov* [1975]; *Ploenjes et al.* [1998]; *Mori et al.* [2001]. These subjects, along with atmospheric studies related to the anomalous isotope enrichment in the upper atmosphere, are the main sources of information to analyse the experimental results.

7.2 Experimental set-up

All the isotope experiments were done with the RF discharge. The experimental set-up and measurement procedure are similar to those described in section 6.2, with few modifications detailed hereinafter. The gas line is slightly modified and an extra branch was added to the gas line upstream the discharge to include a gas bottle of isotopically marked O_2 (99% $^{18}O_2$, Iconisot) and several high precision gas valves. A reduced scheme of the modified gas line is shown in figure 7.1. Only one step of the measurement procedure is modified: the filling of the reactor with appropriate gas mixture before starting the measurement. In previous non-isotopic experiments, the valve next to the pump was closed and the buffer+reactor volume was filled with CO_2 flowing from the gas bottle. Fine pressure adjustment was done with the precision valve close to the pump. Afterwards, the reactor valves were closed isolating the reactor from the buffer volume.

For isotopic measurements the filling process is the following: The whole gas line, including the reactor, is purged and the Teflon valves (V_t) are closed isolating the reactor from the rest of the gas line. With the reactor empty and isolated, the pump valve (V_{pump}) is closed and the by-pass valve ($V_{by-pass}$) opened. The buffer volume is then filled with a given pressure of CO_2. Subsequently, the upstream valve ($V_{non-ISO}$) is closed, isolating the buffer zone. With high pressure in the

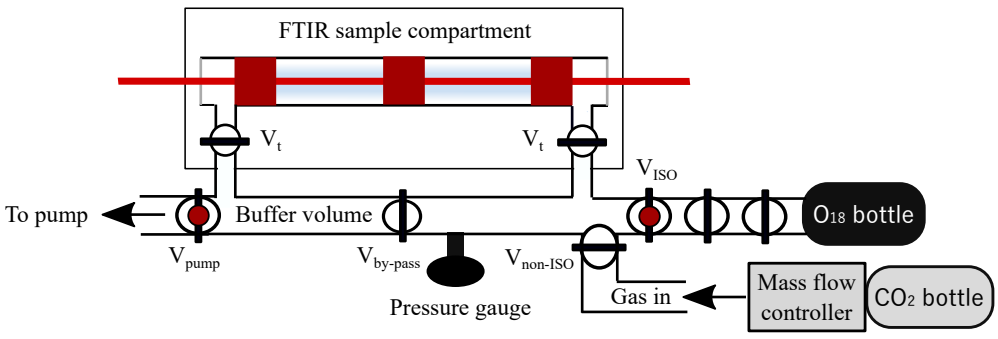

Figure 7.1: Scheme of the gas line used for the building-up experiments with isotopically marked species. The rest of the FTIR set-up can be seen in figure 6.1. V_t, $V_{by-pass}$ and $V_{non-ISO}$ are usual gas valves; V_{pump} and V_{ISO} are high precision gas valves.

isotope gas line, the high precision valve connecting the isotope gas line with the buffer volume (V_{ISO}) is carefully opened until the targeted total pressure is reached and closed again. Finally, the reactor closing valves are opened again so that the pressure in the buffer volume + reactor reaches the targeted pressure for the experiment. A pressure calibration is therefore required to know in advance the pressure needed in the buffer volume to get the desired pressure when opening the reactor. After this process, the reactor is closed again (isolated) and the measurement proceeds similarly to what was described in chapter 6.2. The filling procedure may introduce a certain error in the initial gas mixture fractions, which is estimated to be maximum of 10%. Similarly to the non-isotopically marked building-up experiments, a pre-treatment of the reactor walls was applied before every measurement. This pretreatment, performed in flowing conditions, was done always with non-isotopically labelled gas. The initial adjustment of the match box settings was also done with non-isotopic gas mixtures in the reactor. All the measurements presented in this chapter were done for the same RF power 40 W (reading) ≈27.7 W (real). A summary of the experimental details is given in the experimental box 7.1.

Diagnostics: FTIR (thermal)	**Reactor**: Short	**Pressure**: **2-5** Torr
Discharge: RF	(23 cm)	**Power (RF)**: 40 W (reading)
Pulse: N_{tr}=500 × N_p=10 ×	$\boldsymbol{T_{wall}}$=not	**Gas mixtures**: CO_2-O_2
t_p^{ON}=5 - t_p^{OFF}=10 ms On-Off	controlled	(0.75-0.25/0.5-0.5/0.25-0.75),
(reference pulse Exp.box 6.2)	**Flow**: 0 (Static)	CO-O_2 (0.666-0.333/0.4-0.6)

Experimental box 7.1: General experimental conditions for isotopic experiments.

7.3 Data treatment

7.3.1 Description of the fitting script

The FTIR spectra are fitted with the same MATLAB script used in chapter 6, but adapted to account for a set of 12 isotopes of CO_2 and 6 isotopes of CO, added very recently in HITRAN database *Gordon et al.* [2017]. The isotopes included in the fitting script are listed in table 7.1. Acquiring the spectra in thermal equilibrium is particularly important in complex isotopic mixtures. Indeed, a spectra taken under discharge conditions, out of thermal equilibrium, would require too many fitting parameters (including vibrational temperatures for all the species involved) and lead to large uncertainties. The different masses of the isotopes induce a shift in wavelength in the FTIR absorption spectra. The induced shift is big enough to be resolved with the spectral resolution of the FTIR and consequently, the contribution of the different isotopes can be clearly distinguished and fitted as long as thermal equilibrium can be assumed. Heavier isotopes show an absorption spectra which is shifted towards lower wavenumbers, *i.e.* the vibrational energy levels are at a lower energies for the heavier isotopes. As example $^{12}C^{16}O_2(00^01)$ has an energy of 2349.143 cm^{-1}, whereas for $^{16}O^{12}C^{18}O(00^01)$ is 2332.113 cm^{-1} and for $^{13}C^{16}O_2(00^01)$ is 2283.488 cm^{-1}. Note that, as a consequence, low energy levels of heavier isotopologues can be populated more easily than lighter isotopologues. Figures 7.2, 7.3 and 7.4 show simulated spectra of CO_2 and CO bands for different isotope compositions to illustrate their shift in the spectra. Figures 7.2 and 7.3 show the simulated spectra of the CO_2 band (between 2240 and 2390 cm^{-1}) with different isotopic oxygen

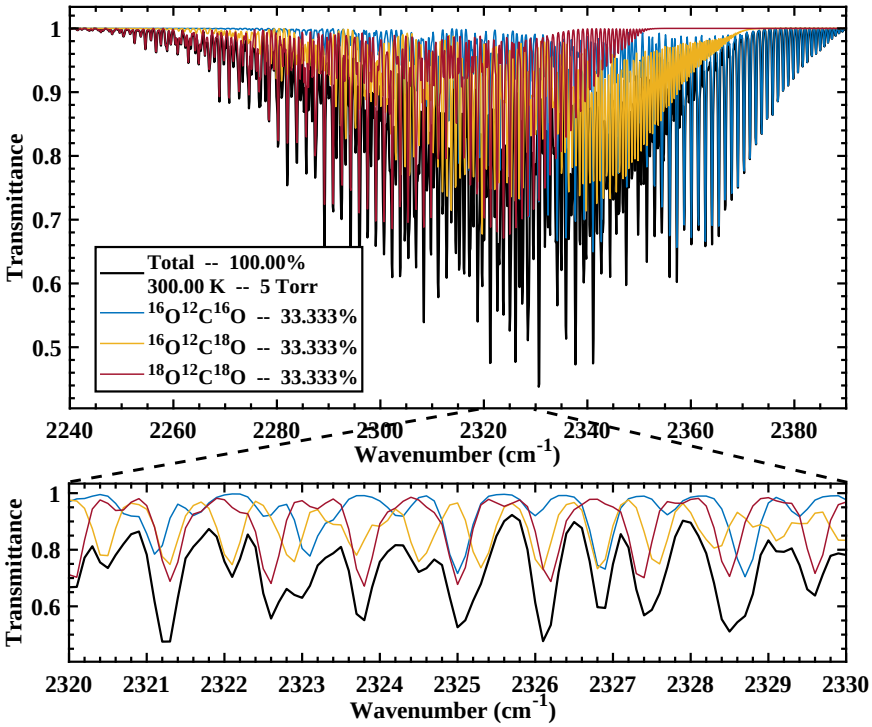

Figure 7.2: Simulated spectra in the CO_2 band region for different CO_2 isotopologues containing ^{12}C and ^{16}O and/or ^{18}O.

or carbon composition, respectively. When comparing CO_2 with O^{16}, O^{17} or O^{18}, we observe that the spectra of the different isotopologues are strongly convoluted. Varying the weight of the central carbon atom induces a much larger wavelength shift. Figure 7.4 shows the simulated spectra of the CO band (between 1950 and 2250 cm^{-1}) with a similar proportion of the three CO isotopes having a ^{12}C included in the script: $^{12}C^{16}O$, $^{12}C^{17}O$ and $^{12}C^{18}O$.

In our experiments CO and CO_2 from an Air Liquide, Alphagaz 2 bottles were used as a source of non-marked CO or CO_2 (with ^{12}C and ^{16}O atoms). However, due to the natural abundance

CO_2 isotopes	Abundance
$^{16}O^{12}C^{16}O$	0.984204
$^{16}O^{13}C^{16}O$	0.0110574
$^{16}O^{12}C^{18}O$	0.00394707
$^{16}O^{12}C^{17}O$	0.000733989
$^{16}O^{13}C^{18}O$	0.0000443446
$^{16}O^{13}C^{17}O$ *	0.00000824623
$^{18}O^{12}C^{18}O$	0.00000395734
$^{17}O^{12}C^{18}O$	0.0000014718
$^{17}O^{12}C^{17}O$ *	0.000000136847
$^{18}O^{13}C^{18}O$	0.00000004446
$^{17}O^{13}C^{18}O$ *	0.0000000165354
$^{17}O^{13}C^{17}O$ *	0.00000000155

CO isotopes	Abundance
$^{12}C^{16}O$	0.986544
$^{13}C^{16}O$	0.0110836
$^{12}C^{18}O$	0.00197822
$^{12}C^{17}O$	0.000367867
$^{13}C^{18}O$	0.000022225
$^{13}C^{17}O$ *	0.0000041329

* Isotopes disabled for the fitting of $C^{16}O_2$-$^{18}O_2$ gas mixtures

Table 7.1: CO_2 and CO isotopologues included in the fitting script with their natural abundance.

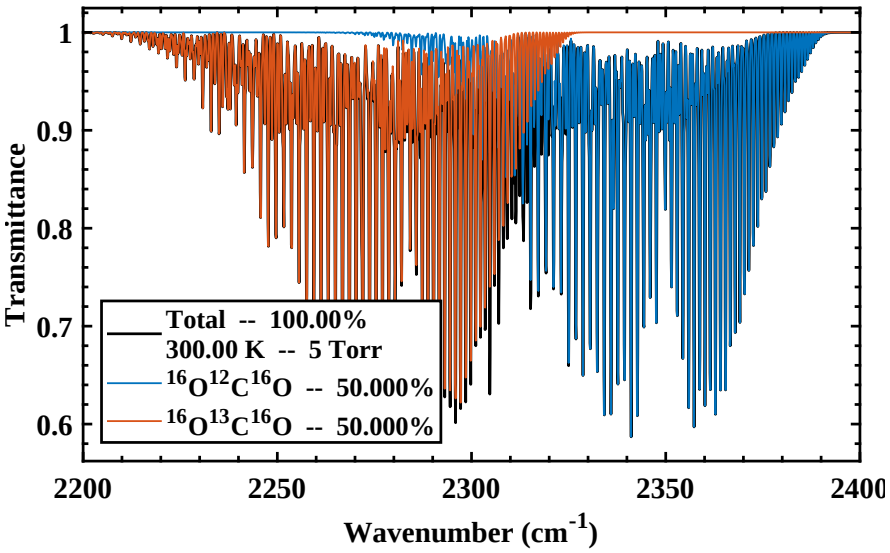

Figure 7.3: Simulated spectra in the CO_2 band region for different CO_2 isotopologues containing ^{16}O and ^{12}C or ^{13}C.

of other isotopes, a non-negligible amount of isotopologues including ^{13}C, ^{17}O and ^{18}O atoms are always present in the gas mixture, as already discussed regarding figure 6.3. The natural abundance of these isotopes obtained from HITRAN database is included in table 7.1.

Measurements performed with labelled molecules were done with a $^{18}O_2$ bottle (99% $^{18}O_2$). The dominant isotopologues in our gas mixture are therefore combinations of ^{12}C, ^{16}O and ^{18}O, but

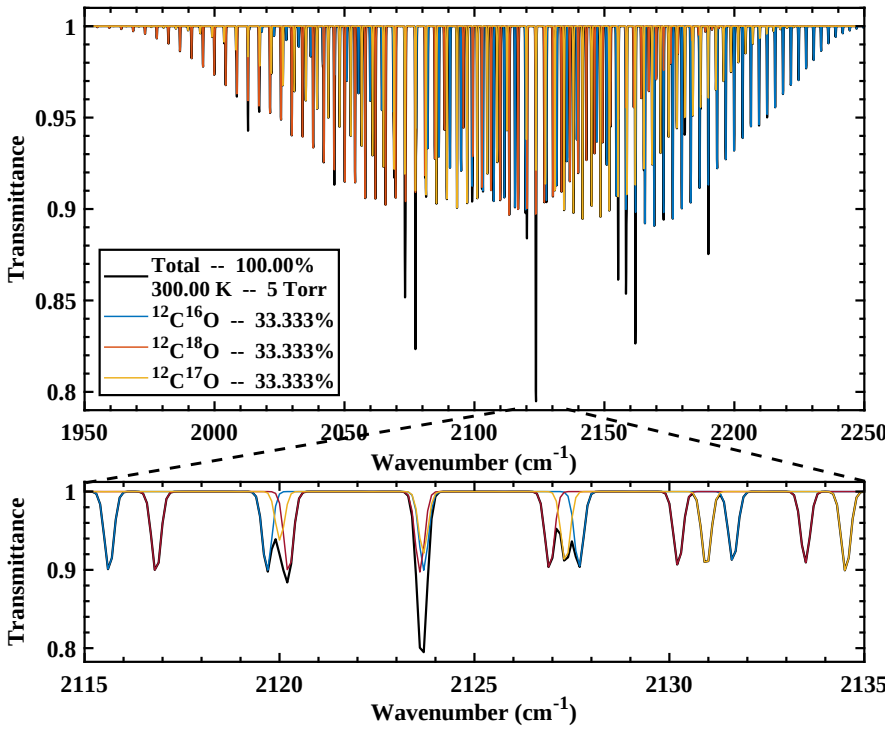

Figure 7.4: Simulated spectra in the CO band region for different CO isotopologues containing ^{12}C and ^{16}O, ^{17}O or ^{18}O.

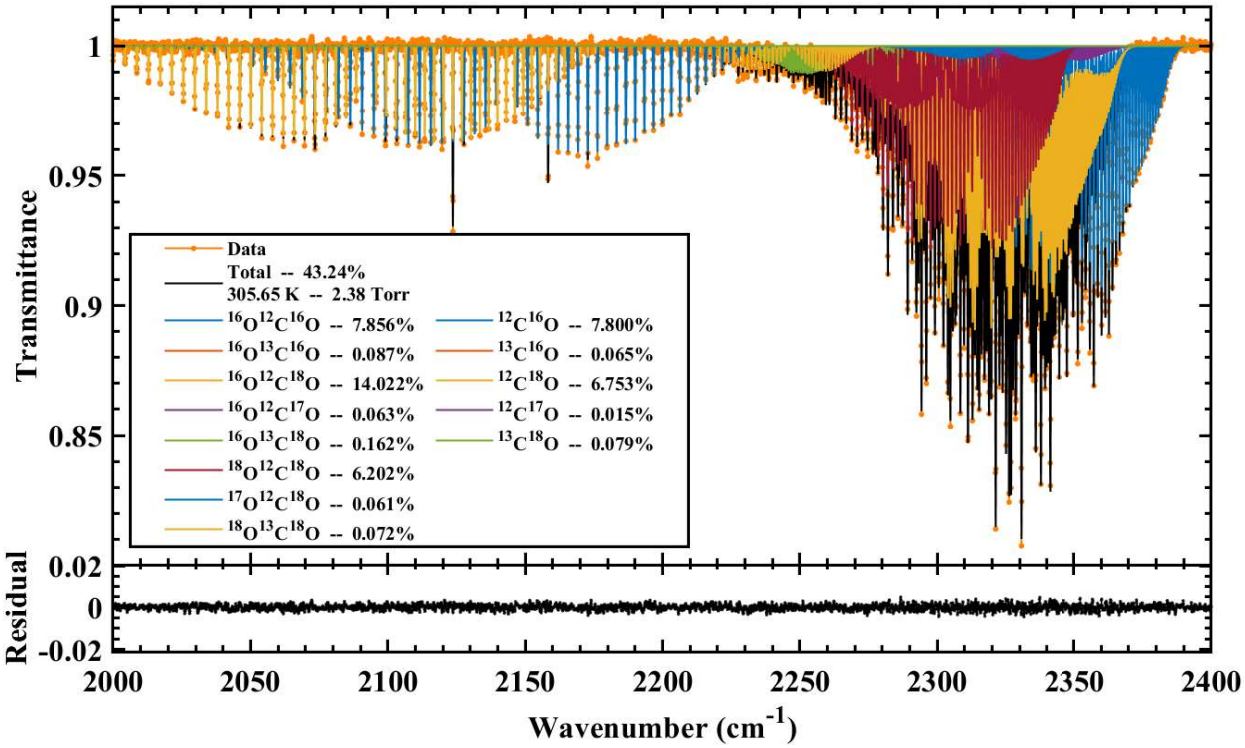

Figure 7.5: Data and fitting of the FTIR spectra obtained in a measurement of $0.5CO_2$-$0.5O_2$ at 2 Torr, 40 W.

the natural abundance and other impurities present in the gas bottles makes necessary to include some of the isotopologues with ^{13}C and ^{17}O atoms that contribute to the spectra. The script is prepared to deal with all the possible combinations of the isotopes of C and O. However, not all of them will be useful for the gas mixtures studied in this chapter and including them leads to noisier fits. Therefore, for measurements with mixtures of non-marked CO_2 and $^{18}O_2$, only isotopes above detection limit were kept for the final fit of the data, whereas the others were disabled. The disabled isotopes (4 for CO_2 and 1 for CO) are marked with symbol * in table 7.1.

An example of a measured spectra corresponding to the last spectra of a building-up taken at 2 Torr, 40 W in a gas mixture of 0.5 $C^{16}O_2$-0.5$^{18}O_2$ and the corresponding fit, showing the contribution of all the different isotopes, is presented in figure 7.5. The percentage of each isotopologue is given in the legend. The increase in pressure and decrease of the percentage of carbonated species in the gas mixture are caused by the accumulation of O_2. The residual of the fit is included below and shows the high quality of the fitting.

7.3.2 Example of isotopic measurement

Figure 7.6 shows an example of the time evolution of the different CO_2 (panel (a)) and CO (panel (b)) isotopologues for a measurement with an initial gas mixture of $0.5CO_2$-$0.5^{18}O_2$ taken at 2 Torr, 40 W and the reference pulse configuration. In panel (a) we observe a decrease of the initial main CO_2 isotopologue, $^{16}O^{12}C^{16}O$, and an increase of the CO_2 isotopes with one or two ^{18}O atoms. The isotopically-marked CO_2 species appear already from the first data point, after only 50 ms of T^{ON}, and monotonically increase until the steady-state equilibrium. These isotopologues can only come from non-marked CO_2 molecules that have undergone an O atom exchange process with atoms that

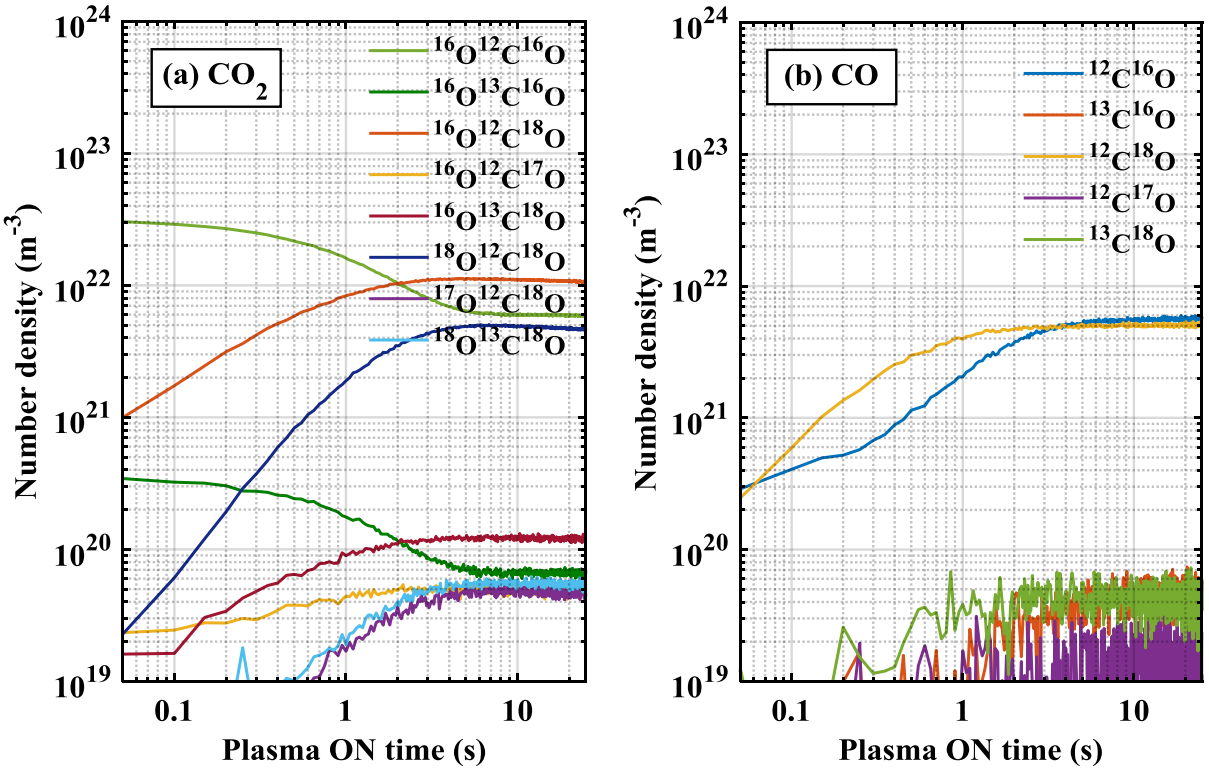

Figure 7.6: Example of time evolution of the fitted number densities corresponding to the CO_2 isotopologues (panel (a)) and CO (panel (b)) for a measurement of $0.5CO_2$-$0.5O_2$ at 2 Torr, 40 W.

come from the dissociation of $^{18}O_2$. All the isotopologues of CO increase with increasing T^{ON}, as expected. Remarkably, the densities of the two main isotopologues, $^{12}C^{16}O$ and $^{12}C^{18}O$ are very similar already at T^{ON}=50 ms and at the end of the measurement. A more detailed analysis of the trends shown in this figure will be given in following sections but it is worth emphasizing the fast isotope incorporation in CO and CO_2 molecules as a significant, and somewhat unexpected, experimental result.

It is also noticeable that $^{16}O^{12}C^{16}O$ and $^{16}O^{13}C^{16}O$ follow the same trend; similarly for $^{16}O^{12}C^{18}O$ and $^{16}O^{13}C^{18}O$, and for $^{18}O^{12}C^{18}O$ and $^{18}O^{13}C^{18}O$, within the experimental error. The isotopologues with ^{13}C reproduce the same behaviour as the isotopologues with ^{12}C as a function of T^{ON}. Considering the significant difference in the vibrational energies of both isotopes (see figure 7.3), the consistent trends for ^{12}C and ^{13}C isotopologues already indicates a negligible role of the vibrational excitation of CO_2 in the dissociation process in our discharge. For CO isotopologues, $^{12}C^{16}O$ and $^{13}C^{16}O$ on the one hand and $^{12}C^{18}O$ and $^{13}C^{18}O$ on the other hand, show also the same time evolution even though they are close to the detection limit. The isotopologues containing ^{17}O, on the contrary, show different variation as a function of time. A hypothesis to explain the specific behaviour of ^{17}O containing isotopologues is given in section 7.5.2. However, the ^{17}O content was not varied in our experiments and the abundance ^{17}O-containing isotopologues is very low in our measurements, it is therefore difficult to extract meaningful information from their time evolution. In the following, all the isotopologues mentioned and included in figure 7.6 are fitted, but only the three main CO_2 isotopologues and the two main CO isotopologues will be extensively discussed to analyse the results.

✓ Isotopically-marked CO_2 molecules appear already after T^{ON}=50 ms.
✓ ^{12}C-containing isotopologues and ^{13}C-containing isotopologues follow similar time evolution → No significant contribution of vibrational excitation to the dissociation in our conditions.

It is also worth mentioning that ^{16}O is naturally present in the Pyrex surface of the tube. The exchange of oxygen atoms between the gas phase and the reactor walls was measured in similar experimental conditions in N_2-O_2 mixtures *Marinov et al.* [2014] and it is expected to take place also in our case. Therefore, the oxygen atoms in the chemical structure of the Pyrex walls could be an extra source of ^{16}O. Nevertheless, the time scale in which this exchange happens is relatively slow, in the order of minutes, and therefore is not expected to have an strong impact in our measurements. The exchange of oxygen atoms between the gas phase and the reactor walls is studied in more detail in chapter 8.

7.4 Experimental results: CO_2-CO-O_2 mixtures

7.4.1 CO_2-O_2 mixtures with isotopically labelled species

Three gas mixtures were investigated using non-marked CO_2 and labelled O_2: 0.75$C^{16}O_2$-0.25$^{18}O_2$, 0.5$C^{16}O_2$-0.5$^{18}O_2$ and 0.25$C^{16}O_2$-0.75$^{18}O_2$. The ratios between the different atoms involved, for example between carbon and oxygen atoms or between both isotopic oxygen atoms are given in table 7.2. These ratios should determine the final abundance of isotopically-labelled CO and CO_2, if no isotope fractionation mechanism is dominating. We also define here the parameter δ corresponding to the fraction of labelled ^{18}O in the total O atom content of the initial gas mixture.

Gas mixture	C:O	^{16}O:^{18}O	$\delta = {}^{18}O/({}^{18}O+{}^{16}O)$	C:^{16}O	C:^{18}O
0.75$C^{16}O_2$-0.25$^{18}O_2$	1:2.667	3:1	0.25	1:2	1:0.667
0.5$C^{16}O_2$-0.5$^{18}O_2$	1:4	1:1	0.5	1:2	1:2
0.25$C^{16}O_2$-0.75$^{18}O_2$	1:8	1:3	0.75	1:2	1:6

Table 7.2: Ratios between the atoms involved in the three CO_2-O_2 gas mixtures investigated with isotopic $^{18}O_2$.

Dissociation fraction in CO_2-O_2 mixtures

Before being able to use labelled $^{18}O_2$ to track O atom exchange processes, it is important to know if a large amount of ^{18}O-containing isotopologues modifies the time evolution of the dissociation fraction and therefore the chemical processes under study. Figure 6.16 compares the variation of α as a function of the accumulated plasma ON time, T^{ON}, measured in a gas mixture with non-marked O_2, $C^{16}O_2$-$^{16}O_2$ (same data shown in figure 6.16), along with the dissociation fraction obtained in gas mixtures of CO_2 with $^{18}O_2$, at 2 Torr, 40 W. $\alpha = {}^{CO}/_{[CO+CO_2]}$ is calculated with the sum of all CO and CO_2 isotopologues. The dissociation fraction with both gas mixtures is very similar, within the reproducibility level of the experiment. Similar results are obtained when

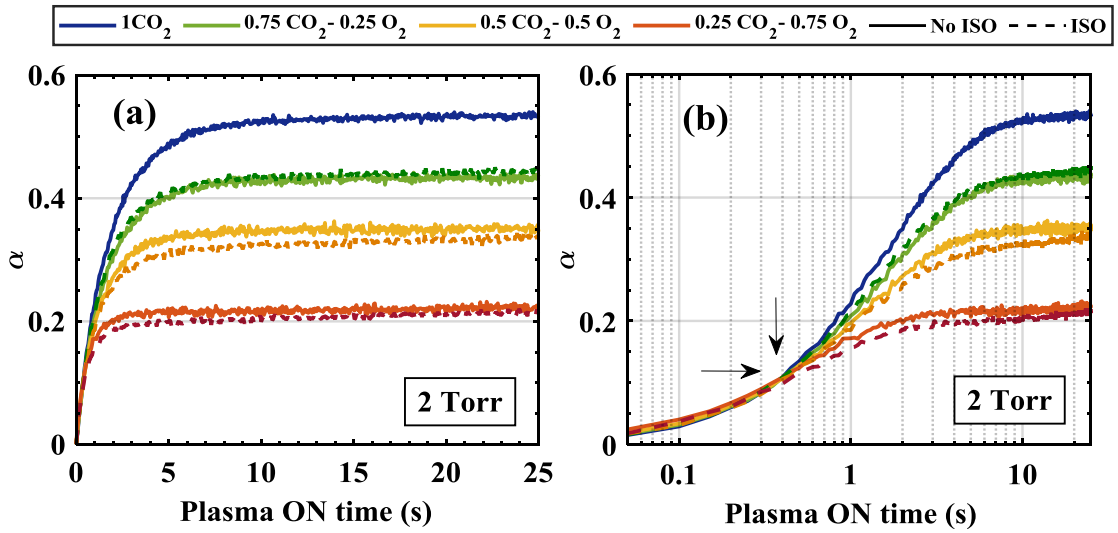

Figure 7.7: Time evolution of the dissociation parameter α for different CO_2-O_2 gas mixtures with O_2^{16}, solid lines (same data shown in figure 6.16), and with O_2^{18}, dotted lines, measured at 2 Torr 40 W. Panels (a) and (b) show the data in linear and logarithmic time scale respectively.

comparing isotopic and non-isotopic gas mixtures at 5 Torr (not shown). The time point at which the curves corresponding to the different gas mixtures diverge from each other is also the same (T^{ON} ~0.5 s). We can therefore conclude that the presence of isotopic species does not alter the overall evolution of the dissociation fraction. A change in the electron kinetics was not expected, but this comparison confirms that there is no relevant change in the reactivity of the neutral species caused by the use of isotopes, and that the change in the vibrational kinetics, less relevant for ^{18}O than for ^{13}C-containing isotopologues, does not influence the chemistry in our plasma conditions. The three time-regions discussed in the previous chapter (see figure 6.6), are still valid and will be also the axis of discussion along this chapter.

✓ The time evolution of the dissociation fraction in isotopically-marked gas mixtures is similar to that in non-isotopically-marked mixtures.
✓ The use of heavier isotopes of oxygen do not alter the characteristic time of any of the dominant chemical process in our conditions

Isotopic exchange in CO_2-O_2 mixtures

In this section we investigate the time evolution of the main isotopologues of CO_2 and CO, for the three gas mixtures under study: $0.75C^{16}O_2$-$0.25^{18}O_2$, $0.5C^{16}O_2$-$0.5^{18}O_2$ and $0.25C^{16}O_2$-$0.75^{18}O_2$. For readability, in order to compare the different gas mixtures, instead of using absolute densities (such as those shown in figure 7.6), which are evidently affected by the variable O_2 content, we will use the fraction of each isotopologue over the total carbon-containing species, defined as:

$$\chi = \frac{f_{Ci}}{\sum_{C_i} f_{C_i}} \tag{7.1}$$

Figures 7.8 and 7.9 show the time evolution in logarithmic scale of the fractions of the three main isotopes of CO_2 (graphs (a), (c) and (d)):$^{16}O^{12}C^{16}O$, $^{16}O^{12}C^{18}O$ and $^{18}O^{12}C^{18}O$ and the two main isotopes of CO (graphs (b), (d) and (e)): $^{12}C^{16}O$ and $^{12}C^{18}O$ for the initial gas mixtures: $0.75C^{16}O_2$-$0.25^{18}O_2$ (panels (a) and (b)), $0.5C^{18}O_2$-$0.5^{18}O_2$ (panels (c) and (d)) and $0.25C^{16}O_2$-$0.75^{18}O_2$ (panels (e) and (f)). Figure 7.8 shows the data obtained at 2 Torr, 40 W and figure 7.9 the data measured at 5 Torr, 40 W.

The fractions of the main isotopes in similar plasma conditions but obtained in the non-isotopic experiments ($^{16}O^{12}C^{16}O$ and $^{12}C^{16}O$), so-called non ISO exp., are also plotted and compared with the sum of the fractions of the main isotopologues obtained in the isotopic measurements, Sum ISO exp. For both CO_2 and CO, at 2 Torr and 5 Torr, the sum of the fractions of the most abundant isotopologues in the isotopic experiments (Sum ISO exp.) matches very well the evolution of the main isotopologues obtained in the non-isotopic measurements ($^{16}O^{12}C^{16}O$ no ISO exp). This good agreement further confirms that the use of isotopically marked species does not disturb significantly the overall chemistry in the plasma.

Generally speaking the observed trends are similar to those shown in the measurement example in figure 7.6. In the graphs corresponding to the CO_2 data, for both pressures and all gas mixtures we observe the decrease of the fraction of the non-labelled $C^{16}O_2$ and the constant growth of the fraction corresponding to the two isotopes that include an ^{18}O atom: $^{16}O^{12}C^{18}O$ and $^{18}O^{12}C^{18}O$. In the case of CO, both isotopologues grow monotonically as a function of the plasma ON time until the steady-state value.

We now analyse separately the isotopologues evolution within each of the three time regions identified in the building up experiment (see chapter 6) which are still visible here: the "initial slope", the "turning region" and the "steady state equilibrium".

→ ***Initial slope***

One of the most remarkable features in figures 7.8 and 7.9 is the fast appearance of isotopically-marked CO_2 species. Already from the very first data point, corresponding to an accumulated total plasma ON time of only 50 ms, the CO_2 isotopologue containing 1 isotopic oxygen represents an important fraction of the total gas mixture, even higher than the fraction of CO produced at the same T^{ON}. For the measurements at 2 Torr, after T^{ON}=50 ms it reaches 3% of the total carbon-containing compounds in the case of the 50%-50% $C^{16}O_2$-$^{18}O_2$ mixture. This percentage is increasing, as expected, with the initial $^{18}O_2$ content (∼9% in 25%-75% $C^{16}O_2$-$^{18}O_2$, ∼1.5% for 75%-25% $C^{16}O_2$-$^{18}O_2$). At 5 Torr the fractions of the isotopically labelled species are lower than at 2 Torr, approximately 0.5%, 1% and 2.5% for 25%-75%, 50%-50% and 75%-25% CO_2-O_2 gas mixtures respectively. The fraction of the isotope of CO_2 with two ^{18}O atoms is lower than for $^{16}O^{12}C^{18}O$, which is expected from the fact that the CO_2 molecule needs to exchange two oxygen atoms. The isotopic fraction at T^{ON}=50 ms and the appearance rate of ^{18}O-containing isotopes increase with the $^{18}O_2$ content in the initial gas mixture and decrease with pressure. In the case of CO, surprisingly, for short T^{ON} the dominant isotopologue is the isotopically-labelled one,$^{12}C^{18}O$. Already from the very first data points and for any gas mixture, even for 75%-25% $C^{16}O_2$-$^{18}O_2$, where the ratio ^{16}O *versus* ^{18}O is 3:1, the fraction of $^{12}C^{18}O$ is significantly larger than that of $^{12}C^{16}O$. Note that, at first, all the CO produced from the direct dissociation of CO_2 is not labelled (*i.e.* $C^{16}O$).

Such fast appearance was not expected considering the results of non-isotopic CO_2-O_2 variation

experiments, shown in figure 7.7 and in the previous chapter, section 6.3.2. The time point where the addition of O_2 to the initial gas mixture seemed to starts having an impact on the dissociation fraction was around T^{ON} ~0.5 s both at 2 and 5 Torr (pointed out by arrows in figure 7.7). The "back reaction", *a priori* the mechanism expected to be responsible of the appearance of these isotopes, was only taking place after a threshold, believed to be related to the densities of reactants. Therefore, a mechanism other than "back reaction" seems to be responsible for O atom exchanges from the very beginning of the the experiment, when the CO density is still very low.

→ ***Turning region***

After the beginning of the experiment and up to the steady-state, all the ^{18}O-containing isotopes grow monotonically. The only exception is a striking bump in the $^{16}O^{12}C^{18}O$ fraction that can be observed for the gas mixture with the highest amount of isotopically marked oxygen, $0.25C^{16}O_2$-$0.75^{18}O_2$, around T^{ON}=1 s and T^{ON}=4 s for 2 and 5 Torr measurements respectively, followed by a little decrease before the stabilization. The bumps happen approximately at the same time-point where the densities of both symmetric isotopes $^{16}O^{12}C^{16}O$ and $^{18}O^{12}C^{18}O$ are the same (crossing point).

When the O^{16} is the dominant oxygen isotope in the gas mixture (δ=0.25 for 75%-25% $C^{16}O_2$-$^{18}O_2$), there is a crossing point between both CO isotopologues, which takes place at 0.7 s for 2 Torr and 4 s for 5 Torr. For even O^{16} and O^{18} fractions (δ=0.5), there is no crossing and both isotopologues tend to reach the same fraction, as expected from the initial abundance, at 4 s at 2 Torr and 10.5 s at 5 Torr.

In figures 7.8 and 7.9, the threshold time-point T^{ON} ~0.5 s is marked in both CO_2 and CO panels with vertical black lines. No clear correlation between the behaviour of the different CO_2 isotopes and the effect of the addition of O_2 in the dissociation fractions is evident in the data presented in these figures. It is however worth pointing out that the maximum difference between the fractions of both CO isotopologues, $^{12}C^{16}O$ and $^{12}C^{18}O$, seems to be close to the threshold time point at which the "back-reaction" seems to start playing a role in the CO_2 conversion (~0.5 s). This effect is particularly visible for the measurements at 5 Torr, although not very clear for the 75%-25% $C^{16}O_2$-$^{18}O_2$ gas mixture at 2 Torr. The higher $^{12}C^{18}O$ fraction is not the cause nor the consequence of higher/lower dissociation. The values of α remain the same with isotopically-marked species. Several hypothesis will be discussed in section 7.5 to explain this transient predominance of $^{12}C^{18}O$.

→ ***Steady-state equilibrium***

At a certain time point the fractions of the different isotopologues studied do not evolve any more, because creation and loss mechanisms are balanced. The steady-state equilibrium for each isotopologue is achieved close, but not always exactly at the same T^{ON} of the steady-state for the dissociation fraction α. The time point T^{ON} where the concentrations of the different CO_2 isotopologues stabilize depends on the pressure. For instance, in the case of CO_2 isotopologues, the steady-state is reached around T^{ON}=3-7 s at 2 Torr but at T^{ON} >15 s at 5 Torr. Additionally, $T^{ON}_{steady-state}$ is slightly different for the different isotopologues. In the case of CO_2 species, the differences are not very large, and seem to decrease with increasing $^{18}O_2$ content. For example at 2 Torr, the maximum differences are observed for the $75\%C^{16}O_2$-$25\%^{18}O_2$ mixture: $T^{ON}_{steady-state}(^{16}O^{12}C^{16}O)$ is ~7 s, $T^{ON}_{steady-state}(^{18}O^{12}C^{16}O)$ is ~5 s and $T^{ON}_{steady-state}(^{18}O^{12}C^{18}O)$ is ~3 s. The two CO isotopologues on the other hand show clearly different stabilization time points. $^{12}C^{18}O$ isotopologue shows a faster

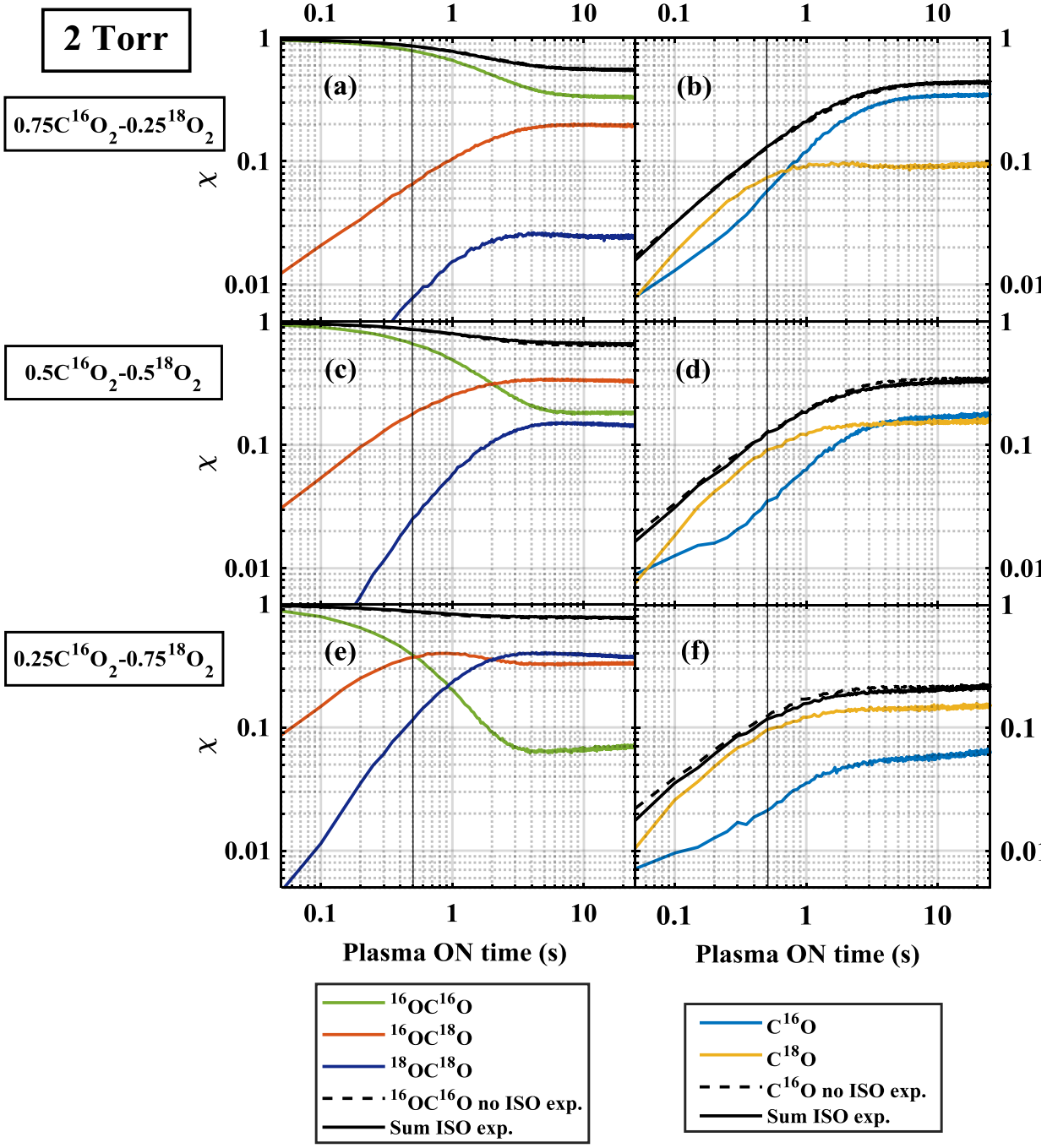

Figure 7.8: Time evolution of the fractions of the three main isotopes of CO_2 (panels (a), (c) and (d)): $^{16}O^{12}C^{16}O$, $^{16}O^{12}C^{18}O$ and $^{18}O^{12}C^{18}O$ and the two main isotopes of CO (panels (b), (d) and (e)): $^{12}C^{16}O$ and $^{12}C^{18}O$ for three different initial gas mixtures: $0.75CO_2$-$0.25O_2$ ((a) and (b)), $0.5CO_2$-$0.5O_2$ ((c) and (d)) and $0.25CO_2$-$0.75O_2$ ((e) and (f)) measured at 2 Torr 40 W.

increase at the beginning of the experiment and an earlier $T^{ON}_{steady-state}$ for all the gas mixtures, when compared with $^{12}C^{16}O$. On the contrary $^{12}C^{16}O$ stabilizes later, making possible that for some conditions, the fraction of this isotope reaches or surpasses the fraction of $^{12}C^{18}O$. As example, at 2 Torr 75%$C^{16}O_2$-25%$^{18}O_2$, $T^{ON}_{steady-state}$($^{12}C^{18}O$)∼1 s whereas $T^{ON}_{steady-state}$($^{12}C^{16}O$)∼8 s. For 50%$C^{16}O_2$-50%$^{18}O_2$ and 25%$C^{16}O_2$-75%$^{18}O_2$ the stabilization times are $T^{ON}_{steady-state}$($^{12}C^{18}O$)∼2-2.5 & 3 s and $T^{ON}_{steady-state}$($^{12}C^{16}O$)∼6 & 4 s.

The steady-state concentrations of the CO_2 isotopologues reproduce well the initial isotopic ratio between ^{16}O and ^{18}O. For instance, in the 50%-50% $C^{16}O_2$-$^{18}O_2$ at 2 Torr, δ=0.5, the two isotopes of CO ($C^{18}O$ and $C^{16}O$) reaches the same final densities, similarly to the two symmetric isotopologues of CO_2 within the experimental error. These errors are mainly caused by the initial mixture preparation, leading to ∼10% inaccuracy in the initial $C^{16}O_2$-$^{18}O_2$ mixture. In this example the targeted ratio is 50%-50% $C^{16}O_2$-$^{18}O_2$, but the real initial mixture was 51.9%-48.1% (∼7.3% error), which induces a slightly higher density of ^{16}O. The fraction of the mixed isotopologue, $^{16}O^{12}C^{18}O$, is roughly twice the fraction of the symmetric isotopologues.

For 2 Torr 75%-25% $C^{16}O_2$-$^{18}O_2$, the final fraction of $^{16}O^{12}C^{18}O$ was approximately 0.32, 0.1 for$^{16}O^{12}C^{18}O$ and 0.025 for $^{18}O^{12}C^{18}O$, which gives a ratio ^{16}O *versus* ^{18}O around 3.3:1, only slightly higher than the input ratio. Small deviations from the expected ratios are believed to be only due to the small inaccuracies in the preparation of the initial gas mixture and possible (little) contribution of ^{16}O from the reactor walls.

The main observations to be remembered from this set of measurements are summarized in the box below. Possible explanations will be given in section 7.5, but additional information obtained from similar experiments performed in CO-O_2 mixtures will be first presented and compared with the CO_2-O_2 case, since they provide more insights to identify the underlying mechanisms.

✓ Isotopically-labelled species appear right away after starting the building-up with even higher densities of labelled CO_2 than CO.
✓ $C^{18}O$ fraction is higher than $C^{16}O$ for the first hundreds of ms in any gas mixture.
✓ The steady-state fractions of the different isotopologues reproduce the initial ^{18}O input ratio δ.
✓ An overshoot of $^{16}OC^{18}O$ is observed at large δ (=0.75).
✓ $C^{18}O$ can also pass through a maximum value especially at high pressure and small δ and reaches steady-state values earlier than $C^{16}O$ at any conditions.

7.4.2 CO-O_2 mixtures

Similarly to the building-up experiments with non-marked O_2 (see section 6.3.2), two CO-O_2 mixtures were studied:

- 0.4CO-0.6O_2: 1 carbon atom for 4 oxygen atoms → similar proportion in terms of carbon *versus* oxygen to a mixture of 0.5CO_2+0.5O_2. The isotopic ratio is ^{16}O:^{18}O → 1:3, different to the 0.5$C^{16}O_2$-0.5$^{18}O_2$ case (^{16}O:^{18}O → 1:1) but similar to a 0.25$C^{16}O_2$-0.75$^{18}O_2$ mixture.
- 0.666CO-0.333O_2: 1 carbon atom for 2 oxygen atoms → similar to a 100% CO_2 plasma (not possible in CO_2-O_2 isotopically-labelled experiments). The proportion of the two isotopes of oxygen is even, ^{16}O:^{18}O → 1:1 (*i.e.* δ = 0.5).

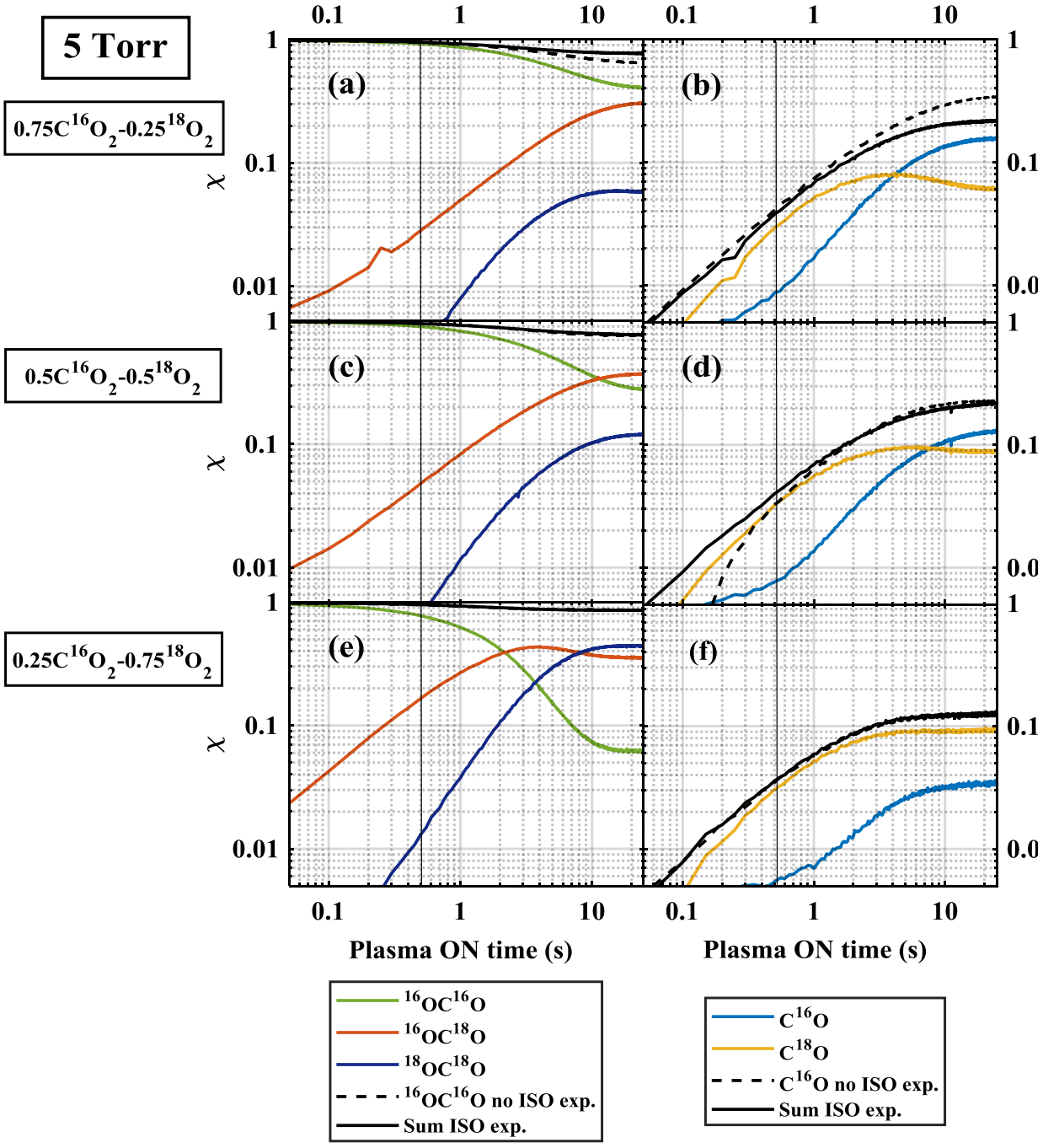

Figure 7.9: Time evolution of the fractions of the three main isotopes of CO_2 (panels (a), (c) and (d)): $^{16}O^{12}C^{16}O$, $^{16}O^{12}C^{18}O$ and $^{18}O^{12}C^{18}O$ and the two main isotopes of CO (panels (b), (d) and (e)): $^{12}C^{16}O$ and $^{12}C^{18}O$ for three different initial gas mixtures: $0.75CO_2$-$0.25O_2$ ((a) and (b)), $0.5CO_2$-$0.5O_2$ ((c) and (d)) and $0.25CO_2$-$0.75O_2$ ((e) and (f)) measured at 5 Torr, 40 W.

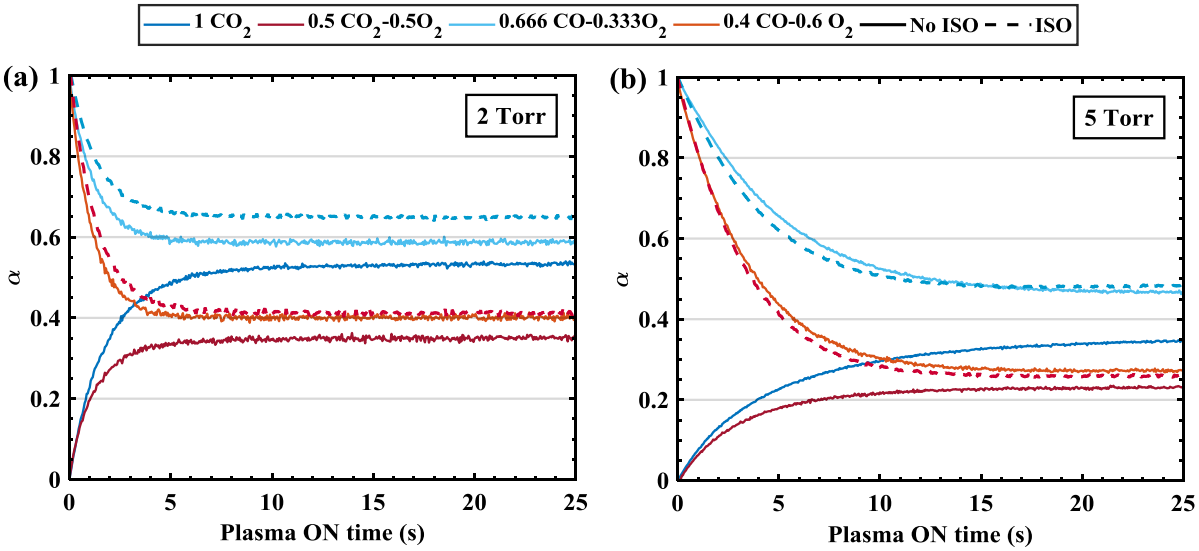

Figure 7.10: Time evolution of the dissociation parameter α for two CO-O_2 mixtures (0.4CO + 0.6O_2 and 0.666CO + 0.333O_2) both isotopically (so-called ISO in the legend) and non-isotopically marked. Equivalent measurements in terms of carbon *versus* oxygen atoms ratio measured in CO_2-O_2 mixtures (1CO_2 and 0.5CO_2-0.5O_2) at (a) 2 Torr and (b) 5 Torr, 40 W are also included. The non-isotopically marked data (no ISO) are the same as shown in figure 6.17 in the previous chapter.

The ratios between the different atoms involved are given in table 7.3:

Gas mixture	**C:O**	**^{16}O:^{18}O**	$\delta = {}^{18}O/({}^{18}O+{}^{16}O)$	**C:^{16}O**	**C:^{18}O**
0.4C^{16}O-0.6$^{18}O_2$	1:4	1:3	0.75	1:1	1:3
0.666C^{16}O-0.333$^{18}O_2$	1:2	1:1	0.5	1:1	1:1

Table 7.3: Ratios between the atoms involved in the CO-O_2 gas mixtures investigated with isotopic $^{18}O_2$.

In order to check if we also obtain a similar evolution of the dissociation fraction α with marked and non-marked CO-O_2 mixtures, figure 7.10 presents the time evolution of α for the two gas mixtures detailed above, with and without isotopically labelled oxygen. These four measurements are also compared to measurements in CO_2-O_2 with the same C:O ratio (therefore in pure CO_2 and in 0.5CO_2:0.5O_2) presented in figure 6.17. As already seen in the previous section for CO_2-O_2 mixtures, the time evolution of α in CO–O_2 mixtures is the same with and without isotopically labelled oxygen within the experimental error (∼10%). The use of ^{18}O-containing isotopologues does not change the chemistry in our plasma conditions. The differences in the final steady-state values between CO-O_2 and CO_2-O_2 mixtures for similar C:O proportions persist with higher final α(plateau) when starting from CO-O_2 mixtures.

The time evolution of the fractions of the different isotopologues for both CO-O_2 mixtures is shown in figure 7.11. The data for 2 Torr is plotted in panels (a) and (c) and the data measured at 5 Torr in panels (b) and (d) for initial gas mixtures of 0.4C^{16}O-0.6 $^{12}O_2$ ((a) and (b)) and 0.666C^{16}O-0.333 $^{12}O_2$ ((c) and (d)), respectively. All the conditions presented in these figures show

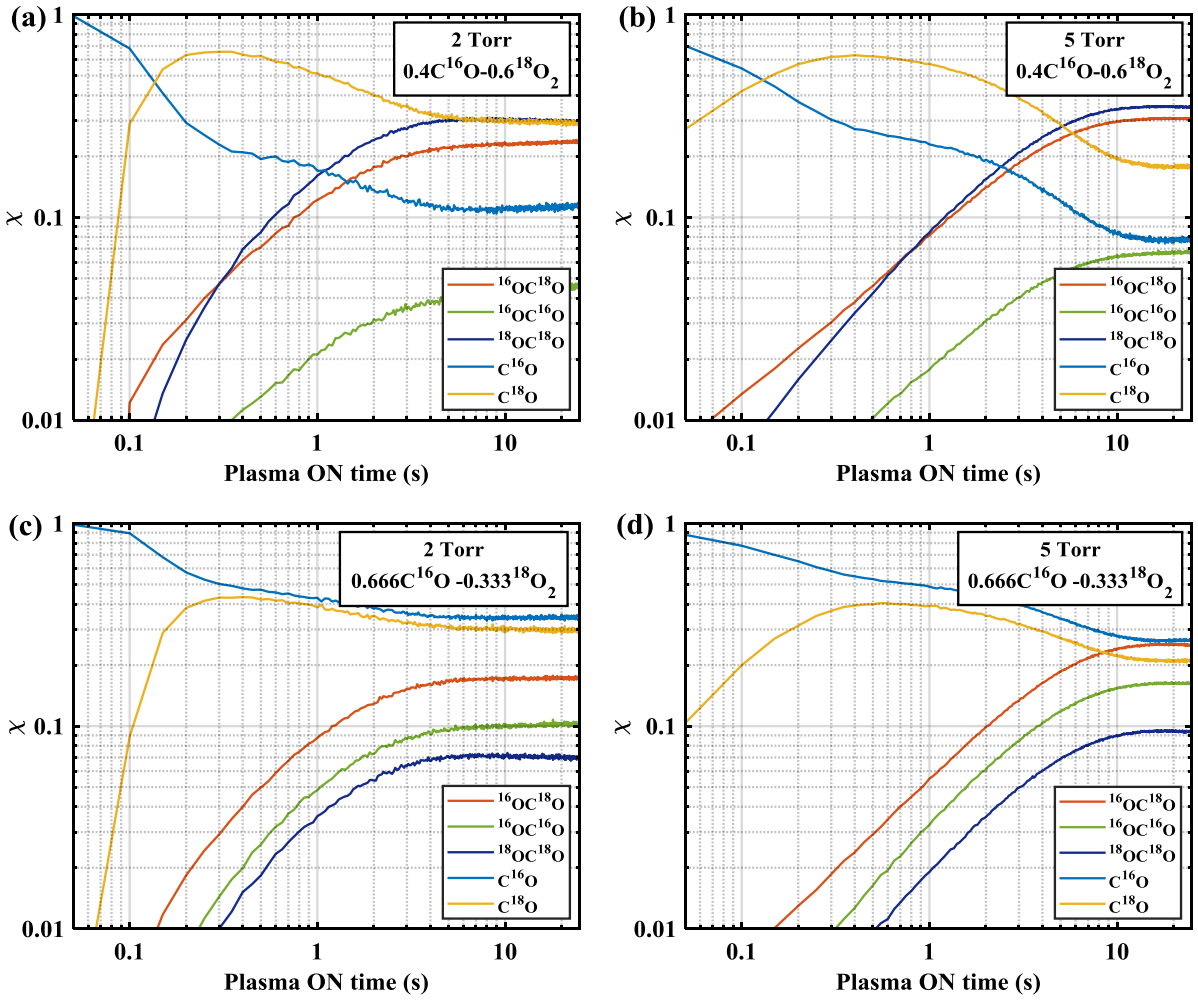

Figure 7.11: Time evolution of the fractions of three main isotopologues of CO_2: $^{16}O^{12}C^{16}O$, $^{16}O^{12}C^{18}O$ and $^{18}O^{12}C^{18}O$ and two main isotopologues of CO: $^{12}C^{16}O$ and $^{12}C^{18}O$ for gas mixture of $0.4C^{16}O$-$0.6^{18}O_2$ (panels (a) and (b)) and $0.666C^{16}O$-$0.333\ ^{18}O_2$ (panels (c) and (d)) measured at 2 Torr ((a) and (c)) and 5 Torr ((b) and (d)), 40 W.

some common trends: A monotonic increase of the three isotopes of CO_2, a continuous decrease of $C^{16}O$ and a fast initial increase of $C^{18}O$ passing through a maximum before slowly decreasing to the final steady-state level. There are however some significant differences between both gas mixtures:

→ $0.666C^{16}O$+$0.333^{18}O_2$ gas mixture:

- The three isotopologues of CO_2 show ∼parallel trends (in log-log scale) all along T^{ON}.
- After an initial decrease of $C^{16}O$ and fast increase of $C^{18}O$, from T^{ON} ∼0.3 s both CO isotopologues evolve also in parallel, and their fractions are similar, within the gas mixture error.

→ $0.4C^{16}O$+$0.6^{18}O_2$ gas mixture:

- $^{18}OC^{18}O$ evolves faster than the other CO_2 isotopologues and its density surpasses that of $^{18}OC^{16}O$ after T^{ON}=0.3 s at 2 Torr and 0.7-0.8 at 5 Torr.
- The crossing point between $^{16}OC^{18}O$ and $^{18}OC^{18}O$ caused by the faster increase of $^{18}OC^{18}O$ takes place at the same T^{ON} at which $\chi(C^{18}O)$ reaches its maximum value.

- $C^{18}O$ and $C^{16}O$ cross each other at T^{ON} ~0.15 s and then evolve in parallel with $\chi(C^{18}O) > \chi(C^{16}O)$ according to the initial δ ratio.

In the ***first steps*** of the building-up the gas mixtures evolve extremely fast. Already at T^{ON} ~0.15 s and 0.3 s for 0.4$C^{16}O$-0.6$^{18}O_2$ (δ=0.25) and 0.666$C^{16}O$-0.333$^{18}O_2$ (δ=0.5) mixtures respectively, the fractions of $C^{18}O$ and $C^{16}O$ become comparable. The fast appearance of labelled species is consistent with the observations made in CO_2-O_2 gas mixtures but they are still surprising if considering isotope incorporation via chemical reactions. Note that such a fast increase of $C^{18}O$ would require to break $^{18}O_2$ and either break CO (at >11 eV) followed by a reaction $C + O$, or the oxidation of CO by ^{18}O to produce $^{16}OC^{18}O$ followed by a dissociation process with in principle even probability to produce $C^{18}O$ or $C^{16}O$.

In the ***"turning region"*** two features are noticeable: (1) The parallel evolution of both $C^{18}O$ and $C^{16}O$. The difference in their fractions seems to be related purely with the ^{16}O:^{18}O ratios (1:3 and 1:1). (2) The occurrence of "bumps". For 0.4$C^{16}O$-0.6 $^{18}O_2$ mixtures there are two "bumps". In the first one, around T^{ON}=0.3 s at 2 Torr and T^{ON}=0.4 s at 5 Torr, only $C^{18}O$ shows a clear peak, while $C^{16}O$ is depleted. This bump happens approximately at the same time-point for which the traces of $\chi(^{16}OC^{18}O)$ and $\chi(^{18}OC^{18}O)$ cross each other. It seems to be related to the fast increase of $C^{18}O$ up to a fraction which reproduces the final ^{16}O:$O^{18}O$ ratio, when compared to the $C^{16}O$ fraction.

In the secondary bump (around T^{ON}=1 s at 2 Torr and T^{ON}=2 s at 5 Torr) both isotopologues show a parallel behaviour and $C^{16}O$ seems to push up the fraction $C^{18}O$. For 0.666$C^{16}O$-0.333$^{18}O_2$ mixtures there is only one "bump" and in this case the increase of $\chi(C^{18}O)$ seems to push up $\chi(C^{16}O)$ around T^{ON}=0.4-0.5 s at 2 Torr and T^{ON}=1 s at 5 Torr. The cause of these bumps is still unclear but the somewhat "pushing-up" behaviour along with the parallel evolution of both CO isotopologues suggests O atom exchange processes between them. The faster increase of $^{18}OC^{18}O$ compared to the other two CO_2 isotopologues when $\chi(C^{18}O)$ is higher than $\chi(C^{16}O)$ (panels (a) and (b)) suggest the occurrence of "back reaction" *i.e.* oxidation of $\chi(C^{18}O)$. In the "turning region" all the CO_2 isotopologues grow towards their final steady-state fraction.

In the ***final steady-state***, the agreement with the initial input ratio of both oxygen isotopes is reasonably good. In some cases, we observe slightly higher fractions of $^{16}OC^{16}O$ compared to $^{18}OC^{18}O$ and of $C^{16}O$ compared to $C^{18}O$ for mixtures where they were expected to be similar. As for the CO_2-O_2 mixtures, this effect can be partly explained by small inaccuracies in the preparation of the initial gas mixture, which is always more difficult at 5 Torr than at 2 Torr. However since the differences always seem to favour an excess of ^{16}O in the final products, a contribution of ^{16}O from the reactor walls is also possible.

✓ In CO-O_2 gas mixtures, both CO isotopologues reach similar fractions very fast (T^{ON}=0.15 s), and evolve in parallel until the end of the experiment according to the δ ratio.
✓ All CO_2 isotopologues monotonically increase with T^{ON} but $^{18}OC^{18}O$ show a faster increase in mixtures with an excess of ^{18}O, compatible with a back reaction mechanism.

7.4.3 Comparison of gas mixtures

In this section we compare the results obtained with CO_2-O_2 and CO-O_2 gas mixtures. The summary of the ratios between the atoms proportions for all the gas mixtures studied is reminded in table 7.4. Two important parameters are considered for the analysis: the ratio $f_{^{18}O}^{CO} = {}^{C^{18}O}/_{(C^{16}O+C^{18}O)}$ corresponding to the proportion of labelled CO among all CO molecules, and the total "fraction of transferred ^{18}O isotopes", $f_{^{18}O}$ defined as:

$$f_{^{18}O} = \frac{2 \cdot \chi(C^{18}O_2) + \chi(^{16}OC^{18}O^{18}) + \chi(C^{18}O)}{2 \cdot \chi(C^{18}O_2) + 2 \cdot \chi(C^{16}O_2) + 2 \cdot \chi(^{16}OC^{18}O) + \chi(C^{18}O) + \chi(C^{16}O)} \tag{7.2}$$

$f_{^{18}O}$ corresponds to the fraction of labelled oxygen contained in all the CO and CO_2 isotopologues, starting from zero at the beginning of the measurement and finishing at δ, the proportion of ^{18}O in the initial gas mixture.

Figure 7.12 panels (a) and (b) show the time evolution of $f_{^{18}O}^{CO} = {}^{C^{18}O}/_{(C^{16}O+C^{18}O)}$, for all the gas mixtures studied at 2 and 5 Torr, 40 W. Note that 0.4CO-0.6O_2 and 0.5CO_2-0.5O_2 have the same ratio of carbon atoms *versus* oxygen atoms (1C:4O) (indicated in the graph), but different O^{16}:O^{18} ratio, whereas 0.666$C^{16}O$-0.333$^{18}O_2$ and 0.5CO_2-0.5O_2 have the same proportion of the two isotopes of oxygen but different ratio C *vs.* O.

The evolution of CO_2-O_2 and CO-O_2 gas mixtures is notably different. In CO-O_2 mixtures ${}^{C^{18}O}/_{(C^{16}O+C^{18}O)}$ increases fast and goes straight to its final δ value, reached between T^{ON} ~0.3 s and 0.6 s, for 2 and 5 Torr respectively. CO_2-O_2 shows different behaviour: first $f_{^{18}O}^{CO}$ increases and passes through a maximum, more pronounced for small initial δ and related to the amplitude of the difference between $C^{16}O$ and $C^{18}O$ densities observed in figures 7.8 and 7.9. The maximum $f_{^{18}O}^{CO}$ reached is relatively similar for all CO_2-O_2 mixtures. Only a small dependence with the isotope content is noticeable mainly at 2 Torr. After the peak, $f_{^{18}O}^{CO}$ decreases until a value that is only determined by δ, where it converges with the corresponding CO-O_2 measurement. The final steady-state equilibrium depends only on the initial $\delta = {}^{^{18}O}/_{(^{18}O+^{16}O)}$ for both CO_2-O_2 and CO-O_2 gas mixtures. Again some discrepancies are caused by the imperfect initial gas mixtures and by small contribution of $C^{16}O$ from the walls.

Figure 7.12 panels (c) and (d) plots the "fraction of transferred ^{18}O isotope" $f_{^{18}O}$ for 2 and 5 Torr respectively. The inner figures show the same data but divided by the value δ for each gas mixture. The most significant information in these graphs can be summarized as follows:

- The incorporation rate of ^{18}O to CO and CO_2, $f_{^{18}O}$, depends only on the pressure but the rate is slower in CO_2-O_2 than in CO-O_2.

Gas mixture	C:O	^{16}O:^{18}O	$\delta = {}^{^{18}O}/_{(^{18}O+^{16}O)}$	C:^{16}O	C:^{18}O
0.4$C^{16}O$-0.6$^{18}O_2$	1:4	1:3	0.75	1:1	1:3
0.666$C^{16}O$-0.333$^{18}O_2$	1:2	1:1	0.5	1:1	1:1
0.75$C^{16}O_2$-0.25$^{18}O_2$	1:2.667	3:1	0.25	1:2	1:0.667
0.5$C^{16}O_2$-0.5$^{18}O_2$	1:4	1:1	0.5	1:2	1:2
0.25$C^{16}O_2$-0.75$^{18}O_2$	1:8	1:3	0.75	1:2	1:6

Table 7.4: Ratios between the atoms involved in all the CO_2-O_2 and CO-O_2 gas mixtures studied.

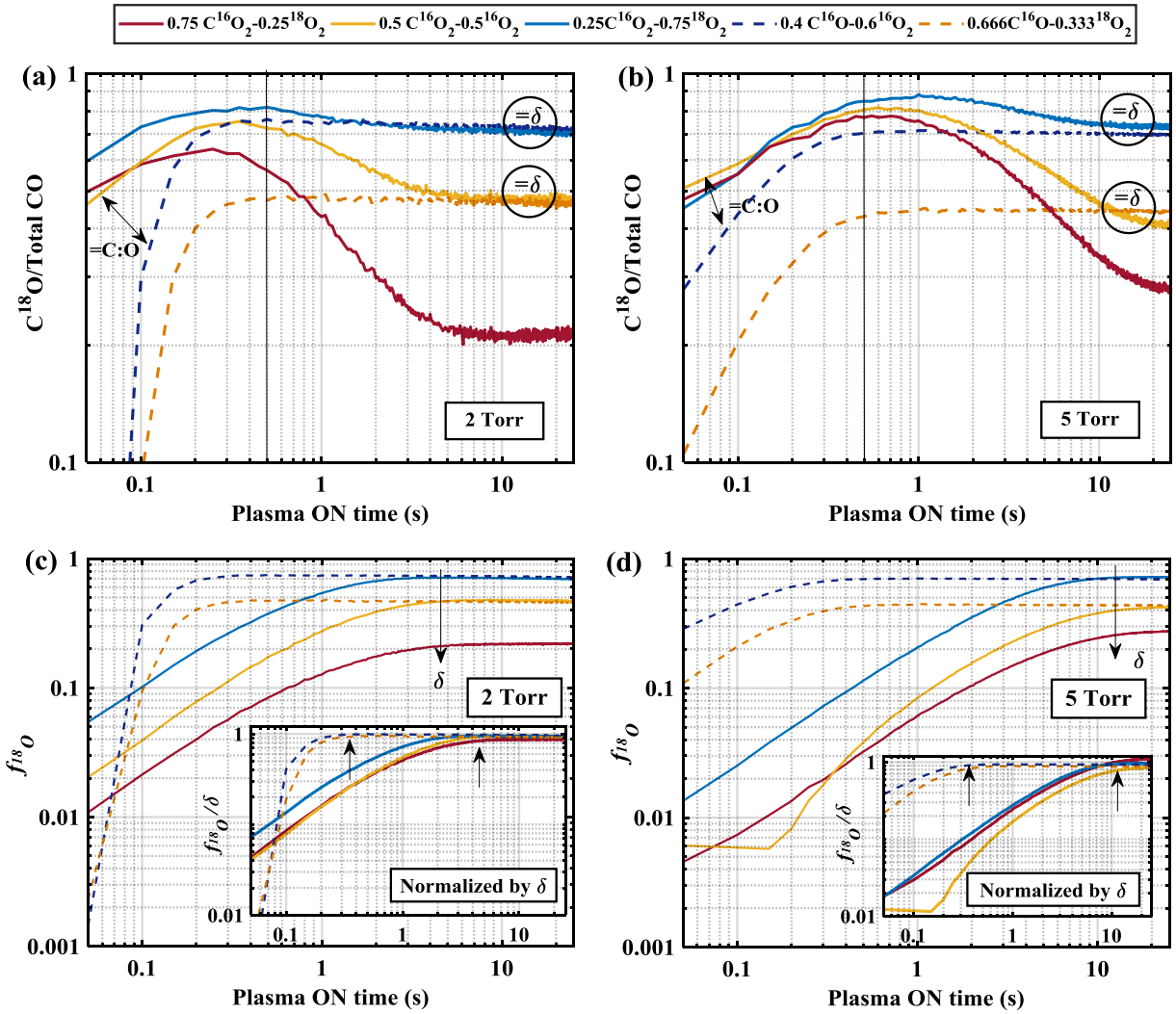

Figure 7.12: Time evolution of the fraction $C^{18}O$ over the total CO (panels (a) and (b)) and of f_O^{18} (panels (c) and (d)) for three gas mixtures of $C^{16}O_2$-$^{18}O_2$ and two mixtures of $C^{16}O$-$^{18}O_2$, measured at 2 (panels (a) and (c)) and 5 (panels (b) and (d)) Torr. The different gas mixtures are colour-coded according to δ.

- When normalizing by δ, the curves follow a ∼single time evolution, again different in CO_2-O_2 than in CO-O_2.

- For CO_2-O_2, $f_{^{18}O}$ is faster at 2 Torr and reaches the steady-state values for shorter T^{ON}, than at 5 Torr (pointed out by arrows in the figure). For CO-O_2, $f_{^{18}O}$ reaches the steady-state for similar T^{ON} at 2 and 5 Torr.

✓ The final steady-state equilibrium depends only on the initial δ for all gas mixture.
✓ The incorporation rate of ^{18}O to CO and CO_2, $f_{^{18}O}$, is faster at low pressure and does not depend on the initial O_2 content.
✓ The incorporation of ^{18}O, $f_{^{18}O}$, is faster when starting from CO-O_2.

7.5 Discussion

This chapter has presented the study of the CO_2 dissociation in different CO_2-CO-O_2 gas mixtures using isotopically marked ^{18}O. A brief summary of the main points revealed by this study is the following:

- No effect of isotopically-labelled species on the overall dissociation fraction.
- Very fast appearance of isotopically marked species for both CO_2 and CO molecules, on a much shorter time scale than the influence of O_2 on α noticed in CO_2-O_2 measurements shown in the previous chapter.
- Predominance of $C^{18}O$ over $C^{16}O$ for any CO_2-O_2 mixture during the first hundreds of milliseconds of total plasma ON time, even for a initial ratio ^{18}O:^{16}O of 1:3.
- Towards the end of the experiment, when the different molecules reach the final steady-state concentrations, the ratio between the different isotopologues reproduces the initial isotopic abundance, within the experimental error.

The behaviour in the steady-state time region is consistent all along this chapter and the previous one: the steady-state value is controlled by non-mass dependent balanced mechanisms. The fast appearance of the isotopically marked species and their evolution in the so-called "turning region" are however surprising and the analysis is not straightforward. Several hypothesis are discussed the in following.

7.5.1 Initial time steps: fast growth of isotopically-labelled CO_2 and CO

The fast appearance of the isotopically marked CO_2 and CO, already from the first train of plasma pulses could have two basic explanations:

- Extremely fast back reaction through any possible mechanism such as CO_2 dissociation $CO_2 \rightarrow CO + O$ followed by the oxidation of CO by a ^{18}O atoms created by the dissociation of $^{18}O_2$, CO electron impact excitation followed by $C^{16}O(a^3\Pi_r) +^{18} O_2 \rightarrow^{18} OC^{16}O +^{18} O$, full CO_2 dissociation reaction $CO_2 \rightarrow C + O + O$ followed by a recombination with ^{18}O atoms available in the gas mixture from the dissociation of O_2, etc.
- Fast atom exchange processes between two species without dissociation.

The first possibility is in contradiction with the time evolution of the dissociation fraction measured in CO_2-O_2 mixtures, with and without isotopically labelled species, where no effect of the addition of O_2 was noticeable until $T^{ON} \approx 0.5$ s. The second possibility seems therefore a more plausible explanation. In fact, the oxygen isotope exchange reaction between $^{18}O(^1D)$ and $^{16}O^{12}C^{16}O$ in ground state is reported in several papers dealing with the anomalous isotope enrichment in the upper atmosphere *Katakis and Taube* [1962]; *Yamazaki and Cvetanovic* [1964]; *Baulch and Breckenridge* [1966]; *Yung et al.* [1991]; *Wen and Thiemens* [1993]; *Perri et al.* [2004]; *Mebel et al.* [2004]. The efficient isotopic exchange of $O(^1D)$, but not $O(^3P)$, with CO_2 was first suggested by *Katakis and Taube* [1962] and confirmed by *ad initio* quantum calculations *Yang et al.* [2005]. O atoms in the ground state, $O(^3P)$, do not have enough energy to undergo isotopic exchange, contrary to the case of $O(^1D)$ *Wen and Thiemens* [1993]. Two possible mechanisms can explain the exchange process:

1. "Knock-off" mechanism which assumes that the incoming excited oxygen atom $O(^1D)$ ejects one O atom from the CO_2 molecule.
2. "Intermediate" mechanism, which would proceed through the intermediate state CO_3^* of short lifetime (in the order of 1-10 ps *DeMore and Dede* [1970]), but long enough for the intramolecular vibrational energy redistribution to be complete (if no energy equilibration occurs, the incoming $O(^1D)$ atom could be efficiently ejected) *Baulch and Breckenridge* [1966].

Both mechanisms can be schematically described by the reaction:

$$^{18}O(^1D)+^{16}O^{12}C^{16}O \rightarrow CO_2+\beta^{16}O+(1\text{-}\beta)^{18}O$$

A "knock-off" mechanism would have an exchange probability β=1. In the "intermediate" mechanism the three oxygen atoms in the CO_3^* intermediate are equivalent, leading to a statistical isotope exchange, *i.e.* $\beta = 2/3$. The intermediate mechanism is supported by the *ab initio* calculations by *Mebel et al.* [2004], which predicts a probability of the incoming $O(^1D)$ atom of being incorporated to the CO_2 molecule close to 2/3, and it has been experimentally verified by *Yamazaki and Cvetanovic* [1964]; *Baulch and Breckenridge* [1966] who also measured an incorporation probability of the $O(^1D)$ atom into the CO_2 molecule of 2/3.

Considering the CO_3^* intermediate mechanism, two reaction channels are reported by *Perri et al.* [2004]: with quenching of the impacting $O(^1D)$ producing a $O(^3P)$ state or without quenching (the O atom remains in the singlet state), according to the following schemes:

$$^{18}O(^1D)+^{16}O^{12}C^{16}O \rightarrow CO_3^* \rightarrow {}^{16}O(^3P)+^{16}O^{12}C^{18}O \quad (R1)$$
$$^{18}O(^1D)+^{16}O^{12}C^{16}O \rightarrow CO_3^* \rightarrow {}^{16}O(^1D)+^{16}O^{12}C^{18}O \quad (R2)$$

The electronic quenching of $O(^1D)$ (reaction R1) was found to be the main channel in crossed molecular beam experiments done at energies of 4.2 and 7.7 kcal/mol. The quenching reaction (R1) is spin-forbidden but the relatively long-lived intermediate CO_3^* allows the isotope exchange and curve-crossing from the singlet to the triplet surface *Perri et al.* [2004]. It is also reported an increase of the branching towards the quenching reaction (R1) when decreasing the collision energy, in good agreement with *ab initio* calculations *Mebel et al.* [2004]. The non-quenching isotope exchange channel (R2) was calculated to account for 16% of all isotope exchange at a collision energy of 4.2 kcal/mol, *Mebel et al.* [2004] and decrease to approximately 5% at collision energies of ∼1.5 kcal/mol. In most of the literature reviewed only the quenching channel is discussed, agreeing with the predominance of this channel for low collision energies. The average kinetic energy of the oxygen atoms in our discharge is much lower. For example, at 2 Torr it is ∼0.03 kcal/mol, suggesting that the quenching process would be dominant in our conditions.

Other possible reactions have been suggested in the literature to contribute to the isotope enrichment of CO_2 molecules. For instance reactions through CO_2 intermediates such as $O(^3P)$ + $CO(^1\Sigma^+) \leftrightarrow CO_2^*(^3B_2) \rightarrow CO_2(^1\Sigma_g^+)$, or in 3-body collisions through $O(^1D)$ + $CO(^1\Sigma^+)$ + M → $CO_2(^1\Sigma_g^+)$ + M have been proposed. However, these reactions were found to be inefficient, in spite of the expected high reactivity of $O(^1D)$ towards CO *Raper and DeMore* [1964]; *Shimizu* [1968], or with significantly lower rates than through the isotope exchange process *Pandey and Bhattacharya* [2006]. At very high collisions energies ∼100 kcal mol^{-1} a possible hyper-thermal isotopic exchange directly through $O(^3P)$+CO_2 and O_2+CO_2 reactions *Yeung et al.* [2009, 2012]

has also been suggested. Finally *de Petris et al.* [2004] studies the possibility of isotope exchange in ionized CO_2-CO mixtures through a $C_2O_3^+$ intermediate. These possibilities are however not expected to play an important role in our conditions due to the low collision energies and/or low ion densities.

The isotopic exchange reaction through quenching of $O(^1D)$ by CO_2 is therefore the most probable isotope incorporation mechanism in our discharge conditions, explaining the fast appearance of ^{18}O-containing CO_2 molecules. In the previous chapter it was demonstrated that electron impact dissociation is the dominant process for the CO_2 dissociation in our discharge, defining the time evolution of the dissociation fraction for short T^{ON}. $O(^1D)$ are therefore created from the electron impact dissociation of CO_2 ($^{16}O(^1D)$ in the initial time steps). On the other hand, the electron impact dissociation of O_2 may proceeds mainly through two dissociation channels either producing two $O(^3P)$, or one $O(^3P)$ and one $O(^1D)$ (all ^{18}O in the initial steps). $^{18}O(^3P)$ could be also excited to the $O(^1D)$ state by direct electron impact excitation. The created $^{18}O(^1D)$ (either from direct electron impact dissociation of O_2 or by excitation of $O(^3P)$) would then undergo isotopic O atom exchange processes with $C^{16}O_2$ generating isotopically mixed CO_2. Note, that it is also possible to create $O(^1S)$ in the discharge that can undergo similar reactions *Yamazaki and Cvetanovic* [1964]. The electron energy required to produce O atom in this state from electron impact is higher than for $O(^1D)$, therefore its density is expected to be lower, but it can in any case contribute to the isotope exchange process.

CO molecules can also undergo isotopic exchange reactions through quenching of $O(^1D)$. This process is spin-forbidden, but similarly to the reaction of $O(^1D)$ with CO_2 there is a possibility of transfer from a singlet potential surface of $O(^1D)$-CO to a triplet surface of $O(^3P)$-CO, through a CO_2^* intermediate *Raper and DeMore* [1964]; *Shimizu* [1968]:

$$O(^1D) + CO \rightarrow CO_2^* \rightarrow O(^3P) + CO$$

As for CO_2, the probability of incorporation of the heavy isotope to the CO molecule through the CO_2^* intermediate is statistical, *i.e.* for CO $\beta = 1/2$ *DeMore et al.* [1990]; *Yung et al.* [1991]. The isotopic exchange through this reaction has not been explored in literature as extensively as for CO_2, perhaps due to the low concentration of CO in the atmosphere. It was briefly suggested by *Katakis and Taube* [1962]; *Pandey and Bhattacharya* [2006], but in other studies it was found to not be the main source of isotopic CO in the atmosphere, contrary to the case of CO_2 *Huff and Thiemens* [1998]. The occurrence of the quenching/exchange reaction in CO molecules is thus less clear than for CO_2, but could still partly explain the fast growth of $C^{18}O$ in CO-O_2 gas mixtures.

To conclude with the initial slope time-region, in section 7.4.3 we showed a faster ^{18}O incorporation rate ($f_{^{18}O}$) in CO-O_2 mixtures compared to CO_2-O_2 mixtures. The most probable reason is the occurrence of "back reaction" from the very beginning of the building-up process, in addition to the O atom exchange process. The absence of threshold for the "back reaction" in CO-O_2 contrary CO_2-O_2 as discussed in the previous chapter supports this hypothesis. In all the isotope exchange reactions discussed along this section the initial required step is always the dissociation of O_2 followed either by the encounter of CO_2 or CO with a $O(^1D)$ atom. The production of this $O(^1D)$ state represent less than 1 out of the 4 O atoms produced in electron impact dissociation of two O_2 molecules (the threshold for electron impact dissociation path of O_2 producing $O(^1D)$ is higher than the other path, see figure 1.4) even though it can also be formed by electron impact excitation

of $O(^3P)$. Nevertheless in CO-O_2 mixtures, already from the beginning we can have the reaction $CO(a^3\Pi_r) + {}^{18}O_2 \rightarrow CO_2 + O$, which only requires the excitation of CO at a energy threshold (6 eV) that is close to the reaction $e + O_2 \rightarrow 2O(^3P)$ (∼5 eV) and lower than for $e + O_2 \rightarrow O(^3P) + O(^1D)$ (∼8 eV) *Phelps* [1985]. The reaction with $CO(a^3\Pi_r)$ would then contribute to the ^{18}O incorporation, explaining the faster $f_{^{18}O}$ in CO-O_2 mixtures.

✓ The fast growth of labelled CO and CO_2 molecules is most probably a consequence of atomic exchange in quenching collisions with $O(^1D)$ state (and possibly $O(^1S)$).
✓ These atoms exchange mechanisms are not possible from $O(^3P)$ and allow to trace the evolution of $O(^1D)$ in time by taking into account the collision frequency with CO and CO_2 as well as the statistical branching of the isotopically-labelled atom exchange ($\beta = 1/2$ for CO, $\beta = 2/3$ for CO_2).

7.5.2 "Turning region": back reaction and effect of the vibrational kinetics

In the so-called "turning region" all the isotopically-marked CO_2 species and both CO isotopologues monotonically grow up to the final steady-state value in CO_2-O_2 mixtures. Only $C^{16}O_2$ decreases, as expected. In CO-O_2 mixtures, $C^{16}O$ decreases while all the CO_2 species increase. After the initial fast increase, $C^{18}O$ slowly decreases in parallel to $C^{16}O$. Several points are worth discussing:

- In 0.4$C^{16}O$-0.6$^{18}O_2$ mixtures a significantly faster increase of $C^{18}O_2$ compared to the other two CO_2 isotopes is observed. This happens only when the fraction of $C^{18}O$ largely exceeds the one of $C^{16}O$. This is probably an indication of "back reaction" from $C^{18}O$.
- The parallel behaviour of $C^{16}O$ and $C^{18}O$ after the first 150 ms of building-up in CO-$^{18}O_2$ mixtures is explained by the even isotope incorporation probability ($\beta = 1/2$) through CO_2^* intermediate.
- The predominance of $C^{18}O$ over $C^{16}O$ in $C^{16}O_2$-$^{18}O_2$ mixtures for T^{ON}, until ≤ 0.7 s at 2 Torr and ≤ 4 s at 5 Torr, even for low ^{18}O content in the initial gas mixture, is very remarkable and not consistent with the experimental results in $C^{16}O$-$^{18}O_2$ mixtures.

When CO is in excess compared to CO_2 (such as in CO-O_2 mixtures), the behaviour is the expected one, and both isotopologues follow parallel evolution with a ratio given only by the initial ^{16}O:^{18}O proportion. When CO_2 is in excess (CO_2-O_2 mixtures), unexpected abundance of $C^{18}O$ is observed. Several possible hypothesis can be discussed:

- Combined effect of the O atom exchange process through quenching with CO molecules and creation of $C^{18}O$ from the dissociation of ^{18}O-containing CO_2. An isotope-dependent effect is not expected in the electron impact dissociation of CO_2 to produce CO and $O(^1D)$, unless there is a significant contribution of electron impact dissociation from vibrationally excited states (discussed below in more detail). CO_2 photo-dissociation experiments *Bhattacharya et al.* [2000] confirmed that dissociation by high energy photons (with energy higher than the [$O(^1D)$+CO] level) was not inducing any isotope difference in the dissociation products. Hence, from the electron impact dissociation of $^{16}O^{12}C^{18}O$, we would expect equal proportion

of $C^{18}O$ or $C^{16}O$. From the dissociation of $^{18}O^{12}C^{18}O$, $C^{18}O$ would be the only product. Therefore both dissociation processes would tend to increase the concentration of $C^{18}O$ in the gas mixture.

However, at the T^{ON} values for which $C^{18}O$ is dominant in comparison to $C^{16}O$, the fractions of $^{16}O^{12}C^{18}O$ and $^{18}O^{12}C^{18}O$ are still relatively low, and the main dissociation products would come from the electron impact dissociation of $^{16}O^{12}C^{16}O$. Moreover, for the gas mixture with lower amount of ^{18}O atoms, the fraction of $C^{18}O$ (over the total carbon compounds) is at some points surprisingly higher than that of $^{16}O^{12}C^{18}O$ at 2 Torr and very similar at 5 Torr (see for instance T^{ON} ≈0.2 s in panel (b) in figure 7.8 and panel (b) in figure 7.9).

- Isopologue-dependent dissociation mechanism. The photo-dissociation by low energy photons, above the $^1B_2$ state of CO_2 but below the [O(^{1}D)+CO] level, did show an isotope enrichment in the dissociation products *Bhattacharya et al.* [2000] explained by the following process:

$$CO_2 + h\nu \rightarrow CO_2(^1B_2)^* \leftrightarrow CO_2(^3B_2)^* \rightarrow O(^3P) + CO(^1\Sigma^+)$$

The crossing between singlet $CO_2(^1B_2)$ and triplet $CO_2(^3B_2)$ states (see figure 1.2) is spin forbidden but it can happen due to perturbations caused by spin-orbit coupling. Anomalous enrichment was seen in the photo-dissociation of ClO_2, explained by this isotopologue-selective spin-orbit coupling *Lim et al.* [1999]. In the case of CO_2, the differences in the vibrational energy levels could affect the spin-orbit coupling leading to an isotopologue-selective crossing *Harding et al.* [1988]; *Bhattacharya et al.* [2000]. Yet, in the literature reviewed the isotope enrichment was found in ^{17}O, not in ^{18}O, suggesting an effect of the nuclear spin *Bhattacharya et al.* [2000]; *Mahata and Bhattacharya* [2009]. This specificity of the species containing ^{17}O, could be one of the reasons of the different variation as a function of time for these isotopologues seen in figure 7.6.

- Effect of the vibrational kinetics. Both CO_2 and CO isotopologues present significant differences in their vibrational energies which is evident already from their infra-red absorption spectra. These differences have been proposed as a possible method for isotope separation by differentiated vibrational pumping *Gordiets and Mamedov* [1975]; *Rich and Bergman* [1986]; *Ploenjes et al.* [1998]; *Mori et al.* [2001, 2002]. The most explored case is for the isotopologues $^{12}C^{16}O$ and $^{13}C^{16}O$ due to the large energy difference between their vibrational levels (see figure 7.4) *Andreev et al.* [1994]; *Savinov et al.* [2002]. Although very little information was found about ^{18}O-containing mixtures, figure 7.13 shows an example of the calculated and partly measured vibrational distribution function (VDF) of $C^{16}O$ and $C^{18}O$ *Bergman et al.* [1983]. The VDF of the heavier isotope is more populated and therefore it could be in principle more reactive. Similar relation between heavier and lighter isotopes is expected in CO_2. If there is a relevant contribution to the total dissociation from electron impact on vibrationally excited levels, it could contribute to increase the density of $C^{18}O$. In $^{13}C^{16}O$-$^{12}C^{16}O$ mixture the pure vibrational CO reaction $CO(\nu) + CO(\omega) \rightarrow CO_2 + C$ *Gorse and Capitelli* [1984]; *Adamovich et al.* [1993]; *Essenhigh et al.* [2006]; *Capitelli et al.* [2017] was found to promote the production of free ^{13}C. Such a reaction is not very probable in our discharge conditions due to the low excitation regime, but this reaction does not necessarily proceed directly from ground state level CO($X^1\Sigma^+$), and it may happen from vibrationally excited CO($a^3\Pi_r$) or CO($A^1\Pi$)

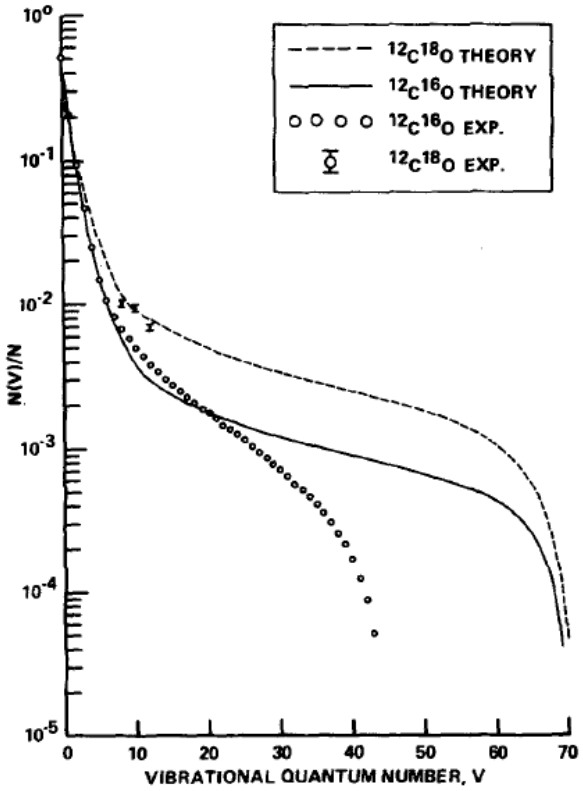

Figure 7.13: VDF for the two CO isotopologues discussed in this chapter extracted from *Bergman et al.* [1983]

Vikis [1978]; *Bergman et al.* [1983]. Other reactions such as $CO(a^3\Pi_r) + CO_2 \rightarrow 2CO + O$ could also be affected by the preferential vibrational excitation of any of the reactants leading to some preference to keep the $C^{18}O$ isotopologue.

The exact mechanisms causing the over population of $C^{18}O$ compared to $C^{16}O$ for short T^{ON} in CO_2-O_2 mixtures are still unclear. They can be related with one or a combination of several of the possibilities discussed above, or with other mechanisms not reported here. It can not be excluded that mechanisms involving vibrationally excited CO could play a role in the differentiated isotope fractions in CO_2-O_2 mixtures. In any case the probably different vibrational temperatures of $C^{18}O$ and $C^{16}O$ does not affect the overall dissociation fraction. As a consequence, a pure vibrational "back reaction" mechanism based on the reaction $CO(\nu) + CO(\omega) \rightarrow CO_2 + C$ *Gorse and Capitelli* [1984]; *Adamovich et al.* [1993]; *Essenhigh et al.* [2006]; *Capitelli et al.* [2017] as briefly discussed in the previous chapter, cannot be the main "back reaction" mechanism in our discharge conditions. Nevertheless a strong CO destroying mechanism must take place in our plasma conditions otherwise, no explanation of the effect of oxygen in CO_2-O_2 and CO-O_2 mixtures such as that shown in figures 7.7 and 7.10 would be possible. If a mechanism involving only $CO(\nu^*)$ was dominating, we should see an effect of the different population of $C^{18}O$ compared to $C^{16}O$ on the time evolution of the dissociation fraction along the building-up experiment. However no effect is observed.

The results presented in this chapter agree with the conclusions of the previous chapter about a negligible role of the vibrational excitation on the dissociation of CO_2, at least in CO_2 or CO_2-O_2 gas mixtures. It therefore reinforces the hypothesis of a "back reaction" mechanism based on

electronically excited species.

✓ The transient excess of $C^{18}O$ in CO_2-O_2 mixtures can not be accounted solely by atomic exchange with $O(^1D)$.
✓ No significant effect of vibrationally excited molecules on the dissociation fraction can be evidenced in spite of the different vibrational temperature of the different isotopes.

7.6 Conclusions and perspectives

This chapter has revealed a fast exchange of oxygen atoms between molecules without undergoing an "usual" back reaction. The use of isotopically labelled species was not successful in tracing this mechanism. However, it has been revealed as a possible way to trace $O(^1D)$ atoms, whose low density and high reactivity, almost at collision rate *Perri et al.* [2004], makes their measurement very challenging. We have been able to keep track of its appearance and activity in a subsidiary way: $O(^1D)$ seems to be effectively quenched by collisions with CO_2 and CO, which in case of isotopic difference can undergo a fast exchange of O atoms in the molecule with statistical probability. The fast exchange of oxygen atoms between molecules through this mechanism is consistent with the fact that the initial slope in building up experiments is driven by the electron impact dissociation of CO_2, discussed in chapter 6.

The occurrence of a significant back reaction mechanism was demonstrated in the previous chapter by comparing the time evolution of the dissociation fraction with different gas mixtures, particularly by CO_2-O_2 and CO-O_2 mixtures. Isotopic measurements discussed in this chapter did not reveal any effect induced by the different vibrational excitation of the different isotopologues, reinforcing the hypothesis of a major role of excited electronic states, in particular $CO(a^3\Pi_r)$, in the "back reaction" mechanism.

Under discharge conditions where the dissociation through vibrational up-pumping can contribute to the total dissociation fraction, the use of isotopes labelling technique appears as a very attractive possibility because of two main reasons:

- Different isotopologues do not impact differently the electron kinetics and do not show significant differences in terms of the chemistry of the heavy neutral species. However, they do have relevant differences in their vibrational kinetics, which opens many possibilities for the study of the role of the vibrational kinetics in the CO_2 conversion process.
- The possibility of tracing the effect of $O(^1D)$. This electronically excited state is constantly produced by electron impact of CO_2 or O_2. However its very fast quenching rates and low densities, makes it very challenging to measure. Being able to trace it and estimate its density could give an indication of the ratio between the dissociation by electron impact or through vibrational up-pumping.

In this regard, experiments with CO_2 containing isotopically labelled O are suggested under high vibrational excitations conditions, as well as with ^{13}C-containing mixtures. The use of isotopes provides a valuable insight in the chemistry of the plasma, an approach that could be further applied in other CO_2/CO-containing plasmas.

Part IV

Surface processes in CO_2 plasmas

Chapter 8

Surface processes in CO_2-O_2 plasmas

Contents

8.1 Introduction 217
8.2 Preliminary comparison between CO_2 and O_2 plasmas 219
8.2.1 O atom densities and loss frequencies in CO_2 and O_2 plasmas 219
8.2.2 O atom loss probabilities in CO_2 and O_2 plasmas 220
8.3 Experimental details and basic parameters in CO_2-O_2 plasmas 224
8.3.1 Experimental details 224
8.3.2 Gas temperature 225
8.3.3 Electric field 226
8.4 O atom densities and loss probabilities in CO_2-O_2 plasmas 226
8.4.1 O atom densities and surface losses under plasma exposure 226
8.4.2 O atom losses in post-discharge 231
8.5 Effect of the wall temperature on the O atom loss processes 234
8.6 Wall reactivity with large SiO_2 effective surfaces 239
8.7 Investigation of surface processes by isotope implantation 243
8.7.1 Oxygen atoms *versus* carbon compounds 244
8.7.2 Effect of the large effective surfaces on isotopic exchange 245
8.8 Preliminary comparison with a surface model 246
8.8.1 Brief description of the model 246
8.8.2 Model results and comparison with experiments 249
8.9 Epilogue: Carbon-based surfaces for enhanced CO_2 dissociation 257
8.10 Conclusions 264

8.1 Introduction

In chapter 3 we presented oxygen atom loss frequencies obtained in CO_2 plasmas, measured under plasma exposure by actinometry in partial-modulated glow discharges. The comparison with rates of gas phase O atom loss processes available in the literature suggested that the O atoms are mostly lost through surface processes in our discharge conditions. While many works have studied the O

atom loss processes in O_2 plasmas reporting atomic oxygen recombination probabilities (γ_O) for different materials and discharge configurations, very few values are given in CO_2 plasmas.

The recombination probability on silica or Pyrex has been studied in O_2 plasma especially for atomic sources and thermal shields for spacecraft re-entry *Paterna et al.* [2002]; *Balat-Pichelin and Bêche* [2010] but even for O_2, the reported values of γ_O are largely scattered for a given surface material. Apart from the uncertainties inherent to certain measurement methods (e.g. titration with NO), among the main reasons for these differences are the pre-treatment history of the surface and the wall (surface) temperature. Another source of discrepancies between the γ_O values obtained comes from the plasma exposure conditions of the surface. Values of γ_O on Pyrex and/or quartz surfaces have been measured in O_2 plasma either in *spatial post-discharge* by measuring a longitudinal profile of O atoms density downstream the plasma *Pejaković et al.* [2008]; *Magne et al.* [1993]; *Wickramanayaka et al.* [1991] sometimes at elevated surface temperature *Kim and Boudart* [1991]; *Greaves and Linnett* [1959], or in *temporal post-discharge* by monitoring the decay of O atoms density after switching off the plasma *Cartry et al.* [1999, 2000, 2006]; *Macko et al.* [2004]; *Marinov et al.* [2013a], or in *stationary discharge* by measuring a spatial gradient of O atoms above the surface studied *Balat-Pichelin et al.* [2003]; *Bedra and Balat-Pichelin* [2005]; *Bedra et al.* [2006]; *Lopaev et al.* [2010a]. Values of γ_O obtained in *spatial post-discharge* are often one order of magnitude lower than values obtained with the surface under direct plasma exposure. The reasons for this effect are still uncertain, but could be connected with surface ions resulting from the discharge electrons or ion fluxes towards the surface *Gordiets and Ferreira* [1998]. At pressures below 1 Torr in O_2 it has been claimed in *Booth et al.* [2019] that ion bombardment can "clean" active sites and increase the chemical activity of the surface. In CO_2 plasma the values of γ_O are much more scarce *Kolesnikov et al.* [2000]; *Afonina et al.* [2002]; *Bousquet et al.* [2007] and obtained in conditions sometimes difficult to compare with the values measured in pure O_2.

In a rather simplified view, surfaces are usually treated as a 2D body defined by a certain density of adsorption sites, where atoms or molecules can get absorbed either reversibly or irreversibly. Reversible adsorption, or "physisorption" takes place when a weak bond (energy ∼0.1-0.3 eV) is established between an atom or molecule and the surface through van der Waals forces. Due to the low-energy of these bonds, physisorbed atoms can diffuse on the surface (surface diffusion) or being desorbed back to the gas phase (thermal desorption). In the case of irreversible adsorption (chemisorption), a true chemical bond between the adsorbed atom and the surface is formed (energy ∼1-3 eV *Lopaev et al.* [2010a]). Chemisorption only occurs on specific surface sites (chemisorption sites), typically associated to impurities or surface defects. The density of chemisorption sites, $\approx 10^{12}$-10^{14} cm^{-2}, is generally much lower than the density of physisorption sites, which is similar to the surface atom density, $\approx 10^{15}$-10^{16} cm^{-2} *Booth et al.* [2019]. In this simplified view, surface processes are described via two mechanisms *Marinov* [2012]: When an incident atom or molecule from the gas phase recombines with an adsorbed atom (physisorbed or chemisorbed) the recombination probability depends on the atom concentration to first order. This process is usually known as Eley-Rideal recombination (E-R mechanism) *Guerra* [2007]. In the recombination with physisorbed atoms, the surface plays a similar role to the third body in gas phase three-body recombination processes *Booth et al.* [2019]. When the recombination process involves two adsorbed atoms (both physisorbed or one physisorbed and one chemisorbed), that encounter each other after surface diffusion, the recombination probability shows either a first or a second order dependence on the atom

or molecule concentration *Guerra* [2007]. This process is commonly called Langmuir-Hinshelwood (L-H) recombination *Kim and Boudart* [1991]; *Guerra* [2007]. The Langmuir-Hinshelwood mechanism is often claimed to be dominant only at low surface temperatures (below ∼250 K), where the thermal desorption of physisorbed atoms is slow. At temperatures close to room temperature or above, the E-R mechanism is believed to be the dominant recombination mechanism *Macko et al.* [2004]. However, a significant contribution of L-H mechanism at higher surface temperatures, such as 370 K *Guerra et al.* [2019], or even 500 K *Gordiets and Ferreira* [1998] has been reported. The surface temperature is therefore one of the main parameters defining the nature of surface processes in a plasma environment. Nevertheless, a clear dependence of the O atom loss frequencies with the gas temperature was found in our experimental conditions (see figure 3.30) and not only with the surface temperature *Booth et al.* [2019].

Molecules such as O_2, CO or CO_2, are believed to interact very weakly with the surface. Nevertheless, ozone formation in surfaces such as Pyrex has been observed *Janssen and Tuzson* [2010]; *Lopaev et al.* [2010a] even in very similar experimental conditions to ours *Marinov et al.* [2012a, 2013a]. In this context, physisorbed O_2 molecules are claimed to play a key role in the ozone production at the surface *Lopaev et al.* [2010b]. In CO/CO_2-containing plasmas, CO_2 molecules and more probably CO may also affect the O atoms surface processes and/or participate in surface reactions. This chapter is devoted to the study of surface processes in CO_2 plasmas, with an emphasis in the O atom surface loss processes. A careful comparison between loss probabilities obtained in O_2 plasmas and CO_2-O_2 gas mixtures is made. The influence of wall temperature in addition to isotopic exchange studies will provide additional information. Moreover, a preliminary comparison with a surface model will provide insights in the different surface mechanisms involved. At the end of the chapter, the interaction between CO_2 plasma and a very peculiar surface will be presented and will constitute at the same time an application of some of the lessons learnt along the chapter and throughout this thesis, as well as a closing point of this work.

8.2 Preliminary comparison between CO_2 and O_2 plasmas

The investigation presented in this chapter was motivated by the comparison of the O atom loss frequency data measured in CO_2 plasmas, shown in chapter 3, and the experimental results obtained in O_2 plasma in similar experimental conditions (same experimental set-up) presented in *Booth et al.* [2019] and discussed in detail in the PhD thesis of Abhyuday Chatterjee. We introduce this comparison as starting point for the discussion of the O atom surface loss processes in CO_2 plasmas. More details about the measurement procedure and data analysis are given in sections 2.4.1 and 3.5.

8.2.1 O atom densities and loss frequencies in CO_2 and O_2 plasmas

Figure 8.1 shows O atom fractions and recombination frequencies measured by actinometry and calculated as the average of the results from two emission lines, O777 and O845, measured in CO_2 plasmas (see section 3.5) and in pure O_2 plasmas measured in the same experimental conditions, shared by J.-P. Booth and D. Lopaev, and partly presented in *Booth et al.* [2019]. Panels (a) and (b) show the O atom loss frequencies for O_2 and CO_2 plasmas respectively, and panels (c) and (d), the corresponding O atom fractions over the total gas density, as a function of pressure, for currents

between 10 and 40 mA. The wall temperature was kept at 50^{o}C in all the experiments.

We observe similar trends in both plasmas. The loss frequency first decreases with pressure, passes through a minimum and then increases. The loss frequency increases with current for all pressures in both discharges. The O atom fraction in the total gas density follows an opposite and complementary trend. $^O/_N$ first increases as a function of pressure, passes through a maximum and then decreases more slowly. The minimum in loss frequency and the maximum in atomic oxygen fraction take place at the same pressure value, suggesting a change of surface processes regime, similar in both discharges. There are however, some noticeable differences between O_2 and CO_2 plasmas:

- The O atom fractions are higher in O_2 than in CO_2 plasmas.
- The loss frequencies are also higher for O_2 than for CO_2 plasmas.
- The minimum in ν_{loss}^{O} and maximum in $^O/_N$ seem to be slightly shifted towards lower pressures in O_2 plasmas (0.75 Torr) compared to CO_2 plasmas (∼1-2 Torr).
- The variation of ν_{loss}^{O} with pressure, both when increasing and when decreasing pressure, is significantly larger in O_2 plasmas than in CO_2 plasmas.

The higher O atom density in O_2 plasmas was to be expected, and can be explained by the electron impact dissociation of O_2 and CO_2. The thresholds for electron impact of O_2 are roughly at 5-6 or 8 eV (see figure 1.4) creating two oxygen atoms on the ground state or one excited and one ground state O atom, respectively *Phelps* [1985]. CO_2 is dissociated by electron impact at ∼7 eV *Polak and Slovetsky* [1976] creating one oxygen atom in O(^{1}D) excited state (which is often assumed to be rapidly quenched into the ground state). The probability to extract an extra O atom from the dissociation of CO is not very high due to the higher energy threshold, >11 eV. The data presented in figure 6.19 already suggested that the dissociation of CO is not contributing significantly to the available oxygen in the gas phase, and it is confirmed by the difference between O_2 and CO_2 plasmas observed in figure 8.1.

The ratio between $(^O/_N)_{max}$ in O_2 and in CO_2 is ∼1.9 (at 40 mA). Considering the lower energy threshold for the electron impact dissociation of O_2, a slightly higher ratio above 2 could have been expected. One possible reason for this behaviour is the lower reduced electric field in O_2 plasmas (shown in section 8.3.3). However, another reason is the remarkably higher loss frequencies observed in pure O_2 plasmas than in CO_2. As an example, at 2 Torr, 40 mA $\nu_O^{loss\ O_2} - \nu_O^{loss\ CO_2}$ ∼14.5 s^{-1} and the ratio is 1.8. At 5 Torr, 40 mA the difference is ∼22.3 s^{-1}, and the ratio reaches its maximum $\nu_O^{loss\ O_2}/\nu_O^{loss\ CO_2}$ ∼1.93. In other words, $\nu_O^{loss\ O_2}$ is almost twice higher than $\nu_O^{loss\ CO_2}$. In the following section we study how this is correlated to the surface O atom loss probability.

8.2.2 O atom loss probabilities in CO_2 and O_2 plasmas

The loss rate due to recombination at the reactor walls can be expressed as *Chantry* [1987]:

$$\tau = \frac{1}{K_{wall}} = \tau_{diff} + \tau_{loss} = \frac{\Lambda_O^2}{D} + \frac{V}{S}\frac{2(2-\gamma)}{\upsilon_{th}\gamma} \tag{8.1}$$

where γ is the wall loss probability (of the O atoms in this case), S is the surface area in contact with the plasma, V is the volume of the plasma, υ_{th} is the thermal velocity of the O atoms given by

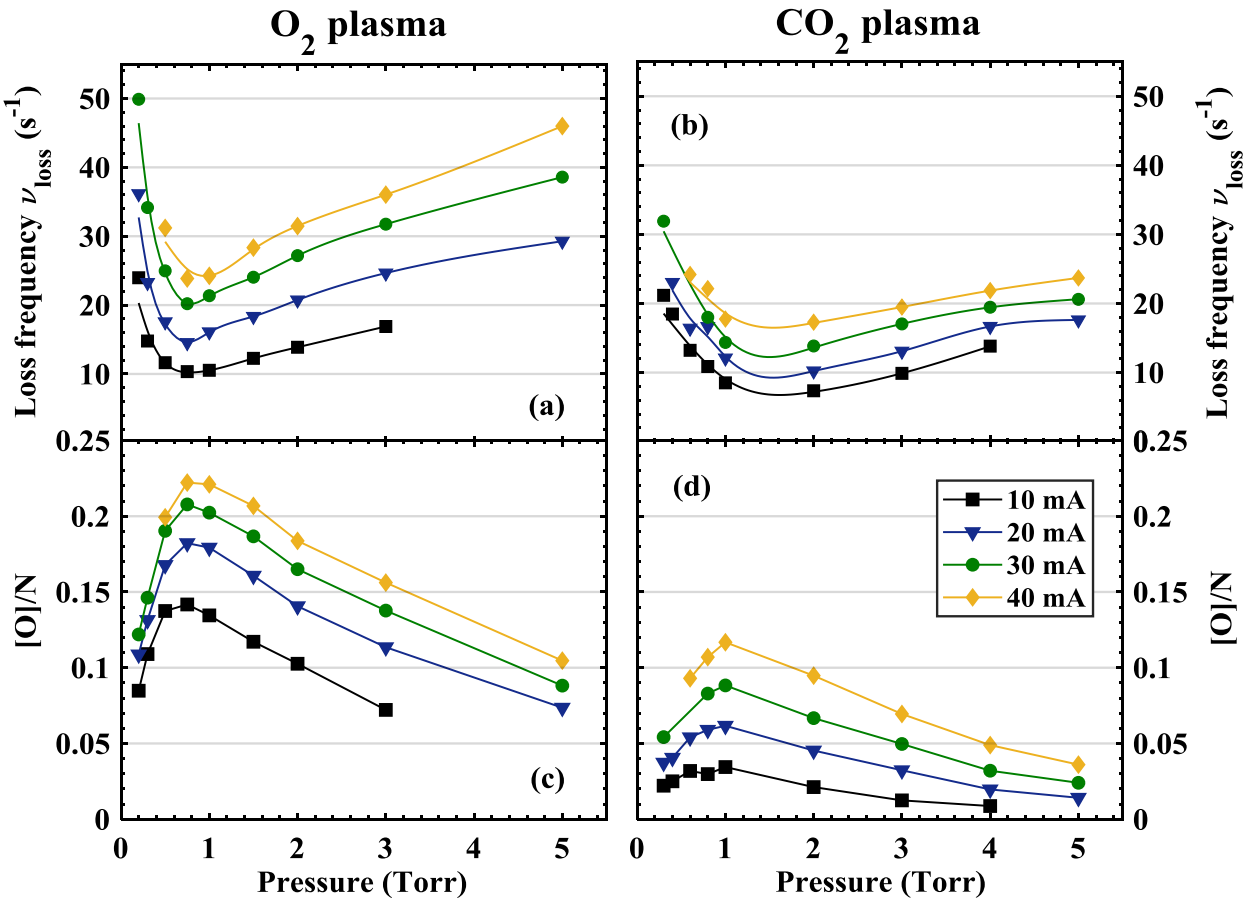

Figure 8.1: Comparison of the loss frequencies and atomic oxygen fractions measured in O_2 plasmas (panels (a) and (c), respectively) and CO_2 plasmas (panels (b) and (d)) as a function of pressure for currents between 10 and 40 mA. The O_2 plasma data in this figure was shared by J.-P. Booth and D. Lopaev, and it is partly presented in *Booth et al.* [2019]). CO_2 plasma data was discussed in detail in section 3.5.

the expression $v_{th} = \sqrt{8k_BT/\pi \cdot m_o}$, where m_o is the mass of the oxygen atoms ($m_o = 2.66 \times 10^{-26}$ kg) and D is the diffusion coefficient of atomic oxygen. Λ_O is the diffusion length, defined in chapter 3 and given by equation (3.3). In our case $\Lambda_O \sim 0.42$ cm. Two expressions were found in literature to calculate the diffusion coefficient of O atoms in CO_2. From *Cenian et al.* [1994]:

$$D = D(0) \cdot P^{-1} \cdot (T/273)^{3/2} \tag{8.2}$$

where $D(0) = 190$ cm^{2}s^{-1} is the diffusion coefficient at 1 Torr and 273 K, P is the pressure in Torr and T is the gas temperature. Or the expression used in chapter 3 to calculate the diffusion coefficient, given by equation (3.4):

$$D = \frac{1}{3} l v_{th} = \frac{1}{3} \left(\frac{k_B T}{\sqrt{2} \cdot P \pi d^2} \right) \cdot \sqrt{\frac{8k_B T}{\pi \cdot m_o}} \tag{8.3}$$

where l is the mean free path, d is the kinetic diameter of the oxygen atom (assumed to be similar to the molecular oxygen, 346 pm *Mehio et al.* [2014]) and v_{th} is the thermal velocity of the oxygen atoms. According to these equations, the maximum of τ_{diff} is for 5 Torr 10 mA (see figure 3.7), and ranges between 1.8 ms (equation (8.2)) and 3.2 ms (equation (8.3)). As the minimum lifetime

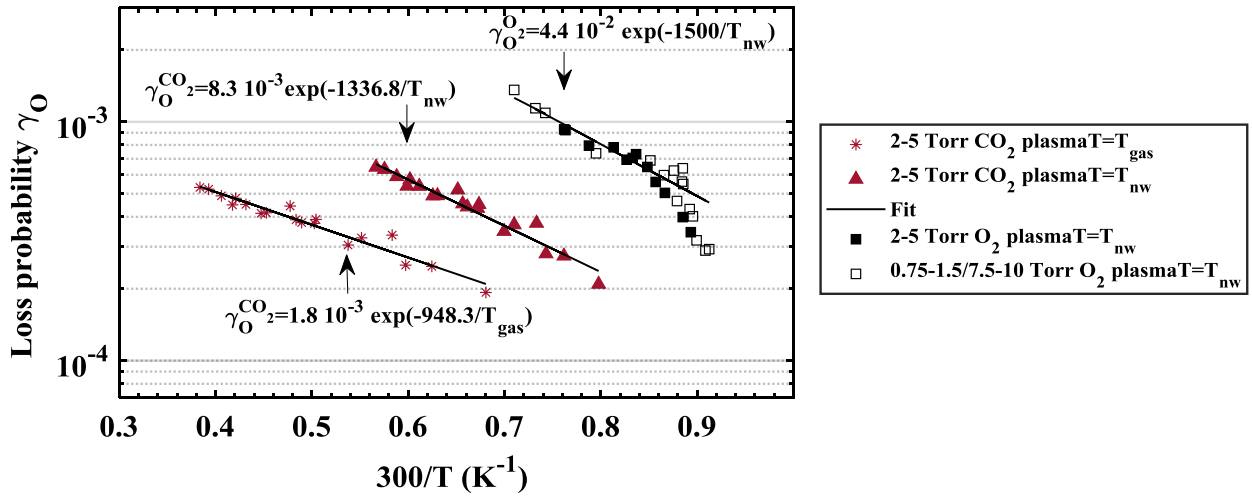

Figure 8.2: Loss probabilities, γ_O, plotted *versus* $^{300}/_{T}$, for O_2 plasma (from *Booth et al.* [2019]) and for CO_2 plasma. In the later case, γ_O values calculated and plotted using T=T_{gas} and T=T_{nw} are included for comparison, with the corresponding exponential fittings. O_2 the data in the same range of pressures as CO_2 data (2-5 Torr) is plotted with filled symbols, data for higher or lower pressures, used for the fitting is plotted with empty symbols.

(τ_{loss}) in our conditions is close to 30 ms we can assume that $\tau = \tau_{diff} + \tau_{loss} \approx \tau_{loss}$ ($\tau_{diff} \ll \tau_{loss}$). Taking this into account in equation (8.1) we calculate the loss probability with the expression:

$$\gamma_O = \frac{2R \cdot \nu_{loss}^O}{\upsilon_{th}} = \frac{2R}{\tau_{wall}\upsilon_{th}} \tag{8.4}$$

In this equation the value of temperature used for the thermal velocity should represent the temperature of the atoms reaching the wall. This temperature, $T_{near\ wall}$=T_{nw}, is significantly lower than T_{gas}, as discussed in section 3.2.4, because of the radial temperature profile in the tube. The low value of the mean free path (the maximum value is <0.25 mm) means that the O atoms will be thermalized to this lower temperature before reaching the wall *Booth et al.* [2019]. The expressions to calculate T_{nw} for O_2 and CO_2 plasmas were already discussed in section 3.2.4:

$$T_{nw}^{O_2} = T_w + 0.28 \cdot (T_{gas} - T_w) \tag{8.5}$$

$$T_{nw}^{CO_2} = T_w + 0.45 \cdot (T_{gas} - T_w) \tag{8.6}$$

In figure 8.2 the loss probabilities derived from experiments in CO_2, between 2 and 5 Torr, and O_2 plasmas are plotted *versus* $300/T_{nw}$. Additionally, CO_2 data calculated using T_{gas} (and plotted versus $300/T_{gas}$) is included for comparison, to illustrate the differences in the activation energies that can be derived from considering different gas temperatures close to the surface. $\gamma_O^{O_2}$ values in O_2 and the corresponding fit were shared by J.-P. Booth and D. Lopaev and are included in *Booth et al.* [2019]. Three main points can be commented about the results shown in figure 8.2:

1. The obtained loss probabilities in CO_2 plasmas are in the range of 2-7 $\times$ 10^{-4}, lower than the measurements in pure O_2 plasma, with $\gamma_O^{O_2}$ ranging from 3 to 10 $\times$ 10^{-4}.
2. For both gases we observe a clear dependence of γ_O on the gas temperature near the wall, following an exponential trend, *i.e.* an Arrhenius dependence, which can be described by

Guerra [2007]:

$$\gamma_O = A \cdot exp\left(-\frac{E_{act}}{k_B T_{near\ wall}}\right) \tag{8.7}$$

3. The derived activation energies, E_{act}, considering T_{nw} are $E_{act}^{CO_2}$=0.115 eV for CO_2 plasma (0.08eV considering T_{gas}) and $E_{act}^{O_2}$ ≈0.13 eV for O_2, higher than in CO_2 plasma.

The gas temperature dependence for both gases suggest a first order process, therefore an Eley-Rideal surface recombination mechanism, where an adsorbed atom or molecule reacts with an atom coming from the gas phase *Kim and Boudart* [1991]. This should be the dominant surface recombination process for the wall temperature used during this experiments (323 K) according to *Macko et al.* [2004]. Three main points can therefore be kept in mind for the following discussion:

- O atom surface recombination seems to occur through an Eley-Rideal mechanism, with either chemisorbed or physisorbed species.
- The recombination depends on the kinetic energy of the incoming gas-phase O atoms, therefore on T_{nw}.
- E-R recombination is a first order process, not limited by the flux of O atoms but by the density of adoption sites.

The kinetic energy of incoming oxygen atoms appears to be a key parameter in the recombination process. The gas temperature near the wall is higher in CO_2 plasmas, and consequently higher loss probabilities could have been expected in CO_2 plasmas. The higher loss probabilities in O_2 than in CO_2 are in this context even more remarkable. According to equation (8.4) this is partly due to the lower gas temperatures in O_2 plasmas but specially due to the higher loss frequencies, shown in figure 8.1, up to ∼2 times higher.

The fact that the E-R mechanism is not limited by the flux of O atoms, contrary to the L-H mechanism implies that in principle the higher $[O/N]_{O_2}$ compared to $[O/N]_{CO_2}$ should not be the cause of the different loss probabilities in CO_2 and O_2 plasmas. A certain contribution of the L-H mechanism cannot be discarded and it will be discussed in more detail in the following sections. Nevertheless it is not expected to be the main loss mechanism according to the experimental dependence with T_{nw} (at least for T_{wall}=50 ^{o}C).

It is worth mentioning that in the literature, only one example was found comparing γ_O ($\propto \nu_O^{loss}$) for CO_2 and O_2 measured in the same experimental conditions (at 0.005 Torr, in a 300W RF plasma ignited in a helicon reactor). The ratio $\gamma_O^{O_2}/\gamma_O^{CO_2}$ reported was ∼ 3.75 *Bousquet et al.* [2007], showing qualitative agreement with our results, in spite of very different plasma sources.

This preliminary comparison already suggests that CO and CO_2 molecules or even C atoms influence the loss mechanisms of O atoms on the surface exposed to CO_2 plasmas. The mechanisms involved are at this stage still unclear. C atoms, CO molecules or even CO_2 could be chemisorbed or physisorbed, changing the surface configuration and competing for the adsorption sites with O atoms and O_2 molecules. Several measurements will be presented to provide insights about the mechanisms responsible for this "passivation" of the surface:

1. Several gas mixtures between 100%CO_2-0%O_2 and 10%-CO_2-90%O_2 will be measured to investigate the role of the O atom flux and CO, CO_2 densities on the recombination probabilities.

2. Different wall temperatures will studied to investigate the possibility of L-H mechanism and the role of physisorbed species.
3. Large effective surface materials (silica fibers, see chapter 5) will be used to vary the density of adsorption sites.
4. Isotope exchange experiments will be perform to study the role of chemisorbed C or CO.

✓ In our discharge conditions, O atom recombination seems to be dominated by an Eley-Rideal mechanism, dependent on the kinetic energy of the incoming O atoms.
✓ O atom loss frequencies and loss probabilities are significantly higher in O_2 plasmas than in CO_2 plasmas.
✓ CO and CO_2 molecules and/or C atoms infuence the surface O atoms losses on Pyrex.

8.3 Experimental details and basic parameters in CO_2-O_2 plasmas

We studied gas mixtures ranging from pure CO_2 to pure O_2 plasmas, keeping the total gas flow constant at 7.4 sccm. In this section we briefly remind the experimental details and provide information about the basic parameters characterizing CO_2-O_2 plasmas in our discharge conditions, required to treat actinometry data and to obtain atomic oxygen densities.

8.3.1 Experimental details

The experimental details concerning the diagnostics of O atom densities and loss frequencies are summarized in the experimental box 8.1. The experimental set-up was similar to the set-up used for previous experiments (preliminary comparison), but another discharge tube was used (also made of Pyrex, with similar dimensions). A pre-treatment based on a pure O_2 plasma at 1.5 Torr, 40 mA was carried out during at least 30 minutes in between measurements for different gas mixtures. In order to measure dissociation fractions and gas temperatures in CO_2-containing mixtures we used FTIR spectroscopy, whose details are given in the experimental box 8.2. For isotopic experiments, the experimental details will be given in section 8.7

Diagnostics: Actinometry, CRDS (Pulsed)	**Reactor**: DW Long tube	**Pressure**: **0.4-7.5** Torr
Discharge: Glow discharge Modulated & Pulsed	T_{wall}: **Carbo-ice + ethanol (∼50)-50°C**	**Current**: **20, 40** mA
	Gas mixture: **CO_2-O_2**	**Flow**: 7.4 sccm (τ_{res} ≈0.46-5 s)

Experimental box 8.1: Measurements of the O atom densities and loss frequencies.

Diagnostics: FTIR	**Reactor**: DW Short tube	**Pressure**: **1, 2 & 5** Torr
Discharge: Glow	DW L-shape	**Current**: **20, 40** mA
Continuous plasma	T_{wall}: **-20-50°C**	**Flow**: 7.4 sccm
In situ & downstream	**Gas mixture**: **CO_2-O_2**	τ_{res} ≈: 0.15-1.6 s

Experimental box 8.2: Measurements of dissociation fraction.

In order to obtain O atom densities, actinometry data was treated with the so-called method 2, using the Boltzmann solver LoKI to calculate iteratively the absolute oxygen densities (see section 2.4.1). Gas temperature, reduced electric field and dissociation fraction α, are input parameters required to run the script. Gas temperature and electric field measurements for these gas mixtures are discussed below. *In situ* dissociation fractions measured at 1, 2 and 5 Torr, 20 and 40 mA are given in section 8.6 and were obtained with the short glow discharge reactor. Similarly to chapter 3, the atomic oxygen data was taken in the long discharge tube. Therefore a conversion procedure to calculate the equivalent dissociation fractions in the long reactor was done based on the dependence of α with the residence time, similar to that described in section 3.4.6. It is also important to point out that α is not changed by the wall temperature between T_{wall}=-20 and 50^{o}C, within the experimental error. Only a small decrease of α was observed at lower T_{wall}, (carbo-ice+ethanol temperatures, T_{wall} ∼-50^{o}C). However, no absolute O atom densities were determined for those conditions and only loss frequencies for carbo-ice+ethanol T_{wall} are discussed in section 8.5.

8.3.2 Gas temperature

Figure 8.3 presents the variation of the gas temperature as a function of the CO_2 fraction in the initial gas mixture with a fixed T_{wall}=50^{o}C, measured with FTIR. Data measured with HR-TALIF at 1 Torr, 20 and 40 mA, is included for comparison. At low pressures the radial temperature gradient is small and FTIR and HR-TALIF values are in very good agreement. The gas temperature in CO_2 plasmas is higher than in O_2 plasmas. For a given pressure, current and wall temperature, the gas temperature increases ∼linearly with the CO_2 content in the initial gas mixture. Therefore, knowing the gas temperature in O_2 and CO_2 plasmas for a given condition, we can interpolate the temperature for any gas mixture. Moreover, previous FTIR and TALIF measurements at different wall temperatures show that for a given pressure, current and gas mixture, T_{gas} varies linearly with T_{wall} (see example in figure 3.8). Therefore the gas temperature has been inter/extrapolate for all T_{wall} and gas mixtures for which we did not have direct measurement. Gas temperatures measured

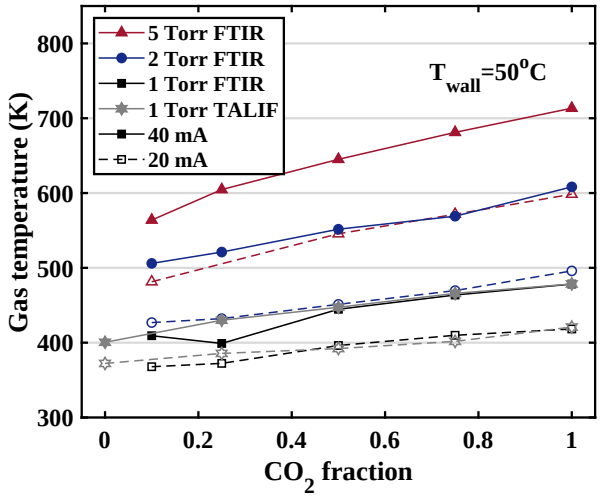

Figure 8.3: Variation of the gas temperature with the initial CO_2 fraction measured with FTIR at 1, 2 and 5 Tor, 20 mA (dashed lines, empty symbols) and 40 mA (solid lines, filled symbols), at T_{wall}=50^{o}C. HR-TALIF data at 1 Torr, 20 and 40 mA, is also included for comparison.

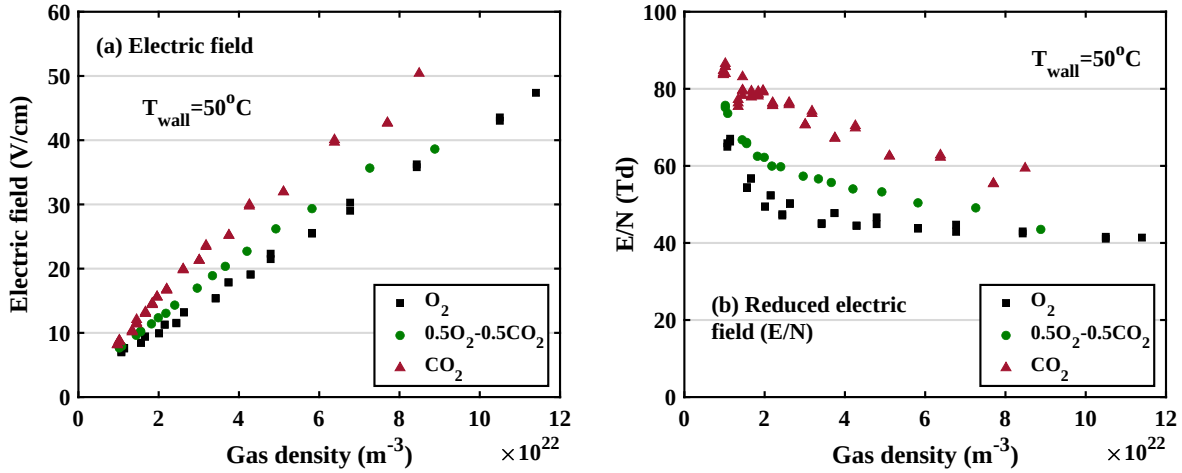

Figure 8.4: Electric field (panel (a)) and reduced electric field (panel (b) measured in three gas mixtures: 100%O_2, 50%O_2-50%CO_2 and 100%CO_2, between 0.4 and 7.5 Torr, 20 and 40 mA at T_{wall}=50^{o}C.

in pure O_2 plasma for T_{wall}=5 and 50^{o}C were shared by J.-P. Booth and D. Lopaev and can be found in the PhD thesis of Abhyuday Chatterjee and in *Booth et al.* [2019]. In order to calculate the temperature near the wall in O_2 and CO_2 plasmas, equations (8.5) and (8.6) were used. For other gas mixtures, the radial profile was not studied but T_{nw} is assumed to be proportional to the CO_2 fraction in the initial mixture, similarly to T_{gas}.

8.3.3 Electric field

Electric field values are recorded simultaneously with actinometry data. The measured values and the calculated reduced electric fields for one wall temperature (50 ^{o}C), as illustrative example, are shown in figure 8.4. For a given gas mixture, a single linear dependence with the gas density is observed. However, the slope clearly depends on the O_2 content. Data for different T_{wall} values falls in the same line (not shown). The reduced electric field varies significantly with the gas mixture and in O_2-containing plasmas is lower than in pure CO_2 as expected from the lower energy losses on vibrations.

8.4 O atom densities and loss probabilities in CO_2-O_2 plasmas

8.4.1 O atom densities and surface losses under plasma exposure

The effect of the CO_2 content in the initial gas mixture was studied by measuring the O atom densities and O atom loss frequencies under plasma exposure in partial modulated discharges for five different CO_2-O_2 mixtures: pure CO_2, 0.75CO_2-0.25O_2, 0.5CO_2-0.5O_2, 0.25CO_2-0.75O_2 and pure O_2, for pressures between 0.4 and 7.5 Torr, at 20 and 40 mA. The variation of the O atom density as a function of current and pressure was discussed in detail for CO_2 plasmas in section 3.5, and it has been compared for a similar range of pressures and currents with the data measured in O_2 plasma in similar conditions *Booth* [2019] in section 8.2.1. The purpose of this section is not to repeat the analysis but to show how the parameters under study evolve between both extreme gas mixtures. Most of the experiments in this section were carried out at a fixed wall temperature,

T_{wall}=25^{o}C. Nevertheless, γ_o data at T_{wall}=50^{o}C is briefly presented to be compared with previous experiments.

Figure 8.5 presents the experimental results for the absolute O atom density. The plot is built as a 3D map where the variation of the absolute O atom density is plotted both as a function of the CO_2 fraction in the initial gas mixture and as a function of pressure. The individual data points are kept and represented with the symbol "o". The top layer represents the absolute oxygen data taken at 40 mA. The bottom layer, only partly visible, plots the data at 20 mA, which follows a parallel variation to the data at 40 mA (similar to figure 8.1). For all gas mixtures, the atomic oxygen density increases with pressure, passes through a maximum and then slowly starts decreasing when the pressure is further increased. The maximum seems to slightly drift toward higher pressures when increasing the O_2 content. For a mixture of 100% CO_2 the maximum is between 2-3 Torr, similarly to figure 3.24, whereas at 100% O_2 the maximum takes places at pressure around 5 Torr. The variation of the O atom density as a function of the gas mixture follows a *quasi* linear increase as a function of the O_2 content, but the slope is strongly depending on pressure. For the lowest pressures (0.4 Torr), the O atom density barely increases when increasing the amount of O_2 in the initial gas mixture. When the pressure is increased the slope reaches up to $[O]_{max}$ (5 Torr) and then starts decreasing. The absolute atomic oxygen values in CO_2 are in good agreement with the data presented in chapter 3, section 3.5, with a maximum absolute atomic oxygen density around 3×10^{21} m^{-3} at 2 Torr, 40 mA.

Figure 8.6 presents the O atom fraction $^O/_N$ (panel (a)) and O atom loss frequency (panel (b)).

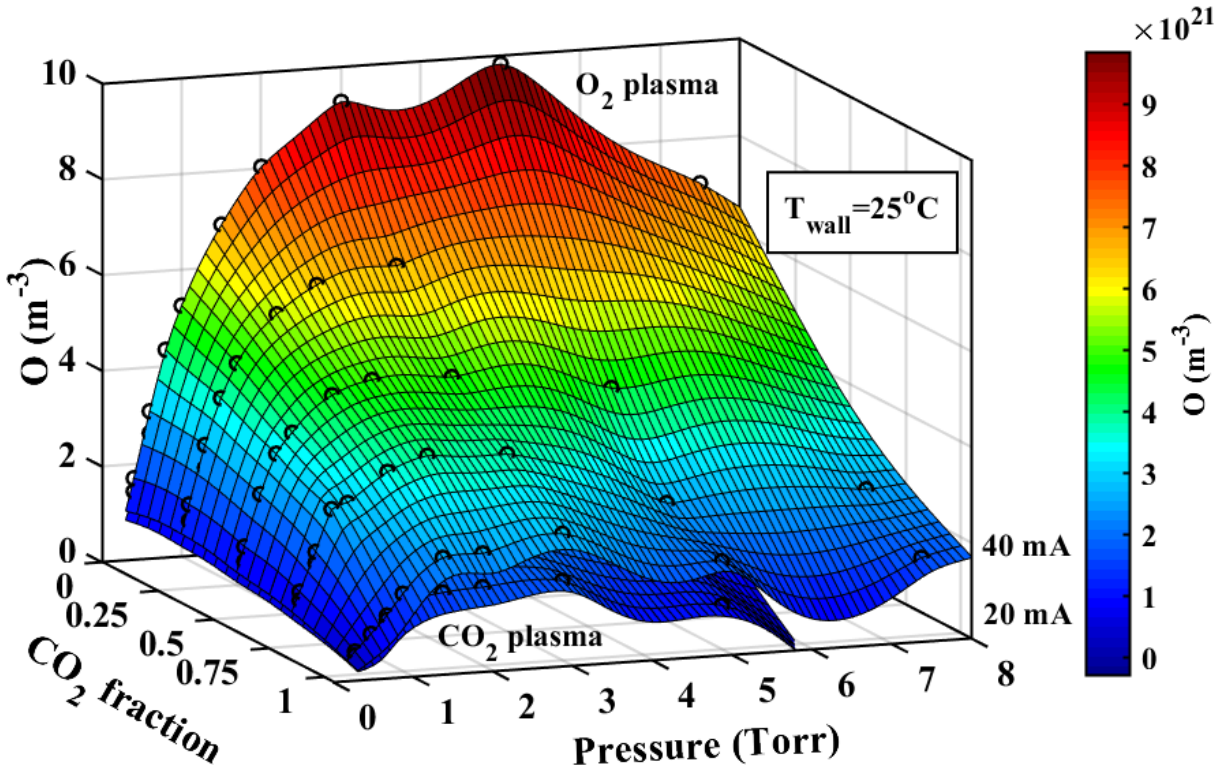

Figure 8.5: Variation of the absolute O atom density as a function of pressure and CO_2 fraction in the initial gas mixture for 20 mA (bottom layer) and 40 mA (top layer), measured by actinometry (the data presented is the average of both emission lines studied O777 and O845) for a T_{wall}=25^{o}C.

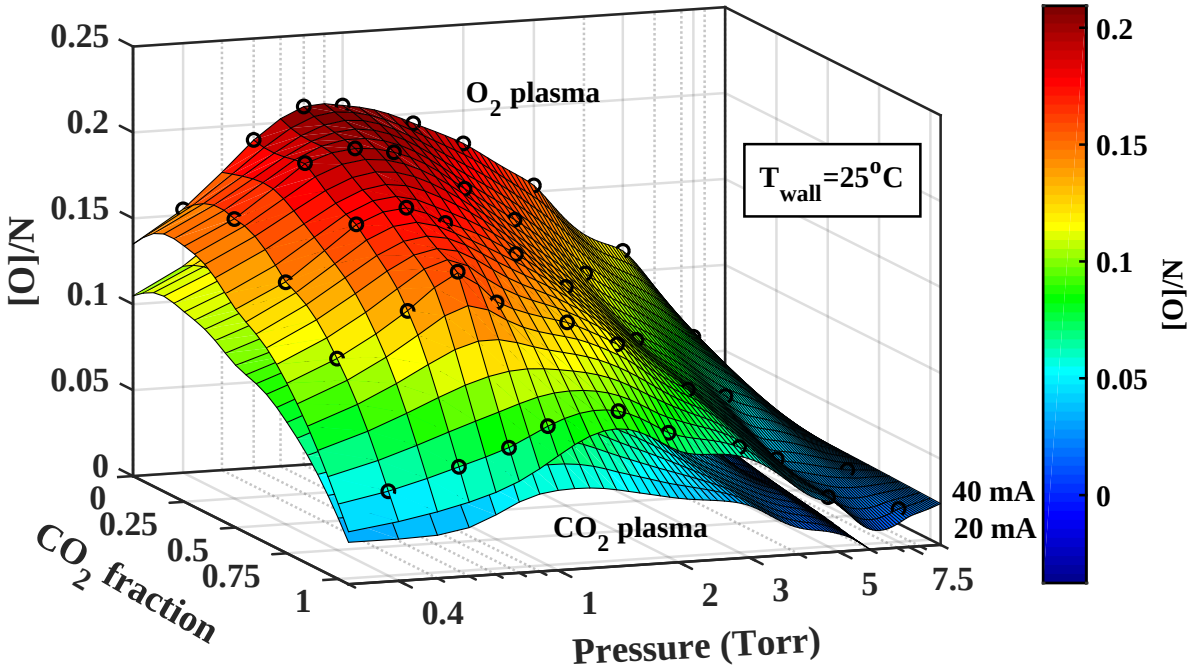

(a) O atom fraction, $^{O}/_{N}$

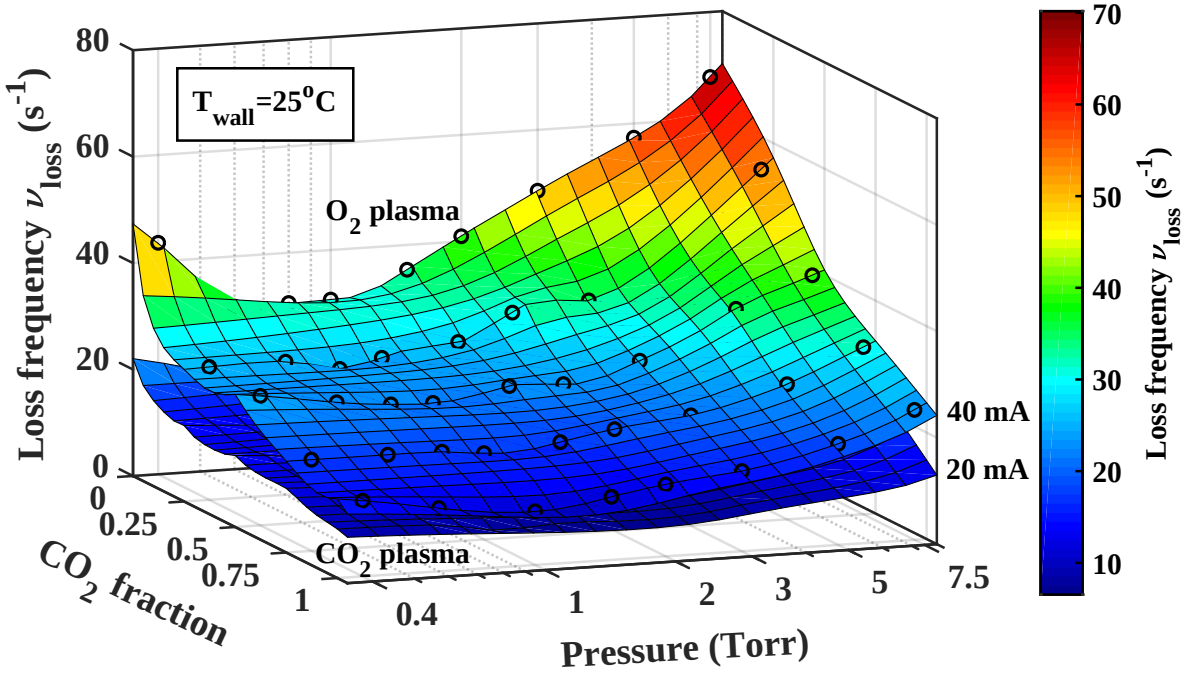

(b) O atom loss frequency, ν_{loss}

Figure 8.6: Variation of the O atom fraction (panel (a)) and O atom loss frequency (panel (b)) as a function of pressure and CO_2 fraction in the initial gas mixture for 20 mA (bottom layer) and 40 mA (top layer), measured by actinometry (the data presented is the average of both emission lines studied O777 and O845) at T_{wall}=25^{o}C. The pressure axis is plotted in log scale for readability of the graph.

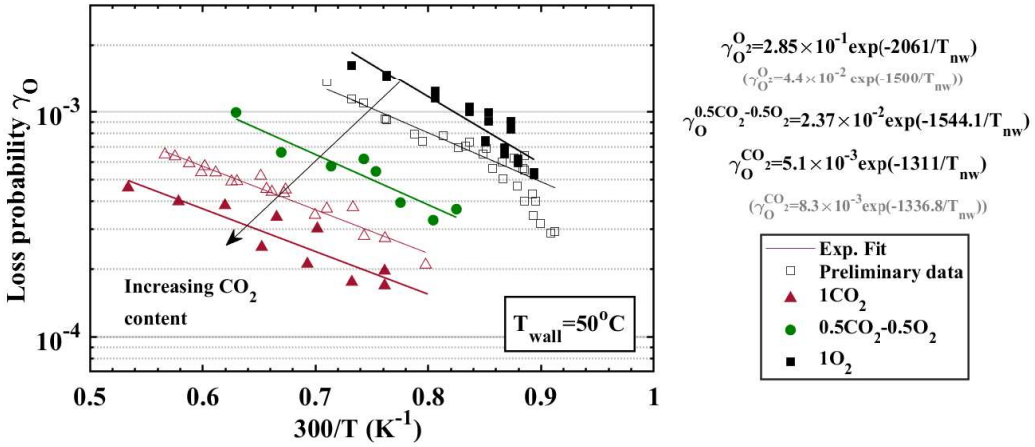

(a) T_{wall}=50°C, including previous data from figure 8.2.

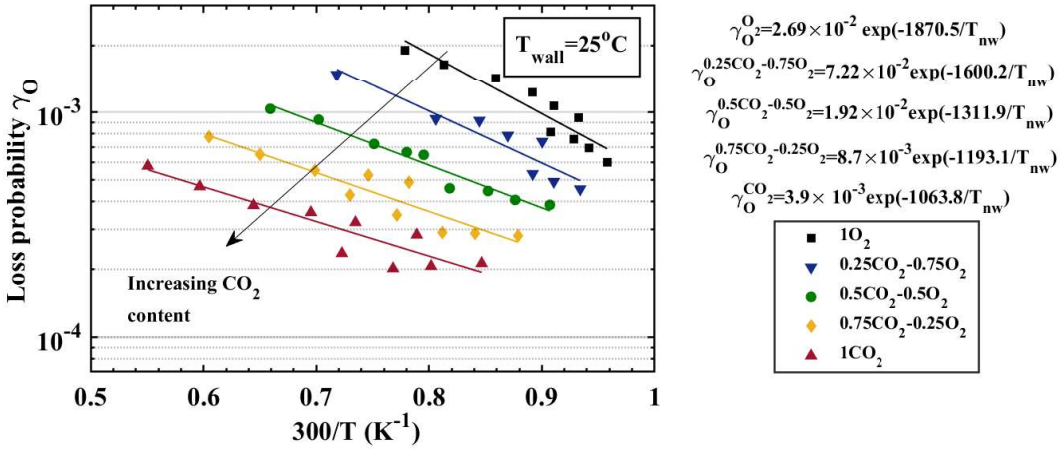

(b) T_{wall}=25°C. γ_O values derived from data presented in figure 8.6 (b).

Figure 8.7: Loss probabilities γ_O for gas mixtures ranging from 100%O_2 to 100%CO_2, calculated and plotted versus $^{300}/_{T}$ being T=T_{nw}, for two different wall temperatures: (a) T_{wall}=50°C for the comparison with previous data from figure 8.2; and (b) T_{wall}=25°C.

Both plots are complementary and very consistent with the trends previously analysed in section 8.2. $^{O}/_{N}$ increases as a function of the O_2 content. The variation is only ~linear for pressures above $(^{O}/_{N})_{max}$. At $(^{O}/_{N})_{max}$ the O atom fraction increases faster for low O_2 content probably due to the combined effects of increasing O atom density and decreasing gas temperature at different rates. For pressures below $(^{O}/_{N})_{max}$, the O atom fraction first increases as a function of the O_2 content, passes though a maximum and then decreases due to the increase in ν_{loss}. A shift in $(^{O}/_{N})_{max}$ is also noticeable. In CO_2 plasma it is at 1.5 Torr (previously it was at 1 Torr, but no data point was taken at 1.5 Torr), but already for the first gas mixture containing O_2, 0.25O_2-0.75CO_2, the maximum shifts to 0.75 Torr and remains there for all the other O_2-containing gas mixtures. The loss frequencies evolve smoothly between CO_2 and O_2 plasmas, showing that the loss frequencies are clearly enhanced at the lowest and highest pressures by the increase of the O_2 content.

The derived loss probabilities are plotted as a function of $^{300}/_{T_{nw}}$ in figure 8.7. Note that only data for "high" pressures, above the minimum of loss frequency were kept for the calculation of the

loss probability. Panel (a) shows data obtained at T_{wall}=50^{o}C for the comparison with previous data from figure 8.2. Panel (b) shows data at T_{wall}=25^{o}C, *i.e.* calculated from the loss frequency values in figure 8.6. In panel (a) we observe that for O_2 plasma the new loss probabilities and the "slope" of the exponential fit are higher. The corresponding activation energy, E_{act} for the new set of experiments is $E_{act}^{O_2}$ ≈0.175 eV, higher than the previous data, $E_{act}^{O_2}$ ≈0.13 eV, but still in very good agreement with activation energies available in the literature such as $E_{act}^{O_2}$ ≈0.17 eV *Kim and Boudart* [1991] or close to the average value found in the literature ∼0.155 eV *Pagnon et al.* [1995]; *Booth et al.* [2019]. Several reasons could explain the difference between both sets of data such as a slightly different composition of the tube (Pyrex, but modified during the manufacturing process) or small changes in the "cleaning" pre-treatment carried out before any measurement with gas mixture variation.

In the O_2 data, two slightly differentiated groups appear: one that tends to fall below the fitted curve for higher $^{300}/_{T_{nw}}$ values (data taken at 20 mA), and another group that tends to be above the fitted curve (data taken at 40 mA). This effect is visible for all wall temperatures, and mostly for high O_2 content (see for instance figure 8.12 (c)). The reason is still unclear, but could be a consequence of the gas temperature considered. Not taking into account the data at 20 mA in the fitting would reduce the slope of the fit, giving values closer to the previous activation energy. For CO_2, the new data shows lower loss probabilities, but the activation energy $E_{act}^{CO_2}$=0.113 eV is very similar to the previous value.

For both wall temperatures, the loss probability decreases with CO_2 content, in good agreement with the previous data. The activation energies also decrease progressively with the amount of CO_2. A possible explanation for the lower recombination frequencies in CO_2 than O_2 could be that part of the adsorption sites are occupied by species only available in CO_2 plasmas, such as CO_{ads} or even carbon atoms, and not only by O_{ads}. The possibility of CO adsorbed in the walls was already suggested by Cenian *et al.* *Cenian et al.* [1994], where the rate for the O+O recombination at the wall is dependent on the CO concentration in the gas phase (reaction 11 in table 3.1). The argument is that the adsorption of CO on the walls happens preferentially to the absorption of oxygen, and therefore limits the recombination of O atoms into O_2. The decrease of γ_O when N_2 is added to O_2 plasmas was already pointed out by *Gordiets et al.* [1995]. Similarly, lower O densities were found in pure O_2 plasmas compared with O_2 + small amounts of fluorinated compounds, which was explained by the passivation of the surface by F atoms in *Booth and Sadeghi* [1991].

Concerning the gas temperature dependence of the loss frequencies and the experimental T_{wall}, we could *a priori* assume that O atom recombination is driven by E-R mechanism. In this case, several possible reactions involving O atoms could be competing at the wall in CO_2-O_2 mixtures (without differentiating between chemisorbed or physisorbed species): $O + CO_{ads} \rightarrow CO_2$ and $O + Ads \rightarrow O_{ads}$ followed by either $O + O_{ads} \rightarrow O_2$ or $CO + O_{ads} \rightarrow CO_2$. There is very little information in the literature about reactions between adsorbed O or CO with atoms or molecules from the gas phase. Loss probabilities have been given for $O + O_{ads} \rightarrow O_2$ and $CO + O_{ads} \rightarrow CO_2$ in *Kovalev et al.* [2005]; *Bykova et al.* [1997] obtained in different experimental conditions (higher temperatures, 3000-7000 K, simulating entry into the Martian atmosphere). In these works, the loss probability given for $CO + O_{ads} \rightarrow CO_2$ is claimed to be higher than for $O + O_{ads} \rightarrow O_2$.

$$CO + O_{ads} \rightarrow CO_2 \quad \gamma = 0.15 \cdot exp\left(^{-15(kJ/mol)}/_{RT_{wall}}\right)$$

$$O + O_{ads} \rightarrow O_2 \quad \gamma = 0.15 \cdot exp\left(^{-25(kJ/mol)}/_{RT_{wall}}\right)$$

Extrapolated to our temperatures, the proposed expression for $CO + O_{ads} \rightarrow CO_2$ gives values between 1.5 and 2 times lower than our results. However, the probabilities given for $O+O_{ads} \rightarrow O_2$ in *Kovalev et al.* [2005] are very low, ∼10 times lower than our values. If the reaction $CO+O_{ads} \rightarrow CO_2$ was the dominant surface recombination process, the densities of O and CO, and their evolution as a function of pressure would be more comparable (see section 3.6). Therefore, although the probability given for $CO + O_{ads} \rightarrow CO_2$ could be compatible with our results, the probability for $O + O_{ads} \rightarrow O_2$ should be necessarily higher. There is no information in these works about the reaction with adsorbed CO ($O + CO_{ads} \rightarrow CO_2$) but this is probably not the dominant process either for the same reason mentioned above.

The reason for the different activation energy as a function of the gas mixture is not clear yet. It will be discussed in section 8.8 in light of preliminary modelling results, but already several hypothesis can be formulated, such as an influence of a higher heat flux towards the wall in CO_2 plasmas, an extra energy flux, for example from vibrationally excited molecules (or other excited states) from the gas phase towards the surface, the involvement of vibrationally excited molecules in surface reactions, or even the excitation of molecules directly on the surface *Armenise and Kustova* [2018]. The vibrational temperatures shown in chapter 4 for CO_2 or CO reach 1000 K for the asymmetric stretch vibrational mode of CO_2 and 1500 K for CO, ∼0.086 eV and 0.13 eV respectively. The differences in the gas mixture could also modify the population of adsorbed species on the surface affecting the global activation energy.

8.4.2 O atom losses in post-discharge

It is known in O_2 plasma literature that the O atom loss probabilities in post-discharge are lower than under plasma exposure *Gordiets and Ferreira* [1998]; *Cartry et al.* [2006]; *Bousquet et al.* [2007]. In this section, we compare γ_O values measured under plasma exposure and in temporal post-discharge for the five gas mixtures under study, ranging from pure O_2 to pure CO_2. For that purpose we performed CRDS measurements in pulsed plasma (full-modulation) in a cycle of 196-196 ms On-Off, the same pulse duration as for the modulated discharge used in previous sections and long enough to reach the steady-state O atom concentration towards the end of the pulse. Note that short pulse durations (5-10 ms On-Off) were showing a flat evolution of the O atom density along the pulse (see section 3.7.2), due to the relatively long lifetime of the oxygen atoms. The measurements were carried out at T_{wall}=50^{o}C and 2 Torr, 40 mA, close to the maximum of O density and the minimum of loss frequency.

Figure 8.8 presents the time evolution of the absolute O atom density during and after the plasma pulse for the five gas mixtures. For all the gas mixtures O atom density increases during the plasma pulse, and slowly decays exponentially when the plasma is switched off. We observe a deep in the O density a few milliseconds right after the end of the pulse, which is probably an artefact. The previous O atom density level is rapidly recovered and the fast perturbation does not affect the temporal evolution in the post-discharge. Such an effect can be caused either by noise in the data acquisition when the plasma is switched OFF or by the correction applied to the CRDS absorbance signal to account for the change in the gas temperature. For short pulses (5-10 ms On-Off, see section 3.7.2), the time evolution of T_{rot} measured with FTIR (see figure 3.4) was used for the correction. However, for long plasma pulses we assume that the steady-state gas temperature is immediately reached when the plasma is started and in the post-discharge we assume that the

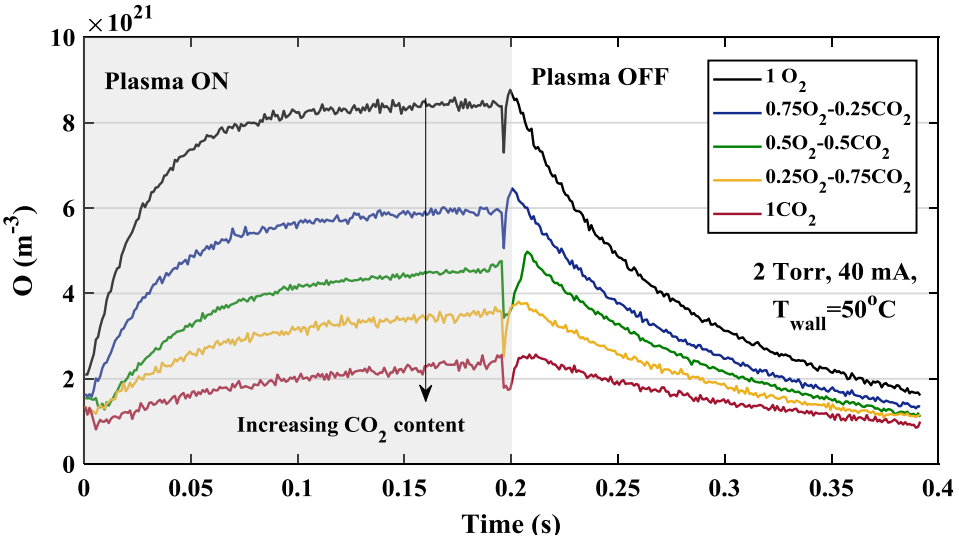

Figure 8.8: Time evolution of the absolute O atom density along a plasma pulse of 196-196 ms On-Off measured with CRDS at 2 Torr, 40 mA (7.4 sccm, gas flow) for five gas mixtures ranging from 100%O_2 to 100%CO_2.

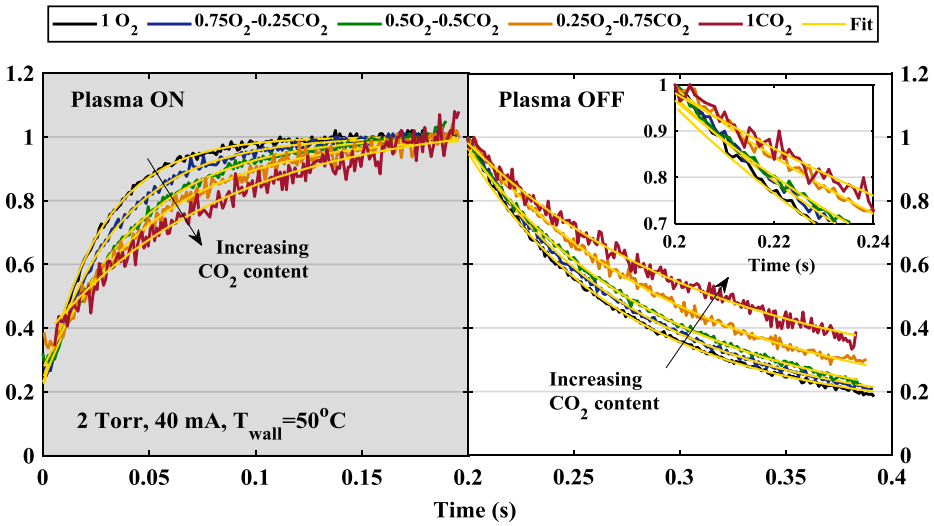

Figure 8.9: Time evolution of the O atom density normalized to the maximum along a plasma pulse of 196-196 ms On-Off measured with CRDS at 2 Torr, 40 mA (7.4 sccm, gas flow) for five gas mixtures ranging from 100%O_2 to 100%CO_2. The fitting of the data according to a single exponential is included.

gas temperature is equal to the wall temperature. This is in principle a reasonable approximation since the time required to reach the steady-state T_{gas} value is ∼4 ms (see section 3.2.2), much shorter than the time scales discussed here. Future calculations will take the gas temperature time evolution into account to better correct the early post-discharge. Figure 8.9 shows the same data, either normalized to the values at the end of the pulse for the ON phase, or to the peak in the early post-discharge for the OFF phase. The deep in the early post discharge was not considered for the fitting and is not included in the figure. Both figures, 8.8 and 8.9 bring some important observations:

- The O atom density increases with the O_2 content in the initial gas mixture, as expected.

- The O atom densities measured close to the end of the pulse are in very good agreement with the measurements obtained in partial-modulated discharge with actinometry for a similar On-Off cycle (see figure 8.5), confirming the agreement between CRDS and actinometry discussed in section 3.5.
- The evolution of the O atom density when the O_2 content is large is significantly faster during the plasma pulse than in the post-discharge.
- During the plasma pulse, the O atom density evolution is significantly faster for O_2 plasmas than for CO_2, showing a clear dependence with the initial CO_2 content.
- In general, the time evolution of the O atom density follows a single-exponential both in the ON and the OFF phases, as can be appreciated from the fits of the increase and decrease, included in the figure (in yellow).

The overall time evolution in the post-discharge is well described by a single exponential. Nevertheless, it is worth mentioning that in the early post- discharge (first milliseconds after switching off the plasma), the fit does not reproduce perfectly the data (see inner graph in figure 8.9), suggesting a non-single exponential decay in the very first milliseconds of the post discharge. The deviation from the single exponential fit seems to be larger for larger O_2 amounts in the initial gas mixture and it is in agreement with literature in pure O_2 discharges *Magne et al.* [1993]; *Cartry et al.* [2006]. However, the time resolution in the experiment does not allow for a more detailed analysis of this short time scale.

The derived loss probabilities in post-discharge and under plasma exposure are shown in figure 8.10 as a function of the CO_2 fraction in the initial gas mixture. Data measured with actinometry in partial modulated discharges at the same wall temperature (shown in figure 8.7) is also included,

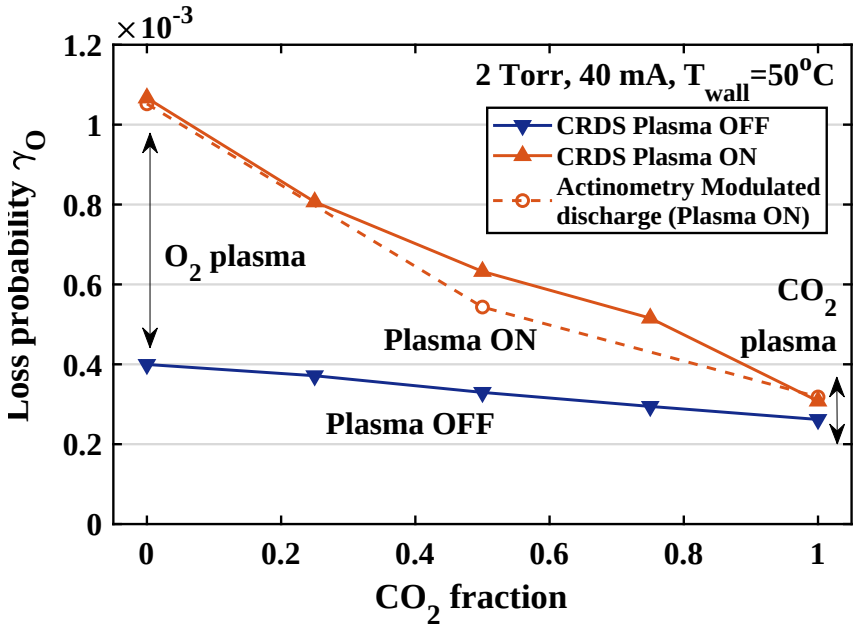

Figure 8.10: Variation of the loss probability, γ_O, as a function of the CO_2 fraction in the initial gas mixture, measured at 2 Torr, 40 mA T_{wall}=50^{o}C, in a pulsed plasma of 196-196 ms On-Off with CRDS (γ_O for ON and OFF phases are plotted separately) and measured with actinometry in a modulated discharge of 196-196 ms Up-Down for the same pressure, current and T_{wall}.

showing a very good agreement with the loss probabilities measured with CRDS during the pulse. The difference between the γ_O variation as a function of CO_2 content in post-discharge or under plasma exposure is highly remarkable. Although the loss probabilities in post-discharge are always lower than under plasma exposure, the difference in pure CO_2 is significantly smaller than in O_2 plasma.

The results support the hypothesis of surface passivation by gas phase compounds in CO_2-containing plasmas. The different behaviour in CO_2 or O_2 plasmas shows that the higher γ_O under plasma exposure than in the post-discharge is not caused by higher gas temperature, otherwise $\gamma_O^{ON} - \gamma_O^{OFF}$ should be larger in CO_2 plasmas. A possible reason given in the literature for the larger γ_O under plasma exposure in O_2 is the ion bombardment, modifying the surface state and/or inducing the desorption of adsorbed species *Cartry et al.* [1999]. Adsorption sites created in this way could then be filled with O atoms from the gas phase inducing a faster adsorption-recombination cycle. This mechanism could be prevented in CO_2 plasmas, for instance, by the presence of adsorbed species more strongly bond to the surface.

✓ γ_O increases with the O_2 content in the initial gas mixture in both ON and OFF phases of the pulsed discharge, but it increases more under plasma exposure.
✓ γ_O^{ON}-γ_O^{OFF} is remarkably larger in O_2 plasmas than in CO_2 plasmas.
✓ γ_O measured under plasma exposure by CRDS in pulsed discharge agrees very well with actinometry measurements in partially-modulated discharges.

8.5 Effect of the wall temperature on the O atom loss processes

The surface wall temperature, T_{wall}, was varied between -20 and 50^{o}C by changing the temperature of the thermostat controlling the circulation of a mixture of water+ethanol in between the double wall of the glow discharge reactor. T_{wall} variation experiments were carried out in three gas mixtures, 100%CO_2, 50%CO_2-50%O_2 and 100%O_2. Additionally a few measurements were done immersing the glow discharge reactor in a bath of ethanol+carbo-ice, whose temperature was approximately -50^{o}C. Figure 8.11 plots the loss frequencies for CO_2 plasma (panel (a)) and O_2 plasma (panel (b)), and figure 8.12 the O atom fractions in similar conditions. Similarly to previous sections, the pressure axis is plotted in logarithmic scale for readability of the graph.

Both gases show a very similar evolution of the O atom loss frequency as a function of T_{wall}, although the loss frequencies are systematically higher in O_2 plasmas compared to CO_2. So far, for measurements at T_{wall}=25 or 50^{o}C, we have observed two pressure regimes: below $^O/_{N_{max}}$, at either 0.75 or 1.5 Torr, $^O/_N$ shows a fast increase with pressure, whereas ν_{loss}^O drops; above $^O/_{N_{max}}$, the atom fraction decreases moderately and ν_{loss}^O increases as a function of pressure. Surprisingly ν_{loss}^O varies with T_{wall} in opposite direction depending on the pressure regime: For low pressures ν_{loss}^O increases with T_{wall}, whereas it strongly decreases with T_{wall} for high pressures. At the lowest wall temperature studied, T_{wall}(ethanol+carbo-ice)$\sim$-50^{o}C, the two pressure regimes are not visible any more and a continuous increase of ν_{loss}^O as a function of pressure is observed. The variation of ν_{loss}^O as a function of T_{wall} is then discussed separately for the low and the high pressure regimes:

→ **Low pressure regime** ($P < P[(^O/_N)_{max}]$)

For high T_{wall} (25 or 50^{o}C) at low pressure, we have previously seen that ν_{loss}^{O} does not follow a clear dependence with the gas temperature (see figure 3.30) but it increases when the pressure is decreased. This behaviour suggests that below $P[(^O/_N)_{max}]$ we could have plasma enhanced surface recombination processes by ion bombardment. Below 1 Torr, the collisionality of the sheath is reduced causing an increase of the mean energy of the ions reaching the wall, with decreasing pressure. Therefore, ion bombardment can either create more chemisorption sites where recombination can occur, or enhance the desorption of species and free adsorption sites, which then increase the recombination frequencies, as suggested in pure oxygen plasmas *Cartry et al.* [2006]; *Booth et al.* [2019].

When T_{wall} is decreased, two effects have to be considered: on the one hand the desorption of physisorbed species decreases; on the other hand the density near the wall increases due to the lower temperature near the wall. The surface could then be more covered and the sheath become more

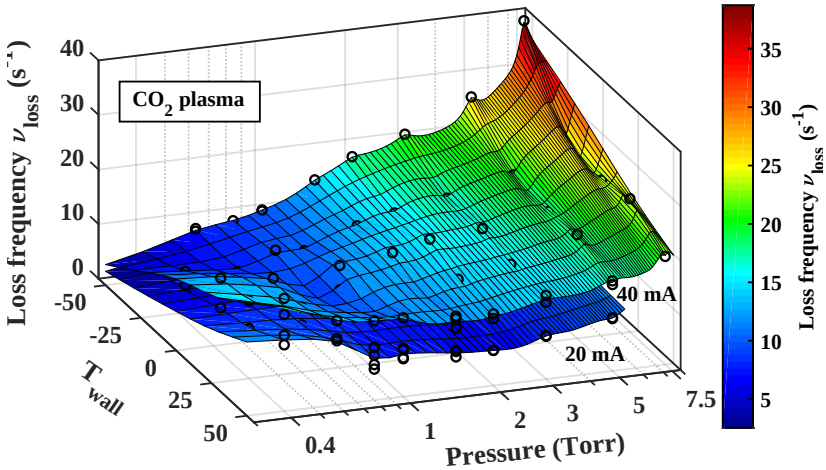

(a) CO_2 plasma

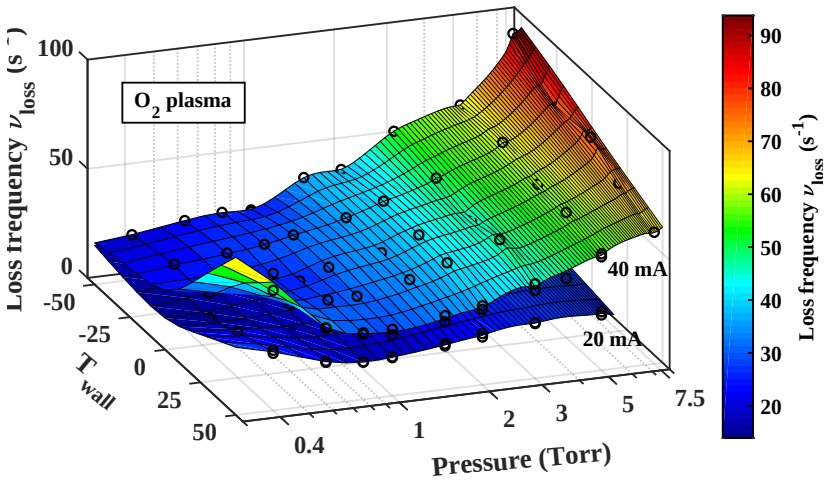

(b) O_2 plasma

Figure 8.11: Variation of the O atom loss frequency, ν_{loss}, as a function of pressure and T_{wall} for 20 mA (bottom layer) and 40 mA (top layer), in CO_2 plasma (panel (a)) and O_2 plasma (panel (b)) measured by actinometry (the data presented is the average of both emission lines studied, O777 and O845). The pressure axis is plotted in log scale for readability of the graph.

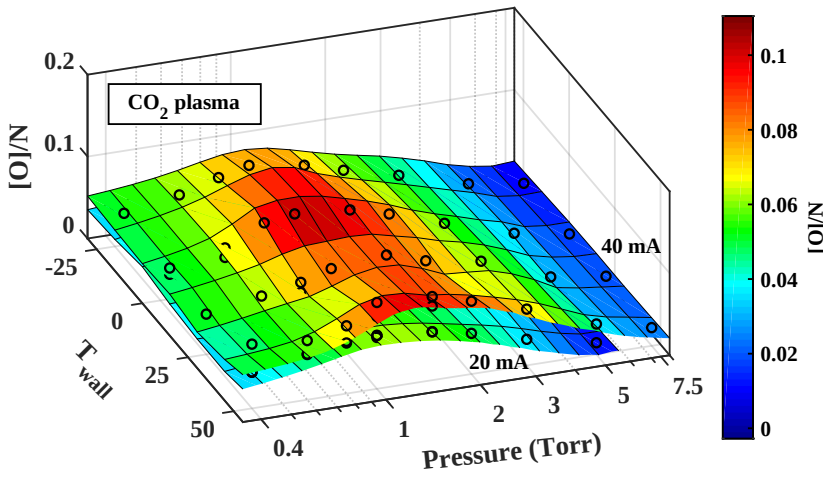

(a) CO_2 plasma

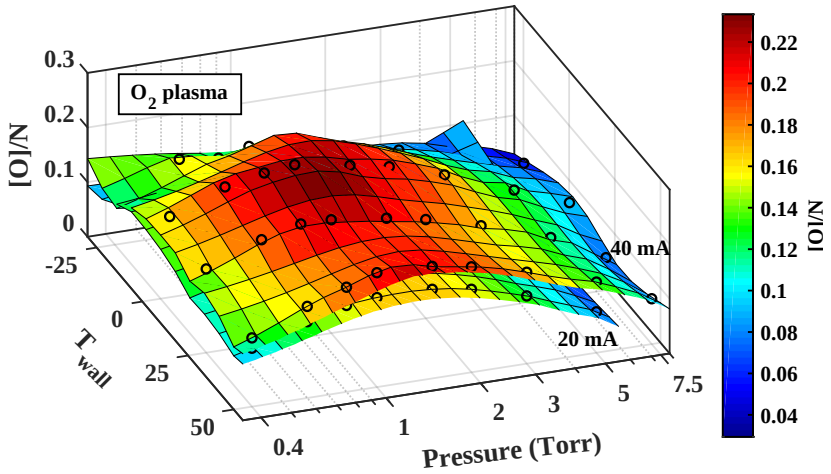

(b) O_2 plasma

Figure 8.12: Variation of the O atom fraction measured in CO_2 plasma (panel (a)) and O_2 plasma (panel (b)) as a function of pressure and T_{wall} for 20 mA (bottom layer) and 40 mA (top layer), measured by actinometry (the data presented is the average of both emission lines, O777 and O845). The pressure axis is plotted in log scale for readability of the graph.

collisional due to the higher gas density. The creation of new adsorption sites by ion bombardment would then be more difficult. Looking at ν_{loss}^{O} at 0.4 Torr, decreasing T_{wall} from 50^{o}C to -50^{o}C seems indeed to have a similar effect as increasing the pressure (when remaining in the low pressure regime below 1 Torr).

→ **High pressure regime ($P > P[(O/N)_{max}]$)**

At high pressure the sheath is collisional and the creation of adsorption sites by ion bombardment is less relevant. However, as the absolute O atom density increases, the ratio of adsorption-recombination sites versus the total number of O atoms available decreases. In this high pressure range the loss frequencies increase when T_{wall} is decreased, and the variation as a function of pressure becomes steeper. Several mechanisms could contribute to this behaviour. When T_{wall} is decreased the density of physisorbed species increases. Therefore, we could expect an increase of the contribution of Langmuir-Hishelwood recombination mechanism, as predicted by *Macko et al.* [2004]. In

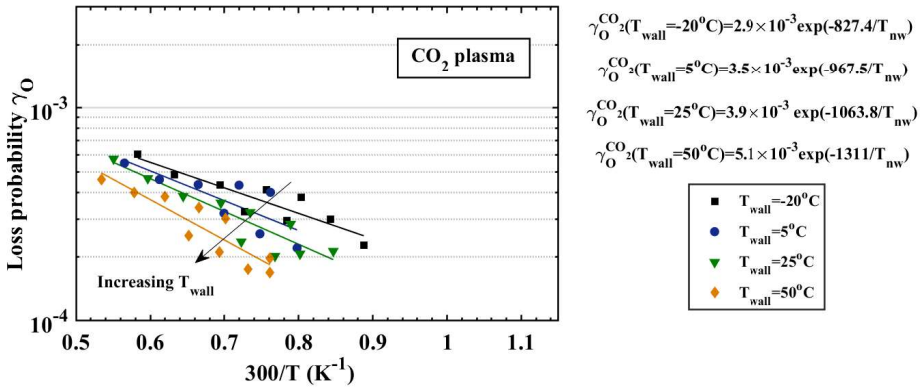

(a) CO_2 plasma

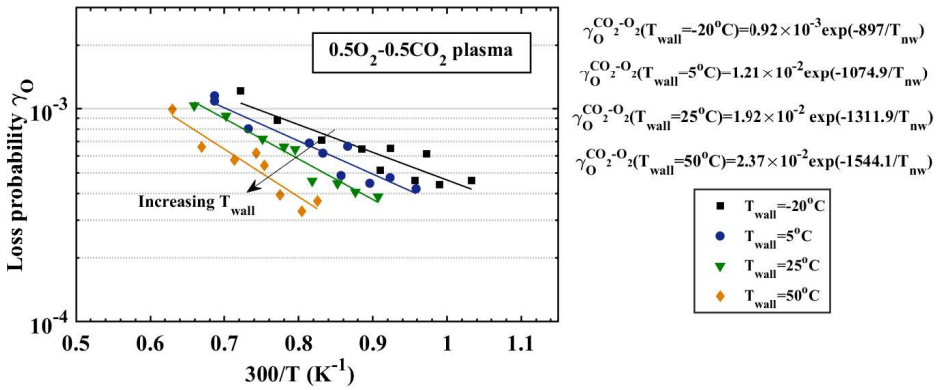

(b) $0.5CO_2$-$0.5O_2$ plasma

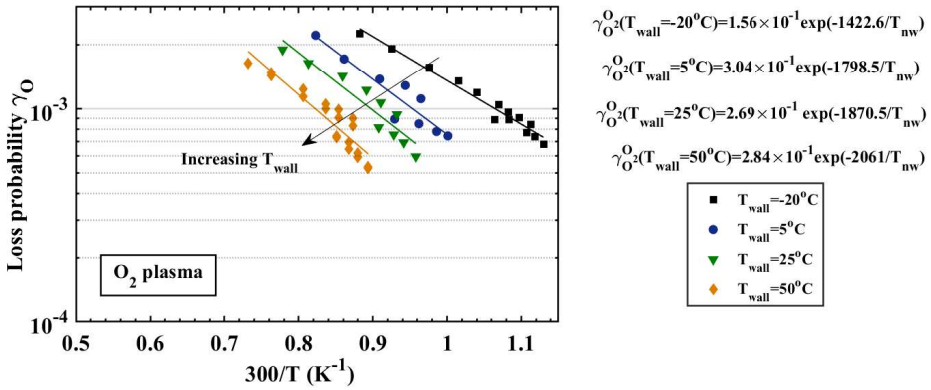

(c) O_2 plasma

Figure 8.13: Loss probabilities γ_O plotted as a function of $^{300}/_{T}$ (being T=T_{nw}) obtained for three gas mixtures ranging from 100%CO_2 plasma to 100%O_2 for T_{wall}=-20, 5, 25 and 50^{o}C.

this case, the thermal flux of O atoms to the wall, defined as:

$$\phi_O = \frac{\upsilon_{th} \cdot [O]}{4} \tag{8.8}$$

becomes an important parameter. When decreasing T_{wall} the thermal velocity decreases, but the atomic density increases more due to the decrease of T_{nw}, partly explaining the evolution of the variation as a function of pressure. The data at low T_{wall} and high pressure could still be well

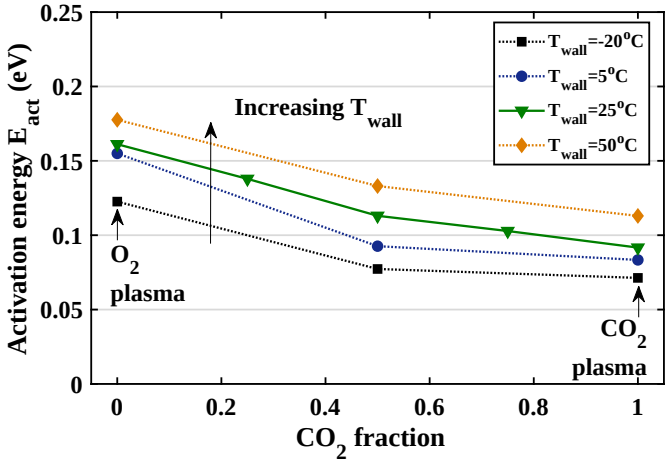

Figure 8.14: Activation energies derived from the fitting of the loss probabilities represented in figures 8.7 (b) and 8.13, according to an Arrhenius fitting given by equation (8.7).

fitted with a single exponential, whereas a hyperbolic decay would be expected in a second order recombination process. Note here that a L-H mechanism in the limit case of a short diffusion radius on the surface (because of fast desorption or high surface coverage) and would probably not differ strongly from a first order decay. Another possible contribution could come from an increased Eley-Rideal recombination with physisorbed species.

The derived loss probabilities for data between T_{wall}=-20-50^{o}C are presented in figure 8.13. Figure 8.14 summarizes the activation energies obtained form the Arrhenius fitting for gas mixture variation and T_{wall} variation experiments. For all the wall temperatures studied, we see a clear effect of the gas mixture, consistent with the pulsed plasma experiments. There seems to be also an effect of the wall temperature in the activation energy. However this effect is small and in the limit of accuracy of the fit (for instance at 20 mA, data always tend to fall bellow the fitted curve which increases the "slope"). In addition, for high T_{wall} we expect a dominant E-R recombination mechanism on chemisorbed atoms which imply a well defined activation energy. However for lower T_{wall}, significant contributions from other mechanisms involving physisorbed atoms could deviate from the single exponential fit. No change in the activation energy comparing T_{wall}= 5 and 50^{o}C was found in O_2 plasma by *Booth et al.* [2019].

In any case, as shown on figure 8.14, the activation energy is decreasing when the CO_2 content is increased for all wall temperatures. This effect could in principle be a consequence of different surface reactions responsible for O atoms losses with carbonated species. It is however surprising to observe a decay of both E_{act} and γ_O together with increasing CO_2 content. Several hypothesis could explain it. First of all a possible surface reaction of O atoms with C, CO or CO_2 would lead to the loss of only one O atom instead of two with the recombination into O_2. It is also possible that adsorbed carbonated species occupy recombination sites of O atoms therefore reducing γ_O. The lowering of E_{act} would then be the result either of different O atoms adsorption energy because of neighbouring adsorbed species, or a higher temperature at the surface because of higher energy flux (heat flux or excited species) towards the wall in CO_2 plasmas. The adsorption of carbonated species on SiO_2 surface and their possible reactivity needs to be considered. A larger surface of SiO_2 could then enhance these effects, which will be checked in the following section.

✓ For high pressures (P>$P[(O/N)_{max}]$), ν_{loss}^{O} decreases with T_{wall} while for low pressures ν_{loss}^{O} increases with T_{wall}.
✓ The loss probabilities, γ_O and activation energies, E_{act}, decrease with T_{wall} for all CO_2-O_2 mixtures.
✓ E_{act} decreases with the CO_2 content for all T_{wall} values, suggesting an influence of adsorbed carbonated species (C, CO, CO_2) and/or higher surface temperature in CO_2 plasma.

8.6 Wall reactivity with large SiO_2 effective surfaces

In chapter 5 we introduced a surface configuration based on a layer of silica (SiO_2) fibers rolled around the inner reactor wall. The objective was to increase the surface-to-volume ratio and maximize the effect of the surface on the plasma dynamics. The density of oxygen atoms in the gas phase was drastically reduced in the presence of the fibers (see section 5.3.3) due to the enhanced O atom surface recombination caused by the higher adsorption capability of the fibers (higher density of recombination sites). In spite of the removal of O atoms with the fibers, no effect was found on the dissociation fraction α in pure CO_2 (see figure 5.5). In the previous section we have seen that the adsorption of carbonated species on SiO_2 surface could maybe be responsible for the change of γ_O in CO_2/O_2 mixture. Therefore we present here complementary measurements of dissociation fraction α obtained with and without silica fibers for different CO_2/O_2 ratio. Measurements performed both downstream and *in situ* with infra-red absorption are discussed in this section.

Figure 8.15 presents the dissociation fractions obtained for three pressures (1, 2 and 5 Torr) and two discharge currents, 20 and 40 mA, measured *in situ* and downstream the discharge (using the L-shaped reactor discussed in section 3.4.4). Five different gas mixtures were studied, from 100%CO_2 to 10%CO_2-90%O_2, taken with the bare tube and with the silica fibers attached to the walls of the plasma reactor. Gas mixtures with lower CO_2 content were not possible because of the low IR absorption signal. The graphs are organized by pressure (1 Torr: panel (a.x), 2 Torr: panel (b.x) and 5 Torr: panel (c.x)), by type of experiment: downstream (panel (x.1)) or *in situ versus* downstream (panels (x.2) and (x.3)), and by current (20 mA: panel (x.2) and 40 mA: panel(x.3)). Note that all the data in this figure was taken at 7.4 sccm, *i.e* τ_{res} ≈0.15-1.6 s. Several observations can be extracted from these graphs:

- For pure CO_2 the dissociation fraction with and without fibers is the same within experimental errors, which is consistent with previous data.
- An increase of the initial O_2 content decreases α for all pressures and currents studied, both *in situ* and downstream.
- The decay of α with O_2 content is more pronounced at higher pressure.
- The difference in α between 40 and 20 mA decreases with increasing O_2 content. The difference between 20 and 40 mA is especially smaller at 5 Torr both downstream and *in situ*, with and without the fibers. As example in pure CO_2, α(40 mA)-α(20 mA)∼0.11 for every pressure. However, with an initial gas mixture of 0.1CO_2-0.9CO_2, at 1 Torr the difference is ∼0.057 and at 5 Torr the difference is negligible.

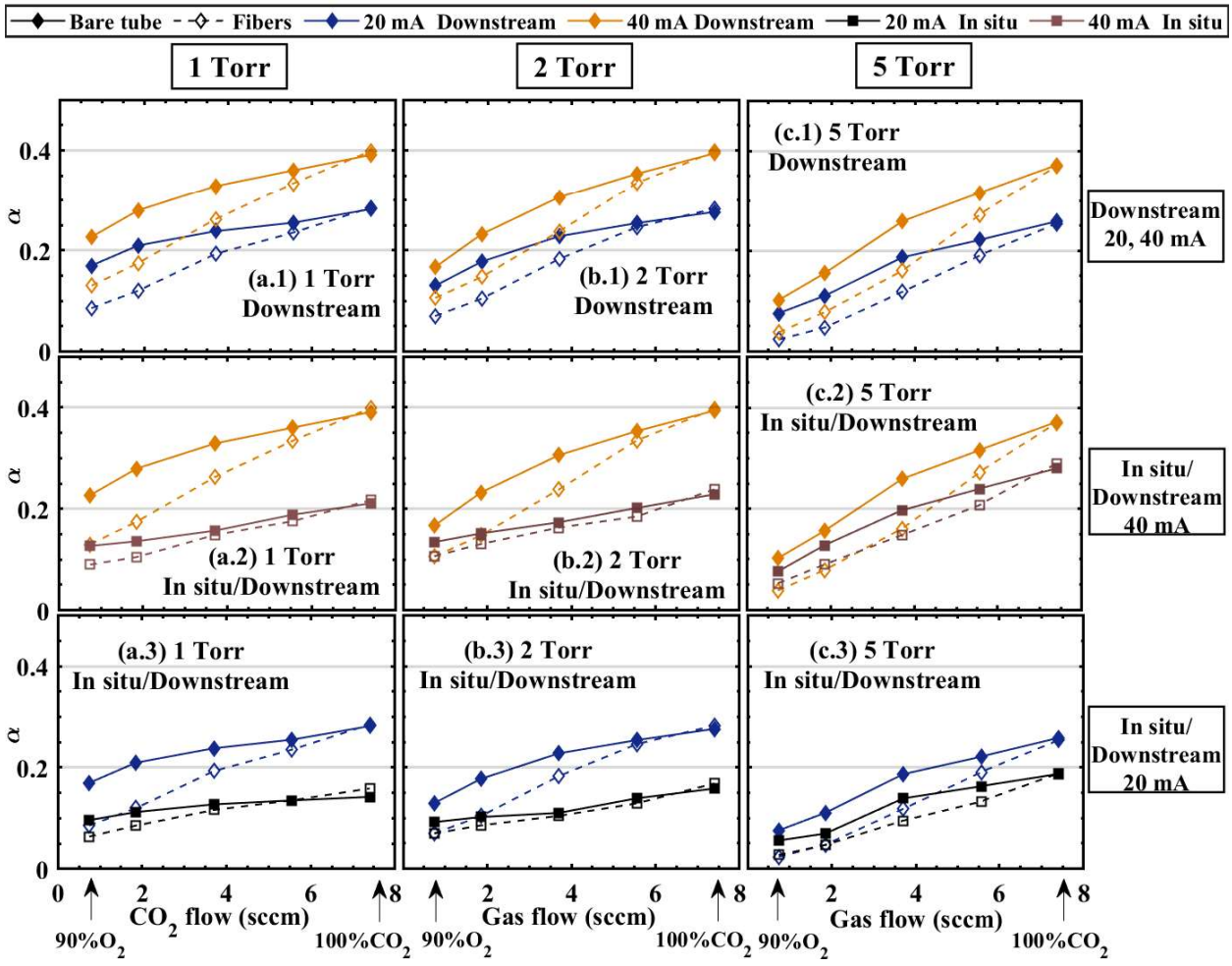

Figure 8.15: Variation of the conversion factor α with the CO_2 content in CO_2-O_2 gas mixtures for a constant total gas flow of 7.4 sccm for three pressures 1 (panels (a.x)), 2 (panels (b.x)) and 5 (panels (c.x)) Torr. Upper panels (x.1) plot downstream data for currents of 20 and 40 mA both with the bare tube and with fibers. Middle panels (x.2) compare downstream and *in situ* data for a current of 40 mA with the bare tube and with fibers, and lower panels (x.3) compare downstream and *in situ* data for a current of 20 mA, for the bare tube and with fibers.

- *In situ* data shows similar α with the bare tube and with fibers. α is only slightly lower with the fibers for large O_2 content. This small difference tends to increase with pressure.
- On the contrary, downstream data show a clear decay of α with the fibers when the O_2 content is increased.

→ Analysis of *in situ* data from figure 8.15

Let us first discuss the data measured *in situ*. With or without fibers, α decreases with the O_2 content in all conditions. The fibers reduce only slightly α *in situ* when the O_2 content is increased, which is more visible at high pressure. The decay of α with increasing O_2 has been already observed in the building-up experiments (see section 6.3.2). The reason could be evidently an increase of "back reaction" in the gas phase. It is not very probable that the mechanism involves oxygen atoms, as already discussed, but could be more efficient with O_2 molecules reacting with electronically excited CO. It is therefore expected that the removal of O atoms due to the fibers is not directly affecting

α. The increase of O_2 because of the faster recombination of O atoms on fibers would only slightly change the background of O_2 molecules available for back reaction mechanism with $CO(a^3\Pi_r)$ for instance, compared to the effect of increasing the O_2 content in the initial gas mixture.

The small decrease of α with fibers for high O_2 content could, on the other hand, correspond to a small contribution from surface recombination involving CO to produce CO_2. This effect would be enhanced at higher pressure mostly because of the higher temperature. In any case, these results together with previous data suggest that the probability of "back reactions" on the surface, such as $O + CO_{ads} \rightarrow CO_2$ or $CO + O_{ads} \rightarrow CO_2$, must be significantly lower than the recombination between O atoms, otherwise the fibers should significantly decrease the dissociation fraction measured *in situ*. The passivation of the surface lowering γ_O in previous section can still be due to adsorption of carbonated species, in particular CO, but with only a weak reactivity towards O. The possibility of CO adsorption on the fibers was already suggested in section 5.6.2, when discussing the time resolved evolution of the dissociation fraction in a pulsed glow discharge. In order to study more in detail this possibility and its contribution to surface back reaction with CO, which could happen with a slower characteristic time, two additional tests were performed:

1. α_{input} variation: With the glow discharge in flowing conditions (ϕ=7.4 sccm corresponding roughly to τ_{res} ~0.6 s at 2 Torr, 40 mA), we vary the initial CO_2-CO-O_2 mixture, keeping constant the proportion between C and O atoms as if all molecules were produced from pure CO_2 dissociation (*i.e.* O_2=1/2CO).

2. Building-up experiment with fibers: In the RF discharge, we took three measurements, a usual building-up with the bare tube, a building-up experiment with fibers, both starting from pure CO_2, and a building-up starting from the steady-state gas mixture measured with the bare tube at the same power and pressure.

Both tests are in fact checking how the fibers influence the steady-state composition, at which the production and loss processes of CO should be exactly balanced. The output of both tests is shown in figures 8.16 and 8.17 respectively. In figure 8.16, the 1:1 black line gives the α value corresponding to the gas composition imposed at the entrance of the reactor (α_{input}) and verified by measuring it with plasma OFF (fitted with the thermal equilibrium script). When the plasma is switched ON, if α_{input} was lower than the steady-state dissociation fraction, the measured α increases. On the contrary, when α_{input} is higher than the equilibrium dissociation fraction, α decreases because of the oxidation of CO. There is one α_{input} value for which no change is observed, which corresponds exactly to the steady-state composition. The steady-state value measured in the bare tube is α ~0.6, in good agreement with the steady-state value measured in building-up experiments in the glow discharge, shown in figure 6.20. This value is different from the "usual" value shown for instance in figure 8.15, because of the dependence on the residence time (see section 3.4.4), which is roughly τ_{res}=0.6 s at 2 Torr, 40 mA. In this experiment, we are "forcing" the dissociation to reach the steady-state, as if τ_{res} was ~5 s. The dotted line in figure 8.16 represents the data obtained with the fibers. The steady-state value is shifted towards lower α. These data suggest that for a similar α_{input} with the bare tube and the fibers, CO is more oxidized with the fibers.

Figure 8.17 gives the results of the second test. Starting from pure CO_2, the fibers are lowering α from approximately T^{ON} ~2 s compared to the bare tube. Thus the fibers are not modifying

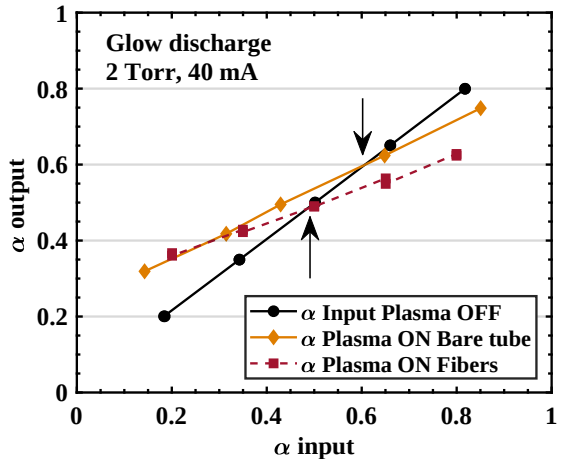

Figure 8.16: Variation of α measured *in situ* as a function of the input α in the initial gas mixture, for plasma OFF (only gas flow), and for 2 Torr, 40 mA (7.4 sccm, gas flow) with the bare tube and with fibers.

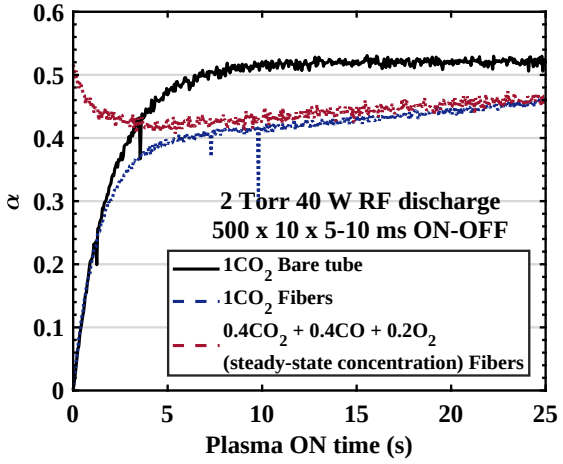

Figure 8.17: Time evolution α measured in a building-up experiment (in static conditions at 2 Torr, 40 W) starting for pure CO_2 with and without fibers and starting from the steady-state concentration with fibers.

the initial slope (confirming that the electron energy is not strongly influenced by the fibers), but when the CO is already produced in quantity large enough, the fibers seem to have a detrimental effect on α. Contrary to the bare tube case, which reaches a steady-state value at T^{ON} ~10 s with α(plateau)$\gtrsim$0.5, with the fibers α keeps rising slowly during all the measurement. When starting from a gas mixture corresponding to the steady-state composition measured with the bare tube, but placing the fibers on the walls, α shows an initial fast decrease. After T^{ON} ~7 s, α is almost the same as the value obtained starting from pure CO_2 and it slowly increases with the same slope as in the pure CO_2 experiment. The fast initial decrease is not believed to be related with CO oxidation, because the measurement shows a tendency to re-gain the initial level over time. It seems likely that CO is first quickly adsorbed when the measurement starts. The depletion of CO could be an enhanced adsorption of CO under plasma exposure. The slow rise observed for T^{ON} >7s could then be the result either of a saturation of the CO adsorption sites, consistent with the hypothesis that CO passivates SiO_2 surface but almost does not react.

These two tests confirm the adsorption of CO on SiO_2 materials and suggest the possibility of surface "back reaction", but on longer time scales than the usual τ_{res} corresponding to our reference conditions at 7.4 sccm. These results also confirm that the probability of recombination of CO with O at the wall is lower than the recombination of O with O into O_2. Indeed the fibers reduce the concentration down to 5% of the O atom density measured in the bare tube (see figure 5.6), whereas the reduction of the CO density, even in static conditions is significantly lower.

→ Analysis of downstream data from figure 8.15

Let us go back to figure 8.15 to analyse the downstream data. This figure shows a remarkable effect of the fibers on the ratio of α measured downstream *versus in situ* ($R_{d/i}$). This ratio has been discussed in detail in chapter 3. We concluded that the difference in α measured *in situ* and downstream is not due to a longitudinal gradient of dissociation fraction (see section 3.4.3). It is also not due to an artefact of the fitting script or due to de-excitation of electronically excited states, as shown in the building-up plasma On-Off experiments (see section 6.3.1). We also saw that $R_{d/i}$ tends

to 1 for long residence times (see figure 3.19). In section 3.4 we proposed the possibility of chemical reactions occurring only in the early post-discharge. However, in the building-up On-Off experiment no increase of α was observed during the post-discharge. Therefore, the mechanism responsible for the increase of α should take place *ex situ*, *i.e.* in the temporal and spatial post-discharge, which is surprising.

Figure 8.15 gives a few more insights on the causes for having $R_{d/i} > 1$. The fibers are not changing the downstream α in pure CO_2, but contrary to the *in situ* measurements, the fibers reduce α measured downstream when the O_2 content increases (see curves yellow on panel x.2 and blue on panel x.3). For the highest O_2 content (90% O_2 - 10% CO_2) there is almost no difference any more for all pressures and $R_{d/i} \sim 1$. The difference between α downstream with and without fibers increases with O_2 content. It seems therefore that an oxygen specie removed by the fibers is involved in the increase of α in the early post-discharge. The fact that $R_{d/i}(> 1)$ is higher for low pressure suggests that the O atoms, that are removed by the fibers, could be involved. However, other relatively long-lived excited species such as $O_2(a^1\Delta_g)$, or other electronically excited species, could also play a role and be quenched by the fibers. In pure CO_2 the fibers do not prevent this effect and $R_{d/i}$ can be almost ∼2 at 1 Torr. A reasonable explanation would be that carbonated coating is formed in the spatial post-discharge (which would happen more for higher CO_2 content) and get oxidized by atomic oxygen (or $O_2(a^1\Delta_g)$) at the exit of the plasma volume. However, no carbon deposit was seen by eye. Moreover, the whole L-shaped reactor was cleaned with long continuous O_2 plasma before any measurement, and no change in the ratio downstream *vs. in situ* was observed in subsequent measurements, which seems in contradiction with the formation of a carbon coating in the close vicinity of the plasma volume. The mechanisms responsible for the change of α downstream remain therefore unclear. Spatially resolved measurements in the spatial post-discharge in flowing conditions are suggested to bring physical insight into these phenomena.

✓ The possibility of CO adsorption on SiO_2 materials under plasma exposure is demonstrated.
✓ Slow "back reaction" mechanims in the surface are evidenced, although their probability is lower compared to the recombination into O_2.

8.7 Investigation of surface processes by isotope implantation

In order to investigate the possible implantation of atoms or molecules in the surface we have performed building-up experiments such as those described in chapters 6 and 7 with $^{18}O_2$ or $^{13}CO_2$ isotopes. The general experimental details are briefly reminded in the experimental box 8.3. The measurement procedure is similar, except the pre-treatment step. Previously, the pre-treatment process was consisting in 15 minutes of continuous O_2 plasma (1.5 Torr, 40W), followed by 10 minutes of CO_2 gas flow. For the surface isotope experiments, the reactor is filled with pure isotopic gas, either $^{18}O_2$ or $^{13}CO_2$ and a continuous RF plasma at 1.5 Torr 40 W is ran for 15 minutes. Labelled atoms can then be grafted onto the reactor walls. After this first treatment, the reactor is emptied and filled again, repeating the process four times, i.e. we run 4x15 minutes of $^{18}O_2$ or $^{13}CO_2$ plasma in static conditions. Subsequently, the reactor is emptied and filled with

non-isotopic CO_2 and a building-up measurement is started. For initial tests, we did measurements with the reference pulse configuration, N_{tr}=500 × N_p=10 × t_p^{ON}=5 - t_p^{OFF}=10 ms On-Off, and a total plasma ON time, T^{ON}=25 s. However, the amount of isotopes extracted from the surface was relatively low. In order to visualize the extraction of the isotopically-labelled species, longer plasma pulses, N_p=300 × t_p^{ON}=2.08 t_p^{OFF}= 2.08 s On-Off, were studied and are presented in this section.

Diagnostics: FTIR	**Reactor**: SW Short tube	**Pressure**: 2 Torr
Discharge: RF Pulsed plasma	$\boldsymbol{T_{wall}}$: not controlled	**Current**: 40 W
300×2.08-2.08 s On-Off		**Flow**: 0 (static)

Experimental box 8.3: Measurements of isotope implantation in the surface.

8.7.1 Oxygen atoms *versus* carbon compounds

Figure 8.18 shows the absolute densities of all the CO and CO_2 isotopologues during the plasma of pure $^{12}C^{16}O_2$ ran after pre-treating the surface with 4x15 minutes of isotopically labelled molecules. Several isotopologues necessarily coming from the surface are showing a clear evolution (not at the noise levels) for the two pre-treatment cases: $^{18}O_2$ plasma (panel (a)) and $^{13}C^{16}O_2$ (panel (b)). The objective is to compare the possible implantation of ^{18}O atoms with the implantation of ^{13}C atoms or ^{13}CO molecules. Both experiments show significant differences and some similarities:

- As expected both experiments show first a fast decrease of the main CO_2 isotopologue, $^{12}C^{16}O_2$, and the increase of $^{12}C^{16}O$ on similar time scales as for usual building-up experiments. For long T^{ON} however, CO tends to slowly decrease while CO_2 tends to re-increase. The decrease of CO and increase of CO_2 are faster for the pretreatment with $^{13}C^{16}O_2$.

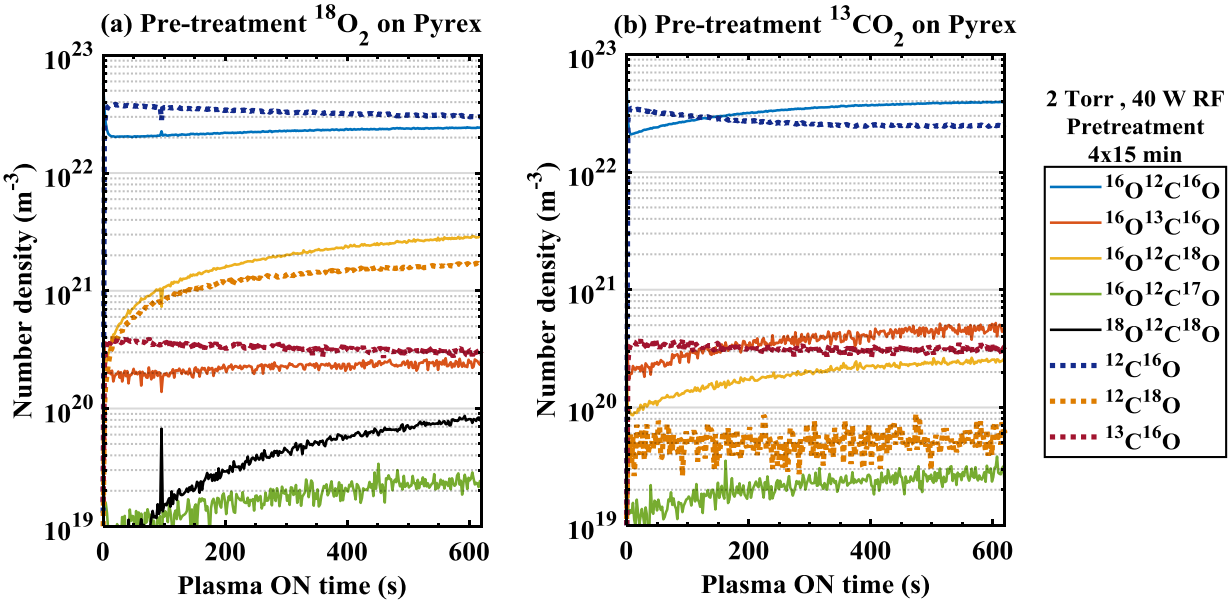

Figure 8.18: Building-up experiment at 2 Torr, 40 W (N_p=300 × t_p^{ON}=2.08 t_p^{OFF}= 2.08 s On-Off) after pre-treatment for isotope implantation of ^{18}O (panel (a)) and ^{13}C (panel (b)) in the bare Pyrex discharge tube.

- In panel (a) we see a continuous growth of isotopologues containing ^{18}O: ^{16}OC^{18}O, C^{18}O and ^{18}OC^{18}O. ^{13}C-containing isotopologues reproduce the time evolution of the equivalent ^{12}C-containing isotopologues.

- In panel (b), no special growth of ^{18}O isotopologues is observed they follow the same evolution as similar non-labelled species and their density is significantly lower than in panel (a). ^{13}C-containing isotopologues also reproduce the time evolution of the equivalent ^{12}C-containing isotopologues. Their densities are in the same range as in the $^{18}O_2$-pretreatments experiment, No effect of the $^{13}C^{16}O_2$ pre-treatment is noticeable in this case.

Figure 8.18 (a) therefore shows the slow extraction of chemisorbed ^{18}O and proves that O atoms are indeed implanted in the surface and remain strongly bonded. The lack of significant amounts of extracted ^{13}C suggests that C atoms or CO and CO_2 molecules are not implanted in the surface and that their contribution to surface processes as active reactants or passivating the surface could be only through weakly bonded (physisorbed) species. Both experiments shown in figure 8.18 were done after a pre-treatment at a RF power of 40 W. A similar experiment was done after a $^{13}C^{16}O_2$ pretreatment at 80 W of continuous plasma, but no extraction of ^{13}C-containing compounds was noticeable either.

The extraction of isotopically-labelled species is progressive, in agreement with the results from *Donnelly et al.* [2011]; *Guerra et al.* [2014], which suggest that the adsorbed species are not either physisorbed or chemisorbed but that there is a continuum of bond energies. The ^{18}O extraction rate is roughly 4.8×10^{12} atoms·cm^{-2}s^{-1} comparable to the rate measured in similar conditions in N_2-O_2 mixtures *Marinov* [2012], which was 1.2×10^{13} atoms·cm^{-2}s^{-1}. This extraction rate is insufficient to explain the measured γ_O, however it accounts only for isotopes incorporated to C-containing gas phase compounds. The extraction of isotopic oxygen by reactions such as $^{16}O + {}^{18}O_{ads} \rightarrow {}^{16}O^{18}O$ cannot be detected by infra-red absorption. The detected ^{18}O comes either from surface reactions such as $C^{16}O + {}^{18}O_{ads} \rightarrow {}^{16}OC^{18}O$ or from gas phase reaction between ^{18}O, $^{18}O_2$ or ^{16}O^{18}O with CO or CO_2.

8.7.2 Effect of the large effective surfaces on isotopic exchange

Similar $^{18}O_2$ pre-treatment experiments were done with the fibers and are compared with the experiment in the bare tube in figure 8.19. The overall temporal evolution of the different isotopologues is qualitatively similar. Nevertheless, two important points can be noticed: the faster time evolution and the larger amount of isotopically-labelled species produced, due to the larger surface available for implantation. There is also a clear difference in the trend shown by $C^{16}O_2$. Whereas C^{16}O, is similar in both surface configurations, $C^{16}O_2$ drops more with the fibers and does not re-increase. This evolution is partly compensated by the large increase of isotopically marked species. In particular C^{18}O continues to increase when ^{16}OC^{18}O seem already stabilized.

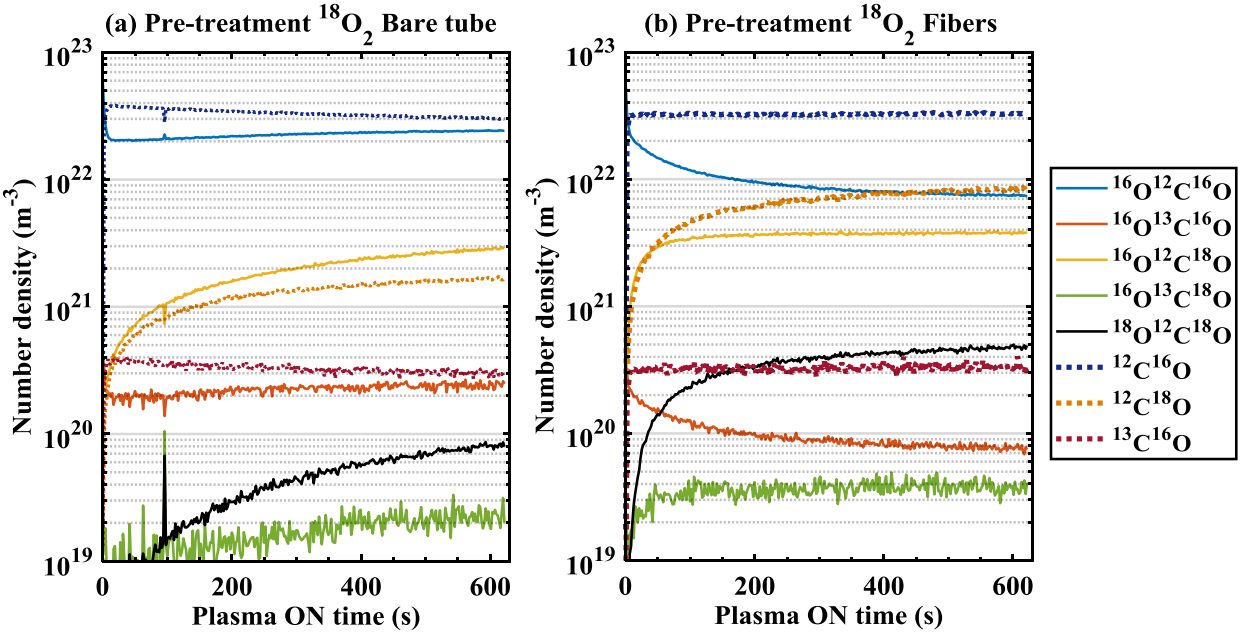

Figure 8.19: Building-up experiment at 2 Torr, 40 W (N_p=300 × t_p^{ON}=2.08 t_p^{OFF}= 2.08 s On-Off) after pre-treatment for isotope implantation of ^{18}O in the bare Pyrex discharge tube (panel (a)) and in the discharge tube with the walls covered by SiO_2 fibers (panel (b)).

✓ Isotopic exchange experiments show that C atoms, CO or CO_2 molecules are not efficiently implanted in the surface.
✓ The ocupation of chemisorption sites by C-containing species does not seem to be the main cause of surface passivation.
✓ On the contrary, O atoms are implanted in the surface and can slowly be extracted during a building-up experiment.

8.8 Preliminary comparison with a surface model

A preliminary comparison of the experimental loss probabilities with the output of an surface model is discussed in this section. The model, partially adapted, was developed by V. Guerra and it is described in detail in *Guerra* [2007]. The model was benchmarked against a MonteCarlo surface model in *Marinov et al.* [2017b]. We first give a brief summary of the main characteristics of the model and subsequently show a first comparison of the model results with the experimental data obtained in O_2 and CO_2 plasmas. For this comparison we will use the data discussed in section 8.2.

8.8.1 Brief description of the model

A list of variables and reaction types included in the model as well as default values of relevant model parameters are given in table 8.1. The model is ready to account for reactions involving O atoms (all the reactions listed), O_2 (reactions R1, R2, R4F and R4S ($\rightarrow O_3$), R6F and R6S ($\rightarrow O_3$) and RH, chemisorption of O_2 is not considered) and CO (all the reaction listed, including chemisorption of CO). CO_2 or C carbon atoms are not considered for any surface reactions, except CO_2 as a product

of the recombination of CO+O. The possibility of reactions between O_2 and CO is not taken into account. Evidently, the number of parameters is significant, and there is not enough experimental information to constraint many of them, such as ozone densities, for instance. Therefore, as initial approach, only reactions involving exclusively oxygen atoms will be discussed, which are in any case expected to be the most relevant in our discharge conditions.

The surface is considered to be fully covered by physisorption sites, being [F]=1.5×10^{19} m^{-2}. Chemisorption sites density is estimated by the prevalence of -OH groups in silica to be $[S] = 3{\times}10^{13}$ cm^{-2} *Guerra* [2007]; *Guerra and Marinov* [2016]. The density of chemisorption sites is not used as parameter in the code, it is introduced through the parameter ϕ, the fraction of surface covered by chemisorption sites, defined as:

$$\phi = \frac{[S]}{[F] + [S]} \tag{8.9}$$

where [F] and [S] are the densities of physisorption and chemisorption sites, respectively. Desorption from chemisorption sites is not considered due to the strength of the bond which for temperatures below $\sim$ 2000K results in a low desorption rate *Kim and Boudart* [1991].

The rates for **physisorption (R1)**, **chemisorption (R3)** and the **Eley-Rideal recombinations (R4S) and (R4F)** are given by reaction rates of the type:

List of variables

Symbol	Description
F_V	Vacant physisorption site
S_V	Vacant chemisorption sites
A_F	Physisorbed species
A_S	Chemisorbed species
$[F]$	Density of physisorption sites
$[S]$	Density of chemisorption sites
R_i	Reaction type
r_i	Reaction rate
k_i^0	Steric factor
$k_i^{'}$	Sticking probability

Default model parameters

Parameter	Notation	Value
Density phys sites *	[F]	$1.5{\times}10^{19}$ m^{-2}
Fraction chem. sites **	ϕ	$2{\times}10^{-2}$
Desorption frequency	$\nu_{de\,O}$	$1{\times}\ 10^{15}$ s^{-1}
Desorption energy	$E_{de\,O}$	30 $^{kJ}/_{mol}$
Diffusion frequency	$\nu_{di\,O}$	$1{\times}\ 10^{13}$ s^{-1}
Diffusion energy	$E_{di\,O}$	15 $^{kJ}/_{mol}$
E-R phys. O atom (R4F)	E_{O+O_F}	0 $^{kJ}/_{mol}$
E-R chem. O atom (R4S)	E_{O+O_S}	17.5 $^{kJ}/_{mol}$
L-H phys.+phys. (R6F)	$E_{O_F+O_F}$	0 $^{kJ}/_{mol}$
L-H phys.+phys. (R6S)	$E_{O_F+O_F}$	17.5 $^{kJ}/_{mol}$

* Density of physisorption sites.
** Fraction of the surface covered by chemisorption sites.

List of reactions

Reaction type	Reaction	Description
R1	$A + F_V \xrightarrow{r_1} A_F$	Physisorption
R2	$A_F \xrightarrow{r_2} A + F_V$	Thermal desorption from physorption sites
R3	$A + S_V \xrightarrow{r_3} A_S$	Chemisorption
R4S	$A + A_S \xrightarrow{r_4 S} A_2 + S_V$	E-R recombination with a chemisorbed atom
R4F	$A + A_F \xrightarrow{r_4 F} A_2 + S_V$	E-R recombination with a physisorbed atom
R5	$A_F + S_V \xrightarrow{r_5} F_V + A_S$	Chemisorption via surface diffusion of physisorbed atoms
R6S	$A_F + A_S \xrightarrow{r_6 S} A_2 + F_V + S_V$	L-H recombination of a physis- and a chemisorbed atom
R6F	$A_F + A_F \xrightarrow{r_6 F} A_2 + F_V + F_V$	L-H recombination between two physisorped atoms
RH	$A_F + F_V \xrightarrow{r_H} F_V + A_F$	Change of physisorption site (hoping)

Table 8.1: Tables describing relevant variables, a list of the computed reactions and the default model parameters.

$$r_i = k_i^{'} \cdot \frac{\phi_O}{[F] + [S]} \tag{8.10}$$

Where $k_i^{'}$ are the sticking probabilities $k_i^{'}$ calculated with the expression:

$$k_i^{'} = k_i^0 \cdot \exp\left(\frac{-E_{act}}{k_B T}\right) \tag{8.11}$$

where k_i^0 are the corresponding steric factors. All the steric factors for the computed (enabled) reactions are considered equal to 1. E_{act} is the activation energy for the corresponding reaction. With regard to reactions R1 and R3, the activation energies are considered zero, therefore any gas phase O atom arriving from the surface at an empty physisorption or chemisorption site is adsorbed. Activation energies for recombination reactions with chemisorbed oxygen atoms range from E_r = 12.5kJmol^{-1} *Booth et al.* [2019], 14 kJmol^{-1}*Kim and Boudart* [1991], 15.8 kJmol^{-1} *Lopaev et al.* [2010a, b], 25.5 kJmol^{-1} *Guerra* [2007]. As default, we consider E_r = 17.5 kJmol^{-1} *Guerra and Marinov* [2016] for the E-R recombination with chemisorbed atomic oxygen, in line with the hypothesis that $E_{act} \approx E_{di}$, where E_{di} is the energy barrier for diffusion. For recombination with physisorbed O atoms either we consider E_{act}=0 or 2.5 kJmol^{-1}. The values used for the temperature T are discussed below. ϕ_O is the thermal flux of O atoms towards the wall defined as:

$$\phi_O = \frac{\upsilon_{th} \cdot [O]}{4} \tag{8.12}$$

where υ_{th} is the thermal velocity of the incoming O atoms ($= \sqrt{8k_B T_g/\pi M_O}$) and $[O]$ is the O atom density, also commented below.

The rate for **thermal desorption (R2)** rate is given by:

$$r_2 = \nu_{de} \exp\left(\frac{-E_{de}}{k_B T_w}\right) \tag{8.13}$$

Where ν_{de} is the frequency of the vibrations of physisorbed atoms in the direction perpendicular to the surface $\nu_{de} \approx 10^{14} - 10^{16}$s^{-1}. Our default value is $\nu_{de} = 10^{15}$s^{-1}. E_{de} is the activation energy for desorption. We consider E_d=30 kJmol^{-1}, similar to *Lopaev et al.* [2010a, b] and to *Gordiets and Ferreira* [1998] (33 kJmol^{-1}), although values as a high as 51 kJmol^{-1} can be found in the literature *Kim and Boudart* [1991]. $T_w = T_{wall}$.

The **rates of reactions after diffusion, including Langmuir-Hinshelwood recombination (RH, R5, R6S and R6F)** depend on the rate for the diffusion process:

$$\tau_{di}^{-1} = \nu_{di} \exp\left(-\frac{E_{di}}{kT_{wall}}\right) \tag{8.14}$$

Where τ_{di} is the the average time between diffusion events. ν_{di} is the characteristic diffusion frequency $\nu_{di} = 10^{13}$s^{-1} and E_{di}, the energy barrier for diffusion, is $\approx 0.5E_{de}$ *Kim and Boudart* [1991]. If the diffusion happens, the subsequent process depends on the occupancy of the site where the particle was diffused and the rate for that process, which is given by the corresponding sticking probability. Therefore the rates for reactions of the type R5, R6S and R6F are given by the expression *Marinov et al.* [2017b]:

$$r_i = k_i^{'} \cdot \tau_{di}^{-1} \tag{8.15}$$

The recombination probability is calculated as the sum of the recombination probabilities of all the individual reactions, given by:

$$\gamma_O = \gamma_O^{(E-R)_F(R4F)} + \gamma_O^{(E-R)_S(R4F)} + \gamma_O^{(L-H)_F(R6F)} + \gamma_O^{(L-H)_S(R6S)} = \\ = \frac{2[O_S](r_4^S + \theta_F \cdot r_6^S) + 2[O_F](r_4^F + \theta_F \cdot r_6^F)}{\phi_O} \quad (8.16)$$

where $[O]_F$ and $[O]_S$ are the physisorbed and chemisorbed O atom densities, and $\theta_F = {}^{[O]_F}/_{[F]}$ is the surface coverage of physisorbed O atoms. More details on the deduction of these expressions and the parameters involved are given in *Guerra* [2007]. The recombination probability is the main output of the code, along with the surface coverage, and it will be the parameter that will be compared to the experimental results.

Few modifications were implemented in the model. The most relevant one is the use of the temperature near the wall, $T = T_{nw}$ in the calculation of all the rates involving incoming oxygen atoms (R1,R3, R4F and R4S), in equation (8.11). The O atom densities used in the calculation of the flux of oxygen towards the surface are corrected accordingly:

$$O_{nw} = O \cdot \left(\frac{T_{gas}}{T_{nw}}\right) \quad (8.17)$$

In principle, all the reactions involving adsorbed species (R2, RH, R5, R6S and R6F) are calculated using $T = T_{wall}$. Nevertheless, as a purely exploratory test, we introduced a new parameter in the code T_{ws}, so-called "effective surface/wall temperature", which is defined as:

$$T_{ws} = T_{wall} + s \cdot (T_{nw} - T_{wall}) \quad (8.18)$$

where s is an adjustable parameter between 0 and 1, *i.e.* T_{ws} varies between T_{wall} and T_{nw}. The underlying idea is that kinetic energy and vibrational energy brought by colliding particles, or even the energy transmitted by electronically excited states is not instantaneously relaxed and may influence the surface reactions of the adsorbed species. A more accurate description would imply the use of accommodation coefficients. However, the purpose for now is to investigate the effect of a higher surface temperature in the calculated loss probabilities. This parameter will be used, as a test, in equation (8.14) and in the calculation of the sticking probabilities for reactions R5, R6S, R6F and RH, instead of the wall temperature, and it is only briefly discussed in the following section. As default, we keep the use of T_{wall}, unless explicitly specified in the text or in the figures.

In all the model tests we will use the experimental O atom densities and gas temperatures in O_2 plasmas (shared by J.-P. Booth and D. Lopaev, more details are given in the PhD thesis of A. Chatterjee and in *Booth et al.* [2019]) and our experimental values in CO_2 plasmas (see section 8.2), as input parameters for the code.

8.8.2 Model results and comparison with experiments

O_2 plasma

→Surface model results

Figure 8.20 plots the experimental loss probabilities calculated from data taken at T_{wall}=5 and

50^{o}C, for currents between 10 and 40 mA and pressures between 0.75 and 10 Torr. The data taken at T_{wall}=50^{o}C were already discussed in figure 8.2. The output of the model is also plotted, including the total O atom loss probabilities and the γ_O values for each individual recombination process obtained from the surface model with the default parameters (see table 8.1). We observe three different behaviours for the various reactions considered:

- E-R recombination with chemisorbed oxygen, $O+O_S$, follows a single "linear" (in logarithmic scale) dependence with T_{nw}. $\gamma_O^{O+O_S}$ decreases as a function of $^1/_{T_{nw}}$.
- L-H recombination with chemisorbed oxygen, O_F+O_S, shows no dependence on T_{nw}, and only depends on T_{wall}. $\gamma_O^{O_F+O_S}$ slightly decreases as a function of $^1/_{T_{nw}}$.
- Both reactions involving only gas phase O atoms and/or physisorbed O atoms, $O+O_F$ and O_F+O_F, show similar variation as a function of $^1/_{T_{nw}}$ similar to a "knee" shape. $\gamma_O^{O+O_F}$ and $\gamma_O^{O_F+O_F}$ decrease as a function of $^1/_{T_{nw}}$, but significantly increase when T_{wall} is decreased.

The default model parameters are not far from reproducing the experimental results, although the model results at T_{wall}=50^{o}C are slightly underestimated. A better match can be obtained simply by decreasing the activation energy for the reaction $O+O_S$, which is the dominant recombination reaction at T_{wall}=50^o C, to a value of 13 kJmol^{-1}. The results of these tests are shown in figure 8.21. Panel (a) shows the model results with the default parameters for comparison, panels (b) and (c) plot the "best match" conditions. The contribution of the E-R recombination with a chemisorbed oxygen is increased, closely following the experimental data at T_{wall}=50^{o}C. The difference between panel (b) and panel (c) is given by the consideration of a small energy barrier for the L-H recombination between physisorbed O atoms, as suggested in *Guerra and Marinov* [2016]. The energy barrier decreases the contribution of this reaction, and the model results follow more closely

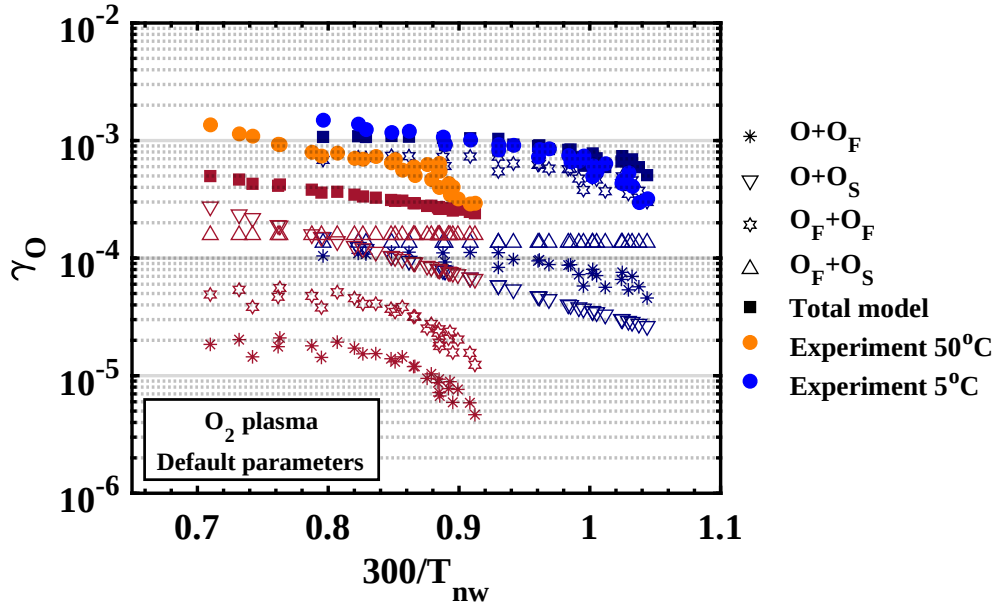

Figure 8.20: Recombination probabilities obtained from the experiments in *Booth et al.* [2019] compared to the model with the default parameters for T_{wall} 50 and 5^o C, detailing the contribution of the different reactions at the surface.

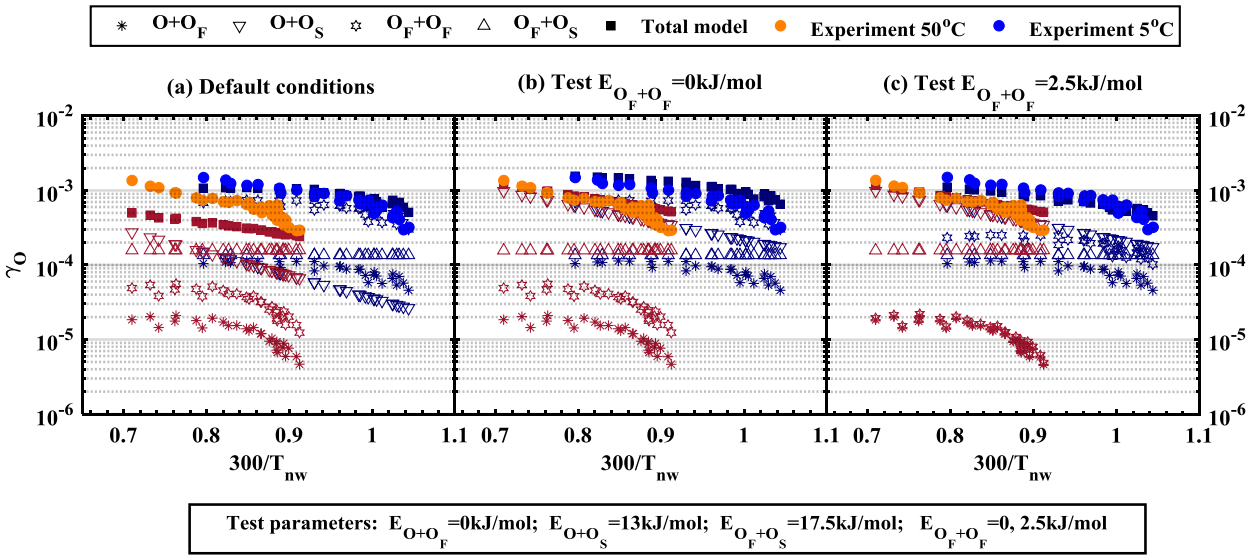

Figure 8.21: Recombination probabilities in O_2 plasma compared to the model results. Panel (a) shows the model results with the default parameters for reference, panels (b) and (c) plot the "best match" conditions obtained with close parameters detailed in the text box at the bottom. Panel (b) and panel (c) show the effect of a low energy barrier for the L-H recombination between physisorbed O atoms.

the experimental data. Without any energy barrier the L-H recombination between physisorbed O atoms is the dominant surface reaction at T_{wall}=5^{o}C. Including the E_{act}=2.5 kJmol^{-1} barrier, the contribution from this reaction and from E-R with chemisorbed oxygen is comparable for the lowest pressures (higher $^{300}/_{T_{nw}}$ values) and E-R still dominates for higher pressures. According to *Macko et al.* [2004], in our range of surface temperatures, we should always be dominated by E-R mechanisms. E-R and L-H become comparable only at surface temperatures close to 225-250 K. However, L-H contribution at surface temperatures up to 500 K has already been claimed in the literature *Guerra et al.* [2019]; *Gordiets and Ferreira* [1998]. In our calculations we observe a significant contribution of L-H mechanism at slightly higher surface temperatures. The differences can be partly explain by the effect of the temperature near the wall, not taken into account in *Macko et al.* [2004].

Looking more closely to the "best match" results in figure 8.21 we could argue that the model does not completely capture the dependence with T_{nw}. For larger $^{300}/_{T_{nw}}$ values, γ_O is slightly over-estimated, and for smaller values, it is slightly under-estimated. Partly for that reason, we introduced the concept of effective surface temperature. In figure 8.22, the best match conditions without taking into account T_{ws} (s =0) are compared with the best match conditions for a T_{ws} calculated with s =0.4. The introduction of this parameter for the calculation of surface reactions involving adsorbed O atoms shows a clear impact in the temperature dependence of $\gamma_O^{O_F+O_S}$ and $\gamma_O^{O_F+O_F}$. In the case of $\gamma_O^{O_F+O_S}$, instead of a flat variation as a function of $^1/_{T_{nw}}$, and only a small "stair-type" decrease with T_{wall}, using T_{ws} we observe now two parallel decreasing slopes as a function of $^{300}/_{T_{nw}}$, similar to the dependence shown by E-R mechanism with O_S. Concerning $\gamma_O^{O_F+O_F}$, using T_{ws} gives also a small slope in the "tail" (far from the "knee", for smaller $^{300}/_{T_{nw}}$ values). The value of s defines the "slope" of the temperature dependence. Note that the temperature correction is not large, but the effect is significant. As example, for T_{wall}=50^{o}C=323.15 K and T_{gas}=600 K

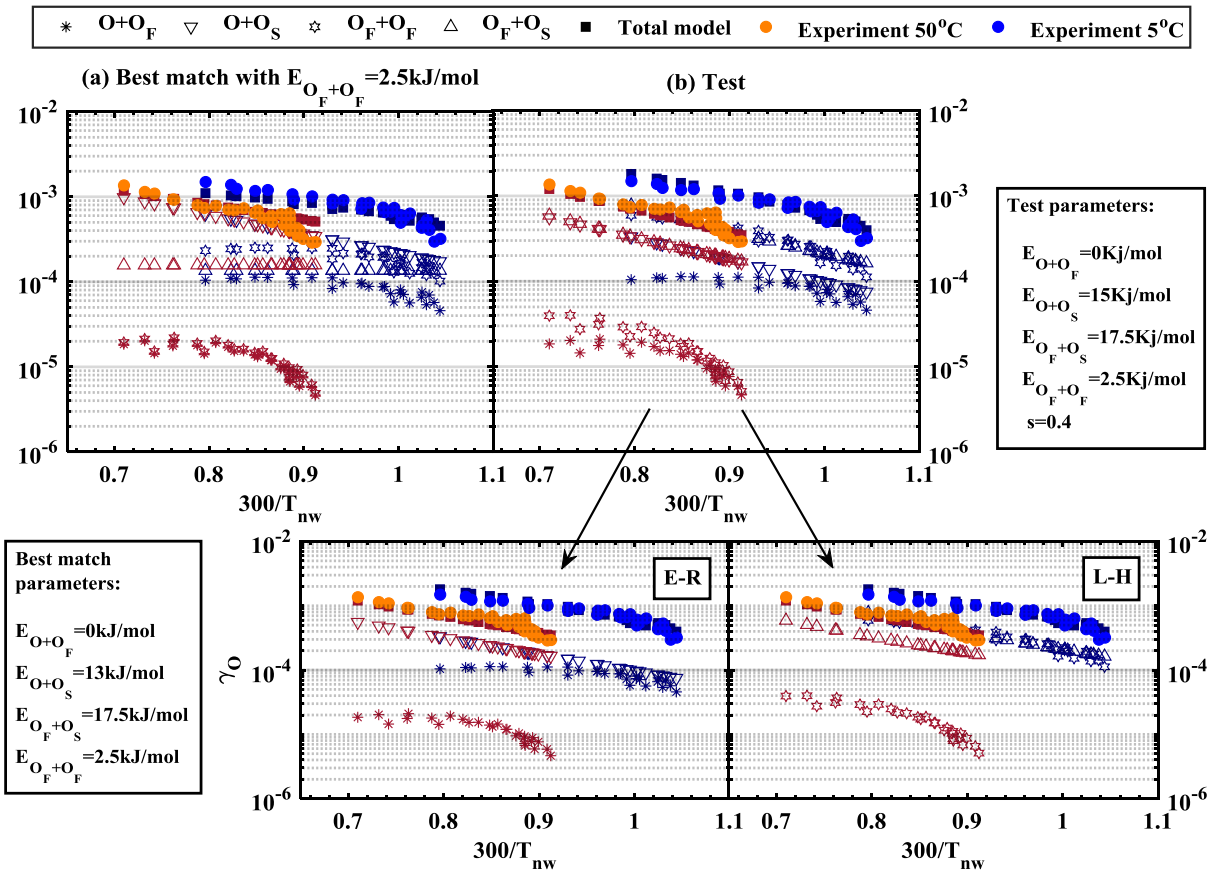

Figure 8.22: Recombination probabilities in O_2 plasma compared to the model results. Panel(a) shows the model results with the default parameters for reference and panel (b) the results using the model parameters detailed in the box. T_{ws} was calculated with a value s=0.4. Bottom panels plot separately the contributions of E-R (right) and L-H (left) mechanisms for readability.

in pure O_2 plasma, T_{nw}=400.7 K and T_{ws}=354.2 K. Including this parameter, the slope of the experimental data is better captured and the relation between the activation energies for the different reactions is more coherent ($E_{act}^{O_F+O_S} = E_{act}^{O+O_S} + E_{act}^{O_F+O_F}$). However, the importance of L-H recombination increases and is similar to that of E-R even at T_{wall}=50^{o}C. It is worth mentioning that the effect of the "effective surface temperature" T_{ws} could help to explain why the activation energies decrease with the CO_2 content in the gas mixture. T_{ws} depends on T_{nw} and therefore on T_{gas}, which increases with the CO_2 content. The surface temperature would be higher in CO_2-containing plasmas, contributing to reduce the activation energy required for the recombination process.

→ ***Comparison with a phenomenological model***

The experimental loss probabilities in O_2 plasma were discussed in detail in *Booth et al.* [2019], accompanied by a phenomenological model. This work has been done by the group of D. Lopaev from MSU (Moscow) but we remind the main results here for comparison with the model described before. In the phenomenological model only two reactions are considered: Eley-Rideal (E-R) recombination with chemisorbed O atoms ($O + O_S$) and E-R recombination with physisorbed O atoms ($O + O_F$). Two cases are explored:

- Case 1: Same activation energy for E-R recombination with physisorbed and chemisorbed O atoms: $E_{ER}^S = E_{ER}^F$

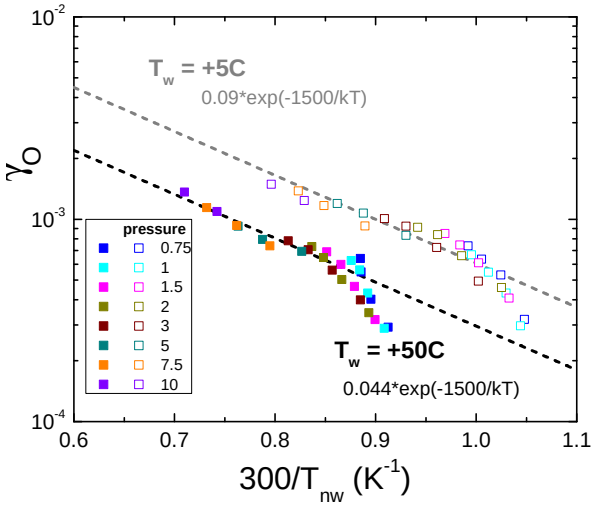

Figure 8.23: Experimental O atom loss probabilities measured at T_{wall}=5 and 50^{o}C for pressures between 0.75 and 10 Torr and currents between 10 and 40 mA. Figure extracted from *Booth et al.* [2019].

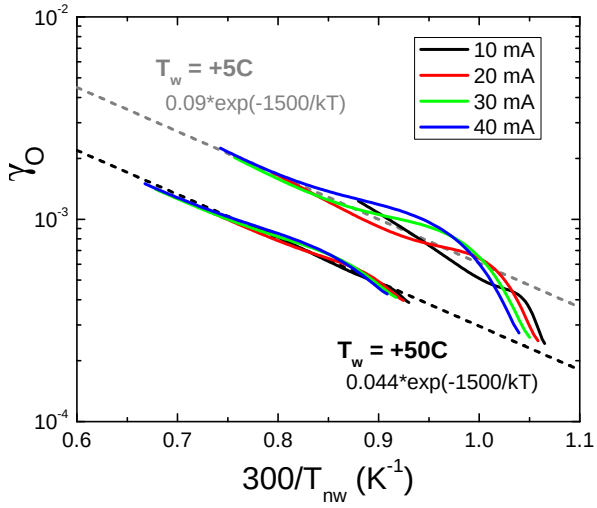

Figure 8.24: O atom loss probabilities calculated from the phenomenological model for the Case 1, for currents between 10 and 40 mA and for T_{wall}=5 and 50^{o}C. Figure extracted from *Booth et al.* [2019].

- Case 2: The activation energies for both processes are different and E^F_{ER}=gas phase 3-body recombination with the surface playing the role of the 3^{rd} body $\rightarrow E^F_{ER} = 0$.

The detailed model parameters are included in table 8.2. The experimental recombination probabilities and the output from the model in the best matching case are shown respectively in figures 8.23 and 8.24. With the input values for the variables $[S]$ and $[F]$: ϕ=0.0148. The best matching with the data is obtained for the case 1. Only this case will be compared to the results of the surface model. The reaction rates are calculated on the basis of two reactions:

$$O + A \xrightarrow{k_0} O_A \qquad O + O_A \xrightarrow{K^A_{ER}} O_2 + A \tag{8.19}$$

where A represents S or F for recombination with chemisorbed or physisorbed O atoms respectively. The rate coefficient for this reaction (k^A_{ER}), according to the rate equation:

$$\frac{d[O]}{dt} = K^A_{ER}[O][O_A] \tag{8.20}$$

is given by the expression:

Model parameter	**Value case 1** $\mathbf{E^S_{act}}$=$\mathbf{E^F_{act}}$	**Value case 2** $\mathbf{E^S_{act}}$; $\mathbf{E^F_{act}}$=**0**
Activation energy E_{act}	0.13 eV=12.543kJ/mol	0.163 eV=15.727kJ/mol
O atom desorption energy $E_{de\,O}$	0.302 eV=29.138kJ/mol	0.172 eV=16.595kJ/mol
Desorption frequency $\nu_{de\,O}$ (s^{-1})	1×10^{13}	1×10^{13}
Adsorption rate constant k_0 ($cm^{-2}s^{-1}$)	2×10^{-10}	2×10^{-10}
Reaction probability P_0	0.044	0.12
Density of chemisorption sites $[S]$ (cm^{-2})	1.5×10^{14}	1.5×10^{14}
Density of physisorption sites $[F]$ (cm^{-2})	1×10^{16}	1×10^{16}

Table 8.2: Input values for the phenomenological model *Booth et al.* [2019].

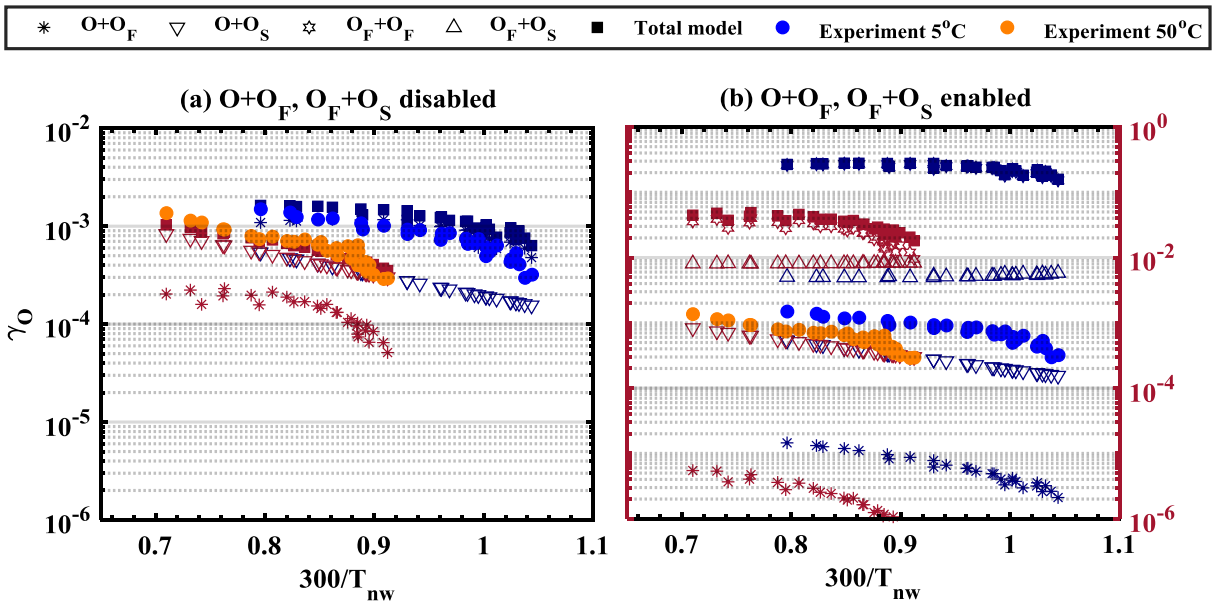

Figure 8.25: Recombination probabilities in O_2 plasma compared to the model results using the model parameters suggested in *Booth et al.* [2019] (case 1). Panel (a) plots results obtained disabling L-H recombination reactions and panel (b) with L-H enabled.

$$K_{ER}^{A} = k_0 * P = k_0 \cdot P_0 \exp\left(-\frac{E_{act}^{A}}{RT_{nw}}\right) \tag{8.21}$$

where P is the elementary reaction probability, P_0 is a function of the properties of the surface and is used as a fitting parameter. k_0 ($cm^2 s^{-1}$) is the effective collision frequency of gas phase atoms with chemisorbed atoms, which can be estimated as $k_0 \sim a^2 \cdot \upsilon_{th} \cdot S/V$, where a≈0.25 nm is the distance between surface atoms *Booth et al.* [2019]. P_0 and k_0 are input parameters for the model and are detailed in table 8.2. Figure 8.25 (a) shows the result of the surface model for the case 1, *i.e.* disabling both L-H recombination reactions. The model results show very good agreement with the experimental data and show that the γ_O at T_{wall}=5^{o}C are dominated by E-R with physisorbed O atoms whereas at T_{wall}=50^{o}C are dominated by E-R with chemisorbed O atoms. The phenomenological model, which inspired the present comparison with the surface model, is very successful in predicting the "knee" shape when the contribution of physisorbed O atoms starts to become important.

Nevertheless, panel (b) in figure 8.25 shows the model results when both L-H reactions ($O_F + O_F$ and $O_F + O_S$) are computed with the default input values ($E_{act}^{O_F+O_F}$=0 kJmol^{-1}, $E_{act}^{O_F+O_S}$=17.5 kJmol^{-1} and E_{di}=15kJmol^{-1}) but keeping the proposed $\nu_{de\,O}$=10^{13} s^{-1}. The graph shows that these reactions would be dominant in the conditions given in the Case 1 when compared with E-R reactions ($O + O_F$ and $O + O_S$), not reproducing the dependence with T_{nw} seen in the experimental data and giving very high γ_O values, above 0.1. The main reason is the strong effect of the low desorption frequency values used by the phenomenological model ($\nu_{de\,O}$=10^{13} s^{-1}) calculated taking into account the frequency of the atom oscillation in the physisorption well, with Morse approximation. The output of the surface model shows that we cannot neglect the contribution of L-H processes, particularly at such low desorption frequency.

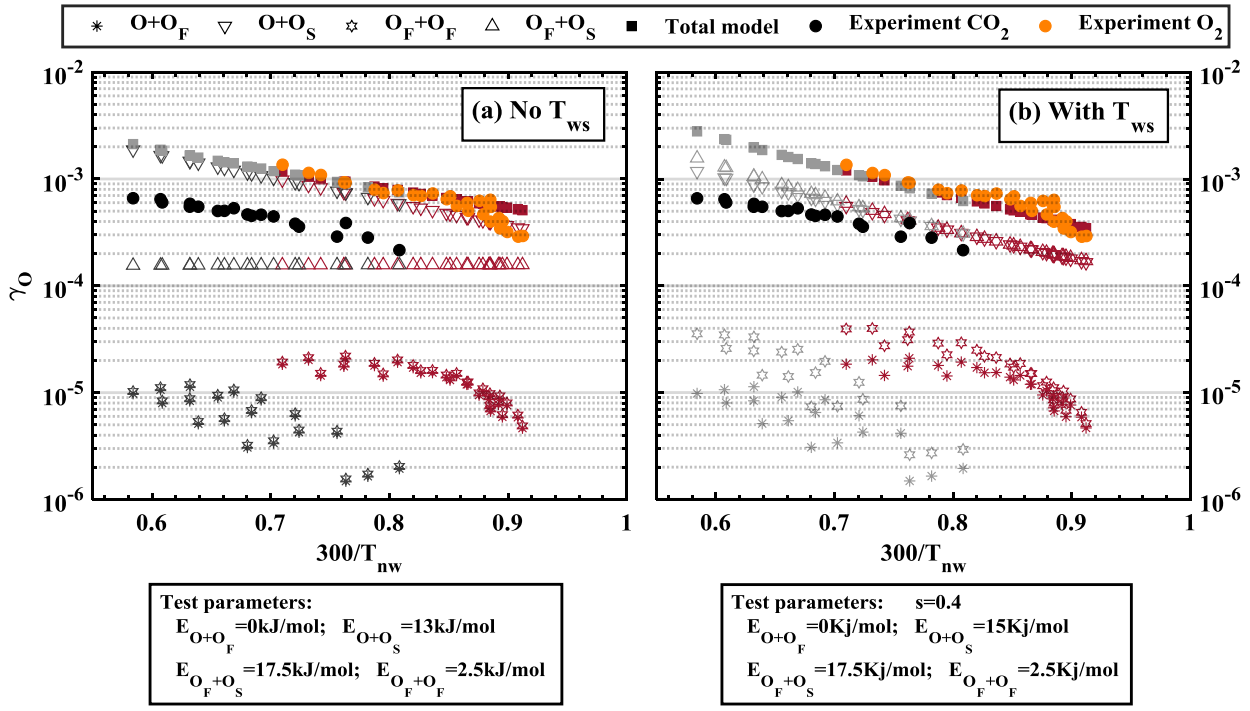

Figure 8.26: Recombination probabilities in CO_2 plasma compared to O_2 plasma at T_{wall}=50^{o}C and to the model results considering only O atom reactions. Panel (a) shows the model results with the "best match" conditions, without considering T_{ws} (s=0). Panel (b) shows the model results with the "best match" conditions but considering T_{ws} calculated with s=0.4.

CO_2 plasma

Including all the reactions involving CO and O in the model, even without considering O_2 reactions, leads to a significant increase of the number of model parameters. For most of them there is no information available in the literature. Preliminary tests show that using similar activation energies as for O atom reactions leads to a predominance of the recombination between atomic oxygen and CO, due to its higher density. From the experimental results we know that the O atom loss processes are significantly more effective than the CO loss processes (see section 3.6). Therefore the activation energies for reactions involving CO must be higher. In such case the O atoms loss processes are in fact controlled by the same reactions discussed for the case of O_2 plasmas. We assume that the activation energies for reaction involving CO are significantly higher and, as a very preliminary approach we neglect all reactions with CO. Figure 8.26 shows the model results in the "best match" cases without using the parameter T_{ws} (panel (a)) or using it (panel (b)).

Both graphs show a similar behaviour, and predict the increase of γ_O as a function of T_{nw}, which could not be avoided unless low activation energies for CO reactions are considered. As a result, the model largely overestimates the loss probability in CO_2 plasma compared to our experiment results. The dependence of γ_O with $^{300}/_{T_{nw}}$ is strongly driven by the E-R recombination with chemisorbed oxygen, for the default model approach or by E-R and L-H with O_S if T_{ws} is considered. As a matter of fact, the only possibility found to match the experimental results with the model predictions at this stage was to use a different value of the parameter $\phi = {}^{[S]}/_{([S]+[F])}$, the fraction of surface covered by chemisorption sites. Figure 8.27 shows the results of this test using a value of ϕ=0.65 $\times 10^{-2}$

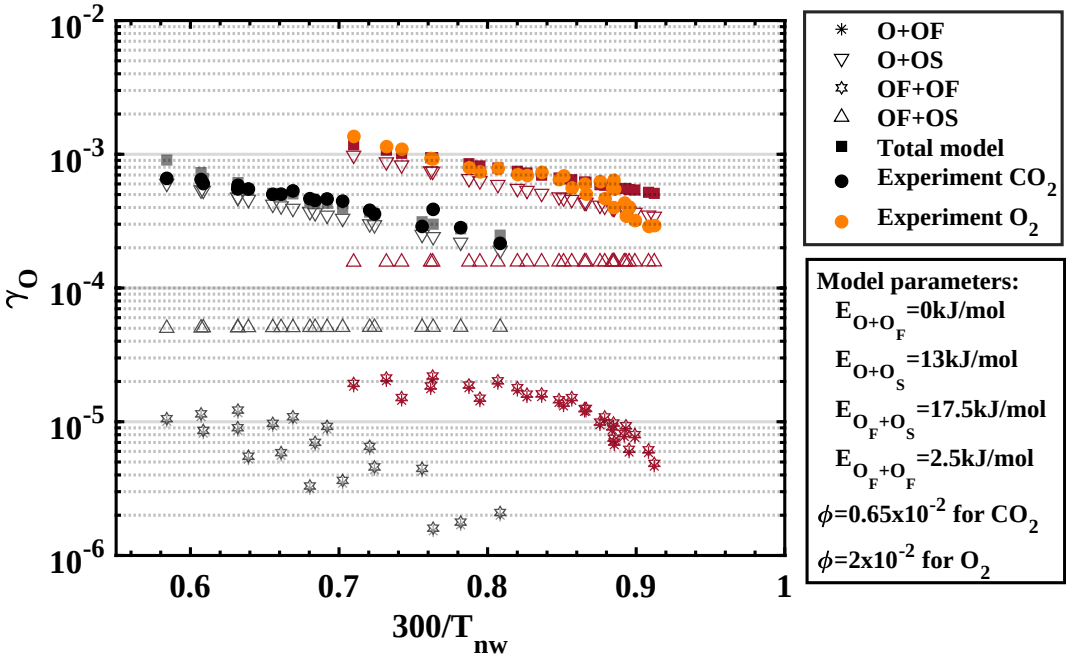

Figure 8.27: Recombination probabilities in CO_2 plasma compared to O_2 plasma at T_{wall}=50^{o}C and to the model results considering only O atom reactions. CO_2 model values were obtained with ϕ=0.65×10^{-2} instead of the default value ϕ=2×10^{-2}, used for reactions in O_2 plasma.

for CO_2 data while for O_2 the default value ϕ=2 ×10^{-2} was kept. A good agreement between the model and the experiment for CO_2 plasma is observed in this case. Note that these values imply that roughly 67% of the active sites or chemisorbed oxygen available for recombination are suppressed by the presence of CO.

These results suggests that CO (or other species present in CO_2 plasma) have the role of either passivating chemisorption sites, not participating actively in recombination reactions, or to "block" chemisorbed oxygen atoms preventing them from participating in recombination reactions. From the isotopic exchange experiments, we do not expect a significant density of chemisorbed CO or C atoms. It is possible that they were very strongly implanted and could not be removed with the building-up experiment procedure. However, the surface of the Pyrex tube is easily regenerated: $\gamma_O^{O_2}$ are reproducible after a CO_2 plasma simply running a cleaning O_2 plasma for ∼10 minutes. The possibility of physisorbed CO on top of a chemisorbed O atoms, not reacting but preventing any reaction could explain the observed results. From a modelling point of view, it would be interesting to vary the desorption and diffusion energies of CO to verify this point. On the other hand, the model follows the view of two types of adsorption sites, physisorbed and chemisorbed, with very different bond energies. However, experiments such as the extraction of isotopes from the Pyrex surface shown in section 8.7 or experiments described in *Donnelly et al.* [2011]; *Marinov* [2012]; *Guerra et al.* [2014] show that the distribution of bond energies is more continuous. This distribution of adsorption energy could be different for CO compared to oxygen atoms.

✓ A surface model was used to reproduce the loss probabilities measured in pure O_2 plasma and shows a predominance of E-R mechanisms, but L-H represents also a significant contribution even at relatively high surface temperature.
✓ An "effective temperature" T_{ws} is introduced to account for a possible influence of the heat flux and/or the impact of excited states (vibrational or electronic) on the surface processes. This parameter allows to obtain a better match with the experimental γ_O values.
✓ In CO_2 plasmas γ_O values could not be reproduced by the model without reducing the number of chemisorption sites for O recombination, which is believed to be a consequence of CO adsorption on free adsorption sites or on top of adsorbed O atoms.

8.9 Epilogue: Carbon-based surfaces for enhanced CO_2 dissociation

The aim of this section is to show an example of application of some of the lessons learnt along this thesis in general, and in particular those concerning the surface kinetics in our experimental conditions. We will make use of different set-ups and experiments described throughout this thesis. Some of these "lessons" are summarized in the following list:

- The O atom loss processes are dominated by surface recombination in our discharge conditions.
- The surface recombination of atomic oxygen is mostly into O_2. Recombination with CO molecules into CO_2 is possible but less efficient.
- The recombination probability depends significantly on the kinetic energy of the incoming O atoms.
- Gas phase "back reaction" mechanisms are efficient and partly define the time evolution of the dissociation fraction.
- Any "back reaction" mechanism necessarily involves oxygen, either in the form of free atomic oxygen or in form of O_2. The amount of oxygen available determines the steady-state dissociation fraction.
- O atoms behave as the main quenchers of the vibrational excitation of CO_2 and CO molecules. Possible reactions involving vibrationally excited CO_2 and O atoms to enhance the dissociation are not significant in our experimental conditions.

So far in this thesis we have worked only with SiO_2-based surface materials: a "smooth" Pyrex tube or SiO_2 micro-structured fibers. In this section we investigate the possibility of using the incoming oxygen in surface reactions to enhance the final dissociation fraction. For this purpose, we performed preliminary experiments on carbon-based surfaces. The underlying idea is to avoid introducing any new component in the discharge, such as catalytic materials or any element not previously discussed that can modify significantly our discharge conditions. Carbon atoms are naturally present in any CO_2 plasma, *i.e.* in all our previous experiments, mostly in the form of CO, or CO_2, and therefore they will undergo similar reactions as those discussed in previous

experiments. We modify however the balance between oxygen and carbon atoms and the balance between different reactions. For these preliminary experiments we will use a well defined carbon-based surface material, graphite, as test case. Evidently a deep study of graphite's behaviour under CO_2 plasma exposure would require a much more detailed description of the surface reactions, which is out the scope of this thesis. Consequently the following analysis is somewhat superficial but serves the illustrative purpose of this section.

Graphite pellets (Sigma-Aldrich, reagent grade) were partially embedded in the inner part of a Pyrex cylinder, similar to the usual Pyrex glow or RF discharge reactors. No glue or adhesive substance was used. The Pyrex tube was partially melted while graphite pellets were flown in the tube (hand-crafted work by the glass blower J.-M. Wierniezky). As a result, a dense and rough layer of graphite pellets stuck in the Pyrex surface was obtained. The pellets could be removed by hand or by a strong gas flow, but they were stable under the low flow used in glow discharge tests or in static conditions in the RF experiments. The graphite tubes have a slightly smaller diameter than the usual reactor, just enough to be able to introduce them inside the usual glow or RF reactors. The slightly smaller diameter implied a slightly higher current density (for the same imposed current) and a slightly shorter residence time when working in flowing conditions. Therefore, a similar Pyrex tube ("blank"), with the same diameter as the graphite tubes, was used for the comparison of both surfaces. It is also worth mentioning that this method to have a graphite surface compatible with the available experimental set-ups, and comparable with previous results, significantly perturbs the functioning of the RF discharge. In the usual configuration the metallic electrodes are rolled around the single-walled discharge reactor. With either the graphite tubes or the blank Pyrex tubes, two concentric independent Pyrex layers were separating the electrodes from the gas. Consequently, higher powers are required to ignite the plasma (above 90W) and the power calibration presented in section 2.2.2 and applicable in chapters 6 and 7, is not valid any more. The power values shown below are merely a qualitative indication of the power dissipated in the discharge. The experimental results presented in this section must be considered only as preliminary tests, supporting and exemplifying the conclusions detailed above, and as a starting point for future work.

Dissociation fraction and O atom density in the glow discharge

We firstly study the basic dissociation parameters in the glow discharge. Figure 8.28 shows the variation as a function of pressure of the O atom fraction measured by actinometry (panel (a)) and the dissociation fraction, α (panel (b)) measured by infra-red absorption:

→ ***O atom fraction***

Figure 8.28 (a) compares the O atom fraction measured with the graphite tube and the Pyrex ("blank") tube. The data taken in the usual short glow discharge reactor with the same current, 40 mA (see figure 5.13) is also shown for comparison. The Pyrex ("blank") tube and the previous data in the usual glow discharge show evident differences believed to be related to the slightly different diameter, current density and residence time. However, both show comparable $(O/N)_{max}$ values, and qualitatively similar trends passing through a maximum shifted from 1 to 2 Torr with the "blank". Remarkable differences are obtained with the graphite tube, which shows a fast decrease of O/N with pressure up to 2 Torr, and remains basically constant at a very low value (∼10% of the oxygen density in the Pyrex tube) when the pressure is further increased. We therefore conclude that the

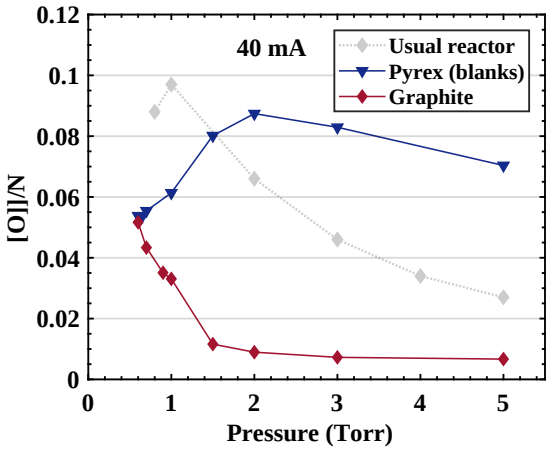

(a) O atom fraction variation *versus* pressure

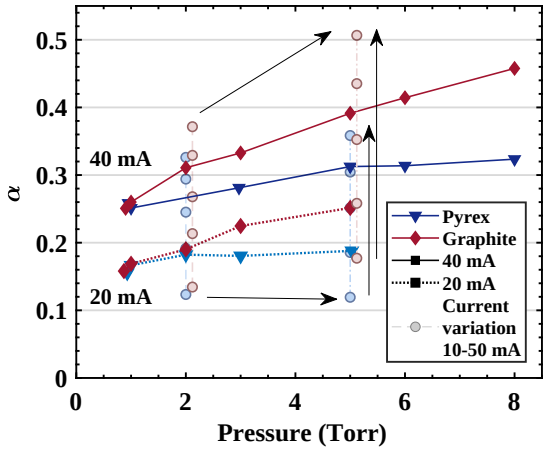

(b) Dissociation fraction variation *versus* pressure

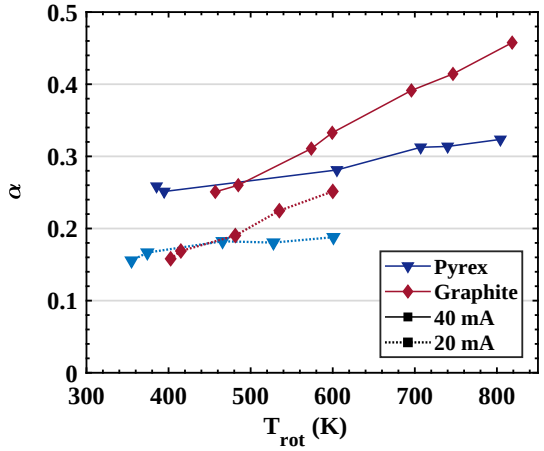

(c) Dissociation fraction variation *versus* T_{rot}

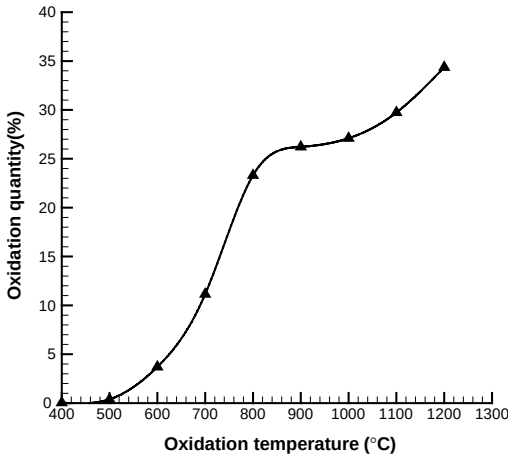

(d) Oxidation fraction versus temperature. Figure extracted from *Xiaowei et al.* [2004]

Figure 8.28: (a) Variation of the O atom fraction in the glow discharge as a function of pressure measured at 40 mA with the graphite tube and with the blanks, and compared to the measurements in the usual Pyrex reactor. (b) Variation of α as a function of pressure and current measured with the Pyrex or with the graphite tube in the glow discharge. (c) Same data as the pressure variation experiments shown in panel (b) but plotted as a function of the gas temperature. (d) Oxidation fraction as a function of the gas temperature (in ^{o}C). Figure extracted from *Xiaowei et al.* [2004].

presence of the graphite significantly decreases the O atom density in gas phase. It is however less efficient than the silica fibers, particularly at low pressure. With the SiO_2 fibers, $(O/N)_{max}$ was below 10% of the O atom density with the bare tube at any pressure, and for instance at 1 Torr $(O/N)_{fibers}$ was already only 5% of $(O/N)_{bare\ tube}$ (see figure 5.6), whereas with the graphite it is roughly 50%. The vibrational temperatures (not shown) show an increase consistent with the removal of the atomic oxygen similar to the effect seen with the fibers in chapter 5.

→ ***Dissociation fraction***

Figure 8.28 (b) shows the variation of the dissociation fraction as a function of pressure for two currents 20 and 40 mA, for the blank and the graphite tube. Additionally current variation measurements taken at 2 and 5 Torr between 10 and 50 mA are also included. With the bare tube we

see a very little increase of α, consistent with data taken in the usual glow discharge reactor (see for instance figure 3.14). With the graphite tube, the dissociation fraction clearly increases both with pressure and current. The same data is plotted in figure 8.28 (c), but as a function of the fitted rotational temperature. It is interesting to notice a common threshold for the "graphite effect" for both currents studied, around 500 K. This temperature value is significantly lower than the ignition temperature of graphite surfaces (flame) which is around 1000 K *Hedman and McDonald* [1965]; *Zhang et al.* [1997]; *Makino et al.* [2003]. It is lower than the thermal oxidation of graphite, which starts to be noticeable at temperatures close to 500^{o}C (800 K), as shown in panel (d). This figure, extracted from *Xiaowei et al.* [2004], represents the oxidation degree of graphite under dry air flow, kept at a fixed temperature during 4 hours. Our experiments are performed in flowing conditions with residence times in the order of seconds. The time in between different data points is in the order of minutes. The oxidation rate is therefore significantly faster under plasma conditions. Two main reasons can explain these differences:

1. Availability of atomic oxygen: O_2 molecules either dissociatively adsorb at vacancy sites of graphite, exothermically and without energy barrier, or form molecular precursor states, depending on the geometry and surface state of the graphite *Lee et al.* [1999]. Atomic oxygen chemisorbs on graphite at near ambient temperatures *Wong et al.* [1983] in any adsorption site. Both processes have therefore very low activation energies but they have different reaction pathways leading to different reaction rates *Wong et al.* [1983]. At 500^{o}C the rate of oxidation by atomic oxygen was estimated to be at least five orders of magnitude faster than by molecular oxygen *Pattabiraman et al.* [1990].

2. Effect of the excited species: The species formed in the graphite surface under plasma exposure are similar to those produced by thermal treatment of carbon but their relative concentration is different, being attributed to the high reactivity of excited species formed in the plasma (ions, electrons, radicals). These plasma species are claimed to help breaking the ordered structure of graphite, generating defects and adsorption sites, and help the desorption of the by-products favoring substitution reactions *Holland and Ojha* [1976]; *Hueso et al.* [2007]

In principle, the temperature threshold could be related with the activation energy of the oxygen adsorption on graphite, the oxidation of graphite or the activation energy of the desorption of the created molecule. The removal of carbon atoms from the lattice plane of graphite requires a very low activation energy, *Marsh et al.* [1963]; *Gleit et al.* [1963]; *Holland and Ojha* [1976]; *Wong et al.* [1983]. Both dissociative chemisorption of O_2 or chemisorption or O atoms are claimed to happen at very low activation energy. Once the oxygen is chemisorbed it is irreversibly bound to the surface and it is only released as a carbon oxide *Blyholder and Eyring* [1957] when the temperature is raised above 200^{o}C (∼500 K) *Holland and Ojha* [1976]. The desorption step is therefore claimed to be the limiting step of the process *Blyholder and Eyring* [1957]; *Barton et al.* [1973], explaining our experiments and the experiments reported by *Xiaowei et al.* [2004] under very different experimental conditions. Carbon monoxide was found to be the main product of the oxidation of graphite *Blyholder and Eyring* [1957]; *Lee et al.* [1999]; *Hahn* [2005], and not CO_2, as is the case under certain experimental conditions. For instance CO_2 was found to be the main product in the oxidation of graphene due to the different surface oxidation pathways followed by graphite or graphene under O_2-containing plasmas *Sun et al.* [2011]; *Koizumi et al.* [2013].

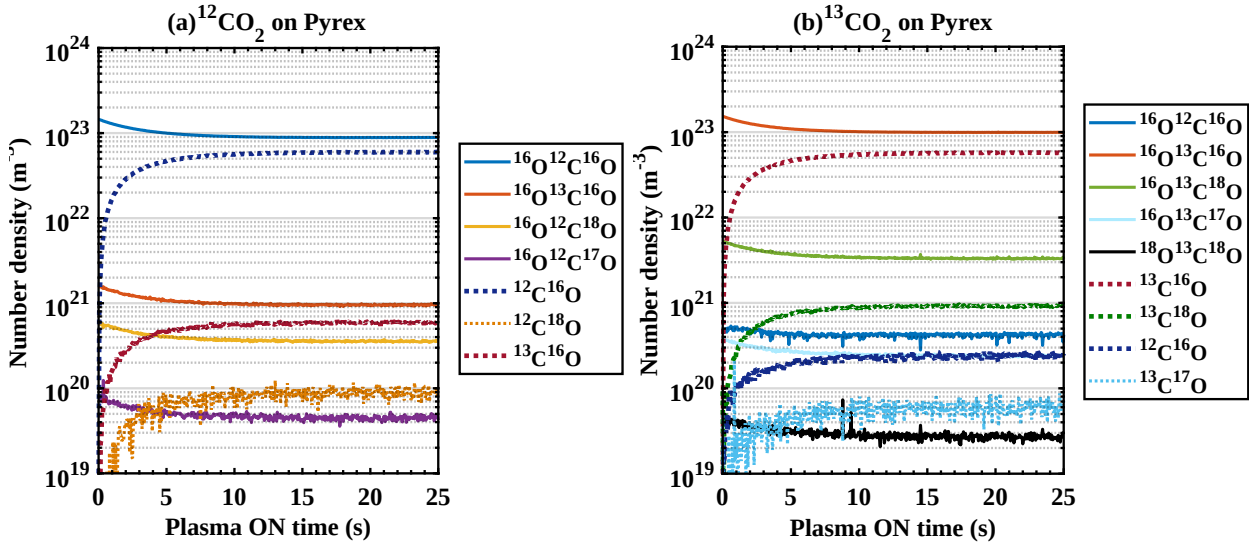

Figure 8.29: Building-up experiments at 5 Torr, 50 W (N_{tr}=500× N_p=10 × t_p^{ON}=5 t_p^{OFF}= 10 ms On-Off) with $^{12}CO_2$ (panel (a)) and $^{13}CO_2$ (panel (b)), taken with the bare Pyrex tube inserted in the RF reactor.

Surface reactivity traced by isotopic exchange

In order to confirm that the increase of dissociation is due to the oxidation of graphite we have performed preliminary isotopic exchange experiments with isotopically-labelled carbon atoms. The graphite structure is essentially composed by ^{12}C. A building-up experiment with $^{13}CO_2$ plasma can provide insight in the extraction of carbon from the graphite surface and its incorporation to the gas phase CO and CO_2 molecules. We first characterize the $^{13}CO_2$ building-up in the usual Pyrex reactor, and compare it with a usual $^{12}CO_2$ building-up already discussed in chapters 6 and 7. Figure 8.29 (a) shows the usual building-up with $^{12}CO_2$ at 5 Torr 50 W (reading power). All the isotopes included in table 7.1 are included in the fitting but only isotopologues showing a clearly defined time evolution are kept in the figure. All CO isotopologues show a parallel fast initial increase, and then stabilize between T^{ON}=10-15 s. CO_2 isotopologues slowly decrease and stabilize at a similar time point. The number densities of ^{12}C-containing isotopologues are roughly two orders of magnitude higher than ^{13}C-containing isotopologues, which are always present due to their natural abundance in the CO_2 bottle (see table 7.1). Figure 8.29 (b) shows the same experiment but with $^{13}CO_2$. The time evolution is similar (the dissociation fraction, not shown, is also similar) confirming the negligible role of the different vibrational kinetics of both isotopologues in our discharge conditions, discussed in chapter 7. Nevertheless, the population of the different isotopologues is very different, as expected. Note that the colour code is the same in both panels, *i.e.* the common isotopologues (*e.g.* $^{16}O^{13}C^{16}O$ and $^{13}C^{16}O$) keep the same colour. In this case, ^{13}C-containing isotopologues are more than two and a half orders of magnitude higher than ^{12}C-containing isotopologues.

Experiments with the graphite tube were done at 2 Torr, 90 and 120 W (reading power). It was not possible to ignite the plasma at lower power values, due to the effect of the double tube in the RF reactor. Longer pulses were also required to sustain the plasma. The pulse configuration in these experiments was N_{tr}=500 × N_p=1 × t_p^{ON}=100 t_p^{OFF}= 100 ms On-Off. A O_2 plasma pre-treatment of 5 minutes at 1.5 Torr 90W was done to remove possible water adsorbed in the graphite surface before the building-up experiment. Figure 8.30 shows the time evolution of the dissociation fraction

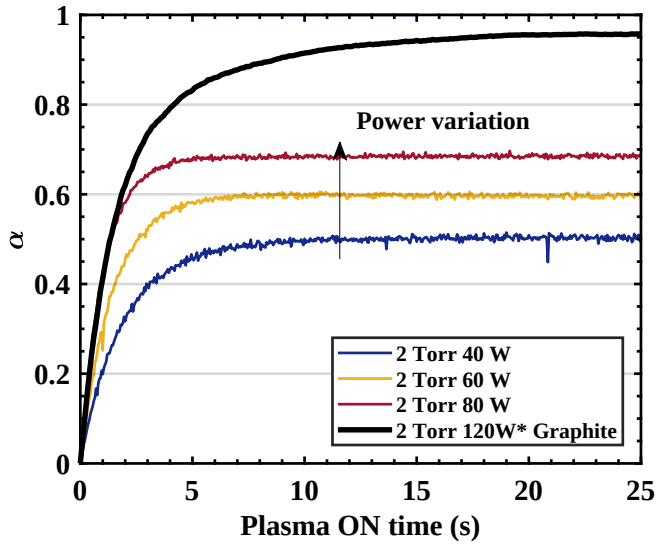

Figure 8.30: Dissociation fraction α measured in building-up experiments at 2 Torr (N_{tr}=500 × N_p=10 × t_p^{ON}=5 t_p^{OFF}= 10 ms On-Off), for different powers in the bare tube: 40, 60 and 80 W reading powers (same data as in figure 6.5) and with the graphite tube (N_{tr}=500 × N_p=1 × t_p^{ON}=100 t_p^{OFF}= 100 ms On-Off) at ∼120 W.

for a measurement at 2 Torr, 120 W, and compares it with power variation measurements at 2 Torr (same as shown in figure 6.5). Although this is a qualitative comparison some comments can be put forward:

- The dissociation fraction measured with the graphite tube shows a fast initial increase similar to the measurements done in the Pyrex tube.
- After the initial slope, in the "turning region", the measurements on Pyrex deviate from the initial slope towards the final steady-state, which shows a flat time evolution.
- The dissociation fraction in the measurements with the graphite keeps increasing until the end of the experiment, although with a slower slope.
- The dissociation values measured with the graphite tube after 25 s of total plasma ON time are above 95%.

The time evolution of the dissociation fraction follows similar time regions as in the Pyrex tube. The initial slope seems to still be controlled by the electron impact dissociation of the CO_2 available in the gas phase. Although in principle the input power in the graphite experiments should be higher than previous experiments, the slope matches very well the data in the usual Pyrex reactor at 80 W (corresponding to a real power dissipated in the discharge of 44.2 W). The probable less efficient power transfer to the plasma with the double Pyrex layer required by the graphite experiments, makes plausible that the real power was relatively close to the experiments at 80W in the bare tube.

In the "turning region" the time evolution of α deviates from the initial linear slope and progress towards the final steady-state. In the steady-state all the measurements done in the Pyrex tube, for any power, show a flat evolution as a function of time. The evolution in these time regions was shown to be controlled by back reaction mechanisms dependent on the available oxygen in gas phase

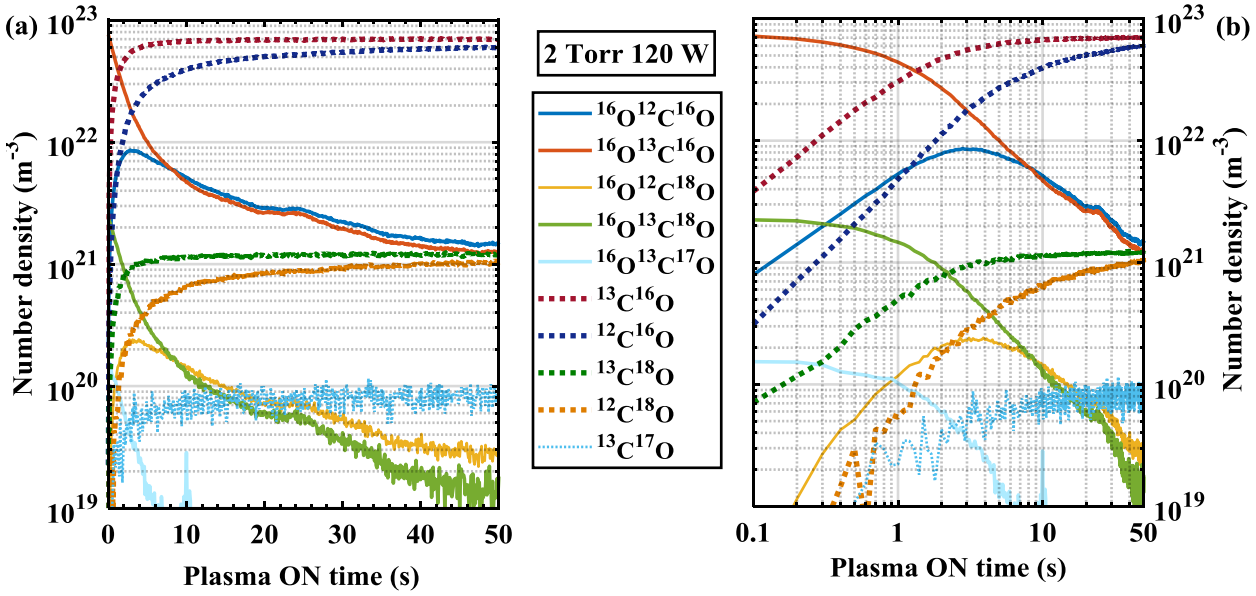

Figure 8.31: Building-up experiment at 2 Torr, ∼120 W (N_{tr}=500 × N_p=1 × t_p^{ON}=100 t_p^{OFF}= 100 ms On-Off) with the graphite tube (^{12}C) and $^{13}CO_2$ gas plotted in linear (panel (a)) and logarithmic (panel (b)) time scale.

either in the form of atomic oxygen or more probably as molecular oxygen (see section 6.3.2). The measurements done with the graphite tube show a different time evolution in the "turning region", which suggests a significant decrease of the back reaction, probably related to the lack of oxygen available. In addition, the dissociation fraction keeps increasing in the "steady-state" region (to keep the notation). The increasing rate of α in this region is similar to that shown in figure 8.17, suggesting that this increase is compatible with surface reactions and/or desorption processes. The dissociation value after 25 s of plasma ON time is very high, close to 95%. At T^{ON}=50 s (not shown in figure 8.30, but in figure 8.31) the dissociation fraction reaches values as high as 97.9%, very close to a pure CO discharge, and keeps the slow increasing trend.

The time evolution of the different isotopologues corresponding to the graphite measurement in figure 8.30, is shown in figure 8.31, in linear time scale (panel (a)) and logarithmic time scale (panel (b)). There are four groups of isotopologues:

1. ^{13}*C-containing isotopologues*:
   - **^{13}CO** with ^{16}O, ^{18}O or ^{17}O shows a fast increase at the beginning of the experiment to be expected from the electron impact dissociation of $^{13}CO_2$ in the gas phase. They reach a steady-state number density at T^{ON}∼10 s, following a similar evolution to that in a Pyrex tube (see figure 8.29).
   - **$^{13}CO_2$** with 2^{16}O, 1^{16}O+1^{18}O or 1^{16}O+1^{17}O shows a constant decreasing trend. Contrary to isotopic measurements in the Pyrex tube (see figure 8.29), their densities do not stabilize and decrease until the end of the experiment.
2. ^{12}*C-containing isotopologues*:
   - **^{12}CO** with ^{16}O or ^{18}O shows a constant increase during all the experiment. The growth rate is slower than for ^{13}CO isotopologues, but the densities of ^{13}CO and ^{12}CO tend to

converge towards the end of the experiment.

- $^{12}\mathbf{CO_2}$ with 2^{16}O or 1^{16}O+1^{18}O shows an initial increasing trend, passes through a maximum at $T^{ON}\sim$3 s and then decreases joining the decreasing trend of $^{13}CO_2$ isotopologues. The reason of the initial increase is not clear yet. Possible hypothesis include a certain desorption of CO_2 from the graphite surface or, more probably, the oxidation of carbon deposited or CO created by the pre-treatment of the graphite and adsorbed in the Pyrex parts of the reactor and gas pipes that are close to the graphite tube but not covered and still in contact with the plasma.

The extraction of ^{12}C from the graphite surface is clear. For each CO produced from the gas phase dissociation of CO_2, one oxygen atom is also created. The similar densities of ^{13}CO and ^{12}CO at the end of the experiment for all the equivalent isotopologues suggest that almost every O atom produced undergoes a carbon oxidation reaction in the graphite surface and that the CO produced is desorbed to the gas phase. To conclude, the use of a carbon-based surface such as graphite has been proven to be an efficient method to trap the oxygen, preventing "back reaction" in the gas phase and increasing the total dissociation rate up to values above 95%.

8.10 Conclusions

In our experimental conditions, the O atom densities are shown to strongly depend on surface loss processes. In this chapter we have studied the surface processes, with a particular attention to the O atom surface recombination, in CO_2 and O_2 plasmas and their mixtures. Two clearly differentiated regimes were found in the range of pressures studied:

- At low pressures, below 0.75-1.5 Torr, the surface loss processes seems to be enhanced by ion bombardment.
- At pressures above 1.5 Torr the loss frequency increases with pressure and current. The surface loss probability, derived from the loss frequency, shows an Arrhenius dependence with the temperature near the wall, suggesting in principle a dominant loss process based on surface recombination through an Eley-Rideal mechanism, although a contribution from Langmuir-Hinshelwood mechanism could be significant.

The two regimes evolve differently when the wall temperature is decreased. For low pressures the loss frequencies decrease when the wall temperature is decreased, whereas for high pressures the loss frequencies increase. Both CO_2 and O_2 plasmas show qualitatively a similar behaviour. However, the values of the derived loss probabilities are lower for CO_2 plasma. In this regard two observations can be put forward:

- Significant influence of the gas phase compounds in the surface loss processes. O atom loss frequencies and loss probabilities are higher in O_2 plasma than in CO_2 plasma particularly under plasma exposure but also in post-discharge. Gas phase species present in CO_2 plasma, seem to play an important role inhibiting the O atom recombination in CO_2 plasmas.
- Large effect of the surface processes in the gas phase chemistry, controlling the "back reaction" through the control of the O atoms and O_2 densities in the gas phase.

Adsorbed species, probably CO, which is adsorbed in SiO_2 surfaces, seem to effectively passivate the Pyrex surface. Modelling results show that to justify the experimental results more than 60% of the chemisorption sites or chemisorbed oxygen should be passivated under CO_2 plasma. However, no chemisorption of C atoms or CO was observed by isotope exchange experiments. A plausible hypothesis is therefore the adsorption of CO on chemisorbed oxygen.

The role of CO and CO_2 molecules in surface mechanisms is in any case an important aspect to study for a better control of O atoms reactivity in CO_2 plasma conversion. In addition, the experimental results shown in this chapter demonstrate the huge possibilities of surface processes for the improvement of the efficiency in the CO_2 conversion, exemplified here by the suppression of "back reaction" with the graphite surface.

Chapter 9

Conclusions

The objective of this thesis was the investigation of fundamental processes in CO_2 plasmas. We performed experiments in conditions simple enough to identify and investigate single processes, while still working under plasma conditions with all the complexity of coupled mechanisms. The low excitation regime typical in the glow discharge, made possible to study independently the vibrational kinetics and the chemistry of gas phase species. The low pressure range allowed to isolate different processes due to their characteristic times, for example differentiating electron-driven processes (e-V excitation or electron impact dissociation), from vibrational-vibrational energy transfer mechanisms, vibrational-to-translation relaxation or surface processes. The followed approach lead to a successful comparison with volume and surface kinetic models. The main conclusions of this thesis, can be summarized as follows:

- **Electron impact dissociation** is the main dissociation mechanism in our discharge conditions. No evidence of contribution from vibrational up-pumping mechanism was found. Possible contribution of electron impact dissociation from vibrationally excited molecules could explain the higher dissociation rates observed in CO_2-N_2 mixtures. The predominance of electron impact dissociation, and a careful experimental approach allowed us to provide an experimental validation of the CO_2 electron impact dissociation cross section. In spite of being one of the most important mechanisms in any CO_2 gas discharge, significantly different values were proposed in the literature, hindering the understanding of the dissociation mechanisms in CO_2 plasmas. With the experimental validation of the theoretical cross section calculated by *Polak and Slovetsky* [1976] through two complementary methods, this key mechanism is now more clear.
- **Vibrational kinetics**. The de-excitation of the vibrational levels of CO_2 was found to be strongly controlled by the gas temperature, through its influence in the rate coefficients of V-V' and V-T processes and the increased collision rate. We have observed a significant impact of the dissociation products in the CO_2 vibrational kinetics, particularly O atoms and CO, which enhances the excitation of $CO_2(\nu_3)$ through near-resonant V-V' transfers. The performed experiments and the comparison with a 0D kinetic model describing the vibrational kinetics of the low energy levels, validated the rates for V-V' and V-T transfer reported by *Blauer and Nickerson* [1973], along with the used scaling laws.
- **Role of oxygen atoms**. The amount of oxygen atoms that remain free in continuous plasma

is significant, reaching values as high as 10% of the total gas mixture. The O atoms do not contribute significantly to any back reaction mechanism in our conditions, in agreement with the rate coefficients available in the literature. However, atomic oxygen was found to be the main quencher of the vibrational excitation of CO_2 and CO, dominating the V-T de-excitation processes. The density of oxygen atoms is controlled by surface loss processes in our discharge conditions.

- **Electronically excited states** seem to have a relevant role in the chemistry of CO_2 plasmas. Their fast reaction rates make them very challenging to detect. However, they carry a significant amount of energy which can influence relevantly the vibrational kinetics or the gas phase chemistry. In this thesis two electronically excited states were mainly discussed: $CO(a^3\Pi_r)$ and $O(^1D)$. The latter is a key electronically excited state that brings information of the dissociation process. $CO(a^3\Pi_r)$ is believed to contribute significantly to the **back reaction mechanism**, which would involve O_2 and not atomic oxygen. Back reaction mechanisms involving vibrationally excited CO are possible but they are probably not dominant in our discharge conditions.
- **Surface processes**. We have seen that even non active surfaces such as Pyrex (or SiO_2-based materials) can influence significantly the gas phase kinetics, for instance by controlling the O atom and O_2 densities, therefore strongly impacting the vibrational kinetics and the gas phase chemistry. At the same time, the plasma itself significantly affects the behaviour of the surface. A clear example is the passivation of the Pyrex walls probably by adsorbed CO, decreasing the O atom loss probabilities. In addition, the exchange of oxygen atoms between the gas phase and the Pyrex surface, where they become strongly bonded, even at pressure as a high as 2 Torr was proven by isotope implantation.

One of the main challenges of plasma chemistry is the control of the selectivity towards a concrete reaction path. An interesting possibility to promote certain reaction mechanisms is "tayloring the EEDF". Another option is the use of surfaces to catalyse specific reactions, which is the main focus of the plasma catalysis field, or the use of membranes to extract and separate the dissociation products, preventing certain mechanisms. In our experimental conditions we have shown the possibilities of using surfaces to control the amount of oxygen atoms in the gas phase. If this oxygen is used for instance to enhance the overall dissociation fraction with carbon-based surfaces, the occurrence of gas phase back reactions, which necessarily involves oxygen in form of atomic oxygen or in form of O_2, can be prevented.

Surfaces can affect the vibrational kinetics of CO_2, not only through de-excitation of vibrations in the walls, but through their influence in the gas phase species. Oxygen atoms have a significant effect on the vibrational kinetics of CO_2, behaving as the main quenchers of the vibrational excitation of CO_2 and enhancing the V-T de-excitation processes. The reaction $O + CO_2(\nu^*) \rightarrow CO + O_2$ was not observed in our conditions, probably due to the low excitation regime. However, understanding this reaction and in general any chemical reaction involving vibrational excited species is necessary to take advantage of the vibrational excitation to increase energy and conversion efficiencies, and still requires more fundamental investigation.

Very little is known about electronically excited states an their role in the CO_2 plasma dynamics. These states carry a relevant amount of energy, and could have a significantly impact on the

final dissociation fraction. The lack of information in a CO_2, or even an O_2, plasma environment with regard to the effect of O atoms, O_2, CO or CO_2 electronically excited states, is evident and more fundamental research is required to determine the reaction rates for those states and their dependence with other plasma parameters. No good description of the gas phase chemistry in CO_2 plasma is possible without taking into account these states. The fast reaction rates make them also difficult to control for instance by surface processes. In addition their density is expected to be very low, being very challenging to measure. We have discussed two electronically excited states in this thesis, not directly measured. However, $O(^1D)$ could be detected through an indirect method, by isotopic exchange processes. From a diagnostics point of view, tracing $O(^1D)$ opens the possibility to use it as marker of the electron impact dissociation path, compared to dissociation through vibrational up-pumping.

For all these processes a wider knowledge of the fundamental mechanisms from a quantum mechanics point of view could help to understand the balance between different mechanism and to try to enhance the selectivity through some dissociation paths.

Bibliography

Adamovich, I., S. Saupe, M. Grassi, O. Schulz, S. Macheret, and J. Rich (1993), Vibrationally stimulated ionization of carbon monoxide in optical pumping experiments, *Chemical Physics*, *173*(3), 491 – 504, doi:https://doi.org/10.1016/0301-0104(93)80163-4.

Adamovich, I., S. D. Baalrud, A. Bogaerts, P. J. Bruggeman, M. Cappelli, V. Colombo, U. Czarnetzki, U. Ebert, J. G. Eden, P. Favia, D. B. Graves, S. Hamaguchi, G. Hieftje, M. Hori, I. D. Kaganovich, U. Kortshagen, M. J. Kushner, N. J. Mason, S. Mazouffre, S. M. Thagard, H.-R. Metelmann, A. Mizuno, E. Moreau, A. B. Murphy, B. A. Niemira, G. S. Oehrlein, Z. L. Petrovic, L. C. Pitchford, Y.-K. Pu, S. Rauf, O. Sakai, S. Samukawa, S. Starikovskaia, J. Tennyson, K. Terashima, M. M. Turner, M. C. M. van de Sanden, and A. Vardelle (2017), The 2017 Plasma Roadmap: Low temperature plasma science and technology, *Journal of Physics D: Applied Physics*, *50*(32), 323,001, doi:https://doi.org/10.1088/1361-6463/aa76f5.

Adamovich, I. V., S. O. Macheret, J. W. Rich, and C. E. Treanor (1998), Vibrational energy transfer rates using a forced harmonic oscillator model, *Journal of Thermophysics and Heat Transfer*, *12*(1), 57–65, doi:https://doi.org/10.2514/2.6302.

Aerts, R., T. Martens, and A. Bogaerts (2012), Influence of vibrational states on CO_2 splitting by dielectric barrier discharges, *The Journal of Physical Chemistry C*, *116*(44), 23,257–23,273, doi:https://doi.org/10.1021/jp307525t.

Aerts, R., R. Snoeckx, and A. Bogaerts (2014), *In-situ* chemical trapping of oxygen in the splitting of carbon dioxide by plasma, *Plasma Processes and Polymers*, *11*(10), 985–992, doi:https://doi.org/10.1002/ppap.201400091.

Afonina, N., V. Gromov, and V. Kovalev (2002), Investigation of the influence of different heterogeneous recombination mechanisms on the heat fluxes to a catalytic surface in dissociated carbon dioxide, *Fluid dynamics*, *37*(1), 117–125, doi:10.1023/A:1015195119243.

Amorim, J., and G. Baravian (2001), The two-photon absorption laser induced stimulated emission as a hydrogen atoms diagnostic tool: modelling and experiment, *Optics Communications*, *192*(3), 277 – 286, doi:https://doi.org/10.1016/S0030-4018(01)01227-5.

Amorim, J., G. Baravian, and G. Sultan (1996), Absolute density measurements of ammonia synthetized in N_2–H_2 mixture discharges, *Applied Physics Letters*, *68*(14), 1915–1917, doi:https://doi.org/10.1063/1.116293.

Amorim, J., G. Baravian, and J. Jolly (2000), Laser-induced resonance fluorescence as a diagnostic technique in non-thermal equilibrium plasmas, *Journal of Physics D: Applied Physics*, *33*(9), R51–R65, doi:https://doi.org/10.1088/0022-3727/33/9/201.

Andreev, S., A. Mazurenko, M. Kerimkulov, V. Ochkin, S. Y. Savinov, and S. Tskhai (1994), Isotope effects in the dissociation of carbon dioxide in nonequilibrium gas-discharge plasmas, *Technical Physics C/C of Zhurnal Tekhnicheskoi Fiziki*, *39*, 466–466.

Andreev, S., V. Zakharov, V. Ochkin, and S. Savinov (2004), Plasma-chemical CO_2 decomposition in a non-self-sustained discharge with a controlled electronic component of plasma, *Spectrochimica Acta Part A: Molecular and Biomolecular Spectroscopy*, *60*(14), 3361 – 3369, doi:https://doi.org/10.1016/j.saa.2004.01.034.

Andreev, Y., I. A. Semiokhi, V. A. Sirotkin, Y. M. Voronkov, and V. A. Kaigorod (1971), Dissociation of carbon diaxide in a pulse discharge, *Russian Journal of Physical Chemistry, USSR*, *45*(11), 1587.

Annušová, A., D. Marinov, J.-P. Booth, N. Sirse, M. L. da Silva, B. Lopez, and V. Guerra (2018), Kinetics of highly vibrationally excited O_2(X) molecules in inductively-coupled oxygen plasmas, *Plasma Sources Science and Technology*, *27*(4), 045,006, doi:https://doi.org/10.1088/1361-6595/aab47d.

Armenise, I., and E. Kustova (2013), State-to-state models for CO_2 molecules: From the theory to an application to hypersonic boundary layers, *Chemical Physics*, *415*, 269 – 281, doi:https://doi.org/10.1016/j.chemphys.2013.01.034.

Armenise, I., and E. Kustova (2018), Mechanisms of coupled vibrational relaxation and dissociation in carbon dioxide, *The Journal of Physical Chemistry A*, *122*(23), 5107–5120, doi:https://doi.org/10.1021/acs.jpca.8b03266.

Armenise, I., P. Reynier, and E. Kustova (2016), Advanced models for vibrational and chemical kinetics applied to Mars entry aerothermodynamics, *Journal of Thermophysics and Heat Transfer*, *30*(4), 705–720, doi:https://doi.org/10.2514/1.T4708.

Asisov, R. I., A. K. Vakar, V. K. Jivotov, M. F. Krotov, O. A. Zinoviev, B. V. Potapkin, A. A. Rusanov, V. D. Rusanov, and A. A. Fridman (1983), Non-equilibrium plasma-chemical process of CO_2 decomposition in a supersonic microwave discharge, *Proceedings of the USSR Academy of Sciences*, *1*, 271.

Aymar, M., and M. Coulombe (1978), Theoretical transition probabilities and lifetimes in Kr I and Xe I spectra, *Atomic Data and Nuclear Data Tables*, *21*(6), 537 – 566, doi:https://doi.org/10.1016/0092-640X(78)90007-4.

Azzolina-Jury, F., D. Bento, C. Henriques, and F. Thibault-Starzyk (2017), Chemical engineering aspects of plasma-assisted CO_2 hydrogenation over nickel zeolites under partial vacuum, *Journal of CO_2 Utilization*, *22*, 97 – 109, doi:https://doi.org/10.1016/j.jcou.2017.09.017.

Babu, D. J., S. Yadav, T. Heinlein, G. Cherkashinin, and J. J. Schneider (2014), Carbon dioxide plasma as a versatile medium for purification and functionalization of vertically aligned carbon

nanotubes, *The Journal of Physical Chemistry C*, *118*(22), 12,028–12,034, doi:https://doi.org/10.1021/jp5027515.

Bak, M. S., S. Im, and M. Cappelli (2015), Nanosecond-pulsed discharge plasma splitting of carbon dioxide, *IEEE Transactions on Plasma Science*, *43*(4), 1002–1007, doi:https://doi.org/10.1109/TPS.2015.2408344.

Bal, K. M., S. Huygh, A. Bogaerts, and E. C. Neyts (2018), Effect of plasma-induced surface charging on catalytic processes: application to CO_2 activation, *Plasma Sources Science and Technology*, *27*(2), 024,001, doi:https://doi.org/10.1088/1361-6595/aaa868.

Balat-Pichelin, M., and E. Bêche (2010), Atomic oxygen recombination on the ODS PM 1000 at high temperature under air plasma, *Applied Surface Science*, *256*(16), 4906–4914, doi:https://doi.org/10.1016/j.apsusc.2010.03.002.

Balat-Pichelin, M., J. Badie, R. Berjoan, and P. Boubert (2003), Recombination coefficient of atomic oxygen on ceramic materials under earth re-entry conditions by optical emission spectroscopy, *Chemical Physics*, *291*(2), 181 – 194, doi:https://doi.org/10.1016/S0301-0104(03)00152-6.

Baluja, K. L., and C. J. Zeippen (1988), M1 and E2 transition probabilities for states within the $2p^4$ configuration of the O I isoelectronic sequence, *Journal of Physics B: Atomic, Molecular and Optical Physics*, *21*(9), 1455–1471, doi:https://doi.org/10.1088/0953-4075/21/9/007.

Bamford, D. J., L. E. Jusinski, and W. K. Bischel (1986), Absolute two-photon absorption and three-photon ionization cross sections for atomic oxygen, *Physical Review A*, *34*, 185–198, doi:https://doi.org/10.1143/jjap.30.289710.1103/PhysRevA.34.185.

Barton, S. S., B. H. Harrison, and J. Dollimore (1973), Surface studies on graphite: desorption of surface oxide, *Journal of the Chemical Society, Faraday Transactions 1: Physical Chemistry in Condensed Phases*, *69*, 1039–1048, doi:https://doi.org/10.1039/F19736901039.

Baulch, D. L., and W. H. Breckenridge (1966), Isotopic exchange of $O(^1D)$ with carbon dioxide, *Transactions of the Faraday Society*, *62*, 2768–2773, doi:https://doi.org/10.1039/TF9666202768.

Bedra, L., and M. J. Balat-Pichelin (2005), Comparative modeling study and experimental results of atomic oxygen recombination on silica-based surfaces at high temperature, *Aerospace Science and Technology*, *9*(4), 318 – 328, doi:https://doi.org/10.1016/j.ast.2005.01.011.

Bedra, L., M. Rutigliano, M. Balat-Pichelin, and M. Cacciatore (2006), Atomic oxygen recombination on quartz at high temperature: Experiments and molecular dynamics simulation, *Langmuir*, *22*(17), 7208–7216, doi:https://doi.org/10.1021/la060032l.

Benedictis, S. D., M. Capitelli, F. Cramarossa, and C. Gorce (1987), Non-equilibrium vibrational kinetics of CO pumped by vibrationally excited nitrogen molecules: A comparison between theory and experiment, *Chemical Physics*, *111*(3), 361 – 370, doi:https://doi.org/10.1016/0301-0104(87)85086-3.

Berden, G., R. Peeters, and G. Meijer (2000), Cavity ring-down spectroscopy: Experimental schemes and applications, *International Reviews in Physical Chemistry*, *19*(4), 565–607, doi:https://doi.org/10.1080/014423500750040627.

Bergman, R. C., G. F. Homicz, J. W. Rich, and G. L. Wolk (1983), ^{13}C and ^{18}O isotope enrichment by vibrational energy exchange pumping of CO, *The Journal of Chemical Physics*, *78*(3), 1281–1292, doi:https://doi.org/10.1063/1.444866.

Berthelot, A., and A. Bogaerts (2016), Modeling of plasma-based CO_2 conversion: lumping of the vibrational levels, *Plasma Sources Science and Technology*, *25*(4), 045,022, doi:https://doi.org/10.1088/0963-0252/25/4/045022.

Berthelot, A., and A. Bogaerts (2017), Modeling of CO_2 plasma: effect of uncertainties in the plasma chemistry, *Plasma Sources Science and Technology*, *26*(11), 115,002, doi:https://doi.org/10.1088/1361-6595/aa8ffb.

Beuthe, T. G., and J.-S. Chang (1997), Chemical kinetic modelling of non-equilibrium Ar-CO_2 thermal plasmas, *Japanese Journal of Applied Physics*, *36*(Part 1, No. 7B), 4997–5002, doi:https://doi.org/10.1143/jjap.36.4997.

Bhattacharya, S. K., J. Savarino, and M. H. Thiemens (2000), A new class of oxygen isotopic fractionation in photodissociation of carbon dioxide: Potential implications for atmospheres of Mars and Earth, *Geophysical Research Letters*, *27*(10), 1459–1462, doi:https://doi.org/10.1029/1999GL010793.

Bird, R. B., J. O. Hirschfelder, and C. F. Curtiss (1954), *Molecular theory of gases and liquids*, John Wiley, doi:https://doi.org/10.1002/aic.690010225.

Black, G., H. Wise, S. Schechter, and R. L. Sharpless (1974), Measurements of vibrationally excited molecules by Raman scattering. II. Surface deactivation of vibrationally excited N_2, *The Journal of Chemical Physics*, *60*(9), 3526–3536, doi:https://doi.org/10.1063/1.1681570.

Blauer, J., and G. Nickerson (1973), A survey of vibrational relaxation rate data for processes important to CO_2-N_2-H_2O infrared plume radiation ultrasystems.

Blyholder, G., and H. Eyring (1957), Kinetics of graphite oxidation, *The Journal of Physical Chemistry*, *61*(5), 682–688, doi:https://doi.org/10.1021/j150551a039.

Bogaerts, A., and E. C. Neyts (2018), Plasma technology: An emerging technology for energy storage, *ACS Energy Letters*, *3*(4), 1013–1027, doi:https://doi.org/10.1021/acsenergylett.8b00184.

Bogaerts, A., W. Wang, A. Berthelot, and V. Guerra (2016), Modeling plasma-based CO_2 conversion: crucial role of the dissociation cross section, *Plasma Sources Science and Technology*, *25*(5), 055,016, doi:https://doi.org/10.1088/0963-0252/25/5/055016.

Bongers, W., H. Bouwmeester, B. Wolf, F. Peeters, S. Welzel, D. van den Bekerom, N. den Harder, A. Goede, M. Graswinckel, P. W. Groen, J. Kopecki, M. Leins, G. van Rooij, A. Schulz, M. Walker, and R. van de Sanden (2017), Plasma-driven dissociation of CO_2 for fuel synthesis, *Plasma Processes and Polymers*, *14*(6), 1600,126, doi:https://doi.org/10.1002/ppap.201600126.

Booth, J.-P. (2019), Atomic oxygen kinetic radius. *Private communication.*

Booth, J. P., and N. Sadeghi (1991), Oxygen and fluorine atom kinetics in electron cyclotron resonance plasmas by time-resolved actinometry, *Journal of Applied Physics*, *70*(2), 611–620, doi:https://doi.org/10.1063/1.349662.

Booth, J.-P., D. Marinov, M. Foucher, O. Guaitella, D. Bresteau, L. Cabaret, and C. Drag (2015), Gas temperature measurements in oxygen plasmas by high-resolution Two-Photon Absorption Laser-induced Fluorescence, *Journal of Instrumentation*, *10*(11), C11,003–C11,003, doi:https://doi.org/10.1088/1748-0221/10/11/c11003.

Booth, J. P., O. Guaitella, A. Chatterjee, C. Drag, V. Guerra, D. Lopaev, S. Zyryanov, T. Rakhimova, D. Voloshin, and Y. Mankelevich (2019), Oxygen (^{3}P) atom recombination on a Pyrex surface in an O_2 plasma, *Plasma Sources Science and Technology*, *28*(5), 055,005, doi:https://doi.org/10.1088/1361-6595/ab13e8.

Bouchoul, N., E. Fourré, J.-M. Tatibouët, and C. Batiot-Dupeyrat (2019), Plasma-catalytic dry reforming of CH_4 over calcium oxide: Catalyst structural and textural modifications, *Plasma Chemistry and Plasma Processing*, pp. 1–15, doi:https://doi.org/10.1007/s11090-019-09966-9.

Bousquet, A., G. Cartry, and A. Granier (2007), Investigation of O-atom kinetics in O_2, CO_2, H_2O and O_2/HMDSO low pressure radiofrequency pulsed plasmas by time-resolved optical emission spectroscopy, *Plasma Sources Science and Technology*, *16*(3), 597–605, doi:https://doi.org/10.1088/0963-0252/16/3/020.

Brehmer, F., S. Welzel, M. C. M. van de Sanden, and R. Engeln (2014), CO and by-product formation during CO_2 reduction in dielectric barrier discharges, *Journal of Applied Physics*, *116*(12), 123,303, doi:https://doi.org/10.1063/1.4896132.

Brehmer, F., S. Welzel, B. L. M. Klarenaar, H. J. van der Meiden, M. C. M. van de Sanden, and R. Engeln (2015), Gas temperature in transient CO_2 plasma measured by Raman scattering, *Journal of Physics D: Applied Physics*, *48*(15), 155,201, doi:https://doi.org/10.1088/0022-3727/48/15/155201.

Britun, N., G. Chen, T. Silva, T. Godfroid, M.-P. Delplancke-Ogletree, and R. Snyders (2017), Enhancing the greenhouse gas conversion efficiency in microwave discharges by power modulation, in *Green Chemical Processing and Synthesis*, edited by I. Karame and H. Srour, chap. 1, IntechOpen, doi:https://doi.org/10.5772/67875.

Britun, N., T. Silva, G. Chen, T. Godfroid, J. van der Mullen, and R. Snyders (2018), Plasma-assisted CO_2 conversion: Optimizing performance via microwave power modulation, *Journal of Physics D: Applied Physics*, *51*(14), 144,002, doi:https://doi.org/10.1088/1361-6463/aab1ad.

Brown, S. S., A. R. Ravishankara, and H. Stark (2000), Simultaneous kinetics and ring-down: Rate coefficients from single cavity loss temporal profiles, *The Journal of Physical Chemistry A*, *104*(30), 7044–7052, doi:https://doi.org/10.1021/jp0013715.

Buchwald, M. I., and G. J. Wolga (1975), Vibrational relaxation of CO_2(001) by atoms, *The Journal of Chemical Physics*, *62*(7), 2828–2832, doi:https://doi.org/10.1063/1.430819.

Busch, K. W., and M. A. Busch (1999), *Cavity-ring down spectroscopy: an ultratrace-absorption measurement technique*, ACS Publications, doi:https://doi.org/10.1021/bk-1999-0720.

Butterworth, T., R. Elder, and R. Allen (2016), Effects of particle size on CO_2 reduction and discharge characteristics in a packed bed plasma reactor, *Chemical Engineering Journal*, *293*, 55 – 67, doi:https://doi.org/10.1016/j.cej.2016.02.047.

Bykova, N., S. Vasil'evskii, A. Gordeev, A. F. Kolesnikov, I. Fershin, and M. Yakushin (1997), Determination of the effective probabilities of catalytic reactions on the surfaces of heat shield materials in dissociated carbon dioxide flows, *Fluid dynamics*, *32*(6), 876–886, doi:https://doi.org/10.1007/BF03374545.

Byron, S. R., and H. Apter (1992), Model of gas composition and plasma properties in sealed cw CO_2 lasers, *Journal of Applied Physics*, *71*(4), 1976–1991, doi:https://doi.org/10.1063/1.351162.

Cabaret, L., and C. Drag (2010), Highly scannable injection seeded nanosecond Ti:sapphire ring laser, *The European Physical Journal - Applied Physics*, *51*(2), 20,702, doi:https://doi.org/10.1051/epjap/2010089.

Capezzuto, P., F. Cramarossa, R. D'Agostino, and E. Molinari (1976), Contribution of vibrational excitation to the rate of carbon dioxide dissociation in electrical discharges, *The Journal of Physical Chemistry*, *80*(8), 882–888, doi:https://doi.org/10.1021/j100549a024.

Capitelli, M. (2012), *Nonequilibrium vibrational kinetics*, vol. 39, Springer Science & Business Media, doi:https://doi.org/10.1007/978-3-642-48615-9.

Capitelli, M., D. Bruno, and A. Laricchiuta (2013), *Fundamental aspects of plasma chemical physics*, vol. 74, Springer, doi:https://doi.org/10.1007/978-1-4419-8185-1.

Capitelli, M., G. Colonna, G. D'Ammando, and L. D. Pietanza (2017), Self-consistent time dependent vibrational and free electron kinetics for CO_2 dissociation and ionization in cold plasmas, *Plasma Sources Science and Technology*, *26*(5), 055,009, doi:https://doi.org/10.1088/1361-6595/aa6427.

Cartry, G., L. Magne, and G. Cernogora (1999), Atomic oxygen recombination on fused silica: experimental evidence of the surface state influence, *Journal of Physics D: Applied Physics*, *32*(15), L53–L56, doi:https://doi.org/10.1088/0022-3727/32/15/101.

Cartry, G., L. Magne, and G. Cernogora (2000), Atomic oxygen recombination on fused silica: modelling and comparison to low-temperature experiments (300 K), *Journal of Physics D: Applied Physics*, *33*(11), 1303–1314, doi:https://doi.org/10.1088/0022-3727/33/11/309.

Cartry, G., X. Duten, and A. Rousseau (2006), Atomic oxygen surface loss probability on silica in microwave plasmas studied by a pulsed induced fluorescence technique, *Plasma Sources Science and Technology*, *15*(3), 479–488, doi:https://doi.org/10.1088/0963-0252/15/3/025.

Castle, K. J., K. M. Kleissas, J. M. Rhinehart, E. S. Hwang, and J. A. Dodd (2006), Vibrational relaxation of $CO_2(\nu_2)$ by atomic oxygen, *Journal of Geophysical Research: Space Physics*, *111*(A9), doi:https://doi.org/10.1029/2006JA011736.

Castle, K. J., L. A. Black, M. W. Simione, and J. A. Dodd (2012), Vibrational relaxation of $CO_2(\nu_2)$ by $O(^3P)$ in the 142–490 K temperature range, *Journal of Geophysical Research: Space Physics*, *117*(A4), doi:https://doi.org/10.1029/2012JA017519.

Cenian, A., A. Chernukho, V. Borodin, and G. Śliwiński (1994), Modeling of plasma-chemical reactions in gas mixture of CO_2 lasers I. Gas decomposition in pure CO_2 glow discharge, *Contributions to Plasma Physics*, *34*(1), 25–37, doi:https://doi.org/10.1002/ctpp.2150340105.

Cenian, A., A. Chernukho, and V. Borodin (1995), Modeling of plasma-chemical reactions in gas mixture of CO_2 lasers. II. Theoretical model and its verification, *Contributions to Plasma Physics*, *35*(3), 273–296, doi:https://doi.org/10.1002/ctpp.2150350309.

Center, R. E. (1973), Vibrational relaxation of CO by O atoms, *The Journal of Chemical Physics*, *58*(12), 5230–5236, doi:https://doi.org/10.1063/1.1679135.

Centi, G., and S. Perathoner (2009), Opportunities and prospects in the chemical recycling of carbon dioxide to fuels, *Catalysis Today*, *148*(3), 191 – 205, doi:https://doi.org/10.1016/j.cattod.2009.07.075.

Chantry, P. J. (1987), A simple formula for diffusion calculations involving wall reflection and low density, *Journal of Applied Physics*, *62*(4), 1141–1148, doi:https://doi.org/10.1063/1.339662.

Chedin, A. (1979), The carbon dioxide molecule: Potential, spectroscopic, and molecular constants from its infrared spectrum, *Journal of Molecular Spectroscopy*, *76*(1), 430 – 491, doi:https://doi.org/10.1016/0022-2852(79)90236-4.

Chen, F. F., and J. P. Chang (2012), *Lecture notes on principles of plasma processing*, Springer Science & Business Media, doi:https://doi.org/10.1007/978-1-4615-0181-7.

Chen, G., N. Britun, T. Godfroid, V. Georgieva, R. Snyders, and M.-P. Delplancke-Ogletree (2017a), An overview of CO_2 conversion in a microwave discharge: the role of plasma-catalysis, *Journal of Physics D: Applied Physics*, *50*(8), 084,001, doi:https://doi.org/10.1088/1361-6463/aa5616.

Chen, G., T. Godfroid, N. Britun, V. Georgieva, M.-P. Delplancke-Ogletree, and R. Snyders (2017b), Plasma-catalytic conversion of CO_2 and CO_2/H_2O in a surface-wave sustained microwave discharge, *Applied Catalysis B: Environmental*, *214*, 114 – 125, doi:https://doi.org/10.1016/j.apcatb.2017.05.032.

Chen, H., Y. Mu, Y. Shao, S. Chansai, S. Xu, C. E. Stere, H. Xiang, R. Zhang, Y. Jiao, C. Hardacre, and X. Fan (2019), Coupling non-thermal plasma with Ni catalysts supported on BETA zeolite for catalytic CO_2 methanation, *Catal. Sci. Technol.*, *9*, 4135–4145, doi:https://doi.org/10.1039/C9CY00590K.

Chen, H.-F., H.-C. Chiang, H. Matsui, S. Tsuchiya, and Y.-P. Lee (2009), Distribution of vibrational states of CO_2 in the reaction $O(^1D)+CO_2$ from time-resolved Fourier transform infrared emission spectra, *The Journal of Physical Chemistry A*, *113*(15), 3431–3437, doi:https://doi.org/10.1021/jp807501c.

Coburn, J. W., and M. Chen (1980), Optical emission spectroscopy of reactive plasmas: A method for correlating emission intensities to reactive particle density, *Journal of Applied Physics*, *51*(6), 3134–3136, doi:https://doi.org/10.1063/1.328060.

Colonna, G., I. Armenise, D. Bruno, and M. Capitelli (2006), Reduction of state-to-state kinetics to macroscopic models in hypersonic flows, *Journal of Thermophysics and Heat Transfer*, *20*(3), 477–486, doi:https://doi.org/10.2514/1.18377.

Corvin, K. K., and S. J. B. Corrigan (1969), Dissociation of carbon dioxide in the positive column of a glow discharge, *The Journal of Chemical Physics*, *50*(6), 2570–2574, doi:https://doi.org/10.1063/1.1671416.

Cosby, P. C., and H. Helm (1992), Dissociation rates of diatomic molecules.

Cramp, J., and J. Lambert (1973), Vibrational relaxation of $CO_2(\nu_3)$ by O atoms, *Chemical Physics Letters*, *22*(1), 146 – 149, doi:https://doi.org/10.1016/0009-2614(73)80555-X.

Dagdigian, P. J., B. E. Forch, and A. W. Miziolek (1988), Collisional transfer between and quenching of the 3p 3P and 5P states of the oxygen atom, *Chemical Physics Letters*, *148*(4), 299 – 308, doi:https://doi.org/10.1016/0009-2614(88)87276-2.

Dang, C., J. Reid, and B. K. Garside (1982), Detailed vibrational population distributions in a CO_2 laser discharge as measured with a tunable diode laser, *Applied Physics B*, *27*(3), 145–151, doi:https://doi.org/10.1007/BF00694640.

Dang, C., J. Reid, and B. Garside (1983), Dynamics of the CO_2 upper laser level as measured with a tunable diode laser, *IEEE Journal of Quantum Electronics*, *19*(4), 755–764, doi:https://doi.org/10.1109/JQE.1983.1071913.

Davidson, J. A., H. I. Schiff, T. J. Brown, and C. J. Howard (1978), Temperature dependence of the deactivation of $O(^1D)$ by CO from 113–333 K, *The Journal of Chemical Physics*, *69*(3), 1216–1217, doi:https://doi.org/10.1063/1.436657.

Davies, P. B., and P. A. Martin (1990), Diode-laser spectroscopy of $a^3\pi$ CO, *Molecular Physics*, *70*(1), 89–106, doi:https://doi.org/10.1080/00268979000100861.

de la Fuente, J. F., S. H. Moreno, A. I. Stankiewicz, and G. D. Stefanidis (2016), A new methodology for the reduction of vibrational kinetics in non-equilibrium microwave plasma: application to CO_2 dissociation, *React. Chem. Eng.*, *1*, 540–554, doi:https://doi.org/10.1039/C6RE00044D.

de la Fuente, J. F., S. H. Moreno, A. I. Stankiewicz, and G. D. Stefanidis (2017), On the improvement of chemical conversion in a surface-wave microwave plasma reactor for CO_2 reduction with hydrogen (The reverse water-gas shift reaction), *International Journal of Hydrogen Energy*, *42*(18), 12,943 – 12,955, doi:https://doi.org/10.1016/j.ijhydene.2017.04.040.

de Lara-Castells, M. P., M. I. Hernández, G. Delgado-Barrio, P. Villarreal, and M. López-Puertas (2006), Vibrational quenching of $CO_2(010)$ by collisions with $O(^3P)$ at thermal energies: A quantum-mechanical study, *The Journal of Chemical Physics*, *124*(16), 164,302, doi:https://doi.org/10.1063/1.2189860.

de Petris, G., A. Cartoni, M. Rosi, A. Troiani, G. Angelini, and O. Ursini (2004), Isotope exchange in ionised CO_2/CO mixtures: The role of asymmetrical $C_2O_3^+$ ions, *Chemistry – A European Journal*, *10*(24), 6411–6421, doi:https://doi.org/10.1002/chem.200400483.

Dębek, R., F. Azzolina-Jury, A. Travert, F. Maugé, and F. Thibault-Starzyk (2019), Low-pressure glow discharge plasma-assisted catalytic CO_2 hydrogenation-The effect of metal oxide support on the performance of the Ni-based catalyst, *Catalysis Today*, *337*, 182 – 194, doi:https://doi.org/10.1016/j.cattod.2019.03.039.

DeMore, W., S. Sander, R. Hampson, M. Kurylo, D. Golden, C. Howard, A. Ravishankara, and M. Molina (1990), Chemical kinetics and photochemical data for use in stratospheric modeling, eval. 9, jpl publ. 90-1, *Jet Propulsion Lab., Pasadena, Calif.*

DeMore, W. B., and C. Dede (1970), Pressure dependence of carbon trioxide formation in the gas-phase reaction of $O(^1D)$ with carbon dioxide, *The Journal of Physical Chemistry*, *74*(13), 2621–2625, doi:https://doi.org/10.1021/j100707a006.

den Harder, N., D. C. M. van den Bekerom, R. S. Al, M. F. Graswinckel, J. M. Palomares, F. J. J. Peeters, S. Ponduri, T. Minea, W. A. Bongers, M. C. M. van de Sanden, and G. J. van Rooij (2017), Homogeneous CO_2 conversion by microwave plasma: Wave propagation and diagnostics, *Plasma Processes and Polymers*, *14*(6), 1600,120, doi:https://doi.org/10.1002/ppap.201600120.

Depraz, S., M. Perrin, P. Rivière, and A. Soufiani (2012a), Infrared emission spectroscopy of CO_2 at high temperature. Part II: Experimental results and comparisons with spectroscopic databases, *Journal of Quantitative Spectroscopy and Radiative Transfer*, *113*(1), 14 – 25, doi:https://doi.org/10.1016/j.jqsrt.2011.09.013.

Depraz, S., M. Perrin, and A. Soufiani (2012b), Infrared emission spectroscopy of CO_2 at high temperature. Part I: Experimental setup and source characterization, *Journal of Quantitative Spectroscopy and Radiative Transfer*, *113*(1), 1 – 13, doi:https://doi.org/10.1016/j.jqsrt.2011.09.002.

Diomede, P., M. C. M. van de Sanden, and S. Longo (2018), Vibrational kinetics in plasma as a functional problem: A flux-matching approach, *The Journal of Physical Chemistry A*, *122*(39), 7918–7923, doi:https://doi.org/10.1021/acs.jpca.8b05623.

Donahue, T. M. (1971), Aeronomy of CO_2 atmospheres: A review, *Journal of the Atmospheric Sciences*, *28*(6), 895–900, doi:https://doi.org/10.1175/1520-0469(1971)028⟨0895:AOCAAR⟩2.0.CO;2.

Donnelly, V. M., J. Guha, and L. Stafford (2011), Critical review: Plasma-surface reactions and the spinning wall method, *Journal of Vacuum Science & Technology A*, *29*(1), 010,801, doi:https://doi.org/10.1116/1.3517478.

Doyennette, L., M. Margottin-Maclou, H. Gueguen, A. Carion, and L. Henry (1974), Temperature dependence of the diffusion and accommodation coefficients in nitrous oxide and carbon dioxide excited into the (00^01) vibrational level, *The Journal of Chemical Physics*, *60*(2), 697–702, doi:https://doi.org/10.1063/1.1681095.

Drag, C. *et al.* (2020), Direct measurement of two-photon excitation cross section of Xe by absorption. *In preparation.*

Duan, X., Y. Li, W. Ge, and B. Wang (2015), Degradation of CO_2 through dielectric barrier discharge microplasma, *Greenhouse Gases: Science and Technology*, *5*(2), 131–140, doi:https://doi.org/10.1002/ghg.1425.

Dumitrache, C., A. Gallant, N. Minesi, S. Stepanyan, G. D. Stancu, and C. O. Laux (2019), Hydrodynamic regimes induced by nanosecond pulsed discharges in air: Mechanism of vorticity generation, *Journal of Physics D: Applied Physics*, *52*(36), 364,001, doi:https://doi.org/10.1088/1361-6463/ab28f9.

Esposito, F., I. Armenise, G. Capitta, and M. Capitelli (2008), O–O_2 state-to-state vibrational relaxation and dissociation rates based on quasiclassical calculations, *Chemical Physics*, *351*(1), 91 – 98, doi:https://doi.org/10.1016/j.chemphys.2008.04.004.

Essenhigh, K. A., Y. G. Utkin, C. Bernard, I. V. Adamovich, and J. W. Rich (2006), Gas-phase boudouard disproportionation reaction between highly vibrationally excited CO molecules, *Chemical Physics*, *330*(3), 506 – 514, doi:https://doi.org/10.1016/j.chemphys.2006.09.033.

ETH Zurich (2018), ETH Zurich, High Voltage Laboratory database, available in LXCat, www.lxcat.net, retrieved on September 27, 2018.

Fahmy, A., and A. Schönhals (2016), Reaction of CO_2 gas with (radicals in) plasma-polymerized acrylic acid (and formation of COOH-rich polymer layers), *Plasma Processes and Polymers*, *13*(5), 499–508, doi:https://doi.org/10.1002/ppap.201500128.

Feofilov, A., A. Kutepov, C.-Y. She, A. Smith, W. Pesnell, and R. Goldberg (2012), $CO_2(\nu_2)$-O quenching rate coefficient derived from coincidental SABER/TIMED and Fort Collins lidar observations of the mesosphere and lower thermosphere, *Atmospheric Chemistry and Physics*, *12*(19), 9013–9023, doi:https://doi.org/10.5194/acpd-11-32583-2011.

Flament, C., T. George, K. Meister, J. Tufts, J. Rich, V. Subramaniam, J.-P. Martin, B. Piar, and M.-Y. Perrin (1992), Nonequilibrium vibrational kinetics of carbon monoxide at high translational mode temperatures, *Chemical Physics*, *163*(2), 241 – 262, doi:https://doi.org/10.1016/0301-0104(92)87106-J.

Fox, J. L., and A. Dalgarno (1979), Ionization, luminosity, and heating of the upper atmosphere of Mars, *Journal of Geophysical Research: Space Physics*, *84*(A12), 7315–7333, doi:https://doi.org/10.1029/JA084iA12p07315.

Fridman, A. (2008), *Plasma Chemistry*, Cambridge University Ppress, doi:https://doi.org/10.1017/CBO9780511546075.

Gancarz, I., G. Poźniak, and M. Bryjak (1999), Modification of polysulfone membranes 1. CO_2 plasma treatment, *European Polymer Journal*, *35*(8), 1419 – 1428, doi:https://doi.org/10.1016/S0014-3057(98)00240-7.

Gao, L.-f., S.-m. Xiong, B.-c. Li, and Y.-d. Zhang (2005), High reflectivity measurement with cavity ring-down technique, in *Advances in Optical Thin Films II*, vol. 5963, pp. 660 – 667, International Society for Optics and Photonics, SPIE, doi:https://doi.org/10.1117/12.627774.

Gibson, A. R., M. Foucher, D. Marinov, P. Chabert, T. Gans, M. J. Kushner, and J.-P. Booth (2017), The role of thermal energy accommodation and atomic recombination probabilities in low pressure oxygen plasmas, *Plasma Physics and Controlled Fusion*, *59*(2), 024,004, doi:https://doi.org/10.1088/1361-6587/59/2/024004.

Gilijamse, J. J., S. Hoekstra, S. A. Meek, M. Metsälä, S. Y. T. van de Meerakker, G. Meijer, and G. C. Groenenboom (2007), The radiative lifetime of metastable CO($a^3\pi$, ν=0), *The Journal of Chemical Physics*, *127*(22), 221,102, doi:https://doi.org/10.1063/1.2813888.

Gleit, C., W. Holland, and R. Wrigley (1963), Reaction kinetics of the atomic oxygen-graphite system, *Nature*, *200*(4901), 69–69, doi:https://doi.org/10.1038/200069a0.

Godyak, V. A., and R. B. Piejak (1990), In situ simultaneous radio frequency discharge power measurements, *Journal of Vacuum Science & Technology A*, *8*(5), 3833–3837, doi:https://doi.org/10.1116/1.576457.

Goehlich, A., T. Kawetzki, and H. F. Döbele (1998), On absolute calibration with xenon of laser diagnostic methods based on two-photon absorption, *The Journal of Chemical Physics*, *108*(22), 9362–9370, doi:https://doi.org/10.1063/1.476388.

Gokus, T., R. R. Nair, A. Bonetti, M. Böhmler, A. Lombardo, K. S. Novoselov, A. K. Geim, A. C. Ferrari, and A. Hartschuh (2009), Making graphene luminescent by oxygen plasma treatment, *ACS Nano*, *3*(12), 3963–3968, doi:https://doi.org/10.1021/nn9012753.

Gordiets, B. F., and C. M. Ferreira (1998), Self-consistent modeling of volume and surface processes in air plasma, *AIAA Journal*, *36*(9), 1643–1651, doi:https://doi.org/10.2514/2.566.

Gordiets, B. F., and S. S. Mamedov (1975), Isotope separation in chemical reactions of vibrationally excited molecules, *Soviet Journal of Quantum Electronics*, *5*(9), 1082–1084, doi:https://doi.org/10.1070/qe1975v005n09abeh011907.

Gordiets, B. F., C. M. Ferreira, V. L. Guerra, J. M. A. H. Loureiro, J. Nahorny, D. Pagnon, M. Touzeau, and M. Vialle (1995), Kinetic model of a low-pressure N_2-O_2 flowing glow discharge, *IEEE Transactions on Plasma Science*, *23*(4), 750–768, doi:https://doi.org/10.1109/27.467998.

Gordon, I., L. Rothman, C. Hill, R. Kochanov, Y. Tan, P. Bernath, et al. (2017), The HITRAN2016 molecular spectroscopic database, *Journal of Quantitative Spectroscopy and Radiative Transfer*, *203*, 3 – 69, doi:https://doi.org/10.1016/j.jqsrt.2017.06.038.

Gordon, S., B. McBride, and F. J. Zeleznik (1984), Computer program for calculation of complex chemical equilibrium compositions and applications. Supplement 1: Transport properties.

Gorse, C., and M. Capitelli (1984), Kinetic processes in non-equilibrium carbon monoxide discharges. II. Self-consistent electron energy distribution functions, *Chemical Physics*, *85*(2), 177 – 187, doi:https://doi.org/10.1016/0301-0104(84)85031-4.

Grangeon, F., C. Monard, J.-L. Dorier, A. A. Howling, C. Hollenstein, D. Romanini, and N. Sadeghi (1999), Applications of the cavity ring-down technique to a large-area RF-plasma reactor, *Plasma Sources Science and Technology*, *8*(3), 448–456, doi:https://doi.org/10.1088/0963-0252/8/3/315.

Graves, C., S. D. Ebbesen, M. Mogensen, and L. K. S. (2011), Sustainable hydrocarbon fuels by recycling CO_2 and H_2O with renewable or nuclear energy, *Renewable and Sustainable Energy Reviews*, *15*(1), 1 – 23, doi:https://doi.org/10.1016/j.rser.2010.07.014.

Greaves, J. C., and J. W. Linnett (1959), Recombination of atoms at surfaces. Part 6. Recombination of oxygen atoms on silica from 20^0c to 600^0C, *Transactions of the Faraday Society*, *55*, 1355–1361, doi:https://doi.org/10.1039/TF9595501355.

Grofulović, M. (2019), Energy storage and transfer in non-equilibrium CO_2 plasmas, Ph.D. thesis, Instituto Superior Técnico, Technical University of Eindhoven.

Grofulović, M., L. L. Alves, and V. Guerra (2016), Electron-neutral scattering cross sections for CO_2: A complete and consistent set and an assessment of dissociation, *Journal of Physics D: Applied Physics*, *49*(39), 395,207, doi:https://doi.org/10.1088/0022-3727/49/39/395207.

Grofulović, M., T. Silva, B. L. M. Klarenaar, A. S. Morillo-Candas, O. Guaitella, R. Engeln, C. D. Pintassilgo, and V. Guerra (2018), Kinetic study of CO_2 plasmas under non-equilibrium conditions. II. Input of vibrational energy, *Plasma Sources Science and Technology*, *27*(11), 115,009, doi:https://doi.org/10.1088/1361-6595/aadb60.

Grofulović, M., B. L. M. Klarenaar, O. Guaitella, V. Guerra, and R. Engeln (2019), A rotational Raman study under non-thermal conditions in pulsed CO_2–N_2 and CO_2–O_2 glow discharges, *Plasma Sources Science and Technology*, *28*(4), 045,014, doi:https://doi.org/10.1088/1361-6595/ab1240.

Guerra, V. (2007), Analytical model of heterogeneous atomic recombination on silicalike surfaces, *IEEE Transactions on Plasma Science*, *35*(5), 1397–1412, doi:https://doi.org/10.1109/TPS.2007.902028.

Guerra, V., and D. Marinov (2016), Dynamical Monte Carlo methods for plasma-surface reactions, *Plasma Sources Science and Technology*, *25*(4), 045,001, doi:https://doi.org/10.1088/0963-0252/25/4/045001.

Guerra, V., P. A. Sá, and J. Loureiro (2003), Electron and metastable kinetics in the nitrogen afterglow, *Plasma Sources Science and Technology*, *12*(4), S8–S15, doi:https://doi.org/10.1088/0963-0252/12/4/314.

Guerra, V., D. Marinov, O. Guaitella, and A. Rousseau (2014), NO oxidation on plasma pretreated Pyrex: the case for a distribution of reactivity of adsorbed o atoms, *Journal of Physics D: Applied Physics*, *47*(22), 224,012, doi:https://doi.org/10.1088/0022-3727/47/22/224012.

Guerra, V., T. Silva, P. Ogloblina, M. Grofulović, L. Terraz, M. L. da Silva, C. D. Pintassilgo, L. L. Alves, and O. Guaitella (2017), The case for *in situ* resource utilisation for oxygen production on Mars by non-equilibrium plasmas, *Plasma Sources Science and Technology*, *26*(11), 11LT01, doi:https://doi.org/10.1088/1361-6595/aa8dcc.

Guerra, V., A. Tejero-del Caz, C. D. Pintassilgo, and L. L. Alves (2019), Modelling N_2–O_2 plasmas: volume and surface kinetics, *Plasma Sources Science and Technology*, *28*(7), 073,001, doi:https://doi.org/10.1088/1361-6595/ab252c.

Guerra, V. *et al.*. (2019), Cross sections for CO electron impact excitation. IST-Lisbon database. *Private communication.*

Gusev, O., M. Kaufmann, K.-U. Grossmann, F. Schmidlin, and M. Shepherd (2006), Atmospheric neutral temperature distribution at the mesopause altitude, *Journal of Atmospheric and Solar-Terrestrial Physics*, *68*(15), 1684 – 1697, doi:https://doi.org/10.1016/j.jastp.2005.12.010.

Hagelaar, G. J. M., and L. C. Pitchford (2005), Solving the Boltzmann equation to obtain electron transport coefficients and rate coefficients for fluid models, *Plasma Sources Science and Technology*, *14*(4), 722–733, doi:https://doi.org/10.1088/0963-0252/14/4/011.

Hahn, J. (2005), Kinetic study of graphite oxidation along two lattice directions, *Carbon*, *43*(7), 1506 – 1511, doi:https://doi.org/10.1016/j.carbon.2005.01.032.

Hake, R. D., and A. V. Phelps (1967), Momentum-transfer and inelastic-collision cross sections for electrons in O_2, CO and CO_2, *Physical Review*, *158*, 70–84, doi:https://doi.org/10.1103/PhysRev.158.70.

Halmann, M. M. (2018), *Chemical Fixation of Carbon Dioxide Methods for Recycling CO_2 into Useful Products*, CRC press, doi:https://doi.org/10.1201/9781315139098.

Harding, D. R., R. E. Weston, and G. W. Flynn (1988), Energy transfer to CO(ν) in the O(^{1}D)+CO($^1\Sigma_g^+$) reaction, *The Journal of Chemical Physics*, *88*(6), 3590–3598, doi:https://doi.org/10.1063/1.453908.

Hedman, P. O., and A. J. McDonald (1965), Erosion of graphite in solid-propellant combustion gases and effects on heat-transfer, *AIAA Journal*, *3*(7), 1250–1257, doi:https://doi.org/10.2514/3.3117.

Heijkers, S., R. Snoeckx, T. Kozák, T. Silva, T. Godfroid, N. Britun, R. Snyders, and A. Bogaerts (2015), CO_2 conversion in a microwave plasma reactor in the presence of N_2: Elucidating the role of vibrational levels, *The Journal of Physical Chemistry C*, *119*(23), 12,815–12,828, doi:https://doi.org/10.1021/acs.jpcc.5b01466.

Heijkers, S., L. M. Martini, G. Dilecce, P. Tosi, and A. Bogaerts (2019), Nanosecond pulsed discharge for CO_2 conversion: Kinetic modeling to elucidate the chemistry and improve the performance, *The Journal of Physical Chemistry C*, *123*(19), 12,104–12,116, doi:https://doi.org/10.1021/acs.jpcc.9b01543.

Herdrich, G., M. Auweter-Kurtz, H. L. Kurtz, T. Laux, and M. Winter (2002), Operational behavior of inductively heated plasma source IPG3 for entry simulations, *Journal of Thermophysics and Heat Transfer*, *16*(3), 440–449, doi:https://doi.org/10.2514/2.6698.

Herzberg, G. (1950), *Molecular spectra and molecular structure. Vol. 1: Spectra of diatomic molecules*, Van Nostrand Reinhold.

Herzberg, G. (1966), *Molecular Spectra and Molecular Structure: III Electronic structure of polyatomic molecules*, Van Nostrand Reinhold.

Herzberg, G. (1991), *Electronic spectra and electronic structure of polyatomic molecules*, vol. 2, Krieger Publishing Company.

Holland, L., and S. Ojha (1976), The chemical sputtering of graphite in an oxygen plasma, *Vacuum*, *26*(2), 53 – 60, doi:https://doi.org/10.1016/S0042-207X(76)80624-0.

Horiguchi, H., R. S. F. Chang, and D. W. Setser (1981), Radiative lifetimes and two-body collisional deactivation rate constants in Ar for Xe($5p^5 6p$), Xe($5p^5 6p$), and Xe($5p^5 7p$) states, *The Journal of Chemical Physics*, *75*(3), 1207–1218, doi:https://doi.org/10.1063/1.442169.

Hoskins, L. C. (1975), Pure rotational Raman spectroscopy of diatomic molecules, *Journal of Chemical Education*, *52*(9), 568, doi:https://doi.org/10.1021/ed052p568.

Houston, P. L., and R. P. Merrill (1988), Gas-surface interactions with vibrationally excited molecules, *Chemical Reviews*, *88*(4), 657–671, doi:https://doi.org/10.1021/cr00086a005.

Huang, Q., D. Zhang, D. Wang, K. Liu, and A. W. Kleyn (2017), Carbon dioxide dissociation in non-thermal radiofrequency and microwave plasma, *Journal of Physics D: Applied Physics*, *50*(29), 294,001, doi:https://doi.org/10.1088/1361-6463/aa754e.

Huang, X., D. W. Schwenke, S. A. Tashkun, and T. J. Lee (2012), An isotopic-independent highly accurate potential energy surface for CO_2 isotopologues and an initial $^{12}C^{16}O_2$ infrared line list, *The Journal of Chemical Physics*, *136*(12), 124,311, doi:https://doi.org/10.1063/1.3697540.

Huddleston, R., and E. Weitz (1981), A laser-induced fluorescence study of energy transfer between the symmetric stretching and bending modes of CO_2, *Chemical Physics Letters*, *83*(1), 174 – 179, doi:https://doi.org/10.1016/0009-2614(81)80314-4.

Hueso, J., J. Espinós, A. Caballero, J. Cotrino, and A. González-Elipe (2007), XPS investigation of the reaction of carbon with NO, O_2, N_2 and H_2O plasmas, *Carbon*, *45*(1), 89 – 96, doi:https://doi.org/10.1016/j.carbon.2006.07.021.

Huestis, D., J. Marschall, G. Billing, and R. Maclagan (2002), Theoretical and experimental studies of O-CO_2 collisions, in *AGU Fall Meeting Abstracts*.

Huff, A. K., and M. H. Thiemens (1998), $^{17}O/^{16}O$ and $^{18}O/^{16}O$ isotope measurements of atmospheric carbon monoxide and its sources, *Geophysical Research Letters*, *25*(18), 3509–3512, doi:https://doi.org/10.1029/98GL02603.

Indarto, A., D. R. Yang, J.-W. Choi, H. Lee, and H. K. Song (2007), Gliding arc plasma processing of CO_2 conversion, *Journal of Hazardous Materials*, *146*(1), 309 – 315, doi:https://doi.org/10.1016/j.jhazmat.2006.12.023.

IST-LXCat (2018), IST-Lisbon database, available in LXCat, www.lxcat.net, retrieved on 16 August, 2018.

Itikawa, Y., and N. Mason (2005), Cross sections for electron collisions with water molecules, *Journal of Physical and Chemical Reference Data*, *34*(1), 1–22, doi:https://doi.org/10.1063/1.1799251.

Janssen, C., and B. Tuzson (2010), Isotope evidence for ozone formation on surfaces, *The Journal of Physical Chemistry A*, *114*(36), 9709–9719, doi:https://doi.org/10.1021/jp1017899.

Jones, J.-P., G. K. S. Prakash, and G. A. Olah (2014), Electrochemical CO_2 reduction: Recent advances and current trends, *Israel Journal of Chemistry*, *54*(10), 1451–1466, doi:https://doi.org/10.1002/ijch.201400081.

Katakis, D., and H. Taube (1962), Some photochemical reactions of O_3 in the gas phase, *The Journal of Chemical Physics*, *36*(2), 416–422, doi:https://doi.org/10.1063/1.1732521.

Katsch, H. M., A. Tewes, E. Quandt, A. Goehlich, T. Kawetzki, and H. F. Döbele (2000), Detection of atomic oxygen: Improvement of actinometry and comparison with laser spectroscopy, *Journal of Applied Physics*, *88*(11), 6232–6238, doi:https://doi.org/10.1063/1.1315332.

Khvorostovskaya, L., I. Potekhin, G. Shved, V. Ogibalov, and T. Uzyukova (2002), Measurement of the rate constant for quenching $CO_2(01^10)$ by atomic oxygen at low temperatures: Reassessment of the rate of cooling by the CO_2 15-μm emission in the lower thermosphere, *Izvestiya - Atmospheric and Oceanic Physics*, *38*, 613–624.

Kim, Y. C., and M. Boudart (1991), Recombination of oxygen, nitrogen, and hydrogen atoms on silica: kinetics and mechanism, *Langmuir*, *7*(12), 2999–3005, doi:https://doi.org/10.1021/la00060a016.

Klarenaar, B. L. (2018), Vibrational kinetics of CO_2 in non-thermal plasma, Ph.D. thesis, Technical University of Eindhoven.

Klarenaar, B. L. M., F. Brehmer, S. Welzel, H. J. van der Meiden, M. C. M. van de Sanden, and R. Engeln (2015), Note: Rotational Raman scattering on CO_2 plasma using a volume Bragg grating as a notch filter, *Review of Scientific Instruments*, *86*(4), 046,106, doi:https://doi.org/10.1063/1.4918730.

Klarenaar, B. L. M., R. Engeln, D. C. M. van den Bekerom, M. C. M. van de Sanden, A. S. Morillo-Candas, and O. Guaitella (2017), Time evolution of vibrational temperatures in a CO_2 glow discharge measured with infrared absorption spectroscopy, *Plasma Sources Science and Technology*, *26*(11), 115,008, doi:https://doi.org/10.1088/1361-6595/aa902e.

Klarenaar, B. L. M., M. Grofulović, A. S. Morillo-Candas, D. C. M. van den Bekerom, M. A. Damen, M. C. M. van de Sanden, O. Guaitella, and R. Engeln (2018), A rotational Raman study under non-thermal conditions in a pulsed CO_2 glow discharge, *Plasma Sources Science and Technology*, *27*(4), 045,009, doi:https://doi.org/10.1088/1361-6595/aabab6.

Klarenaar, B. L. M., A. S. Morillo-Candas, M. Grofulović, M. C. M. van de Sanden, R. Engeln, and O. Guaitella (2019), Excitation and relaxation of the asymmetric stretch mode of CO_2 in a pulsed glow discharge, *Plasma Sources Science and Technology*, *28*(3), 035,011, doi:https://doi.org/10.1088/1361-6595/aada5e.

Koelman, P., S. Heijkers, S. Tadayon Mousavi, W. Graef, D. Mihailova, T. Kozak, A. Bogaerts, and J. van Dijk (2017), A comprehensive chemical model for the splitting of CO_2 in non-equilibrium plasmas, *Plasma Processes and Polymers*, *14*(4-5), 1600,155, doi:https://doi.org/10.1002/ppap.201600155.

Koelman, P., D. Yordanova, W. Graef, S. T. Mousavi, and J. van Dijk (2019), Uncertainty analysis with a reduced set of input uncertainties selected using pathway analysis, *Plasma Sources Science and Technology*, *28*(7), 075,009, doi:https://doi.org/10.1088/1361-6595/ab0738.

Koizumi, K., M. Boero, Y. Shigeta, and A. Oshiyama (2013), Atom-scale reaction pathways and free-energy landscapes in oxygen plasma etching of graphene, *The Journal of Physical Chemistry Letters*, *4*(10), 1592–1596, doi:https://doi.org/10.1021/jz400666h.

Kolesnikov, A. F., I. S. Pershin, S. A. Vasil'evskii, and M. I. Yakushin (2000), Study of quartz surface catalycity in dissociated carbon dioxide subsonic flows, *Journal of Spacecraft and Rockets*, *37*(5), 573–579, doi:https://doi.org/10.2514/2.3629.

Kono, M., Y. He, K. G. H. Baldwin, and B. J. Orr (2016), Sub-Doppler two-photon-excitation Rydberg spectroscopy of atomic xenon: mass-selective studies of isotopic and hyperfine structure, *Journal of Physics B: Atomic, Molecular and Optical Physics*, *49*(6), 065,002, doi:https://doi.org/10.1088/0953-4075/49/6/065002.

Korolov, I., Z. Donkó, G. Hübner, L. Bischoff, P. Hartmann, T. Gans, Y. Liu, T. Mussenbrock, and J. Schulze (2019), Control of electron dynamics, radical and metastable species generation in atmospheric pressure RF plasma jets by Voltage Waveform Tailoring, *Plasma Sources Science and Technology*, *28*(9), 094,001, doi:https://doi.org/10.1088/1361-6595/ab38ea.

Kovacs, M., D. Ramachandra Rao, and A. Javan (1968), Study of diffusion and wall de-excitation probability of (00^01) state in CO_2, *The Journal of Chemical Physics*, *48*(7), 3339–3341, doi:https://doi.org/10.1063/1.3000461.

Kovalev, V., N. Afonina, and V. Gromov (2005), Heat transfer modelling to catalytic protection systems of space vehicles entering into martian atmosphere, in *Shock Waves*, pp. 597–602, Springer, doi:https://doi.org/10.1007/978-3-540-27009-6_89.

Kozák, T., and A. Bogaerts (2014a), Splitting of CO_2 by vibrational excitation in non-equilibrium plasmas: a reaction kinetics model, *Plasma Sources Science and Technology*, *23*(4), 045,004, doi:https://doi.org/10.1088/0963-0252/23/4/045004.

Kozák, T., and A. Bogaerts (2014b), Evaluation of the energy efficiency of CO_2 conversion in microwave discharges using a reaction kinetics model, *Plasma Sources Science and Technology*, *24*(1), 015,024, doi:https://doi.org/10.1088/0963-0252/24/1/015024.

Kramida, A., Yu.Ralchenko, J.Reader, and and NIST ASD Team (2018), NIST Atomic Spectra Database (ver. 5.5.6), Available: https://physics.nist.gov/asd [2018, August 30]. National Institute of Standards and Technology, Gaithersburg, MD.

Krauss, M., S. R. Mielczarek, D. Neumann, and C. E. Kuyatt (1971), Mechanism for production of the fourth positive band system of CO by electron impact on CO_2, *Journal of Geophysical Research (1896-1977)*, *76*(16), 3733–3737, doi:https://doi.org/10.1029/JA076i016p03733.

Krupenie, P. H. (1972), The spectrum of molecular oxygen, *Journal of Physical and Chemical Reference Data*, *1*(2), 423–534, doi:https://doi.org/10.1063/1.3253101.

Kunze, H.-J. (2009), *Introduction to plasma spectroscopy*, vol. 56, Springer Science & Business Media, doi:https://doi.org/10.1007/978-3-642-02233-3.

Kustova, E., M. Mekhonoshina, and A. Kosareva (2019), Relaxation processes in carbon dioxide, *Physics of Fluids*, *31*(4), 046,104, doi:https://doi.org/10.1063/1.5093141.

Kutasi, K., V. Guerra, and P. Sá (2010), Theoretical insight into Ar–O_2 surface-wave microwave discharges, *Journal of Physics D: Applied Physics*, *43*(17), 175,201, doi:https://doi.org/10.1088/0022-3727/43/17/175201.

Laher, R. R., and F. R. Gilmore (1990), Updated excitation and ionization cross sections for electron impact on atomic oxygen, *Journal of Physical and Chemical Reference Data*, *19*(1), 277–305, doi:https://doi.org/10.1063/1.555872.

Lambert, J. D. (1972), Vibration-translation and vibration-rotation energy transfer in polyatomic molecules, *Journal of the Chemical Society, Faraday Transactions 2: Molecular and Chemical Physics*, *68*, 364–373, doi:https://doi.org/10.1039/F29726800364.

Laricchiuta, A., L. D. Pietanza, M. Capitelli, and G. Colonna (2018), Electron-CO excitation and ionization cross sections for plasma modeling, *Plasma Physics and Controlled Fusion*, *61*(1), 014,009, doi:https://doi.org/10.1088/1361-6587/aae16b.

LeClair, L. R., and J. W. McConkey (1994), On O(^{1}S) and CO($a^3\pi$) production from electron impact dissociation of CO_2, *Journal of Physics B: Atomic, Molecular and Optical Physics*, *27*(17), 4039–4055, doi:https://doi.org/10.1088/0953-4075/27/17/026.

Lee, S. M., Y. H. Lee, Y. G. Hwang, J. R. Hahn, and H. Kang (1999), Defect-induced oxidation of graphite, *Physical Review Letters*, *82*, 217–220, doi:https://doi.org/10.1103/PhysRevLett.82.217.

Levko, D., M. Pachuilo, and L. L. Raja (2017), Particle-in-cell modeling of streamer branching in CO_2 gas, *Journal of Physics D: Applied Physics*, *50*(35), 354,004, doi:https://doi.org/10.1088/1361-6463/aa7e6c.

Li, L., H. Zhang, X. Li, X. Kong, R. Xu, K. Tay, and X. Tu (2019), Plasma-assisted CO_2 conversion in a gliding arc discharge: Improving performance by optimizing the reactor design, *Journal of CO_2 Utilization*, *29*, 296 – 303, doi:https://doi.org/10.1016/j.jcou.2018.12.019.

Liang, Z., W. Evans, and P. Keblinski (2013), Equilibrium and nonequilibrium molecular dynamics simulations of thermal conductance at solid-gas interfaces, *Physical Review E*, *87*, 022,119, doi:https://doi.org/10.1103/PhysRevE.87.022119.

Lim, G.-I., S.-M. Lim, S. K. Kim, and Y. S. Choi (1999), Unexpectedly large $O^{37}ClO/O^{35}ClO$ intensity ratios of the fluorescence from the low-energy vibrational levels of OClO ($\tilde{A}^2$ A_2), *The Journal of Chemical Physics*, *111*(2), 456–459, doi:https://doi.org/10.1063/1.479325.

Lin, X., L. Z. Chen, J. P. Li, F. Li, and X. L. Yu (2018), Experimental and numerical study of carbon-dioxide dissociation for Mars atmospheric entry, *Journal of Thermophysics and Heat Transfer*, *32*(2), 503–513, doi:https://doi.org/10.2514/1.T5152.

Liu, J.-L., H.-W. Park, W.-J. Chung, and D.-W. Park (2016), High-efficient conversion of CO_2 in AC-pulsed tornado gliding arc plasma, *Plasma Chemistry and Plasma Processing*, *36*(2), 437–449, doi:https://doi.org/10.1007/s11090-015-9649-2.

Liu, Y., F. Rehman, and W. B. Zimmerman (2017), Reaction engineering of carbon monoxide generation by treatment with atmospheric pressure, low power CO_2 DBD plasma, *Fuel*, *209*, 117 – 126, doi:https://doi.org/10.1016/j.fuel.2017.07.097.

Liu, Y. S., R. A. McFarlane, and G. J. Wolga (1975), Measurement of vibrational–vibrational energy transfer probabilities in CO–CO collisions by a fast flow approximation, *The Journal of Chemical Physics*, *63*(1), 228–234, doi:https://doi.org/10.1063/1.431049.

Long, D. A. (2002), *The Raman Effect: A Unified Treatment of the Theory of Raman Scattering by Molecules*, Wiley Chichester, doi:https://doi.org/10.1002/0470845767.

Lopaev, D., and A. Smirnov (2004), Diagnostics of heterogeneous processes with the participation of radicals by time-resolved actinometry, *Plasma physics reports*, *30*(10), 882–893, doi:https://doi.org/10.1134/1.1809405.

Lopaev, D. V., E. M. Malykhin, and S. M. Zyryanov (2010a), Surface recombination of oxygen atoms in O_2 plasma at increased pressure: I. The recombination probability and phenomenological model of surface processes, *Journal of Physics D: Applied Physics*, *44*(1), 015,201, doi:https://doi.org/10.1088/0022-3727/44/1/015201.

Lopaev, D. V., E. M. Malykhin, and S. M. Zyryanov (2010b), Surface recombination of oxygen atoms in O_2 plasma at increased pressure: II. Vibrational temperature and surface production of ozone, *Journal of Physics D: Applied Physics*, *44*(1), 015,202, doi:https://doi.org/10.1088/0022-3727/44/1/015202.

Lopez-Puertas, M., F. W. Taylor, et al. (2001), *Non-LTE radiative transfer in the atmosphere*, vol. 3, World Scientific, doi:https://doi.org/10.1142/4650.

Lottigier, P., A. Jucha, L. Cabaret, C. Blondel, P. Drag, CLottigier, A. Jucha, L. Cabaret, C. Blondel, and C. Drag (2019), Single-mode scannable nanosecond Ti:sapphire laser for high resolution Two-photon Absorption Laser Induced Fluorescence (TALIF), *Applied Physics B*, *125*(1), 14, doi:https://doi.org/10.1007/s00340-018-7124-5.

Lowke, J. J., A. V. Phelps, and B. W. Irwin (1973), Predicted electron transport coefficients and operating characteristics of CO_2–N_2–He laser mixtures, *Journal of Applied Physics*, *44*(10), 4664–4671, doi:https://doi.org/10.1063/1.1662017.

López-Puertas, M., M. A. López-Valverde, C. P. Rinsland, and M. R. Gunson (1992), Analysis of the upper atmosphere $CO_2(\nu_2)$ vibrational temperatures retrieved from ATMOS/Spacelab 3 observations, *Journal of Geophysical Research: Atmospheres*, *97*(D18), 20,469–20,478, doi:https://doi.org/10.1029/92JD02026.

Mack, J. A., K. Mikulecky, and A. M. Wodtke (1996), Resonant vibration–vibration energy transfer between highly vibrationally excited O_2 ($X^3\Sigma_g^-$,ν=15-26) and CO_2, N_2O, N_2 and O_3, *The Journal of Chemical Physics*, *105*(10), 4105–4116, doi:https://doi.org/10.1063/1.472259.

Macko, P., G. Cunge, and N. Sadeghi (2001), Density of $N_2(X^1\Sigma_g^+; \nu = 18)$ molecules in a DC glow discharge measured by cavity ring-down spectroscopy at 227 nm; validity domain of the technique, *Journal of Physics D: Applied Physics*, *34*(12), 1807–1811, doi:https://doi.org/10.1088/0022-3727/34/12/307.

Macko, P., P. Veis, and G. Cernogora (2004), Study of oxygen atom recombination on a Pyrex surface at different wall temperatures by means of time-resolved actinometry in a double pulse discharge technique, *Plasma Sources Science and Technology*, *13*(2), 251–262, doi:https://doi.org/10.1088/0963-0252/13/2/009.

Magne, L., H. Coitout, G. Cernogora, and G. Gousset (1993), Atomic oxygen recombination at the wall in a time afterglow, *Journal de Physique III*, *3*(9), 1871–1889.

Mahata, S., and S. K. Bhattacharya (2009), Anomalous enrichment of O^{17} and C^{13} in photodissociation products of CO_2: Possible role of nuclear spin, *The Journal of Chemical Physics*, *130*(23), 234,312, doi:https://doi.org/10.1063/1.3153845.

Makino, A., T. Namikiri, and K. Kimura (2003), Combustion rates of graphite rods in the forward stagnation field with high-temperature airflow, *Combustion and Flame*, *132*(4), 743 – 753, doi:https://doi.org/10.1016/S0010-2180(02)00537-0.

Margottin-Maclou, M., L. Doyennette, and L. Henry (1971), Relaxation of vibrational energy in CO, HCl, CO_2, and N_2O, *Applied Optics*, *10*(8), 1768–1780, doi:https://doi.org/10.1364/AO.10.001768.

Marieu, V., P. Reynier, L. Marraffa, D. Vennemann, F. D. Filippis, and S. Caristia (2007), Evaluation of SCIROCCO plasma wind-tunnel capabilities for entry simulations in CO_2 atmospheres, *Acta Astronautica*, *61*(7), 604 – 616, doi:https://doi.org/10.1016/j.actaastro.2006.12.006.

Marinov, D. (2012), Reactive adsorption of molecules and radicals on surfaces under plasma exposure, Ph.D. thesis, Ecole Polytechnique.

Marinov, D., O. Guaitella, J.-P. Booth, and A. Rousseau (2012a), Direct observation of ozone formation on SiO_2 surfaces in O_2 discharges, *Journal of Physics D: Applied Physics*, *46*(3), 032,001, doi:https://doi.org/10.1088/0022-3727/46/3/032001.

Marinov, D., D. Lopatik, O. Guaitella, M. Hübner, Y. Ionikh, J. Röpcke, and A. Rousseau (2012b), Surface vibrational relaxation of N_2 studied by CO_2 titration with time-resolved quantum cascade laser absorption spectroscopy, *Journal of Physics D: Applied Physics*, *45*(17), 175,201, doi:https://doi.org/10.1088/0022-3727/45/17/175201.

Marinov, D., V. Guerra, O. Guaitella, J.-P. Booth, and A. Rousseau (2013a), Ozone kinetics in low-pressure discharges: vibrationally excited ozone and molecule formation on surfaces, *Plasma Sources Science and Technology*, *22*(5), 055,018, doi:https://doi.org/10.1088/0963-0252/22/5/055018.

Marinov, D., D. Lopatik, O. Guaitella, Y. Ionikh, J. Röpcke, and A. Rousseau (2013b), Surface deactivation of vibrationally excited N_2 studied using infrared titration combined with quantum cascade laser absorption spectroscopy, *Journal of Physics D: Applied Physics*, *47*(1), 015,203, doi:https://doi.org/10.1088/0022-3727/47/1/015203.

Marinov, D., O. Guaitella, T. de los Arcos, A. von Keudell, and A. Rousseau (2014), Adsorption and reactivity of nitrogen atoms on silica surface under plasma exposure, *Journal of Physics D: Applied Physics*, *47*(47), 475,204, doi:https://doi.org/10.1088/0022-3727/47/47/475204.

Marinov, D., C. Drag, C. Blondel, O. Guaitella, J. Golda, B. Klarenaar, R. Engeln, V. S. von der Gathen, and J.-P. Booth (2016), Pressure broadening of atomic oxygen two-photon absorption laser induced fluorescence, *Plasma Sources Science and Technology*, *25*(6), 06LT03, doi:https://doi.org/10.1088/0963-0252/25/6/06lt03.

Marinov, D., J.-P. Booth, C. Drag, and C. Blondel (2017a), Measurement of the isotope shift of the $2p^4\ ^3P_2 \rightarrow 2p^3 3p\ ^3P_2$ two-photon transition of O I and a revision of the triplet energy levels of atomic oxygen, *Journal of Physics B: Atomic, Molecular and Optical Physics*, *50*(6), 065,003, doi:https://doi.org/10.1088/1361-6455/aa5a88.

Marinov, D., C. Teixeira, and V. Guerra (2017b), Deterministic and Monte Carlo methods for simulation of plasma-surface interactions, *Plasma Processes and Polymers*, *14*(1-2), 1600,175, doi:https://doi.org/10.1002/ppap.201600175.

Marsh, H., E. O'hair, R. Reed, and W. Wynne-Jones (1963), Reaction of atomic oxygen with carbon, *Nature*, *198*(4886), 1195–1196, doi:https://doi.org/10.1038/1981195a0.

Martini, L. M., N. Gatti, G. Dilecce, M. Scotoni, and P. Tosi (2017), Laser induced fluorescence in nanosecond repetitively pulsed discharges for CO_2 conversion, *Plasma Physics and Controlled Fusion*, *60*(1), 014,016, doi:https://doi.org/10.1088/1361-6587/aa8bed.

Martini, L. M., S. Lovascio, G. Dilecce, and P. Tosi (2018), Time-resolved CO_2 dissociation in a nanosecond pulsed discharge, *Plasma Chemistry and Plasma Processing*, *38*(4), 707–718, doi:https://doi.org/10.1007/s11090-018-9893-3.

Mebel, A. M., M. Hayashi, V. V. Kislov, and S. H. Lin (2004), Theoretical study of oxygen isotope exchange and quenching in the $O(^1D)+CO_2$ reaction, *The Journal of Physical Chemistry A*, *108*(39), 7983–7994, doi:https://doi.org/10.1021/jp049315h.

Médard, N., J.-C. Soutif, and F. Poncin-Epaillard (2002), Characterization of CO_2 plasma-treated polyethylene surface bearing carboxylic groups, *Surface and Coatings Technology*, *160*(2), 197 – 205, doi:https://doi.org/10.1016/S0257-8972(02)00407-3.

Mehio, N., S. Dai, and D.-e. Jiang (2014), Quantum mechanical basis for kinetic diameters of small gaseous molecules, *The Journal of Physical Chemistry A*, *118*(6), 1150–1154, doi:https://doi.org/10.1021/jp412588f.

Mei, D., X. Zhu, C. Wu, B. Ashford, P. T. Williams, and X. Tu (2016), Plasma-photocatalytic conversion of CO_2 at low temperatures: Understanding the synergistic effect of plasma-catalysis, *Applied Catalysis B: Environmental*, *182*, 525 – 532, doi:https://doi.org/10.1016/j.apcatb.2015.09.052.

Misewich, J., C. N. Plum, G. Blyholder, P. L. Houston, and R. P. Merrill (1983), Vibrational relaxation during gas–surface collisions, *The Journal of Chemical Physics*, *78*(6), 4245–4249, doi:https://doi.org/10.1063/1.445101.

Misewich, J., P. L. Houston, and R. P. Merrill (1985), Vibrational relaxation of carbon dioxide (101) and carbon monoxide (ν=2) during gas–surface collisions, *The Journal of Chemical Physics*, *82*(3), 1577–1584, doi:https://doi.org/10.1063/1.448433.

Moore, C. B., R. E. Wood, B. Hu, and J. T. Yardley (1967), Vibrational energy transfer in CO_2 lasers, *The Journal of Chemical Physics*, *46*(11), 4222–4231, doi:https://doi.org/10.1063/1.1840527.

Mori, S., H. Akatsuka, and M. Suzuki (2001), Carbon and oxygen isotope separation by plasma chemical reactions in carbon monoxide glow discharge, *Journal of Nuclear Science and Technology*, *38*(10), 850–858, doi:https://doi.org/10.1080/18811248.2001.9715105.

Mori, S., H. Akatsuka, and M. Suzuki (2002), Numerical analysis of carbon isotope separation by plasma chemical reactions in carbon monoxide glow discharge, *Journal of Nuclear Science and Technology*, *39*(6), 637–646, doi:https://doi.org/10.1080/18811248.2002.9715244.

Morillo-Candas, A. S., C. Drag, J.-P. Booth, T. C. Dias, V. Guerra, and O. Guaitella (2019), Oxygen atom kinetics in CO_2 plasmas ignited in a DC glow discharge, *Plasma Sources Science and Technology*, *28*(7), 075,010, doi:https://doi.org/10.1088/1361-6595/ab2b84.

Morillo-Candas, A. S., T. Silva, B. L. M. Klarenaar, M. Grofulović, V. Guerra, and O. Guaitella (2020), Electron impact dissociation of CO_2, *Plasma Sources Science and Technology*, *29*(1), 01LT01, doi:https://doi.org/10.1088/1361-6595/ab6075.

Moss, M. S., K. Yanallah, R. W. K. Allen, and F. Pontiga (2017), An investigation of CO_2 splitting using nanosecond pulsed corona discharge: effect of argon addition on CO_2 conversion and energy efficiency, *Plasma Sources Science and Technology*, *26*(3), 035,009, doi:https://doi.org/10.1088/1361-6595/aa5b1d.

Muiño, R. D., and H. F. Busnengo (2013), *Dynamics of gas-surface interactions*, vol. 50, Springer, doi:https://doi.org/10.1007/978-3-642-32955-5.

Mumma, M. J., E. J. Stone, and E. C. Zipf (1975), Nonthermal rotational distribution of $CO(A^1\pi)$ fragments produced by dissociative excitation of CO_2 by electron impact, *Journal of Geophysical Research (1896-1977)*, *80*(1), 161–167, doi:https://doi.org/10.1029/JA080i001p00161.

Nick, K.-P., and V. Helbig (1984), Argon branching ratios and absolute transition probabilities in the 4s–4p transition array, *Physica Scripta*, *T8*, 100–103, doi:https://doi.org/10.1088/0031-8949/1984/t8/016.

Niemi, K., V. S. von der Gathen, and H. F. Döbele (2001), Absolute calibration of atomic density measurements by laser-induced fluorescence spectroscopy with two-photon excitation, *Journal of Physics D: Applied Physics*, *34*(15), 2330–2335, doi:https://doi.org/10.1088/0022-3727/34/15/312.

Niemi, K., V. S. von der Gathen, and H. F. Döbele (2005), Absolute atomic oxygen density measurements by two-photon absorption laser-induced fluorescence spectroscopy in an RF-excited atmospheric pressure plasma jet, *Plasma Sources Science and Technology*, *14*(2), 375–386, doi:https://doi.org/10.1143/jjap.30.289710.1088/0963-0252/14/2/021.

Nighan, W. L. (1969), Effect of molecular dissociation and vibrational excitation on electron energy transfer in CO_2 laser plasmas, *Applied Physics Letters*, *15*(11), 355–357, doi:https://doi.org/10.1063/1.1652857.

Nikitin, E. (1964), Theory of non-adiabatic vibrational relaxation in atom-molecular collisions, *Molecular Physics*, *7*(4), 389–396, doi:https://doi.org/10.1080/00268976300101151.

Nourbakhsh, A., M. Cantoro, T. Vosch, G. Pourtois, F. Clemente, M. H. van der Veen, J. Hofkens, M. M. Heyns, S. D. Gendt, and B. F. Sels (2010), Bandgap opening in oxygen plasma-treated graphene, *Nanotechnology*, *21*(43), 435,203, doi:https://doi.org/10.1088/0957-4484/21/43/435203.

Nunnally, T., K. Gutsol, A. Rabinovich, A. Fridman, A. Gutsol, and A. Kemoun (2011), Dissociation of CO_2 in a low current gliding arc plasmatron, *Journal of Physics D: Applied Physics*, *44*(27), 274,009, doi:https://doi.org/10.1088/0022-3727/44/27/274009.

Pagnon, D., J. Amorim, J. Nahorny, M. Touzeau, and M. Vialle (1995), On the use of actinometry to measure the dissociation in O_2 DC glow discharges: determination of the wall recombination probability, *Journal of Physics D: Applied Physics*, *28*(9), 1856–1868, doi:https://doi.org/10.1088/0022-3727/28/9/014.

Pandey, A., and S. K. Bhattacharya (2006), Anomalous oxygen isotope enrichment in CO_2 produced from O+CO: Estimates based on experimental results and model predictions, *The Journal of Chemical Physics*, *124*(23), 234,301, doi:https://doi.org/10.1063/1.2206584.

Patel, C. K. N. (1965), Cw laser on vibrational-rotational transitions of CO, *Applied Physics Letters*, *7*(9), 246–247, doi:https://doi.org/10.1063/1.1754400.

Paterna, D., R. Monti, R. Savino, and A. Esposito (2002), Experimental and numerical investigation of Martian atmosphere entry, *Journal of Spacecraft and Rockets*, *39*(2), 227–236, doi:https://doi.org/10.2514/2.3804.

Pattabiraman, P., N. Rodriguez, B. Jang, and R. Baker (1990), A study of the interaction of atomic oxygen with various carbonaceous materials, *Carbon*, *28*(6), 867 – 878, doi:https://doi.org/10.1016/0008-6223(90)90335-V.

Pejaković, D. A., J. Marschall, L. Duan, and M. P. Martin (2008), Nitric oxide production from surface recombination of oxygen and nitrogen atoms, *Journal of Thermophysics and Heat Transfer*, *22*(2), 178–186, doi:https://doi.org/10.2514/1.33073.

Perathoner, S., and G. Centi (2014), CO_2 recycling: A key strategy to introduce green energy in the chemical production chain, *ChemSusChem*, *7*(5), 1274–1282, doi:https://doi.org/10.1002/cssc.201300926.

Pérez-Mendoza, M., M. Domingo-García, and F. López-Garzón (1999), Modifications produced by O_2 and CO_2 plasma treatments on a glassy carbon: comparison with molecular gases, *Carbon*, *37*(9), 1463 – 1474, doi:https://doi.org/10.1016/S0008-6223(99)00009-3.

Perri, M. J., A. L. Van Wyngarden, J. J. Lin, Y. T. Lee, and K. A. Boering (2004), Energy dependence of oxygen isotope exchange and quenching in the $O(^1D)+CO_2$ reaction: A crossed molecular beam study, *The Journal of Physical Chemistry A*, *108*(39), 7995–8001, doi:https://doi.org/10.1021/jp0485845.

Phelps, A. (1985), Tabulations of collision cross sections and calculated transport and reaction coefficients for electron collisions with O_2, *JILA information center Report. Univ. Colorado*, *28*.

Pietanza, L., G. Colonna, G. D'Ammando, A. Laricchiuta, and M. Capitelli (2016a), Non equilibrium vibrational assisted dissociation and ionization mechanisms in cold CO_2 plasmas, *Chemical Physics*, *468*, 44 – 52, doi:https://doi.org/10.1016/j.chemphys.2016.01.007.

Pietanza, L., G. Colonna, V. Laporta, R. Celiberto, G. D'Ammando, A. Laricchiuta, and M. Capitelli (2016b), Influence of electron molecule resonant vibrational collisions over the symmetric mode and direct excitation-dissociation cross sections of CO_2 on the electron energy distribution function and dissociation mechanisms in cold pure CO_2 plasmas, *The Journal of Physical Chemistry A*, *120*(17), 2614–2628, doi:https://doi.org/10.1021/acs.jpca.6b01154.

Pietanza, L. D., G. Colonna, G. D'Ammando, and M. Capitelli (2016c), Time-dependent coupling of electron energy distribution function, vibrational kinetics of the asymmetric mode of CO_2 and dissociation, ionization and electronic excitation kinetics under discharge and post-discharge conditions, *Plasma Physics and Controlled Fusion*, *59*(1), 014,035, doi:https://doi.org/10.1088/0741-3335/59/1/014035.

Pietanza, L. D., G. Colonna, G. D'Ammando, A. Laricchiuta, and M. Capitelli (2016d), Electron energy distribution functions and fractional power transfer in "cold" and excited CO_2 discharge and post discharge conditions, *Physics of Plasmas*, *23*(1), 013,515, doi:https://doi.org/10.1063/1.4940782.

Pietanza, L. D., G. Colonna, and M. Capitelli (2017), Non-equilibrium plasma kinetics of reacting CO: an improved state to state approach, *Plasma Sources Science and Technology*, *26*(12), 125,007, doi:https://doi.org/10.1088/1361-6595/aa93bd.

Pintassilgo, C. D., V. Guerra, O. Guaitella, and A. Rousseau (2014), Study of gas heating mechanisms in millisecond pulsed discharges and afterglows in air at low pressures, *Plasma Sources Science and Technology*, *23*(2), 025,006, doi:https://doi.org/10.1088/0963-0252/23/2/025006.

Plönjes, E., P. Palm, W. Lee, M. D. Chidley, I. V. Adamovich, W. R. Lempert, and J. Rich (2000), Vibrational energy storage in high pressure mixtures of diatomic molecules, *Chemical Physics*, *260*(3), 353 – 366, doi:https://doi.org/10.1016/S0301-0104(00)00257-3.

Ploenjes, E., I. Adamovich, V. Subramaniam, and J. Rich (1998), Isotope separation in optically pumped thomson discharges, in *36th AIAA Aerospace Sciences Meeting and Exhibit*, doi:https://doi.org/10.2514/6.1998-993.

Polak, L., and D. Slovetsky (1976), Electron impact induced electronic excitation and molecular dissociation, *International Journal for Radiation Physics and Chemistry*, *8*(1), 257 – 282, doi:https://doi.org/10.1016/0020-7055(76)90070-X.

Pollock, D. S., G. B. I. Scott, and L. F. Phillips (1993), Rate constant for quenching of $CO_2(010)$ by atomic oxygen, *Geophysical Research Letters*, *20*(8), 727–729, doi:https://doi.org/10.1029/93GL01016.

Ponduri, S., M. M. Becker, S. Welzel, M. C. M. van de Sanden, D. Loffhagen, and R. Engeln (2016), Fluid modelling of CO_2 dissociation in a dielectric barrier discharge, *Journal of Applied Physics*, *119*(9), 093,301, doi:https://doi.org/10.1063/1.4941530.

Popov, N. A. (2001), Investigation of the mechanism for rapid heating of nitrogen and air in gas discharges, *Plasma Physics Reports*, *27*(10), 886–896, doi:https://doi.org/10.1134/1.1409722.

Powell, H. T. (1973), Vibrational relaxation of carbon monoxide using a pulsed discharge, *The Journal of Chemical Physics*, *59*(9), 4937–4941, doi:https://doi.org/10.1063/1.1680709.

Premathilake, D., R. A. Outlaw, R. A. Quinlan, and C. E. Byvik (2019), Oxygen generation by carbon dioxide glow discharge and separation by permeation through ultrathin silver membranes, *Earth and Space Science*, *6*(4), 557–564, doi:https://doi.org/10.1029/2018EA000521.

Puech, V., and L. Torchin (1986), Collision cross sections and electron swarm parameters in argon, *Journal of Physics D: Applied Physics*, *19*(12), 2309–2323, doi:https://doi.org/10.1088/0022-3727/19/12/011.

Puliyalil, H., D. Lašič Jurković, V. D. B. C. Dasireddy, and B. Likozar (2018), A review of plasma-assisted catalytic conversion of gaseous carbon dioxide and methane into value-added platform chemicals and fuels, *RSC Adv.*, *8*, 27,481–27,508, doi:https://doi.org/10.1039/C8RA03146K.

Qin, Y., G. Niu, X. Wang, D. Luo, and Y. Duan (2018), Status of CO_2 conversion using microwave plasma, *Journal of CO_2 Utilization*, *28*, 283 – 291, doi:https://doi.org/10.1016/j.jcou.2018.10.003.

Raizer, Y. P. (1991), *Gas discharge physics*, Springer.

Ramakers, M., I. Michielsen, R. Aerts, V. Meynen, and A. Bogaerts (2015), Effect of argon or helium on the CO_2 conversion in a dielectric barrier discharge, *Plasma Processes and Polymers*, *12*(8), 755–763, doi:https://doi.org/10.1002/ppap.201400213.

Ramakers, M., G. Trenchev, S. Heijkers, W. Wang, and A. Bogaerts (2017), Gliding arc plasmatron: Providing an alternative method for carbon dioxide conversion, *ChemSusChem*, *10*(12), 2642–2652, doi:https://doi.org/10.1002/cssc.201700589.

Ramos, S., G. Vasconcelos, E. Antunes, A. Lobo, V. Trava-Airoldi, and E. Corat (2010), Wettability control on vertically-aligned multi-walled carbon nanotube surfaces with oxygen pulsed DC plasma and CO_2 laser treatments, *Diamond and Related Materials*, *19*(7), 752 – 755, doi:https://doi.org/10.1016/j.diamond.2010.01.044.

Raper, O. F., and W. B. DeMore (1964), Reaction of $O(^1D)$ with CO, *The Journal of Chemical Physics*, *40*(4), 1053–1057, doi:https://doi.org/10.1063/1.1725247.

Ray, D., R. Saha, and S. Ch. (2017), DBD plasma assisted CO_2 decomposition: Influence of diluent gases, *Catalysts*, *7*(9), doi:https://doi.org/10.3390/catal7090244.

Rich, J. W., and R. C. Bergman (1986), *Isotope Separation by Vibration-Vibration Pumping*, pp. 271–293, Springer Berlin Heidelberg, Berlin, Heidelberg, doi:https://doi.org/10.1007/978-3-642-48615-9_9.

Rivallan, M., S. Aiello, and F. Thibault-Starzyk (2010), Microsecond time-resolved Fourier transform infrared analytics in a low pressure glow discharge reactor, *Review of Scientific Instruments*, *81*(10), 103,111, doi:https://doi.org/10.1063/1.3492094.

Romanini, D., A. Kachanov, N. Sadeghi, and F. Stoeckel (1997), Cw cavity ring down spectroscopy, *Chemical Physics Letters*, *264*(3), 316 – 322, doi:https://doi.org/10.1016/S0009-2614(96)01351-6.

Rothman, L., I. Gordon, R. Barber, H. Dothe, R. Gamache, A. Goldman, et al. (2010), HITEMP, the high-temperature molecular spectroscopic database, *Journal of Quantitative Spectroscopy and Radiative Transfer*, *111*(15), 2139 – 2150, doi:https://doi.org/10.1016/j.jqsrt.2010.05.001.

Röpcke, J., P. B. Davies, N. Lang, A. Rousseau, and S. Welzel (2012), Applications of quantum cascade lasers in plasma diagnostics: a review, *Journal of Physics D: Applied Physics*, *45*(42), 423,001, doi:https://doi.org/10.1088/0022-3727/45/42/423001.

Rusanov, V., A. Fridman, and G. Sholin (1979), Population of vibrationally excited states of diatomic molecules in a nonequilibrium plasma in the diffusion approximation, *Soviet Physics Technical Physics*, *24*, 554–561.

Rusanov, V. D., A. A. Fridman, and G. V. Sholin (1981), The physics of a chemically active plasma with nonequilibrium vibrational excitation of molecules, *Soviet Physics Uspekhi*, *24*(6), 447–474, doi:https://doi.org/10.1070/pu1981v024n06abeh004884.

Sabadil, H., and S. Pfau (1985), Measurements of the degree of dissociation in oxygen DC discharges: Comparison of the ozone method with the Wrede-Harteck method, *Plasma chemistry and plasma processing*, *5*(1), 67–79, doi:https://doi.org/10.1007/BF00567910.

Sadeghi, N., D. W. Setser, A. Francis, U. Czarnetzki, and H. F. Döbele (2001), Quenching rate constants for reactions of $Ar(4p'[1/2]_0$, $4p[1/2]_0$, $4p[3/2]_2$, and $4p[5/2]_2)$ atoms with 22 reagent gases, *The Journal of Chemical Physics*, *115*(7), 3144–3154, doi:https://doi.org/10.1063/1.1388037.

Sahai, A., B. Lopez, C. O. Johnston, and M. Panesi (2017), Adaptive coarse graining method for energy transfer and dissociation kinetics of polyatomic species, *The Journal of Chemical Physics*, *147*(5), 054,107, doi:https://doi.org/10.1063/1.4996654.

Saidia, L., A. Belasri, S. Baadj, and Z. Harrache (2019), Physico-chemical investigation of pulsed discharge in CO_2/O_2 gas mixture, *Plasma Physics Reports*, *45*(5), 501–516, doi:https://doi.org/10.1134/S1063780X1905009X.

Saloman, E. B. (2004), Energy levels and observed spectral lines of xenon, Xe I though Xe LIV, *Journal of Physical and Chemical Reference Data*, *33*(3), 765–921, doi:https://doi.org/10.1063/1.1649348.

Savinov, S. Y., H. Lee, H. K. Song, and B.-K. Na (2002), The decomposition of CO_2 in glow discharge, *Korean Journal of Chemical Engineering*, *19*(4), 564–566, doi:https://doi.org/10.1007/BF02699296.

Saxon, R. P., and J. Eichler (1986), Theoretical calculation of two-photon absorption cross sections in atomic oxygen, *Physical Review A*, *34*, 199–206, doi:https://doi.org/10.1143/jjap.30.289710.1103/PhysRevA.34.199.

Scapinello, M., L. M. Martini, G. Dilecce, and P. Tosi (2016), Conversion of CH4 /CO_2 by a nanosecond repetitively pulsed discharge, *Journal of Physics D: Applied Physics*, *49*(7), 075,602, doi:https://doi.org/10.1088/0022-3727/49/7/075602.

Scarduelli, G., G. Guella, D. Ascenzi, and P. Tosi (2011), Synthesis of liquid organic compounds from CH_4 and CO_2 in a dielectric barrier discharge operating at atmospheric pressure, *Plasma Processes and Polymers*, *8*(1), 25–31, doi:https://doi.org/10.1002/ppap.201000044.

Schulman, M. B., F. A. Sharpton, S. Chung, C. C. Lin, and L. W. Anderson (1985), Emission from oxygen atoms produced by electron-impact dissociative excitation of oxygen molecules, *Physical Review A*, *32*, 2100–2116, doi:https://doi.org/10.1103/PhysRevA.32.2100.

Schwartz, R. N., Z. I. Slawsky, and K. F. Herzfeld (1952), Calculation of vibrational relaxation times in gases, *The Journal of Chemical Physics*, *20*(10), 1591–1599, doi:https://doi.org/10.1063/1.1700221.

Schweitzer, C., and R. Schmidt (2003), Physical mechanisms of generation and deactivation of singlet oxygen, *Chemical Reviews*, *103*(5), 1685–1758, doi:https://doi.org/10.1021/cr010371d.

Seeber, K. N. (1971), Radiative and collisional transitions between coupled vibrational modes of CO_2, *The Journal of Chemical Physics*, *55*(10), 5077–5081, doi:https://doi.org/10.1063/1.1675625.

Sepka, S., Y.-K. Chen, J. Marschall, and R. A. Copeland (2000), Experimental investigation of surface reactions in carbon monoxide and oxygen mixtures, *Journal of Thermophysics and Heat Transfer*, *14*(1), 45–52, doi:https://doi.org/10.2514/2.6488.

Sharma, R. D., and C. A. Brau (1969), Energy transfer in near-resonant molecular collisions due to long-range forces with application to transfer of vibrational energy from ν_3 mode of CO_2 to N_2, *The Journal of Chemical Physics*, *50*(2), 924–930, doi:https://doi.org/10.1063/1.1671145.

Sharma, R. D., and P. P. Wintersteiner (1990), Role of carbon dioxide in cooling planetary thermospheres, *Geophysical Research Letters*, *17*(12), 2201–2204, doi:https://doi.org/10.1029/GL017i012p02201.

Shields, F. D., C. C. Warf, and H. E. Bass (1973), Acoustical method of obtaining vibrational transition rates tested on CO_2/N_2 mixtures, *The Journal of Chemical Physics*, *58*(9), 3837–3840, doi:https://doi.org/10.1063/1.1679737.

Shimizu, M. (1968), The recombination mechanism of CO and O in the upper atmospheres of Venus and Mars, *Icarus*, *9*(1), 593 – 597, doi:https://doi.org/10.1016/0019-1035(68)90051-1.

Shved, G., L. Khvorostovskaya, I. Y. Potekhin, A. Demyanikov, A. Kutepov, and V. Fomichev (1991), Measurement of the rate constant or $CO_2(01^10)$ deactivation by atomic oxygen and the significance of its value for the energetics and emission of the lower thermosphere, *Izv. Akad. Nauk SSSR, Fiz. Atmos. Okeana*, *27*(4), 431–437.

Siemsen, K., J. Reid, and C. Dang (1980), New techniques for determining vibrational temperatures, dissociation, and gain limitations in cw-CO_2 lasers, *IEEE Journal of Quantum Electronics*, *16*(6), 668–676, doi:https://doi.org/10.1109/JQE.1980.1070536.

Silva, T., and V. Guerra (2020), *In preparation.*

Silva, T., N. Britun, T. Godfroid, and R. Snyders (2014), Optical characterization of a microwave pulsed discharge used for dissociation of CO_2, *Plasma Sources Science and Technology*, *23*(2), 025,009, doi:https://doi.org/10.1088/0963-0252/23/2/025009.

Silva, T., M. Grofulović, B. L. M. Klarenaar, A. S. Morillo-Candas, O. Guaitella, R. Engeln, C. D. Pintassilgo, and V. Guerra (2018), Kinetic study of low-temperature CO_2 plasmas under non-equilibrium conditions. I. Relaxation of vibrational energy, *Plasma Sources Science and Technology*, *27*(1), 015,019, doi:https://doi.org/10.1088/1361-6595/aaa56a.

Skrzypkowski, M. P., T. Gougousi, R. Johnsen, and M. F. Golde (1998), Measurement of the absolute yield of $CO(a^3\pi)$+O products in the dissociative recombination of CO_2^+ ions with electrons, *The Journal of Chemical Physics*, *108*(20), 8400–8407, doi:https://doi.org/10.1063/1.476267.

Slanger, T. G., and G. Black (1974), Electronic-to-vibrational energy transfer efficiency in the $O(^1D)$-N_2 and $O(^1D)$-CO systems, *The Journal of Chemical Physics*, *60*(2), 468–477, doi:https://doi.org/10.1063/1.1681064.

Slanger, T. G., B. D. Sharpee, D. A. Pejaković, D. L. Huestis, M. A. Bautista, R. L. Gattinger, E. J. Llewellyn, I. C. McDade, D. E. Siskind, and K. R. Minschwaner (2011), Atomic oxygen emission intensity ratio: Observation and theory, *Eos, Transactions American Geophysical Union*, *92*(35), 291–292, doi:https://doi.org/10.1029/2011EO350005.

Slovetsky, D. I. (1980), *Chemical reactions mechanisms in nonequilibrium plasmas*, Nauka, Moscow (in russian).

Snoeckx, R., and A. Bogaerts (2017), Plasma technology – a novel solution for CO_2 conversion?, *Chem. Soc. Rev.*, *46*, 5805–5863, doi:https://doi.org/10.1039/C6CS00066E.

Spencer, L. F., and A. D. Gallimore (2011), Efficiency of CO_2 dissociation in a radio-frequency discharge, *Plasma Chemistry and Plasma Processing*, *31*(1), 79–89, doi:https://doi.org/10.1007/s11090-010-9273-0.

Spiridonov, M. V., S. McKenna-Lawlor, and S. Y. Savinov (1994), Diagnostics of the active medium of a waveguide CO_2 laser: Vibrational distributions and plasma-chemical processes, *Journal of Quantitative Spectroscopy and Radiative Transfer*, *52*(5), 621 – 630, doi:https://doi.org/10.1016/0022-4073(94)90028-0.

Stancu, G. D., F. Kaddouri, D. A. Lacoste, and C. O. Laux (2010), Atmospheric pressure plasma diagnostics by OES, CRDS and TALIF, *Journal of Physics D: Applied Physics*, *43*(12), 124,002, doi:https://doi.org/10.1088/0022-3727/43/12/124002.

Stocker, T., D. Qin, G. Plattner, M. Tignor, S. Allen, J. Boschung, A. Nauels, Y. Xia, V. Bex, and P. M. Midgley (2013), Climate change 2013: The Physical Science Basis. Contribution of Working Group I to the Fifth Assessment Report of the Intergovernmental Panel on Climate Change (IPCC).

Studt, F., M. Behrens, E. L. Kunkes, N. Thomas, S. Zander, A. Tarasov, J. Schumann, E. Frei, J. B. Varley, F. Abild-Pedersen, J. K. Nørskov, and R. Schlögl (2015), The mechanism of CO and CO_2 hydrogenation to methanol over Cu-based catalysts, *ChemCatChem*, *7*(7), 1105–1111, doi:https://doi.org/10.1002/cctc.201500123.

Sun, S., H. Wang, D. Mei, X. Tu, and A. Bogaerts (2017), CO_2 conversion in a gliding arc plasma: Performance improvement based on chemical reaction modeling, *Journal of CO_2 Utilization*, *17*, 220 – 234, doi:https://doi.org/10.1016/j.jcou.2016.12.009.

Sun, T., S. Fabris, and S. Baroni (2011), Surface precursors and reaction mechanisms for the thermal reduction of graphene basal surfaces oxidized by atomic oxygen, *The Journal of Physical Chemistry C*, *115*(11), 4730–4737, doi:https://doi.org/10.1021/jp111372k.

Tan, X., and D. B. Go (2019), Rational design of plasma-enhanced catalysis at microscale dimensions for the dissociation of CO_2, *Journal of Electrostatics*, *97*, 71 – 74, doi:https://doi.org/10.1016/j.elstat.2018.12.003.

Taylan, O., and H. Berberoglu (2014), Dissociation of carbon dioxide using a microhollow cathode discharge plasma reactor: effects of applied voltage, flow rate and concentration, *Plasma Sources Science and Technology*, *24*(1), 015,006, doi:https://doi.org/10.1088/0963-0252/24/1/015006.

Taylor, R. L., and S. Bitterman (1969), Survey of vibrational relaxation data for processes important in the CO_2-N_2 laser system, *Rev. Mod. Phys.*, *41*, 26–47, doi:https://doi.org/10.1103/RevModPhys.41.26.

Tejero-del Caz, A., V. Guerra, D. Gonçalves, M. Lino da Silva, L. Marques, N. Pinhão, C. D. Pintassilgo, and L. L. Alves (2019), The LisbOn KInetics boltzmann solver, *Plasma Sources Science and Technology*, *28*(4), 043,001, doi:https://doi.org/10.1088/1361-6595/ab0537.

Terraz, L., T. Silva, A. S. Morillo-Candas, O. Guaitella, A. T. del Caz, L. L. Alves, and V. Guerra (2019), Influence of N_2 on the CO_2 vibrational distribution function and dissociation yield in non-equilibrium plasmas, *Journal of Physics D: Applied Physics*, *53*(9), 094,002, doi:https://doi.org/10.1088/1361-6463/ab55fb.

Toebaert, D., P. Muys, and E. Desoppere (1995), Spatially resolved measurement of the vibrational temperatures of the plasma in a DC-excited fast-axial-flow CO_2 laser, *IEEE Journal of Quantum Electronics*, *31*(10), 1774–1778, doi:https://doi.org/10.1109/3.466051.

Treanor, C. E., J. W. Rich, and R. G. Rehm (1968), Vibrational relaxation of anharmonic oscillators with exchange-dominated collisions, *The Journal of Chemical Physics*, *48*(4), 1798–1807, doi:https://doi.org/10.1063/1.1668914.

Tsutsumi, T., A. Greb, A. R. Gibson, M. Hori, D. O'Connell, and T. Gans (2017), Investigation of the radially resolved oxygen dissociation degree and local mean electron energy in oxygen plasmas in contact with different surface materials, *Journal of Applied Physics*, *121*(14), 143,301, doi:https://doi.org/10.1063/1.4979855.

Urbanietz, T., M. Böke, V. S. von der Gathen, and A. von Keudell (2018), Non-equilibrium excitation of CO_2 in an atmospheric pressure helium plasma jet, *Journal of Physics D: Applied Physics*, *51*(34), 345,202, doi:https://doi.org/10.1088/1361-6463/aad4d3.

Uytdenhouwen, Y., S. Van Alphen, I. Michielsen, V. Meynen, P. Cool, and A. Bogaerts (2018), A packed-bed DBD micro plasma reactor for CO_2 dissociation: Does size matter?, *Chemical Engineering Journal*, *348*, 557 – 568, doi:https://doi.org/10.1016/j.cej.2018.04.210.

Vacher, D., M. L. da Silva, P. André, G. Faure, and M. Dudeck (2008), Radiation from an equilibrium CO_2–N_2 plasma in the [250–850 nm] spectral region: I. Experiment, *Plasma Sources Science and Technology*, *17*(3), 035,012, doi:https://doi.org/10.1088/0963-0252/17/3/035012.

van den Bekerom, D. C. M., J. M. P. Linares, E. M. van Veldhuizen, S. Nijdam, M. C. M. van de Sanden, and G. J. van Rooij (2018), How the alternating degeneracy in rotational Raman spectra of CO_2 and C_2H_2 reveals the vibrational temperature, *Applied Optics*, *57*(20), 5694–5702, doi:https://doi.org/10.1364/AO.57.005694.

van den Bekerom, D. C. M., J. M. P. Linares, T. Verreycken, E. M. van Veldhuizen, S. Nijdam, G. Berden, W. A. Bongers, M. C. M. van de Sanden, and G. J. van Rooij (2019), The importance of thermal dissociation in CO_2 microwave discharges investigated by power pulsing and rotational Raman scattering, *Plasma Sources Science and Technology*, *28*(5), 055,015, doi:https://doi.org/10.1088/1361-6595/aaf519.

van Rooij, G. J., H. N. Akse, W. A. Bongers, and M. C. M. van de Sanden (2017), Plasma for electrification of chemical industry: a case study on CO_2 reduction, *Plasma Physics and Controlled Fusion*, *60*(1), 014,019, doi:https://doi.org/10.1088/1361-6587/aa8f7d.

Vargas, J., B. Lopez, and M. Lino da Silva (2019), Heavy impact dissociation of carbon dioxide. *Poster presented in 63rd Course Cold Plasmas: Fundamentals and Applications, Erice 2019.*

Vermeiren, V., and A. Bogaerts (2019), Improving the energy efficiency of CO_2 conversion in nonequilibrium plasmas through pulsing, *The Journal of Physical Chemistry C*, *123*(29), 17,650–17,665, doi:https://doi.org/10.1021/acs.jpcc.9b02362.

Vesel, A., M. Mozetic, A. Drenik, and M. Balat-Pichelin (2011), Dissociation of CO_2 molecules in microwave plasma, *Chemical Physics*, *382*(1), 127 – 131, doi:https://doi.org/10.1016/j.chemphys.2011.03.015.

Viegas, P., M. C. M. van de Sanden, S. Longo, and P. Diomede (2019), Validation of the Fokker–Planck approach to vibrational kinetics in CO_2 plasma, *The Journal of Physical Chemistry C*, *123*(37), 22,823–22,831, doi:https://doi.org/10.1021/acs.jpcc.9b06576.

Vikis, A. (1978), Carbon-13 isotope enrichment in the photolysis of CO with the 123.58 nm Kr resonance radiation, *Chemical Physics Letters*, *53*(3), 565 – 567, doi:https://doi.org/10.1016/0009-2614(78)80070-0.

Wachman, H. Y. (1962), The thermal accommodation coefficient: A critical survey, *ARS Journal*, *32*(1), 2–12, doi:https://doi.org/10.2514/8.5939.

Wang, W., D. Mei, X. Tu, and A. Bogaerts (2017), Gliding arc plasma for CO_2 conversion: Better insights by a combined experimental and modelling approach, *Chemical Engineering Journal*, *330*, 11 – 25, doi:https://doi.org/10.1016/j.cej.2017.07.133.

Welzel, S., F. Hempel, M. Hübner, N. Lang, P. B. Davies, and J. Röpcke (2010), Quantum cascade laser absorption spectroscopy as a plasma diagnostic tool: An overview, *Sensors*, *10*(7), 6861–6900, doi:https://doi.org/10.3390/s100706861.

Wen, J., and M. H. Thiemens (1993), Multi-isotope study of the $O(^1D)+CO_2$ exchange and stratospheric consequences, *Journal of Geophysical Research: Atmospheres*, *98*(D7), 12,801–12,808, doi:https://doi.org/10.1029/93JD00565.

Wickramanayaka, S., N. Hosokawa, and Y. Hatanaka (1991), Variation of the recombination coefficient of atomic oxygen on pyrex glass with applied RF power, *Japanese Journal of Applied Physics*, *30*(Part 1, No. 11A), 2897–2900, doi:https://doi.org/10.1143/jjap.30.2897.

Wiegand, W. J., M. C. Fowler, and J. A. Benda (1970), Carbon monoxide formation in CO_2 lasers, *Applied Physics Letters*, *16*(6), 237–239, doi:https://doi.org/10.1063/1.1653177.

Witteman, W. J. (2013), *The CO_2 laser*, vol. 53, Springer, doi:https://doi.org/10.1007/978-3-540-47744-0.

Wong, C., R. T. Yang, and B. L. Halpern (1983), The mode of attack of oxygen atoms on the basal plane of graphite, *The Journal of Chemical Physics*, *78*(6), 3325–3328, doi:https://doi.org/10.1063/1.445198.

Wu, D., R. A. Outlaw, and R. L. Ash (1996), Extraction of oxygen from CO_2 using glow-discharge and permeation techniques, *Journal of Vacuum Science & Technology A*, *14*(2), 408–414, doi:https://doi.org/10.1116/1.580098.

Wyckoff, S., and J. Theobald (1989), Molecular ions in comets, *Advances in Space Research*, *9*(3), 157 – 161, doi:https://doi.org/10.1016/0273-1177(89)90255-X.

Xiaowei, L., R. Jean-Charles, and Y. Suyuan (2004), Effect of temperature on graphite oxidation behavior, *Nuclear Engineering and Design*, *227*(3), 273 – 280, doi:https://doi.org/10.1016/j.nucengdes.2003.11.004.

Xu, L. T., R. L. Jaffe, D. W. Schwenke, and M. Panesi (2017a), The effect of the spin-forbidden $CO(^1\Sigma^+)+O(^3P) \rightarrow CO_2(^1\Sigma_g^+)$ recombination reaction on afterbody heating of Mars entry vehicles, in *47th AIAA Thermophysics Conference*, doi:https://doi.org/10.2514/6.2017-3486.

Xu, S., J. C. Whitehead, and P. A. Martin (2017b), CO_2 conversion in a non-thermal, barium titanate packed bed plasma reactor: The effect of dilution by Ar and N_2, *Chemical Engineering Journal*, *327*, 764 – 773, doi:https://doi.org/10.1016/j.cej.2017.06.090.

Xu, S., P. I. Khalaf, P. A. Martin, and J. C. Whitehead (2018), CO_2 dissociation in a packed-bed plasma reactor: effects of operating conditions, *Plasma Sources Science and Technology*, *27*(7), 075,009, doi:https://doi.org/10.1088/1361-6595/aacd6a.

Yalin, A. P., R. N. Zare, C. O. Laux, and C. H. Kruger (2002), Temporally resolved cavity ringdown spectroscopy in a pulsed nitrogen plasma, *Applied Physics Letters*, *81*(8), 1408–1410, doi:https://doi.org/10.1063/1.1500427.

Yamazaki, H., and R. J. Cvetanovic (1964), Isotopic exchange of the excited oxygen atoms with CO_2^{18} and their collisional deactivation, *The Journal of Chemical Physics*, *40*(2), 582–585, doi:https://doi.org/10.1063/1.1725160.

Yaney, P. P., and J. W. Parish (1999), Studies of surface deactivation of vibrationally-excited homonuclear molecules in gaseous discharge media using Coherent Anti-Stokes Raman Spectroscopy (CARS), *Dayton University OH*.

Yang, G., L. Yao, X. Zhang, Q. Meng, and K.-L. Han (2005), Theoretical study of the mechanism for spin-forbidden quenching process $O(^1D)+CO_2(^1\Sigma) \rightarrow O(^3P)+CO_2(^1\Sigma)$, *International Journal of Quantum Chemistry*, *105*(2), 154–159, doi:https://doi.org/10.1002/qua.20672.

Yang, R., D. Zhang, K. Zhu, H. Zhou, X. Ye, A. W. Kleyn, Y. Hu, and Q. Huang (2018), *In situ* study of the conversion reaction of CO_2 and CO_2-H_2 mixtures in radio frequency discharge plasma, *Acta Physico-Chimica Sinica*, *35*(3), 292–298, doi:https://doi.org/10.3866/PKU.WHXB201803121.

Yap, D., J.-M. Tatibouët, and C. Batiot-Dupeyrat (2015), Carbon dioxide dissociation to carbon monoxide by non-thermal plasma, *Journal of CO2 Utilization*, *12*, 54 – 61, doi:https://doi.org/10.1016/j.jcou.2015.07.002.

Yeung, L. Y., M. Okumura, J. T. Paci, G. C. Schatz, J. Zhang, and T. K. Minton (2009), Hyperthermal O-atom exchange reaction O_2+CO_2 through a CO_4 intermediate, *Journal of the American Chemical Society*, *131*(39), 13,940–13,942, doi:https://doi.org/10.1021/ja903944k.

Yeung, L. Y., M. Okumura, J. Zhang, T. K. Minton, J. T. Paci, A. Karton, J. M. L. Martin, J. P. Camden, and G. C. Schatz (2012), $O(^3P)+CO_2$ collisions at hyperthermal energies: Dynamics of nonreactive scattering, oxygen isotope exchange, and oxygen-atom abstraction, *The Journal of Physical Chemistry A*, *116*(1), 64–84, doi:https://doi.org/10.1021/jp2080379.

Young, R. A., and G. Black (1967), Deactivation of $O(^1D)$, *The Journal of Chemical Physics*, *47*(7), 2311–2318, doi:https://doi.org/10.1063/1.1703312.

Yung, Y. L., W. B. DeMore, and J. P. Pinto (1991), Isotopic exchange between carbon dioxide and ozone via $O(^1D)$ in the stratosphere, *Geophysical Research Letters*, *18*(1), 13–16, doi:https://doi.org/10.1029/90GL02478.

Zangwill, A. (1988), *Physics at surfaces*, Cambridge university press, doi:https://doi.org/10.1017/CBO9780511622564.

Zasavitskii, I. I., R. S. Islamov, M. A. Kerimkulov, Y. B. Konev, V. N. Ochkin, S. Y. Savinov, N. N. Sobolev, M. V. Spiridonov, and A. P. Shotov (1990), Kinetics of formation of the CO_2 molecule distributions over the vibrational-rotational levels in the active medium of a waveguide CO_2 laser, *Journal of Soviet Laser Research*, *11*(4), 361–375, doi:https://doi.org/10.1007/BF01120633.

Zhang, K., G. Zhang, X. Liu, A. N. Phan, and K. Luo (2017), A study on CO_2 decomposition to CO and O_2 by the combination of catalysis and dielectric-barrier discharges at low temperatures and ambient pressure, *Industrial & Engineering Chemistry Research*, *56*(12), 3204–3216, doi:https://doi.org/10.1021/acs.iecr.6b04570.

Zhang, L.-M., Z.-C. Tan, S.-D. Wang, and D.-Y. Wu (1997), Combustion calorimetric and thermogravimetric studies of graphite and coals doped with a coal-burning additive, *Thermochimica Acta*, *299*(1), 13 – 17, doi:https://doi.org/10.1016/S0040-6031(97)00130-5, 14th IUPAC Conference on Chemical Thermodynamics.

Zhu, L., T. G. Kreutz, S. A. Hewitt, and G. W. Flynn (1990), Diode laser probing of vibrational, rotational, and translational excitation of CO_2 following collisions with $O(^1D)$. I. Inelastic scattering, *The Journal of Chemical Physics*, *93*(5), 3277–3288, doi:https://doi.org/10.1063/1.458861.

Zipf, E. C. (1969), The collisional deactivation of metastable atoms and molecules in the upper atmosphere, *Canadian Journal of Chemistry*, *47*(10), 1863–1870, doi:https://doi.org/10.1139/v69-305.

université PARIS-SACLAY

ECOLE DOCTORALE N°572:
ONDES ET MATIERES (EDOM)

Titre: Étude des mécanismes fondamentaux des plasmas de CO_2

Mots clés: CO_2 plasma, recyclage de CO_2, plasma froid, interaction plasma-surface, excitation vibrationnelle, excitation électronique.

Résumé: Le recyclage du CO_2 est un enjeu environnemental, sociétal et économique majeur. Parmi toutes les technologies envisagées pour convertir le CO_2, les plasmas froids ont l'avantage de transférer une grande partie de l'énergie électrique dans l'excitation vibrationnelle du CO_2. Cela peut permettre d'augmenter l'efficacité de conversion tout en minimisant le coût énergétique en induisant un milieu hors-équilibre permettant de dépasser les limites thermodynamiques des méthodes traditionnelles. Toutefois les plasmas de CO_2 sont encore trop mal compris pour optimiser ces procédés. De nombreux processus de base ne sont pas bien décrits et le manque de connaissances sur les interactions des molécules de CO_2 excitées avec d'autres espèces empêchent leur développement. Cette thèse présente une étude fondamentale des principaux mécanismes contrôlant la dynamique des plasmas de CO_2. Des sources plasma DC et RF homogènes et reproductibles ont été étudiées à l'aide de diagnostiques optiques de pointe pour comprendre les mécanismes d'excitation, de dissociation et de recombinaison du CO_2. Les résultats expérimentaux ont été comparés avec des codes de simulation des plasmas de CO_2. L'interaction du plasma avec des surfaces a également été étudiées ouvrant la voie à l'utilisation de catalyseurs pour améliorer l'efficacité du plasma.

Title: Investigation of fundamental mechanisms of CO_2 plasmas

Keywords : CO_2 plasma, CO_2 recycling, cold plasma, plasma-surface interactions, vibrational excitation, electronic excitation.

Abstract: CO_2 recycling is a major environmental, societal and economic issue. Among all the technologies considered to convert CO_2, cold plasmas have the advantage of transferring a large part of the electrical energy into the vibrational excitation of CO_2, inducing a non-equilibrium medium that can help to overcome the limitations of the traditional thermodynamic methods, increasing the efficiency while minimizing energy costs. However, CO_2 plasmas are still poorly understood. Many basic processes are not well described and the lack of knowledge on the interactions of excited CO_2 molecules with other species prevents technological developments. This thesis presents a fundamental study of the main mechanisms controlling the dynamics of CO_2 plasmas. Homogeneous and reproducible DC and RF plasma sources were studied using advanced optical diagnostics to understand CO_2 excitation and dissociation processes. The experimental results were compared, when possible, with CO_2 plasma simulation codes. The interaction of plasma with surfaces was also studied, paving the way for the use of catalysts to improve efficiency of CO_2 recycling by plasma.

Université Paris-Saclay
Espace Technologique / Immeuble Discovery
Route de l'Orme aux Merisiers RD 128 / 91190 Saint-Aubin, France